

Copyright
by
Justin Lockheart Burt
2007

The Dissertation Committee for Justin Lockheart Burt Certifies that this is the approved version of the following dissertation:

Formation of Noble Metal Nanocrystals in the Presence of Biomolecules

Committee:

Miguel Jose Yacaman, Supervisor

Benny D. Freeman

Brian A. Korgel

Keith J. Stevenson

Thomas M. Truskett

Formation of Noble Metal Nanocrystals in the Presence of Biomolecules

by

Justin Lockheart Burt, B.S.Ch.E., M.S.E.

Dissertation

Presented to the Faculty of the Graduate School of

The University of Texas at Austin

in Partial Fulfillment

of the Requirements

for the Degree of

Doctor of Philosophy

The University of Texas at Austin

May 2007

Dedication

To Erika and our daughter, Bernadette Genevieve

To my parents, Diana and Gary

To all who labor in the pursuit of truth

Ad Majorem Dei Gloriam

Acknowledgements

Gloria in excelsis Deo. I thank God for the gift of life. I thank Him for the gift of a rational soul, by means of which we perceive the manifestation of His glory in this world. Through contemplation of that which has been created, may we be brought to contemplation of the Creator.

Et in terra pax hominibus bonæ voluntatis. I express my love and gratitude to my family for their unconditional love and unwavering support. I thank my beloved wife, Erika, who graciously deigned to share her life with me. I thank her for giving the greatest gift any person could ever receive, our firstborn child, Bernadette Genevieve.

I thank all those who have helped me arrive at this point in my academic career. Before all others, I must acknowledge my first and best teachers, my parents. I thank Dr. Hsueh-Chia Chang and Dr. Pavlo Takhistov for giving me my first exposure to academic research at the University of Notre Dame. I am grateful to Jose Berbel for introducing me to industrial research, and for his friendship. I express my gratitude to my research advisor at The University of Texas at Austin, Dr. Miguel Jose Yacaman, for granting me the intellectual freedom to pursue truly original ideas. I thank the members of the Yacaman research group for their insight, support, and friendship.

I acknowledge all who contributed to my development in the science and art of transmission electron microscopy, especially Dr. J.P. Zhou, Dr. Mario Miki Yoshida, and

Dr. Jose Reyes Gasga. I thank Dr. Rozamond Y. Sweeney for her invaluable help in studying the interaction of protein-functionalized gold nanocrystals with bacteria. I am grateful to Dr. Javier Guerra for his generous assistance in studying the catalytic activity of protein-functionalized platinum nanocrystals. I express my gratitude to Dr. Humberto Lara, Dr. Jose Luis Elechiguerra, and Jose Ruben Morones for our collaboration in studying the interaction of protein-functionalized silver nanocrystals with HIV.

I express my profound thanks to the National Science Foundation for generously supporting my academic pursuits through the Graduate Research Fellowship program. Finally, I am grateful to The University of Texas at Austin College of Engineering for their generous support through the Thrust 2000 Robert L. and Jane G. Mitchell Endowed Graduate Fellowship in Engineering, and the George J. Heuer, Jr. Ph.D. Endowed Graduate Fellowship.

Formation of Noble Metal Nanocrystals in the Presence of Biomolecules

Publication No. _____

Justin Lockheart Burt, Ph.D.

The University of Texas at Austin, 2007

Supervisor: Miguel Jose Yacaman

One of the most promising, yet least studied routes for producing biocompatible nanostructures involves synthesis in the presence of biomolecules. I hypothesized that globular proteins could provide a suitable framework to regulate the formation of noble metal nanocrystals. As proof of concept, I designed two novel synthesis protocols utilizing bovine serum albumin (BSA) protein to regulate the formation of gold nanocrystals. In the first case, the standard protocol for polyol reduction was modified by replacing ethylene glycol with glycerin, replacing synthetic polymers with BSA as protecting agent, and decreasing the reaction temperature. In the second case, the Brust-Schiffrin two-phase reduction was modified by replacing alkylthiols with BSA as protecting agent, which facilitated a strictly aqueous phase synthesis.

Due to superior product yield and rapid reduction at room temperature, the aqueous protocol became the foundation for subsequent studies. I extended this approach to produce well-dispersed ~2nm silver, gold, and platinum nanocrystals. Having demonstrated the feasibility of BSA-functionalized nanocrystals, some potential uses were explored. BSA-functionalized silver nanocrystals were employed in a broader study

on the interaction of silver nanocrystals with HIV. BSA-functionalized gold nanocrystals were utilized for *in vivo* dosage of a contrast enhancing agent to bacteria. BSA-functionalized platinum nanocrystals were studied as hydrogenation catalysts.

Since many intriguing uses for protein-functionalized nanocrystals involve incorporation into biosystems, I sought to enhance biocompatibility by using ascorbic acid as reducing agent. Initial experiments revealed elongated and branched nanocrystals. Such structures were not observed in previous synthesis protocols with BSA, so I hypothesized ascorbic acid was driving their formation. To test my assertion, I reduced ionic gold in an aqueous solution of ascorbic acid, thereby discovering a new method for producing multiply-branched gold nanocrystals.

Two conditions were necessary to achieve multiply-branched structures: rapid kinetics, and strongly acidic pH. By exploiting ascorbic acid complexation with BSA to moderate reaction kinetics, and using sodium hydroxide to provide basic pH, the two conditions for branching were negated, and well-dispersed ~2.5nm gold nanocrystals were obtained. This protocol represents a novel, environmentally benign approach to producing biocompatible nanocrystals, relying on proteins, ascorbic acid, sodium hydroxide, and water, all at ambient temperature.

Table of Contents

List of Tables	xiv
List of Figures.....	xv
Chapter 1: Introduction.....	1
1.1 Properties of Noble Metal Nanocrystals.....	4
1.1.1 Surface to Volume Ratio.....	5
1.1.2 Fluctuating Morphology and High Surface Activity	6
1.1.3 Quantum Size Effects	7
1.1.4 Proper Size for Interaction with Biological Systems.....	11
1.2 Synthesis of Noble Metal Nanocrystals via Colloidal Reduction.....	13
1.3 Bioconjugation of Noble Metal Nanocrystals.....	17
1.3.1 Conventional Nanocrystal Bioconjugation Techniques.....	17
1.3.2 Formation of Nanocrystals Directly in the Presence of Biomolecules	18
1.4 Properties of Serum Albumin Protein.....	20
1.5 On the High Angle Annular Dark Field Technique.....	22
1.6 Dissertation Overview	24
Chapter 2: Polyol Synthesis of Protein-Stabilized Gold Nanocrystals.....	27
2.1 Introduction.....	27
2.2 Experimental Procedure.....	29
2.3 Results and Discussion	31
2.3.1 Reduction of Ionic Gold in the Absence of Surface-Protecting Molecules.....	31
2.3.2 Formation of Gold Nanocrystals in the Presence of BSA at 65°C	37
2.3.3 Formation of Gold Nanocrystals in the Presence of BSA at 95°C	56
2.4 Conclusions.....	68

Chapter 3: Aqueous Synthesis of Protein-Stabilized Gold Nanocrystals via Chemical Reduction with Sodium Borohydride	70
3.1 Introduction.....	70
3.2 Experimental Procedure.....	71
3.3 Results and Discussion	73
3.3.1 Determination of the Optimal Sequence and Rate of Addition	73
3.3.2 Formation of Gold Nanocrystals Directly Functionalized by BSA Protein.....	82
3.4 Conclusions.....	93
Chapter 4: Aqueous Synthesis of Protein-Stabilized Silver, Gold, and Platinum Nanocrystals via Chemical Reduction with Sodium Borohydride	94
4.1 Introduction.....	94
4.2 Experimental Procedure.....	95
4.3 Results and Discussion	98
4.3.1 On the Selection of Reaction Conditions.....	98
4.3.2 Formation of Silver Nanocrystals Directly Functionalized by BSA Protein.....	99
4.3.3 Formation of Gold Nanocrystals Directly Functionalized by BSA Protein.....	112
4.3.4 Formation of Platinum Nanocrystals Directly Functionalized by BSA Protein.....	127
4.3.5 Comparison of Silver, Gold, and Platinum Nanocrystals Formed in the Presence of BSA Protein Molecules	140
4.4 Conclusions.....	143
Chapter 5: Interactions of Serum Albumin-Functionalized Noble Metal Nanocrystals with External Systems.....	144
5.1 Serum Albumin-Functionalized Silver Nanocrystals as Antivirals: Interaction with HIV	145
5.1.1 Introduction.....	145
5.1.2 Experimental Procedure.....	145
5.1.3 Results and Discussion	148
5.1.4 Conclusions.....	158

5.2 Serum Albumin-Functionalized Gold Nanocrystals: Toward In Vivo Dosage of Contrast-Enhancing Agents for the Imaging of Microorganisms	159
5.2.1 Introduction.....	159
5.2.2 Experimental Procedure.....	160
5.2.3 Results and Discussion	162
5.2.4 Conclusions.....	168
5.3 Serum Albumin-Functionalized Platinum Nanocrystals as Hydrogenation Catalysts.....	169
5.3.1 Introduction.....	169
5.3.2 Experimental Procedure.....	171
5.3.3 Results and Discussion	172
5.3.4 Conclusions.....	187
Chapter 6: Aqueous Synthesis of Gold Nanocrystals via Reduction with Ascorbic Acid: From Aggregation to Diffusion-Driven Growth via Addition of Bovine Serum Albumin.....	188
6.1 Introduction.....	188
6.2 Experimental Procedure.....	189
6.3 Results and Discussion	191
6.3.1 Preliminary Considerations – the Significance of Excess Ascorbic Acid.....	191
6.3.2 Synthesis of Gold Nanocrystals in the Presence of BSA via Reduction with Ascorbic Acid.....	199
6.3.3 TEM Analysis of the Gold Nanocrystals Obtained from Reduction with Ascorbic Acid in the Presence of BSA.....	208
6.4 Conclusions.....	226
Chapter 7: Aqueous Synthesis of Star Polyhedral Gold Nanocrystals via Reduction with Ascorbic Acid	228
7.1 Introduction.....	228
7.2 Experimental Procedure.....	232
7.3 Results and Discussion	234
7.3.1 Product Overview	234
7.3.2 Proposed Structural Models.....	238

7.3.3	Structural Analysis of Multiple-Twinned Star Polyhedra	239
7.3.4	Structural Analysis of Monocrystalline Star Polyhedra.....	244
7.3.5	Merits of the Synthesis Approach.....	246
7.3.6	Preferential Growth of {111} Surfaces.....	247
7.3.7	Characteristic Structural Defects	248
7.3.8	Absorption Spectroscopy	249
7.3.9	Structural Stability of Star Polyhedral Gold Nanocrystals	251
7.3.10	On the Relative Significance of Reaction Kinetics and Solution pH	255
7.3.11	On the Formation and Stability of Super-Stellated Gold Nanocrystals.....	258
7.3.12	On the Initial Rate of Nucleation and Growth.....	264
7.3.13	Proposed Model for Growth of Star Polyhedral Gold Nanocrystals	269
7.4	Conclusions.....	271
Chapter 8: Aqueous Synthesis of Gold Nanocrystals via Reduction with Ascorbic Acid: Controlled Growth in the Presence of Bovine Serum Albumin.....		
8.1	Introduction.....	273
8.2	Experimental Procedure.....	274
8.3	Results and Discussion	276
8.3.1	Synthesis of Gold Nanocrystals via Addition of Chloroauric Acid to a Pre-Existing Aqueous Solution of Ascorbic Acid and BSA..	276
8.3.2	Synthesis of Gold Nanocrystals via Addition of Chloroauric Acid to a Pre-Existing Aqueous Solution of Ascorbic Acid, BSA, and Sodium Hydroxide.....	291
8.3.3	Synthesis of Gold Nanocrystals via Addition of Chloroauric Acid to a Pre-Existing Aqueous Solution of Ascorbic Acid and BSA, with Subsequent Addition of Sodium Hydroxide	305
8.4	Conclusions.....	312
Chapter 9: Conclusions and Recommendations		
9.1	Conclusions.....	314
9.1.1	Polyol Synthesis of Protein-Stabilized Gold Nanocrystals.....	314

9.1.2 Aqueous Synthesis of Protein-Stabilized Silver, Gold, and Platinum Nanocrystals via Chemical Reduction with Sodium Borohydride .	314
9.1.3 Serum Albumin-Functionalized Silver Nanocrystals as Antivirals: Interaction with HIV	315
9.1.4 Serum Albumin-Functionalized Gold Nanocrystals: Toward In Vivo Dosage of Contrast-Enhancing Agents for the Imaging of Microorganisms	316
9.1.5 Serum Albumin-Functionalized Platinum Nanocrystals as Catalysts for the Aqueous Phase Hydrogenation of Allyl Alcohol	316
9.1.6 Synthesis of Star Polyhedral Gold Nanocrystals via Reduction with Ascorbic Acid	317
9.1.7 Synthesis of Gold Nanocrystals via Reduction with Ascorbic Acid: Controlled Growth in Basic Reaction Media and in the Presence of Bovine Serum Albumin	318
9.2 Recommendations	319
9.2.1 Aqueous Synthesis of Protein-Stabilized Noble Metal Nanocrystals	319
9.2.2 Serum Albumin-Functionalized Silver Nanocrystals as Antivirals	320
9.2.3 Serum Albumin-Functionalized Nanocrystals as Heterogeneous Catalysts	321
9.2.4 Star Polyhedral Gold Nanocrystals	321
Bibliography	323

Vita 333

List of Tables

Table 2.1: Reaction conditions for the various systems tested.	30
Table 3.1: Reaction conditions for the various systems tested.	72
Table 3.2: Theoretical and experimentally-obtained S: Au Ratios.	82
Table 4.1: Reaction conditions for the various systems tested – silver.	96
Table 4.2: Reaction conditions for the various systems tested – gold.	96
Table 4.3: Reaction conditions for the various systems tested – platinum.	97
Table 4.4: Theoretical and experimentally-obtained S: Ag Ratios.	105
Table 4.5: Theoretical and experimentally-obtained S: Au Ratios.	118
Table 4.6: Theoretical and experimentally-obtained S: Pt Ratios.	131
Table 5.1: Activity of BSA-Functionalized Platinum Nanocrystals for the Catalytic Hydrogenation of Allyl Alcohol	179
Table 6.1: Reaction conditions for the various systems tested.	190
Table 6.2: Preliminary ratios of ascorbic acid to gold.	192
Table 8.1: Protein amounts for the various systems tested.	275

List of Figures

Figure 1.1: The Lycurgus Cup. (British Museum)	2
Figure 1.2: The Rose Window. (Cathedral of Notre Dame, Paris).....	3
Figure 1.3: Surface to volume ratio versus total number of atoms in a close-packed cubic crystal.	6
Figure 1.4: STEM images of the E2E3 subcomplex of the <i>Escherichia coli</i> PDH complex, obtained by Frey and Frey.....	12
Figure 1.5: Protein-functionalized gold nanocrystals targeting various regions of intact HepG2 cells, as reported by Feldheim and colleagues.	13
Figure 1.6: Free energy of formation versus embryo radius.....	15
Figure 1.7: Tertiary structure of human serum albumin (PDB1BJ5), a structural analogue to BSA	21
Figure 2.1: Reaction at 65°C in absence of BSA.....	33
Figure 2.2: Reaction at 65°C in absence of BSA – high resolution HAADF images.	35
Figure 2.3: Reaction at 65°C in absence of BSA – conventional TEM images.	36
Figure 2.4: Reaction time at 65°C as a function of BSA concentration.....	37
Figure 2.5: Color and clarity of each system studied at 65°C.	39
Figure 2.6: (6:1) Au:BSA at 65°C.....	40
Figure 2.7: (12:1) Au:BSA at 65°C.....	42
Figure 2.8: (12:1) Au:BSA at 65°C – conventional TEM analysis.	43
Figure 2.9: (24:1) Au:BSA at 65°C – nanometric crystals.....	45
Figure 2.10: (24:1) Au:BSA at 65°C – HAAADF images of large crystals.....	47
Figure 2.11: Growth model for an FCC-type platelet resulting from planar twinning....	49
Figure 2.12: Model of five perfect tetrahedra joined at a common axis.....	50
Figure 2.13: (96:1) Au:BSA at 65°C – nanometric crystals.....	52
Figure 2.14: (96:1) Au:BSA at 65°C – HRTEM images.....	53
Figure 2.15: (96:1) Au:BSA at 65°C – large crystals resulting from cyclic twinning. ...	54
Figure 2.16: (96:1) Au:BSA at 65°C – large crystals resulting from planar twinning. ...	55
Figure 2.17: (12:1) Au:BSA at 95°C – nanometric crystals.....	58
Figure 2.18: (12:1) Au:BSA at 95°C – large crystals.....	59
Figure 2.19: (24:1) Au:BSA at 95°C – nanometric crystals.....	60
Figure 2.20: (24:1) Au:BSA at 95°C – large crystals.....	61
Figure 2.21: Electron microscopy of a gold triangular platelet oriented on edge.	63
Figure 2.22: (96:1) Au:BSA at 95°C – nanometric crystals.....	64
Figure 2.23: (96:1) Au:BSA at 95°C – large crystals.....	65
Figure 2.24: (96:1) Au:BSA at 95°C – HRTEM of crystals with parallel twin planes. ...	66
Figure 2.25: (96:1) Au:BSA at 95°C – HRTEM images of elongated crystals.....	67
Figure 3.1: Dropwise addition of sodium borohydride.....	75
Figure 3.2: Rapid addition of chloroauric acid to a pre-existing aqueous solution of BSA and sodium borohydride..	77
Figure 3.3: Rapid addition of chloroauric acid to a pre-existing aqueous solution of BSA and sodium borohydride – HAADF images of gold aggregates.....	78
Figure 3.4: Rapid addition of sodium borohydride to a pre-existing solution of BSA and chloroauric acid.....	79

Figure 3.5: Representative EDS spectrum of the protein-functionalized nanocrystals. . .	83
Figure 3.6: HRTEM images of BSA-functionalized nanocrystals.	84
Figure 3.7: HAADF images of BSA films at (7:1) Au:BSA and (28:1) Au:BSA molar ratios, demonstrating the effective protection of the crystals by BSA.	85
Figure 3.8: Size distributions of BSA-functionalized gold nanocrystals, each based on the measurement of 500 nanocrystals.	86
Figure 3.9: Tertiary structure of human serum albumin (PDB1BJ5), a structural analogue to BSA.	87
Figure 3.10: Infrared spectra.	89
Figure 3.11: Raman spectra.	91
Figure 3.12: UV-visible absorption spectra.	92
Figure 4.1: (24:1) Ag:BSA.	100
Figure 4.2: (24:1) Ag:BSA – HRTEM images.	102
Figure 4.3: EDS spectra of protein-functionalized silver nanocrystals.	104
Figure 4.4: UV-visible absorption spectra of the various silver systems.	106
Figure 4.5: HAADF comparison of silver nanocrystal size distributions.	107
Figure 4.6: (96:1) Ag:BSA.	108
Figure 4.7: (96:1) Ag:BSA – TEM images of larger nanocrystals with high densities of twins and stacking faults.	109
Figure 4.8: (96:1) Ag:BSA – representative images of a larger elongated crystal with length in excess of 100 nm.	111
Figure 4.9: (24:1) Au:BSA.	113
Figure 4.10: (24:1) Au:BSA – Conventional TEM analysis.	114
Figure 4.11: (24:1) Au:BSA – HRTEM images.	115
Figure 4.12: EDS spectra of the protein-functionalized gold nanocrystals.	117
Figure 4.13: UV-visible absorption spectra of the various gold systems.	119
Figure 4.14: HAADF comparison of gold nanocrystal size distributions.	121
Figure 4.15: (96:1) Au:BSA.	122
Figure 4.16: (96:1) Au:BSA – HRTEM of FCC single crystals.	123
Figure 4.17: (96:1) Au:BSA – HRTEM of multiple-twinned crystals with fivefold symmetry.	124
Figure 4.18: (96:1) Au:BSA – HRTEM of crystals with parallel twinning structural defects.	125
Figure 4.19: (24:1) Pt:BSA.	127
Figure 4.20: (24:1) Pt:BSA – HRTEM images.	129
Figure 4.21: EDS spectra of the protein-functionalized platinum nanocrystals.	130
Figure 4.22: HAADF images of platinum-rich protein aggregates.	132
Figure 4.23: UV-visible absorption spectra of the various platinum systems.	133
Figure 4.24: HRTEM analysis of single-twinned crystals observed at (48:1) Pt:BSA.	134
Figure 4.25: HAADF analysis of a large platinum aggregate in the (96:1) Pt:BSA system.	135
Figure 4.26: (96:1) Pt:BSA.	136
Figure 4.27: (96:1) Pt:BSA – HRTEM of elongated crystals – aspect ratios <2.	137
Figure 4.28: (96:1) Pt:BSA – HRTEM of elongated crystals – aspect ratios >2.	138
Figure 5.1: Interaction of Silver Nanocrystals with HIV-1.	152

Figure 5.2: Inhibition of HIV-1 by silver nanocrystals.	155
Figure 5.3: Toxicity of silver nanocrystals against MT-2 cells, determined by Trypan Blue exclusion assay.	156
Figure 5.4: HAADF images of gold-functionalized <i>Pseudomonas aeruginosa</i>	163
Figure 5.5: Growth kinetics for <i>Pseudomonas aeruginosa</i> in an as-synthesized solution of BSA-functionalized gold nanocrystals.	165
Figure 5.6: HAADF images of <i>Pseudomonas aeruginosa</i> after 24 hours incubation at 30°C.	167
Figure 5.7: $(1/r)$ vs $(1/[Cat])$ for (24:1) Pt:BSA nanocrystals.	174
Figure 5.8: (r) vs $([Cat])$ for (24:1) Pt:BSA nanocrystals.	175
Figure 5.9: Turnover frequency vs stirring rate for (24:1) Pt:BSA crystals (110 μM).	176
Figure 5.10: Turnover frequency vs stirring rate for platinum crystals at (48 μM).	177
Figure 5.11: HAADF analysis of (24:1) Pt:BSA (48 μM) after 3 hours of reaction.	181
Figure 5.12: HAADF analysis of (24:1) Pt:BSA (48 μM) after 24 hours of reaction. ...	182
Figure 5.13: (96:1) Pt:BSA (48 μM) after 3 hours of reaction.	183
Figure 5.14: (96:1) Pt:BSA (48 μM) after 24 hours of reaction.	185
Figure 5.15: HAADF analysis of (24:1) Pt:BSA (110 μM) after 3 hours of reaction. ..	186
Figure 6.1: (24:1) Au:BSA at (4:1) AA:Au.	193
Figure 6.2: (24:1) Au:BSA at (16:1) AA:Au.	195
Figure 6.3: (24:1) Au:BSA at (32:1) AA:Au – polycrystalline aggregates with dimensions in the range of 40–50 nm.	196
Figure 6.4: (12:1) Au:BSA at (16:1) AA:Au – TEM images.	197
Figure 6.5: (12:1) Au:BSA at (32:1) AA:Au – TEM images.	199
Figure 6.6: Reaction time as a function of BSA concentration for each system studied at a molar ratio of (40:1) AA:Au.	201
Figure 6.7: Color and clarity of each system studied at a molar ratio of (40:1) AA:Au, viewed in transmitted light.	202
Figure 6.8: UV-visible absorption spectra of the systems studied at a molar ratio of (40:1) AA:Au.	204
Figure 6.9: Representative TEM images and size distributions for each system studied at a molar ratio of (40:1) AA:Au.	207
Figure 6.10: (96:1) Au:BSA – 35–50 nm polycrystalline aggregates.	208
Figure 6.11: (96:1) Au:BSA – 20–35 nm gold multipods.	209
Figure 6.12: (48:1) Au:BSA – 45–75 nm polycrystalline aggregates.	210
Figure 6.13: (48:1) Au:BSA – 15–25 nm crystals with small pyramids emanating from a primary-sized nanocrystal.	211
Figure 6.14: (24:1) Au:BSA – multipods with branches emanating from a common core.	212
Figure 6.15: (12:1) Au:BSA – multipods.	213
Figure 6.16: (12:1) Au:BSA – elongated crystals, with twinning planes parallel to the direction of elongation.	214
Figure 6.17: (12:1) Au:BSA – elongated crystals, resulting from pentagonal primary-sized nanocrystals with preferential diffusional growth of one or more monocrystalline domains.	215
Figure 6.18: (12:1) Au:BSA – concave crystals with sizes ranging from 10–25 nm. ...	216

Figure 6.19: (12:1) Au:BSA – concave crystals with sizes ranging from 40–55 nm. .	217
Figure 6.20: (6:1) Au:BSA – elongated crystals with lengths ranging from 10–20 nm.	218
Figure 6.21: (6:1) Au:BSA – planar multipods with dimensions ranging from 15–30 nm.	219
Figure 6.22: (6:1) Au:BSA – concave crystals with sizes ranging from 10–20 nm.	220
Figure 6.23: (6:1) Au:BSA – rounded convex crystals with sizes ranging from 5–15 nm.	221
Figure 6.24: (9:2) Au:BSA – gold tripods with dimensions of 15–25 nm.	222
Figure 6.25: (9:2) Au:BSA – elongated crystals with lengths ranging from of 10–20 nm.	223
Figure 6.26: (9:2) Au:BSA – concave crystals with sizes ranging from 10–15 nm.	224
Figure 6.27: (9:2) Au:BSA – concave crystals with sizes ranging from 20–30 nm.	225
Figure 6.28: (9:2) Au:BSA – rounded convex crystals with sizes ranging from 5–10 nm.	226
Figure 7.1: The five Platonic solids, as depicted by Johannes Kepler along with their philosophical connotations.....	229
Figure 7.2: Artistic renditions of regular star polyhedra.	229
Figure 7.3: The small stellated dodecahedron (left) and great stellated dodecahedron (right), each depicted by Johannes Kepler in two different perspectives.	230
Figure 7.4: TEM analysis of the as-synthesized product, formed in water at a molar ratio of (40:1) AA: Au, in the absence of other chemical or molecular species.	235
Figure 7.5: Star polyhedral gold nanocrystals.	237
Figure 7.6: The two classes of star polyhedral gold nanocrystals.	238
Figure 7.7: TEM tilt sequence for a multiple-twinned star nanocrystal.	240
Figure 7.8: Multiple-twinned star nanocrystals.	242
Figure 7.9: Monocrystalline star polyhedral gold nanocrystals.....	244
Figure 7.10: Characteristic structural defects for multiple-twinned and monocrystalline star polyhedral gold nanocrystals.....	248
Figure 7.11: UV-visible absorption spectra of star polyhedral gold nanocrystals.....	250
Figure 7.12: Representative TEM images illustrate the structural stability of star polyhedral gold nanocrystals.	252
Figure 7.13: SEM images illustrating structural degradation of star polyhedral gold nanocrystals in solution.....	253
Figure 7.14: TEM images illustrating structural degradation of star polyhedral nanocrystals in an ultrasonic bath.	254
Figure 7.15: Low-magnification TEM images of the as-synthesized product, using the standard reaction protocol.....	256
Figure 7.16: TEM images illustrating the extensive coalescence observed when sodium hydroxide is added to the reaction system.	257
Figure 7.17: TEM images illustrating the super-stellated gold nanocrystals, formed in approximately one-third of the (160:1) AA: Au reaction systems.	259
Figure 7.18: Stability of star polyhedral gold nanocrystals in the electron beam.	261
Figure 7.19: Stability of super-stellated gold nanocrystals in the electron beam.	264

Figure 7.20: SEM images illustrating the product distribution observed when the reaction occurs at room temperature, and in ice bath.	265
Figure 7.21: Product distribution for the standard reaction carried out in ice bath.	266
Figure 7.22: Product distribution for the standard reaction protocol carried out with a dropwise addition of chloroauric acid.....	268
Figure 8.1: (24:1) Au:BSA systems at (40:1) AA: Au.	278
Figure 8.2: (24:1) Au:BSA systems formed by addition of ionic gold to an equilibrated solution of ascorbic acid and BSA protein.	279
Figure 8.3: (24:1) Au:BSA system at a molar ratio of (160:1) AA: Au.	281
Figure 8.4: Size distributions for (24:1) Au:BSA system.....	282
Figure 8.5: Size distributions for (18:1) Au:BSA system.....	284
Figure 8.6: Size distributions for (72:5) Au:BSA system.....	285
Figure 8.7: HAADF analysis of the internal structure of polycrystalline spheres in the (18:1) Au:BSA system.....	287
Figure 8.8: HAADF analysis of the primary-sized crystals visible along the perimeter of the polycrystalline spheres in the (18:1) Au:BSA system.	288
Figure 8.9: HAADF structural analysis of a polycrystalline aggregate produced in the (24:1) Au:BSA system at a molar ratio of (40:1) AA: Au.....	289
Figure 8.10: HAADF analysis of polycrystalline aggregates produced in the (24:1) Au:BSA system at a molar ratio of (160:1) AA: Au.	290
Figure 8.11: Nanocrystals formed by the addition of ionic gold to a pre-existing solution of ascorbic acid, BSA, and sodium hydroxide.....	293
Figure 8.12: UV-visible absorption spectra resulting from addition of ionic gold to a pre-existing solution of ascorbic acid, BSA, and sodium hydroxide.....	295
Figure 8.13: (18:1) Au:BSA HRTEM – Multiply-branched nanocrystals.	296
Figure 8.14: (18:1) Au:BSA HRTEM – Elongated nanocrystals.	297
Figure 8.15: (18:1) Au:BSA HRTEM – Nanocrystals in the range of 5–10 nm.	298
Figure 8.16: (18:1) Au:BSA HRTEM – Nanocrystals less than 5 nm in diameter.	299
Figure 8.17: (12:1) Au:BSA HRTEM – Multiply-branched nanocrystals with irregular morphologies, and exhibiting a high density of twinning defects.	300
Figure 8.18: (12:1) Au:BSA HRTEM – Elongated nanocrystals.	301
Figure 8.19: (12:1) Au:BSA HRTEM – Nanocrystals in the range of 5–10 nm	303
Figure 8.20: (12:1) Au:BSA HRTEM – Nanocrystals less than 5 nm in diameter.	304
Figure 8.21: Nanocrystals formed by the addition of ionic gold to a pre-existing solution of ascorbic acid and BSA, with subsequent addition of sodium hydroxide.	308
Figure 8.22: UV-visible absorption spectra resulting from addition of ionic gold to a pre-existing solution of ascorbic acid and BSA, with subsequent addition of sodium hydroxide.	309
Figure 8.23: (12:1) Au:BSA – conventional TEM analysis.	310
Figure 8.24: (12:1) Au:BSA – HRTEM analysis.	311

Chapter 1: Introduction

Nanoscience provides the ability to engineer the properties of materials by controlling their size and shape, and this has driven research toward a multitude of potential uses for nanomaterials. (1) For example, metallic nanocrystals have been employed as catalysts, (2) photocatalysts, (3) and sensors, (4) and have been incorporated into optoelectronic devices (5,6) and fuel cell electrodes for the direct conversion of chemical energy into electricity. (7) By definition, a nanomaterial possesses at least one characteristic dimension on the order of a billionth of a meter, and exhibits some type of unique electromagnetic, optical, structural, or other physicochemical property that is a direct consequence of its nanometric size. Nanomaterials constitute a transitional regime, intermediate to the macroscopic world of bulk materials, where classical physics provides an adequate description of material properties, and the microscopic world of individual atoms and molecules, where quantum mechanics dominates.

Ancient civilizations produced and utilized gold nanocrystals, albeit unknowingly, centuries before the advent of modern synthesis and characterization techniques. Gold has enthralled mankind for millennia, and the forerunners of modern-day chemists, the alchemists, were driven by their pursuit of gold. The Romans added gold salt to their glass preparations, which was reduced to colloidal gold when the glass was annealed, producing a transparent ruby-red glass. (8) One of the earliest examples of colloidal gold used for aesthetic purposes is the Lycurgus cup, which dates from the 5th or 4th century B.C. The appearance of the glass is green in normal lighting, but when illuminated from the interior, its color is an intense ruby red. This iridescence is due to the presence of colloidal gold in the glass (Figure 1.1). (9)



Figure 1.1: The Lycurgus Cup, dating from the 5th or 4th century B.C. Colloidal gold causes the glass to appear green in reflected light, but ruby-red in transmitted light. (British Museum)

In the Middle Ages, colloidal gold was employed by artisans to produce bright red and purple colors in stained glass windows. For example, the red and purple hues of the Rose Window of the Cathedral of Notre Dame are due to the presence of colloidal gold (Figure 1.2). (10) In medieval times, colloidal gold also gained renowned for its reputed curative properties. Colloidal gold was employed to treat maladies including heart problems, epilepsy, venereal diseases, and dysentery. In fact, the primary medicinal use of colloidal gold in the Middle Ages was for diagnosis of syphilis, and although the test was not completely reliable, the technique remained in use until the 20th century. (11)

Many books were written on the subject of colloidal gold prior to the work of Faraday in the mid-19th century. Francisci Antonii, a philosopher and medical doctor, published what is considered to be the first book on colloidal gold in 1618. (12) A complete treatise on colloidal gold was published in 1718 by Hans Heinrich, another philosopher and doctor. (13) The idea of stabilizing agents for colloidal gold first

appeared in this work, when Heinrich observed that the use of boiled starch in the preparation of drinkable gold noticeably enhanced its stability. Indeed, the full conception of colloidal gold was beginning to come to fruition by the mid-18th century, as evidenced by a French dictionary on chemistry dated 1769. In this dictionary, the entry for “*or potable*” stated that “drinkable gold contains gold in its elementary form, but under extreme sub-division, suspended in a liquid.” (14)

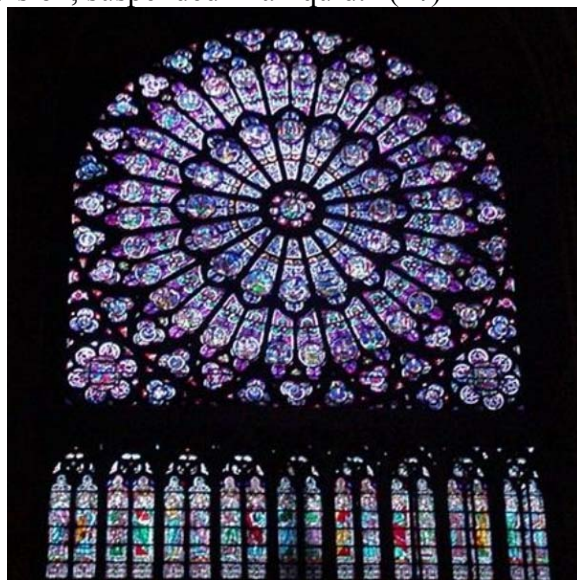


Figure 1.2: Rose Window of the Cathedral of Notre Dame. The bright red and purple colors are the result of colloidal gold. (Cathedral of Notre Dame, Paris)

The first documented synthesis protocol for gold nanocrystals was reported by Michael Faraday in 1857. (15) His work detailed the formation of colloidal gold by reduction of an aqueous solution of chloroauric acid with phosphorous and in the presence of CS₂. His gold solutions had a stable, deep red color that he attributed to the presence of “exceedingly fine particles.” Faraday prepared thin films from his dried colloidal solutions, and noted a reversible color change, from bluish-purple to green, upon mechanical compression of the films. Subsequent developments in the study of nanocrystals were limited until the invention of the electron microscope by Ruska in

1932. (16) The first commercially-produced electron microscope was introduced by Siemens in 1939, and increasing numbers of scientists were armed with the technology to directly relate the properties of colloidal crystals with their structural morphology. With continued advances in instrumentation, image acquisition, and automation, the past 50 years have witnessed rapid advances in the field of electron microscopy, and consequently in the study of nanoscience. (17)

1.1 PROPERTIES OF NOBLE METAL NANOCRYSTALS

Some of the most promising applications for nanocrystals involve biological systems. Many bio-oriented applications for metallic nanocrystals are currently being explored, including image contrast enhancement, (18) bioelectronic sensing, (19) colorimetric bioassays, (20) photothermally-induced drug delivery, (21) and bio-encoded product labeling. (22) Noble metal nanocrystals 2–5 nm in diameter are highly desirable for several types of biologically-oriented (as well as conventional) applications for four primary reasons. (i) A large percentage of the atoms are surface atoms, and are thus available to interact with external species. (ii) Due to the small energy difference between local minimum energy configurations for noble metal nanocrystals in this size range, these nanocrystals have a highly fluctuating structure, resulting in high surface activity. (iii) Due to the onset of quantum size effects, the electromagnetic response of noble metal nanocrystals in this size range can be controllably manipulated. (iv) These nanocrystals are comparable in size to biological molecules, and their small size gives them the ability to penetrate more complex biological systems. We will briefly discuss each of these points in turn.

1.1.1 Surface to Volume Ratio

For bulk metal crystals, less than 1% of the constituent atoms are surface atoms. In contrast, one of the distinguishing characteristics of nanocrystals is their large percentage of surface atoms. (23) One common growth mechanism for nanocrystals formed via colloidal reduction involves the addition of successive full shells of atoms surrounding a central atom, with each shell possessing a close-packed structure. (24) In this case, the number of atoms contained in the n^{th} shell is:

$$N_s = 10n^2 + 2 \quad (1.1)$$

The total number of atoms contained within the volume of a cluster of n shells is:

$$N = \frac{10n^3 + 15n^2 + 11n + 3}{3} \quad (1.2)$$

Thus, the surface to volume ratio for an n^{th} shell nanocrystal can be obtained from the ratio of (N_s/N) , (25) presented graphically in Figure 1.3. The number of gold atoms in a nanocrystal of a given diameter can be estimated from a spherical volume, using the density of bulk FCC gold. Based on this approximation, a gold nanocrystal 2 nm in diameter contains ~245 atoms, while a gold nanocrystal 5 nm in diameter contains ~3870 atoms. In terms of Figure 1.3, the percentage of surface atoms will range from 26% in the case of 5 nm crystals, to 56% surface atoms in the case of 2 nm crystals. By working in the 2–5 nm size range, we can affect large changes in the percentage of surface atoms with only modest changes in nanocrystal dimensions.

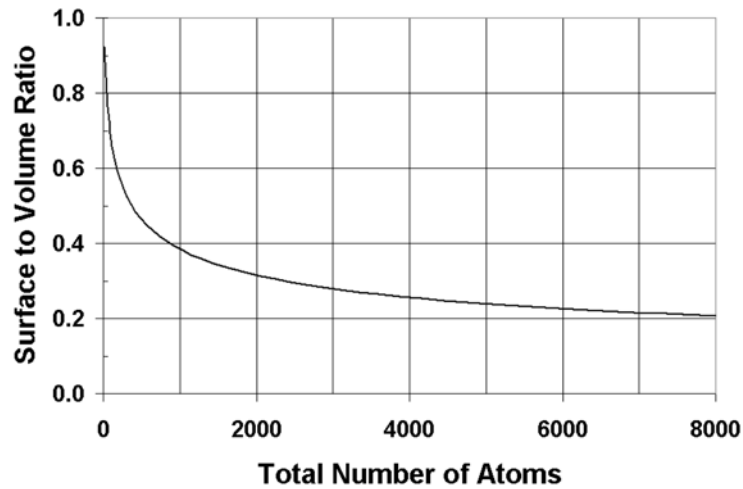


Figure 1.3: Surface to volume ratio versus total number of atoms in a close-packed cubic crystal.

1.1.2 Fluctuating Morphology and High Surface Activity

Structural fluctuations of ~ 2 nm gold nanocrystals were first reported by Bovin *et al.* (26) Soon thereafter, Ijima and Ichihashi documented a ~ 2 nm gold nanocrystal fluctuating between cuboctahedral, icosahedral, and single-twinned morphologies. (27) Since these initial investigations, numerous transmission electron microscopy (TEM) studies have demonstrated that for metallic nanocrystals with diameters less than 5 nm, minor energy excitations are sufficient to induce structural fluctuations, and the frequency of such fluctuations increase with decreasing nanocrystal size. (28, 29)

Theoretical calculations reveal that that the total potential energy of a nanocrystal consists of several local minima, corresponding to different crystal morphologies. (30,31) It has been predicted that for nanocrystals with diameters less than 5 nm, the energy barriers between these local minima are sufficiently small ($\sim kT$ at room temperature), so that thermal fluctuations provide sufficient energy to induce structural transformations. (32) This model is in agreement with the experimental evidence from TEM analysis that

sub-5 nm nanocrystals possess highly fluctuating structures. Marks describes this phenomenon as quasimelting, whereby a nanocrystal samples multiple structural configurations with similar energies and low energy barriers without true melting and recrystallization. (33)

The result of this fluctuating structural character is a highly-active nanocrystal surface. Another important contribution to the high surface energy of nanocrystals is from their large percentage of surface atoms, discussed in the previous section. Since surface atoms lack their full complement of coordination atoms, they possess higher chemical activity than atoms stabilized in the interior of the crystal. Furthermore, as the nanocrystal dimensions decrease to the 2–5 nm size range, an increasing percentage of surface atoms are at crystal edges and vertices, as opposed to the crystal faces. Among the highly-active atoms comprising the crystal surface, edges and vertices are highest in energy, again due to their smaller number of nearest-neighbor atoms. Thus, the large percentage of highly-energetic, fluctuating surfaces promotes the superior chemical activity of 2–5 nm nanocrystals.

1.1.3 Quantum Size Effects

The most basic approach to describing the origin of quantum size effects is through the “Particle in a Box” problem. Consider that an electron in a nanocrystal can be approximated as a three-dimensional particle of mass (m) in a rectangular box of dimensions (L_x), (L_y), (L_z). Within the box the potential energy is zero, while outside the box the potential is infinite (the particle is confined to the box). The three-dimensional Schrödinger wave equation for the particle within the dimensions of the box can be written as:

$$\frac{-\hbar^2}{2m} \left(\frac{\partial^2 \psi}{\partial x^2} + \frac{\partial^2 \psi}{\partial y^2} + \frac{\partial^2 \psi}{\partial z^2} \right) = E \psi \quad (1.3)$$

The wave function (Ψ) is separable into three independent functions:

$$\psi(x, y, z) = X(x)Y(y)Z(z) \quad (1.4)$$

The kinetic energy (E) is separable into x-, y-, and z- components:

$$E(x, y, z) = E_x + E_y + E_z \quad (1.5)$$

Recasting Equation 1.3 in terms of Equations 1.4 and 1.5 yields three separate equations. It is only necessary to solve one equation, as the other two yield analogous solutions. Consider (X):

$$-\frac{\hbar^2}{2m} \left(\frac{d^2 X}{dx^2} \right) = E_x X \quad (1.6)$$

Solving for (X), and applying the boundary conditions ($X = 0$ at $x = 0$ and $x = L_x$):

$$X_n = \sqrt{\frac{2}{L_x}} \sin\left(\frac{n\pi x}{L_x}\right) \quad (1.7)$$

Substituting Equation 1.7 into Equation 1.6 to obtain the quantized energy eigenvalue:

$$E_x = \frac{n^2 \hbar^2}{8mL_x^2} \quad (1.8)$$

Substituting Equation 1.8, and the analogous equations for the y- and z- components of the kinetic energy, into Equation 1.5, and taking into account the existence of three independent quantum numbers, we obtain the three-dimensional quantized energy eigenvalues:

$$E(n_1, n_2, n_3) = \left[\left(\frac{n_1}{L_x} \right)^2 + \left(\frac{n_2}{L_y} \right)^2 + \left(\frac{n_3}{L_z} \right)^2 \right] \frac{\hbar^2}{8m} \quad (1.9)$$

From Equation 1.9, we observe that the separation between adjacent energy levels is inversely proportional to the square of the dimensions of the box. For bulk crystals with macroscopic dimensions, the separation between energy levels is exceedingly small, and the electronic structure is accurately approximated as continuous bands. However, as the crystal dimensions are decreased to the microscopic scale, Equation 1.8 indicates that

the separation between adjacent energy levels increases, and the electronic structure is modified from continuous bands to discrete energy levels. This changeover from bulk electronic structure to quantized energy levels gives rise to the phenomenon of quantum size effects. For noble metal nanocrystals in the range of 2–10 nm, the onset of quantum size effects is pronounced, and their electronic structure is strongly size-dependent. (1)

The response of a nanocrystal to an external electromagnetic field is intimately related to its electronic structure. Consequently, nanocrystals also exhibit unique optical properties. For example, the optical response of noble metal nanocrystals is a consequence of their surface plasmon resonance, which results from the coherent motion of conduction band electrons caused by interaction with an external electromagnetic field. (34) The theoretical origins of the plasmon resonance were first elucidated by Mie in 1908. (35) According to Mie theory, an external electromagnetic field induces polarization of the conduction electrons of a spherical particle, which can be approximated as free electrons with respect to the much heavier metallic core. The resulting net charge difference acts as a restoring force, creating a coherent dipolar oscillation of electrons. When the frequency of the external field is resonant with the coherent electron oscillation, a strong absorption occurs. Of the noble metals, gold and silver are notable for their strong plasmon resonances in the visible region of the electromagnetic spectrum. (36)

According to classic Mie theory, the plasmon resonance is not a function of the particle size. However, experimental evidence demonstrates a strong size-dependence for the plasmon resonance of metallic nanocrystals with dimensions smaller than 20 nm. As the nanocrystal diameter decreases below 10 nm, the plasmon resonance is damped, and becomes practically undetectable for nanocrystals less than 2 nm in diameter. (37) This size-dependent plasmon resonance is a direct result of the size-dependent dielectric

function and discretization of electronic states in metallic nanocrystals due to the onset of quantum size effects. Accounting for quantum effects, and the fact that the mean free path of the conduction electrons (~40–50 nm for silver and gold) is constrained by the physical dimension of a sub-20 nm nanocrystal, the plasmon resonance bandwidth and intensity is found to be inversely proportional to the nanocrystal diameter, as observed experimentally. (34)

The optical response of noble metal nanocrystals is also extremely sensitive to aggregative effects. If the interparticle spacing becomes smaller than the nanocrystal dimensions, the plasmon resonance will be red-shifted due to plasmon-plasmon interactions between adjacent nanocrystals. (34) This phenomenon was famously exploited by Mirkin and colleagues for the colorimetric detection of polynucleotides. (38) Briefly, two separate populations of 13 nm gold nanocrystals were conjugated with thiol-modified oligonucleotides of type *a* and *b*, respectively, being complimentary to sequences *a'* and *b'* on a target nucleotide. Introduction of the target nucleotide to a solution of these bioconjugated nanocrystals caused the *a*-type crystals to bind to the complimentary *a'* sequence, and *b*-type crystals to bind to the *b'* sequence, resulting in the formation of a polymeric network of nanocrystals linked by target molecules. Analogous to the color change that Faraday observed in his colloidal gold films when adjacent crystals were brought into intimate proximity as a result of mechanical compression, this target-induced aggregation caused a dramatic change in solution color (from red to bluish purple upon aggregation), and a corresponding shift in the surface plasmon resonance (from a sharp maximum at 524 nm, to a broad maximum at 576 nm upon aggregation). (39) Due to the strong plasmon resonance of gold, this colorimetric approach can detect femtomolar concentrations of a target molecule, which is 50 times more sensitive than conventional techniques.

1.1.4 Proper Size for Interaction with Biological Systems

In addition to their large percentage of surface atoms, high surface activity, and tunable electromagnetic response, noble metal nanocrystals in the size range of 2–5 nm are of great interest for incorporation into biological systems on the basis of their size alone. Common biological molecules are on the order of 10 nm in size, and decorating these molecules with nanocrystals can reveal detailed structural information. (40) For example, Frey and Frey used gold nanocrystals to elucidate the structure of the pyruvate dehydrogenase (PDH) complex of *Escherichia coli*. (41) PDH is a tri-enzyme complex, consisting of 24 subunits of pyruvate dehydrogenase (E1), 24 subunits of dihydrolipoyl acetyltransferase (E2), and 12 subunits of dihydrolipoyl dehydrogenase (E3). The structure of each enzyme was known, but their spatial orientations within the E2E3 subcomplex of PDH was not known.

The disulfide bonds in the E2E3 subcomplex were reduced, and gold nanocrystals (0.8 nm in diameter) were introduced. Due to the affinity of gold nanocrystals for sulfur, the nanocrystals were preferentially bound to the exposed sulfhydryl groups. The samples were imaged using scanning transmission electron microscopy (STEM), and several pairs of bright round spots were observed, corresponding to the positions of the gold nanocrystals bound to exposed sulfhydryl groups (Figure 1.4b). Since the locations of the disulfide bonds in the individual enzymes were known, mapping the locations of the gold-labeled sulfhydryl groups allowed Frey and Frey to determine the spatial orientations of the enzymes within the E2E3 subcomplex. (41)

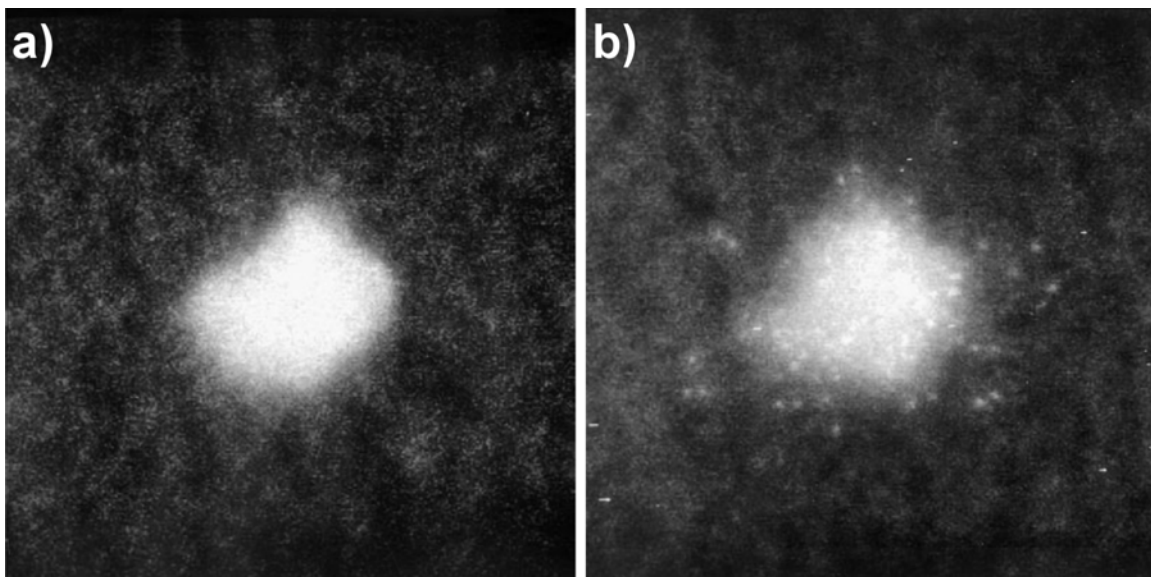


Figure 1.4: STEM images of the E2E3 subcomplex of the *Escherichia coli* PDH complex, obtained by Frey and Frey. (a) Unlabeled subcomplex. (b) Gold-labeled subcomplex. The gold nanocrystals are visible in (b) as bright round spots. (41)

In addition to functionalizing small enzymatic complexes, noble metal nanocrystals have potential for labeling more complex biosystems, such as eukaryotic cells. For example, Feldheim and colleagues reported the use of protein-functionalized gold nanocrystals for targeting the nuclear envelope of intact HepG2 cells. (42) Commercially-obtained gold nanocrystals were crosslinked with bovine serum albumin protein molecules (~160 protein molecules per 20 nm gold nanocrystal), and then derivatized with various peptide targeting sequences. This strategy allowed for the selective targeting of the endosomal cytoplasmic regions (Figure 1.5b), the nuclear envelope (Figure 1.5c), and the interior of the nucleus (Figure 1.5d). To accomplish this type of biotargeting, the nanocrystals employed must be small enough to penetrate the cellular and nuclear membranes. Thus, nanocrystals in the range of 2–5 nm would be prime candidates for size-dependent interactions with more complex biosystems.

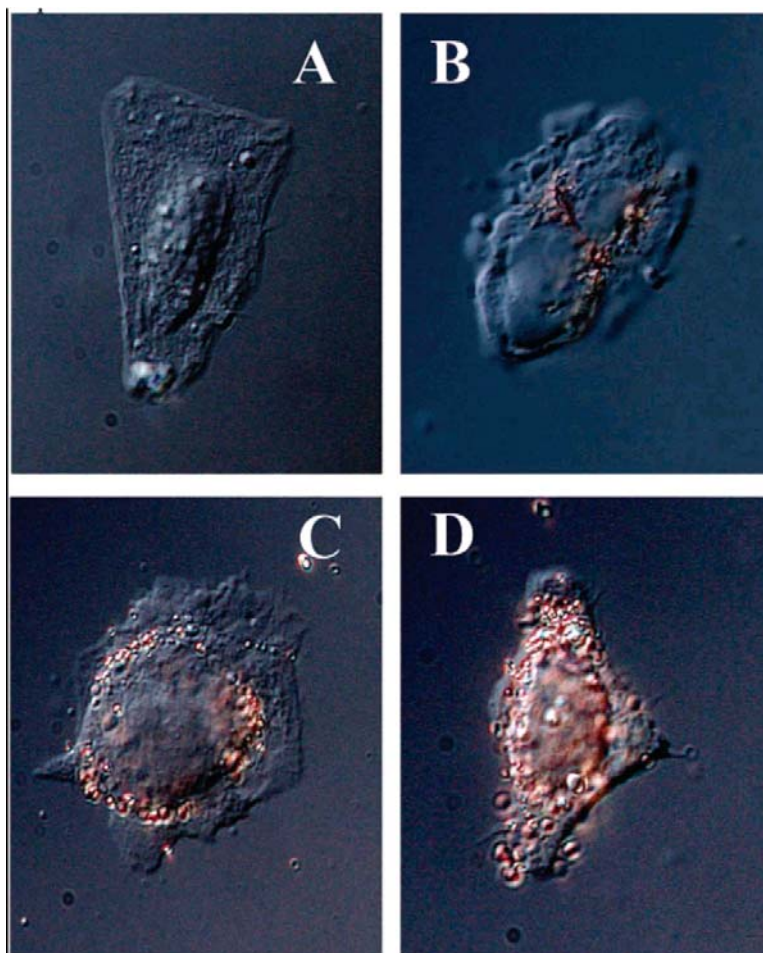


Figure 1.5: Protein-functionalized gold nanocrystals targeting various regions of intact HepG2 cells, as reported by Feldheim and colleagues. (a) Untreated cell; (b)-(d) nanocrystals targeting (b) the endosomal regions, (c) the nuclear envelope, and (d) the interior of the nucleus. (42)

1.2 SYNTHESIS OF NOBLE METAL NANOCRYSTALS VIA COLLOIDAL REDUCTION

The numerous synthesis routes that exist for production of metallic nanocrystals can be grouped into two main categories: “top-down” and “bottom-up” methods. (1) The top-down methods involve lithographic techniques, which are highly effective at producing large areas of patterned surfaces, consisting of periodic arrays of nanocrystals. Although lithographic techniques provide exquisite control over interparticle spacing and

pattern design, the cost of production is high and the size, shape, and crystallographic morphology of individual nanocrystals is highly variable.

The bottom-up approach involves the assembly of individual atoms into nanocrystals. Among the most versatile and reliable bottom-up approaches for the formation of well-dispersed noble metal nanocrystals is the colloidal reduction technique, whereby nanocrystals are formed in solution by the coalescence of atoms that have been generated by *in situ* reduction of ionic precursors. At its most basic level, the general mechanism for the solution-phase formation of metallic nanocrystals involves the controlled precipitation of a solid phase, which can be considered in two distinct stages: nucleation and growth. (1)

The first step in nanocrystal formation occurs when metal atoms are generated in solution by the reduction of an oxidized metallic species. The zerovalent atoms are essentially insoluble, and due to their inherent instability they will spontaneously associate into small atomic clusters called embryos. These embryos continuously form and re-dissolve in solution. The stability of any individual embryo is related to the change in free energy upon formation of the embryo. The total change in free energy is the sum of two contributions: the volume free energy change due to the association of individual insoluble atoms into a crystal lattice (drives embryo formation), and the surface free energy change due to the interfacial tension at the crystal surface (opposes formation). Taking these contributions into account, the total free energy change is:

$$\Delta G_T = -\frac{4}{3}\pi r^3 \Delta G_V + 4\pi r^2 \gamma \quad (1.10)$$

Where (ΔG_T) is the total free energy change upon embryo formation, (r) is the radius of the embryo, (ΔG_V) is the free energy change per volume of embryo created, and (γ) is the interfacial tension per crystal surface area created. The free energy of formation as a function of embryo radius is illustrated in Figure 1.6.

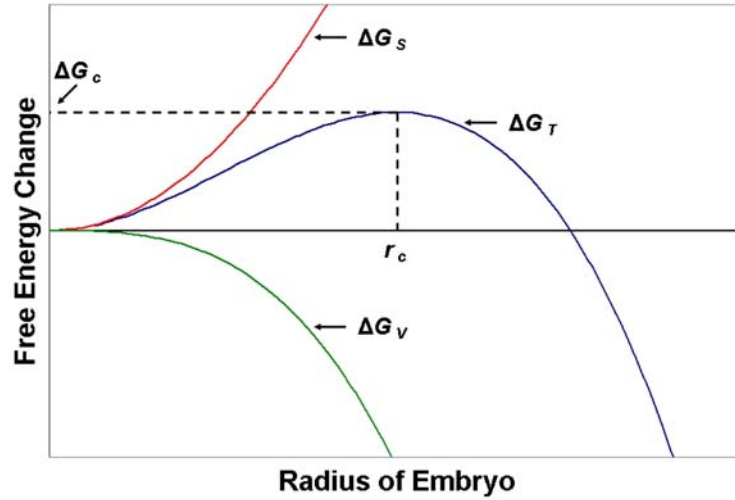


Figure 1.6: Free energy of formation versus embryo radius. The green curve represents the volume free energy change, the red curve represents the surface free energy change, and the blue curve represents the total free energy change of formation. Embryos with radii greater than (r_c) separate from solution and continue to grow as stable nuclei.

From Figure 1.6, we see that a maximum in the total free energy of formation (ΔG_c) exists at the critical radius (r_c). Embryos with radii smaller than the critical radius will re-dissolve into solution. For an embryo whose radius is exactly equal to the critical radius, the addition of one more atom from solution produces a reduction in the total free energy of formation. Thus, it becomes energetically favorable for this embryo to grow rather than to dissociate. From this point on, the embryo will separate from solution and continue to grow as a stable nucleus. The critical radius can be easily obtained from Equation 1.10. Before proceeding, it is useful to first express the volume free energy change in terms of the concentration of atoms in solution:

$$\Delta G_v = -\frac{RT \ln\left(\frac{C}{C_{eq}}\right)}{V} \quad (1.11)$$

Where (R) is the universal gas constant, (T) is the temperature, (C) and (C_{eq}) are the actual and equilibrium concentrations of atoms in solution, respectively, and (V) is the atomic volume. Substituting Equation 1.11 into Equation 1.10, and solving for the critical radius:

$$r_c = \frac{2V\gamma}{RT \ln\left(\frac{C}{C_{eq}}\right)} \quad (1.12)$$

From Equation 1.12, we see that nucleation is favored when the solution is supersaturated with metal atoms. As nuclei are formed, the concentration of atoms remaining in solution decreases. Once the solution is no longer supersaturated, the nucleation phase ends, and subsequent growth will be restricted to previously-existing nuclei. Well-controlled colloidal syntheses are often characterized by a short burst of rapid nucleation that generates all the crystals that will be present at the conclusion of the reaction, followed by a sustained period of crystal growth. (1)

The initially-formed nuclei are still relatively unstable, and the primary growth phase consists of nuclei growing into primary-sized nanocrystals by continued diffusional addition of individual atoms. In the secondary growth phase, two possible routes for the subsequent growth of primary-sized nanocrystals exist: (i) continued diffusion of individual atoms onto existing nanocrystals, and (ii) aggregation of existing nanocrystals. In the case of diffusional growth, the final product will exhibit well-defined crystalline morphologies, while for aggregative growth, the final product will consist of much larger spherical polycrystalline structures. Due to their high surface energies, nanocrystals are thermodynamically unstable. To arrest their growth in the nanometric range, surface-protecting agents are employed that both stabilize the surface of the crystal, and provide a physical barrier to inhibit the coalescence of nanocrystals. (43)

1.3 BIOCONJUGATION OF NOBLE METAL NANOCRYSTALS

Not only is it necessary for an effective synthesis technique to produce nanocrystals with well-defined sizes and shapes, but the surface chemistry must be compatible with the environment in which the product will be utilized, an aqueous environment in the case of biosystems. A major obstacle to the direct synthesis of biocompatible metallic nanocrystals in the size range of 2–5 nm has been selection of suitable surface protecting agents. Colloidal chemistry techniques for the synthesis of metallic nanocrystals 2–5 nm in diameter are well-documented. (44) Stabilizing molecules densely passivate the surface of the colloid, shielding it from aggregation and coalescence. To maintain dimensional stability, well-protected nanocrystals in this size range often require protecting agents (e.g. alkanethiols) that render the crystals insoluble in polar solvents, thus precluding their use in aqueous solution. (45)

1.3.1 Conventional Nanocrystal Bioconjugation Techniques

Conventional approaches for the preparation of bioconjugated metal nanocrystals in the range of 2–5 nm involve crosslinking previously-existing nanocrystals with biomolecules. Typically, the desired biological molecule is incubated in the presence of previously-synthesized nanocrystals and in a solution with carefully-controlled pH conditions and ionic salt content. (46) In many cases, the process is aided by the addition of bound ligands, either to the nanocrystal surface or to the biomolecule, that facilitate the crosslinkage of the two moieties. Due to the presence of crosslinking agents and surface-protecting agents from their initial synthesis, these bioconjugated nanocrystals will have densely-passivated surfaces, with minimal free surface area for direct interaction with external species. On the other hand, some bioconjugation protocols involve the synthesis of weakly-protected nanocrystals in water, followed by ligand exchange with the thiol-, amine-, or phosphate-bearing ligands of the desired biological molecule. In this case, the

time that elapses between the synthesis of the nanocrystal and the bioconjugation event is critical, since these poorly-protected crystals tend to aggregate rapidly in solution. In both cases, the solution is centrifuged at the conclusion of the incubation period to remove the fraction of nanocrystals that were not successfully bioconjugated.

With conventional bioconjugation approaches, the loss of a sizeable percentage of nanocrystals during the workup is a fact of life, albeit a fact that is often glossed over. One example of a report that addresses the issue forthrightly is from Mirkin and colleagues on the colorimetric detection of polynucleotide sequences, described previously. (38) Recall that in their system, 13 nm gold nanocrystals were bioconjugated with thiol-modified oligonucleotides. In a subsequent report, Mirkin and colleagues note that 25–30% of the original gold nanocrystals were lost during the bioconjugation process. (39) The fate of such non-conjugated nanocrystals is irreversible aggregation during the centrifugation step. Now, noble metal nanocrystals are highly value-added commodities, especially when produced with well-controlled dispersions and size distributions, and conventional bioconjugation protocols that routinely destroy 25% or more of the nanocrystals employed leave much room for improvement.

Stability is a major concern even for successfully bioconjugated nanocrystals, as they typically must be stored at near-freezing temperatures to maintain dimensional stability. Under these circumstances, the bioconjugated product tends to remain stable for only a period of a few months. Bioconjugated nanocrystals also exhibit a strong tendency to aggregate with even mild processing, such as drying to form a thin film. (45)

1.3.2 Formation of Nanocrystals Directly in the Presence of Biomolecules

One of the most promising, yet least studied avenues for producing biocompatible nanostructures involves growing nanocrystals in the presence of biomolecules. Nature employs specifically-designed biomolecules to regulate a plethora of biological processes

with exquisite precision, and biomolecules should be interesting candidates for regulating inorganic processes as well, such as the nucleation and growth of nanocrystals. By incorporating biomolecules directly into a synthesis protocol, we can eliminate the need for crosslinking agents or weakly-effective intermediate stabilizing agents, while producing nanocrystals with a degree of built-in biocompatibility.

Furthermore, biomolecules possess the proper framework for direct linkage to metallic nanocrystals. For example, proteins are composed of amino acids that, in addition to terminal amines, possess sulfur-, oxygen-, and nitrogen-bearing side groups that can stabilize the nanocrystal surface. Short, thiol-terminated peptides have been used as protecting agents for the aqueous synthesis of gold nanocrystals, most notably tiopronin (Cys-Gly) by Murray and colleagues, (47) and glutathione (γ -Glu-Cys-Gly) by Whetten and colleagues. (48) In both cases, well-stabilized, water-soluble, sub-2 nm crystals were produced in high yield. However, the actual mechanism of surface protection was analogous to the conventional approaches, with several peptide chains densely passivating the nanocrystal surface. In fact, it was determined that ~85 tiopronin ligands were functionalizing the surface of each 1.8 nm diameter gold nanocrystal, (47) and ~16 glutathione ligands were functionalizing the surface of each 0.9 nm diameter gold nanocrystal. (48)

In the course of my dissertation work, I have developed a different approach to surface protection that can be exploited when working with biological macromolecules. Rather than growing a nanocrystal with surfaces densely protected by several small biomolecules, I hypothesized that it should be possible to grow a nanocrystal within the confines of one biological macromolecule. In this way, the nanocrystal surface will still experience surface-stabilizing interactions with various residues of the macromolecule, while at the same time the bulk of the molecule will provide steric protection to the

nanocrystal surface. Due to this added steric protection, it may not be necessary to have the nanocrystal surface be so densely passivated with directly-bound ligands, and this could allow for the highly-active surfaces of the nanocrystal to more efficiently interact with the external environment.

In fact, prior to my undertaking the research efforts described herein, one report did exist of silver nanocrystals directly functionalized by bovine serum albumin (BSA), a macromolecular protein, with nanocrystal diameters ranging from 25–45 nm. (49) However, these nanocrystal diameters were several times larger than the dimensions of the protein molecule, indicating the nanocrystal surfaces are again protected by multiple protein molecules. In essence, this report presented the same strategy of protecting a nanocrystal surface with multiple surface-protecting biomolecules, only on a larger scale.

1.4 PROPERTIES OF SERUM ALBUMIN PROTEIN

The biological macromolecule I chose to work with in the course of my investigations was bovine serum albumin (BSA) protein. Since I will frequently refer to this molecule throughout my dissertation, I will now address some of its distinguishing characteristics. The physical properties of bovine serum albumin (BSA, molecular mass 66 411 Da) have been thoroughly characterized, and it finds extensive use in biochemical studies as a model protein. (50) Serum albumin is the most abundant protein in blood plasma, and one of its primary physiological roles is to transport hydrophobic molecules through the bloodstream, including hematin, bilirubin, hormones, vitamins, amino acids, and fatty acids. Additionally, serum albumin has a crucial role in regulating both the pH and osmotic pressure of blood by forming complexes with excess ionic solutes. (51)

From a structural standpoint, BSA is a globular protein composed of a single 583-residue polypeptide chain, and its secondary structure is highly alpha helical. The tertiary structure of BSA is comprised of three homologous domains, with cysteine residues

forming disulfide bonds to produce a double-loop bridging pattern, illustrated in the inset of Figure 1.7. (52) This loop-linked structure is critical, in that it allows for the rapid expansion, contraction, and flexing of serum albumin. In fact, serum albumin has been described as a “kicking and screaming” molecule that rapidly accommodates itself to form complexes with a wide variety of ligands. (53)

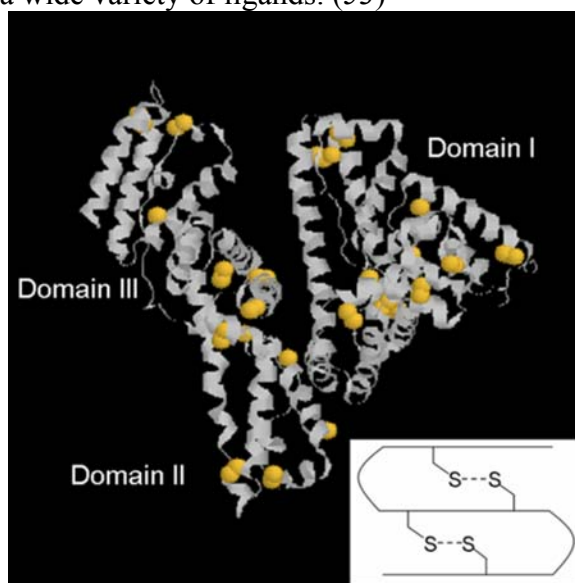


Figure 1.7: Tertiary structure of human serum albumin (PDB1BJ5), (54) a structural analogue to BSA. Sulfurs within the protein molecule are displayed as space-filled atoms. The inset illustrates the formation of double-loop disulfide bridging by cysteine residues. (52)

Although detailed structural models for BSA are not available, the tertiary structure of human serum albumin, a structural analogue to BSA, has been determined by Curry *et al.* from X-ray diffraction. (54) Their analysis indicates that the space group is C121, with cell constants $a = 189.18 \text{ \AA}$, $b = 38.96 \text{ \AA}$, $c = 96.40 \text{ \AA}$, and $\beta = 105.31^\circ$. Several residues of BSA have sulfur-, oxygen-, and nitrogen-bearing groups that can potentially stabilize the surfaces of noble metal nanocrystals. Of these, the most

attractive sites for interaction with nanocrystals would likely involve the 35 thiol-bearing cysteine residues.

1.5 ON THE HIGH ANGLE ANNULAR DARK FIELD TECHNIQUE

Electron microscopy is among the most powerful analytical tools employed in the study of nanomaterials. When a high-energy beam of electrons impinges upon a sample, multiple signals are generated that provide detailed information about its structural and chemical composition. One of the greatest benefits of electronic microscopy is that multiple analyses can be performed concurrent to atomic resolution imaging, which allows for direct correlation between specimen structure and observed properties. In the course of my dissertation work, I have made extensive use of electron microscopy. Most of the electron microscopy techniques I employed are well-established throughout the scientific community (transmission electron microscopy, scanning electron microscopy, energy dispersive X-ray spectroscopy, and electron diffraction), and detailed discourses on these topics are readily available. (55,56) However, one electron microscopy technique stood out among all others as being essential to the characterization of biofunctionalized noble metal nanocrystals, and merits special discussion: the high angle annular dark field technique.

High angle annular dark field (HAADF) is achieved using a TEM in scanning transmission electron microscopy (STEM) mode. In brief, a sub-nanometer electron probe is rastered over the sample, and incoherently scattered electrons are collected by means of a high-angle annular detector. Incoherent images are more intuitive than traditional coherent images, as the signal intensity is the convolution of the specimen function with the probe intensity distribution, and can be directly related to the structure of the object being imaged. (57,58) The signal is collected at sufficiently high angles that most Bragg scattering is excluded, and the specimen function approximates a Rutherford-

like scattering cross section. (59) As a result, the intensity of scattered electrons is dependent upon the mass of the incident atom, yielding spatially resolved chemical information. The incoherent electron scattering is approximated by the Rutherford scattering function:

$$\frac{d\sigma(\theta)}{d\Omega} = \frac{e^4 Z^2}{16E_0^2 \sin^4\left(\frac{\theta}{2}\right)} \quad (1.13)$$

The left side of Equation 1.13 denotes differential scattering cross sections as a function of the scattering angle (θ), while (E_0) is the incident beam energy, (e) is the electron charge, and (Z) is the atomic number of the scattering nucleus. This equation predicts that for a sufficiently high scattering angle, the intensity of the scattered electrons will be dependent on the square of the atomic number. For thin, defect-free specimens, the spatial resolution is limited only by the probe size, and the resulting images will be a compositional map in which image contrast denotes atomic contrast, commonly referred to as the Z^2 -contrast phenomenon. (60,61) As a good approximation, in HAADF images of thin, defect-free specimens, lighter elements appear dark and heavier elements appear bright. To take an example from my own work, due to the large differences in atomic number, noble metal nanocrystals are easily distinguished from the organic material that composes biological molecules.

Recall that HAADF images are formed by electrons that have undergone high angle scattering. Therefore, any crystal feature that increases the amount of high-angle scattering can induce a change in contrast of the HAADF image. Thus, in addition to the previously-discussed Rutherford-like scattering, significant contributions to HAADF contrast can also arise from specimen thickness and structural defects. (62) As electrons travel through thicker regions of the specimen and interfere with more scattering centers, the probability for high angle scattering increases. Therefore, thicker specimen regions

generally have brighter contrast. On the other hand, in the vicinity of crystal defects and strain fields, increased inelastic dispersion occurs as the electron beam encounters atoms that deviate from their ideal lattice positions. The image contrast arising from this time-independent atom displacement is known as Huang scattering contrast, and is valuable in the study of defects. (63)

1.6 DISSERTATION OVERVIEW

One of the most promising, yet least studied routes for producing biocompatible nanostructures involves growing nanocrystals in the presence of biomolecules. By incorporating biomolecules directly into a synthesis protocol, we can produce nanomaterials with built-in biocompatibility. Naturally-occurring biomolecules are renewable resources, which could prove beneficial from a cost perspective when contemplating large-scale production of nanomaterials. Nature employs a plethora of molecules to regulate processes in living organisms with exquisite precision, and biomolecules should be interesting candidates for regulating inorganic processes as well, such as the nucleation and growth of nanocrystals.

The starting point for the investigations described in this dissertation was the general hypothesis: *Due to their innate structural and functional properties, certain naturally-occurring globular proteins may provide a suitable framework to regulate the formation and growth of noble metal nanocrystals with well-controlled morphologies, in the size range of 2–5 nm.* The globular protein I chose to focus my research on was bovine serum albumin (BSA). Serum albumin is the most abundant protein in blood plasma. Since it is a carrier protein with a highly flexible structure that accommodates a variety of molecules, I hypothesized that BSA could alternatively carry an inorganic cargo – a metallic nanocrystal.

In the initial stage of my work, I designed two novel synthesis protocols to gauge the feasibility of utilizing BSA to regulate the formation of gold nanocrystals. In the first case, outlined in Chapter 2, the standard protocol for polyol reduction was modified by replacing ethylene glycol with glycerin, replacing synthetic polymers with BSA as protecting agent, and decreasing the reaction temperature to less than 100°C. In the second case, described in Chapter 3, the standard protocol for the Brust-Schiffrin two-phase reduction was modified by replacing alkylthiols with BSA as protecting agent, which facilitated a strictly aqueous synthesis route.

In both the glycerin- and aqueous-based experiments, I discovered that BSA can be utilized as a surface-protecting agent for the formation of gold nanocrystals in the size range of 2–5 nm. However, due to a superior product yield and rapid reduction at room temperature, the aqueous-based protocol became the foundation for subsequent studies. In Chapter 4, I describe the extension of this approach to produce well-dispersed ~2nm silver, gold, and platinum nanocrystals, grown within and directly functionalized by serum albumin protein molecules. This method has several attractive features, including a high yield of biofunctionalized nanocrystals with well-defined sizes and robust dimensional stability, combined with the ease of synthesis under conditions that are non-destructive to the protein molecule.

Having demonstrated the feasibility of BSA-functionalized nanocrystals, some representative potential uses were explored in Chapter 5. BSA-functionalized silver nanocrystals were employed in a broader study on the interaction of silver nanocrystals with HIV. In the case of gold, BSA-functionalized nanocrystals were utilized for *in vivo* dosage of a contrast enhancing agent to bacteria. Finally, BSA-functionalized platinum nanocrystals were studied as catalysts for aqueous-phase hydrogenation of allyl alcohol.

Since many intriguing uses for protein-functionalized nanocrystals involve incorporation into biosystems, I sought to enhance the biocompatibility of my preparations by using ascorbic acid as reducing agent. The initial results, outlined in Chapter 6, revealed numerous elongated and branched nanocrystals. Such structures were not observed in the previous synthesis protocols I had developed with BSA, so I hypothesized ascorbic acid was driving their formation. To test my assertion, I prepared a simplified system, where ionic gold was reduced in an aqueous solution of ascorbic acid. In doing so, I discovered a new method for producing multiply-branched gold nanocrystals, described in Chapter 7.

Two conditions were necessary to achieve multiply-branched structures: rapid kinetics, and strongly acidic pH. I hypothesized that by negating these two conditions, I could utilize ascorbic acid in the presence of BSA to produce gold nanocrystals of well defined size and shape. In Chapter 8, I demonstrate that by exploiting ascorbic acid complexation with BSA to moderate reaction kinetics, and using sodium hydroxide to provide basic pH, well-dispersed ~2.5 nm gold nanocrystals can be obtained. This protocol represents a novel, environmentally benign approach to producing biocompatible nanocrystals, relying on proteins, ascorbic acid, sodium hydroxide, and water, all at ambient temperature.

Chapter 2: Polyol Synthesis of Protein-Stabilized Gold Nanocrystals

2.1 INTRODUCTION

The polyol method is one of the most widely-utilized colloidal reduction techniques for the formation of metallic nanocrystals. This approach employs solution-phase redox chemistry, with metal ions being reduced to atoms via the oxidation of a polyol species. (64) Metallic nanocrystals are formed within the liquid polyol, which serves both as the solvent and the reducing agent. The reaction is carried out at elevated temperatures to promote oxidation of the polyol species. Surface-protecting molecules are added to solution to stabilize the resulting crystals within the nanometric scale. For a given polyol species, significant variables that affect nanocrystal synthesis include (i) reaction temperature, (ii) reaction time, (iii) dilution of the polyol solution with water, (iv) addition rate, order of addition, and relative molar concentrations of the metal ionic precursor and surfactant molecules. By controlling these parameters, nanocrystals with reasonably-controlled sizes and morphologies can be obtained. (65)

A polyol-based synthetic approach to the formation of biocompatible nanocrystals could have two significant advantages. First, the method is relatively straightforward when compared with other colloidal reduction techniques. Indeed, the reaction kinetics, and therefore the reaction products, can be controlled to a large extent simply by varying the temperature of reaction, with additional layers of complexity being subsequently introduced for more finely-tuned control of the final product characteristics. Second, the most-commonly employed polyol solvents are miscible with water. Thus, water-soluble surface-protecting molecules, such as biological molecules, may be directly incorporated into the polyol method.

For a conventional polyol synthesis involving gold, nanocrystals would be formed by reduction of chloroauric acid at a temperature range of 100–200°C in ethylene glycol, with poly-vinyl pyrrolidone (PVP) used as a surface-stabilizing agent. (65) This standard version of the polyol method has two grave disadvantages when contemplating the synthesis of gold nanocrystals directly functionalized with biological molecules. First, ethylene glycol is a toxic substance, being the primary constituent of automobile antifreeze solutions. Therefore, much of the potential utility of a nanocrystalline product with built-in biocompatibility would be lost due to the toxicity of the solvent, and an inordinate number of purification steps might be required to remove the viscous solvent. Second, the reaction must be carried out at temperatures above 100°C, a temperature range where most biological molecules undergo structural degradation. This thermally-induced denaturation could decrease the effectiveness of biological molecules as surface-protecting agents, resulting in decreased control over the nanocrystal morphologies.

In light of these considerations, I chose to pursue a modified version of the polyol method, using glycerin in place of ethylene glycol. Both ethylene glycol [(CH₂OH)₂] and glycerin [(CH₂OH)₂CHOH] are vicinal glycols in which each constituent carbon atom is bound to a hydroxyl group. Glycerin possesses one additional hydroxyl group per molecule when compared with ethylene glycol. Thus, considering equivalent reaction temperatures, glycerin will have a higher oxidation rate than ethylene glycol, and a greater number of electrons will be available for reduction. Alternatively stated, considering equivalent rates of oxidation, a reaction in glycerin can be carried out at a lower temperature than the same reaction in ethylene glycol. As a result, the use of glycerin for the reduction of chloroauric acid to atomic gold will allow us to access a lower range of reaction temperatures than is typically attainable using ethylene glycol.

This opens the possibility of forming gold nanocrystals in a temperature range that does not induce structural instability in biological molecules.

The use of glycerin also removes the previously-mentioned concerns about solvent toxicity. In contrast with the toxicity of ethylene glycol, glycerin is not only a biocompatible molecule, but is of paramount biological importance as a precursor to the formation of triglycerides. (66) Glycerin is ubiquitous in products used in our daily lives, being a common component in topical creams, gels, and soaps, as well as food items and various pharmaceutical preparations. Due to its biocompatibility, miscibility with water, and potentially desirable gelation properties, glycerin is one of the most robust choices available for preparing a biocompatible nanocomposite.

In this Chapter, I have employed a thorough transmission electron microscopy (TEM) analysis to explore the feasibility of using the polyol method to grow gold nanocrystals in the size range of 2–5 nm in the presence of a macromolecular protein. The polyol solution employed was glycerin, and the surface-protecting agent used was bovine serum albumin (BSA) protein. In addition to varying the relative concentrations of gold atoms and protein molecules, the effects of conducting the reaction below and above the denaturation temperature of the protein were also investigated. This work presents the first report of metallic nanocrystals formed by the polyol method and stabilized by macromolecular protein molecules.

2.2 EXPERIMENTAL PROCEDURE

Synthesis. Gold nanocrystals were synthesized by reducing in air chloroauric acid trihydrate ($\text{HAuCl}_4 \cdot 3\text{H}_2\text{O}$; 99.9+%; Aldrich) in 1,2,3-propanetriol (Glycerin; $\geq 99\%$; Fisher) in the presence of bovine serum albumin (BSA; Fraction V – heat shock treated; Fisher). An aqueous solution of ionic gold precursor was prepared by adding 1 g of $\text{HAuCl}_4 \cdot 3\text{H}_2\text{O}$ to 25 mL of deionized water. All materials were used without further

treatment. In a typical experiment, the desired amount of BSA protein was dissolved in 4 mL deionized water, then added to a round bottom flask containing 45 mL of glycerin under vigorous stirring. The resulting solution was heated in a mineral oil bath, and the solution temperature was allowed to stabilize at either 65°C or 90°C for at least one hour. Then, 1 mL of the ionic gold precursor solution (100 $\mu\text{mol Au}$) was added to the reaction vessel under vigorous stirring. For experiments conducted at 65°C, the reaction was allowed to proceed for 120 hours, while those conducted at 90°C were allowed to proceed for 60 hours. Solution temperature was maintained within $\pm 2.5^\circ\text{C}$ throughout the duration of each experiment. At the conclusion of the experiment, the flask was removed from the mineral oil bath and allowed to cool to room temperature.

Table 2.1: Reaction conditions for the various systems tested.

Temp. ($^\circ\text{C}$)	$\mu\text{mol BSA}$	[Au]:[BSA]
65	0.000	N/A
65	16.666	6:1
65	8.333	12:1
90	"	"
65	4.166	24:1
90	"	"
65	1.042	96:1
90	"	"

Table 2.1 summarizes the reaction conditions for each system tested. The third column of this chart indicates the molar ratios of gold atoms to protein molecules present in solution. All ratios are calculated on the basis of 100 μmol of Au added to the system (1 mL of a 0.1 M solution of chloroauric acid). For example, in the system where 16.666 μmol of BSA were added, the molar ratio is calculated as [100 $\mu\text{mol Au atoms}$]:[16.666

μmol BSA molecules], or 6:1. For convenience, throughout this chapter each system will be referenced by its molar ratio, for example “(6:1) Au:BSA.”

Characterization. Transmission electron microscopy (TEM) and weak beam dark field (WBDF) analysis were performed using a JEOL 2010F TEM equipped with Schottky-type field emission gun, ultra-high resolution pole piece ($C_s = 0.5$ mm), an Energy Dispersive X-ray spectrometer (EDS), and a scanning transmission electron microscope (STEM) unit with high angle annular dark field (HAADF) detector operating at 200 kV. Samples for TEM analysis were prepared by diluting the original reaction product with deionized water (a five-fold dilution by volume), then allowing a drop of the diluted solution to evaporate on a lacey carbon-coated copper TEM grid. The nanocrystals formed in each system were analyzed via EDS to confirm their elemental identity as gold.

2.3 RESULTS AND DISCUSSION

2.3.1 Reduction of Ionic Gold in the Absence of Surface-Protecting Molecules

Among globular proteins, serum albumin exhibits an uncommon degree of tolerance for elevated temperatures. By FDA regulation, commercially available human serum albumin preparations (and most bovine serum albumin preparations) are heated for at least 10 hours at $60 \pm 0.5^\circ\text{C}$ to deactivate any pathogens, and the serum albumin molecules retain their structural integrity after this treatment. (50) Thorough investigations of the heat-induced denaturation of human serum albumin have been undertaken by circular dichroism, as well as infrared and laser-Raman spectroscopy. (67,68) These studies concur that the onset of temperature-induced structural changes begins at about 62°C , with protein denaturation occurring at 75°C .

It would be desirable to produce BSA-protected gold nanocrystals below the protein denaturation temperature of 75°C . Since serum albumin maintains its structural

stability at 60°C, and the onset of heat-induced structural change is at 62°C, it was decided that a reasonable reaction temperature to study would be 65°C. This is a lower temperature than is typically employed for the synthesis of gold nanocrystals via the polyol method. (65) To test the feasibility of this approach, it was determined to first attempt the reduction of ionic gold in glycerin at 65°C, in the absence of BSA.

As mentioned in the experimental section, in the subsequent experiments in which BSA was employed, the protein was first dissolved in deionized water. This was done because the dissolution of the commercially-obtained, powder-like flakes of BSA was much more rapidly achieved in water, than when direct solvation of BSA in the much more viscous glycerin was attempted. Since water and glycerin are miscible, it was a simple matter to add the aqueous solution of dissolved protein to the glycerin. Now, the oxidation of glycerin can proceed by many pathways, some of which include dehydration of the molecule to form acetaldehyde and acrolein. (69) Therefore, we expect the addition of water to decrease the oxidation rate of glycerin and the reduction rate of ionic gold. Anticipating the addition of aqueous protein solution in subsequent reactions, and assuming that 4 mL of deionized water would be sufficient to dissolve the largest concentration of protein we might desire to investigate, a total of 5 mL water (4 mL in anticipation of the protein solution, and 1 mL from the ionic gold solution) were added to 45 mL of glycerin. Thus, the reaction system was 10% water by volume.

From visual observation of color changes in solution, the reduction occurred within less than 48 hours. The solution color changed from bright yellow immediately after the addition of the chloroauric acid, to clear and colorless with large golden aggregates visible in solution, indicating the formation of bulk gold. These aggregates were washed, dried and weighed, and found to constitute ~95% of the original mass of gold added to the system. The plastic-coated magnetic stirring bar, which was introduced

within the round bottom flask to provide agitation as the reaction proceeded, had a light coating of what appeared to be golden brown dust. The magnetic stirring bar was removed from solution, washed in water, and a TEM grid was prepared. As seen in Figure 2.1, several nanoscale structures were present.

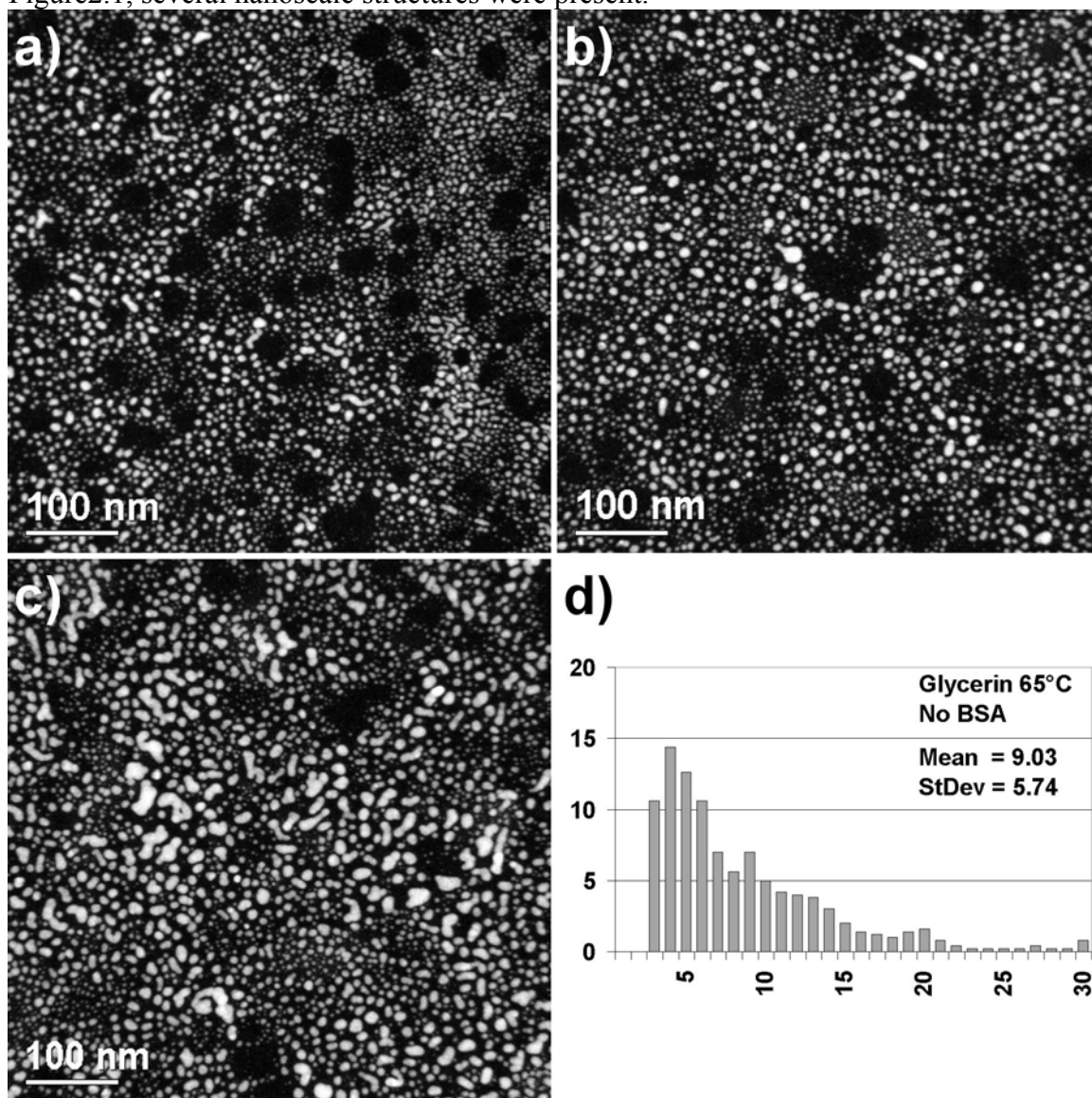


Figure 2.1: Reaction at 65°C in absence of BSA. (a) to (c) HAADF images of product obtained from stirring bar. (d) Size distribution, diameter in nanometers versus percentage frequency.

For this system, and for all systems discussed subsequently in this chapter (unless explicitly stated otherwise), size distributions were obtained from HAADF analysis by counting 500 individual nanocrystals at high magnification, such as those presented in Figure 2.2. For elongated and irregular crystals, the longest dimension was recorded. The nanocrystals produced by adsorption on the magnetic stirring bar surface exhibit a broad size distribution, with a standard deviation of more than 63%, indicating poorly protected crystals. Although nearly 25% of the gold nanocrystals obtained from the stirring bar were less than 5 nm in diameter, more than one-third were larger than 10 nm and exhibited a variety of irregular morphologies.

The nanocrystals greater than 5 nm in diameter also possess a great deal of structural strain. This is evident from the strain contrast in the HAADF images of Figure 2.2. Recall that HAADF images are formed by electrons that have undergone high angle scattering. (62) Therefore, any crystal feature that increases the amount of high-angle scattering can induce a change in contrast of the HAADF image. In the vicinity of crystal defects and strain fields, increased inelastic dispersion occurs as the electron beam encounters atoms that deviate from their ideal lattice positions. The resulting strain contrast is known as Huang-scattering contrast. (63) Referring to Figure 2.2, several crystals can be observed in which one region of the crystal possesses a different contrast. These correspond to strain fields within the crystal, and examples of these types of structures are circled in Figure 2.2b and c. Additionally, planar defects can be clearly delineated through Huang scattering contrast, appearing in the crystal as linear bands of alternating intensity. Examples of nanostructures with parallel planar twinning defects are circled in Figure 2.2a and d. The lattice strain present in these nanocrystals is also evident through conventional TEM analysis (Figure 2.3).

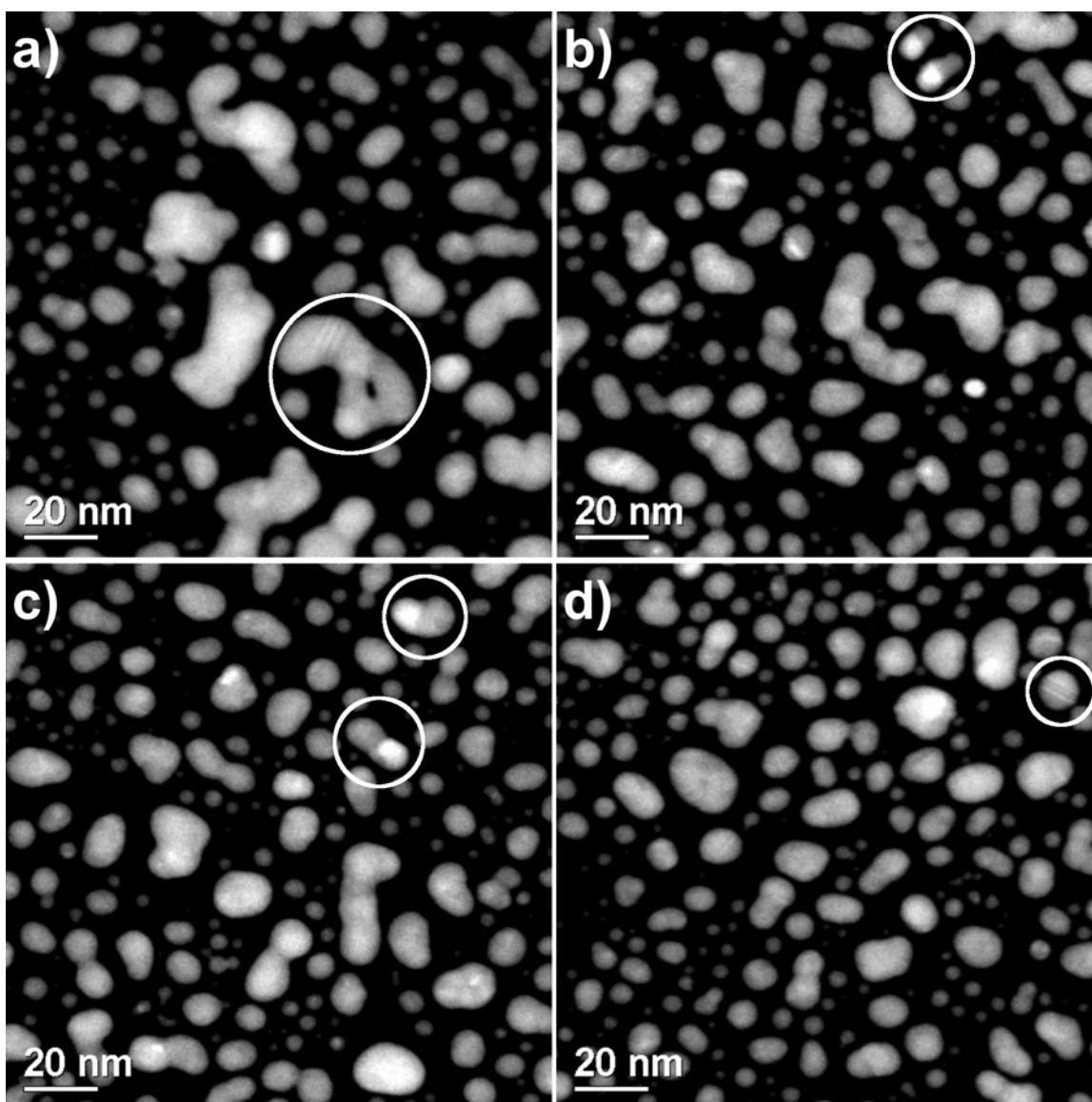


Figure 2.2: Reaction at 65°C in absence of BSA – high resolution HAADF images. Circled crystals in (a) and (d) exhibit contrast consistent with parallel planar twinning, while circled crystals in (b) and (c) exhibit strain field contrast.

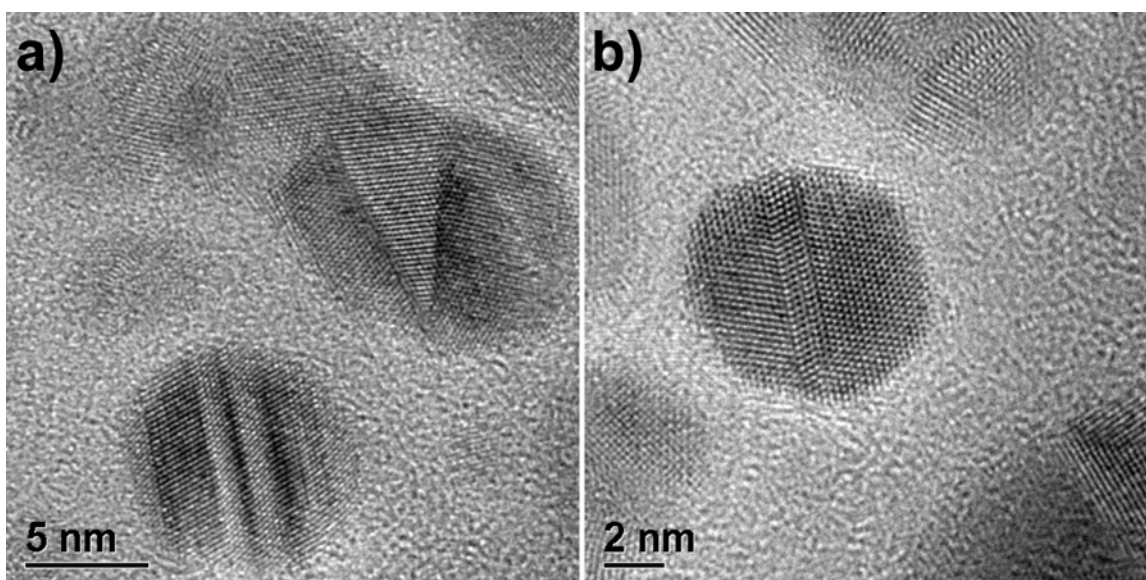


Figure 2.3: Reaction at 65°C in absence of BSA – conventional TEM images.

We can summarize these results as follows. First, reduction of ionic gold in glycerin at 65°C is possible, with a total reaction time of ~48 hours in the absence of BSA. Second, the vast majority of the product forms bulk gold, which is not surprising since a surface-stabilizing agent was not added. Third, adsorbed gold crystals in the sub-5 nm range are stabilized on the magnetic stirring bar. This is promising because the surface of a stirring bar is a poor stabilizing agent, so the introduction of even a moderately effective surface-protecting agent into this system could be sufficient to stabilize a large number of nanocrystals in the sub-5 nm range. Finally, nanocrystals of this size have extremely high surface energies, so it is not surprising that the majority of gold crystals adsorbed on the stirring bar have grown via coalescence into progressively larger structures. (33)

2.3.2 Formation of Gold Nanocrystals in the Presence of BSA at 65°C

Comparison of reaction times at 65°C

Since each reaction was completed in more than 24 hours, an imperceptibly slow rate of change in solution color was observed. Thus, the reaction time was determined as follows. A fully-reacted sample was placed in a round-bottom flask under vigorous stirring, directly next to the reaction vessel. The two vessels were compared at twelve hour intervals, and when the color and intensity of the reacting solution matched the previously-reacted sample, the reaction was considered completed. All reactions were performed in triplicate, so two measures of reaction time were obtained for each system.

The reaction times for each system will be treated separately in following sections, but the overall trend in measured reaction times at 65°C is presented graphically in Figure 2.4. Reaction time exhibited an exponential dependence on the concentration of BSA. According to the regression, the reaction time in the complete absence of BSA, but with 10% water content, should be ~44 hours. This is in agreement with the experimentally-observed time of ~48 hours.

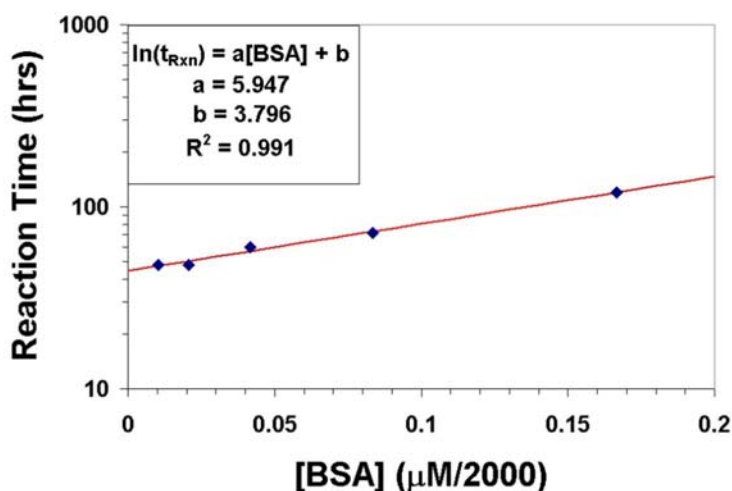


Figure 2.4: Reaction time at 65°C as a function of BSA concentration.

Comparison of solution appearance at 65°C

In addition to reaction time, the solution color was recorded at the conclusion of each reaction. In the (6:1) Au:BSA system, the final product developed a deep red-wine color, indicative of gold nanocrystals <20 nm in diameter. Upon dilution with water, the solution was transparent, indicating a solution of small nanocrystals, rather than a suspension of larger crystals. For the (12:1) Au:BSA system, the final product developed a deep violet color, indicating the presence of gold nanocrystals <5 nm in diameter. This solution was also observed to be transparent upon dilution with water. The final product in the (24:1) Au:BSA system developed a deep red-wine color, but with a strong violet tinge that was not observed in the (6:1) Au:BSA system. Again, the diluted solution was transparent. The color of the final product in the (96:1) Au:BSA system was a rusty burnt orange. Unlike the other systems explored at 65°C, this solution was not transparent upon dilution, but rather was translucent.

Figure 2.5 demonstrates the appearance of each system investigated at 65°C in reflected (Figure 2.5a) and transmitted (Figure 2.5b) light. The solutions were prepared by four-fold dilution of the as-synthesized product in deionized water. The light source for backlighting was a florescent lamp. The appearance of (6:1) Au:BSA (far left vial) and (12:1) Au:BSA (second from left) were unchanged in reflected or transmitted light, with solution colors of red-wine and violet, respectively. The solution color in reflected and transmitted light for (24:1) Au:BSA (third from left) was a violet-tinged red-wine. However, in transmitted light, a limited amount of iridescence was observed, adding a blue undertone to the solution. This is symptomatic of larger, anisotropic gold crystals, on the order of ~100 nm. Thus, it would seem that in addition to nanocrystals <20 nm in diameter, this system also has a limited number of ~100 nm gold crystals. Finally, the appearance of (96:1) Au:BSA (far right vial) was markedly different in reflected and

transmitted light. In reflected light (Figure 2.5a), the solution was translucent with a rusty burnt orange color. In transmitted light (Figure 2.5b), this solution was transparent with a light orange color, and a larger degree of iridescence was observed, giving the solution a brilliant blue-violet appearance. Again, this indicates the presence of ~ 100 nm anisotropic gold crystals, and the greater degree of iridescence suggests a greater quantity of large crystals than in the (24:1) Au:BSA system. I will now briefly summarize the results from each system studied at 65°C .

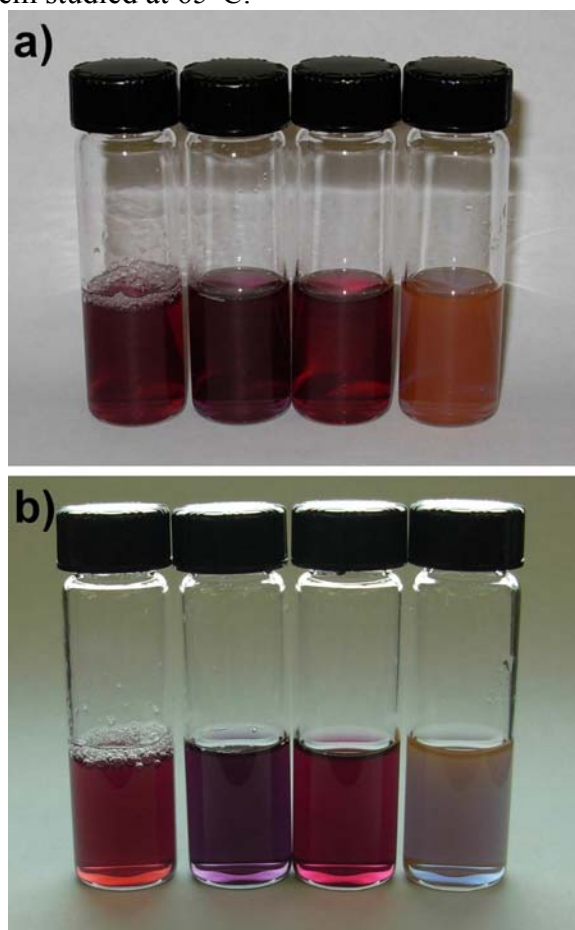


Figure 2.5: Color and clarity of each system studied at 65°C . The solutions were viewed in (a) reflected light and (b) transmitted light. In both (a) and (b), the vials from left to right contain (6:1) Au:BSA, (12:1) Au:BSA, (24:1) Au:BSA, and (96:1) Au:BSA.

(6:1) Au:BSA

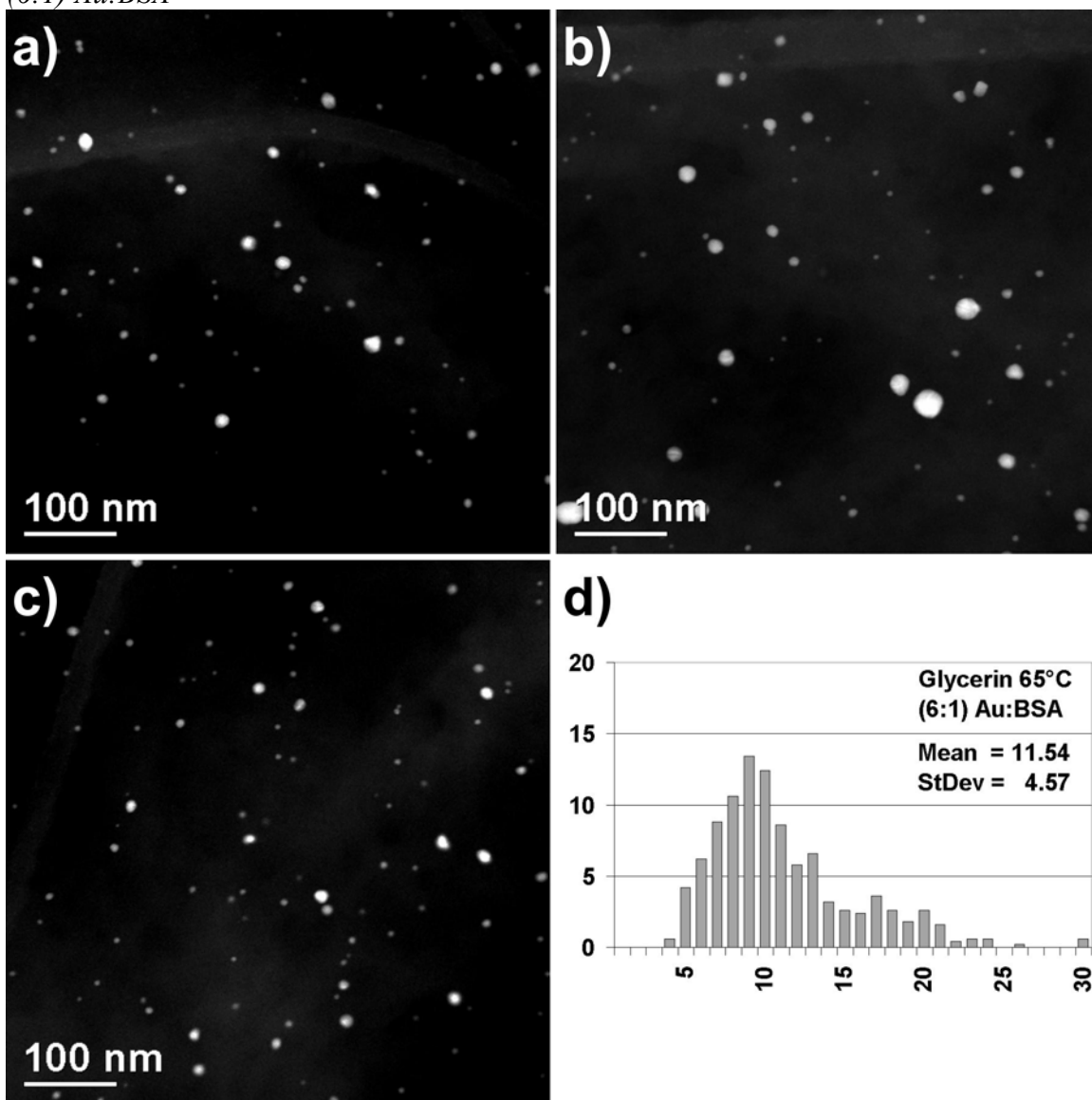


Figure 2.6: (6:1) Au:BSA at 65°C. (a) to (c) HAADF images. (d) Size distribution, diameter in nanometers versus percentage frequency.

Figure 2.6 presents an overview of the product at a molar ratio of (6:1) Au:BSA. Although nearly 44% of the product was smaller than 10 nm in diameter, the size distribution was still quite broad, with a standard deviation of nearly 40%. Additionally,

we note that in this system, and all other systems studied where BSA was added, no nanocrystals were adsorbed on the surface of the magnetic stirring bar.

The (6:1) Au:BSA reaction time was ~120 hours, 2.5 times longer than the system without BSA. However, recall that in the system with no BSA added, ~95% of the product consisted of bulk gold, whereas in the case of (6:1) Au:BSA, no bulk gold was formed. Indeed, no nanocrystals greater than 35 nm were found. Furthermore, no nanocrystals with highly tortuous, irregular morphologies were observed. This represents a vast improvement in the yield of nanoscale products, but when compared with other systems to be discussed in the following paragraphs, the size distribution for (6:1) Au:BSA is much broader, and the reaction time is inordinately long; therefore, further investigation of this reaction condition was not pursued.

(12:1) Au:BSA

Figure 2.7 provides an overview of (12:1) Au:BSA. This system represents a vast improvement over the previously-discussed (6:1) Au:BSA system in every regard. The reaction time was ~72 hours, a 40% decrease from the (6:1) Au:BSA system. The product uniformity obtained was outstanding, with a measured size distribution of 2.015 ± 0.212 nm, or a standard deviation of slightly more than 10%. This represented 98% of the observed nanocrystals. The remaining 2% of the product consisted of larger, rounded nanocrystals, such as the one visible in Figure 2.7b. Since so few of these larger crystals were encountered, it was not possible to count 500 for a distribution (the same will be true for the sub-population of large crystals discussed in each of the ensuing systems); from those crystals measured, their sizes ranged from 5–15 nm.

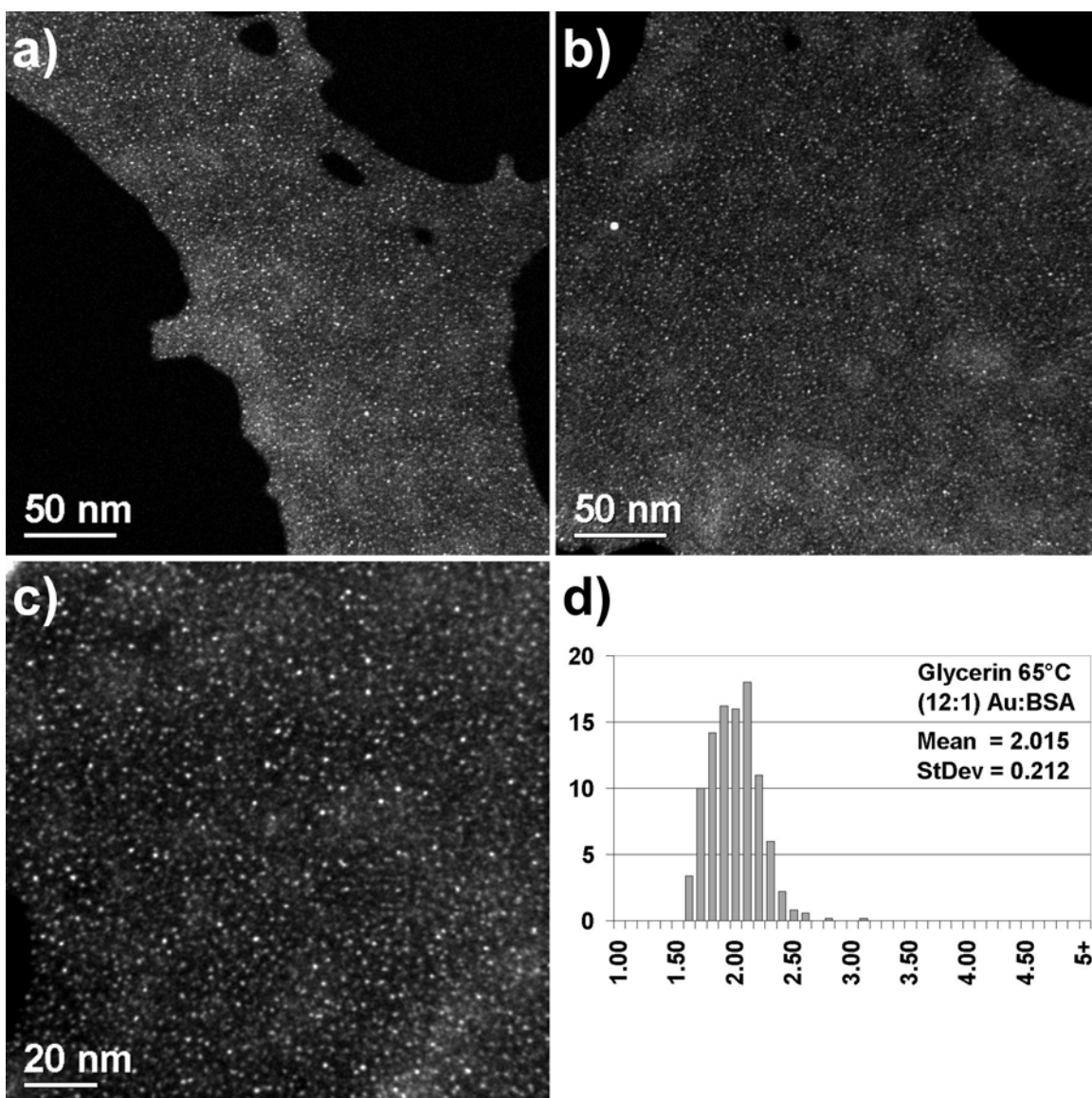


Figure 2.7: (12:1) Au:BSA at 65°C. (a) to (c) HAADF images. (d) Size distribution, diameter in nanometers versus percentage frequency.

The size difference between the ~ 2 nm crystals and the 5–15 nm crystals was small, and the larger crystals could have easily been included in the size distribution calculations. However, in systems to be discussed in ensuing paragraphs, a much greater difference exists between the smallest, nanometric scale crystals, and the largest crystals,

and they will be considered as distinct sub-populations. Therefore, to be consistent, the (12:1) Au:BSA system was also divided into two sub-populations: ~ 2 nm crystals, comprising 98% of the product, and 5–15 nm crystals, comprising 2 % of the product.

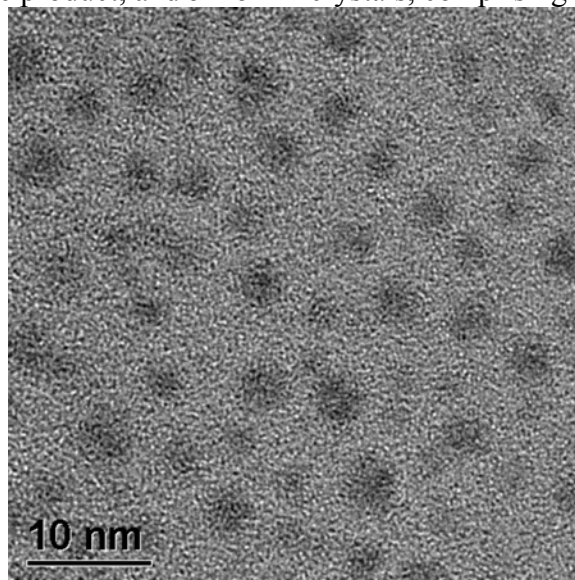


Figure 2.8: (12:1) Au:BSA at 65°C – conventional TEM analysis.

Due to the large excess of protein in this system, the thickness of the sample was too great to allow for high-resolution TEM (HRTEM) analysis. Figure 2.8 is an example of the conventional TEM images obtained from this system. The atomic structure of the nanocrystals was not discernible, as their atomic resolution was obscured by the enveloping protein. Indeed, it is not even clear where the edges of the individual nanocrystals terminate, making these images unsuitable for determining a size distribution. Comparison of this image with Figure 2.7 reveals the power of the HAADF technique for imaging small nanocrystals. Due to the Z^2 -contrast phenomenon discussed previously, it was possible to unambiguously observe the ~ 2 nm gold nanocrystals through HAADF imaging. In Figure 2.7, the film of protein molecules is composed of C, N, O, and S and appears as a faint gray cloudy background, while the gold nanocrystals

are the bright, round structures within the protein matrix. The black areas on the lower left and upper right corners of Figure 2.7a are holes in the protein film, regions where no sample is present.

(24:1) Au:BSA

Figure 2.9 provides an overview of (24:1) Au:BSA. The reaction time was 60 hours, versus 72 hours for the (12:1) Au:BSA system. The visible appearance of the final product solution was comparable to the (12:1) Au:BSA system, with one notable difference. The product was stored in glass vials, and it was found that after approximately one month of storage in solution at room temperature, a small amount of precipitation was observed at the bottom of the vial that had the appearance of fine metallic gold. The amount of precipitated material did not increase further after this initial precipitation event, and the size and structural distribution of the solvated product as observed by TEM did not change within a six month period of observation. We interpret this as the gravity-induced size separation of a larger fraction of gold crystals that were formed during the initial reaction period. Furthermore, we propose that these larger gold crystals were the cause of the iridescence observed previously in the optical transmittance of the sample (Figure 2.5b). Due to the viscosity of the glycerin solution, it is not surprising that larger crystals might take a number of weeks to precipitate.

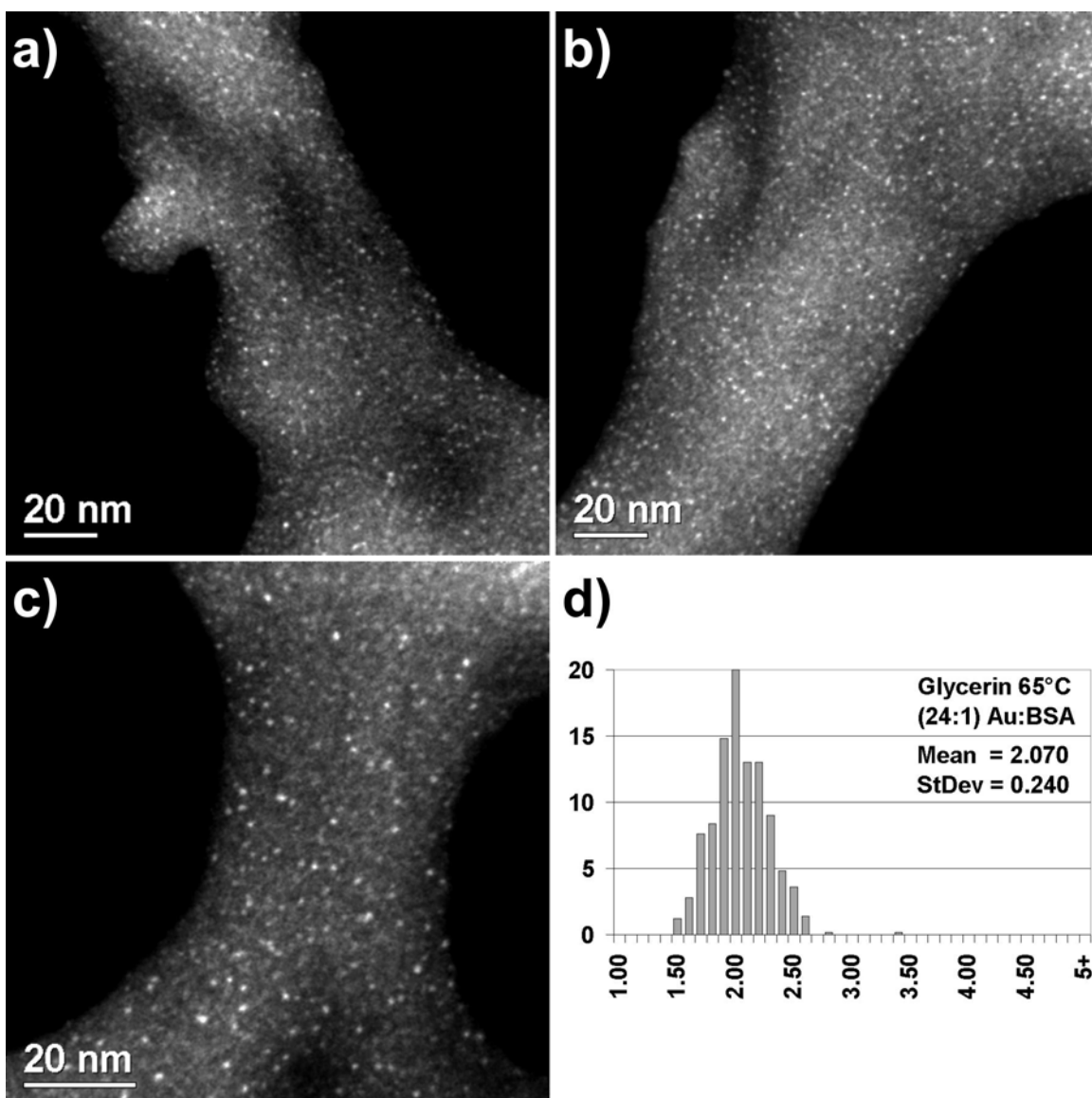


Figure 2.9: (24:1) Au:BSA at 65°C – nanometric crystals. (a) to (c) HAADF images. (d) Size distribution, diameter in nanometers versus percentage frequency.

The measured distribution of the nanometric-scale crystals was 2.070 ± 0.240 nm, representing a deviation of less than 12%, which compares favorably with the (12:1) Au:BSA system. The remainder of the product consisted of much larger crystals, with dimensions on the order of 100–150 nm. If one simply considers the number of large

crystals versus the number of ~ 2 nm crystals present in the sample, the ~ 2 nm crystals represents over 99% of all structures observed, and the larger crystals would constitute less than 1%. However, if considered as a percentage of the total mass of gold present in the sample, the amount of gold present as 100–150 nm crystals would be larger than 1%. In fact, the mass fraction of gold present in the two sub-populations was roughly approximated by calculating the average number of ~ 2 nm nanocrystals and large crystals observed per square micron in HAADF images, estimating the average volume of a ~ 2 nm nanocrystal as a sphere of radius 1 nm, and the average volume of a large crystal as the volume of a decahedron with edge length 90 nm. Based on these approximations, $\sim 94\%$ of the gold by mass is present as ~ 2 nm nanocrystals, and $\sim 6\%$ is present as 100–150 nm crystals. Although rudimentary, this approach gives us a means to estimate the yield of small (2–5 nm) nanocrystals in the (24:1) Au:BSA system.

The 100–150 nm crystals were anisotropic structures, with faceted surfaces and well-defined shapes (Figure 2.10). If these larger crystals were forming as the result of some structural instability in the initially-formed ~ 2 nm crystals, one would expect the growth to proceed by a process of aggregation and coalescence. In the absence of sufficient thermal energy to anneal them into equilibrium shapes, the larger crystals would possess polycrystalline structures with poorly defined morphologies. The fact that faceted crystals with well-defined shapes are observed supports our hypothesis that the larger gold crystals were formed during the initial reaction period. This is not at all surprising, as the reaction is strongly thermodynamically-driven, which favors the formation of larger, stable, faceted crystals.

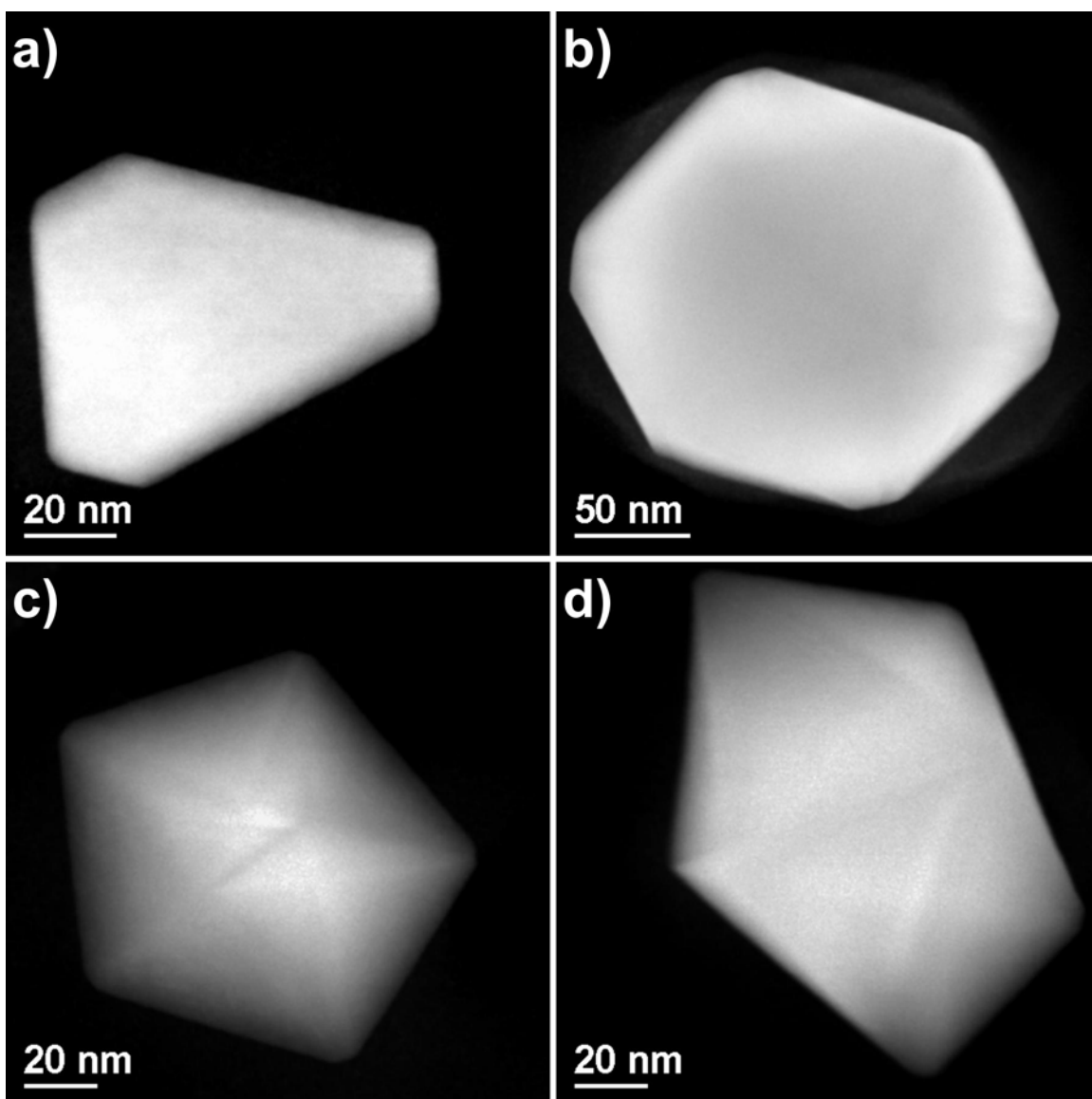


Figure 2.10: (24:1) Au:BSA at 65°C – HAAADF images of large crystals. Truncated (a) triangular and (b) hexagonal platelets. (c) and (d) Decahedral crystals, in which the fivefold symmetric twinned structure is clearly observed.

Two distinct classes of crystal morphologies were observed: (i) two-dimensional platelets, and (ii) multiple-twinned crystals with fivefold symmetry. Both classes of anisotropic morphologies are commonly observed in gold nanocrystal synthesis, and are the result of planar twinning and cyclic twinning, respectively. Below, I will provide a

brief description of how these structures arise; for a thorough treatment of the role of twinning in the formation of anisotropic noble metal nanocrystals, please refer to the work of Elechiguerra *et al.* (70)

Recall that because HAADF images are formed by electrons that have undergone high angle scattering, any crystal feature that increases the amount of high-angle scattering can induce a change in contrast of the HAADF image. As the electron beam travels through thicker regions of a specimen and interfere with more atoms, the probability for high angle scattering increases. Therefore, thicker regions will have brighter contrast. In Figure 2.10a-b, we observe a constant signal intensity, which indicates there is no variation in the thickness of these crystals, and they are in fact two-dimensional structures. Due to the low stacking fault energy of gold, planar twinning between the [111] type close-packed planes is a common occurrence. (71) Gold platelets resulting from planar twinning typically exhibit a hexagonal profile due to the hexagonal symmetry of the FCC close-packed planes from which they originate (Figure 2.10b). The introduction of a twin plane causes the edges of the hexagonal prism to terminate in alternating concave (A-type) and convex (B-type) {111} faces (Figure 2.11). An extra atom added to a B-type surface will be inherently unstable due to a limited number of nearest neighbors, and will tend to re-dissolve into solution, while an atom added to an A-type surface will be stabilized by the presence of additional nearest neighbors. As a result, the A-type surfaces are fast-growth surfaces, and in this manner a hexagonal platelet can give rise to a triangular platelet (Figure 2.10a).

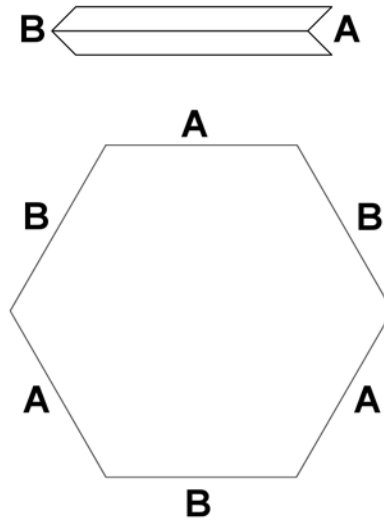


Figure 2.11: Growth model for an FCC-type platelet resulting from planar twinning, adapted from (71). The upper cartoon is a lateral view that illustrates how the twin plane gives rise to concave (A-type) and convex (B-type) faces. The lower cartoon is a frontal view, which shows the alternating A- and B-type faces along the perimeter of the hexagonal platelet.

Due to its low twinning energy, gold also readily undergoes cyclic twinning, resulting in the formation of decahedral crystals (Figure 2.10c and d). (72) The multiple-twinned structure of these nanocrystals is a direct result of their fivefold symmetry. (73) It is not possible to fill space by joining five perfect tetrahedra to form a center with fivefold rotational symmetry, because a gap of $\sim 7.5^\circ$ remains between the final two tetrahedral units (Figure 2.12). (74) When crystals possessing fivefold symmetry are formed, such as the decahedron, defects must be introduced at the tetrahedral boundaries to accommodate the structure. (75) Thus, the structure of an FCC decahedron can be understood as five tetrahedral, monocrystalline domains, joined by a fivefold array of cyclic twinning.

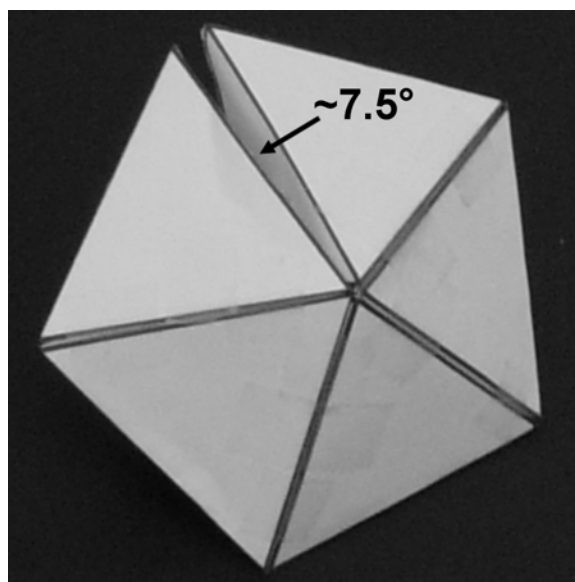


Figure 2.12: Model of five perfect tetrahedra joined at a common axis. The five tetrahedra cannot fill space, as a gap of $\sim 7.5^\circ$ remains between the final two tetrahedral units.

(96:1) Au:BSA

Figure 2.13 provides an overview of the (96:1) Au:BSA system. The observed reaction time was 48 hours, a 20% decrease from the (24:1) Au:BSA system. As noted previously, the final product had a rusty burnt-orange color, and golden flakes were visibly observed in suspension. After one month of storage in solution at room temperature, a fine gold precipitant was observed. The amount of precipitant appeared to be more than in the (24:1) Au:BSA system.

The measured size distribution of the nanometric-scale crystals was 3.345 ± 0.561 nm, representing a standard deviation of slightly less than 17%. Although this is greater than both the $\sim 10\%$ deviation in the (12:1) Au:BSA system and the $\sim 12\%$ deviation in the (24:1) Au:BSA system, it is still less than the 20% deviation generally considered as an upper bound on an acceptable percentage deviation for nanocrystals in this size range. The average diameter of nanometric-size crystals in this system is more than fifty percent

greater than the average diameter in the (24:1) Au:BSA system. Due to a lower concentration of BSA, fewer of the initially-formed gold nuclei are stabilized by protein molecules, and with fewer protein-stabilized nuclei present, each nucleus grows to a larger average size. When moving from (96:1) Au:BSA to (24:1) Au:BSA, if we assume that by adding four times as much BSA, four times as many nuclei will be stabilized, we would expect that for a given amount of gold atoms, the volume of the resulting nanometric-sized crystals at (24:1) Au:BSA would be one-fourth the volume of those at (96:1) Au:BSA. In fact, using the experimentally-determined average nanocrystal diameters, and assuming spherical volumes for simplicity, we find the nanocrystal volume ratio is 0.237.

This nanometric-scale portion of the Au (96:1) system represented well over 99% of the total population by number. The remainder of the product consisted of larger anisotropic crystals with dimensions on the order of 150–200 nm, possessing faceted surfaces and well-defined shapes, much as was the case in the (24:1) Au:BSA system. The mass fraction of gold present in the two sub-populations was roughly approximated by calculating the average number of crystals observed per square micron, and estimating an average crystal volume for each sub-population. In this case, the approximate yield was determined to be ~82% of the gold by mass present as ~3.35 nm nanocrystals, and ~18% present as large, faceted crystals. Comparing this with the (24:1) Au:BSA system, by adding one-fourth as much BSA we increase the mass percentage of gold present as large crystals by an approximate factor of three.

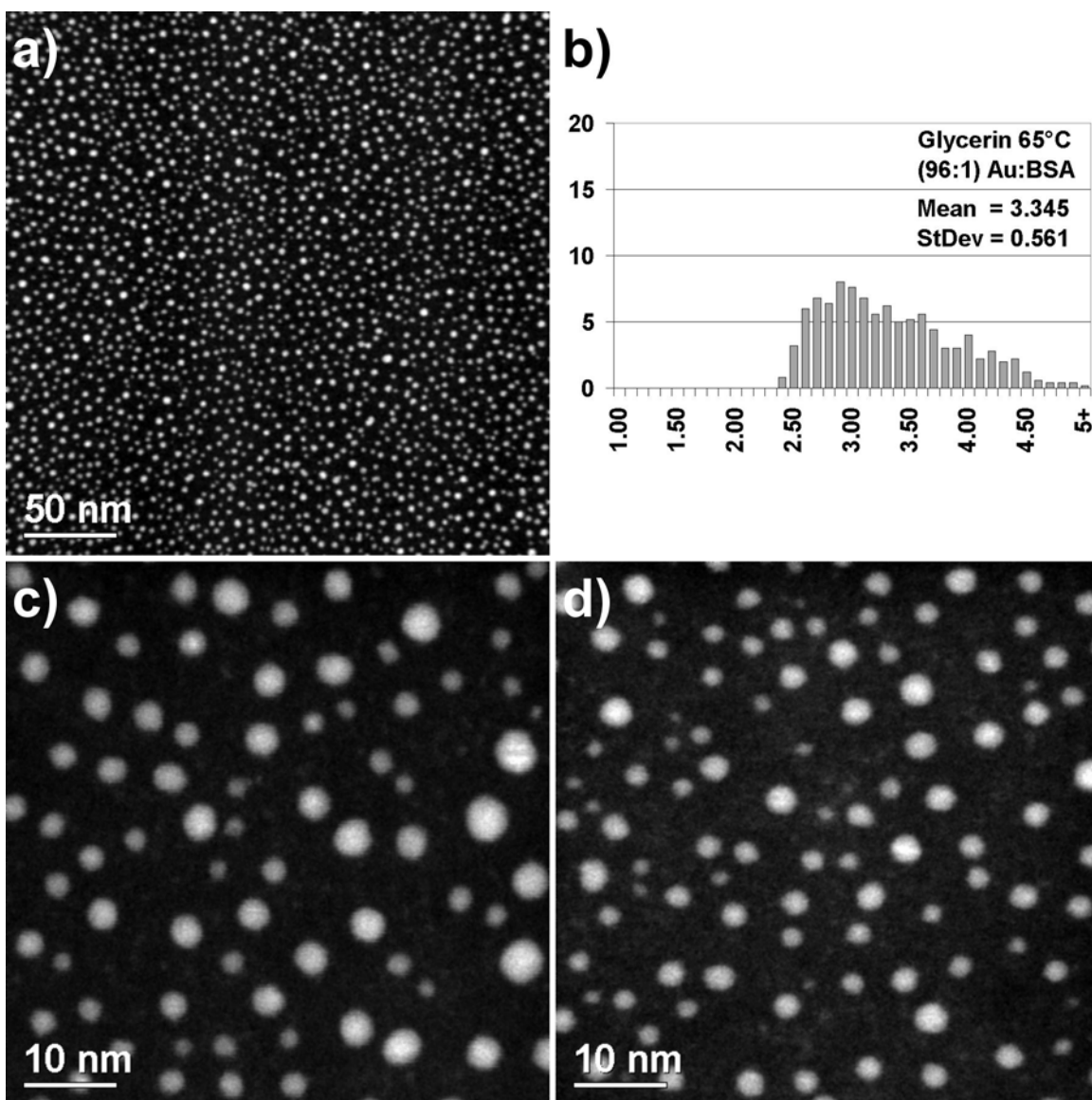


Figure 2.13: (96:1) Au:BSA at 65°C – nanometric crystals. (a), (c), and (d) HAADF images. (b) Size distribution, diameter in nanometers versus percentage frequency.

Due to the smaller amount of protein in this system, samples prepared for TEM analysis were sufficiently thin to allow for HRTEM analysis of the nanometric-scale crystals. Figure 2.14 presents HRTEM images characteristic of the ~3 nm crystals present in this system. In this size range, the most stable gold nanocrystal morphologies

are multiple-twinned crystals with fivefold symmetry (decahedral and icosahedral), as well as FCC single crystals (typically cuboctahedral). Both classes of nanocrystals are found in this system.

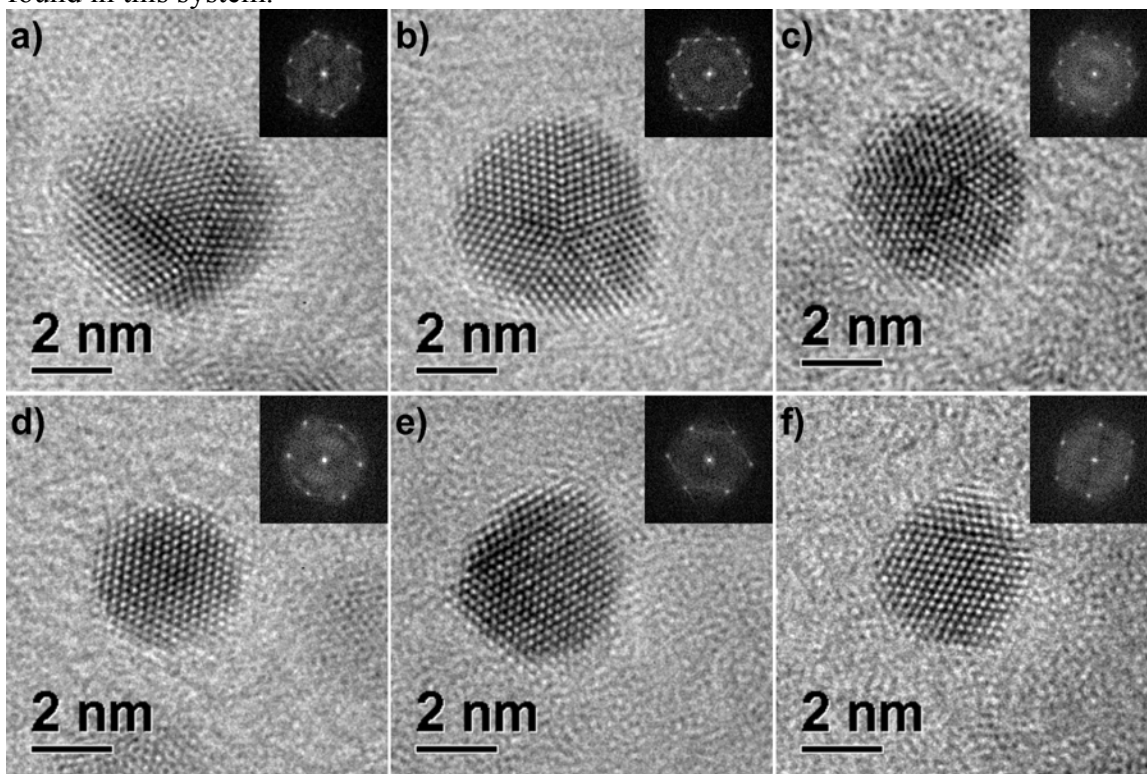


Figure 2.14: (96:1) Au:BSA at 65°C – HRTEM images. (a) to (c), Multiple-twinned crystals with fivefold symmetry. (d) to (f) FCC single crystals. The fast Fourier transform (FFT) of each image is included as an inset.

Two distinct classes of morphologies were observed for the larger crystals: multiple-twinned crystals with fivefold symmetry (decahedrons and nanowires with pentagonal cross-section, as in Figure 2.15), and two-dimensional platelets (triangular platelets and wire-like platelets, as in Figure 2.16). The formation of wire-like platelets (Figure 2.16a-d) can readily be interpreted in terms of Figure 2.11. If a second twinning event occurs that prevents growth of one of the fast-growing A-type faces, the hexagonal

nucleus will be limited to growth on the remaining two A-type faces, resulting in the formation of a wire-like platelet.

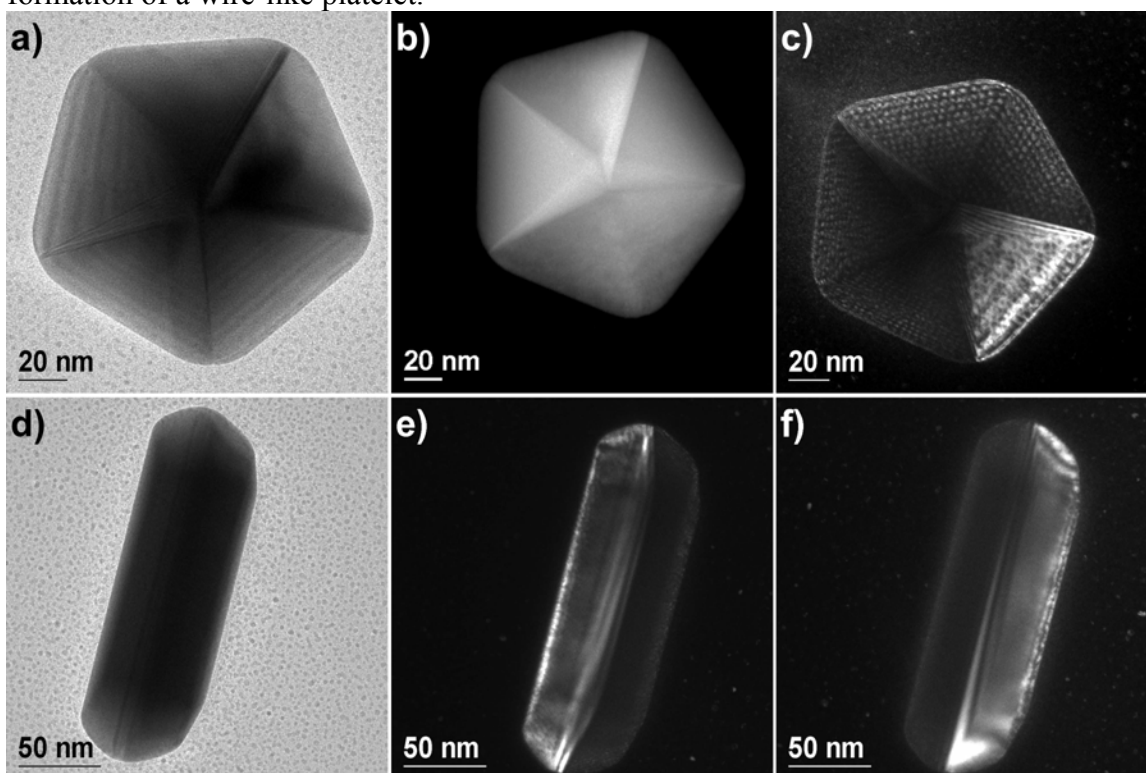


Figure 2.15: (96:1) Au:BSA at 65°C – large crystals resulting from cyclic twinning. (a) to (c) Decahedron imaged by (a) conventional TEM, (b) HAADF, and (c) WBDF. (d) to (f) Nanowire with pentagonal cross-section imaged by (d) conventional TEM, and (e), (f) WBDF.

The two most-commonly observed crystallographic habits were decahedrons and triangular platelets. Interestingly, when compared with the (24:1) Au:BSA system, few hexagonal platelets were observed, and many more triangular platelets were present. As mentioned previously, the edges of a hexagonal nucleus will preferentially grow along the A-type faces, producing a triangular platelet if a sufficient supply of atoms is present in solution. The presence of hexagonal platelets in a reaction product indicates the supply of atoms in solution was exhausted before triangular platelets could form. (71)

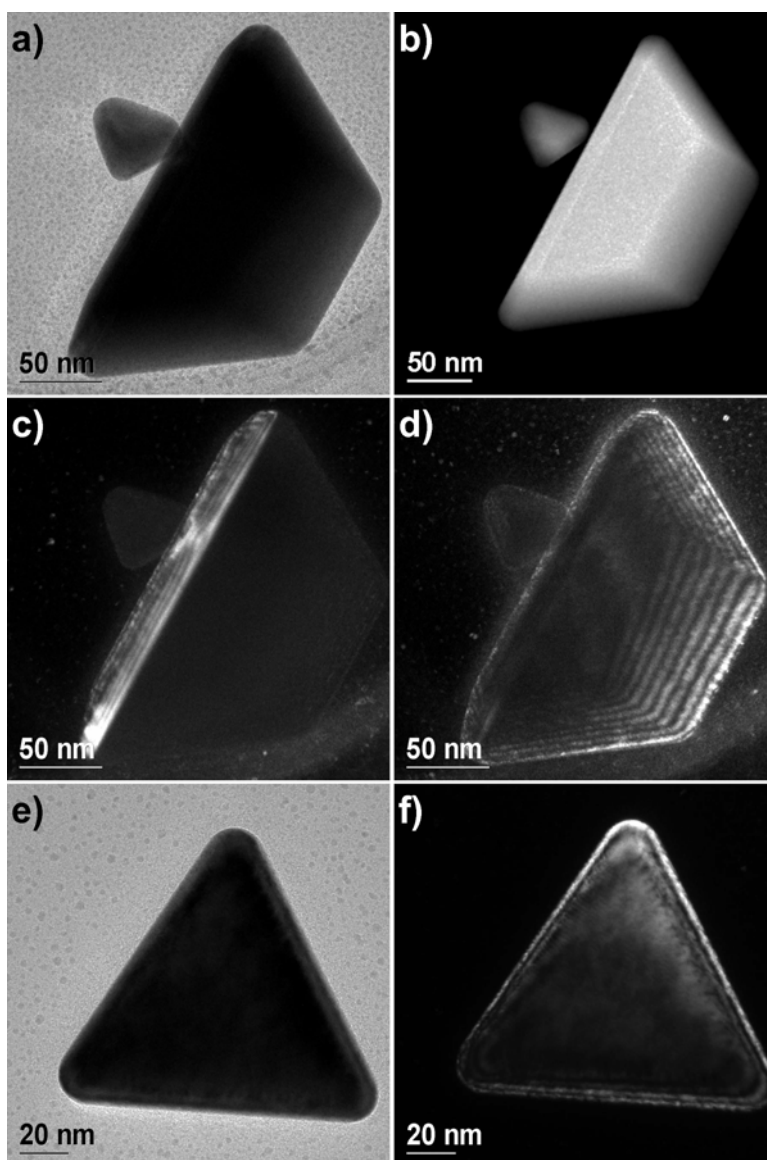


Figure 2.16: (96:1) Au:BSA at 65°C – large crystals resulting from planar twinning. (a) to (d) Wire-like platelet imaged by (a) conventional TEM, (b) HAADF, and (c), (d) WBDF. (e) and (f) Triangular platelet imaged by (e) conventional TEM, and (f) WBDF.

In the context of our systems, the presence of hexagonal platelets in the (24:1) Au:BSA system, and their large absence in the (96:1) Au:BSA system, indicates that fewer gold atoms were available for growth of large platelets in the (24:1) Au:BSA

system. Alternatively, we can say that more of the gold atoms in the (24:1) Au:BSA system were present as protein-stabilized nanocrystals in the ~ 2 nm size range, and a smaller percentage of gold was present as larger crystals. This is in agreement with our previous observations.

Summary of the systems investigated at 65°C

The results at 65°C can be summarized as follows. Adding more BSA provides more protection for the initially-formed nuclei, resulting in more primary nanocrystals being stabilized, but more BSA also decreases the rate of reaction. For reaction times greater than ~ 72 hours, substantially fewer nuclei are formed, causing each nucleus to grow to a larger average size. Due to the dimensional constraints of BSA, the protein molecule will no longer be able to effectively protect nanocrystals as they grow beyond a critical average size, resulting in less well-controlled subsequent growth and a broader size distribution with non-uniform morphologies, as seen in the (6:1) Au:BSA system. For all other Au:BSA ratios studied, the rate of reaction is sufficient to promote the growth of more nuclei, and BSA is effective at protecting the nanometric-scale crystals. However, as the concentration of BSA is decreased, there is not a sufficient excess of protein molecules to protect all of the gold nuclei formed. As the reaction is strongly thermodynamically driven, the unprotected nuclei grow into stable, faceted nanocrystals with well-defined morphologies. It should be noted that these larger faceted crystals are easily size-separated from the remainder of the nanometric-scale crystals, and thus a highly uniform dispersion of gold nanocrystals on the order of 2–5 nm is in fact attainable at 65°C.

2.3.3 Formation of Gold Nanocrystals in the Presence of BSA at 95°C

Recalling the (12:1) Au:BSA system at 65°C, it was noted that nearly the entire final product consisted of ~ 2 nm nanocrystals. The number of gold atoms in a

nanocrystal of diameter D can be estimated from a spherical volume, using the density of bulk FCC gold:

$$N_{Au} = \left(59.07 \frac{\text{atoms}}{\text{nm}^3} \right) \frac{\pi}{6} (D)^3 \quad (2.1)$$

Thus, a gold nanocrystal of 2 nm in diameter consists of ~245 gold atoms. In terms of the (12:1) Au:BSA system, there are 20 BSA molecules present for every ~2 nm nanocrystal. Due to the structural dimensions of BSA (18.9 x 9.6 x 3.9 nm), it is improbable that twenty BSA molecules are interfaced with each ~2 nm nanocrystal. Rather, it appears that with the thermodynamically-driven conditions, formation of large, faceted crystals is highly favored, and a large excess of protein is necessary to protect the gold nuclei as they form, and prevent growth beyond the ~2 nm size range.

Higher reaction temperatures will bring about a greater oxidation rate for glycerin, a more rapid reduction of gold atoms, and ultimately a more kinetically-driven reaction. This could result in the formation of fewer large, faceted crystals, and a higher yield of 2–5 nm nanocrystals. Unfortunately, the use of a biomolecule as surface-protecting agent constrains us in the potential temperatures we can pursue. The reactions conducted at 65°C were below the temperature where thermally-induced denaturation of BSA protein occurs. Protein denaturation in reactions conducted above 75°C could decrease the efficacy of BSA in protecting ~2 nm nanocrystals, resulting in less-well controlled morphologies, and prolonged boiling can induce BSA to form a gel. I undertook to study the effects of conducting our experiments above the denaturation temperature of BSA by pursuing a second series of reactions at 95°C.

(12:1) Au:BSA

Figure 2.17 provides an overview of the (12:1) Au:BSA system at 95°C. The reaction time was ~36 hours, a 25% decrease from the most rapid reaction studied at 65°C, and a 50% decrease when compared with the (12:1) Au:BSA system at 65°C. The

measured size distribution of the nanometric-scale crystals was 2.626 ± 0.424 nm, or a standard deviation of slightly more than 16%. This represented 94% of the observed product. The remaining 6% of the product consisted of larger, rounded nanocrystals, with diameters in the range of 10–30 nm (Figure 2.18).

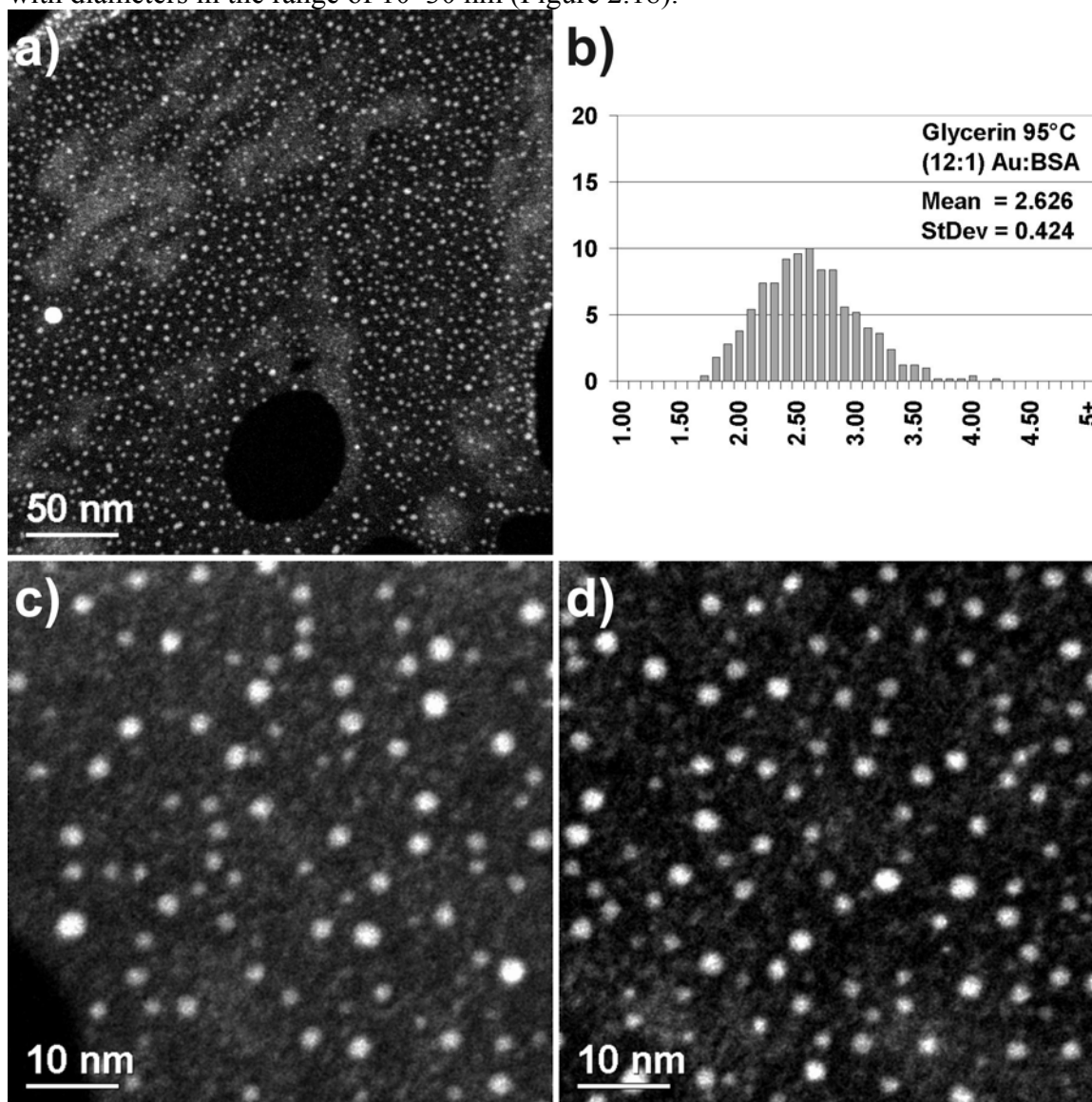


Figure 2.17: (12:1) Au:BSA at 95°C – nanometric crystals. (a), (c)-(d) HAADF images. (b) Size distribution, diameter in nanometers versus percentage frequency.

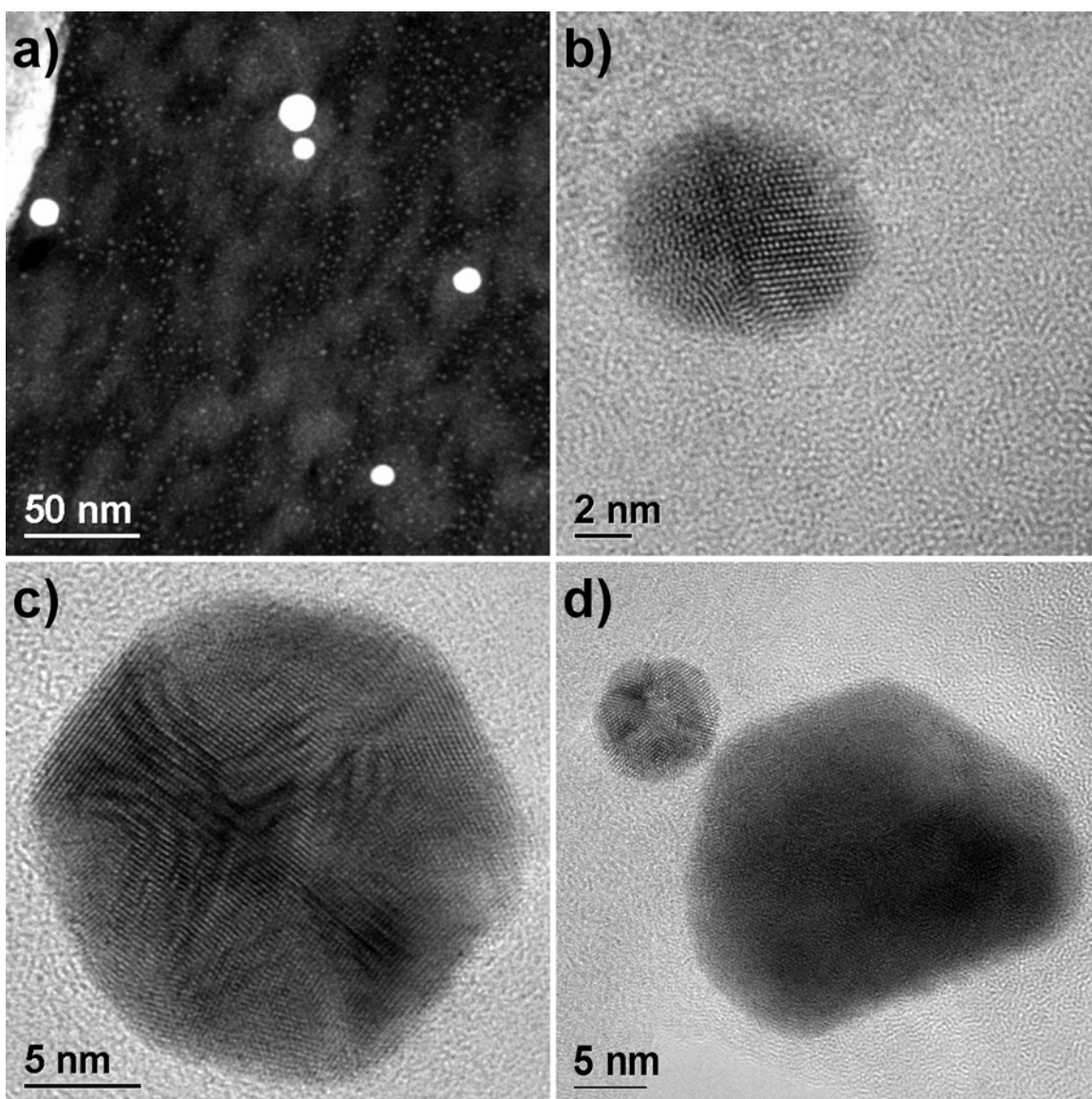


Figure 2.18: (12:1) Au:BSA at 95°C – large crystals. (a) HAADF, (b)-(d) TEM images.

In comparison with (96:1) Au:BSA, the most rapid reaction studied at 65°C, this system provides a greater yield of nanometric-scale crystals, with ~20% smaller average diameter and a comparable percent deviation, in 25% less reaction time. However, the major drawback is that in this system, the 10–30 nm crystals do not separate by gravity,

whereas in the (96:1) Au:BSA system at 65°C, a sample containing solely the nanometric-scale product is easily attainable.

(24:1) Au:BSA

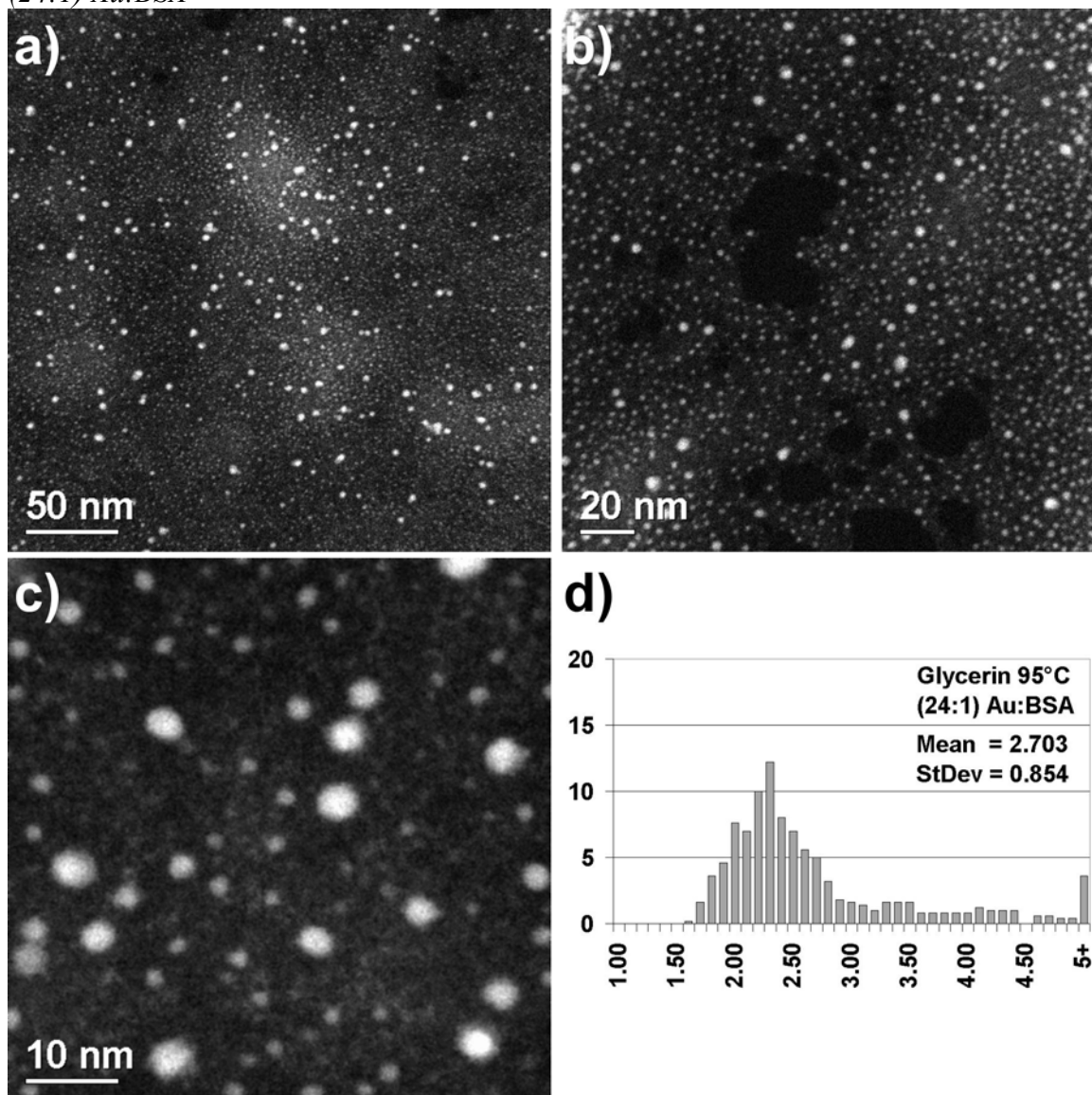


Figure 2.19: (24:1) Au:BSA at 95°C – nanometric crystals. (a)-(c) HAADF images. (d) Size distribution, diameter in nanometers versus percentage frequency.

Figure 2.19 provides an overview of (24:1) Au:BSA at 95°C. The reaction time was ~36 hours, as observed for the (12:1) Au:BSA system at 95°C. The measured size

60

distribution of the nanometric-scale crystals was 2.703 ± 0.854 nm, or a standard deviation of nearly 32%. This is nearly three times greater than the percent deviation observed for this system at 65°C. The other sub-population consisted of decahedra and triangular platelets with dimensions in the range of 30–100 nm (Figure 2.20).

The anisotropic crystals obtained in this system are approximately half the size of those obtained in the (24:1) Au:BSA system at 65°C (Figure 2.10). Additionally, note that the corners on the triangular platelet appear rounded. It is common for the corners of faceted nanocrystals produced under more kinetically-driven conditions to terminate in terraced steps, and these surface steps give the corners a rounded appearance. (76,77)

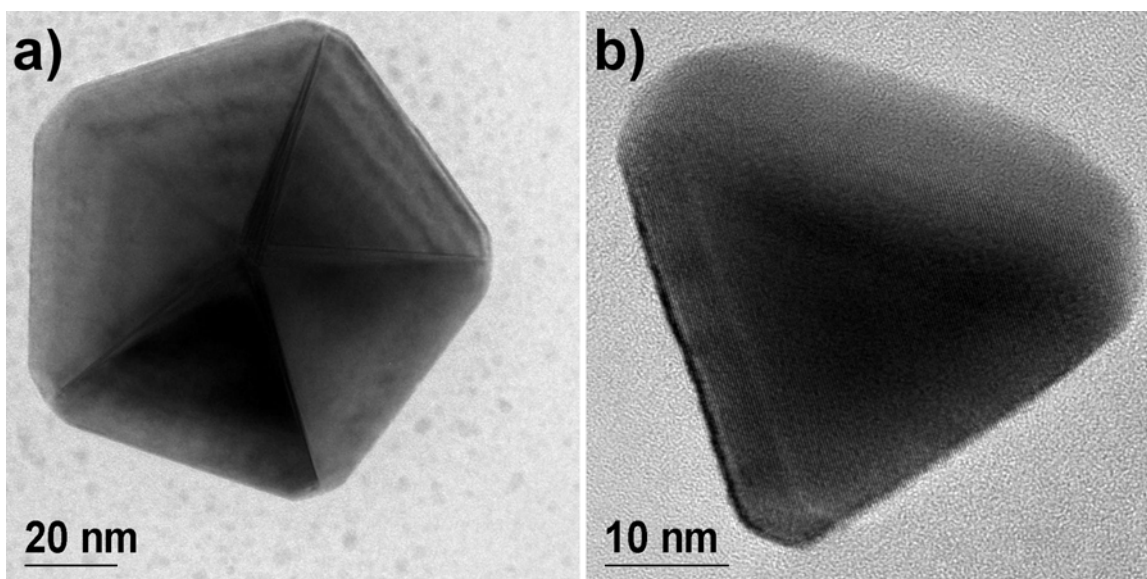


Figure 2.20: (24:1) Au:BSA at 95°C – large crystals. TEM images of (a) decahedral crystal and (b) triangular platelet.

The most common anisotropic crystals observed in this system, and indeed in most of the systems studied where faceted crystals were formed, were decahedral, resulting from cyclic twinning, and triangular platelets, resulting from planar twinning. When a decahedral crystal lies flat on the substrate, the fivefold twin axis is nearly

parallel to the electron beam and the fivefold symmetric twinned structure is clearly observed, as demonstrated previously (e.g. Figure 2.10c, Figure 2.15a-c, Figure 2.20a). However, when a triangular platelet lies flat on the substrate, the electron beam is orthogonal to the twin planes, and the planar defects that give rise to the two-dimensional structure are not clearly observed (e.g. Figure 2.16e-f). In the course of analyzing this system, a triangular platelet was found on edge, presented in Figure 2.21, which provides an excellent opportunity to demonstrate the planar twinning that gives rise to this type of structure. The planar twins are evident to a limited extent along the exposed edge in the conventional TEM image (Figure 2.21a). However, from the TEM image alone, it is not clear if these defects extend throughout the entire body of the crystal. To demonstrate this, we turn to the weak beam dark field (WBDF) technique.

For WBDF, a diffraction-contrast image is formed by tilting the sample out of the Bragg condition to increase inelastic scattering. In the vicinity of a defect, lattice distortions cause the crystallographic planes to be locally tilted back to the Bragg condition, so defects are clearly delineated. (56) In Figure 2.21c, the bright bands extending about the edges of the platelet represent twin planes present within the crystal. In Figure 2.21d, one specific twin plane is illuminated, providing visible confirmation that the twin plane does indeed extend throughout the body of the crystal.

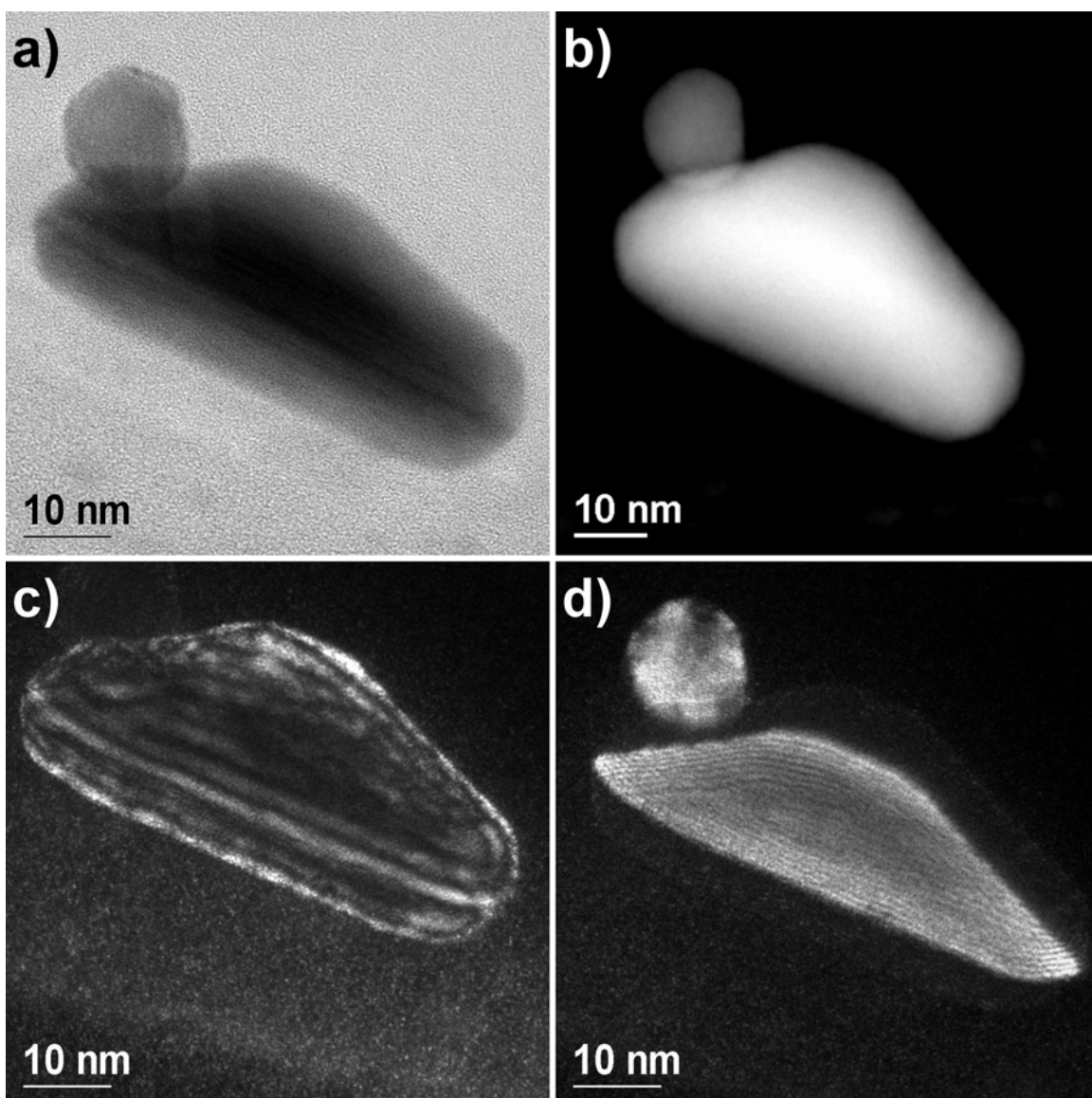


Figure 2.21: Electron microscopy of a gold triangular platelet oriented on edge. (a) conventional TEM, (b) HAADF, and (c)-(d) WBDF images.

(96:1) Au:BSA

Figure 2.22 provides an overview of the (96:1) Au:BSA system at 95°C. The reaction time was ~36 hours, as observed for the other two systems at 95°C. Several of the nanometric-scale crystals in this sample exhibited an elongated structure. Measured

along the longest direction of each crystal, the size distribution was calculated as 3.283 ± 0.992 nm, and the average aspect ratio was 1.289.

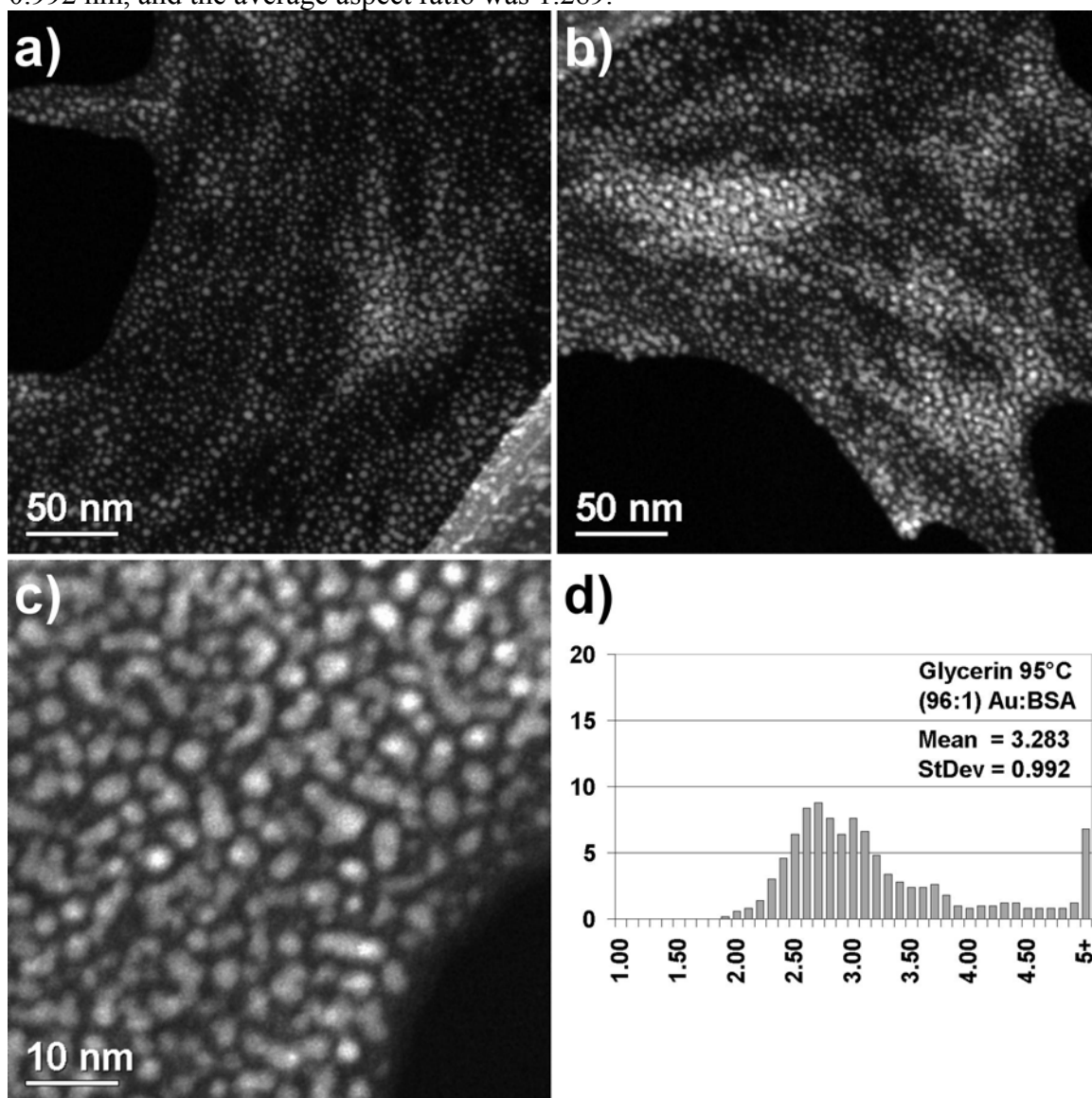


Figure 2.22: (96:1) Au:BSA at 95°C – nanometric crystals. (a)-(c) HAADF images. (d) Size distribution, diameter in nanometers versus percentage frequency.

The larger sub-population of this product consisted of decahedra and triangular platelets with dimensions in the range of 30–60 nm (Figure 2.23). The visibly rounded

edges on these larger crystals are consistent with formation under more kinetically-driven conditions than were encountered at 65°C.

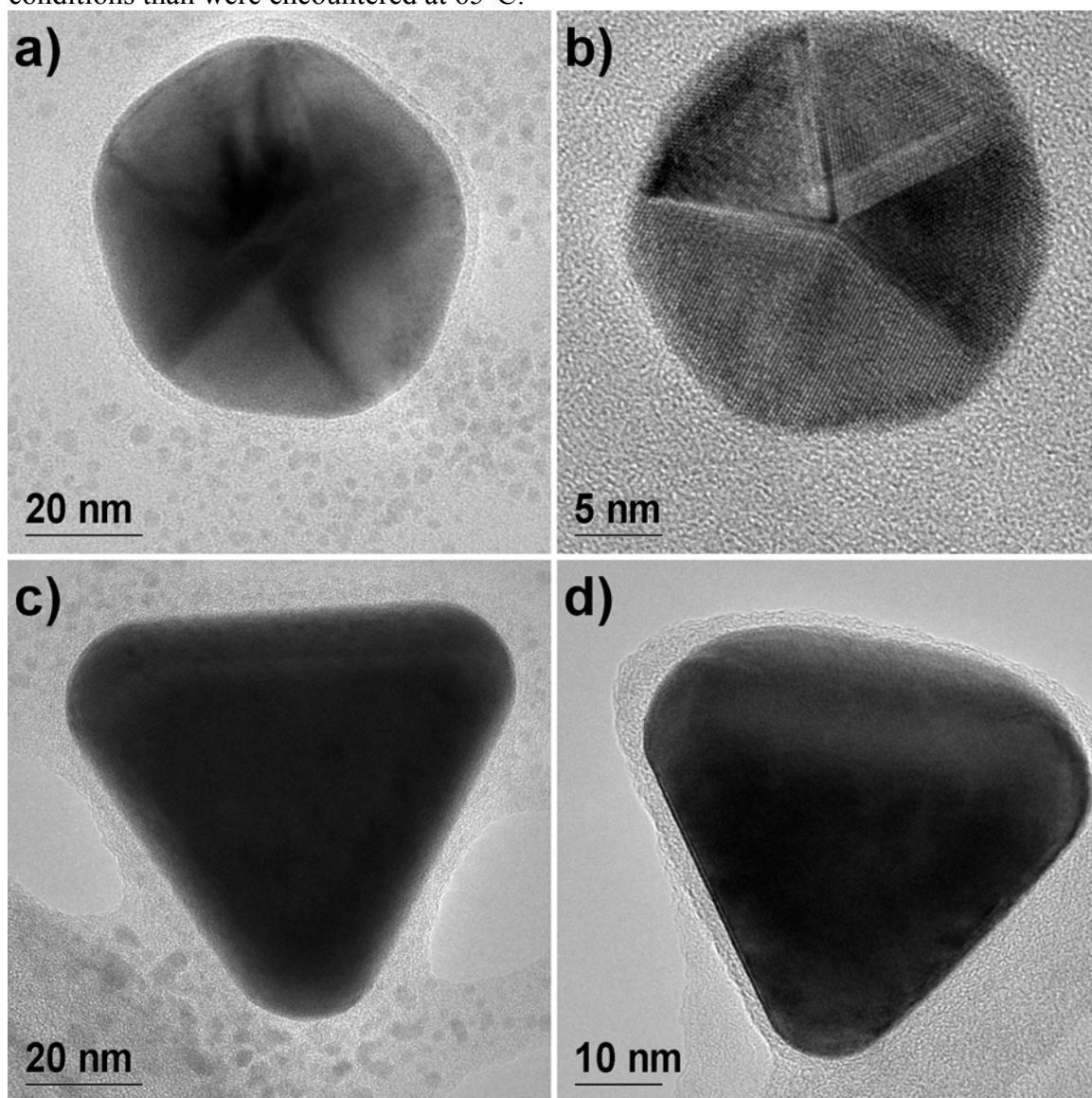


Figure 2.23: (96:1) Au:BSA at 95°C – large crystals. TEM images of (a)-(b) decahedral crystals and (c)-(d) triangular platelets.

Due to the lower concentration of protein in this system, HRTEM analysis of the nanometric-scale crystals was possible. Figure 2.24 presents characteristic HRTEM images of nanocrystals with aspect ratio ~ 1 . The visible parallel twinning planes within

each crystal are symptomatic of a high degree of lattice strain. Structural defects are also evident from the characteristic spot splitting and/or streaking visible in the FFT of each crystal. This is in contrast to the observed nanostructures at 65°C (Figure 2.14), which exhibited stable morphologies.

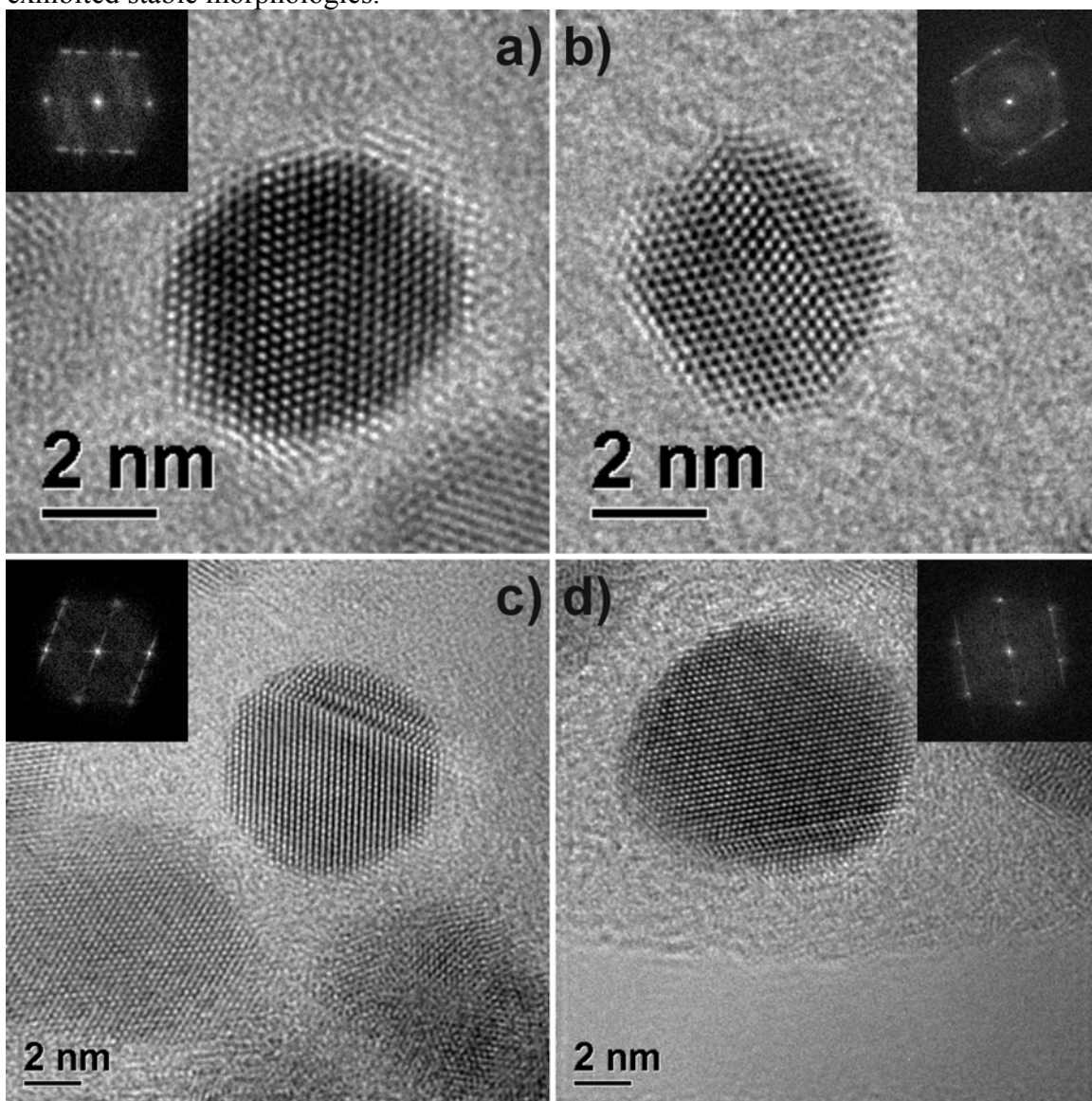


Figure 2.24: (96:1) Au:BSA at 95°C – HRTEM images of crystals with parallel twinning planes. The fast Fourier transform (FFT) of each image is included as inset.

Figure 2.25 presents characteristic HRTEM images of elongated nanocrystals obtained from the (96:1) Au:BSA system at 95°C. Two types of elongated crystals were observed. The first type exhibited lamellar twinning planes orthogonal to the direction of elongation (Figure 2.25a). These crystals had the largest aspect ratios, and also the most variability in length. The second type of elongated structure arose from pentagonal structures, in which at least one monocrystalline domain exhibited preferential growth at the expense of other domains (Figure 2.25b). These crystals were limited to an aspect ratio of ~2, most likely due to the increasing lattice strain imposed upon the growing domain by neighboring domains that do not experience preferential growth.

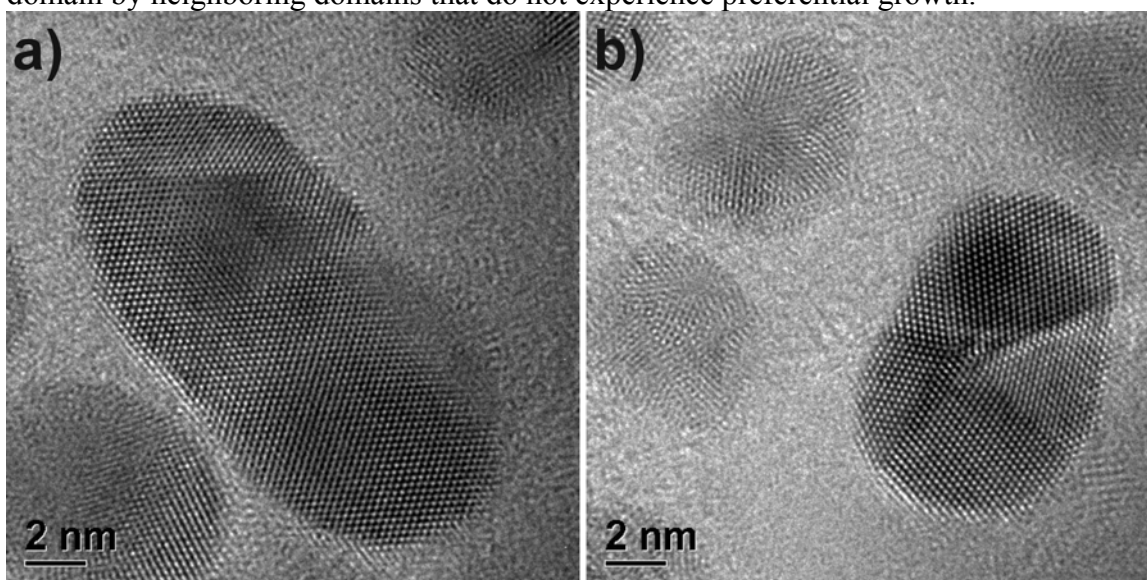


Figure 2.25: (96:1) Au:BSA at 95°C – HRTEM images of elongated crystals.

From the crystal structures examined in Figures 2.24 and 2.25, it is apparent that a large degree of coalescence of primary particles has occurred. Due to the relatively low reaction temperature, these structures do not have sufficient thermal energy to anneal themselves into thermodynamically stable structures, resulting in a large number of elongated nanocrystals, as well as rounded crystals with a high degree of internal strain.

Summary of the systems investigated at 95°C

At 95°C, the reaction time is essentially independent of the concentration of BSA. The primary observed effect of decreasing the BSA concentration was a decreasing degree of protection for the nanometric-scale crystals. Increasing the reaction temperature did in fact decrease the number and size of faceted, anisotropic nanocrystals in the (24:1) Au:BSA and (96:1) Au:BSA systems. However, it is also apparent that thermal denaturation of BSA decreased its effectiveness as a surface-protecting agent. This is especially evident in the case of (96:1) Au:BSA, where elongated and strained nanocrystals indicate a significant amount of coalescence of primary particles. Even the (12:1) Au:BSA system, which was well-controlled at 65°C, exhibited a larger percent deviation of crystal sizes at 95°C, and the formation of multiple-twinned structures as large as 30 nm, which were not present at 65°C.

2.4 CONCLUSIONS

In summary, it was demonstrated that bovine serum albumin can be incorporated into a polyol method to regulate the formation and growth of gold nanocrystals with controlled morphologies in the size range of 2–5 nm. Reactions were conducted below and above 75°C, the temperature where thermally-induced denaturation of BSA protein occurs. It was found that below the denaturation temperature, the concentration of BSA added had a significant role in controlling the reaction time, while above the onset temperature, the reaction time was largely unchanged at various BSA concentrations. Controlled size distributions and stable nanocrystal morphologies on the order of 2–5 nm were observed at 65°C, whereas at 95°C, the nanometric size and shape distributions were broader, and the crystal structures were much more strained. We propose this is a result of the thermally-induced denaturation of BSA protein at 95°C, which decreases its efficacy in protecting 2–5 nm nanocrystals.

If a well-controlled, uniform product is desired with a minimal loss of gold to the formation of large, faceted, anisotropic crystals, the most desirable system is (12:1) Au:BSA at 65°C. However, if one seeks a reasonable degree of control over size distribution, and a more reasonable reaction time, the best system would be (96:1) Au:BSA at 65°C. This system provides ~82% yield by mass of 2–5 nm gold nanocrystals in ~48 hours, and the faceted crystals that form are easily removed via size separation.

Chapter 3: Aqueous Synthesis of Protein-Stabilized Gold Nanocrystals via Chemical Reduction with Sodium Borohydride

3.1 INTRODUCTION

The synthesis and study of gold nanocrystals has grown precipitously since the landmark report of the Brust-Schiffrin method in 1994. Inspired by Faraday's two-phase system of 1857, the Brust-Schiffrin technique involves colloidal reduction in a two-phase system, and uses thiolated alkanes that strongly bind gold to protect the nanocrystal surface. (78,79) Chloroauric acid is transferred from the aqueous phase into toluene using tetraoctylammonium bromide as the phase-transfer agent, and is reduced by sodium borohydride, a strong reducing agent, in the presence of dodecanethiol. (80) This method provides a robust platform for the solution-phase synthesis of stable gold nanocrystals with well-controlled dispersion and sizes on the order of ~2 nm. Subsequent publications have presented numerous modifications and adaptations of the original technique, and its extension to the formation of other types of metal nanocrystals.

The Brust-Schiffrin technique produces organic-soluble nanocrystals. Ligand-exchange techniques have been developed to allow for the displacement of the original capping agent by thiolated molecules with various functionalities. (81,82) Thus, water-soluble nanocrystals can be obtained by ligand exchange with thiolated carboxylic acid derivatives. (45) A less-common route to obtain water-soluble nanocrystals involves the aqueous-phase synthesis of metallic nanocrystals directly in the presence of biological molecules. With this approach, intermediate stabilizing agents and ligand exchange procedures are not required to obtain water-soluble nanocrystals. Short thiolated peptide chains have been used as protecting agents for the aqueous synthesis of gold nanocrystals, most notably tiopronin (Cys-Gly) and glutathione (γ -Glu-Cys-Gly). (47,48)

This eliminates the need for a two-phase synthesis, and provides water-soluble gold nanocrystal with built-in biofunctional linkages.

In this Chapter, I will describe a novel technique for the formation of water-soluble, biocompatible gold nanocrystals, grown within and directly functionalized by bovine serum albumin (BSA), a macromolecular globular protein. The synthesis method involves aqueous-phase redox chemistry at ambient conditions. When compared with previously-existing bioconjugation techniques, this approach has several desirable features, including robust dimensional stability of the product, a near-quantitative yield of protein-functionalized nanocrystals, and a well-defined size on the order of 2 nm, obtained at synthesis conditions that are non-destructive for the protein. This is the first report of pure metallic, sub-2 nm nanocrystals grown within and directly functionalized by a macromolecular globular protein, without the use of intermediate stabilizing molecules or cross-linking agents¹.

3.2 EXPERIMENTAL PROCEDURE

Synthesis. Protein-functionalized gold nanocrystals were synthesized in air by reduction in a homogeneous solution at ambient conditions. Chloroauric acid trihydrate (HAuCl₄·3H₂O; 99.9+%; Aldrich) was reduced in water and in the presence of bovine serum albumin (BSA; Fraction V – heat shock treated; Fisher) by the addition of sodium borohydride (NaBH₄; 99%; Aldrich). An aqueous solution of ionic gold precursor was prepared by adding 1.1815 g of HAuCl₄·3H₂O to 25 mL of deionized water. All materials were used without further treatment. In a typical experiment, the desired volume of 0.12 M HAuCl₄ solution was added to a round bottom flask containing an aqueous solution of 8.571 μmol (0.5692 g) dissolved BSA protein. Then, 2.5 mL of a freshly-prepared NaBH₄ aqueous solution was added under vigorous stirring, bringing the

¹ A large portion of this chapter has been published in *Langmuir* 20, 11778–11783 (2004).

total reaction volume to 40.0 mL. The molar ratio of $[\text{BH}_4^-]:[\text{AuCl}_4^-]$ was maintained at 10:1 for each reaction. Introduction of NaBH_4 to the reaction vessel caused rapid protein foaming, and the solution acquired a golden brown hue that developed into a deep brown. The reaction was allowed to proceed under vigorous stirring for 3 hours. The product was purified by precipitation in ethanol (Ethanol; 200 proof spectrophotometric-grade; Aldrich) at -5°C , then re-dissolved in water.

Table 3.1: Reaction conditions for the various systems tested.

0.12 M $[\text{AuCl}_4^-]$	mg NaBH_4	$\mu\text{mol Au}$	$\mu\text{mol NaBH}_4$	$[\text{Au}]:[\text{BSA}]$
0.4mL	18.2	48	480	28:5
0.5 mL	22.7	60	600	7:1
1.0 mL	45.4	120	1200	14:1
2.0 mL	90.8	240	2400	28:1

Table 3.1 summarizes the reaction conditions for each system tested. The fifth column of this chart indicates the molar ratio of gold atoms to protein molecules present in solution. All ratios are calculated on the basis of 8.571 μmol of BSA added to the system (0.5692 g). For example, in the system where 60 μmol of Au was added to the reaction, the ratio is calculated as $[60 \mu\text{mol Au atoms}]:[8.571 \mu\text{mol BSA molecules}]$, or 7:1. For convenience, throughout this chapter each system will be referenced by its molar ratio, for example “(7:1) Au:BSA.”

Characterization. Transmission electron microscopy (TEM) was performed using a JEOL 2010F transmission electron microscope equipped with Schottky-type field emission gun, ultra-high resolution pole piece ($C_s = 0.5 \text{ mm}$), an Energy Dispersive X-ray spectrometer (EDS), and a scanning transmission electron microscope (STEM) unit with high angle annular dark field (HAADF) detector operating at 200 kV. Samples for

TEM analysis were prepared by allowing a drop of the aqueous product to evaporate on a lacey carbon-coated copper TEM grid. By focusing within the holes of the lacey carbon, we were able to obtain TEM and HAADF images of the protein-functionalized nanocrystals without the interference of the lacey carbon support layer. Infrared spectra in the range of 600-3600 cm^{-1} were recorded using a Nicolet Avatar 360 FTIR spectrometer. Samples were prepared by grinding the product with potassium bromide (KBr; FTIR-grade; Aldrich) into a fine powder, which was pressed into a pellet. Raman spectra in the range of 400-600 cm^{-1} were acquired using a Jobin Yvon LabRam HR800 spectrometer in confocal mode. The 514.5 nm Ar^+ excitation line from an external laser source was used at 100 mW. Samples were analyzed as thin films. UV-visible absorption spectra in the range of 240-600 nm were obtained with a Varian Cary 5000 UV-vis NIR spectrometer. Samples for UV-visible absorption analysis were prepared by diluting the original reaction product with deionized water (a twenty-fold dilution by volume). Solution-phase analysis was performed at room temperature using a matched set of quartz cuvettes (path length 10 mm), and operating the spectrometer in dual beam mode. One cuvette was filled with the diluted reaction solution, while the second cuvette contained deionized water.

3.3 RESULTS AND DISCUSSION

3.3.1 Determination of the Optimal Sequence and Rate of Addition

As briefly mentioned in the experimental section, protein foaming started nearly immediately after addition of the first drops of sodium borohydride solution, with a continuous thin layer of foam covering the solution in approximately 1 second. If the reducing agent solution was added rapidly, the foaming proceeded vigorously, reaching the top of the neck of the 100 mL round bottom flask in approximately 5 seconds. The

concern was raised that if the continuous layer of foam was formed prior to the complete addition of the sodium borohydride solution, we would have essentially two phases of addition – an initial phase in which the reducing agent directly enters the reaction solution, and a second phase during which the reducing agent must penetrate a layer of protein foam, whose thickness varies with time, to reach the reaction solution. Not only would this complicate our calculation of the total addition rate of reducing agent, but the non-uniform rate of addition could have adverse effects on the uniformity of the final gold nanocrystal population. Thus, a primary concern was how best to handle the protein foaming upon addition of sodium borohydride. Three approaches were studied.

Dropwise addition of sodium borohydride

In the first approach, the sodium borohydride solution was added dropwise to the reaction vessel. This reaction, as well as the other two reactions mentioned subsequently in this section, was conducted using 60 μmol of gold, designated as (7:1) Au:BSA. It was found that an addition rate of 2 mL/minute (or 480 $\mu\text{mol}/\text{minute}$) of sodium borohydride solution was sufficiently slow to limit protein foaming to an annular region against the walls of the reaction vessel, allowing all drops of the reducing agent to enter directly into the reaction solution without encountering a layer of protein foam. The results of this synthesis are summarized in Figures 3.1.

A broad variation in nanocrystal size and shape was observed. The size distribution in Figure 3.1d was obtained by measuring the short dimension of each nanocrystal. Approximately 30% of the nanocrystals in this system were elongated, with an average aspect ratio of 1.788 calculated for this segment of the population. Clearly, dropwise addition of sodium borohydride yields nanocrystals with poorly-controlled morphologies. This is not surprising, as the original Brust-Schiffrin technique yields the

most uniform product distributions when sodium borohydride is added rapidly to the reaction system. (11)

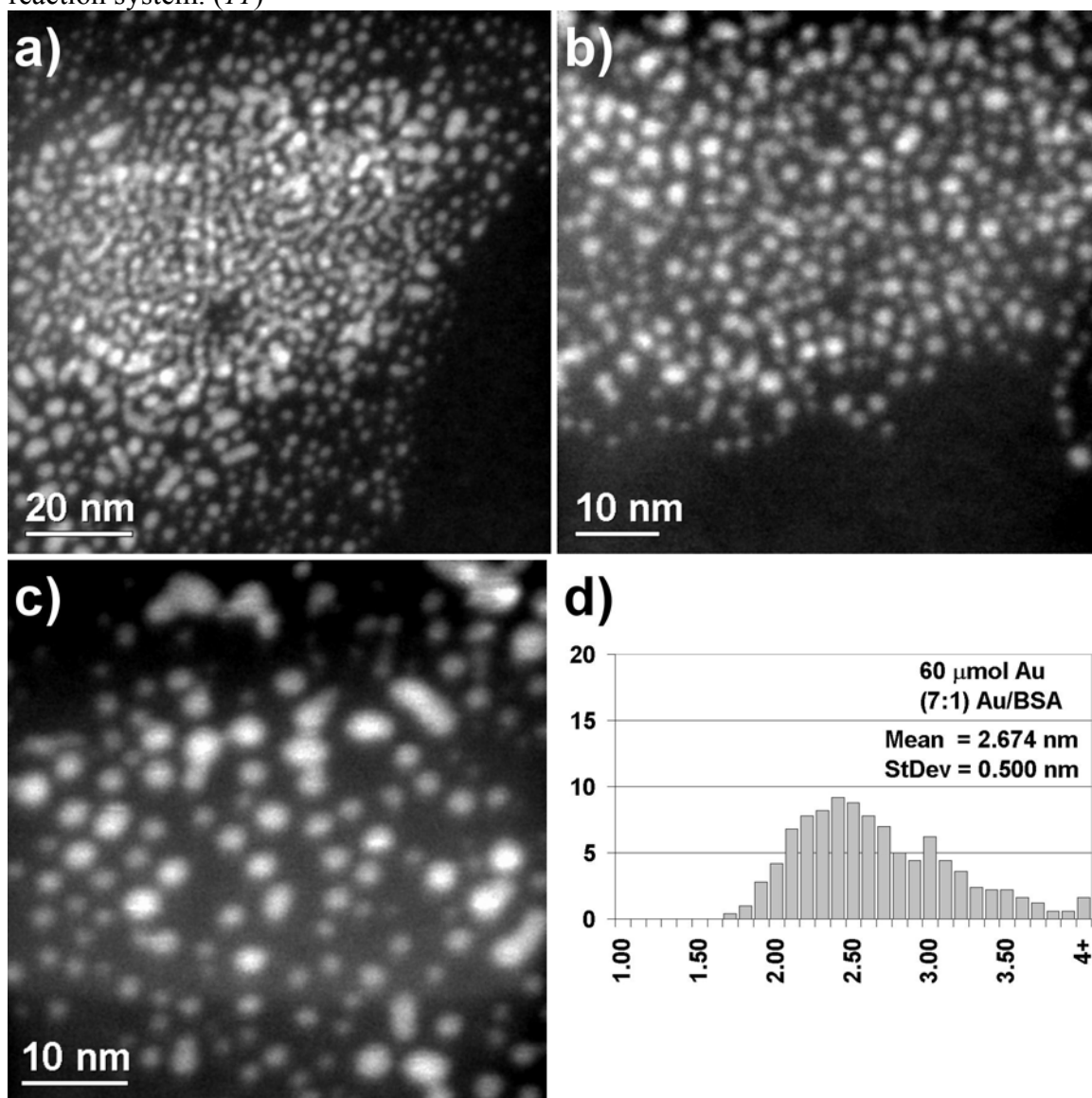


Figure 3.1: Dropwise addition of sodium borohydride. (a) to (c) HAADF images. (d) Size distribution, diameter in nanometers versus percentage frequency.

Addition of sodium borohydride prior to addition of gold

In a second attempt to overcome the effects of protein foaming, the order of addition of sodium borohydride and chloroauric acid was reversed. With this approach,

sodium borohydride was added dropwise at a rate of 2 mL/min (or 480 $\mu\text{mol}/\text{minute}$) to the aqueous solution of BSA. As in the previous case, the dropwise addition limited the initial amount of protein foaming to an annular region against the walls of the reaction vessel. Then, 60 μmol of the ionic gold solution was added directly into the central region of the reaction vessel without interference from the protein foam.

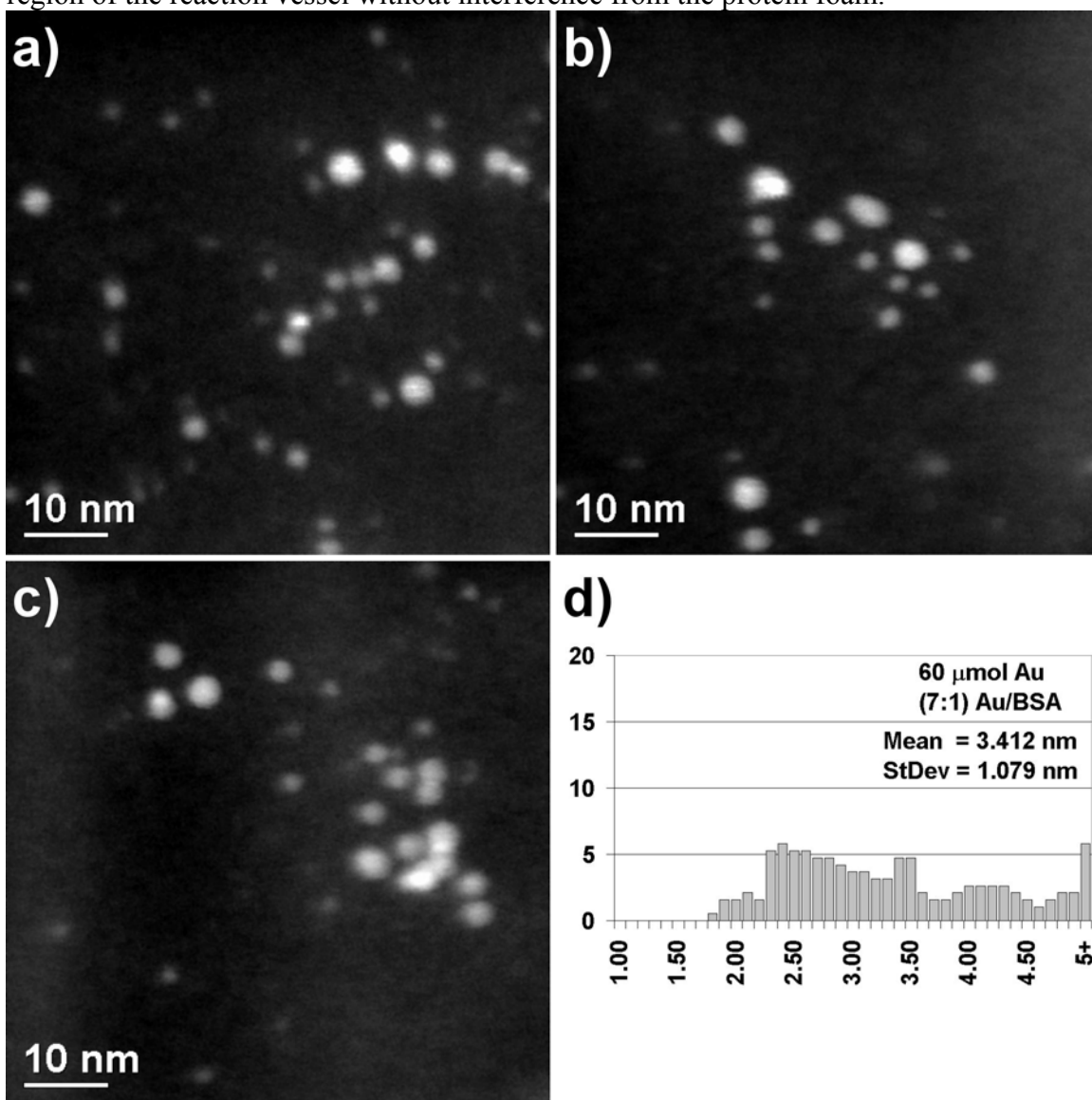


Figure 3.2: Rapid addition of chloroauric acid to a pre-existing aqueous solution of BSA and sodium borohydride. (a) to (c) HAADF images. (d) Size distribution, diameter in nanometers versus percentage frequency.

Upon addition of the chloroauric acid, the reaction solution rapidly acquired a deep purple color, and soon a continuous thin layer of foam developed. The pre-existing annular region of foam was clear in color, whereas the layer of foam formed immediately after the addition of chloroauric acid had an intense pink color. As a result, it was clear that the pre-existing ring of clear protein foam remained segregated above the newly-formed layer of pink protein foam. This suggests that the pre-foamed protein does not contain gold nanocrystals, and the effective concentration of BSA available for protecting nanocrystals is decreased if protein foaming occurs prior to the reduction of ionic gold. This was an important revelation, since BSA is notorious for foaming, and great care was taken in all subsequent experiments to ensure that no protein foam was present prior to the reduction.

The results of this synthesis are summarized in Figure 3.2 and Figure 3.3. Compared with the previously-discussed system, this approach provides better control over the nanocrystal morphologies, with primarily rounded crystals observed, but the size control is still poor, with a percent deviation in excess of 30%. The majority of the rounded nanocrystals observed can be divided into three distinct sub-populations: (i) smaller nanocrystals ~ 2.5 nm in diameter, (ii) intermediate nanocrystals ~ 3.5 nm in diameter, and (iii) larger nanocrystals ~ 4.25 nm in diameter. Additionally, a small number of gold aggregates with dimensions on the order of 10–80 nm were observed (Figure 3.3). It is interesting to note that no such aggregates were formed when sodium borohydride was added to a pre-existing solution of BSA and chloroauric acid. The variability in size of rounded gold nanocrystals suggests that gold nuclei are being

stabilized by BSA protein molecules at different stages of growth, while the presence of gold aggregates indicates that some nuclei are not protected at all by BSA.

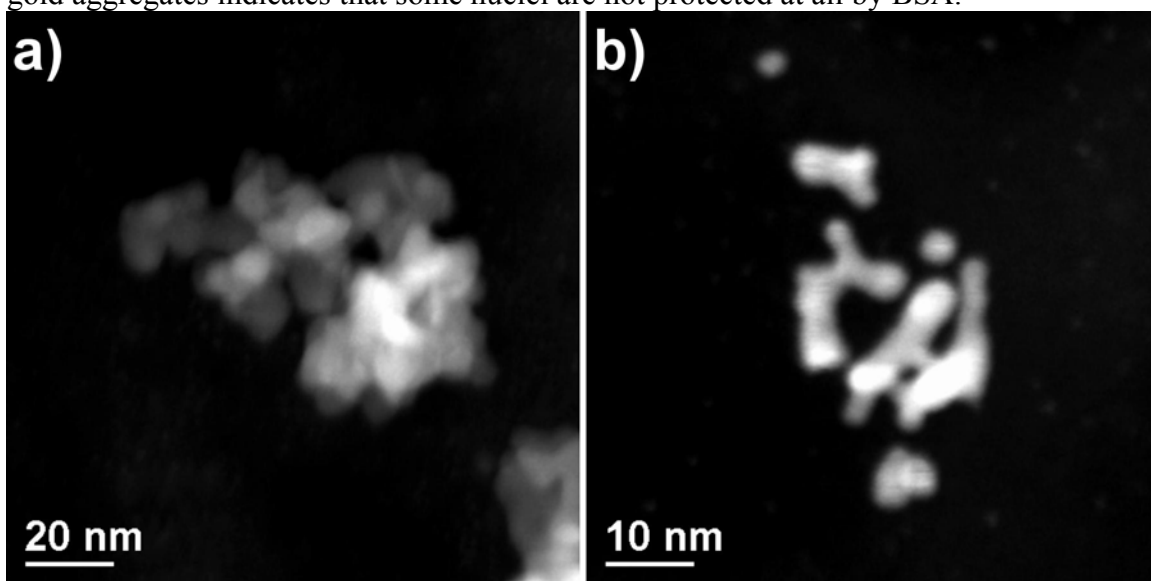


Figure 3.3: Rapid addition of chloroauric acid to a pre-existing aqueous solution of BSA and sodium borohydride – HAADF images of gold aggregates.

Rapid addition of sodium borohydride

In the third approach to overcome the effects of protein foaming, the entire volume of sodium borohydride solution was rapidly injected into the reaction system. As noted previously, upon addition of sodium borohydride to an aqueous solution of BSA and chloroauric acid, approximately 1 second was required for a continuous layer of protein foam to develop. If the entire volume of sodium borohydride is added in less than 1 second, all of the reducing agent can be transferred directly into the reaction solution without the interference of a layer of protein foam. In this final approach, the 2.5 mL of sodium borohydride solution was added by rapid injection with a Pasteur pipette. The total time of addition was less than 0.5 seconds, and all of the reducing agent was added to solution prior to the development of foam. The reduction of gold proceeded rapidly, with the solution acquiring a deep golden-brown color within less than 1 second of

sodium borohydride addition, and the fully-developed intensity of color was attained within 5 seconds. Protein foaming progressed in an analogous fashion, with a continuous layer of foam forming within ~1 second of sodium borohydride addition, expanding to near the top of the neck of the round bottom flask within 5 seconds.

The foam had a uniform brown color, quite similar to the color of the solution. This indicates a homogeneous dispersion of gold nanocrystals within the protein foam, and suggests that the nanocrystals were formed prior to the evolution of the foam. It is also interesting to note that the foam consisted of small, frothy bubbles of uniform size, and was stable for a period of hours. Indeed, in subsequent experiments the uniformity of foam size and color was found to be an accurate indicator of the uniformity of the gold nanocrystals produced.

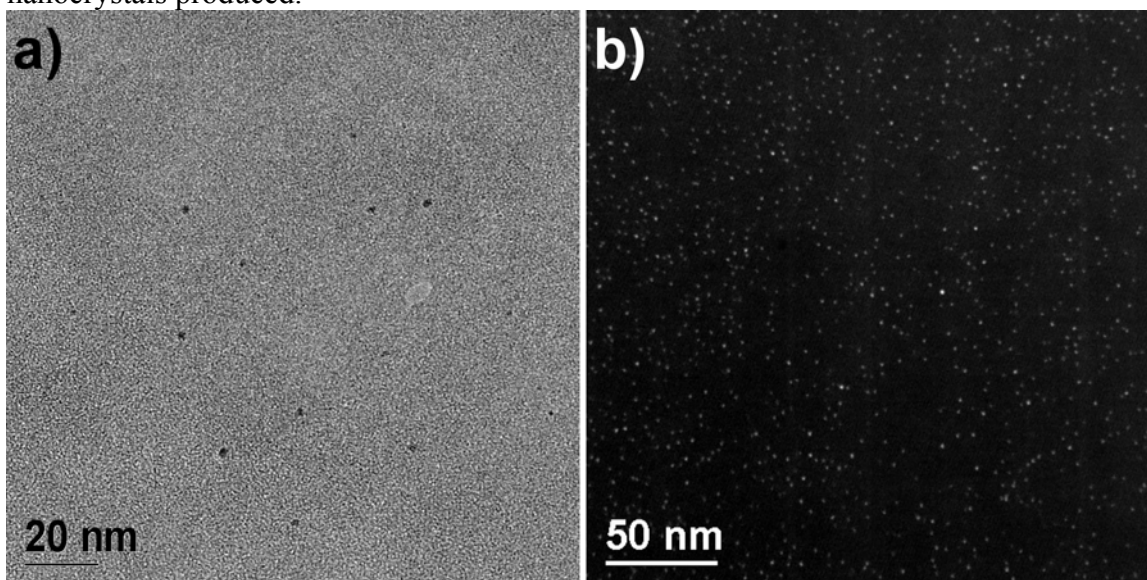


Figure 3.4: Rapid addition of sodium borohydride to a pre-existing solution of BSA and chloroauric acid. (a) Conventional TEM and (b) HAADF images.

Figure 3.4 presents a typical product obtained from rapid addition of sodium borohydride. The gold nanocrystals formed were well-dispersed with an average diameter less than 2 nm, and no aggregates were observed. Discussion of the statistical

distribution will be left to the following sections, when this method will be examined in detail. The presence of a thick, enveloping protein molecule combined with the small dimensions of the gold nanocrystals formed made it difficult to study the size distribution of this sample by conventional TEM analysis (Figure 3.4a). In this image, only the largest fraction of nanocrystals is vaguely visible, and the majority of gold nanocrystals are completely obscured by the protein film. However, due to the Z^2 -contrast phenomenon discussed previously, the gold nanocrystals in our system are clearly visible with HAADF imaging, as seen in Figure 3.4b. As the water content evaporates, neighboring protein molecules interact to form a thin film, so by focusing in the holes of the lacey carbon support, it was possible to unambiguously observe the protein surrounding the nanocrystals. The protein film is composed of C, N, O, and S and appears as a faint gray cloudy background. The gold nanocrystals are the bright, round structures within the protein matrix.

Insights derived from the preliminary methods tested

From these preliminary investigations, two points were made clear: (i) the order of addition should involve adding sodium borohydride to a pre-existing solution of BSA and chloroauric acid, and (ii) a rapid rate of sodium borohydride addition yields a more uniform product than dropwise addition. In terms of point (ii), this is a common observation for synthesis protocols derived from the Brust-Schiffrin technique. (11)

We propose that point (i) can best be explained in terms of the complexation of BSA with chloroauric acid. One of the most outstanding properties of serum albumin as a multifunctional transport protein is its ability to bind a variety of ligands, including heavy metal ions. (50) Binding of copper (II) and nickel (II) by serum albumin has been thoroughly documented. (83) Serum albumin also forms covalent adducts with noble metal ions of Ag(I) and Au(I). (84) Furthermore, serum albumin is known to bind

chlorides and chloride complexes. (85,86) Therefore, it seems probable that serum albumin will bind the AuCl_4^- precursor in our system.

In light of this, we can explain the observed differences when the order of addition of sodium borohydride and chloroauric acid is reversed. In the standard case, the chloroauric acid is added to the BSA solution prior to reduction, and the protein molecules bind a certain percentage of the AuCl_4^- ions. When reduction occurs, those gold ions that were complexed within the protein become atomic gold. There is now a higher local concentration of gold atoms within the protein molecules, and gold will tend to nucleate within the protein molecules. These nuclei will be well-protected from the beginning of their growth by the bulk of the globular protein, and their surfaces will be stabilized by the locally-high availability of sulfur-bearing residues within the protein molecule. As a result, the final product will consist of small, stable gold nanocrystals with a well-controlled distribution.

On the other hand, when chloroauric acid is added to a pre-existing solution of protein molecules and sodium borohydride, reduction begins as soon as the ionic gold enters the reaction solution. There is little opportunity for the ionic gold to bind with BSA prior to reduction, and as a result, many atoms will be reduced and nucleate outside the protein molecules. Several of the growing nuclei will experience surface-stabilizing interactions as they encounter protein molecules in solution, and will become functionalized by them. From this point onwards, their growth will be well-controlled. However, statistically each nucleus will have reached a slightly different stage of growth before encountering a protein molecule, and there will be a broader size distribution among those nanocrystals that become protein-functionalized. Finally, a percentage of gold nuclei will not encounter a protein molecule before they reach the stage of growth

where they are too large to be effectively stabilized by BSA. These poorly-protected crystals will grow by coalescence into various aggregate structures.

3.3.2 Formation of Gold Nanocrystals Directly Functionalized by BSA Protein

Properties of the protein-functionalized product

We will now briefly describe some characteristics of the nanocrystals formed by the rapid addition of sodium borohydride to a pre-existing solution of BSA and chloroauric acid. Robust dimensional stability of the protein-functionalized gold nanocrystals after extensive processing is a remarkable property of this system. The product forms a deep brown solution that is stable indefinitely at ambient conditions. The water content can be evaporated to yield a transparent thin film, the color of which ranges from golden brown to deep brown with increased gold concentration. The film can be ground into a fine, dry powder that can be handled as a simple compound and is easily re-dissolved in water. Size distributions were obtained from HAADF images of the sample before and after processing, which revealed the processing sequence can be repeated multiple times without inducing nanocrystal coalescence.

Table 3.2: Theoretical and experimentally-obtained S:Au Ratios.

Au (μmol)	S:Au (Calc)	S:Au (EDS)
60	5.00	4.92
120	2.50	2.44
240	1.25	1.22

Table 3.2 presents theoretical S:Au molar ratios calculated from the amounts of protein and gold originally added, and compares them with experimentally-obtained EDS measurements. The measured S:Au molar ratios are consistent with the predicted values within experimental error. The S:Au ratio is halved when the moles of gold double, indicating that gold nanocrystals are binding quantitatively with the protein and the

protein has not been saturated beyond its capacity to bind nanocrystals within the concentration range studied.

When the aqueous product is evaporated on a TEM grid, the protein molecules form a thin film. EDS spectra of the protein films, such as the spectrum shown in Figure 3.5, were obtained at 25 k magnification for each sample and confirm the presence of C, N, O, S, and Au. Extensive EDS analysis demonstrates the gold nanocrystals are found only within the protein matrix. The Cu spectral peaks are from the TEM grid, and the Na peak is the result of adsorbed counterions on the protein.

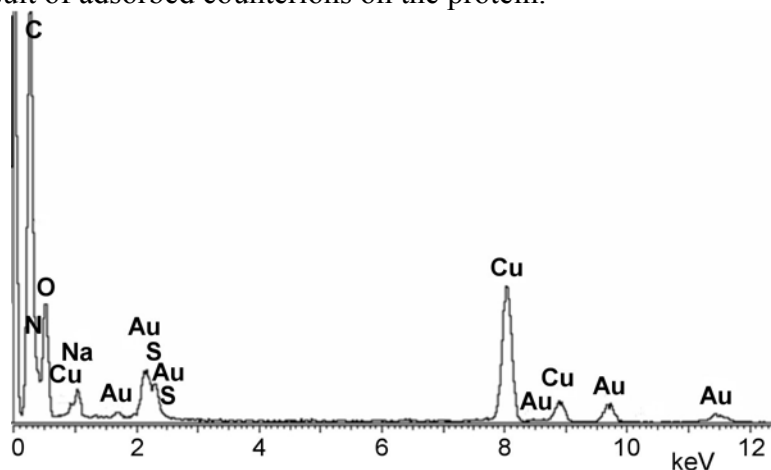


Figure 3.5: Representative EDS spectrum of the protein-functionalized nanocrystals, verifying the presence of C, N, O, S, and Au. The Cu signal is from the TEM grid, and Na is an adsorbed counterion on the protein.

High-Resolution TEM analysis

Figure 3.6 illustrates typical structures observed with high-resolution TEM (HRTEM) analysis. The two gold nanocrystals in Figure 3.6a were among the largest observed. In Figure 3.6b, we see a nanocrystal just under 2 nm in diameter, again larger than the average size. The nanocrystal in Figure 3.6c is approximately 1 nm in diameter and represents the lower range of the size distribution. In each case, the organic material surrounding the gold nanocrystals is a thin protein film. The shapes observed for larger

crystals were primarily pentagonal crystals with fivefold symmetry and FCC single crystals, with no apparent shape preference. These morphologies represent the most stable structures for nanocrystals in this size range. (32) The atomic structure of smaller nanocrystals was typically not discernible, as their atomic resolution was obscured by the enveloping protein.

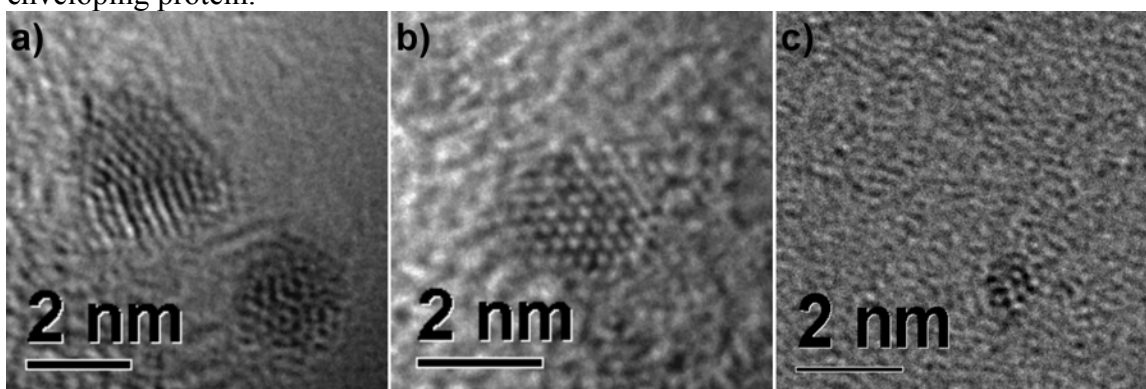


Figure 3.6: HRTEM images of BSA-functionalized nanocrystals. (a) Upper-left nanocrystal is a 2.5 nm pentagonal crystal. Lower-right crystal is a 2.2 nm icosahedron. (b) 2.0 nm FCC octahedral nanocrystal. (c) 1.0 nm nanocrystal with clearly observed crystalline order.

HAADF analysis

Recall that for HAADF microscopy, the signal is primarily formed by electrons that have undergone high angle-scattering, which approximates a Rutherford-like scattering cross section. (57–59) Therefore, image contrast is related to composition, the intensity being proportional to the square of the atomic number. (60,61) As a good approximation, in these images lighter elements appear dark and heavier elements appear bright. The gold nanocrystals in our system are clearly visible with HAADF imaging, as seen in Figure 3.7. The crystals are well dispersed and have a narrow size distribution. Comparison of Figure 3.7a and Figure 3.7b demonstrates that individual nanocrystals are protected from coalescence even as the amount of gold is quadrupled (60 to 240 μmol).

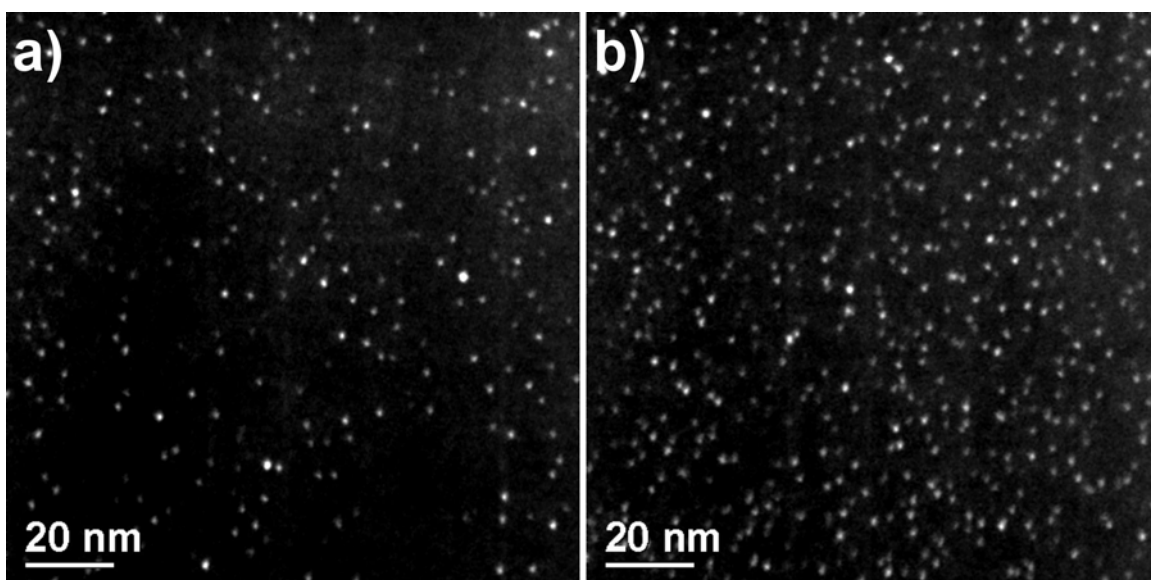


Figure 3.7: HAADF images of BSA films at (a) (7:1) Au:BSA and (b) (28:1) Au:BSA molar ratios, demonstrating the effective protection of the crystals by BSA. The thin protein film appears as a gray, cloudy background, and the gold nanocrystals are the bright, round structures.

Size distributions

Nanocrystal size distributions were obtained from HAADF analysis of each sample at high magnification, such as those demonstrated in Figure 3.7. Figure 3.8 shows the size distribution for each gold concentration investigated, based on measurement of 500 crystals. The (28:5) Au:BSA system produces the smallest average size and the narrowest size distribution, while the (7:1) Au:BSA system exhibits an increase of 0.26 nm in average diameter, with a slight increase in standard deviation.

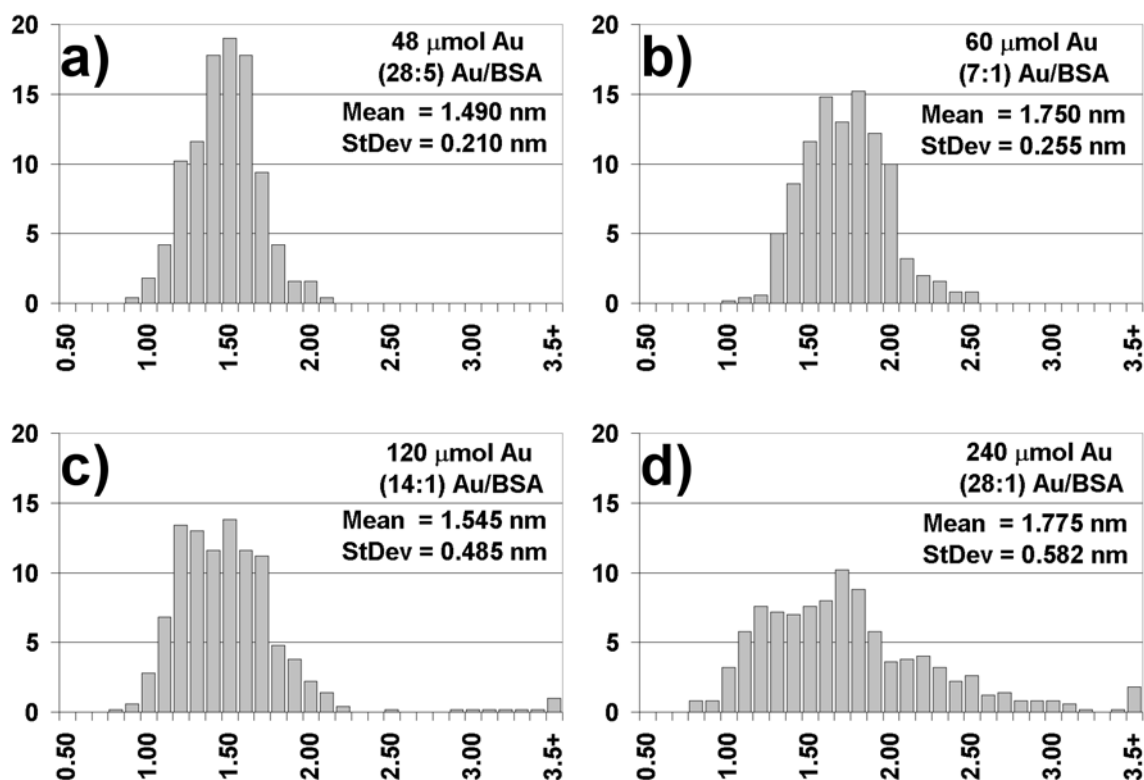


Figure 3.8: Size distributions of BSA-functionalized gold nanocrystals, each based on the measurement of 500 nanocrystals. The abscissa represents the crystal diameter in nanometers, and the ordinate is the percent frequency.

For a constant number of protein molecules in solution, one might expect that with increasing loadings of gold atoms, consistently increasing average nanocrystal diameters would be observed. This was not the case. The nanocrystals produced in the (14:1) Au:BSA and (28:1) Au:BSA systems possess average diameters close to those of the (28:5) Au:BSA and (7:1) Au:BSA systems, respectively. However, the percentage deviation from the mean nanocrystal diameter, which was $\sim 14.5\%$ in the (28:5) Au:BSA and (7:1) Au:BSA systems, more than doubled to $\sim 32\%$ in the (14:1) Au:BSA and (28:1) Au:BSA systems.

These somewhat puzzling trends can be explained in terms of conformational changes in protein structure with changing pH. BSA undergoes a series of reversible isomerizations in the range of pH 2-11. (50) The pH for each system was measured using pH strips. After the reduction was complete, the (28:5) Au:BSA and (7:1) Au:BSA systems were pH ~9. BSA undergoes structural isomerization above pH ~8 from the normal (N) form to the basic (B) form. (87,88) In the B form, Domains I and III separate and the tertiary structure changes from the heart-like shape in Figure 3.9 to a more linear arrangement. Expansion of the secondary structure occurs within Domain II and to a lesser extent within Domain I. For the (14:1) Au:BSA and (28:1) Au:BSA systems, the pH after reduction was ~10. BSA undergoes a second structural isomerization at pH ~10 from the B form to the aged (A) form. (89,90) The A form is an extension of the B isomer, with further expansion in Domains I and II.

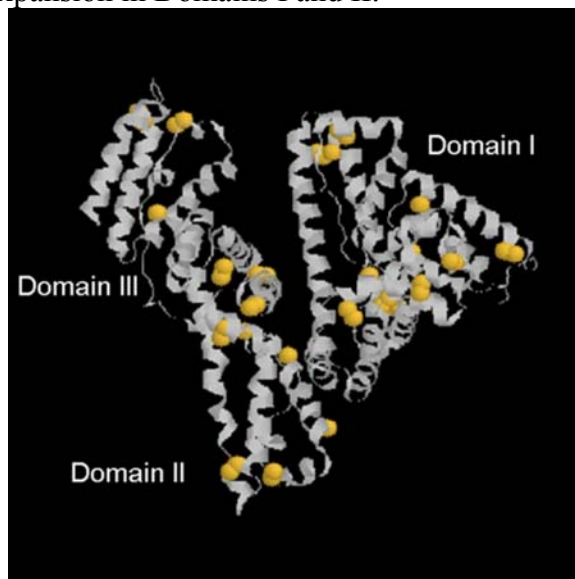


Figure 3.9: Tertiary structure of human serum albumin (PDB1BJ5), (54) a structural analogue to BSA. Sulfur atoms are displayed as space-filled atoms.

In the (28:5) Au:BSA and (7:1) Au:BSA systems we expect that nucleation and growth occur while the protein is in the B form, while in the (14:1) Au:BSA and (28:1)

Au:BSA systems, nucleation and growth can be expected to occur with the protein in the A form. The further-extended A form makes more binding sites available to the nuclei, which accounts for the smaller mean diameter in the (14:1) Au:BSA system compared to the (7:1) Au:BSA system, despite the fact that the (14:1) Au:BSA system has twice as much gold. However, the more extended A form provides less protection via steric hindrance, thus accounting for the ~32% standard deviation in nanocrystal size for the (14:1) Au:BSA and (28:1) Au:BSA systems. Future studies will focus on decreasing the excess amount of sodium borohydride to maintain the protein in the B form during nanocrystal nucleation and growth and to prevent transition to the A form.

Infrared spectroscopy

Infrared spectroscopy was employed to detect the characteristic bands of the protein bonds before and after functionalization with gold nanocrystals. A potential concern with our synthesis method is that sodium borohydride might cleave peptide bonds, so we studied the infrared spectra of our product to examine the possible disappearance or weakening of characteristic bands. The results show that the polypeptide backbone and side-chain functional groups remain intact after functionalization with gold nanocrystals. Spectra from pristine BSA and from the nanocrystal-functionalized protein with maximum gold loading, (28:1) Au:BSA, are presented in Figure 3.10. Assignments of characteristic infrared bands were based on the studies of Grdadolnik. (91) Visual inspection reveals that characteristic bands of the nanocrystal-functionalized protein are conserved, and this was confirmed by measuring the relative peak intensities of each sample.

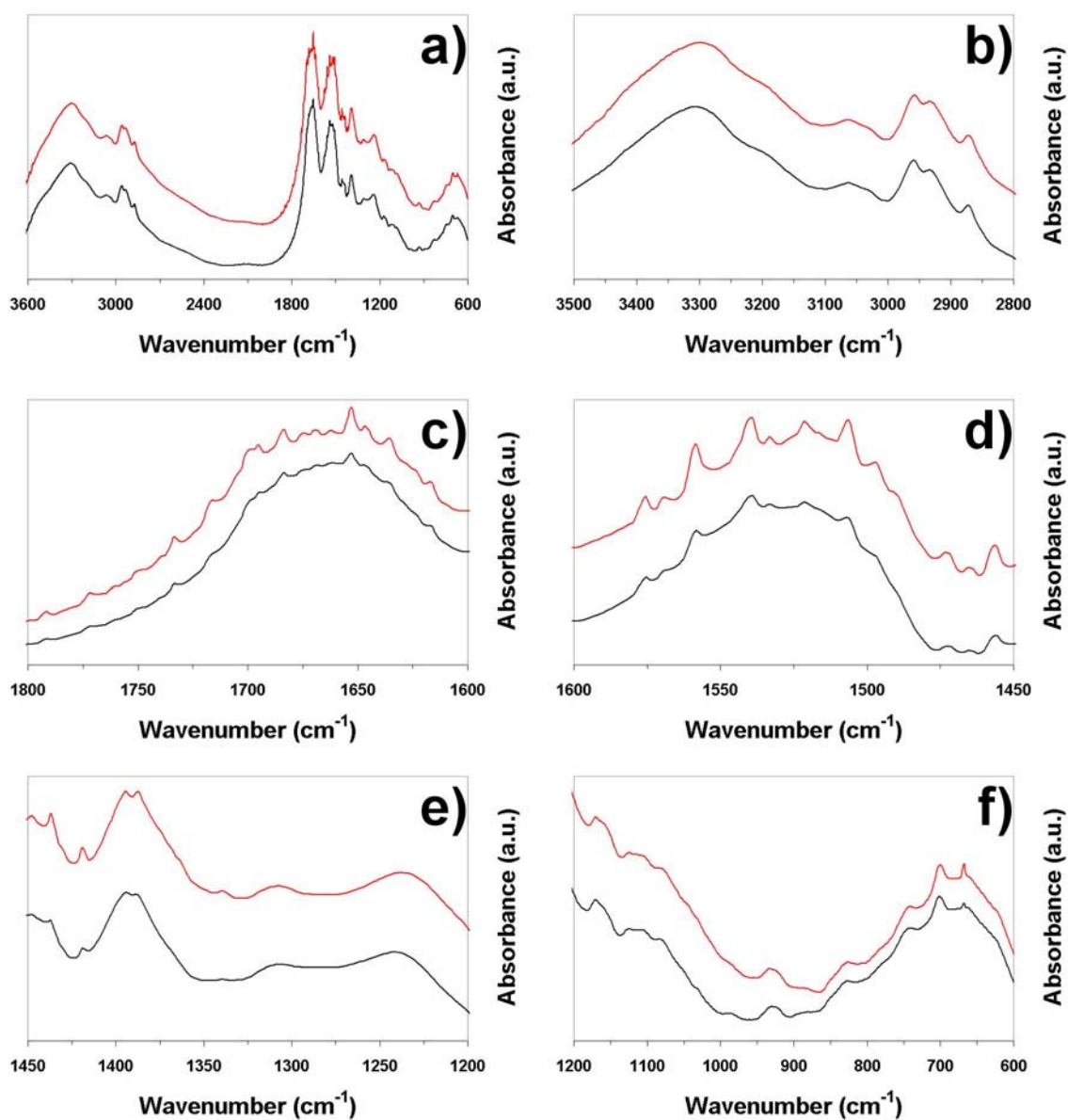


Figure 3.10: Infrared spectra. In each image, the lower spectrum (Black) is pristine BSA, and the upper spectrum (Red) is (28:1) Au:BSA. (a) presents the complete spectra, while (b)-(f) present expanded views of specific spectral regions for clarity of comparison.

The infrared-active modes of the peptide backbone are expressed in the amide bands. The N–H stretching mode is a doublet represented by the Amide A and Amide A'

bands at 3308 and 3062 cm^{-1} , respectively (Figure 3.10b). The Amide I band is primarily a C = O stretching mode and is centered at 1653 cm^{-1} (Figure 3.10c). The Amide II band is a combination of N–H in-plane bending and C–N stretching and is centered near 1550 cm^{-1} (Figure 3.10d). The more-complex Amide III band is centered near 1300 cm^{-1} (Figure 3.10e). Since the amide bands are conserved in the gold-functionalized samples, it is clear the peptide backbone remains intact after nanocrystal conjugation has occurred.

Infrared-active modes attributed to side-chain vibrations include C–H stretching modes at 2962, 2928, and 2870 cm^{-1} (Figure 3.10b) and a –CH₂– bending mode at 1458 cm^{-1} (Figure 3.10d). An aromatic C–C stretch at 1170 cm^{-1} and a C–H bend at 828 cm^{-1} were assigned to the aromatic residue tyrosine, and the C–H bending mode of the aromatic residue tryptophan was detected at 748 cm^{-1} (Figure 3.10f). Additionally, C–S stretching modes from the sulfur-bearing residues cysteine and methionine were detected at 698 and 668 cm^{-1} (Figure 3.10f). Because these infrared modes are conserved, we conclude that the side-chain functional groups, which are critical in determining the bioactivity of the protein, remain intact after nanocrystal conjugation.

Raman spectroscopy

The size distributions in Figure 3.8 demonstrate the gold nanocrystals are well protected from coalescence. This suggests a bond between the gold nanocrystal surface and functional groups of the protein, most likely via Au–S bonding. If the protein is bound to the nanocrystals in this manner, it is likely that free surface area exists since the bulkiness of the protein helps protect the crystals without saturating their surface, and the gold nanocrystals may therefore be active toward certain surface reactions. It is known that sodium borohydride can cleave the disulfide bonds in BSA, (92) so it is possible that free thiolated residues are available for interaction with the gold nanocrystal surface.

Raman spectroscopy was employed to study the disulfide bonds in the gold-functionalized samples. Figure 3.11a presents the complete Raman spectrum obtained from pristine BSA. This spectrum is in agreement with previously reported Raman spectral analyses of BSA. (93,94) Unfortunately, a complete spectrum was not obtainable for the (28:1) Au:BSA system, due to persistent sample burning. It is likely that during the spectral acquisition, laser irradiation at 514.5 nm induced thermal excitation of the gold nanocrystals to the point where the surrounding organic material was burned.

This burning took ~10 seconds to begin, so we decided to focus on obtaining a clear spectral comparison over a range sufficiently narrow to be obtained in less than 10 seconds. The S–S stretching mode is located at 508 cm^{-1} , so we focused our efforts in the spectral range of $600\text{--}400\text{ cm}^{-1}$. Figure 3.11b presents the S–S stretching region for pristine BSA and the (28:1) Au:BSA system. The disulfide stretch at 508 cm^{-1} is absent for the gold-functionalized product, which indicates that the thiol-bearing cysteine residues formerly involved in disulfide bonding should be free to interact with the gold nanocrystal surface.

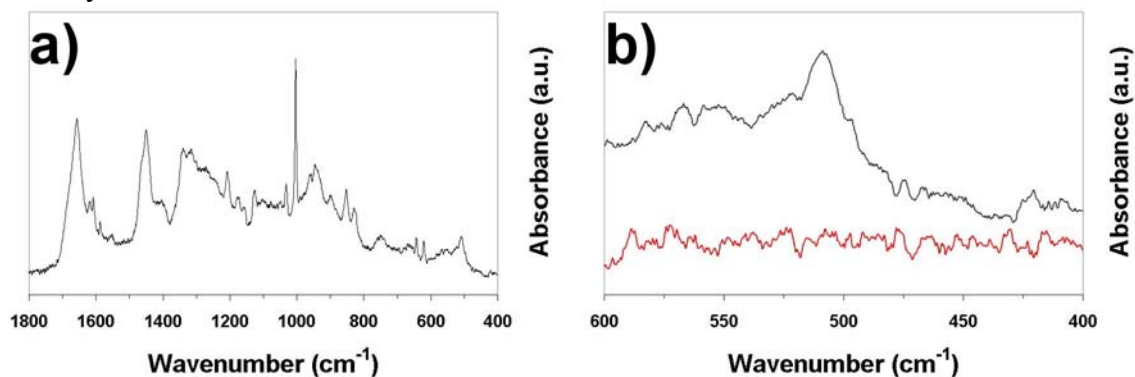


Figure 3.11: Raman spectra. (a) Complete Raman spectrum of pristine BSA. (b) Raman spectra of pristine BSA (upper spectrum, Black), and (28:1) Au:BSA (lower spectrum, Red) in the region of $600\text{--}400\text{ cm}^{-1}$. The disulfide stretching mode corresponds to the peak centered at 508 cm^{-1} .

Absorption spectroscopy

UV-visible absorption spectra of gold nanocrystals <20 nm in diameter exhibit a characteristic surface plasmon resonance peak at ~520 nm that broadens and decreases in intensity as crystal size decreases. (10) For gold nanocrystals below 2 nm in diameter, this plasmon resonance peak is no longer discernable due to the onset of quantum size effects. (34,37) The absorption spectra for our protein-functionalized nanocrystals exhibit no surface plasmon resonance peak, as shown in Figure 3.12, which suggests that they are experiencing quantum confinement. This corroborates our electron microscopy analysis, in which we determined that the gold nanocrystals are <2 nm in diameter.

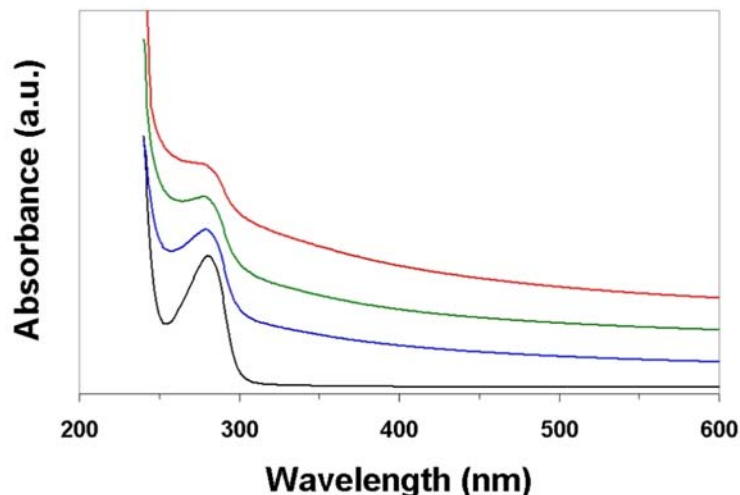


Figure 3.12: UV-visible absorption spectra. From bottom to top, the spectra are pristine BSA (Black), (7:1) Au:BSA (Blue), (14:1) Au:BSA (Green), and (28:1) Au:BSA (Red). Note the diminishing peak intensity at 278 nm with increased gold loading.

Pure BSA exhibits an absorbance maximum at 278 nm and a minimum at 253 nm (bottom spectrum in Figure 3.13). (50) The intensity of this protein-characteristic peak decreases with increased gold loading. The primary sources of this maximum are the aromatic residues tryptophan and tyrosine, with a limited contribution from the disulfide

bonds in the protein. From infrared analysis, we know that the aromatic residues are still present after gold nanocrystal conjugation, and Raman spectroscopy indicated a loss of S–S stretching at 508 cm^{-1} , so the progressive loss of disulfide bonds and formation of Au–S bonds may contribute to the observed decreased absorbance at 278 nm. However, the degree to which the peak intensity decreases is too great to be solely explained by the loss of disulfides. This suggests a conformational change in protein structure upon binding with the gold nanocrystal surface, inducing perturbations in the aromatic residues tryptophan and tyrosine, and resulting in decreased absorbance. We will discuss this point more fully in the following Chapter.

3.4 CONCLUSIONS

In summary, I have developed new method for the synthesis of water-soluble gold nanocrystals, grown within and directly functionalized by bovine serum albumin, a globular protein molecule. The synthesis method employs aqueous chemistry at ambient conditions, and we obtain near-quantitative yield of well-dispersed, protein-functionalized gold nanocrystals with an average diameter less than 2 nm. Infrared spectroscopy confirms that the polypeptide backbone of the protein is not cleaved during the synthesis, and that the side chain functional groups remain intact. The gold nanocrystals are stabilized by a combination of Au–S bonding with the protein and steric protection due to the bulkiness of the protein, so they should have free surface area available for interaction with external species. When compared with previously-existing bioconjugation techniques, this approach has several desirable features, including robust dimensional stability of the product, a near-quantitative yield of protein-functionalized nanocrystals, and a well-defined size of $<2\text{ nm}$, obtained rapidly and at synthesis conditions that are non-destructive for the protein.

Chapter 4: Aqueous Synthesis of Protein-Stabilized Silver, Gold, and Platinum Nanocrystals via Chemical Reduction with Sodium Borohydride

4.1 INTRODUCTION

Chapters 2 and 3 described two distinct and novel methods developed for the synthesis of 2–5 nm gold nanocrystals, stabilized by bovine serum albumin (BSA) protein molecules. The first method, described in Chapter 2, was a polyol-based approach, and involved the formation of gold nanocrystals in glycerin and in the presence of BSA. The two most promising embodiments of this method were found at a reaction temperature of 65°C. In the (12:1) Au:BSA system at 65°C, the glycerin-based method provided ~98% yield by mass of ~2 nm gold nanocrystals in 72 hours. In the (96:1) Au:BSA system at 65°C, the glycerin-based method provided ~82% yield by mass of ~3 nm gold nanocrystals in 48 hours. The remaining ~18% of gold was present as anisotropic crystals with faceted surfaces and regular shapes, with dimensions in the range of 150–200 nm. The second method, described in Chapter 3, was an aqueous-based approach, involving the formation of gold nanocrystals via reduction with sodium borohydride in water at room temperature and in the presence of BSA protein. This method provided a near-100% yield of gold nanocrystals with average diameters of <2 nm. No aggregates or larger crystals of gold were observed, and the reaction was complete in less than five seconds. Due to the superior yield of ~2 nm nanocrystals and rapid reaction time at room temperature, this aqueous-based approach became the foundation for my subsequent studies.

When undertaking the investigations outlined in the current Chapter, I had three primary objectives. My first goal was to determine if the aqueous-based technique for

gold nanocrystal synthesis could be extended to produce analogous silver and platinum nanocrystals directly functionalized with BSA protein molecules. My second objective was to decrease the excess sodium borohydride employed in the synthesis. In Chapter 3, broader nanocrystal distributions were observed at higher gold loadings, and since a constant molar ratio of $[\text{BH}_4^-]:[\text{AuCl}_4^-]$ was maintained for each experiment, higher gold loadings corresponded to more sodium borohydride and a more basic pH. As explained previously, BSA undergoes a series of reversible isomerizations for increasingly basic pH, characterized by opening and expansion of the globular protein structure. Thus, the broader size distributions were attributed to the open structure of the protein at increasingly basic conditions. With a decreased molar excess of sodium borohydride, and therefore a less basic final pH, it is possible that narrower nanocrystal size distributions can be achieved. My third goal was to determine the maximum loading of silver, gold, and platinum atoms that can be effectively stabilized by BSA protein molecules as ~2 nm nanocrystals.

4.2 EXPERIMENTAL PROCEDURE

Synthesis. Protein-functionalized silver, gold, and platinum nanocrystals were synthesized in air by reduction in a homogeneous solution at ambient conditions. Silver nitrate (AgNO_3 ; 0.945 N in water; Aldrich), chloroauric acid trihydrate ($\text{HAuCl}_4 \cdot 3\text{H}_2\text{O}$; 99.9+%; Aldrich), or hexachloroplatinic acid hexahydrate ($\text{H}_2\text{PtCl}_6 \cdot 6\text{H}_2\text{O}$); ACS reagent grade; Aldrich) was reduced in water and in the presence of bovine serum albumin (BSA; Fraction V – heat shock treated; Fisher) by the addition of sodium borohydride (NaBH_4 ; 99%; Aldrich). Desired molarities of ionic silver, gold, and platinum precursors were obtained by dilution with deionized water to a total solution volume of 25 mL. All materials were used without further treatment.

In a typical experiment, 1 mL of 0.6857 M AgNO₃ (685.7 μmol Ag), 2 mL of 0.1000 M HAuCl₄ (200 μmol Au), or 2 mL of 0.0750 M H₂PtCl₆ (150 μmol Pt) were added to an aqueous solution containing a variable amount of dissolved BSA protein. Then, 2 mL of freshly-prepared 0.6 M NaBH₄ aqueous solution (1200 μmol NaBH₄) was added rapidly and under vigorous stirring, bringing the total reaction volume to 40.0 mL. Introduction of NaBH₄ to the reaction vessel caused rapid protein foaming, and within five seconds, the solution acquired a deep brown (Ag), golden brown (Au), or black (Pt) color. Each reaction was allowed to proceed under vigorous stirring for 30 minutes.

Tables 4.1, 4.2, and 4.3 summarize the reaction conditions for each system of silver, gold, and platinum, respectively. The third column of these charts indicates the molar ratios of metal atoms to protein molecules. All ratios are calculated on the basis 685.7 μmol Ag, 200 μmol Au, or 150 μmol Pt added to the system. For example, in the Ag system where 28.571 μmol BSA was added to the reaction, the ratio is calculated as [685.7 μmol Ag]:[28.571 μmol BSA], or 24:1. For convenience, throughout this chapter each system will be referenced by its molar ratio, for example “(24:1) Ag:BSA.”

Table 4.1: Reaction conditions for the various systems tested – silver.

BSA (g)	BSA (μmol)	[Ag]:[BSA]
1.8974	28.571	24:1
0.9487	14.285	48:1
0.4744	7.143	96:1

Table 4.2: Reaction conditions for the various systems tested – gold.

BSA (g)	BSA (μmol)	[Au]:[BSA]
0.5534	8.3333	24:1
0.2767	4.1667	48:1
0.1384	2.0833	96:1

Table 4.3: Reaction conditions for the various systems tested – platinum.

BSA (g)	BSA (μmol)	[Pt]:[BSA]
0.4151	6.2500	24:1
0.2075	3.1250	48:1
0.1038	1.5625	96:1

Characterization. Transmission electron microscopy (TEM) was performed using a JEOL 2010F transmission electron microscope equipped with Schottky-type field emission gun, ultra-high resolution pole piece ($C_s = 0.5$ mm), an Energy Dispersive X-ray spectrometer (EDS), and a scanning transmission electron microscope (STEM) unit with high angle annular dark field (HAADF) detector operating at 200 kV. Samples for TEM analysis were prepared by allowing a drop of the aqueous product to evaporate on a lacey carbon-coated copper TEM grid. As the water content evaporates, neighboring protein molecules interact to form a thin film. By focusing within the holes of the lacey carbon, TEM and HAADF images of the protein-functionalized nanocrystals were obtained without the interference of the lacey carbon support. Size distributions for each sample were obtained from HAADF analysis at high magnification, based on measurement of 500 crystals. UV-visible absorption spectra in the range of 240-700 nm were obtained with a Varian Cary 5000 UV-vis NIR spectrometer. Samples for UV-visible absorption analysis were prepared by diluting the original reaction product with deionized water (a twenty-fold dilution by volume). Solution-phase analysis was performed at room temperature using a matched set of quartz cuvettes (path length 10 mm), and operating the spectrometer in dual beam mode. One cuvette was filled with the diluted reaction solution, while the second cuvette contained deionized water.

4.3 RESULTS AND DISCUSSION

4.3.1 On the Selection of Reaction Conditions

One of the stated goals of this work was to decrease the ratio of $[\text{BH}_4^-]:[\text{AuCl}_4^-]$ from the 10:1 ratio employed in Chapter 3. However, this investigation also involves the concurrent analysis of three metals, each with a distinct redox potential and oxidation state. Preliminary experiments revealed each metallic species required a different relative excess of sodium borohydride to ensure well-controlled nanocrystalline products, and it became clear that a different standard for comparison across metallic species was required. Thus, it was determined to maintain the pH of the product for each metallic species at pH \sim 8. With a final basic pH, we can be sure that sodium borohydride was present in excess during the reduction of the metal ionic precursor, and pH \sim 8 will leave BSA in the basic (B) form. (87–90) Using this approach, isomerization to the aged (A) form of BSA was avoided, while still providing a sufficient excess of sodium borohydride to yield rapid reactions with well-controlled nanocrystalline products.

Solution pH was monitored with pH strips, and the molar ratios required for a final pH \sim 8 were 1.75:1 $[\text{BH}_4^-]:[\text{Ag}^+]$, 6:1 $[\text{BH}_4^-]:[\text{AuCl}_4^-]$, and 8:1 $[\text{BH}_4^-]:[\text{PtCl}_6^{2-}]$. The oxidation states of the ionic precursors were Ag(I), Au(III), and Pt(IV), so the molar ratio of [reducing agent]:[ionic precursor] required to achieve pH \sim 8 was twice the oxidation state of the ionic precursor, except in the case of silver, where the molar ratio was determined to be 1.75:1 rather than 2:1. Recall that the ionic precursors of gold and platinum were acids, whereas silver nitrate is neutral. Therefore, more sodium borohydride is required to neutralize the initially acidic solutions of gold and platinum, or conversely, a lower relative excess of sodium borohydride is required for silver.

To remove any variations that might arise due to different concentrations of sodium borohydride, all experiments were conducted using equal concentrations of

sodium borohydride in the reaction. Thus, the amount of ionic precursor added to each system was normalized such that $(685.7 \mu\text{mol Ag}) \times (1.75 \mu\text{mol NaBH}_4 / \mu\text{mol Ag}) = (200 \mu\text{mol Au}) \times (6 \mu\text{mol NaBH}_4 / \mu\text{mol Au}) = (150 \mu\text{mol Pt}) \times (8 \mu\text{mol NaBH}_4 / \mu\text{mol Pt}) = 1200 \mu\text{mol NaBH}_4$ added to each system. As a result, the systems studied in the present investigation offer a means for direct comparison of reaction products as a sole function of protein concentration, across the three metals tested. We will now discuss the results from each noble metal, in order of increasing oxidation state of the ionic precursor.

4.3.2 Formation of Silver Nanocrystals Directly Functionalized by BSA Protein

(24:1) Ag:BSA

The results of the (24:1) Ag:BSA system are summarized in Figure 4.1. Due to the Z^2 -contrast phenomenon discussed previously, the silver nanocrystals are clearly visible through HAADF imaging (Figure 4.1a-c). By focusing in the holes of the lacey carbon support, it was possible to unambiguously observe the protein surrounding the nanocrystals. The film of protein molecules is composed of C, N, O, and S and appears as a faint gray cloudy background, while the silver nanocrystals are the bright, round structures within the protein matrix. The black area in the upper right corner of Figure 4.1a is a hole in the protein film, where no sample is present.

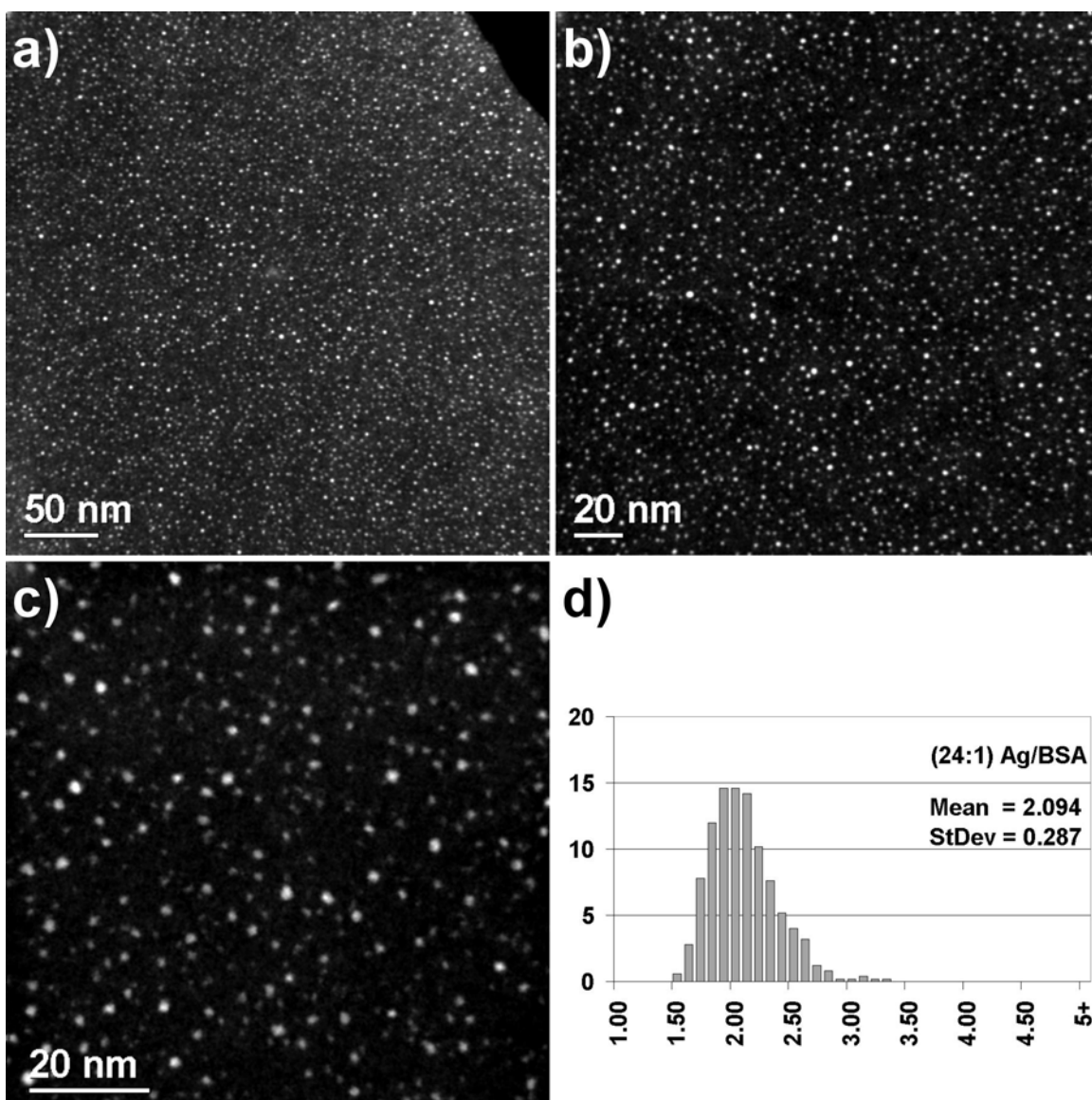


Figure 4.1: (24:1) Ag:BSA. (a)-(c) HAADF images. (d) Size distribution, diameter in nanometers versus percentage frequency.

The silver nanocrystals formed in the (24:1) Ag:BSA system were well-dispersed, with a measured size distribution of 2.094 ± 0.287 nm, or a standard deviation of $\sim 13.7\%$. Recall that in Chapter 3, the (28:5) Au:BSA system possessed the narrowest distribution, with a standard deviation of $\sim 14.1\%$, while the system with the highest loading of gold

atoms, (28:1) Au:BSA, produced a standard deviation of $\sim 32.8\%$. In comparison, (24:1) Ag:BSA provides ~ 2 nm silver nanocrystals with a 57% narrower deviation than the previously-studied (28:1) Au:BSA, with only 15% fewer metal atoms per protein molecule. Alternatively, the current system provides a slightly narrower percent deviation in size than the previously-investigated (28:5) Au:BSA system, with more than four times the number of metal atoms per protein molecule in solution.

High-resolution transmission electron microscopy (HRTEM) analysis was performed to determine the structures of silver nanocrystals produced in the (24:1) Ag:BSA system. Representative images are presented in Figure 4.2. About one-third of the structures were FCC single crystals with either truncated octahedral (Figure 4.2 a-b) or cuboctahedral (Figure 4.2c-d) morphologies. Both of these structures can be considered as resulting from truncation of a cube, resulting in the formation of $\{111\}$ -type surfaces, and they are among the most stable morphologies for nanocrystals in this size range. (32) Another one-third of the observed nanocrystal structures were single-twinned cuboctahedral (Figure 4.2e-g). The formation of structures where a twin plane forms a boundary between subunits with mirror symmetry to each other is quite common in FCC nanocrystals, and especially in silver. (95,96) The final one-third of the structures consisted of multiple-twinned crystals with fivefold symmetry (Figure 4.2h-i). Silver possesses the lowest twinning energy for FCC metals, so it is not surprising that many single-twinned and multiple-twinned nanocrystals of silver are observed. (97)

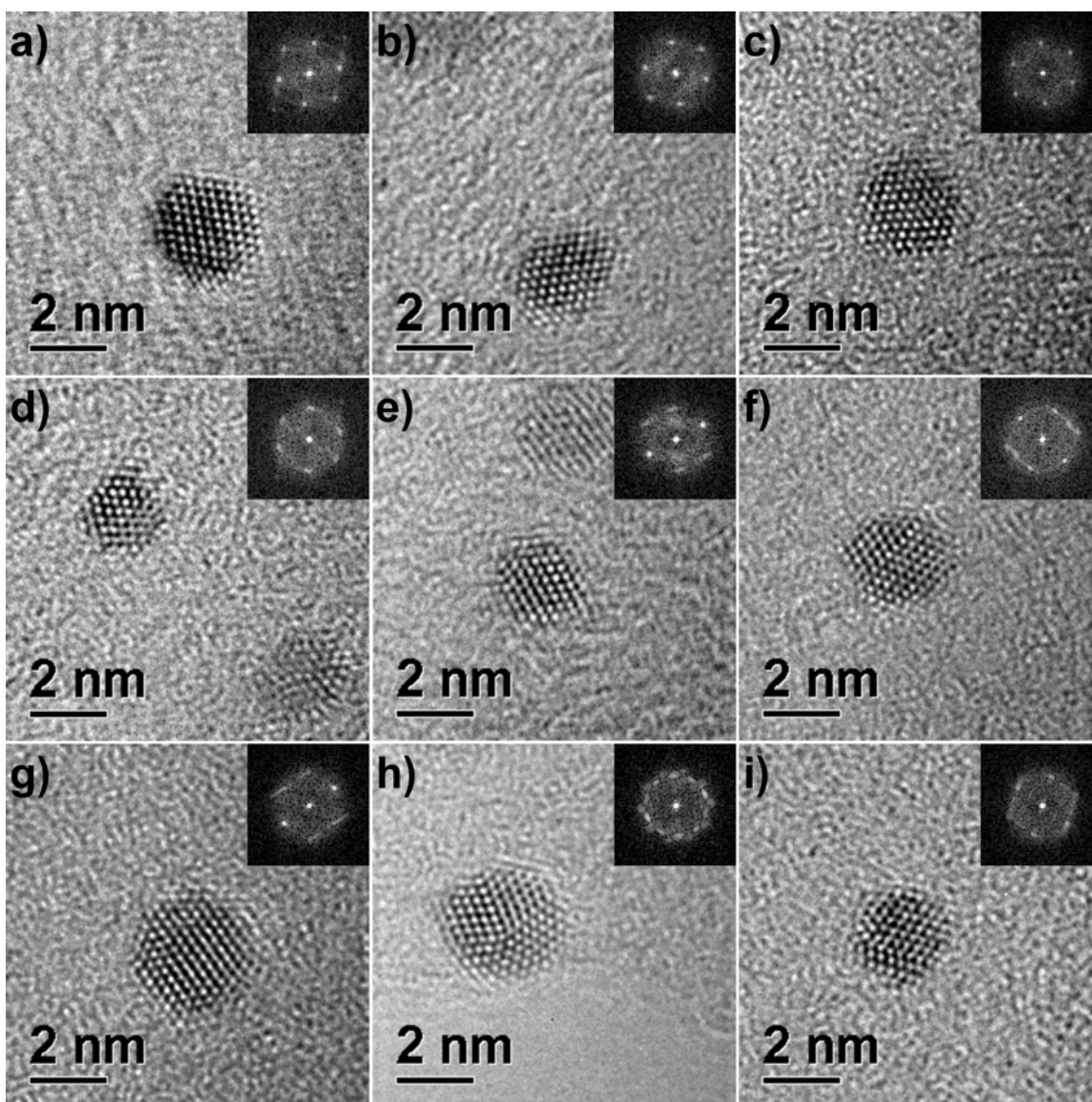


Figure 4.2: (24:1) Ag:BSA – HRTEM images. (a)-(b) FCC truncated octahedral; (c)-(d) FCC cuboctahedral; (e)-(g) single twinned cuboctahedral; (h) Marks decahedron; (i) pentagonal bipyramidal. The fast Fourier transform (FFT) of each image is included as an inset.

The interplanar distances were measured from the FFT of each image in Figure 4.2, and were consistent with the expected values for FCC silver. Figure 4.2a-d are consistent with FCC single crystals in the $\langle 110 \rangle$ zone axis, with $\{111\}$ and $\{200\}$ lattice

planes observed. Figure 4.2e-g are characteristic of single-twinned FCC silver. In all three figures, both twin lamellae share one common set of $\{111\}$ lattice planes, while the spot splitting corresponds to reflections of the $\{111\}$ and $\{200\}$ lattice planes due to the orientation of each twin lamella. Figure 4.2h-i represent FCC cyclic twinned crystals with fivefold symmetry. Figure 4.2h presents a decahedral crystal with the fivefold twinning axis parallel to the electron beam. The corresponding FFT consists of an inner ring of ten symmetric $\{111\}$ -type spots, and an outer ring of ten symmetric $\{200\}$ -type spots. This characteristic pattern results from the superposition of five FCC single crystalline domains in the $\langle 110 \rangle$ zone axis, oriented at 72° angles to each other. Evaluation of the interplanar distances and angular relations of the lattice planes indicates no deviation from the FCC lattice for each of the five individual monocrystalline domains. Figure 4.2i presents another cyclic twinned crystal with fivefold symmetry, but oriented such that only one monocrystalline domains is in the Bragg condition. One set of lattice planes corresponding to an FCC single crystal is clearly observed in the FFT, while the remaining crystalline domains are represented by blurred or streaked spots.

Elemental analysis

EDS spectral analysis was obtained at 25 k magnification for each sample and confirms the presence of C, N, O, S, from the protein molecules, as well as Ag. The Cu spectral peaks are from the TEM grid, while Na is a byproduct from the addition of NaBH_4 . Representative spectra of (24:1) Ag:BSA (Figure 4.3a), (48:1) Ag:BSA (Figure 4.3b), and (96:1) Ag:BSA (Figure 4.3c) are presented. In particular, note the development of the peak intensity of Ag La_1 (2.984 keV) relative to the intensity of S $\text{K}\alpha_1$ (2.307 keV) with increasing silver loadings.

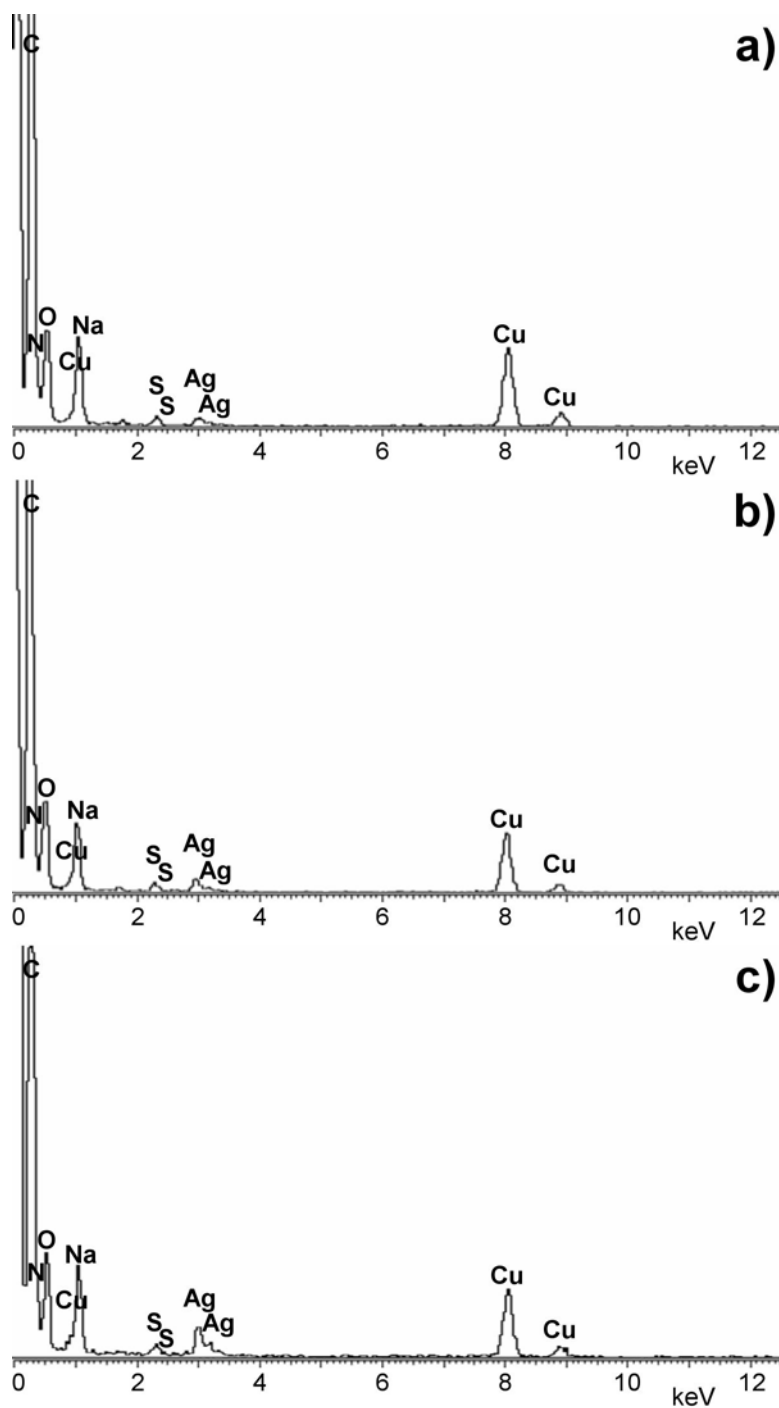


Figure 4.3: EDS spectra of protein-functionalized silver nanocrystals. (a) (24:1) Ag:BSA; (b) (48:1) Ag:BSA; (c) (96:1) Ag:BSA. Note the increasing relative intensity of Ag L α 1 (2.984 keV) with increasing silver loadings.

Table 4.4 presents theoretical S:Ag molar ratios calculated from the amounts of protein and silver originally added, and compares them with EDS measurements, each obtained from the analysis of 10 distinct regions of the sample at 25 k magnification. The measured S:Ag molar ratios are consistent with the predicted values within experimental error, and the S:Ag ratio is halved when the moles of silver double. Taken together, this indicates the silver nanostructures present on the TEM grid are representative of the total population of silver present in the product.

Table 4.4: Theoretical and experimentally-obtained S:Ag Ratios.

(Ag:BSA)	S:Ag (Calc)	S:Ag (EDS)
24:1	1.458	1.419 ± 0.165
48:1	0.729	0.718 ± 0.077
96:1	0.365	0.364 ± 0.047

Absorption spectroscopy

UV-visible absorption spectra of silver nanocrystals <20 nm in diameter exhibit a characteristic surface plasmon resonance peak at ~400 nm. (10) The full-width at half maximum of the surface plasmon resonance is inversely proportional to the nanocrystal diameter, so the absorbance peak becomes broader and less intense as the size of the nanocrystals decrease. (34) For silver nanocrystals ~2 nm in diameter, the surface plasmon resonance can be blue-shifted due to the onset of quantum size effects. The absorption spectrum for (24:1) Ag:BSA exhibits a broad, symmetric peak at ~395 nm. Both the position and the breadth of the surface plasmon resonance suggest the presence of silver nanocrystals ~2 nm in diameter, which is in agreement with our electron microscopy analysis.

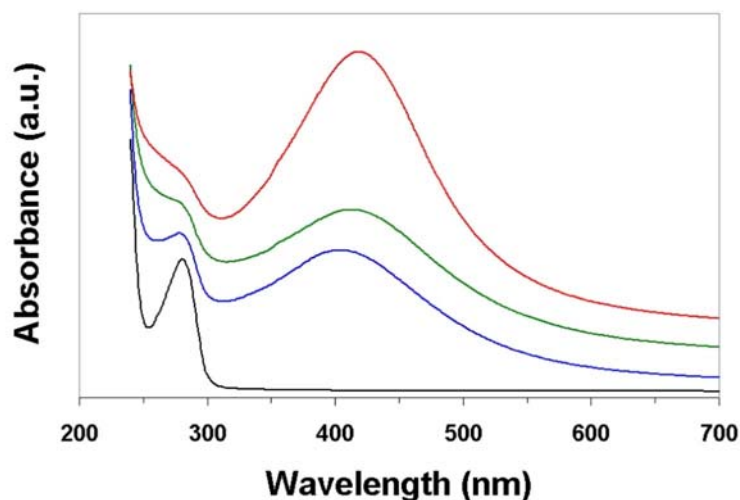


Figure 4.4: UV-visible absorption spectra of the various silver systems. From bottom to top, the spectra are pristine BSA (Black), (24:1) Ag:BSA (Blue), (48:1) Ag:BSA (Green), and (96:1) Ag:BSA (Red). Note the diminishing peak intensity at 278 nm with increased silver loading, and the increased in peak intensity at 410 nm for the (96:1) Ag:BSA system.

The absorption spectrum for (48:1) Ag:BSA also exhibits a broad, symmetric peak, but the absorbance maximum is red-shifted to ~400 nm. This suggests a slightly larger average nanocrystal size than the (24:1) Ag:BSA system, but the breadth and symmetry of the maximum still indicates a well-dispersed population of small silver nanocrystals. Compared to the other two systems, (96:1) Ag:BSA exhibits a narrower, much more intense absorbance maximum that is red-shifted to ~410 nm, indicating the presence of larger silver crystals in this system. Also note that the characteristic absorbance maximum for BSA at 278 nm is progressively quenched with increasing concentrations of silver atoms.

(96:1) Ag:BSA

Figure 4.5 presents a visual comparison of the nanocrystal size distributions observed in the (24:1) Ag:BSA (Figure 4.5a-b) and (48:1) Ag:BSA (Figure 4.5c-d)

systems. Although still well-dispersed, the (48:1) Ag:BSA system exhibits the onset of a bimodal size distribution, with ~20% of the nanocrystals possessing diameters greater than 2.50 nm, as opposed to ~10% of the nanocrystals in the (24:1) Ag:BSA system.

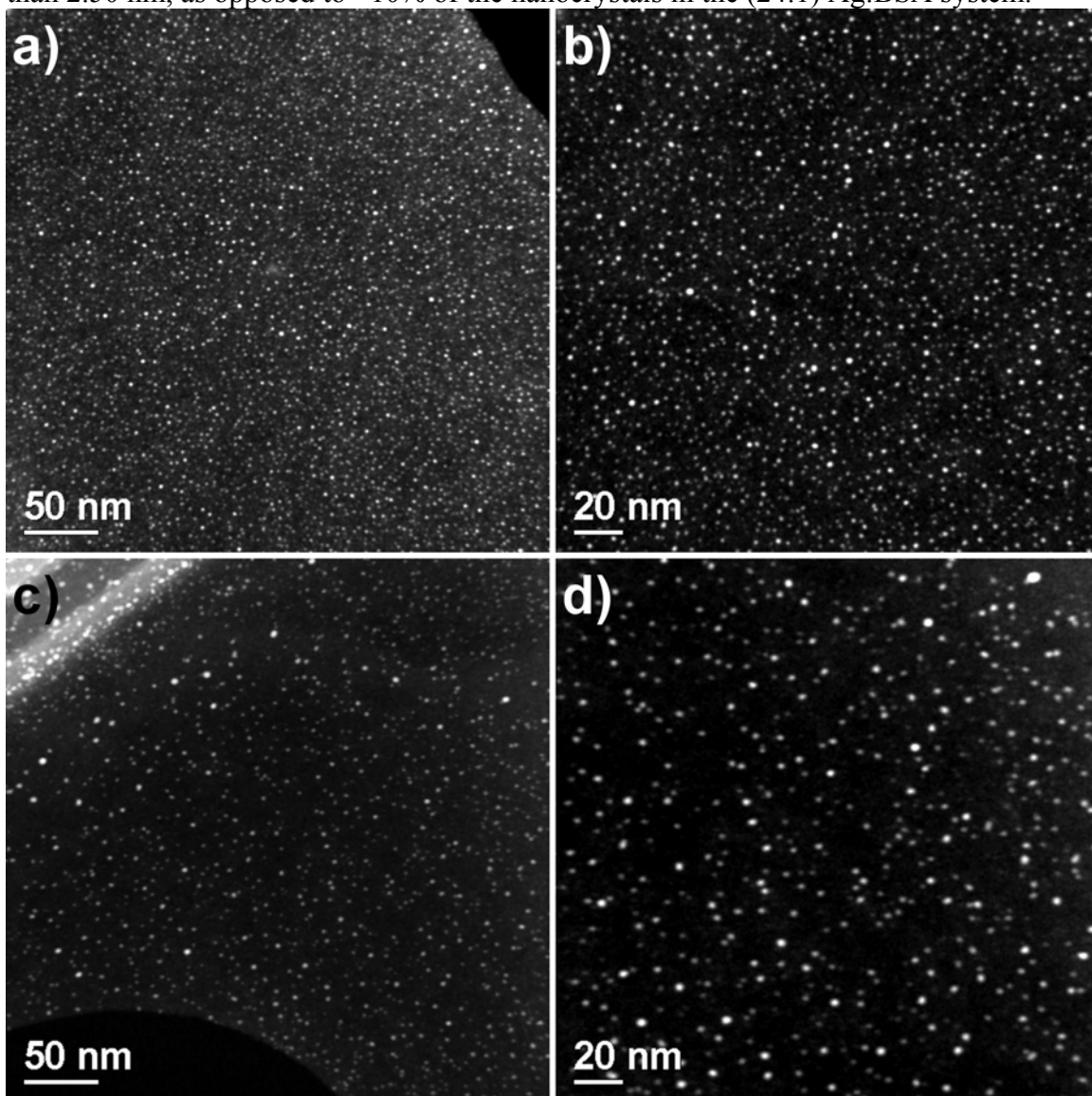


Figure 4.5: HAADF comparison of silver nanocrystal size distributions. (a)-(b) (24:1) Ag:BSA and (c)-(d) (48:1) Ag:BSA.

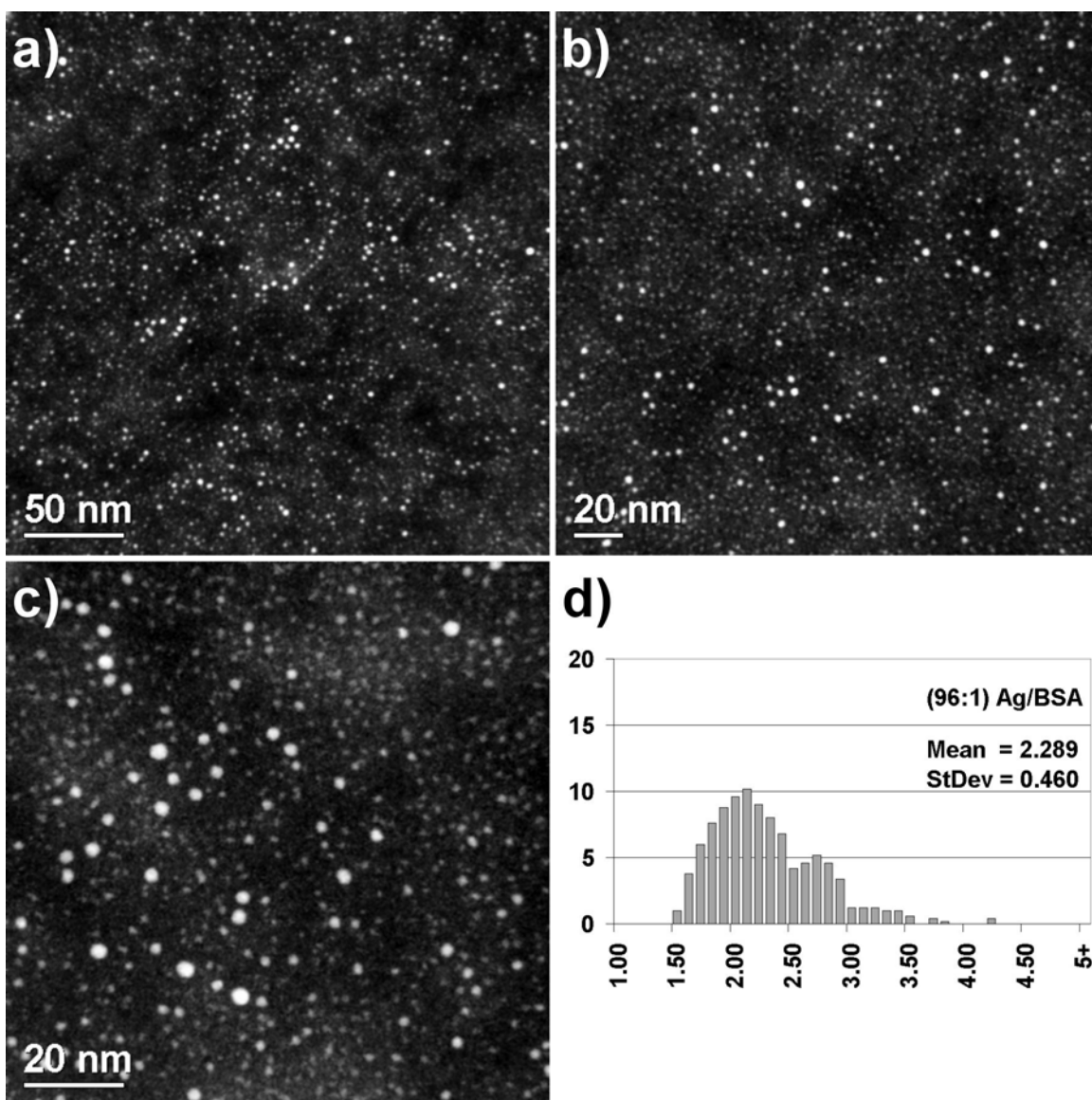


Figure 4.6: (96:1) Ag:BSA. (a) to (c) HAADF images. (d) Size distribution, diameter in nanometers versus percentage frequency.

A bimodal distribution is clearly observed in the (96:1) Ag:BSA system, as summarized in Figure 4.6, with ~30% of the nanometric-scale crystals greater than 2.50 nm in diameter. The size distribution for this system was measured as 2.289 ± 0.460 nm, or a standard deviation of ~20.1%. Although this represents an increase of only ~10% in

the mean particle diameter as compared with the (24:1) Ag:BSA system, the percentage standard deviation in the (96:1) Ag:BSA system is more than 45% greater. The shape distribution of silver nanocrystals was comparable to the (24:1) Ag:BSA system, with many cuboctahedra and decahedra observed.

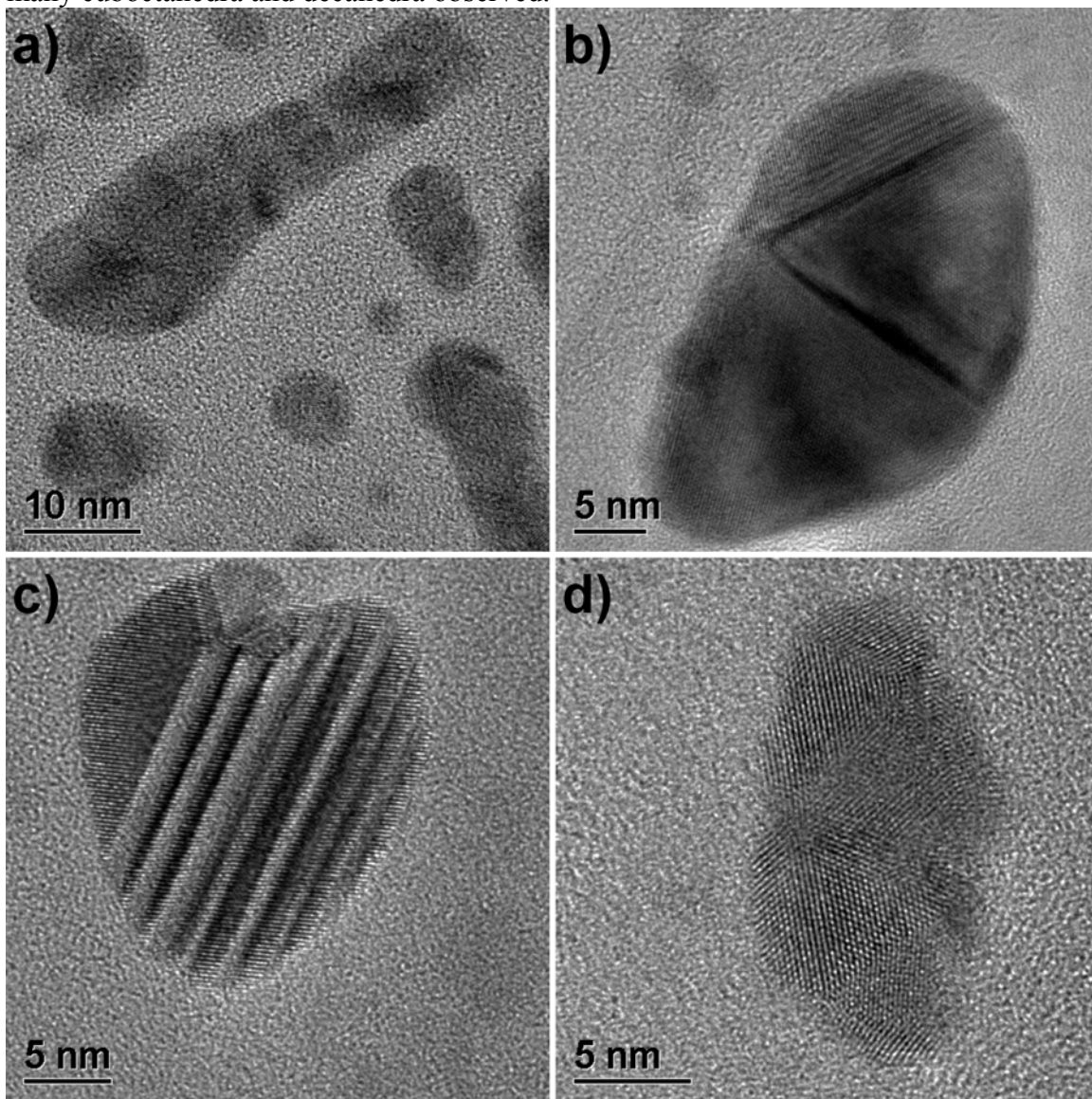


Figure 4.7: (96:1) Ag:BSA – TEM images of larger nanocrystals with high densities of twins and stacking faults.

These ~2 nm nanocrystals represent ~85% of the (96:1) Ag:BSA system. The remaining ~15% of the product, represented in Figure 4.7, consisted of larger crystals with dimensions in the range of 20–80 nm. In contrast, nanocrystals larger than 5 nm were not observed in either the (24:1) Ag:BSA or (48:1) Ag:BSA systems. The large nanocrystals in the (96:1) Ag:BSA system possess a high density of twins and stacking faults, and many of them are elongated. The lattice strain was visibly evident by TEM analysis for several crystals, as in Figure 4.7b-c. Some elongated crystals with lengths in excess of 100 nm were also observed, as seen in Figure 4.8. Although their profile was more regular than the crystals presented in Figure 4.7, a high degree of internal strain was clearly observed through WBDF analysis (Figure 4.8c-d).

In TEM analysis, a constant concern is that the sample on the TEM grid must be representative of the entire sample population being investigated. Since such minute portions of product are utilized, it is possible to draw incorrect conclusions if the sample on the TEM grid inadvertently lacks a certain fraction of the product. As mentioned previously, the S:Ag molar ratios measured by EDS are consistent with the predicted values, and the S:Ag ratio is halved when the moles of silver double. This indicates the silver on the TEM grid is representative of the total amount of silver added to the system. In other words, Figures 4.7 and 4.8 represent the entire sub-population of larger nanocrystals that constitute ~15% of the total product. There is not a fraction of larger crystals that is being neglected in our analysis due to precipitation or sedimentation.

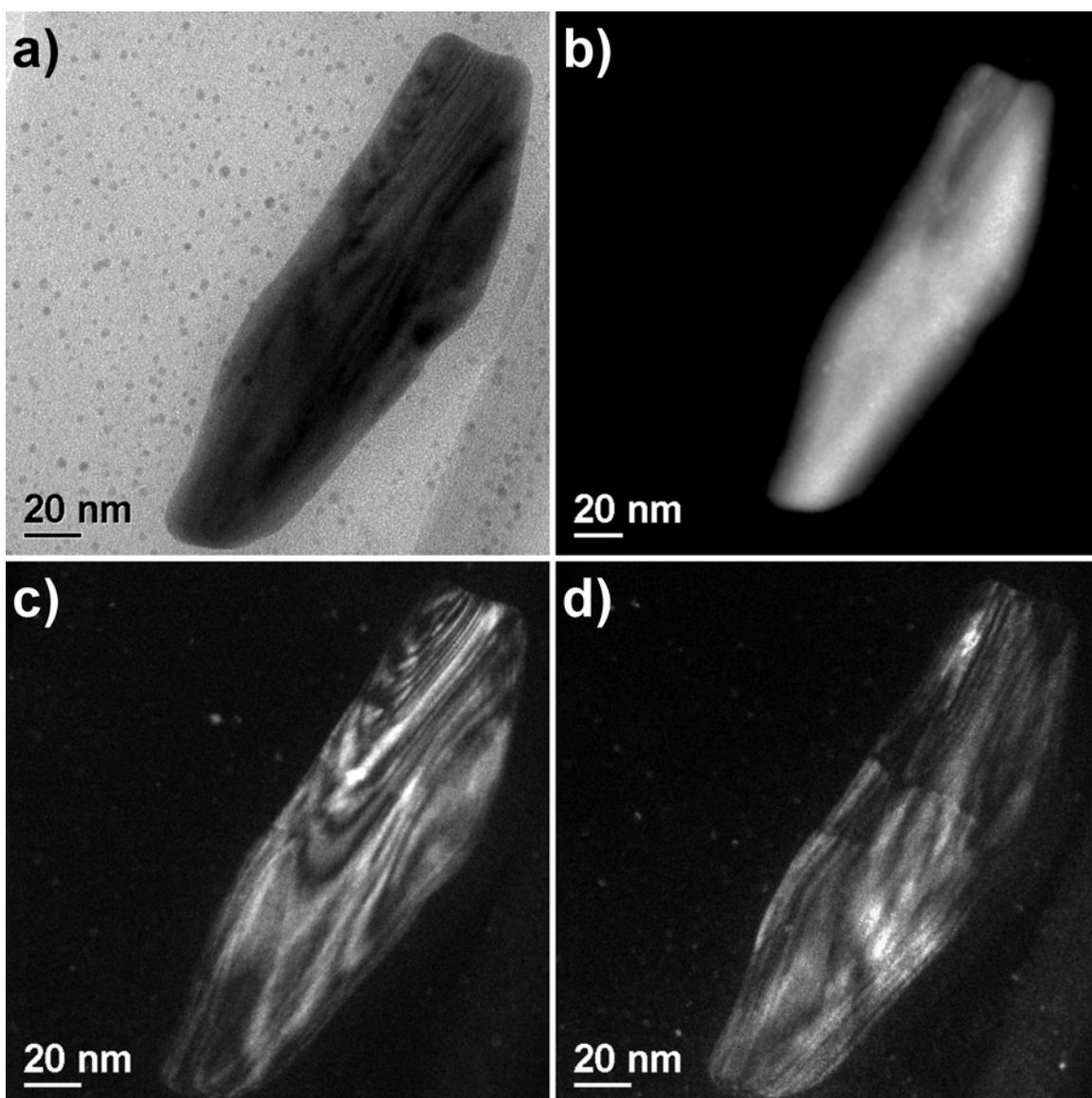


Figure 4.8: (96:1) Ag:BSA – representative images of a larger elongated crystal with length in excess of 100 nm. (a) Conventional TEM image; (b) HAADF image; (c)-(d) WBDF images.

4.3.3 Formation of Gold Nanocrystals Directly Functionalized by BSA Protein

(24:1) Au:BSA

The results of the (24:1) Au:BSA system are summarized in Figure 4.9. The gold nanocrystals are clearly visible through HAADF imaging (Figure 4.9a-c). The film of protein molecules is composed of C, N, O, and S and appears as a faint gray cloudy background, while the gold nanocrystals are the bright, round structures within the protein matrix. The crystals formed in the (24:1) Au:BSA system were well-dispersed, with a size distribution of 1.924 ± 0.282 nm, or a standard deviation of $\sim 14.7\%$.

Recall that in Chapter 3, the (28:5) Au:BSA system possessed the narrowest distribution with a standard deviation of $\sim 14.1\%$, while the system with the highest loading of gold atoms, (28:1) Au:BSA, produced a standard deviation of $\sim 32.8\%$. In comparison, the current embodiment of the (24:1) Au:BSA system provides ~ 2 nm gold nanocrystals with a 55% narrower deviation than the previously-studied (28:1) Au:BSA, with only 15% fewer gold atoms per protein molecule. Alternatively, the current system provides a near-equivalent percent deviation as the previously-investigated (28:5) Au:BSA system, and with more than four times the number of gold atoms per protein molecule in solution.

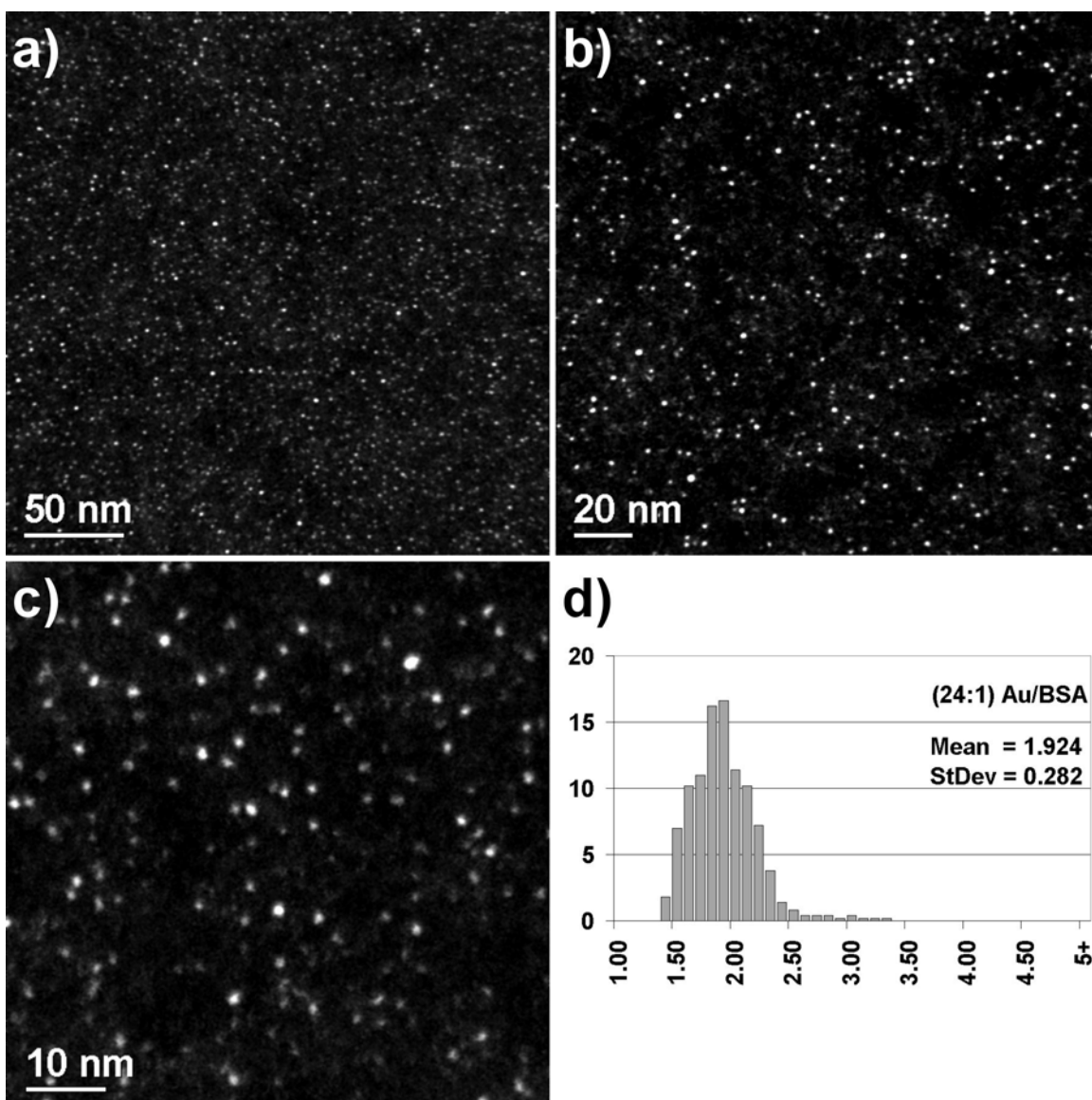


Figure 4.9: (24:1) Au:BSA. (a)-(c) HAADF images. (d) Size distribution, diameter in nanometers versus percentage frequency.

By preparing diluted solutions for TEM analysis, thin films of gold-functionalized protein were deposited on the TEM grid. Focusing in the center of the holes of the lacey carbon support and contracting the electron beam at 1M magnification resulted in localized thinning of the protein film, which allowed for direct imaging of the gold

nanocrystal atomic structure using conventional TEM analysis. During this beam-induced thinning of the protein film, the gold nanocrystals retained their size and structure, and no coalescence of nanocrystals was observed, even when holes developed within the protein film that brought pairs of nanocrystals into intimate proximity of each other (Figure 4.10a). This suggests the gold crystal structures are stable and their surfaces are well-protected by the BSA protein molecules against coalescence. Representative conventional TEM images of the (24:1) Au:BSA system are presented in Figure 4.10. The nanocrystals were well-dispersed, and the average size determined from these images corroborated the size distributions obtained from HAADF analysis.

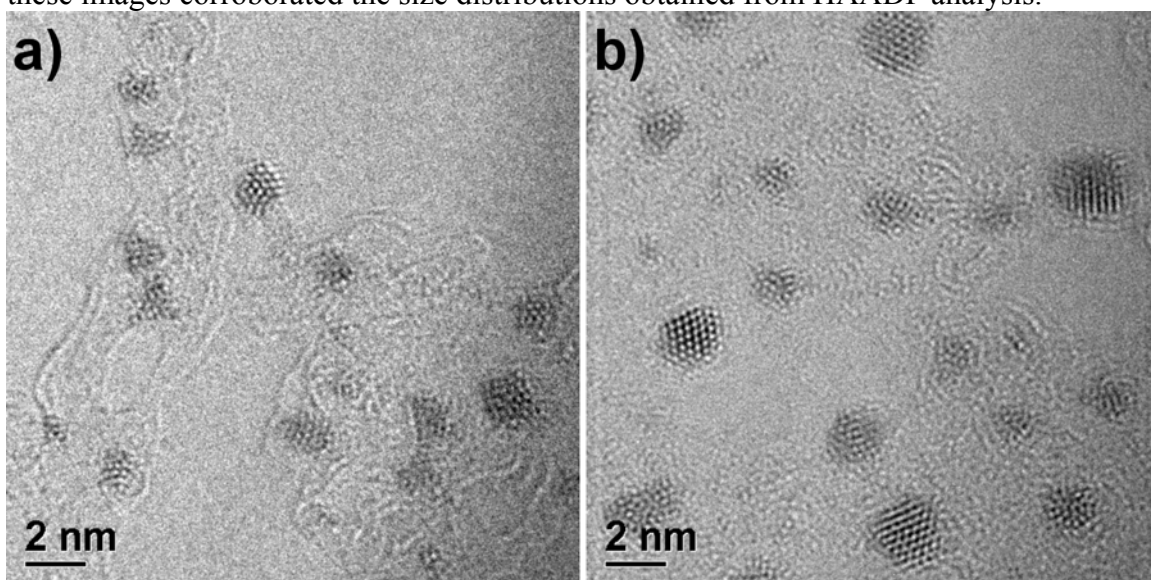


Figure 4.10: (24:1) Au:BSA – Conventional TEM analysis. Thin sections for imaging were obtained by *in situ* beam-induced thinning of the protein film.

HRTEM analysis was performed to determine the structures of gold nanocrystals produced in the (24:1) Au:BSA system. Representative images are presented in Figure 4.11. Approximately two-thirds of the observed structures were FCC single crystals with either truncated octahedral (Figure 4.10 a-c) or cuboctahedral (Figure 4.11d-f) morphologies. The remaining one-third of the structures consisted of either single

twinned FCC crystals (Figure 4.11g) or multiple-twinned crystals with fivefold symmetry, primarily decahedral (Figure 4.11h-i). The twinning energy for gold is among the lower of FCC metals, but is higher than silver. (97) Thus, fewer twinned nanocrystals of gold are observed than was the case with silver.

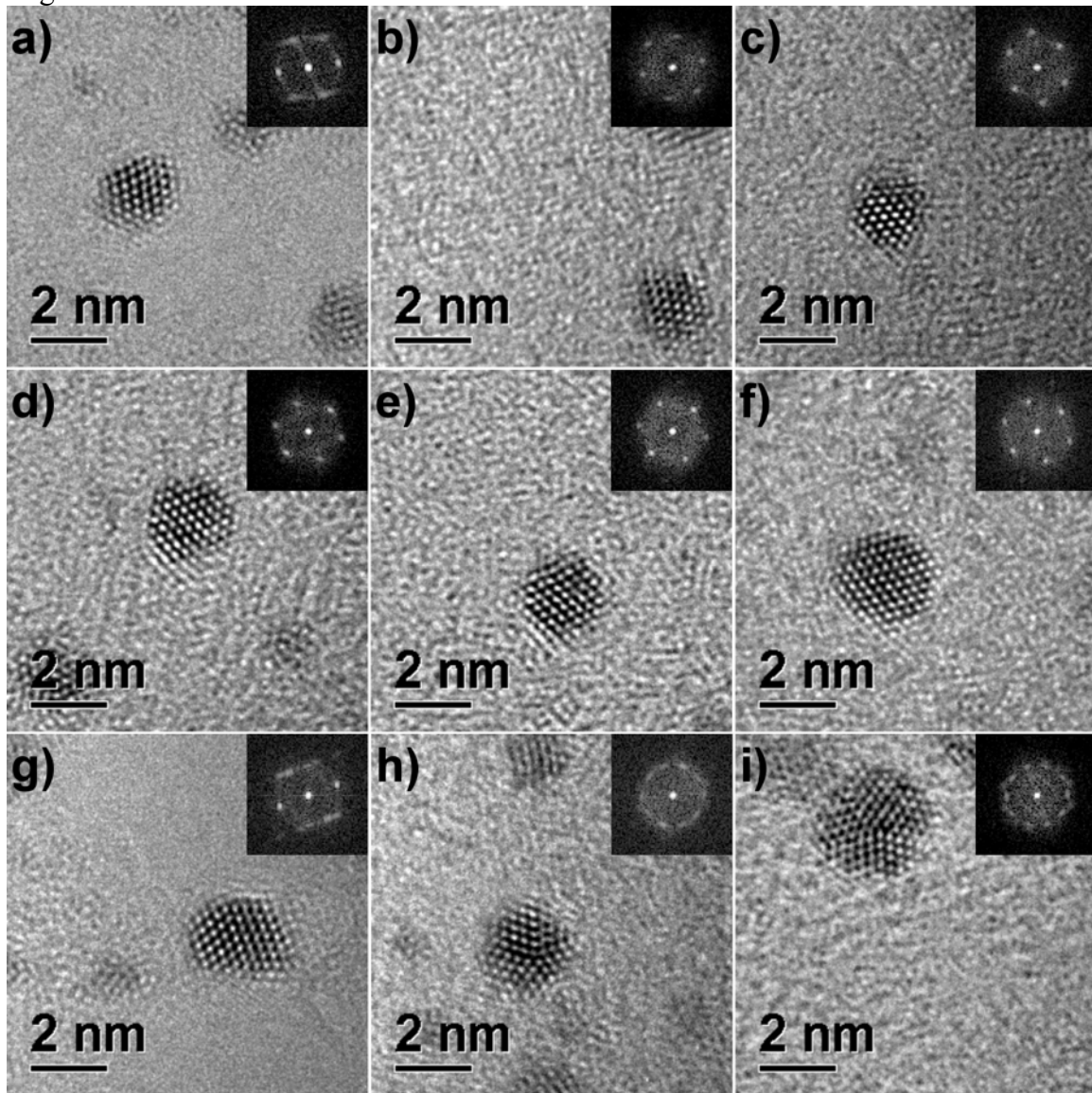


Figure 4.11: (24:1) Au:BSA – HRTEM images. (a)-(c) FCC truncated octahedral; (d)-(f) FCC cuboctahedral; (g) single twinned; (h) pentagonal; (i) Marks decahedron. The FFT of each image is included as an inset.

The interplanar distances were measured from the FFT of each image in Figure 4.11, and were consistent with the expected values for FCC gold. Figure 4.11a-f are consistent with FCC single crystals in the $\langle 110 \rangle$ zone axis, with $\{111\}$ and $\{200\}$ lattice planes observed. Figure 4.11g is characteristic of a single-twinned FCC crystal. Both twin lamellae share one common set of $\{111\}$ lattice planes, while the spot splitting corresponds to reflections of the $\{111\}$ and $\{200\}$ lattice planes due to the orientation of each twin lamella. Figure 4.11h-i represent FCC cyclic twinned crystals with fivefold symmetry, consisting of ten symmetric $\{111\}$ -type spots. Evaluation of the interplanar distances and angular relations of the lattice planes indicates no deviation from the FCC lattice for each of the five individual monocrystalline domains.

Elemental analysis

EDS spectral analysis was obtained at 25 k magnification for each sample and confirms the presence of C, N, O, S, from the protein molecules, as well as Au. The Cu spectral peaks are from the TEM grid, while Na and Cl are byproducts from the addition of NaBH_4 and HAuCl_4 . Representative spectra of (24:1) Au:BSA (Figure 4.12a), (48:1) Au:BSA (Figure 4.12b), and (96:1) Au:BSA (Figure 4.12c) are presented. In particular, note the decrease in peak intensity of S $K\alpha_1$ (2.307 keV) relative to the intensity of Au $M\alpha_1$ (2.123 keV) with increasing gold loadings.

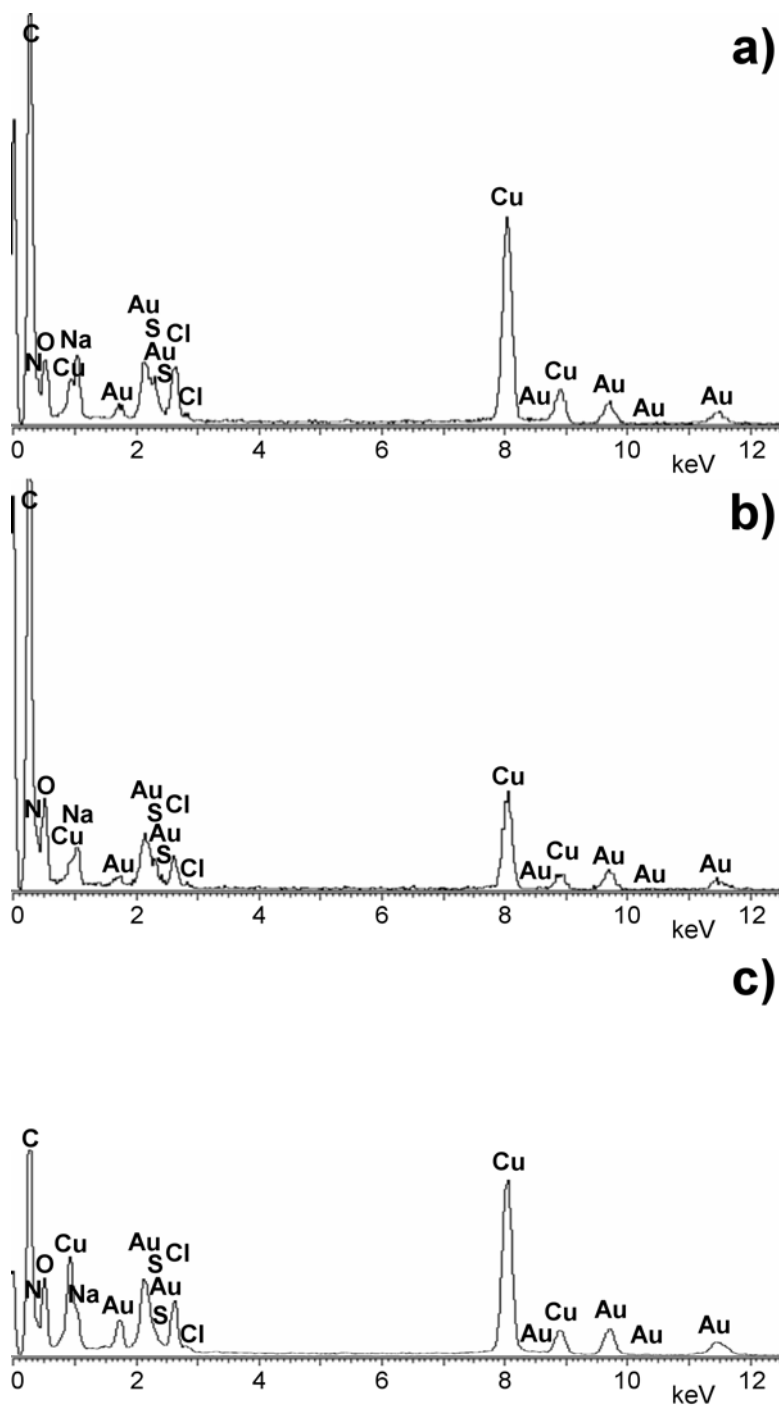


Figure 4.12: EDS spectra of the protein-functionalized gold nanocrystals. (a) (24:1) Au:BSA; (b) (48:1) Au:BSA; (c) (96:1) Au:BSA. Note the decreasing relative peak intensity of S K α 1 (2.307 keV) with increasing gold loadings.

Table 4.5: Theoretical and experimentally-obtained S:Au Ratios.

(Au:BSA)	S:Au (Calc)	S:Au (EDS)
24:1	1.458	1.337 ± 0.160
48:1	0.729	0.680 ± 0.051
96:1	0.365	0.335 ± 0.032

Table 4.5 presents theoretical S:Au molar ratios calculated from the amounts of protein and gold originally added, and compares them with EDS measurements, each obtained from the analysis of 10 distinct regions of the sample at 25 k magnification. The S:Au ratio is halved when the moles of gold added are doubled, as expected. However, the measured S:Au molar ratios are consistently depressed by ~8% when compared with predicted values. This suggests that either ~8% of the protein originally added to the system has been lost, or that ~8% more gold was consistently added to the system than was anticipated. The latter is unlikely; however, the former is possible. Of the three metal species investigated, the most rapid, vigorous foaming occurred in the gold systems. In fact, the protein foam expanded beyond the top of the flask, and out of the reaction vessel. This fraction of foam, which could be as much as 10% of the total solution volume, was not used for analysis.

Protein foaming occurs by the unfolding of individual molecules, giving rise to energetically favorable protein-protein interactions. (98) It is probable that the structural flexibility of a protein molecule decreases when functionalized with a gold nanocrystal. If so, one might expect a smaller percentage of gold-functionalized protein molecules to be incorporated within a stable protein foam, and the foam would be enriched in excess, unreacted protein molecules relative to the total solution composition. This could explain the consistent depression in the experimentally-determined S:Au molar ratios.

Absorption spectroscopy

UV-visible absorption spectra of gold nanocrystals <20 nm in diameter exhibit a characteristic surface plasmon resonance peak at ~520 nm that broadens and decreases in intensity as crystal size decreases. (10) For gold nanocrystals below 2 nm in diameter, this plasmon resonance peak practically disappears due to the onset of quantum size effects. (34,37) As seen in Figure 4.13, (24:1) Au:BSA exhibits no surface plasmon resonance peak, which suggests these nanocrystals are experiencing quantum confinement. This is in agreement with our electron microscopy analysis, where an average diameter of <2 nm was determined.

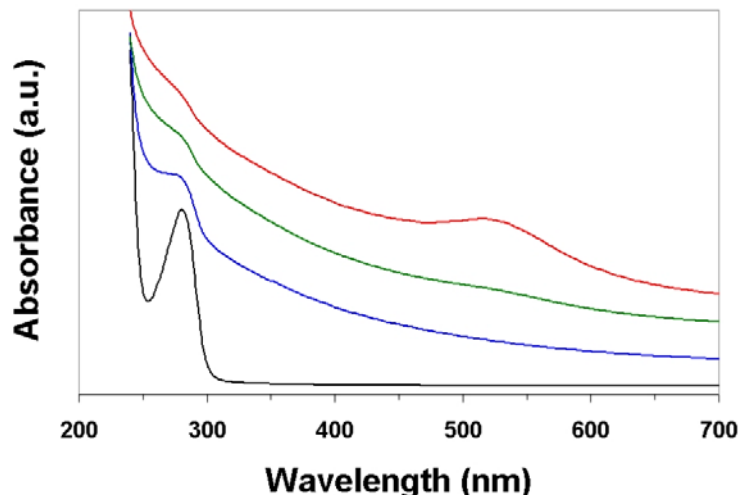


Figure 4.13: UV-visible absorption spectra of the various gold systems. From bottom to top, the spectra are pristine BSA (Black), (24:1) Au:BSA (Blue), (48:1) Au:BSA (Green), and (96:1) Au:BSA (Red). Note the diminishing peak intensity at 278 nm, and the emergence of the surface plasmon resonance at 516 nm, with increasing gold loading.

The absorption spectrum for (48:1) Au:BSA exhibits a broad, symmetric peak of small intensity at 516 nm. This suggests nanocrystals with an average diameter just slightly greater than 2 nm, while the breadth and small intensity of the maximum still indicates a well-dispersed population of small gold nanocrystals. Finally, the spectrum

for (96:1) Au:BSA exhibits a broad, symmetric, but more intense absorbance maximum at 516 nm. The increased intensity suggests these nanocrystals have an appreciably larger average diameter than the previous two systems. Also note that the characteristic absorbance maximum for BSA at 278 nm is progressively quenched with increasing relative concentrations of gold atoms, as was the case for silver.

(96:1) Au:BSA

Figure 4.14 presents a comparison of the nanocrystal size distributions observed in the (24:1) Au:BSA (Figure 4.14a-b) and (48:1) Au:BSA (Figure 4.14c-d) systems. Although still well-dispersed, the (48:1) Au:BSA system exhibits the onset of a broadening size distribution, with ~10% of the nanocrystals possessing diameters greater than 2.50 nm, as opposed to ~3% of the nanocrystals in the (24:1) Au:BSA system.

A broader distribution is clearly observed in the (96:1) Au:BSA system, as summarized in Figure 4.15, with ~30% of the nanocrystals exhibiting diameters larger than 2.50 nm. The size distribution for this system was measured as 2.418 ± 0.813 nm, or a standard deviation of ~33.6%. This represents a ~25% increase in the mean particle diameter as compared with the (24:1) Au:BSA system, and the percentage standard deviation in the (96:1) Au:BSA system is nearly 130% greater.

A cursory comparison of (96:1) Au:BSA (Figure 4.15) with (96:1)Ag:BSA (Figure 4.6) might lead one to believe that the gold nanocrystal distribution at this reaction condition suffers much more than the silver distribution. However, recall that in the case of silver, another 15% of the product in the (96:1) Ag:BSA system consisted of much larger crystals ranging in size from 20 nm to greater than 100 nm (Figures 4.7 and 4.8). In contrast, no gold nanocrystals greater than 10 nm in diameter were observed in the (96:1) Au:BSA system.

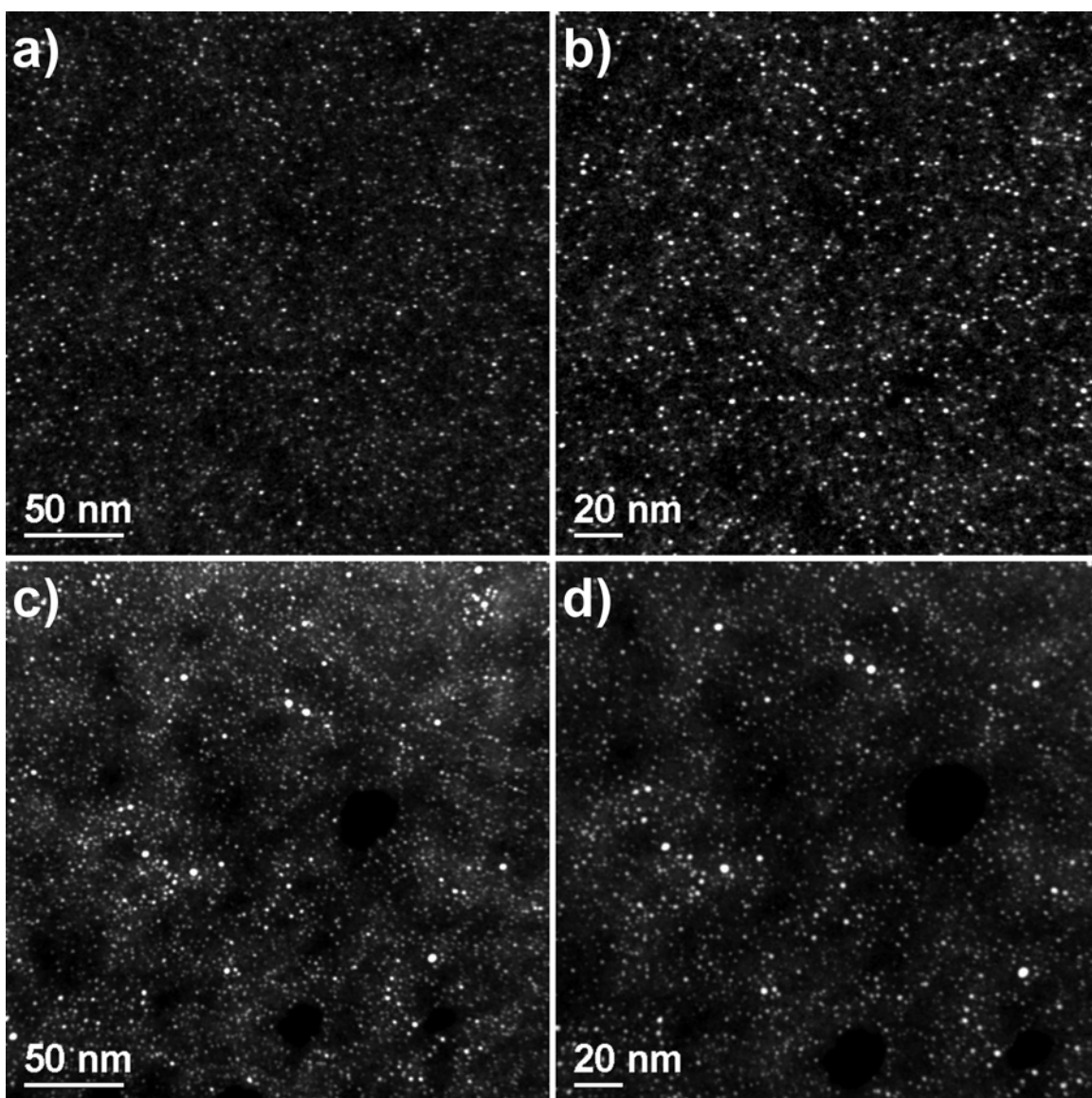


Figure 4.14: HAADF comparison of gold nanocrystal size distributions. (a)-(b) (24:1) Au:BSA and (c)-(d) (48:1) Au:BSA.

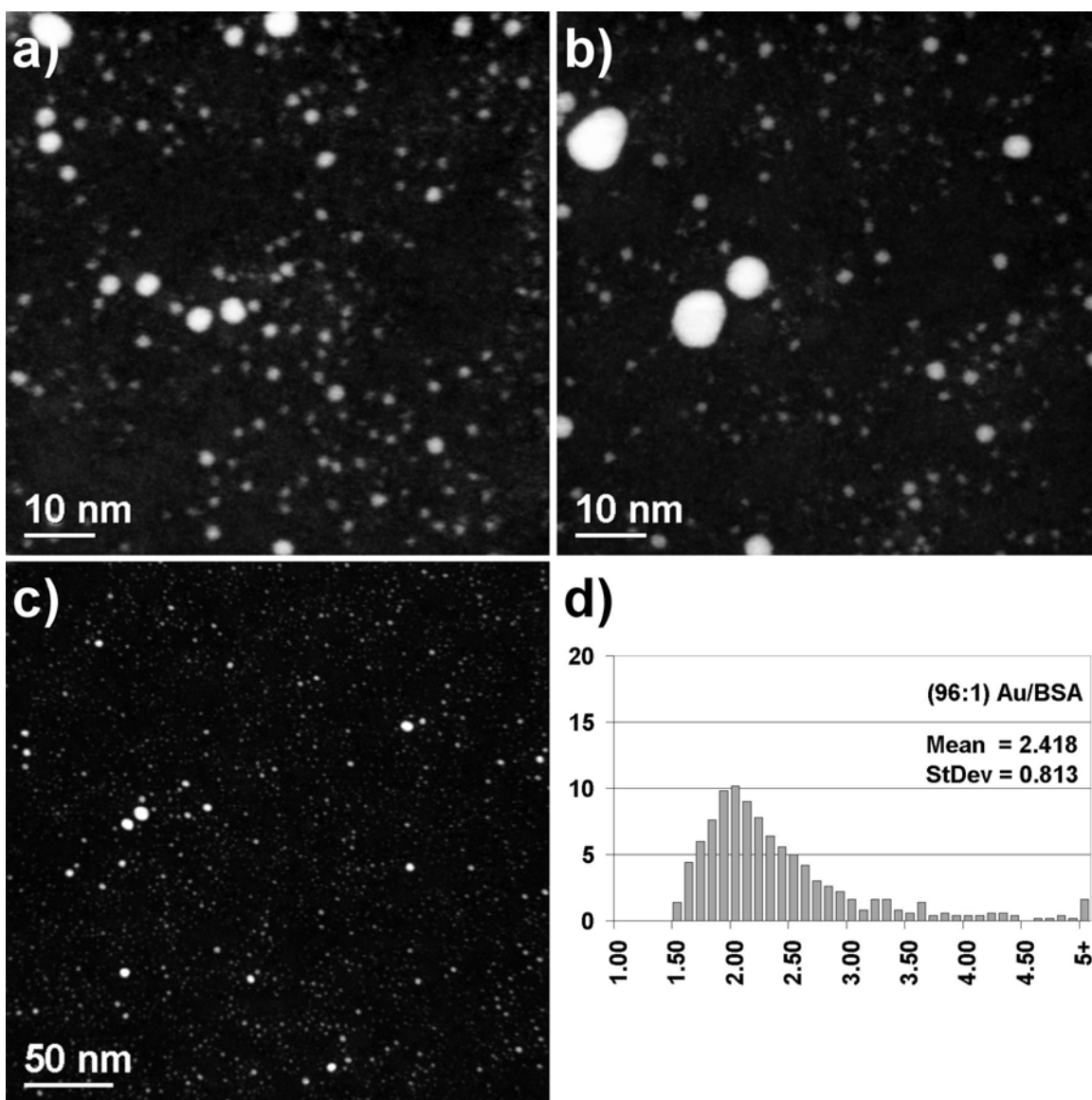


Figure 4.15: (96:1) Au:BSA. (a) to (c) HAADF images. (d) Size distribution, diameter in nanometers versus percentage frequency.

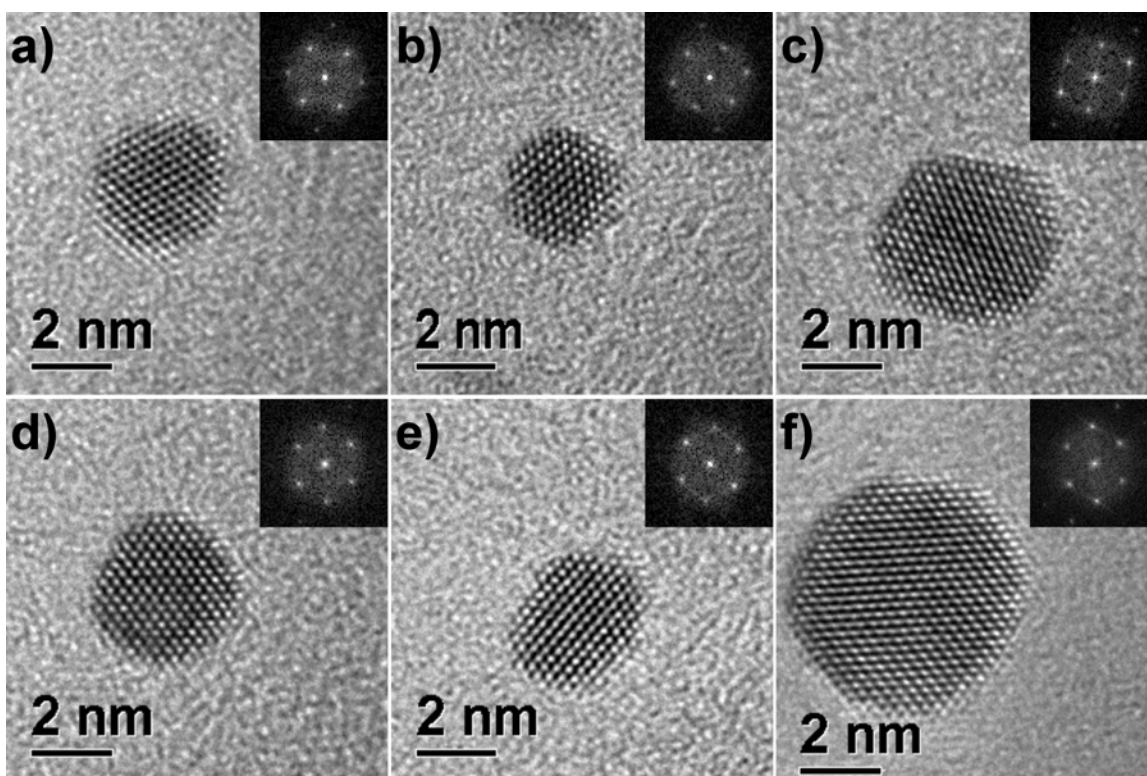


Figure 4.16: (96:1) Au:BSA – HRTEM of FCC single crystals. (a)-(c) FCC cuboctahedral; (d)-(f) FCC truncated octahedral. The FFT of each image is included as an inset.

HRTEM analysis was performed to determine the structures of gold nanocrystals in the (96:1) Au:BSA system. About 45% of the product consisted of FCC single crystals, equally distributed among cuboctahedral (Figure 4.16a-c) and truncated octahedral (Figure 4.16d-f). Another 45% consisted of multiple-twinned crystals with fivefold symmetry, primarily decahedral (Figure 4.17). Finally, ~10% of the (96:1) Au:BSA system consisted of nanocrystals with parallel twinning (Figure 4.18). It is informative to note the larger percentage of decahedral crystals in this system than in the case of (24:1) Au:BSA.

Intermediate-sized (2–5 nm) cyclic twinned nanocrystals can result from two possible growth mechanisms. In one case, they can be considered to be the result of

successive shells of atoms being added to a primary-sized nanocrystal (<2 nm) that had fivefold symmetry. (24) In the second case, we can consider that primary-sized FCC single crystals (tetrahedral or cuboctahedral) are combining to form cyclic twinned structures. As noted previously, less than one-third of the (24:1) Au:BSA system consisted of cyclic twinned crystals. This suggests the second growth mechanism is most likely, and that <2 nm FCC single crystals are growing by cyclic twinning to form multiple-twinned fivefold symmetric structures in the range of 2–5 nm.

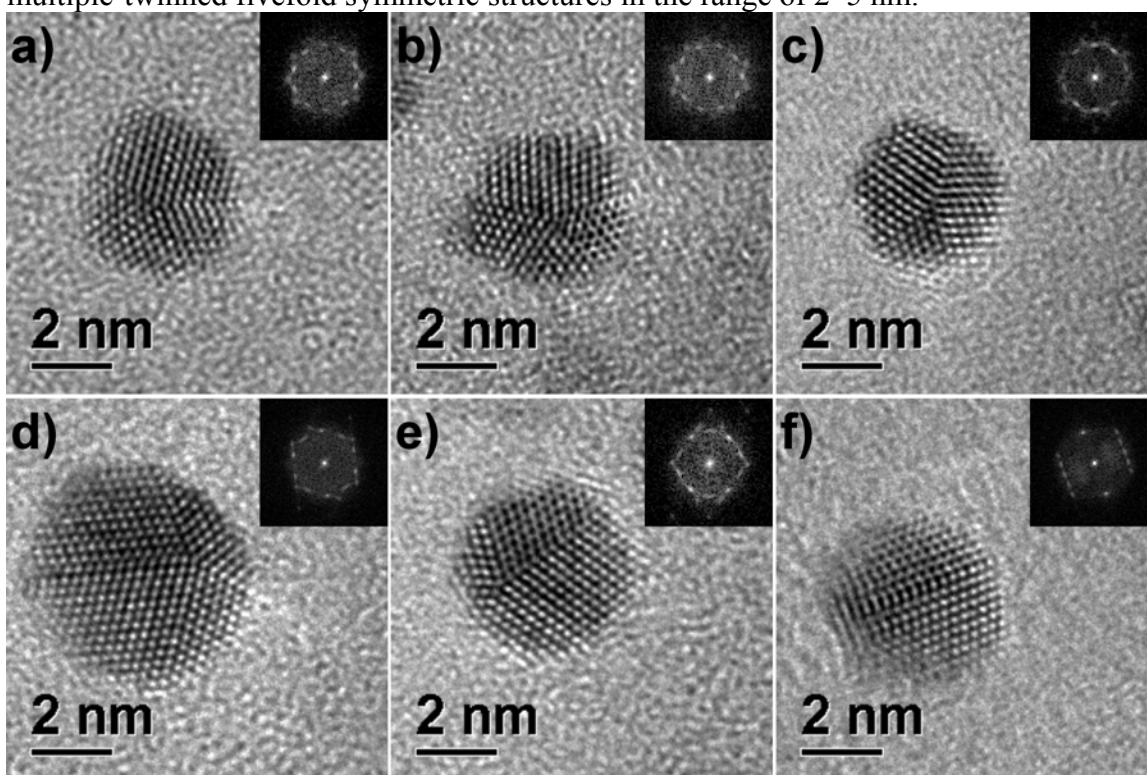


Figure 4.17: (96:1) Au:BSA – HRTEM of multiple-twinned crystals with fivefold symmetry. (a)-(c) decahedra in the fivefold orientation; (d)-(e) decahedra between the twofold and fivefold orientations; (f) decahedron in the twofold orientation. The FFT of each image is included as an inset.

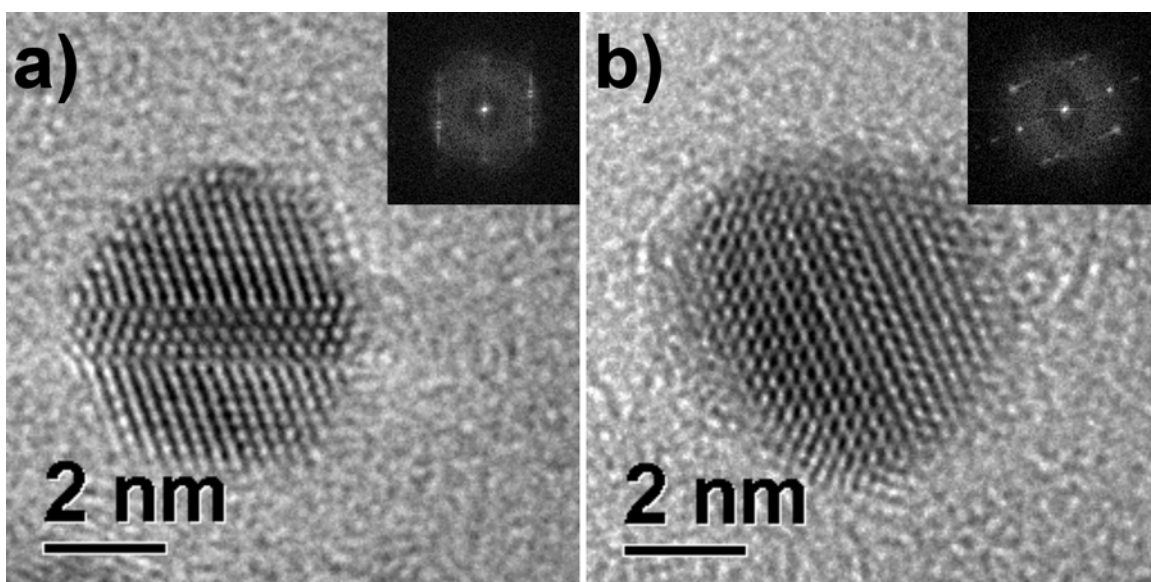


Figure 4.18: (96:1) Au:BSA – HRTEM of crystals with parallel twinning structural defects. The FFT of each image is included as an inset.

The absence of any gold nanostructures larger than ~10 nm, combined with the small percentage of nanocrystals in irregular shapes, suggests that the larger gold crystals in this system are not growing by coalescence. Rather, we propose that the observed distribution in the (96:1) Au:BSA system develops as follows. The protein molecules in solution form complexes with a certain percentage of the AuCl_4^- ions prior to reaction. When these ions are reduced to atoms, there will be a higher local concentration of gold atoms within the protein molecules, and gold will tend to nucleate within the protein. These nuclei will be well-protected by the bulk of the globular protein, and their surfaces will be stabilized by the locally-high availability of sulfur-bearing residues within the protein molecule.

Let us consider the gold atoms within the protein molecules as being sequestered, and effectively reducing the concentration of free gold in solution. For larger excesses of protein, such as in the (24:1) Au:BSA system, a sufficient percentage of the total gold

atoms in the system are sequestered within protein molecules to bring the concentration of free gold in solution below the critical nucleation concentration. Therefore, the free atoms in solution will contribute to the growth of existing protein-stabilized nuclei, and the formation of nuclei outside of the protein molecules is largely avoided.

However, due to the smaller excess of protein molecules in the (48:1) Au:BSA and (96:1) Au:BSA systems, a smaller percentage of the total gold atoms in the system are sequestered within protein molecules, and the concentration of free gold in solution is greater than the critical nucleation concentration. If the number of protein-stabilized nuclei (designated “primary nuclei” for ease of discussion) is sufficiently large, the number of solution-phase nuclei (designated “secondary nuclei”) will be limited, as the formation of a relatively few secondary nuclei will bring the concentration of free gold atoms in solution below the critical nucleation concentration. This is the case in the (48:1) Au:BSA system. For decreasing excesses of protein, as in the (96:1) Au:BSA system, secondary nucleation becomes more significant.

Once the solution-phase concentration of gold atoms decreases beyond the critical nucleation concentration, the remaining free gold atoms will be consumed in the growth of both primary and secondary nuclei. As there is still an excess of protein relative to gold nuclei, the secondary nuclei will eventually encounter free protein molecules in solution and experience surface-stabilizing interactions. Thus, the secondary nuclei will also experience well-controlled growth once they become protein-functionalized. This accounts for the high percentage of stable morphologies, such as FCC single crystals and decahedra, among the larger nanocrystals in the (96:1) Au:BSA system. However, each of the secondary nuclei will statistically have reached a different stage of growth before encountering a protein molecule, and as a result there will be a broader size distribution among those nanocrystals that result from secondary nuclei.

4.3.4 Formation of Platinum Nanocrystals Directly Functionalized by BSA Protein

(24:1) Pt:BSA

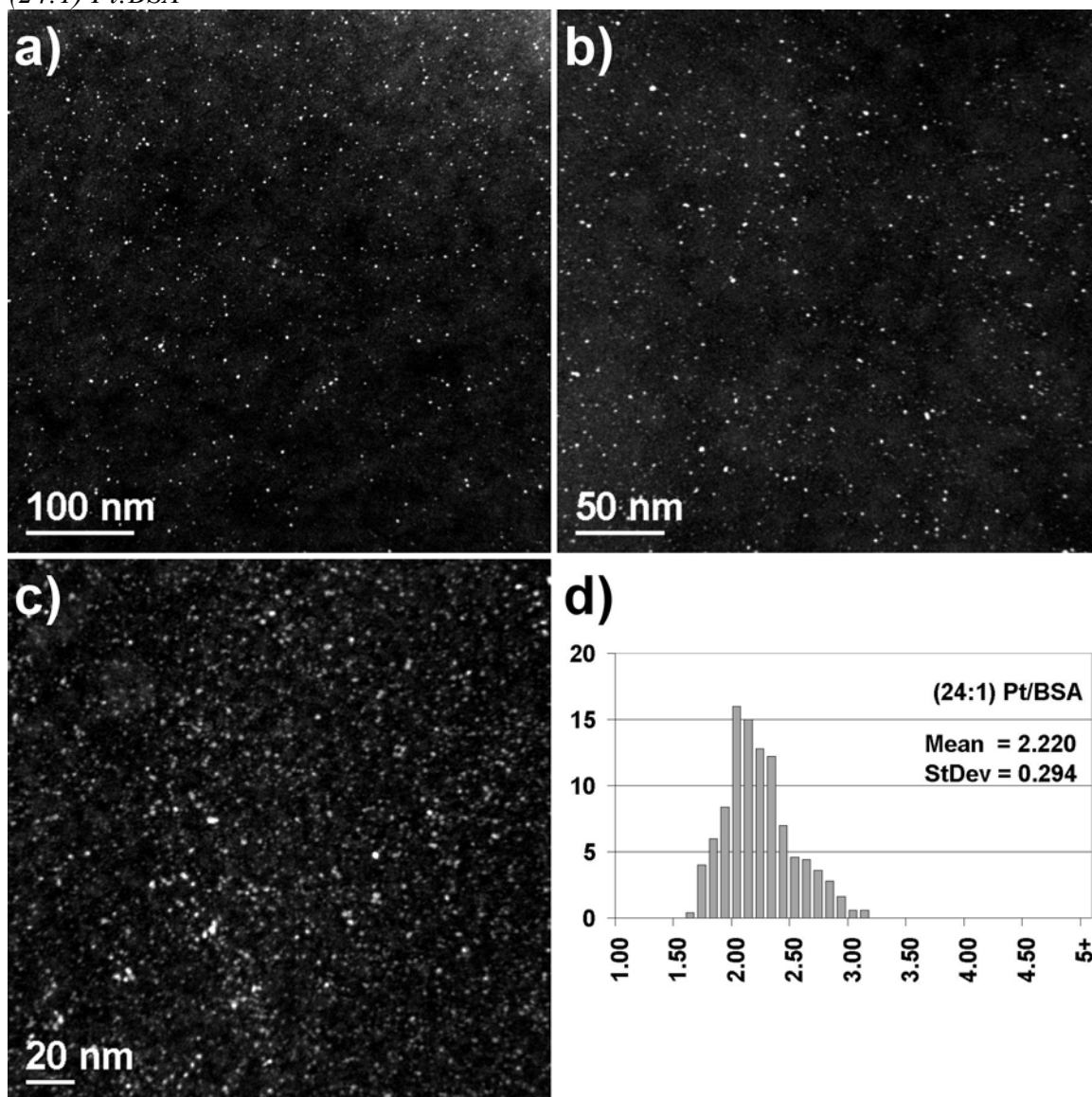


Figure 4.19: (24:1) Pt:BSA. (a)-(c) HAADF images. (d) Size distribution, diameter in nanometers versus percentage frequency.

The results of the (24:1) Pt:BSA system are summarized in Figure 4.19. The platinum nanocrystals are clearly visible through HAADF imaging (Figure 4.19a-c). The

film of protein molecules is composed of C, N, O, and S and appears as a faint gray cloudy background, while the platinum nanocrystals are the bright, round structures within the protein matrix. The platinum nanocrystals formed in the (24:1) Pt:BSA system were well-dispersed, with a measured size distribution of 2.220 ± 0.294 nm, or a standard deviation of $\sim 13.2\%$.

Recall that in Chapter 3, the (28:5) Au:BSA system possessed the narrowest distribution with a standard deviation of $\sim 14.1\%$, while the system with the highest loading of gold atoms, (28:1) Au:BSA, produced a standard deviation of $\sim 32.8\%$. In comparison, (24:1) Pt:BSA provides ~ 2 nm platinum nanocrystals with a 60% narrower deviation than the previously-studied (28:1) Au:BSA, with only 15% fewer metal atoms per protein molecule. Alternatively, the current system provides a narrower percent deviation than the previously-investigated (28:5) Au:BSA system, and with more than four times the number of metal atoms per protein molecule in solution.

HRTEM analysis was performed to determine the structures of platinum nanocrystals produced in the (24:1) Pt:BSA system. Representative images are presented in Figure 4.20. Nearly all observed structures were FCC single crystals with either cuboctahedral (Figure 4.20 a-d) or truncated octahedral (Figure 4.10e-f) morphologies. The twinning energy for platinum is among the highest of all FCC metals, and so cyclic twinning is highly unfavorable in platinum. (99) This explains the paucity of cyclic twinning structures such as decahedra.

The interplanar distances were measured from the FFT of each image in Figure 4.20, and were consistent with the expected values for FCC platinum. Figure 4.20a-f are consistent with FCC platinum single crystals in the $\langle 110 \rangle$ zone axis, with $\{111\}$ and $\{200\}$ lattice planes observed. Evaluation of the interplanar distances and angular relations of the lattice planes indicates no deviation from the bulk FCC lattice.

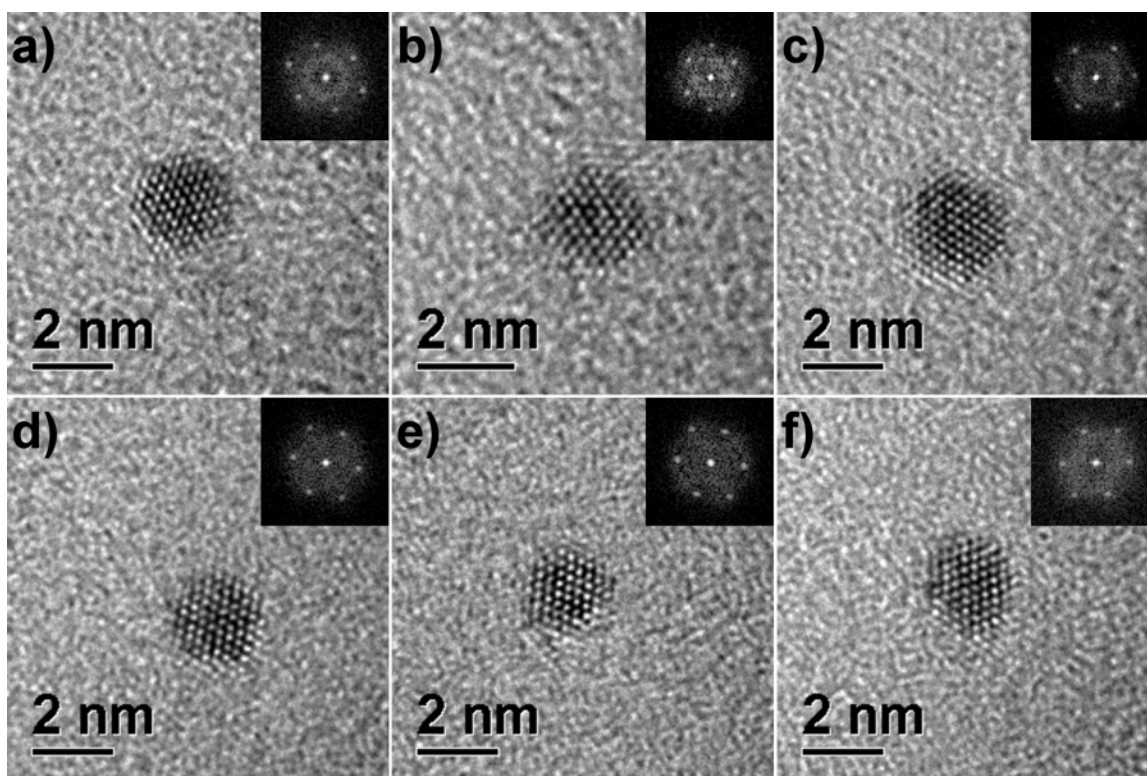


Figure 4.20: (24:1) Pt:BSA – HRTEM images. (a)-(d) FCC cuboctahedral; (e)-(f) FCC truncated octahedral. The FFT of each image is included as an inset.

Elemental analysis

EDS spectral analysis was obtained at 25 k magnification for each sample and confirms the presence of C, N, O, S, from the protein molecules, as well as Pt. The Cu spectral peaks are from the TEM grid, while Na and Cl are byproducts from the addition of NaBH_4 and H_2PtCl_6 . Representative spectra of (24:1) Pt:BSA (Figure 4.21a), (48:1) Pt:BSA (Figure 4.21b), and (96:1) Pt:BSA (Figure 4.21c) are presented. In particular, note the increase in peak intensity of Pt $\text{M}\alpha_1$ (2.051 keV) relative to the intensity of S $\text{K}\alpha_1$ (2.307 keV) with increasing platinum loadings.

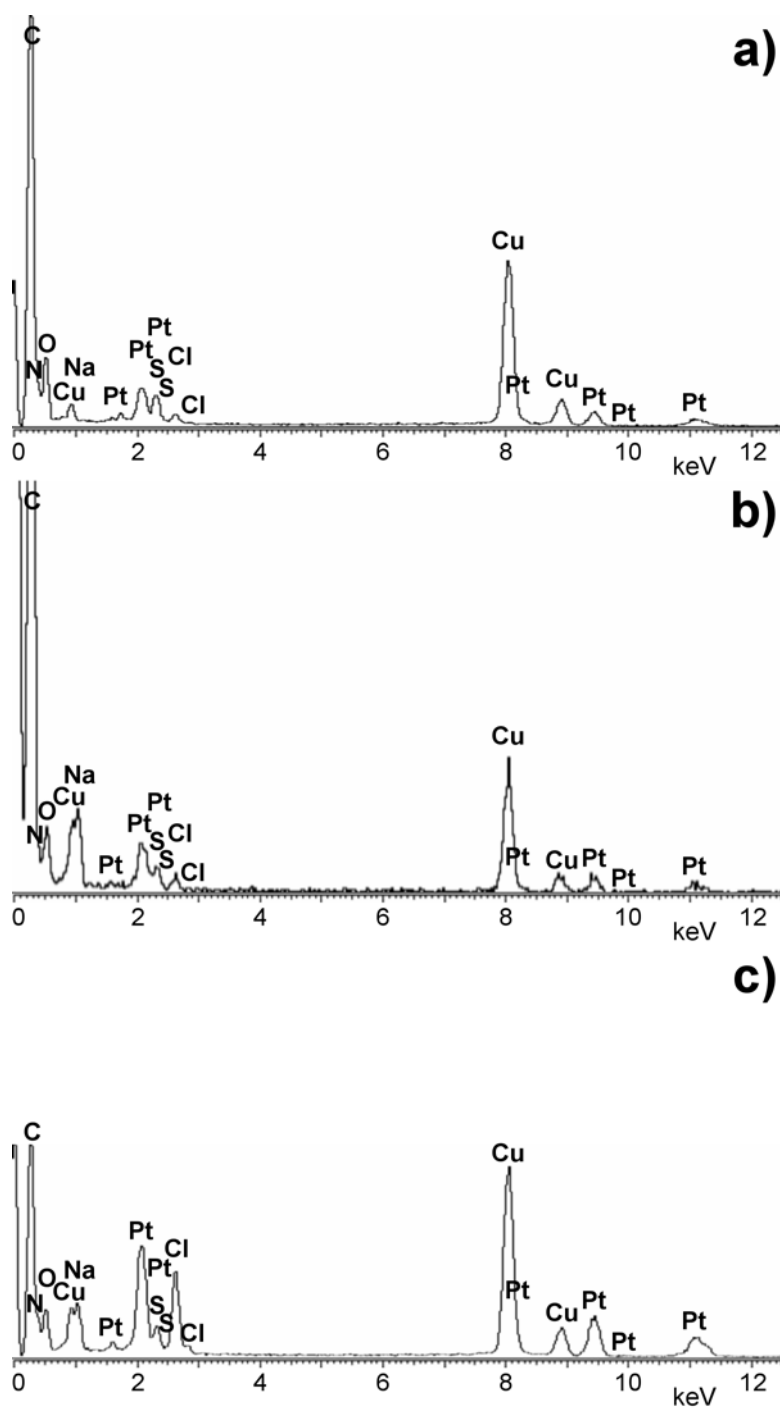


Figure 4.21: EDS spectra of the protein-functionalized platinum nanocrystals. (a) (24:1) Pt:BSA; (b) (48:1) Pt:BSA; (c) (96:1) Pt:BSA. Note the increasing relative peak intensity of Pt M α 1 (2.051 keV) with increasing platinum loadings.

Table 4.6: Theoretical and experimentally-obtained S:Pt Ratios.

(Pt:BSA)	S:Pt (Calc)	S:Pt (EDS)
24:1	1.458	1.510 ± 0.120
48:1	0.729	0.752 ± 0.108
96:1	0.365	0.376 ± 0.092

Table 4.6 presents theoretical S:Pt molar ratios calculated from the amounts of protein and platinum originally added, and compares them with EDS measurements, each obtained from the analysis of 10 distinct regions of the sample at 25 k magnification. The S:Pt ratio is halved when the moles of platinum added are doubled, as expected. However, the measured S:Pt molar ratios are consistently ~3% larger than the predicted values. This suggests that either ~3% of the platinum added to the system has been lost, or that ~3% less platinum was consistently added to the system than was anticipated. The latter is unlikely; however, the former is possible. Of the three metal species investigated, platinum exhibited a tendency to form small, gelatinous protein aggregates in the product. These aggregates were filtered out of solution prior to analysis.

One of these protein aggregates was retrieved, dried, pulverized, and deposited on a TEM grid for analysis. The characteristic HAADF images are presented in Figure 4.22. When compared with the majority of the product (Figure 4.19), these protein aggregates are rich in platinum. It could be that the loss of these gelatinous aggregates rich in platinum are responsible for the observed ~3% disparity between the experimental and predicted S:Pt molar ratios. As an aside, it is interesting to note that even when incorporated into these protein aggregates, the platinum nanocrystals still possess small, uniform size distributions.

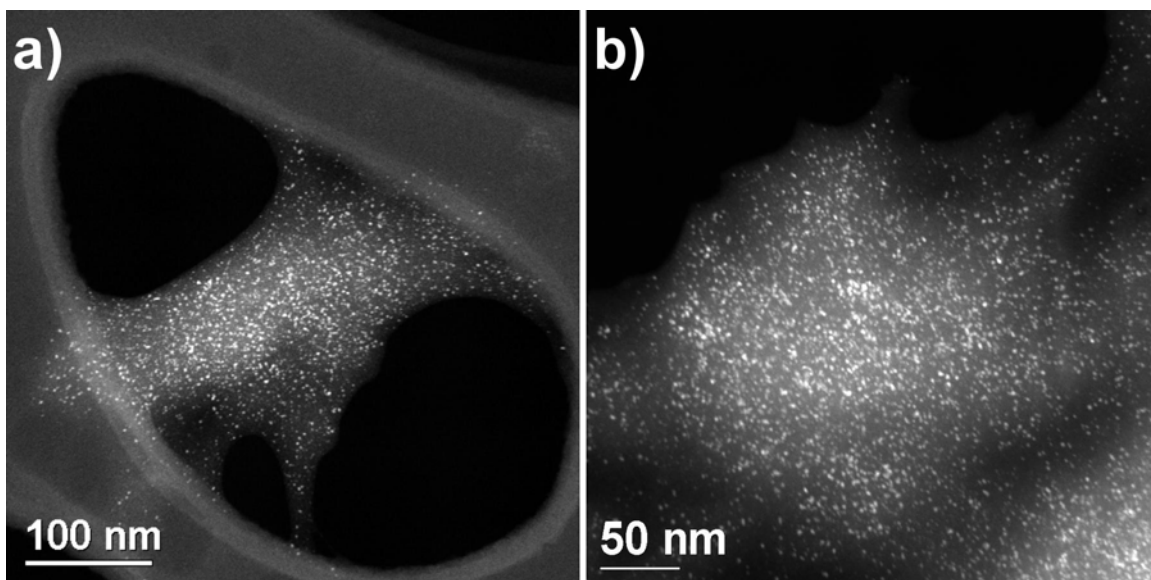


Figure 4.22: HAADF images of platinum-rich protein aggregates.

Absorption spectroscopy

A surface plasmon resonance for platinum is not observable by UV-visible absorption spectroscopy. (100) Nevertheless, absorption spectra for the platinum systems, comparable to those for silver (Figure 4.4) and gold (Figure 4.13), are presented in Figure 4.23. The purpose of this analysis was to study the characteristic absorbance maximum for BSA at 278 nm, which was progressively quenched for increasing concentrations of gold and silver atoms. In fact, the same trend of decreasing intensity at 278 nm was observed with increasing concentrations of platinum.

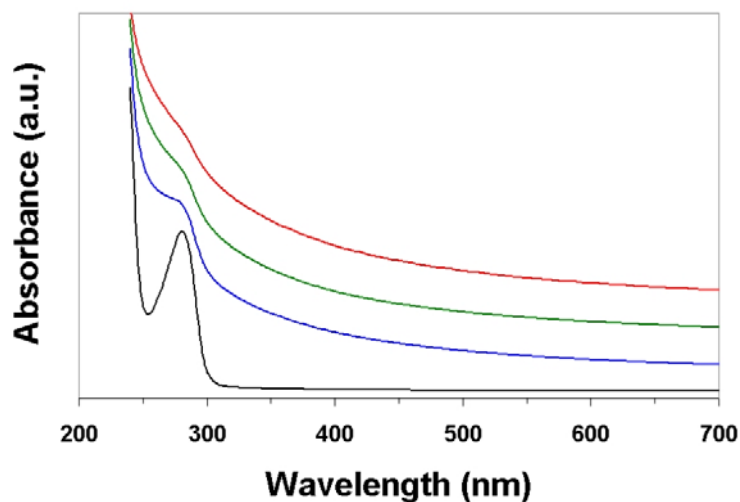


Figure 4.23: UV-visible absorption spectra of the various platinum systems. From bottom to top, the spectra are pristine BSA (Black), (24:1) Pt:BSA (Blue), (48:1) Pt:BSA (Green), and (96:1) Pt:BSA (Red). Note the diminishing intensity of the characteristic absorbance maximum for BSA at 278 nm with increasing platinum loading.

Pure BSA exhibits an absorbance maximum at 278 nm. (50) The primary sources of this maximum are the aromatic residues tryptophan and tyrosine, with a limited contribution from disulfide bonds. Quenching of this maximum has also been documented in the binding of fatty acids (101), steroids (102), and ascorbic acid (103) with BSA. This quenching is generally agreed to reflect ligand-induced conformational changes in the protein, whereby BSA modifies its tertiary structure to better accommodate the bound ligand. (104,105) The quenching observed in our studies suggests a similar conformational change in protein tertiary structure upon binding with the nanocrystal surface. These structural changes induce perturbations in the aromatic residues tryptophan and tyrosine, resulting in the observed absorbance quenching. The degree of quenching in a given spectrum is indicative of the relative fraction of protein molecules involved in binding with silver, gold, or platinum nanocrystals.

(96:1) Pt:BSA

The size distribution in the (48:1) Pt:BSA system was largely unchanged from that observed in the (24:1) Pt:BSA system. The only notable difference was an increase in the number of single twinned crystals, from <5% of the nanocrystals observed in the (24:1) Pt:BSA system, to ~15% of the product in the (48:1) Pt:BSA system. Both single twinned cuboctahedra (Figure 4.24a) and single twinned truncated octahedra (Figure 4.24b) were observed. As a result of their single twinned structure, some of these nanocrystals exhibited slight elongation in the direction orthogonal to the twin plane.

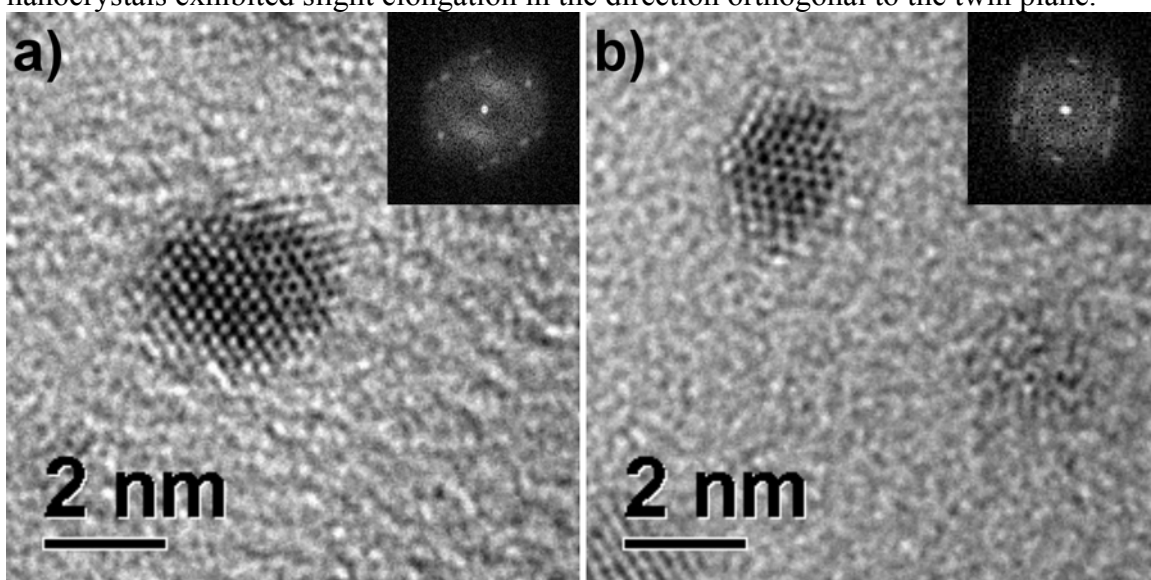


Figure 4.24: HRTEM analysis of single-twinned crystals observed at (48:1) Pt:BSA. (a) single twinned cuboctahedron; (b) single twinned truncated octahedron.

The single twinned platinum nanocrystals represented in Figure 4.24 provided a hint of what we would find in the (96:1) Pt:BSA system, as summarized in Figure 4.25. Low-magnification HAADF imaging revealed massive aggregates of platinum (Figure 4.25a). Intermediate magnification demonstrated these aggregates consisted of individual platinum nanostructures (Figure 4.25b). High-magnification HAADF confirmed a large fraction of these platinum nanostructures were elongated (Figure 4.25c).

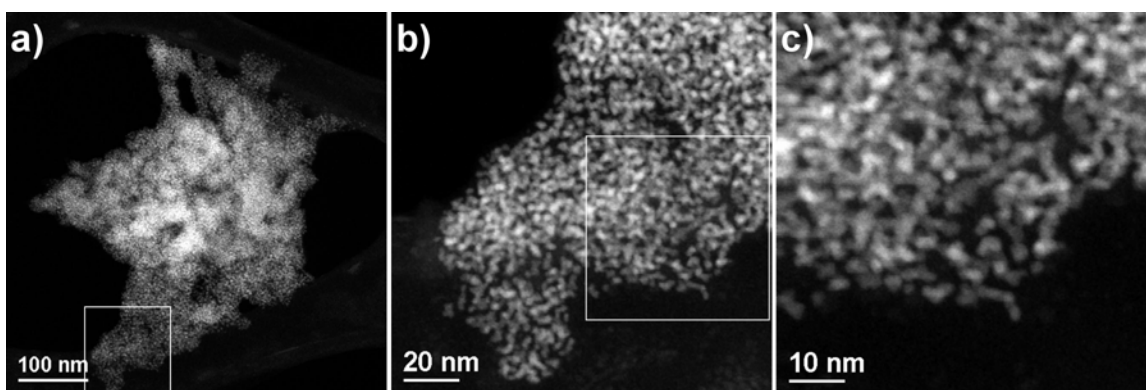


Figure 4.25: HAADF analysis of a large platinum aggregate in the (96:1) Pt:BSA system. Note the presence of elongated platinum nanocrystals in (b) and (c).

Figure 4.26 provides a summary of the (96:1) Pt:BSA system. The average crystal width was 2.233 ± 0.320 nm, or a standard deviation of $\sim 14.3\%$, largely unchanged from the (24:1) Pt:BSA system. However, the average crystal length was determined to be 4.080 ± 1.960 nm, or a standard deviation of nearly 50%. The aspect ratio of each nanocrystal was measured, and the average aspect ratio was found to be 1.830 ± 0.857 . While 16.5% of the nanocrystals exhibited aspect ratios of 1, over 30% of the crystals possessed aspect ratios of 2 or greater.

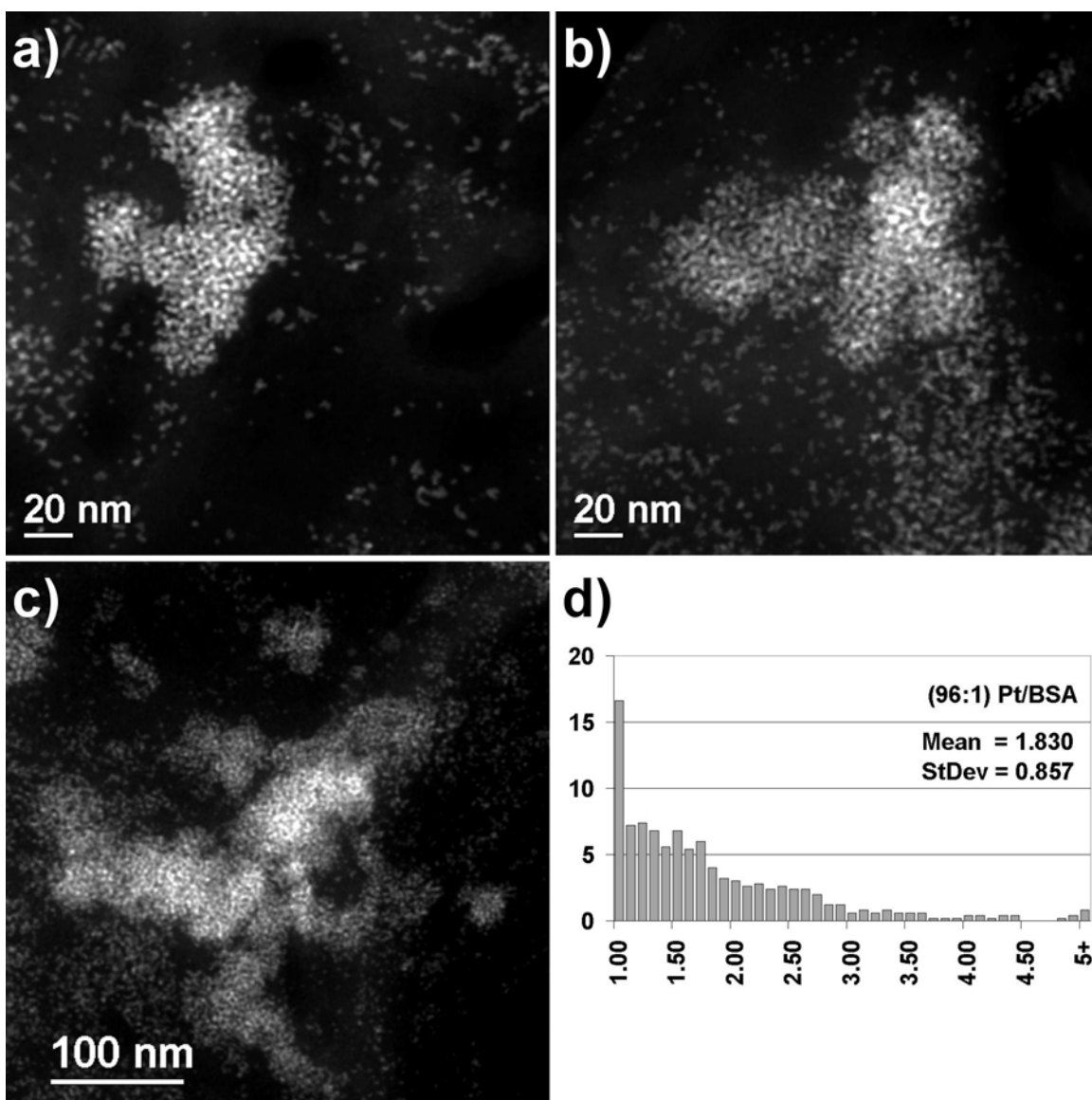


Figure 4.26: (96:1) Pt:BSA. (a) to (c) HAADF images. (d) Product distribution, aspect ratio versus percentage frequency.

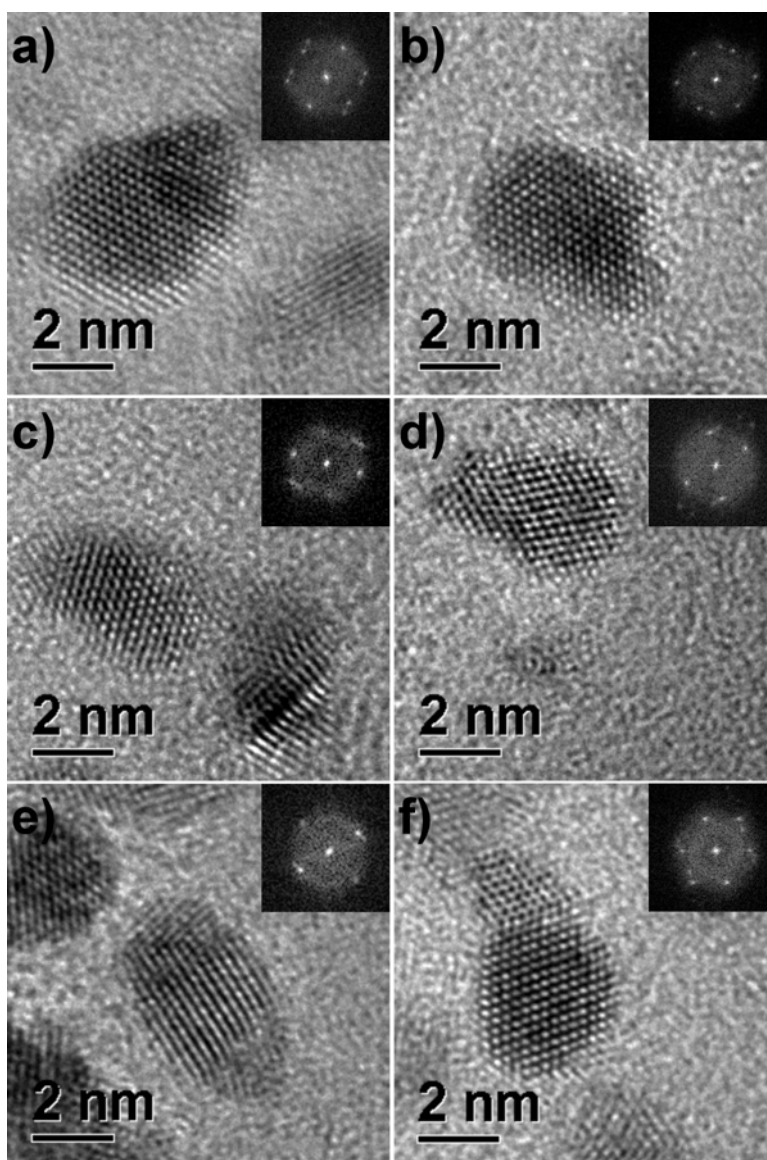


Figure 4.27: (96:1) Pt:BSA – HRTEM of elongated crystals – aspect ratios less than 2. The FFT of each image is included as an inset.

HRTEM analysis was performed to determine the structures of elongated platinum nanocrystals in the (96:1) Pt:BSA system. The analysis was divided into two sub-populations: elongated crystals with aspect ratios less than 2, and those with aspect ratios greater than 2. These two sub-populations are represented in Figures 4.27 and

4.28, respectively. The fast Fourier transform (FFT) of the crystals in Figure 4.27 demonstrate the characteristic spot splitting and/or streaking that is symptomatic of planar twinning. In Figure 4.27a, two distinct linear twin planes are observed.

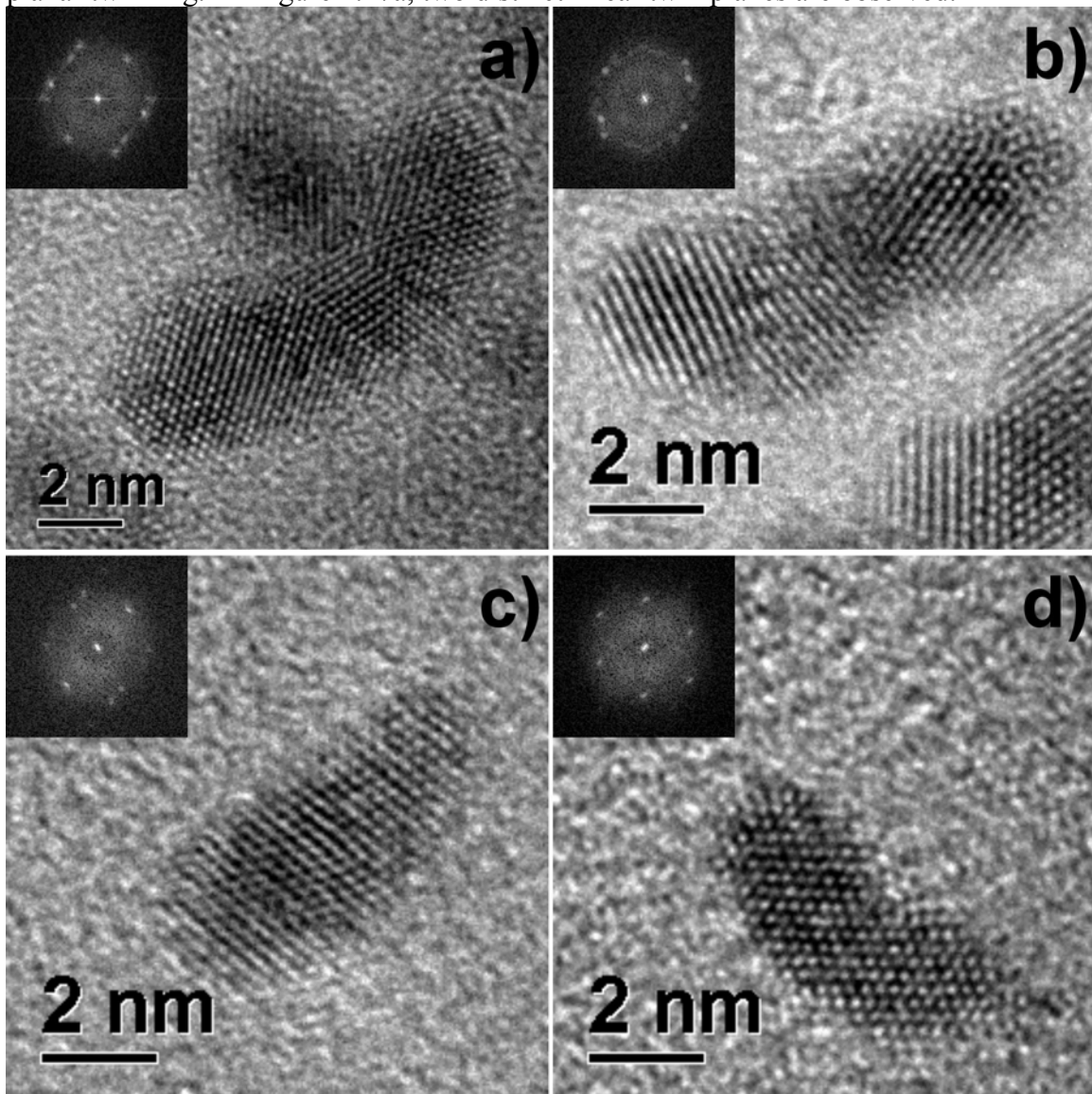


Figure 4.28: (96:1) Pt:BSA – HRTEM of elongated crystals – aspect ratios greater than 2. The FFT of each image is included as an inset.

The longer sub-population of platinum crystals represented in Figure 4.28 typically exhibited multiple parallel twinning planes. This is visually evident in Figure

4.28a and b. However, no twinning is visible in Figure 4.28d, and the FFT does not exhibit spot splitting. It is known that when twin planes are tilted away from the proper zone axis, they become invisible in the electron beam. (106) The FFT of the crystal in Figure 4.28d does not exhibit spot splitting, but it does exhibit spot streaking, which is indicative of twinning, and it is likely that this crystal has also grown by linear twinning.

We propose that the observed distribution in the (96:1) Pt:BSA system proceeds in an analogous manner to that described in the case of (96:1) Au:BSA. However, due to the high twinning energy of platinum, larger nuclei do not grow by assuming cyclic twinning structures, as was the case for gold. Rather, the larger platinum nanocrystals grow by introduction of linear twin planes. Elongated structures resulting from linear twinning have been observed in thermally-annealed platinum crystals, but our crystals are formed at room temperature. (107-109)

Nanocrystal growth occurs in the direction orthogonal to the twin plane, resulting in an elongated structure. Growth in the direction parallel to the twin plane is largely restricted, with the average breadth of the nanocrystals in the (96:1) Pt:BSA system being nearly unchanged from the sizes measured for the (24:1) Pt:BSA system. This restricted growth limits the cross-sectional area of the twin plane, thus limiting its total energy, and in fact this energetic consideration may be driving the preferential elongation. Platinum nanocrystals with aspect ratios greater than 2 are formed by the introduction of multiple linear twinning planes.

It is interesting to note that the percentage of platinum nanocrystals in the (96:1) Pt:BSA system with aspect ratios greater than 2 was ~30%, and that the percentage of gold nanocrystals in the (96:1) Au:BSA system with diameters greater than 2.50 nm was ~30%. Extending this comparison further, the percentage of silver nanocrystals in the

nanometric-scale regime of the (96:1) Ag:BSA system with diameters greater than 2.50 nm was also ~30%.

4.3.5 Comparison of Silver, Gold, and Platinum Nanocrystals Formed in the Presence of BSA Protein Molecules

In the Chapter introduction, I outlined three primary objectives of this investigation: (i) to determine if the aqueous-based gold nanocrystal synthesis technique can be extended to produce silver and platinum nanocrystals directly functionalized with BSA protein; (ii) to determine if narrower size distributions can be obtained by decreasing the excess sodium borohydride; (iii) to determine the maximum loading of silver, gold, and platinum atoms that can be effectively stabilized by BSA protein molecules as ~2 nm nanocrystals. In comparing the results obtained for the gold, silver, and platinum systems, we can address each of these primary objectives.

First, this aqueous-based technique is effective in the formation of silver, gold, and platinum nanocrystals ~2 nm in diameter, directly functionalized by BSA protein molecules. At molar ratios of (24:1) [Au/Ag/Pt]:BSA, ~2 nm nanocrystals are obtained with only ~14% deviation from the mean crystal diameter. Indeed, comparing the HAADF overviews of each system (Figures 4.1, 4.9, and 4.19), it is difficult to distinguish differences based on diameter, percentage size deviation, or nanocrystal dispersion. Each reaction is conducted in water at ambient conditions, and provides a near-quantitative yield of well-protected nanocrystals, within a reaction time of approximately 5 seconds.

Second, the excess sodium borohydride was decreased to bring the final pH of each solution to ~8. By selecting this pH, we have ensured that the BSA protein molecules will remain in the basic (B) form, and will not undergo further structural isomerization to the aged (A) form. The molar ratio of [reducing agent]:[ionic

precursor] required to achieve pH ~ 8 was twice the oxidation state of the ionic precursor, except in the case of silver, where the molar ratio was 1.75:1 rather than 2:1. By decreasing the excess sodium borohydride, ~ 2 nm nanocrystals with only $\sim 14\%$ deviation from the mean crystal diameter were obtained at molar ratios of (24:1) [Ag/Au/Pt]:BSA. In Chapter 3, where the molar ratio of $[\text{BH}_4^-]:[\text{AuCl}_4^-]$ was maintained at 10:1, the (14:1) Au:BSA system yielded ~ 1.55 nm crystals with a percentage deviation of greater than 30%. In comparison, using smaller excesses of sodium borohydride in the current systems, ~ 2 nm nanocrystals can be obtained with half as broad a percentage deviation, and with 70% more metal atoms per protein molecule present in solution.

Third, the molar ratio of (48:1) [Ag/Au/Pt]:BSA is the maximum ratio where a well-controlled product of ~ 2 nm nanocrystals can be obtained in near-quantitative yield. Indeed, at this molar ratio, a broader size distribution is just beginning to be observed. The consistency in the observed size distributions at (24:1) [Ag/Au/Pt]:BSA, combined with the common onset of a broadening size distribution at (48:1) [Ag/Au/Pt]:BSA, suggest that for molar ratios less than (48:1), the protein molecules are controlling nucleation and growth of noble metal nanocrystals. We propose that with greater excesses of BSA, more protein molecules are available to complex with greater numbers of metal ions, thus decreasing the concentration of free metal ions. When reduction occurs, the number of free atoms in solution will be less than the critical nucleation concentration, and nucleation will be limited within the protein molecule, where a locally-higher concentration of metal atoms is found.

At molar ratios of (96:1) [Ag/Au/Pt]:BSA, a smaller percentage of atoms is sequestered within protein molecules, and the concentration of free atoms is greater than the critical nucleation concentration. If the number of protein-stabilized nuclei is still relatively large, the number of solution-phase nuclei will be limited, and when these

nuclei subsequently become protein-functionalized, their sizes will be constrained to a relatively small size range, e.g. less than 10 nm. This is the case in the (96:1) Au:BSA and (96:1) Pt:BSA systems.

The percentage of silver nanocrystals in the nanometric regime of the (96:1) Ag:BSA system with diameters ranging from 2.5–5 nm was also ~30%. However, ~15% of the product consisted of much larger crystals, with sizes ranging from 20 nm to greater than 100 nm. Recall that one of the physiological roles of BSA is to regulate blood pH by forming complexes with the excess species. (51) In the gold and platinum systems, the ionic precursors used were acids. In addition to its normal propensity to form covalent adducts with heavy metal ions and chloride complexes, the moderately acidic solution pH (~4.5 in both cases) could drive BSA molecules to complex more metal ions, in the forms of HAuCl_4 or H_2PtCl_6 , to help regulate the pH of the precursor solution.

Recall the molar ratio of $[\text{BH}_4^-]:[\text{ionic precursor}]$ required to achieve pH ~8 was twice the oxidation state of the ionic precursor for gold and platinum, but in the case of silver, the molar ratio was 1.75:1 rather than 2:1. This difference was attributed to the acidity of the gold and platinum precursors. Thus, the actual ratio of $[\text{BH}_4^-]:[\text{Ag}^+]$ is 12.5% less than expected from comparison with two acidic precursors. If 12.5% less relative excess sodium borohydride is required, it is plausible that ~12.5% less binding between BSA and silver ions occurs due to the absence of pH-driven complexation. We could expect an additional ~12.5% of free silver atoms in the (96:1) Ag:BSA system, and thus a greater probability that some solution-phase nuclei will not encounter surface-stabilizing protein molecules before they grow too large to be effectively stabilized by BSA. Such crystals will grow into large, poorly-controlled structures. Indeed, the larger crystals in the (96:1) Ag:BSA system constituted ~15% of the product. It is plausible this

~15% of large crystals is related to ~12.5% decreased binding between BSA and ionic silver, due to the absence of pH-driven complexation.

4.4 CONCLUSIONS

In summary, I have refined the synthesis method for water-soluble gold nanocrystals described in Chapter 3, and have extended the approach to produce silver, gold, and platinum nanocrystals grown within and directly functionalized by bovine serum albumin, a globular protein molecule. The synthesis method employs aqueous chemistry at ambient conditions, and with a molar ratio of (24:1) [Ag/Au/Pt atoms]/[BSA molecules], we obtain near-quantitative yields of well-dispersed, protein-functionalized nanocrystals with diameters on the order of ~2 nm, and only ~14% standard deviation from the mean particle size. The limit of the protein in efficiently stabilizing all of the nanocrystals as ~2 nm nanocrystals occurs at an approximate molar ratio of (48:1) [Ag/Au/Pt atoms]/[BSA molecules]. Our analysis suggests that for molar ratios less than (48:1), the protein molecules are controlling the nucleation and growth of ~2 nm noble metal nanocrystals. As described previously in Chapter 3, these bioconjugated nanocrystals of silver, gold, and platinum also demonstrate robust dimensional stability, and can be stored indefinitely at ambient conditions as fine, dry powders.

Chapter 5: Interactions of Serum Albumin-Functionalized Noble Metal Nanocrystals with External Systems

Protein-functionalized noble metal nanocrystals with well-defined sizes and robust dimensional stability have an array of potential applications. These nanocrystals are directly conjugated to a macromolecular protein, which provides a degree of built-in biocompatibility and makes them an intriguing choice for incorporation into biological systems. Well-dispersed noble metal nanocrystals on the order of ~ 2 nm are also highly desirable in their own right for more traditional applications such as catalysis.

Ours was the first report of ~ 2 nm silver, gold, and platinum nanocrystals directly functionalized by a globular macromolecular protein. One possible reason this technique was not exploited prior to our work is the concern that the bulk of the macromolecular protein might completely insulate the nanocrystal surface from the external environment. This would preclude their use in catalytic applications, and would hinder their interactions with external biological systems, thus severely limiting their utility.

In this Chapter, we present three distinct examples as proof of concept that serum albumin-functionalized noble metal nanocrystals do indeed have the capacity for interaction with their external environment, and can be utilized to advantage in more complex biosystems. We will briefly describe one representative use for serum albumin-functionalized silver, gold, and platinum nanocrystals. By no means is this meant to be an exhaustive list of applications, but is included merely to illustrate the breadth of potential uses for serum albumin-functionalized noble metal nanocrystals, and to confirm the merits of pursuing the synthesis protocols outlined in the previous two Chapters.

5.1 SERUM ALBUMIN-FUNCTIONALIZED SILVER NANOCRYSTALS AS ANTIVIRALS: INTERACTION WITH HIV

5.1.1 Introduction

The interaction of nanocrystals with biomolecules and microorganisms is an expanding field of research. Within this field, an area that has been largely unexplored is the interaction of metal nanocrystals with viruses. Among noble metal nanomaterials, silver nanocrystals have received considerable attention due to their attractive physicochemical properties. The surface plasmon resonance and large effective scattering cross section of individual silver nanocrystals make them ideal candidates for molecular labeling, (110) where phenomena such as surface enhance Raman scattering (SERS) can be exploited. The antimicrobial action of silver in its various chemical forms has long been recognized, (111-112) but only limited research has been conducted on the antimicrobial properties of silver nanocrystals. For these reasons, we undertook a preliminary study regarding the interaction of silver nanocrystals with the human immunodeficiency virus (HIV). Within the context of this broader study, three types of silver nanocrystals with markedly different surface chemistries were employed. This provided an excellent opportunity (i) to determine if protein-conjugated silver nanocrystals can interact at all with an external biological system, and if interaction does take place, (ii) to measure the efficiency of interaction for protein-conjugated silver nanocrystals with HIV-1, as compared to conventional nanocrystal preparations².

5.1.2 Experimental Procedure

Nanocrystal synthesis. Carbon-coated silver nanocrystals were obtained from Nanotechnologies, Inc. These nanocrystals are produced by a proprietary physical synthesis technique; for more information, visit <http://www.nanoscale.com>.

² The findings in this section have been published in *J. Nanobiotech.* 3:6 (2005).

PVP-coated silver nanocrystals were synthesized by the polyol method, using glycerin as both reducing agent and solvent. Silver sulfate (Ag_2SO_4 ; reagent grade; Aldrich) was reduced in a solution of 1,2,3-propanetriol (Glycerin; $\geq 99\%$; Fisher) and in the presence of poly(N-vinyl-2-pyrrolidone) (PVP-K30; mw = 40,000; Aldrich). All materials were used without further treatment. In a typical experiment, 0.2 g of PVP was added to a 100 mL round bottom flask containing 30 mL of glycerin under vigorous stirring. The resulting solution was heated in a mineral oil bath, and the solution temperature was allowed to stabilize at 140°C for 30 minutes. Then, 2 mL of 0.015 M Ag_2SO_4 (60 μmol Ag) was added to the reaction vessel under vigorous stirring, and the reaction was allowed to proceed for 1 hour.

Silver nanocrystals directly conjugated to serum albumin protein molecules were synthesized in water by reduction of silver nitrate (AgNO_3 ; 0.945 N in water; Aldrich) in the presence of bovine serum albumin (BSA; Fraction V – heat shock treated; Fisher) by the addition of sodium borohydride (NaBH_4 ; 99%; Aldrich). All materials were used without further treatment. Briefly, 0.4 mL of 0.945 M AgNO_3 (378 μmol Ag) was added to a 100 mL round bottom flask containing an aqueous solution of 13.50 μmol (0.8965 g) dissolved BSA protein. Then, 2.5 mL of freshly-prepared NaBH_4 aqueous solution was added under vigorous stirring, bringing the total reaction volume to 40.0 mL. The molar ratio of [Ag atoms]:[BSA molecules] was (28:1), and the molar ratio of [BH_4^-]:[Ag^+] was 1:1. Introduction of NaBH_4 to the reaction caused rapid protein foaming, and within less than five seconds, the solution acquired a deep brown color. The reaction was allowed to proceed under vigorous stirring for 1 hour.

Nanocrystal characterization. Transmission electron microscopy (TEM) was performed using a JEOL 2010F transmission electron microscope equipped with Schottky-type field

emission gun, ultra-high resolution pole piece ($C_s = 0.5$ mm), an Energy Dispersive X-ray spectrometer (EDS), and a scanning transmission electron microscope (STEM) unit with high angle annular dark field (HAADF) detector operating at 200 kV. Samples for TEM analysis were prepared by allowing a drop of each solution of silver nanocrystals to evaporate on a lacey carbon-coated copper TEM grid. The size distributions for carbon-coated and PVP-coated silver nanocrystals were obtained from conventional TEM analysis and HAADF analysis, respectively, based on the measurement of 400 crystals. The size distribution for BSA-conjugated silver nanocrystals was obtained from HAADF analysis at high magnification, based on the measurement of 600 crystals.

Preparation of silver-treated HIV-1 for electron microscopy analysis. Electron microscopy was performed using a JEOL 2010F TEM with the equipment and operating conditions enumerated for the analysis of the silver nanocrystal preparations. Other than the actual TEM analysis, all work related to HIV-1 was performed in a Biosafety Level 3 Laboratory. Samples were prepared for electron microscopy as follows: 10^5 TCID₅₀ samples of HIV-1_{III B} cell free virus were treated with 100 µg/mL solutions of silver nanocrystals. After 30 seconds, 10 µL was deposited on a carbon-coated nickel grid and exposed to 2.5% PBS/glutaraldehyde vapors for 30 minutes.

Silver nanocrystal-mediated inhibition of HIV-1 transmission. Varying concentrations of silver nanocrystals were mixed with samples 10^5 TCID₅₀ of HIV-1_{III B} cell free virus. The initial concentration was 100 µg/mL silver nanocrystals. After 30 seconds, sequential 2-fold dilutions of the initial solution were added to cultures of target cells (2×10^5 MT-2 or 2×10^5 cMAGI HIV-1 reporter cells). Each dilution was introduced to four replicate wells. The cells were incubated at 37°C for 3-5 days. Assessment of HIV-1 mediated

syncytium formation was performed for MT-2 cells, (113,114) while for cMAGI cells, percentage transmission was estimated by the Blue Cell Assay (115,116) as follows: the number of blue-stained cells in the supernatant of each tested well was divided by the number of blue-stained cells in the supernatant of the positive control well.

Cytotoxicity of silver nanocrystals. The cytotoxicity of silver nanocrystals against MT-2 cells was determined using the Trypan Blue exclusion assay. (117) The initial concentration was 50 µg/mL silver nanocrystals, and sequential two-fold dilutions were mixed with 2×10^5 MT-2 cells. The samples were incubated at 37°C, and the cells were evaluated via optical microscopy after 3 hours and 24 hours exposure to silver nanocrystals. An aliquot of the cell suspension was diluted 1:1 (v/v) with 0.4% Trypan Blue and cells were counted using a hemocytometer. Viability was expressed as the percentage of unstained treated cells.

5.1.3 Results and Discussion

On the Nanocrystal Preparations Employed

The physicochemical properties of nanocrystals are strongly dependent upon their interactions with surface-protecting agents. (44) Indeed, nanocrystal surface chemistry can modify their interactions with external systems. For this reason, we tested silver nanocrystals with three markedly different surface chemistries. Carbon-coated nanocrystals were obtained from Nanotechnologies, Inc. These nanocrystals are embedded in a foamy carbon matrix to prevent coalescence during synthesis. The as-received powder was dispersed in deionized water by ultrasonication. TEM analysis showed a significant fraction of nanocrystals are released from the foamy carbon matrix by ultrasonication. These released crystals can be considered as free-surface nanocrystals, and only nanocrystals that escaped from the foamy carbon were available

for interaction with HIV-1. The size distribution of silver nanocrystals released from the foamy carbon matrix by ultrasonication was 16.19 ± 8.68 nm, or a standard deviation of 53.6%.

PVP-coated nanocrystals were synthesized by the polyol method in glycerin. (64) PVP is a linear polymer and stabilizes the nanocrystal surface via bonding with the pyrrolidone ring. Infrared (IR) and X-ray photoelectron spectroscopy (XPS) studies have revealed that both oxygen and nitrogen atoms of the pyrrolidone ring can promote the adsorption of PVP chains onto the surface of silver. (118) The size distribution of PVP-coated silver nanocrystals was 6.53 ± 2.41 nm, or a standard deviation of 36.9%.

Silver nanocrystals directly conjugated to BSA protein molecules were synthesized in aqueous solution. Serum albumin is a globular macromolecular protein, and is the most-abundant protein in blood plasma. (50) Fully 75% of the BSA-conjugated silver crystals were 2.09 ± 0.40 nm in diameter, representing a standard deviation of 19.1%. However, this investigation was conducted before identification of the preferred synthesis conditions reported in Chapter 4. As a result, the product distribution was distinctively bimodal, with the largest 25% of the nanocrystals being 6.22 ± 1.67 nm in diameter, or a standard deviation of 26.9%. Thus, the total measured distribution was 3.12 ± 2.00 nm, or a standard deviation of 64.28%.

Interaction of Silver Nanocrystals with HIV-1

The interaction of silver nanocrystals with HIV-1 was studied via HAADF analysis. Recall that for HAADF microscopy, the signal is primarily formed by electrons that have undergone high angle-scattering, which approximates a Rutherford-like scattering cross section. Therefore, contrast is related to elemental composition, intensity being proportional to the square of the atomic number. As a good approximation, lighter elements appear dark and heavier elements appear bright. (57–61) Due to large

differences in atomic number, silver nanocrystals are easily distinguished from the organic matter that composes the virus. In Figure 5.1, we present HAADF images of the HIV-1 virus with (Figure 5.1a) and without (Figure 5.1b) silver nanocrystals. The presence of silver was independently confirmed by Energy Dispersive X-ray Spectroscopy (EDS), shown in Figure 5.1f. Interestingly, the sizes of nanocrystals bound to the virus (Figure 5.1e) were exclusively within the range of 1-10 nm. Recall that in the case of the free-surface silver nanocrystals, ~40% of the distribution was larger than 10 nm, which suggests a size-dependent interaction.

The nanocrystals seen in Figure 5.1a are not randomly attached to the virus, and regular spatial relationships are observed among groups of three crystals (Figure 5.1a inset). Both the spatial arrangement of nanocrystals and the size dependence of interaction can be explained in terms of the HIV-1 viral envelope. The exterior of the HIV-1 virus is comprised of a lipid membrane interspersed with protruding gp120 glycoprotein knobs, whose main function is to bind with CD4 receptor sites on host cells. (119) These glycoprotein knobs are exposed to the exterior, and should be accessible for interactions with nanocrystals.

Leonard and coworkers (120) reported that the gp120 subunit has nine disulfide bonds, three of which are located in the vicinity of the CD4 binding domain. The tertiary structure of the gp120 subunit is presented in Figure 5.1c (PDB1GC1). (120) The gp120 subunit (grey ribbon structure) is in its complexed state with the CD4 receptor site (blue ribbon structure). The sulfur atoms in the gp120 subunit that participate in the nine disulfide bonds are depicted as yellow space-filled atoms. Exposed disulfide bonds would be the most attractive sites for silver nanocrystals to interact with the virus, and it is plausible that a nanocrystal could experience stabilizing interactions with the disulfide bonds in the vicinity of the CD4 binding domain (shown schematically in Figure 5.1d).

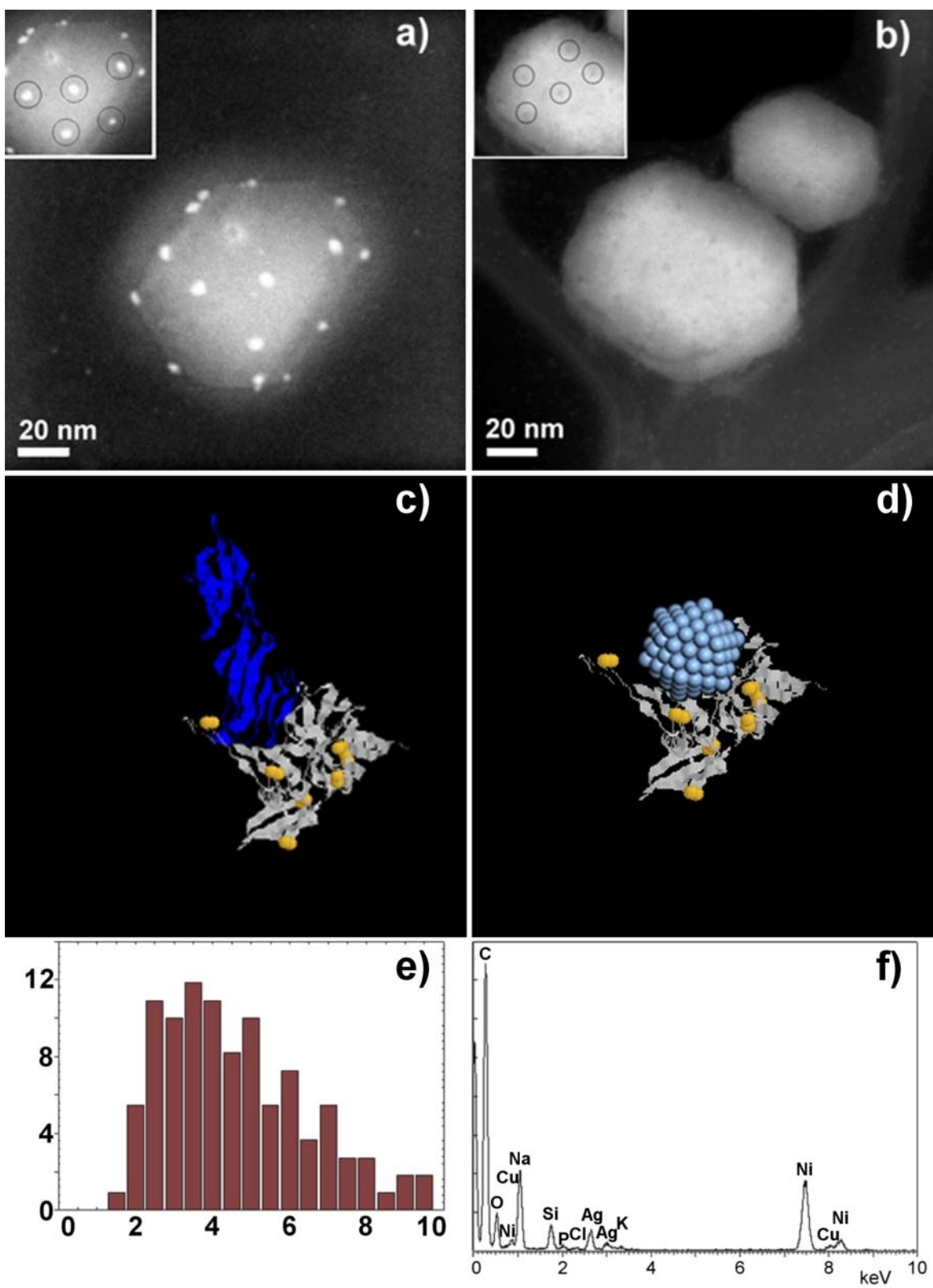


Figure 5.1: Interaction of Silver Nanocrystals with HIV-1. (a) HAADF image of an HIV-1 virus exposed to BSA-conjugated silver nanocrystals. Inset shows the regular spatial arrangement between groups of three nanoparticles. (b) HAADF image of HIV-1 viruses without silver nanocrystal treatment. Inset highlight the regular spatial arrangement observed on the surface of the untreated HIV-1 virus. (c) Tertiary structure of the gp120 subunit (grey ribbon structure) in its complexed state with the CD4 receptor site (blue ribbon structure) (PDB1GC1). (120) Sulfur atoms in the gp120 subunit that participate in the nine disulfide bonds are depicted as yellow space-filled atoms. (d) Schematic of the proposed interaction between a silver nanocrystal and the gp120 glycoprotein. (e) Composite size distribution of silver nanoparticles bound to the HIV-1 virus, derived from all tested preparations. (f) EDS analysis of the treated virus in (a) confirming the presence of Ag. The C signal comes from the TEM grid and the virus, O and P are from the virus, while Na, Cl, and K are present in the culture medium. Ni and Si come from the TEM grid, while Cu is attributed to the sample holder.

Nermut and coworkers have developed a structural model for HIV-1 based on experimental data that consists of an icosahedron with three gp120 knobs per face. (119) The regular spatial relationships among groups of three crystals in Figure 5.1a directly correlate with the proposed positions of the gp120 glycoprotein knobs in this structural model for HIV-1. Regular spatial relationships are also found on the surface of the untreated virus, (Figure 5.1b inset). The observed darker contrast at these sites could indicate the locations of glycoprotein knobs. For materials composed of elements of similar atomic numbers, such as the organic constituents of the virus, local variations in density will provide noticeable HAADF contrast. The majority of the viral envelope consists of a densely-packed lipid membrane. However, for the glycoprotein knobs, we would expect a localized region of lower density due to the presence of membrane-spanning glycoproteins rather than densely-packed lipids. Hence, these areas should appear darker than the rest of the viral envelope.

It has previously been determined that the center-to-center spacing between glycoprotein knobs is ~ 22 nm. (121) In the inset of Figure 5.1a, the average measured

center-to-center spacing between silver nanocrystals is ~28 nm, which correlates with the expected spacing between glycoprotein knobs. The average center-to-center spacing between the small darker regions on the untreated virus (Figure 5.1b inset) is ~22 nm, which again suggests these sites are the gp120 glycoprotein knobs. Thus, the observed spatial arrangement of nanocrystals, the center-to-center distance between nanocrystals, and the fact that the exposed sulfur-bearing residues of the glycoprotein knobs would be attractive sites for nanocrystal interaction strongly suggest that silver nanocrystals interact with the HIV-1 virus via preferential binding to the gp120 glycoprotein knobs.

Presuming that each nanocrystal interacts with a single glycoprotein knob, and that each nearest-neighbor knob is occupied by another nanocrystal, from geometric considerations the theoretical upper limit for the diameter of attached nanocrystals would be ~20 nm. However, if a nanocrystal larger than the diameter of one knob (~14 nm) was attached, (121) only a small fraction of the total crystal surface would be anchored, resulting in a less stable interaction. Thus, if nanocrystals are interacting with HIV-1 via preferential binding at gp120 glycoprotein knobs, we would expect to find primarily nanocrystals less than 14 nm in diameter, as crystals in this size range would have the most stable surface interactions. This corresponds with our experimental observation that crystals greater than 10 nm were not attached to the viral envelope.

In Vitro Inhibition of HIV-1 Transmission

Although the mechanism by which HIV infects host cells is not yet fully understood, two steps are broadly agreed to be critical. The first step involves binding of gp120 to the CD4 receptor site on the host cell. Then, upon binding to CD4, a conformational change is induced in gp120, resulting in exposure of new binding sites for a chemokine receptor. (122–124) An agent that preferentially interacts with gp120 would

block the virus from binding with host cells. Therefore, we measured the inhibitory effects of silver nanocrystals against HIV-1 *in vitro*.

For all three nanocrystal preparations, at silver concentrations above 25 µg/mL, viral infectivity was reduced to an extent that it could not be detected by syncytium formation, as shown graphically in Figure 5.2. For each nanocrystal preparation, we found a dose-dependant inhibition of HIV-1 infectivity, with an IC₅₀ where only moderate cell toxicity was observed, as seen in Figure 5.3.

The congruent *in vitro* inhibition of HIV-1 transmission by all three silver nanocrystal preparations suggests a common mode of interaction between the virus and the nanocrystals. Since the three nanocrystal preparations have markedly-different surface-protecting agents, it stands to reason that a common mode of interaction would entail a direct attachment of the virus to the silver atoms on the surface of the nanocrystals. This is in accord with our proposal, based on electron microscopy analysis, that the silver nanocrystal surfaces are preferentially attaching to the exposed disulfide bonds of the gp120 subunit of the viral envelope glycoprotein.

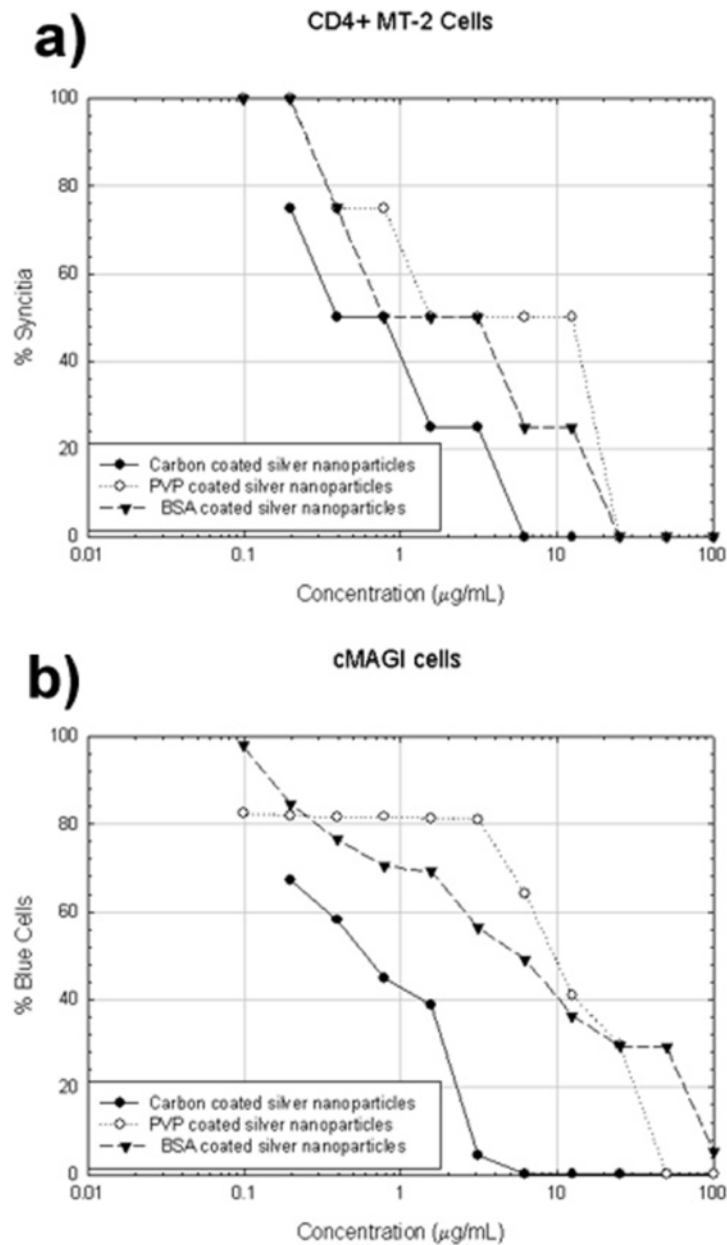


Figure 5.2: Inhibition of HIV-1 by silver nanocrystals. (a) HIV-1 mediated syncytium formation in MT-2 cells. (b) Percentage transmission in cMAGI cells.

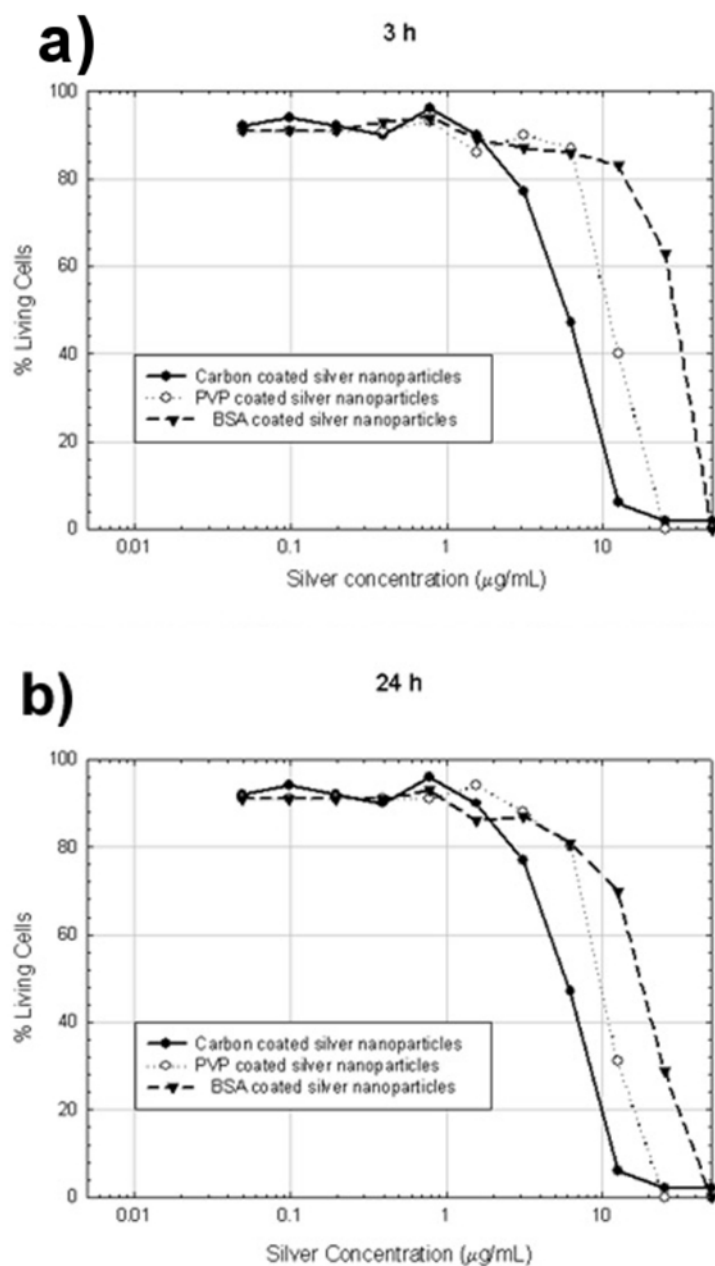


Figure 5.3: Toxicity of silver nanocrystals against MT-2 cells, determined by Trypan Blue exclusion assay. (117) Samples were incubated at 37°C, and the cells were evaluated via optical microscopy after (a) 3 hours and (b) 24 hours exposure to silver nanocrystals.

Comparison of Serum Albumin-Conjugated Silver Nanocrystal Interaction Efficiency

Recall that our stated goals in this analysis were (i) to determine if protein-conjugated silver nanocrystals can interact at all with an external biological system, and (ii) measure the efficiency of interaction for protein-conjugated silver nanocrystals with HIV-1, as compared to the other two conventional nanocrystal preparations. With regard to point (i), we can answer with a resounding yes. In fact, Figure 5.1a depicts the interaction of HIV-1 with BSA-conjugated silver nanocrystals. The fact that BSA-functionalized silver nanocrystals in Figure 5.1a occupy a large percentage of the gp120 receptor sites on the viral envelope demonstrates that there is indeed a strong, site-specific interaction between the glycoprotein knobs of the virus and the silver nanocrystal surface. This confirms that the surfaces of BSA-functionalized silver nanocrystals are able to interact with external systems, despite being directly conjugated to a macromolecular globular protein.

As for point (ii), although the findings regarding interaction with HIV-1 were congruent among nanocrystals with markedly different surface chemistry, the toxicity and inhibition results were not identical. The differences in the trends in HIV-1 inhibition can be explained in terms of the surface chemistry for each nanocrystal preparation. BSA- and PVP-protected nanocrystals exhibit slightly lower inhibition (Figure 5.2) because the nanocrystal surface is directly bound to and encapsulated by a surface-protecting agent. In contrast, silver nanocrystals released from the carbon matrix have greater inhibitory effect due to their essentially free surface area. The fact that carbon-coated nanocrystals present higher cytotoxicity (Figure 5.3) can also be explained in terms of surface chemistry. Since these silver nanocrystals possess essentially free surfaces, they have stronger interactions with host cells, increasing their toxicity.

5.1.4 Conclusions

In the context of a broader study on the interaction of silver nanocrystals with HIV-1, we have demonstrated that BSA-functionalized silver nanocrystals can interact with an external biological system. Three types of silver nanocrystal preparations with markedly different surface chemistries were employed in the course of this investigation, which allowed us to measure the efficiency of interaction for protein-conjugated silver nanocrystals with HIV-1, as compared to the two conventional nanocrystal preparations. The interaction between silver nanocrystals and HIV-1 was found to be congruent among all three nanocrystal preparations, suggesting a common mode of interaction. We proposed that silver nanocrystal surfaces are preferentially attaching to the exposed disulfide bonds of the gp120 subunit of the viral envelope glycoprotein. Since this is a specific interaction between the virus and the nanocrystal surface, these results confirm the surfaces of BSA-functionalized silver nanocrystals are able to interact directly with an external biological system.

Two aspects of our findings have important implications with regard to the protein-functionalized silver nanocrystals. First, a size dependence of interaction with HIV-1 was noted, with only nanocrystals in the range of 1-10 nm bound to the virus. Previously in Chapter 4, I demonstrated that under the proper reaction conditions, well-dispersed BSA-functionalized silver nanocrystals could be obtained in near-100% yield, with size distributions of 2.094 ± 0.287 nm. Thus, the BSA-functionalized product is completely within the proper size range to exploit the size-dependent interaction with HIV-1. In fact, if our proposed mode of interaction is correct, we would expect nanocrystals on the smaller end of the 1-10 nm range to have stronger interactions with HIV-1, since a larger fraction of the crystal surface would be stabilized by exposed disulfide bonds in the vicinity of the CD4 binding domain of gp120.

Secondly, we found that while all silver nanocrystal preparations were effective in inhibiting transmission of HIV-1 at concentrations where only moderate cytotoxicity was observed (Figure 5.2), the BSA-functionalized nanocrystals exhibited the least cytotoxicity (Figure 5.3). Serum albumin is a plasma protein, naturally occurring within the blood and largely confined to circulation in the bloodstream. Attaching nanocrystals to plasma proteins could become a viable strategy for targeted delivery of nanocrystals within the circulatory system, which would be ideal to combat a blood-borne illness such as HIV. This could both reduce the risk of nanocrystal accumulation within deep tissues and critical organs, and reduce the concentration of nanocrystals required to combat blood-borne infections. Of course, the toxicity and long-term health effects of exposure to nanomaterials must be fully explored before any uses of silver nanocrystals in the body are pursued in earnest. However, it is clear that the selection of biocompatible protecting agents, such as plasma proteins, will be crucial for future applications involving the interaction of nanocrystals with viruses and more complex biosystems.

5.2 SERUM ALBUMIN-FUNCTIONALIZED GOLD NANOCRYSTALS: TOWARD IN VIVO DOSAGE OF CONTRAST-ENHANCING AGENTS FOR THE IMAGING OF MICROORGANISMS

5.2.1 Introduction

The use of gold nanocrystals as contrast enhancing agents for imaging biological systems ranging from individual proteins and viruses, to bacteria and eukaryotic cells is well-established. (18) Typically, microorganisms such as bacteria are prepared for microscopy by a sequential process involving fixation with gluteraldehyde vapors, dehydration with ethanol, embedding in a polymer resin, sectioning via microtome, and finally staining with contrast enhancing agents. (125)

The development of contrast-enhancing agents that facilitate *in vivo* imaging of microorganisms would be highly advantageous. One possible approach would be to directly functionalize the contrast-enhancing agent with a biological molecule that the microbe can use as a source of nutrition. The uptake of biological molecules by the microorganism to satisfy its physiological requirements would simultaneously result in accumulation of contrast-enhancing agents on the microorganism. Herein, we report the serendipitous discovery that BSA-functionalized gold nanocrystals may provide a platform for the *in vivo* dosage of contrast-enhancing agents for imaging of microbes. This is the first known report of *in vivo* dosage to microorganisms of a contrast enhancing agent, directly through their source of nutrition.

5.2.2 Experimental Procedure

Nanocrystal synthesis. Protein-functionalized gold and silver nanocrystals were synthesized in air by reduction in a homogeneous solution at ambient conditions. Chloroauric acid trihydrate ($\text{HAuCl}_4 \cdot 3\text{H}_2\text{O}$; 99.9+%; Aldrich) or silver nitrate (AgNO_3 ; 0.945 N in water; Aldrich) was reduced in water and in the presence of bovine serum albumin (BSA; Fraction V – heat shock treated; Fisher) by the addition of sodium borohydride (NaBH_4 ; 99%; Aldrich). All materials were used without further treatment. In the case of gold, 0.5 mL of 0.12 M HAuCl_4 solution (60 μmol Au) was added to a round bottom flask containing an aqueous solution of 8.571 μmol (0.5692 g) dissolved BSA. In the case of silver, 0.1 mL of 0.945 M AgNO_3 (94.5 μmol Ag) was added to a round bottom flask containing an aqueous solution of 13.50 μmol (0.8965 g) dissolved BSA protein. Then, 2.5 mL of freshly-prepared NaBH_4 aqueous solution was added under vigorous stirring, bringing the total volume to 40.0 mL. For the gold synthesis, the molar ratio of $[\text{BH}_4^-]:[\text{AuCl}_4^-]$ was (10:1), and the ratio of $[\text{Au}]:[\text{BSA}]$ was (7:1). For the

silver synthesis, the molar ratio of $[\text{BH}_4^-]:[\text{Ag}^+]$ was (2:1), and the ratio of $[\text{Ag}]:[\text{BSA}]$ was (7:1). Each reaction was allowed to proceed under vigorous stirring for 1 hour.

Inoculation and identification of bacterial species. The initial inoculation of BSA-functionalized gold nanocrystals with bacteria was serendipitous. An aqueous solution of the as-synthesized product was taken to another laboratory for routine sample preparation. Unbeknownst to us at the time, the previous occupant of the shared lab bench had been working with a strain of *Pseudomonas*. The sealed glass vial containing the gold nanocrystal solution was opened for 5 minutes on the lab bench. Prior to inoculation, the solution was transparent and had a deep golden-brown color. Within 24 hours after inoculation, a dense mass of white organic material was observed in the glass vial, causing the solution to become opaque. Colleagues in the aforementioned lab titered the unknown bacterial species on an agar plate, which was incubated for 24 hours at 30°C. Colonies formed on the plate were uniform in appearance, suggesting the presence of a single microorganism. DNA extraction was performed, and polymerase chain reaction (PCR) amplification employed to prepare a sample for DNA sequencing. Automated DNA sequencing was performed using a capillary-based DNA analyzer, and the microbe in our BSA-functionalized gold nanocrystal solution was identified as *Pseudomonas aeruginosa*.

Characterization. Transmission electron microscopy (TEM) was performed using a JEOL 2010F transmission electron microscope equipped with Schottky-type field emission gun, ultra-high resolution pole piece ($C_s = 0.5$ mm), an Energy Dispersive X-ray spectrometer (EDS), and a scanning transmission electron microscope (STEM) unit with high angle annular dark field (HAADF) detector operating at 200 kV. Samples for

TEM analysis were prepared by allowing a drop of the aqueous product to evaporate on a lacey carbon-coated copper TEM grid.

5.2.3 Results and Discussion

On the Microbial Species Present

Recall that the gold nanocrystal solution colonized by *Pseudomonas aeruginosa* only contained the as-synthesized reaction products. Thus, the only chemical species present were water, gold, serum albumin protein, chlorine (from the ionic gold precursor), sodium (from the reducing agent), and boron. No additional growth factors or nutrients were added. To understand better how a bacterial species could colonize a solution with such limited nutritional resources, we should briefly discuss some of the characteristics of this bacterial species.

Pseudomonas aeruginosa is a Gram-negative aerobic rod measuring 0.5-0.8 μm by 1.5-3.0 μm , and member of the bacterial family *Pseudomonadaceae*. Ubiquitous in soil and water, these bacteria occur regularly on plant surfaces. *P. aeruginosa* is also an opportunistic pathogen of humans, exploiting weaknesses in the host to initiate infection. *P. aeruginosa* has minimal nutritional needs. In the laboratory setting, organic growth factors are not required, and it can use more than seventy-five organic compounds for growth. *P. aeruginosa* proliferates in moist environments, a reflection of its natural existence in soil and water. It is tolerant of a variety of physical conditions, can thrive in temperatures as high as 42°C, and is resistant to high concentrations of salts, and many common antibiotics. (126)

Pseudomonas aeruginosa produces three types of extracellular enzyme protease, with protease II being responsible for 75% of the total proteolytic activity. This protease is capable of cleaving high-molecular proteins (such as bovine serum albumin) into low-molecular ones, which are taken up by the bacteria as a source of nutrition. (126) Thus, it

is entirely possible that *P. aeruginosa* could meet its nutritional requirements in an aqueous solution of BSA protein.

HAADF Analysis of the Initially-Inoculated System

A TEM grid for HAADF analysis was prepared 48 hours after the suspected time of initial inoculation. A typical low-magnification image is presented in Figure 5.4a. The presence of elemental gold was confirmed by EDS analysis. The strong contrast apparent in the structure of the bacteria is attributed to the Z^2 -contrast effect described previously. Regions of the bacterial membrane decorated with gold nanocrystals exhibit bright contrast in the HAADF images.

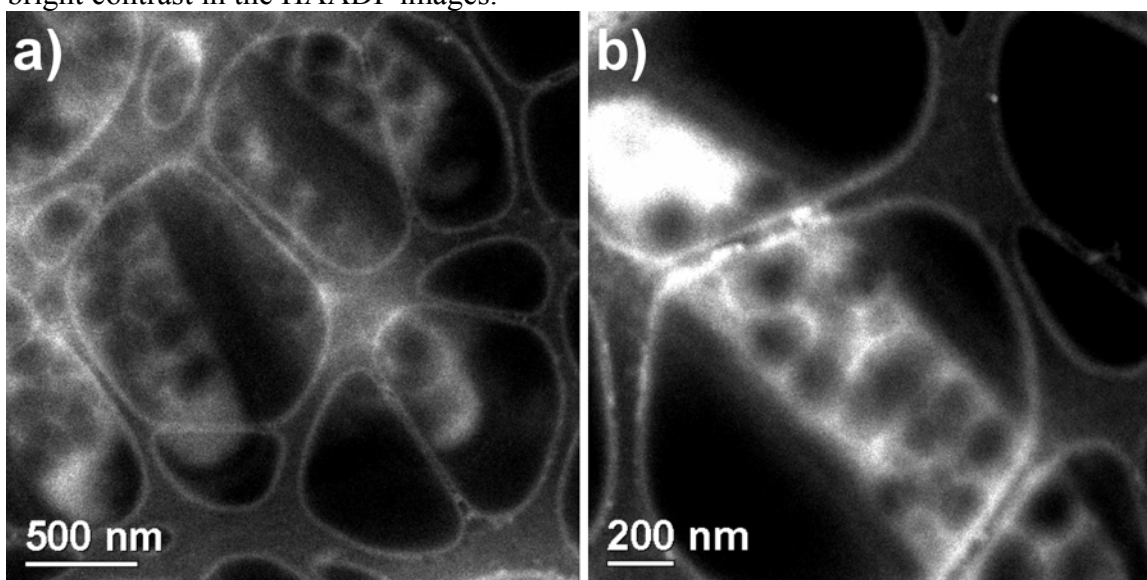


Figure 5.4: HAADF images of gold-functionalized *Pseudomonas aeruginosa*.

In this initially-inoculated sample, we observed numerous bacteria, subsequently identified as *P. aeruginosa*, with their surfaces decorated by gold nanocrystals. However, the surface coverage by gold nanocrystals was not uniform, as greater concentrations of nanocrystals were evident at the poles of the bacteria, as clearly demonstrated in Figure 5.4b. Also, gold nanocrystals were conspicuously absent from certain circular regions

along the length of the bacteria, again clearly seen in Figure 5.4b. It seems the gold nanocrystals are preferentially adsorbed onto specific regions of the bacterial membrane.

Growth Kinetics

The growth kinetics of *Pseudomonas aeruginosa* in an as-synthesized solution of BSA-functionalized gold nanocrystals was determined as follows. A culture of *P. aeruginosa* in Luria-Bertani (LB) growth medium was prepared from a single colony formed on an agar plate, and incubated for 24 hours at 30°C. Then, a 1:1000 (v/v) dilution of the bacterial culture medium was introduced into 1 mL of the as-synthesized BSA-functionalized gold nanocrystals, and incubated at 30°C. After 1 hour, 100 μ L of the inoculated nanocrystal solution was removed, and three successive 1:100 dilutions of the solution were titered on agar plates. The plates were incubated for 24 hours at 30°C. The number of viable cells present in solution at the time of the titering was determined by counting the number of colonies on a plate, and attributing each colony to one original colony forming unit (CFU). The number of colony forming units was divided by the total extent of dilution to obtain the equivalent number of bacteria present in 1 mL of solution. Titering was performed at the time of inoculation, as well as 1, 2, 3, and 4 days after the inoculation of *P. aeruginosa* into the BSA-functionalized gold solution.

The number of viable bacteria (colony forming units) per mL of BSA-functionalized gold nanocrystal solution is presented as a function of time in Figure 5.5. The first 24 hours after inoculation are the exponential growth phase. The second 24 hours constitute the stationary phase, while the final 48 hours constitute the death phase. The features of the growth curve are entirely consistent with the typical phases of growth exhibited by bacteria. It is not surprising that the bacteria enter a death phase after 48 hours, as their nutritional source (BSA protein) was not replenished during the course of these measurements.

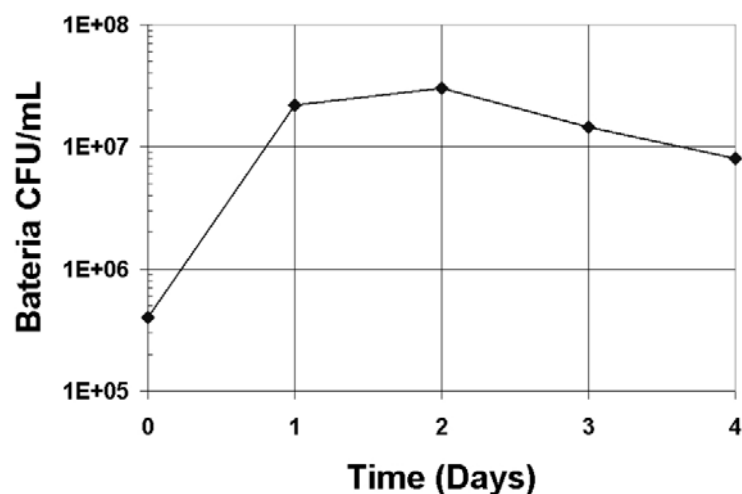


Figure 5.5: Growth kinetics for *Pseudomonas aeruginosa* in an as-synthesized solution of BSA-functionalized gold nanocrystals. The graph presents the number of viable bacteria per mL of gold nanocrystal solution.

The possibility was raised that *P. aeruginosa* might be capable of surviving in the presence of gold nanocrystals because the nanocrystalline surfaces are completely shielded from their external environment by the enveloping macromolecular protein. Thus, we decided to compare the growth kinetics of *P. aeruginosa* in the presence of BSA-functionalized gold and silver nanocrystals. A solution of BSA-functionalized silver nanocrystals was prepared as described in the Experimental Procedure, then diluted with deionized water to the same concentration of BSA protein (0.214 $\mu\text{mol/mL}$) and noble metal atoms (1.5 $\mu\text{mol/mL}$) as were present in the gold nanocrystal solution.

At equivalent concentrations, *P. aeruginosa* did not colonize a solution of BSA-functionalized silver nanocrystals. In fact, BSA-functionalized silver nanocrystals were effective at killing *P. aeruginosa*. Colleagues in our research group have previously determined that free-surface silver nanocrystals are effective at killing *P. aeruginosa* when silver concentrations are greater than 75 $\mu\text{g/mL}$. (127) In our solution of BSA-

functionalized silver nanocrystals, the concentration of silver was 162 $\mu\text{g}/\text{mL}$, more than twice the concentration previously identified as lethal to *P. aeruginosa*. Through our comparison of gold and silver, we found the colonization of BSA-functionalized gold nanocrystal solutions by *P. aeruginosa* was not due to the bulk of the protein completely insulating the crystal surfaces, but was a result of the inherent biocompatibility of gold.

HAADF Analysis of Purposely-Inoculated Systems

A culture of *P. aeruginosa* was prepared from one of the colonies formed on the agar plate, as described previously. A TEM grid was prepared from the culture after 24 hours incubation in LB growth medium. At the same time, a 1:1000 (v/v) dilution of the bacterial culture medium was introduced into 1 mL of the as-synthesized BSA-functionalized gold nanocrystals. After 24 hours of incubation at 30°C, a TEM grid was prepared from the BSA-functionalized gold nanocrystal solution. The two samples were analyzed by HAADF, as presented in Figure 5.6.

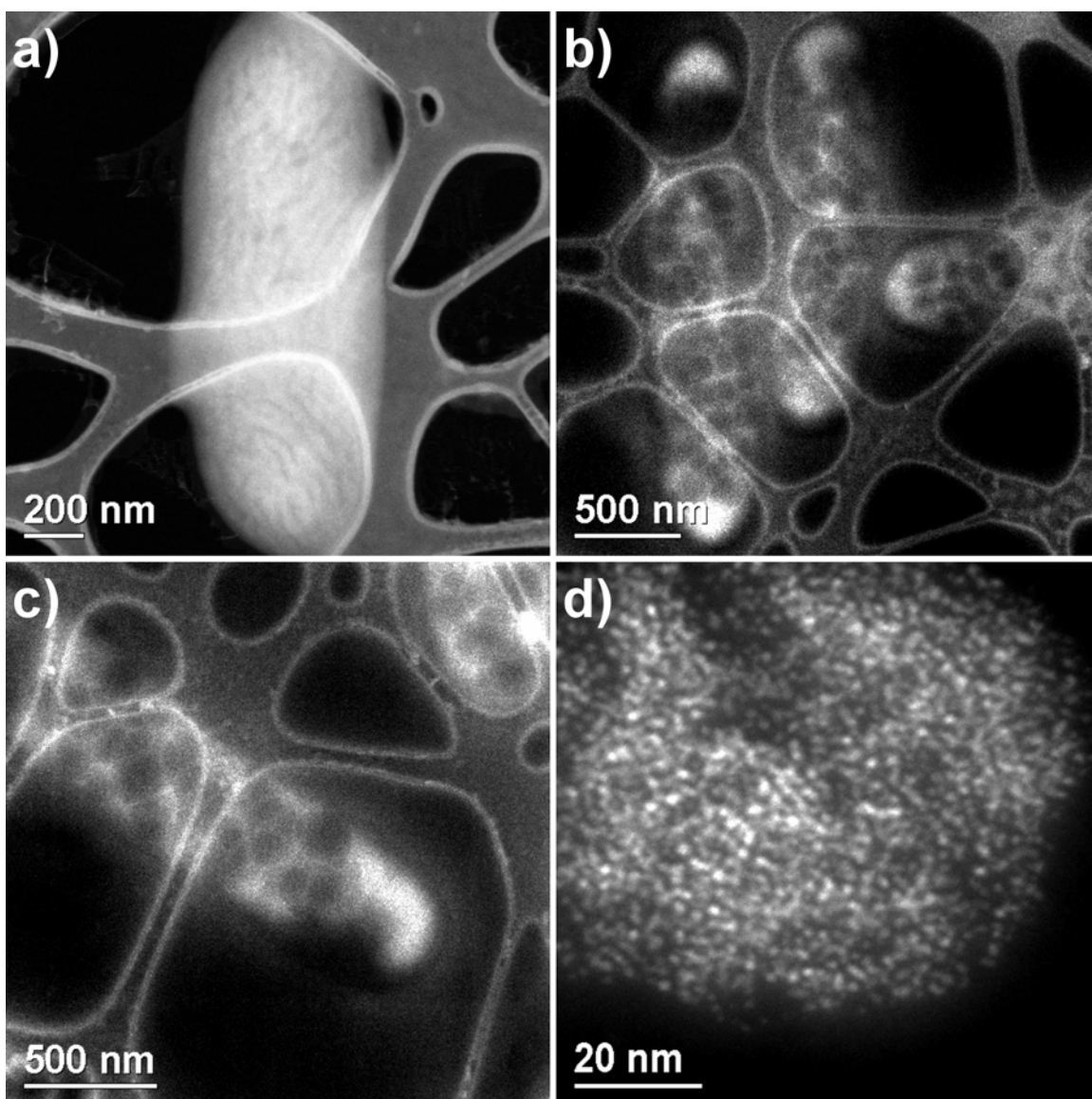


Figure 5.6: HAADF images of *Pseudomonas aeruginosa* after 24 hours incubation at 30°C. (a) Incubated in LB growth medium. (b) Incubated in BSA-functionalized gold nanocrystal solution. One bacterium incubated in the presence of gold (c) at low magnification, and (d) at high magnification, clearly demonstrating that the bright contrast in the polar region is due to the accumulation of ~2 nm gold nanocrystals.

Two facts are readily apparent. First, the clarity of the image obtained at low magnification from the sample incubated in LB growth medium (Figure 5.6a) is much

better than those obtained in BSA-functionalized gold nanocrystal solution (Figure 5.6b-c). This is due to the presence of high concentrations of bulky, macromolecular proteins in the nanocrystal solution, which increases the sample thickness and decreases the resolution. If BSA-functionalized nanocrystals are used as contrast enhancing agents in the future, it is clear that sample washing, or dilution of the protein-rich solution will be required prior to imaging.

Second, the presence of gold nanocrystals once again provides enhanced contrast for imaging the bacteria, revealing surface features that are not at all evident in the bacteria incubated in the standard LB growth medium (Figure 5.6a). The characteristic circular variations in contrast along the length of the bacteria were again revealed by the adsorbed gold nanocrystals. Furthermore, a strong contrast was again noted at the poles of the bacteria, as seen in Figure 5.6c. A high-magnification HAADF image of the pole of this bacterium was captured in Figure 5.6d, one of the few areas in the sample where the film was sufficiently thin to permit analysis at high magnification. This image demonstrates that the bright contrast in the polar regions of the bacteria is due to the accumulation of ~ 2 nm gold nanocrystals.

5.2.4 Conclusions

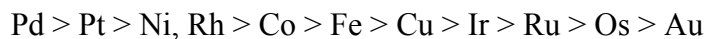
We discovered that BSA-functionalized gold nanocrystals may provide a platform for the *in vivo* dosage of contrast-enhancing agents for imaging of bacteria. Comparison of images of *P. aeruginosa* captured with and without the presence of gold demonstrated that the gold nanocrystals provide enhanced contrast to specific regions of the bacterial surface, particularly the poles. Although the microscopy techniques employed in our study were destructive to the bacteria, the development of *in vivo* dosage platforms for contrast enhancing agents should open promising new alternatives for the imaging of live bacterial cultures via techniques such as Raman microscopy and environmental SEM.

We proposed that *P. aeruginosa* is using the BSA protein as its source of nutrition, and as the bacteria consume the protein molecules to satisfy their physiological requirements, they are simultaneously accumulating contrast-enhancing gold nanocrystals on their surface. Through our comparison of gold and silver, we found that the colonization of BSA-functionalized gold nanocrystal solutions by *P. aeruginosa* was not due to the bulk of the protein completely insulating the nanocrystal surfaces, but was a result of the inherent biocompatibility of gold. To our knowledge, this is the first report of *in vivo* dosage to microorganisms of a contrast enhancing agent directly through their source of nutrition.

5.3 SERUM ALBUMIN-FUNCTIONALIZED PLATINUM NANOCRYSTALS AS HYDROGENATION CATALYSTS

5.3.1 Introduction

The hydrogenation reaction, defined as addition of hydrogen to a π -bond of an unsaturated organic molecule, has great importance in several industries including petroleum engineering, food processing, and production of fine chemicals. Moreover, the hydrogenation reaction has been widely studied, and the mechanism is well-known. A careful choice of the conditions will give rise to a clean reaction crude with high selectivity. The hydrogenation process is catalyzed by transition metals. Group VIII metals display the highest catalytic activity due to their small number of d-vacancies in the outer electronic orbital. In the hydrogenation of ethylene, the order of reactivity follows the trend: (128)



For this reason, we undertook a study on the potential utility of platinum nanocrystals directly conjugated to bovine serum albumin (BSA) protein as catalyst for a model hydrogenation process. The goals of this study were (i) to determine if the surfaces of

platinum nanocrystals directly functionalized with globular macromolecular proteins are available to catalyze the hydrogenation of external species, and (ii) to find a correlation between the crystal structure and the catalytic performance of the platinum nanocrystals.

Small, well-defined nanocrystals are at the border between homogeneous and heterogeneous catalysis. From a classical point of view, these materials are soluble in the solvent where the reaction occurs and where all reactants are located, and would be properly defined as homogeneous catalysts. However, the nanocrystals are supported over another entity (e.g. proteins, dendrimers), and all the concepts inherent to the study of their catalytic activity (e.g. adsorption processes, different catalytic sites) belong to the field of heterogeneous catalysis. Finke defined these species as “soluble heterogeneous catalysts”, (129) a description that agrees with Schwartz’s criterion. (130) According to this point of view, a catalyst is homogeneous if it contains only one kind of catalytic site; otherwise it is considered as heterogeneous.

In this section, we describe the application of BSA-functionalized platinum nanocrystals as catalysts for the aqueous-phase hydrogenation of allyl alcohol. We chose to work with allyl alcohol because it is a terminal olefin, so we can avoid the complication of *cis/trans* isomerism. Furthermore, this olefin is soluble in the aqueous phase, which facilitates the investigation of a water-soluble noble metal catalyst.

The alkene hydrogenation process follows the “Horiuti-Polanyi” or “half-hydrogenated” mechanism. (131) Different steps can be considered in the hydrogenation. An olefin is adsorbed onto the metal surface, facilitating the rupture of the π -bond and giving rise to two new σ -bonds. On this metal surface, there are also two hydrogen atoms that are generated from the dissociative adsorption of H_2 (homolytic rupture of the H–H σ -bond). One of these hydrogen atoms attaches to one former olefinic carbon, providing the half-hydrogenated state. Up until this point, all steps in the process are reversible.

However, once the second hydrogen atom adds to the other former olefinic carbon, the alkane is irreversibly formed, and the newly-generated molecule desorbs from the surface. (132)

5.3.2 Experimental Procedure

Nanocrystal synthesis. Protein-functionalized platinum nanocrystals were synthesized in air by reduction in a homogeneous solution at ambient conditions. Hexachloroplatinic acid hexahydrate ($\text{H}_2\text{PtCl}_6 \cdot 6\text{H}_2\text{O}$); ACS reagent grade; Aldrich) was reduced in water and in the presence of bovine serum albumin (BSA; Fraction V – heat shock treated; Fisher) by the addition of sodium borohydride (NaBH_4 ; 99%; Aldrich). All materials were used without further treatment. Briefly, 2 mL of 0.0750 M H_2PtCl_6 (150 μmol Pt) were added to an aqueous solution containing either 6.2500 μmol (0.4151 g) or 1.5625 μmol (0.1038 g) dissolved BSA protein. Then, 2 mL of freshly-prepared 0.6 M NaBH_4 aqueous solution (1200 μmol NaBH_4) was added rapidly under vigorous stirring, bringing the total volume to 40.0 mL. The molar ratio of $[\text{BH}_4^-]:[\text{PtCl}_6^{2-}]$ was (8:1), and the ratio of [Pt atoms]:[BSA molecules] was either (24:1) or (96:1). Introduction of NaBH_4 to the reaction vessel caused rapid protein foaming, and within less than five seconds, the solution acquired a deep black color. The reaction was allowed to proceed under vigorous stirring for 30 minutes.

Catalytic testing. The catalytic activity was measured in terms of turnover frequency (TOF), or the number of moles of product per mole of catalyst per unit time, under conditions where the catalyst is saturated by the reactants. (133,134) To discern the rate of reaction, the consumption of hydrogen gas was monitored as described elsewhere. (135,136) Briefly, a 20 mL solution containing the platinum catalyst (48 μM Pt) was introduced in a 100 mL three-neck round bottom flask. The system was purged with

hydrogen (~35 mL/min) for 10 minutes under maximum stirring speed (1100 rpm) to evacuate the air contents. Subsequently, the system was sealed and hydrogen was allowed to equilibrate between the aqueous and gas phases for another 10 minutes under maximum stirring speed. Finally, 0.6 mL of 14.667 mM allyl alcohol (8.8 mmol) was injected via syringe. The hydrogenation reaction commenced directly, and the decrease in the pressure of hydrogen was measured electronically.

Characterization. Transmission electron microscopy (TEM) was performed using a JEOL 2010F transmission electron microscope equipped with Schottky-type field emission gun, ultra-high resolution pole piece ($C_s = 0.5$ mm), an Energy Dispersive X-ray spectrometer (EDS), and a scanning transmission electron microscope (STEM) unit with high angle annular dark field (HAADF) detector operating at 200 kV. Samples for TEM analysis were prepared by allowing a drop of the aqueous product to evaporate on a carbon-coated copper TEM grid.

5.3.3 Results and Discussion

Mass-transfer considerations

This system is composed of three distinct phases: the gas, the liquid, and the nanocrystal surface. For this reason, the system has diffusion barriers that can influence in the measurement of catalytic activity. These mass-transfer limitations are critical considerations in any catalysis testing, and are all too often ignored. Previous studies on mass-transfer limitations in catalytic processes provide the means to determine the proper reaction conditions to perform our analysis in an intrinsic kinetic regime. (132,137,138)

In the literature, two different models can be found that predict the behavior of the system, Equation 5.1 (139) and Equation 5.2. (140)

$$\frac{1}{r} = \frac{1}{\eta k_r C_{A,g}} + \frac{d_p \rho_p}{6k_{l,s} C_{A,g}} + \frac{1}{k_{g,l} A_{g,l} C_{A,g}} \quad (5.1)$$

$$\frac{1}{r} = \frac{1}{k_r [Cat]} + \frac{1}{k_M} \quad (5.2)$$

In Equation 5.1, (r) is the reaction rate (mol/s), (W) is the catalyst weight (g), (η) is the effectiveness factor, (k_r) is the intrinsic rate constant (cm³/[s g]), ($C_{A,g}$) is the reactant concentration in the gas phase (mol/cm³), (d_p) is particle diameter (cm), (ρ_p) represents the particle density (g/cm³), ($k_{l,s}$) is the liquid-solid mass transfer coefficient (cm/s), ($k_{g,l}$) is the gas-liquid mass transfer coefficient (cm/s), and ($A_{g,l}$) is the interfacial area between the gas and liquid phases (cm²). For Equation 5.2, (r) is reaction rate (mol/s), (k_r) is the intrinsic rate constant (1/s), [Cat] is the catalyst concentration (mol/L), and (k_M) is the mass transfer constant (mol/[L s]).

Under conditions where the catalyst is saturated by the reactants, the rate depends on a pseudo-first order rate constant and the catalyst concentration, as both models predict. In the equations, secondary terms appear that represent mass transfer. For ideal conditions, the first term should be overwhelmingly larger than the secondary terms, and mass transfer limitations can be neglected. To optimize these conditions, different experiments were carried out. Following Equation 5.2, the reaction rate was measured at different catalyst concentrations of (24:1) Pt:BSA, composed of platinum crystals with aspect ratios of unity, and a size distribution of 2.220 ± 0.294 nm. From this plot (Figure 5.7), we can calculate (k_M) based on regression analysis of the various values of ($k_r[Cat]$).

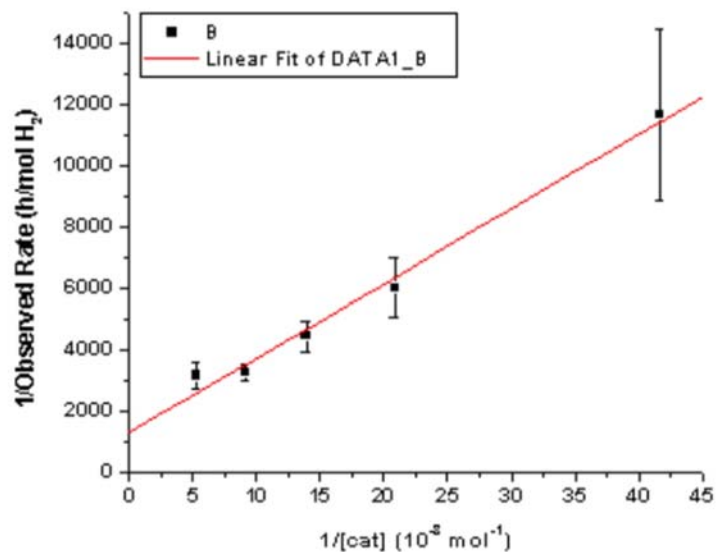


Figure 5.7: $(1/r)$ vs $(1/[Cat])$ for (24:1) Pt:BSA nanocrystals.

From the same experimental data, we can create a plot that represents reaction rate versus catalyst concentration. In this plot (Figure 5.8), two different regions are distinguished. In the first region, the reaction rate is linearly dependent upon the catalyst concentration. In the second region, a plateau is reached where the reaction rate is independent of the catalyst concentration. At this point, the reaction is controlled by mass transfer processes. For this reason, we chose to work at catalyst concentrations of $48 \mu\text{M Pt}$, where (k_M) is five times greater than the term $(k_r[Cat])$. At this concentration, mass transfer effects will have $\sim 17\%$ contribution to the observed measurements.

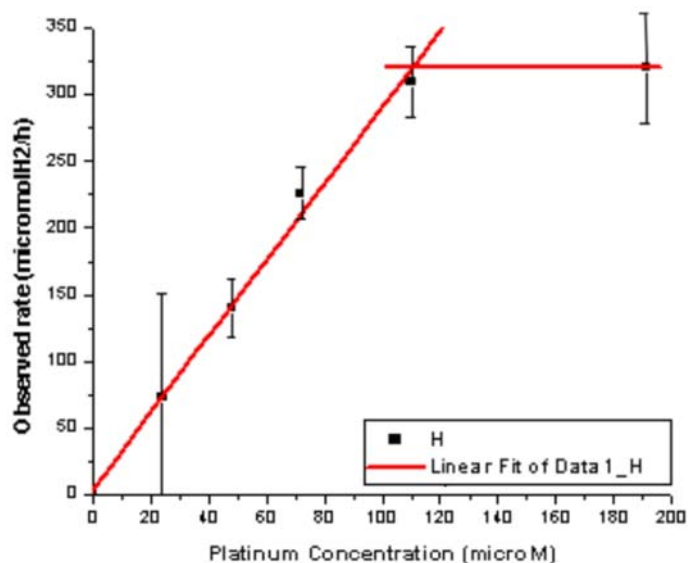


Figure 5.8: (r) vs ($[Cat]$) for (24:1) Pt:BSA nanocrystals.

Varying the stirring rate can also influence the reaction rate, since rapid stirring will allow for the most efficient mass transfer between the phases. If small changes in stirring rate do not induce a change in the reaction rate, then we can consider that the rate of reaction is not being controlled by mass transfer between the liquid and solid phases. Figure 5.9 presents the reaction rate as a function of stirring rate for a 110 μM Pt solution. According to Figure 5.8, this catalyst concentration is located in the mass transfer regime. Thus, it is not surprising that a direct relation between the reaction rate and the agitation speed was observed at this mass-transfer limited catalyst concentration.

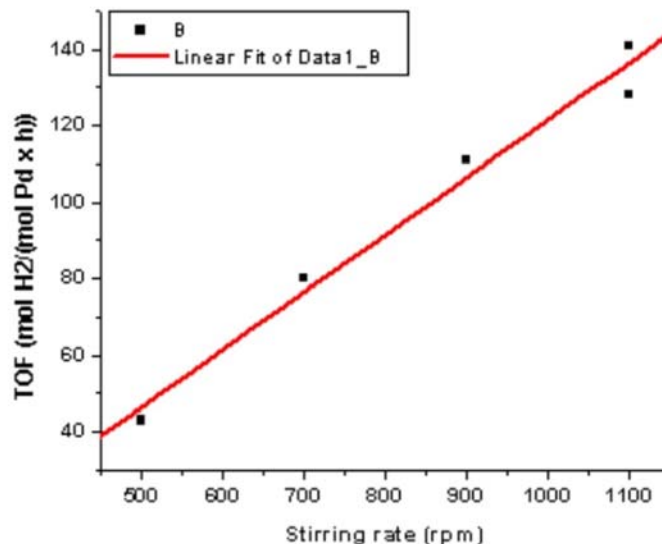


Figure 5.9: Turnover frequency vs stirring rate for (24:1) Pt:BSA nanocrystals (110 μM). The linear increase in TOF indicates this catalyst concentration is in the mass transfer regime.

The effect of stirring rate on TOF was also studied for 48 μM solutions of (24:1) Pt:BSA (Figure 5.10a) and (96:1) Pt:BSA (Figure 5.10b, composed of 70% platinum nanocrystals with aspect ratios <2 , and 30% elongated platinum crystals with widths of 2.233 ± 0.320 nm and lengths of 4.080 ± 1.960 nm). For both 48 μM solutions, the TOF levels off at stirring rates greater than ~ 900 rpm. These results indicate this catalyst concentration is located in the intrinsic kinetic regime, again in agreement with our findings in Figure 5.8.

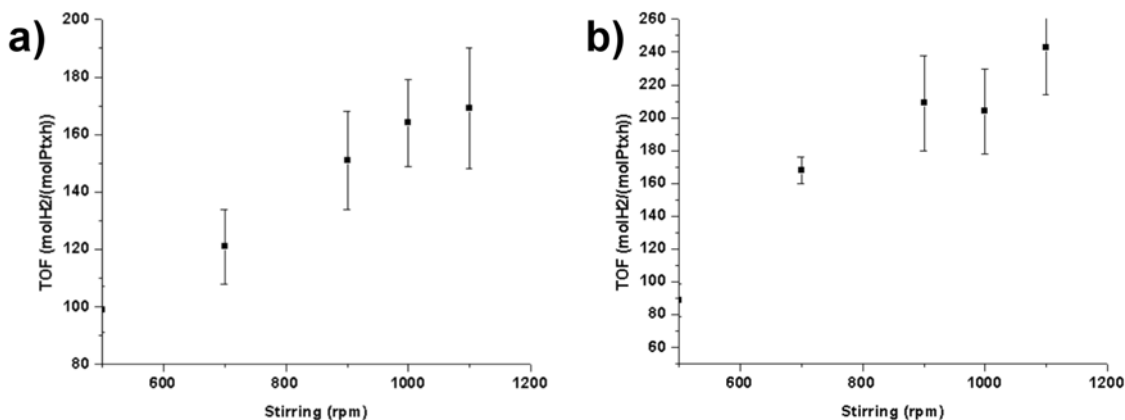


Figure 5.10: Turnover frequency vs stirring rate for platinum nanocrystals at (48 μM). (a) (24:1) Pt:BSA catalyst; (b) (96:1) Pt:BSA catalyst. The leveling off of TOF for stirring rates greater than ~ 900 rpm indicates this catalyst concentration is in the intrinsic kinetic regime.

Catalytic Activity of BSA-Functionalized Platinum Nanocrystals

Two different samples of BSA-functionalized platinum nanocrystals were employed as catalysts for the catalytic hydrogenation of allyl alcohol. The first one, (24:1) Pt:BSA, consists of platinum nanocrystals with aspect ratios of unity, and a size distribution of 2.220 ± 0.294 nm. Previous HRTEM investigations reveal that the morphology of these nanocrystals is FCC single crystalline. The number of platinum atoms in a nanocrystal of diameter D can be estimated from a spherical volume, using the density of bulk FCC platinum:

$$N_{Au} = \left(66.216 \frac{\text{atoms}}{\text{nm}^3} \right) \frac{\pi}{6} (D)^3 \quad (5.3)$$

With this approximation, a platinum nanocrystal 2.075 nm in diameter consists of ~ 310 platinum atoms. We can model these nanocrystals as cuboctahedral, with four complete shells surrounding a central atom, and 309 platinum atoms per crystal. (141-143) The catalytic activity displayed by this material is $\text{TOF}_{10\text{min}} = 169 \pm 21$ [mol H₂/(mol Pt h)].

The second sample studied, (96:1) Pt:BSA, is a mixture of 70% platinum nanocrystals with aspect ratios <2 , and 30% elongated crystals with average dimensions of 2.233×4.080 nm. If we approximate these elongated crystals as cylindrical in shape (we are not proposing their actual morphology is cylindrical, but simply employing cylindrical geometry as an approximation), and taking into account the atomic packing factor for FCC crystals ($APF = 0.74$), each elongated nanocrystal contains 770 atoms. The catalytic activity for the entire sample (70% rounded/single twinned and 30% elongated) is $TOF_{10min} = 243 \pm 29$ [mol H₂/(mol Pt h)]. The selectivity for both (24:1) Pt:BSA and (96:1) Pt:BSA was greater than 99%, as no side product such as propionaldehyde was detected by ¹H-NMR. This indicates platinum is not a good catalyst for oxidative dehydrogenation, a common side reaction in hydrogenation. (144)

Having determined the catalytic activity of these two samples on a per-mole Pt basis, we must consider that the real catalytic sites are located on the crystal surfaces. For (24:1) Pt:BSA, modeled as a four-shell cuboctahedron with 309 atoms, these nanocrystals have 162 atoms on the surface. (136) In terms of surface atoms for the (24:1) Pt:BSA system, $TOF_{surface} = 322 \pm 40$ [mol H₂/(mol Pt_{surface} h)]. For the (96:1) Pt:BSA system, 70% of the nanocrystals are rounded to single-twinned in shape, while the remaining 30% of the nanocrystals can be modeled as cylinders with 508 atoms on the surface and 262 atoms on the interior of the cylinder. Taking these figures into account, $TOF_{surface} = 626 \pm 44$ [mol H₂/(mol Pt_{surface} h)] for the elongated crystals in the (96:1) Pt:BSA system.

The cuboctahedral crystals in the (24:1) Pt:BSA system have 52% surface atoms, and we estimate (based on a cylindrical model) that the elongated crystals in the (96:1) Pt:BSA system have 66% surface atoms. However, in a previous report on palladium nanocrystals with sizes greater than 1.5 nm, Crooks and colleagues determined that

hydrogenation of allyl alcohol occurs preferentially on face atoms. (136) Thus, we must further distinguish between the number of face atoms and edge atoms. Following the same procedure, (136) we calculate there are 78 face atoms for the cuboctahedral crystals in the (24:1) Pt:BSA system. For the elongated crystals in the (96:1) Pt:BSA system, and based on a cylindrical approximation, there are ~468 face atoms. Taking these figures into account, $\text{TOF}_{\text{face}} = 669 \pm 83$ [mol H₂/(mol Pt_{face} h)] for the cuboctahedral crystals in the (24:1) Pt:BSA system, while for the elongated crystals in the (96:1) Pt:BSA system, $\text{TOF}_{\text{face}} = 682 \pm 48$ [mol H₂/(mol Pt_{face} h)]. The measured catalytic activity of each system is summarized in Table 5.1.

Table 5.1: Activity of BSA-Functionalized Platinum Nanocrystals for the Catalytic Hydrogenation of Allyl Alcohol

	$\mu\text{mol Pt}$	TOF [mol H ₂ / (mol Pt h)]	TOF _{surface} [mol H ₂ / (mol Pt _{surface} h)]	TOF _{face} [mol H ₂ / (mol Pt _{face} h)]
(24:1)Pt:BSA	0.96	169 ± 21	322 ± 40	669 ± 83
(96:1)Pt:BSA	0.96	243 ± 29 (total sample)	626 ± 44 (elongated)	682 ± 48 (elongated)

From this analysis, we conclude that the (96:1) Pt:BSA system exhibits a higher catalytic activity than the (24:1) Pt:BSA system. This could be due to the fact that elongated nanocrystals have a greater proportion of face atoms than do cuboctahedral crystals with aspect ratios of unity. Strong support to this hypothesis is provided by the fact that when TOF is calculated based on the number of face atoms per crystal, TOF_{face} is nearly equivalent for the cuboctahedral and elongated crystals. This agrees with the fact that H₂ preferentially dissociates into hydrogen atoms on the faces, rather than the edges, of metal catalysts, since the atoms are stabilized in the threefold hollows present on the faces. (145) Another hypothesis deals with the ratio of protein molecules per nanocrystal. If we assume that the surface of one nanocrystal is protected by one protein

molecule, then a nanocrystal with a smaller surface area (e.g. cuboctahedral) would be better insulated by a protein molecule than a crystal with more surface area (e.g. elongated). This greater degree of protein insulation for rounded crystals could be considered as a poisoning of the crystal surface to some extent.

Comparing the catalytic activity of BSA-functionalized platinum nanocrystals with conventional preparations, the catalytic activity measured for both types of BSA-functionalized nanocrystals is greater than the activity reported for dendrimer-encapsulated catalysts. (146) In that case, a 40-atom platinum nanocrystal was encapsulated inside a hydroxyl-terminated G4-PAMAM dendrimer, and the overall rate was 50 ± 10 [mol H₂/(mol Pt h)]. An important consideration is that due to their smaller size, the dendrimer-encapsulated platinum nanocrystals possess a larger percentage of defect atoms (e.g. edges and vertices) on the crystal surface.

TEM Analysis of Structural Stability

For both the (24:1) Pt:BSA and (96:1) Pt:BSA systems, a precipitant was observed in the reaction crude within 24 hours of catalytic reaction. To investigate the stability of BSA-functionalized platinum nanocrystals in this system, TEM samples were prepared from aliquots after 3 hours and 24 hours of exposure to the hydrogenation reaction. TEM analysis demonstrated coalescence of some nanocrystals. An aggregated colloid is formed during the catalytic reactions, most notably for the (24:1) Pt:BSA system. Recall that for a constant amount of platinum, the (24:1) Pt:BSA system has four times more BSA protein than the (96:1) Pt:BSA system, and we propose that protein aggregation is driving the formation of a precipitant in the reaction crude.

To better understand what was driving the observed precipitation, control experiments were performed for both systems. First, the solution of allyl alcohol and BSA-functionalized platinum catalyst was stirred in the absence of hydrogen, with no

precipitation observed. Second, a solution of BSA-functionalized platinum was stirred in the presence of hydrogen, but in the absence of allyl alcohol, and again no precipitation was observed. After 24 hours, allyl alcohol was added to this system, and the reaction was allowed to proceed for another 24 hours. In this case, precipitation was visually detected in both the (24:1) Pt:BSA and (96:1) Pt:BSA systems.

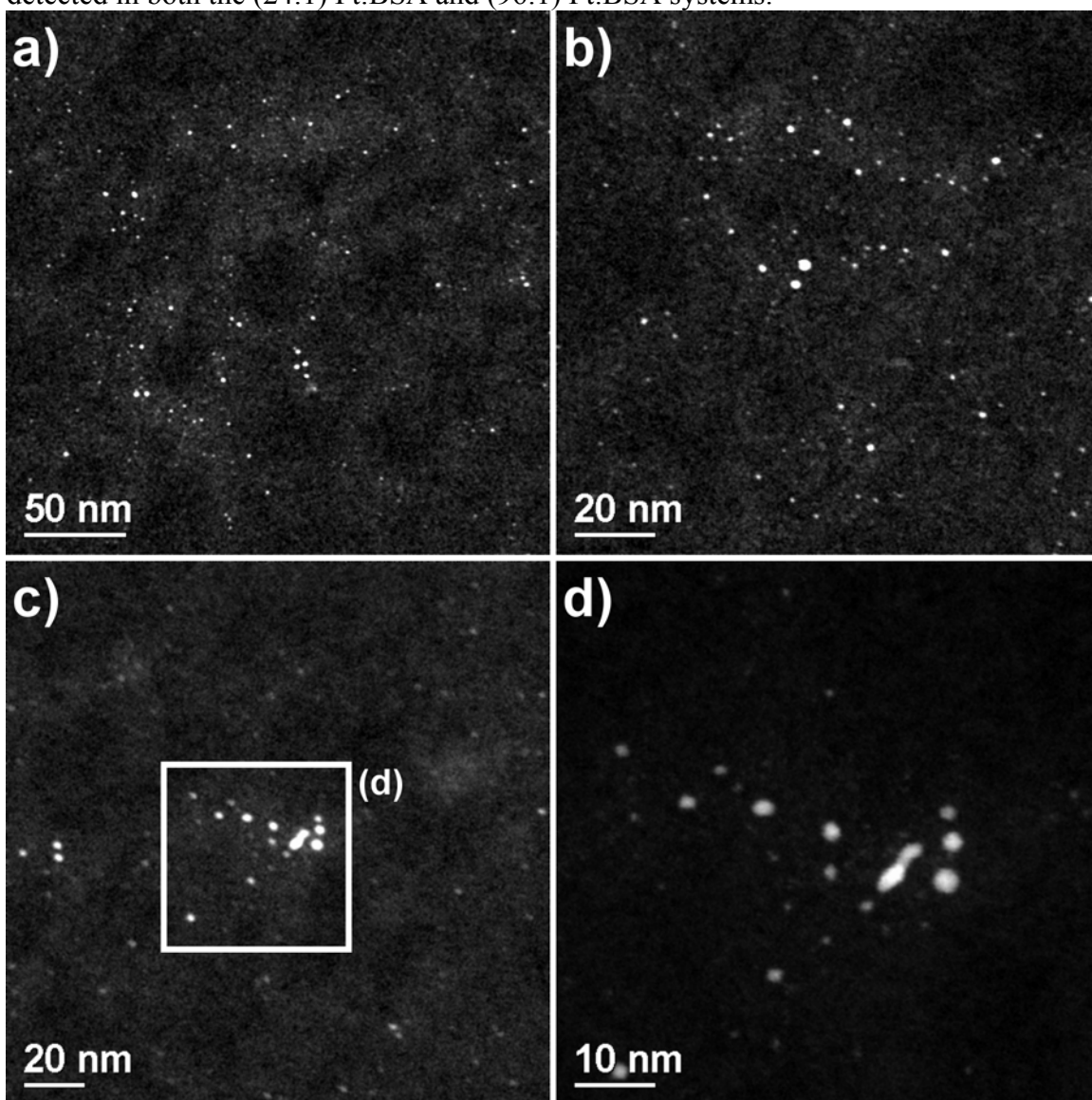


Figure 5.11: HAADF analysis of (24:1) Pt:BSA (48 μ M) after 3 hours of reaction.

For (24:1) Pt:BSA (48 μM) after 3 hours of reaction, HAADF analysis revealed that the nanocrystals are well-dispersed and the size distribution is largely unchanged (Figure 5.11a). However, some evidence of coalescence is observed (Figure 5.11 b-c). Figure 5.11d presents a blowup of the coalesced nanocrystals seen in Figure 5.11c. From this image, we can see that coalescence is causing the growth of larger rounded crystals, as well as elongated crystals.

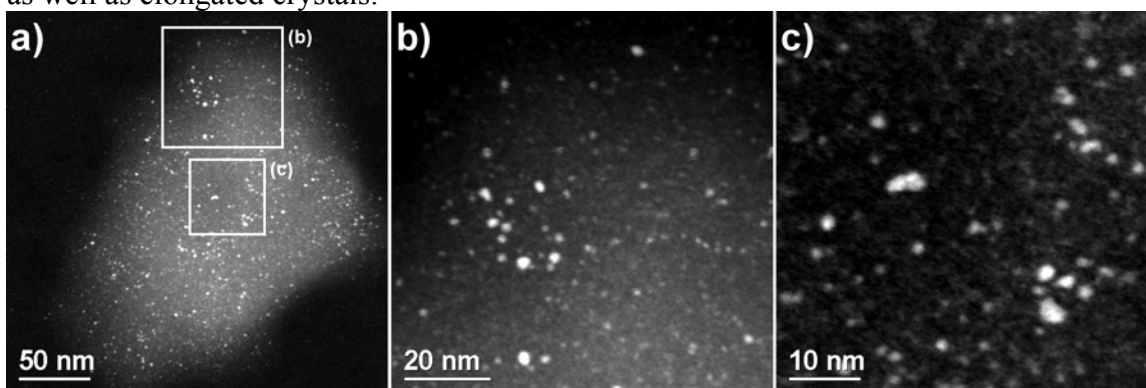


Figure 5.12: HAADF analysis of (24:1) Pt:BSA (48 μM) after 24 hours of reaction. (a) Typical protein aggregate; (b)-(c) blowups of specific regions in the aggregate, demonstrating coalescence among platinum crystals within the protein aggregate.

After 24 hours of reaction, protein aggregation was visibly apparent in the reaction crude, and this was confirmed by HAADF analysis. A characteristic aggregate observed in the (24:1) Pt:BSA system after 24 hours of reaction is presented in Figure 5.12a. These protein aggregates contained greater concentrations of nanocrystals than in the general non-aggregated sample (e.g. Figure 5.11a). There was evidence of extensive coalescence among the nanocrystals within the protein aggregates (Figure 5.12b-c).

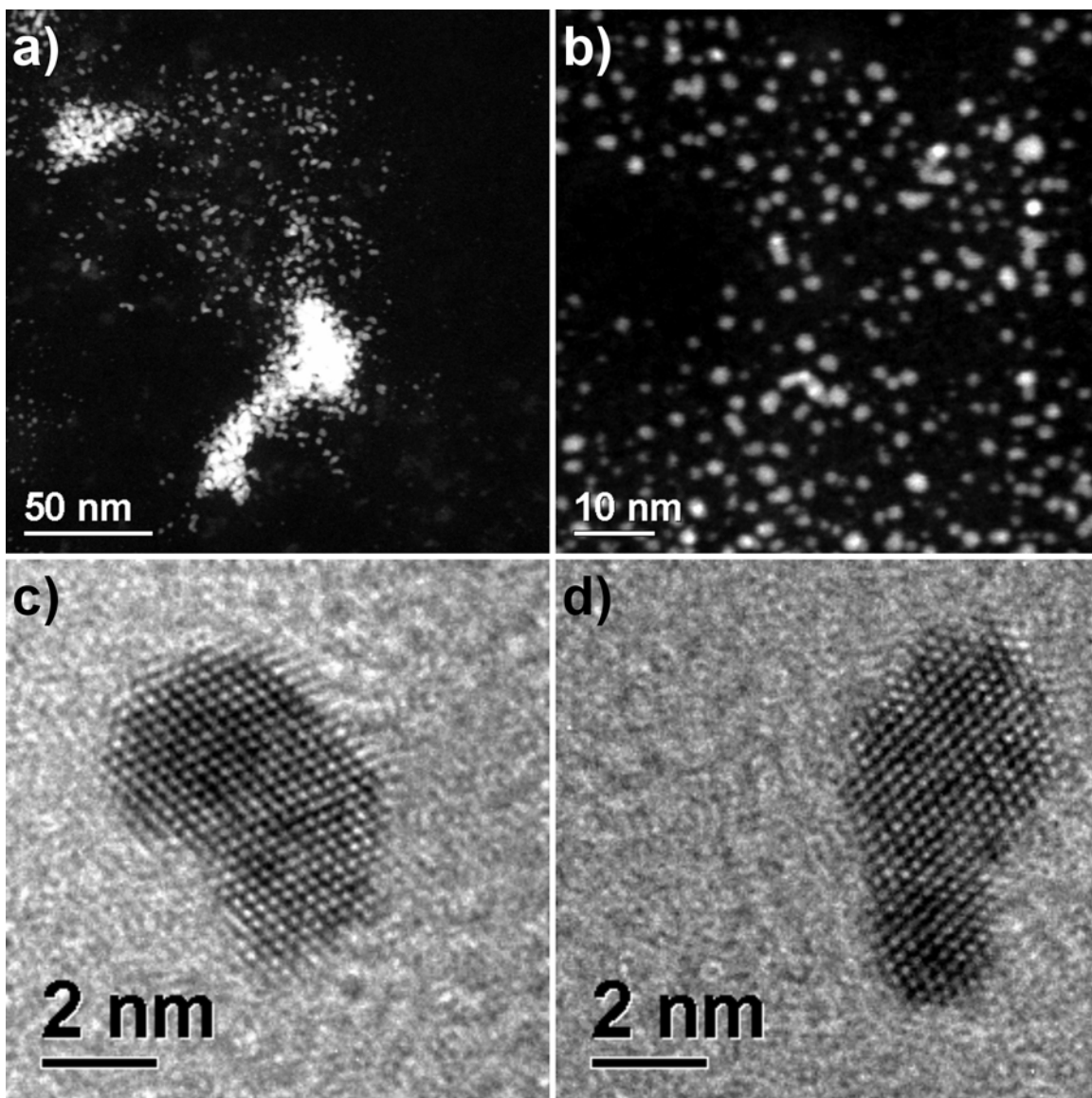


Figure 5.13: (96:1) Pt:BSA (48 μM) after 3 hours of reaction. HAADF of (a) aggregated and (b) dispersed regions of the product. (c)-(d) Characteristic HRTEM images of elongated crystals, with dimensions comparable to those observed in the as-synthesized nanocrystal product.

We propose that the observed protein aggregation is due to the structural degradation of BSA molecules when exposed to the reaction conditions for prolonged intervals. Recall that we are measuring the activity of platinum nanocrystals toward

catalytic hydrogenation, and we have found that the nanocrystals are indeed catalytically active. Now, the BSA protein molecule possesses unsaturated residues, which are in intimate proximity to the nanocrystal surface. Thus, it stands to reason that a certain extent of protein structural degradation will occur via hydrogenation. The results are aggregation among protein molecules, and coalescence among nanocrystals due to a structurally degraded surface-protecting molecule.

For (96:1) Pt:BSA (48 μM), a substantial degree of aggregation was observed after 3 hours of reaction (Figure 5.13a). However, this type of aggregation has also been observed for (96:1) Pt:BSA, independent of the hydrogenation reaction. By analysis of non-aggregated regions of the sample (5.13b) we note the presence of both rounded and elongated nanocrystals, while the aggregated regions are enriched in elongated crystals. HRTEM analysis indicates the elongated crystals maintain the dimensions of the as-synthesized nanocrystals (Figure 5.13c-d).

The aggregation of (96:1) Pt:BSA (48 μM) is more pronounced after 24 hours of reaction, as documented by HAADF analysis in Figure 5.14. The elongated crystals in Figure 5.14a-b are more densely aggregated than was the case after 3 hours of reaction. HRTEM analysis indicated that the elongation of these nanocrystals was more pronounced (Figure 5.14c-d), although extensive coalescence still was not observed.

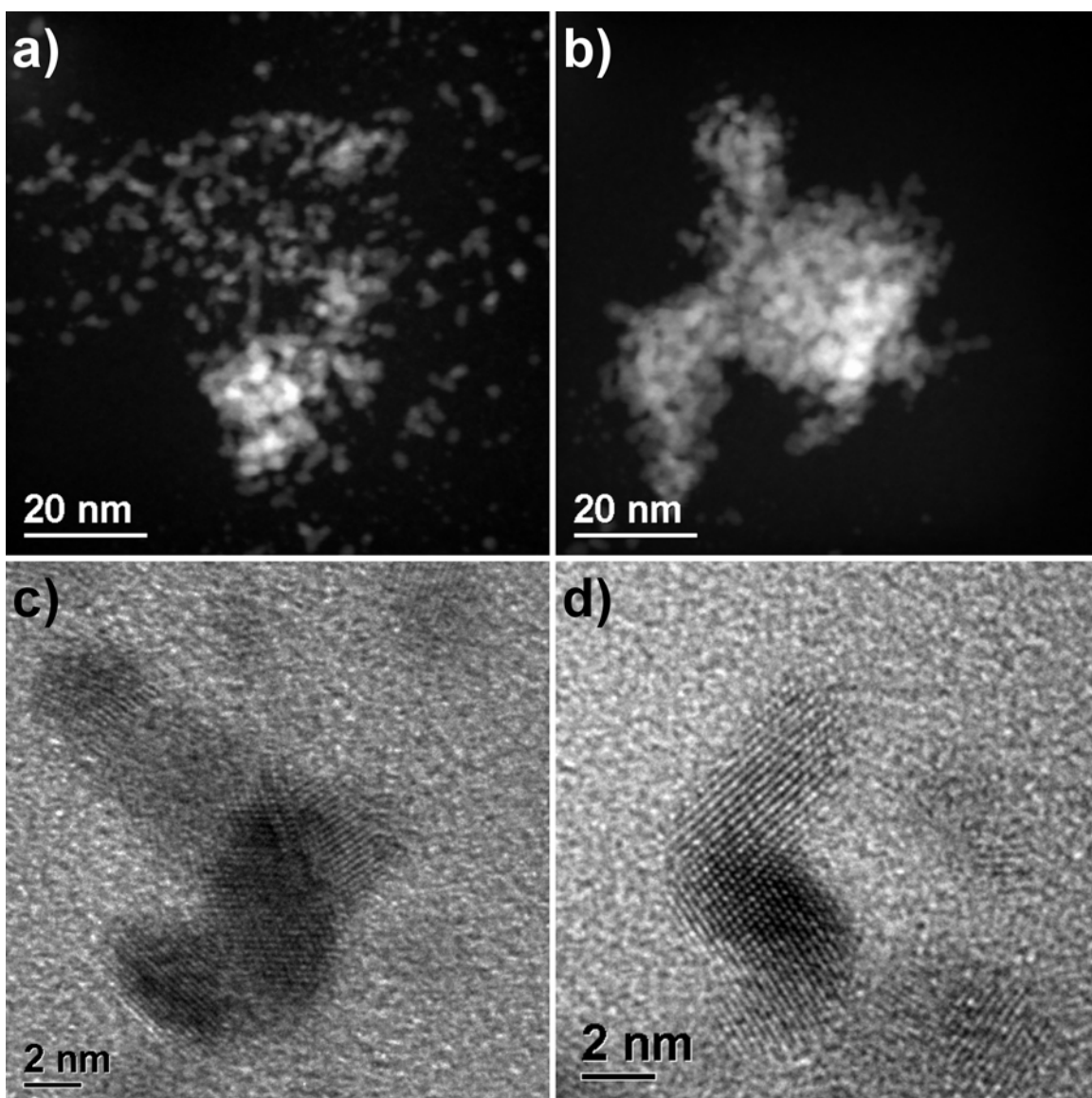


Figure 5.14: (96:1) Pt:BSA ($48 \mu\text{M}$) after 24 hours of reaction. (a)-(b) HAADF images of aggregated crystals. (c)-(d) Characteristic HRTEM images of elongated crystals, demonstrating a more pronounced degree of elongation. Image (c) actually presents two elongated nanocrystals, one on top of the other.

When the reaction was run under mass transfer-limited conditions, extensive protein aggregation and nanocrystal coalescence was observed, even after only 3 hours of reaction. Figure 5.15 presents the (24:1) Pt:BSA system at a concentration of ($110 \mu\text{M}$),

which was previously determined to be a mass-transfer limited catalyst concentration. The significance of mass-transfer limited conditions in relation to the stability of nanoclusters has been previously documented. (137)

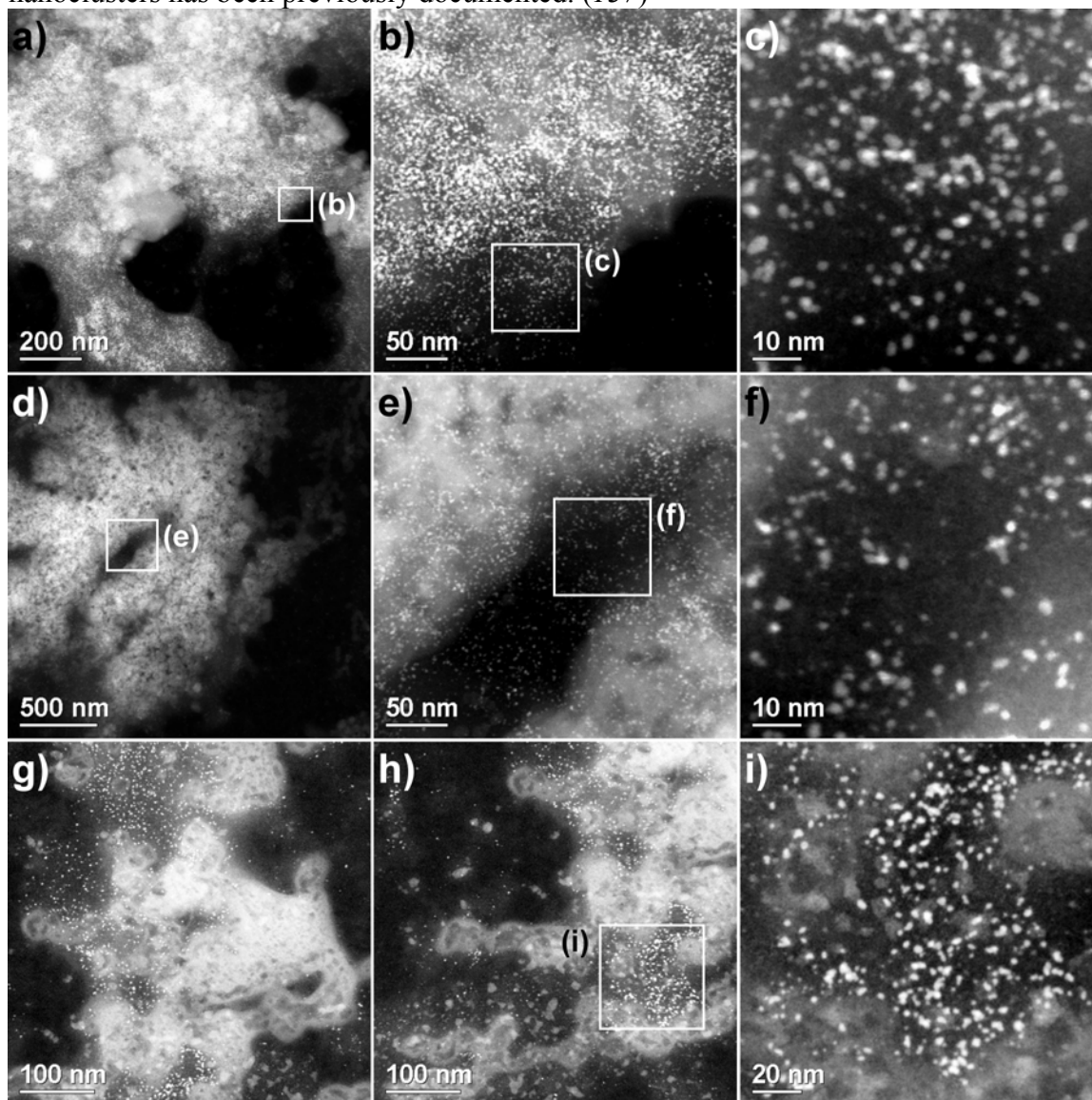


Figure 5.15: HAADF analysis of (24:1) Pt:BSA (110 μM) after 3 hours of reaction. Note the extensive protein aggregation and nanocrystal coalescence observed under mass-transfer limited reaction conditions.

5.3.4 Conclusions

In summary, we have demonstrated that platinum nanocrystals directly conjugated to BSA protein molecules are active toward the catalytic hydrogenation of allyl alcohol. We documented the correlation between nanocrystal structure and catalytic performance, with elongated nanocrystals exhibiting superior activity. We attribute this difference in catalytic activity between rounded and elongated crystals to their relative proportions of exposed face atoms, as demonstrated previously in the case of palladium for nanocrystals with diameters greater than 1.5 nm. (136) We modeled the rounded and elongated nanocrystals as cuboctahedral and cylindrical structures, respectively. When the TOF was calculated based on the number of face atoms per crystal, TOF_{face} was nearly equivalent for the cuboctahedral and elongated crystals.

Comparing the activity of BSA-functionalized platinum nanocrystals with conventional preparations, the catalytic activity measured for both types of BSA-functionalized nanocrystals was superior to the activity reported for dendrimer-encapsulated platinum nanocrystals. (146) However, the long-term dimensional stability of protein-functionalized platinum nanocrystals was compromised under the catalytic reaction conditions, as documented by TEM analysis. Significant coalescence was observed in the (24:1) Pt:BSA catalyst after 24 hours of reaction within the intrinsic kinetic regime, while extensive aggregation and coalescence was found after only 3 hours of reaction within the mass transfer regime. We attribute the observed protein aggregation and nanocrystal coalescence to the structural degradation of BSA molecules when exposed to the hydrogenation reaction conditions for prolonged intervals.

Chapter 6: Aqueous Synthesis of Gold Nanocrystals via Reduction with Ascorbic Acid: From Aggregation to Diffusion-Driven Growth via Addition of Bovine Serum Albumin

6.1 INTRODUCTION

From the investigations described in the previous Chapter, it is clear that serum albumin-functionalized nanocrystals can successfully be incorporated into more complex biological systems, which opens the door to a variety of potential bio-oriented applications. Although the gold and silver nanocrystals utilized in Chapter 5 demonstrated a high degree of biocompatibility in their respective biological environments, these nanocrystals were synthesized using sodium borohydride, a strong reducing agent. I hypothesized that it should be possible to produce protein-functionalized nanocrystals with enhanced biocompatibility by substituting a less harsh reducing agent in the aqueous-based synthesis protocol described in Chapters 3 and 4.

In this respect, the use of a biological molecule as a reducing agent could be ideal, since both the excess reducing agent and its oxidized derivatives would themselves be biocompatible. With this thoroughly bio-inspired approach, the need for stringent purification procedures prior to incorporation into biological systems could be largely avoided. Thus, I chose to pursue the aqueous synthesis of gold nanocrystals in the presence of bovine serum albumin (BSA) via reduction with ascorbic acid, a much gentler reducing agent than sodium borohydride. The preliminary stage of this investigation is described in the current Chapter.

Ascorbic acid [$C_6H_8O_6$], commonly known as Vitamin C, is the most thoroughly-studied of all vitamins. Humans lack the enzyme to produce ascorbic acid, and those who do not obtain sufficient quantities through their diet develop scurvy, a condition in

which synthesis of collagen-containing tissues is impaired. For centuries this malady was common on the high seas, claiming untold numbers of lives among sailors. In 1753, the Scottish naval surgeon James Lind demonstrated that scurvy could be prevented by consuming citrus fruits or their juices. In 1932, ascorbic acid was isolated from lemon juice, and the compound was named for its anti-scurvy activity (*scorbutus* being the Latin equivalent of “scurvy”). In 1933, ascorbic acid became the first vitamin to be structurally characterized and synthesized in the laboratory. (66) In addition to its use as a dietary supplement, ascorbic acid finds broad use as a preservative for foods and pharmaceutical preparations.

Vitamins can be divided into two classes: fat-soluble and water-soluble. Fat-soluble vitamins (Vitamins A, D, E, and K) are stored in fatty tissues, so the body can tolerate periods of dietary deficiency, but if excessive quantities are consumed, their build-up can lead to hypervitaminosis. In contrast, water-soluble vitamins (Vitamins B and C) are excreted by the body and must be consumed regularly. Although many health claims regarding the consumption of large daily doses of Vitamin C remain unsubstantiated, the harmful side effects of consuming substantial quantities of ascorbic acid are minimal. From our standpoint, this means that use of ascorbic acid as a reducing agent will provide an as-synthesized product that would be suitable for a variety of biological applications without the need for extensive purification.

6.2 EXPERIMENTAL PROCEDURE

Synthesis. Gold nanocrystals were synthesized in air by reduction in a homogeneous solution at ambient conditions. Chloroauric acid trihydrate ($\text{HAuCl}_4 \cdot 3\text{H}_2\text{O}$; 99.9+%; Aldrich) was reduced in water and in the presence of bovine serum albumin (BSA; Fraction V – heat shock treated; Fisher) by the addition of ascorbic acid (L-ascorbic acid; ACS reagent grade; Aldrich). An aqueous solution of ionic gold was prepared by adding

1 g $\text{HAuCl}_4 \cdot 3\text{H}_2\text{O}$ to 25 mL of deionized water. All materials were used without further treatment. In a typical experiment, 0.5 mL of 0.10 M HAuCl_4 (50 μmol Au) were added to an aqueous solution containing a variable amount of dissolved BSA protein. Then, 5 mL of freshly-prepared 0.4 M aqueous solution of ascorbic acid (2 mmol ascorbic acid) was added rapidly and under vigorous stirring, bringing the total reaction volume to 40.0 mL. Each reaction was allowed to proceed under vigorous stirring for 24 hours.

Table 6.1 summarizes the reaction conditions for each system investigated. The third column of this chart indicates the molar ratios of gold atoms to protein molecules. All ratios are calculated on the basis 50 μmol Au added to the system. For example, in the system where 2.083 μmol BSA was added to the reaction, the ratio is calculated as [50 μmol Au]:[2.083 μmol BSA], or 24:1. For convenience, throughout this Chapter each system will be referenced by its molar ratio, for example “(24:1) Au:BSA.”

Table 6.1: Reaction conditions for the various systems tested.

BSA (g)	BSA (μmol)	[Au]:[BSA]
0.7379	11.1111	9:2
0.5534	8.3333	6:1
0.2767	4.1667	12:1
0.1384	2.0833	24:1
0.0692	1.0417	48:1
0.0346	0.5208	96:1

Characterization. Transmission electron microscopy (TEM) was performed using a JEOL 2010F transmission electron microscope equipped with Schottky-type field emission gun, ultra-high resolution pole piece ($C_s = 0.5$ mm), an Energy Dispersive X-ray spectrometer (EDS), and a scanning transmission electron microscope (STEM) unit with high angle annular dark field (HAADF) detector operating at 200 kV. Samples for

TEM analysis were prepared by allowing a drop of the aqueous product to evaporate on a lacey carbon-coated copper TEM grid. Nanocrystal size distributions for each system were obtained from conventional TEM analysis, based on measurement of 250 crystals. The nanocrystals formed in each system were analyzed via EDS to confirm their elemental identity as gold. UV-visible absorption spectra in the range of 350-800 nm were obtained with a Varian Cary 5000 UV-vis NIR spectrometer. Samples for UV-visible absorption analysis were prepared by diluting the original reaction product with deionized water (a twenty-fold dilution by volume). Solution-phase analysis was performed at room temperature using a matched set of quartz cuvettes (path length 10 mm), and operating the spectrometer in dual beam mode. One cuvette was filled with the diluted reaction solution, while the second cuvette contained deionized water.

6.3 RESULTS AND DISCUSSION

6.3.1 Preliminary Considerations – the Significance of Excess Ascorbic Acid

Prior to studying the effects of protein concentration on the reaction, we first needed to understand the significance of the amount of excess reducing agent introduced into the system. A range of molar ratios of [ascorbic acid molecules]:[gold ions] was investigated, as summarized in Table 6.2. All ratios are calculated on the basis 50 μmol Au added to the system. For convenience, ascorbic acid will be abbreviated as “AA” when molar ratios are discussed throughout the remainder of this section.

Table 6.2: Preliminary ratios of ascorbic acid to gold.

AA (g)	AA (μmol)	[AA]:[Au]
0.0352	200	4:1
0.1409	800	16:1
0.2818	1600	32:1

(24:1) Au:BSA at various excesses of ascorbic acid

From the aqueous-based synthesis described in Chapters 3 and 4, it was found that serum albumin protein was effective in protecting virtually all of the gold nuclei formed at molar ratios of (24:1) Au:BSA, providing a near-quantitative yield of well-dispersed ~ 2 nm crystals. Thus, it was decided to begin the current investigation at the molar ratio of (24:1) Au:BSA. The results for this system at a molar ratio of (4:1) AA:Au are presented in Figure 6.1. The product distribution was broad (Figure 6.1a-b), with crystals ranging from 175–550 nm in diameter. The measured distribution was 316 ± 120 nm, or a standard deviation of nearly 38%.

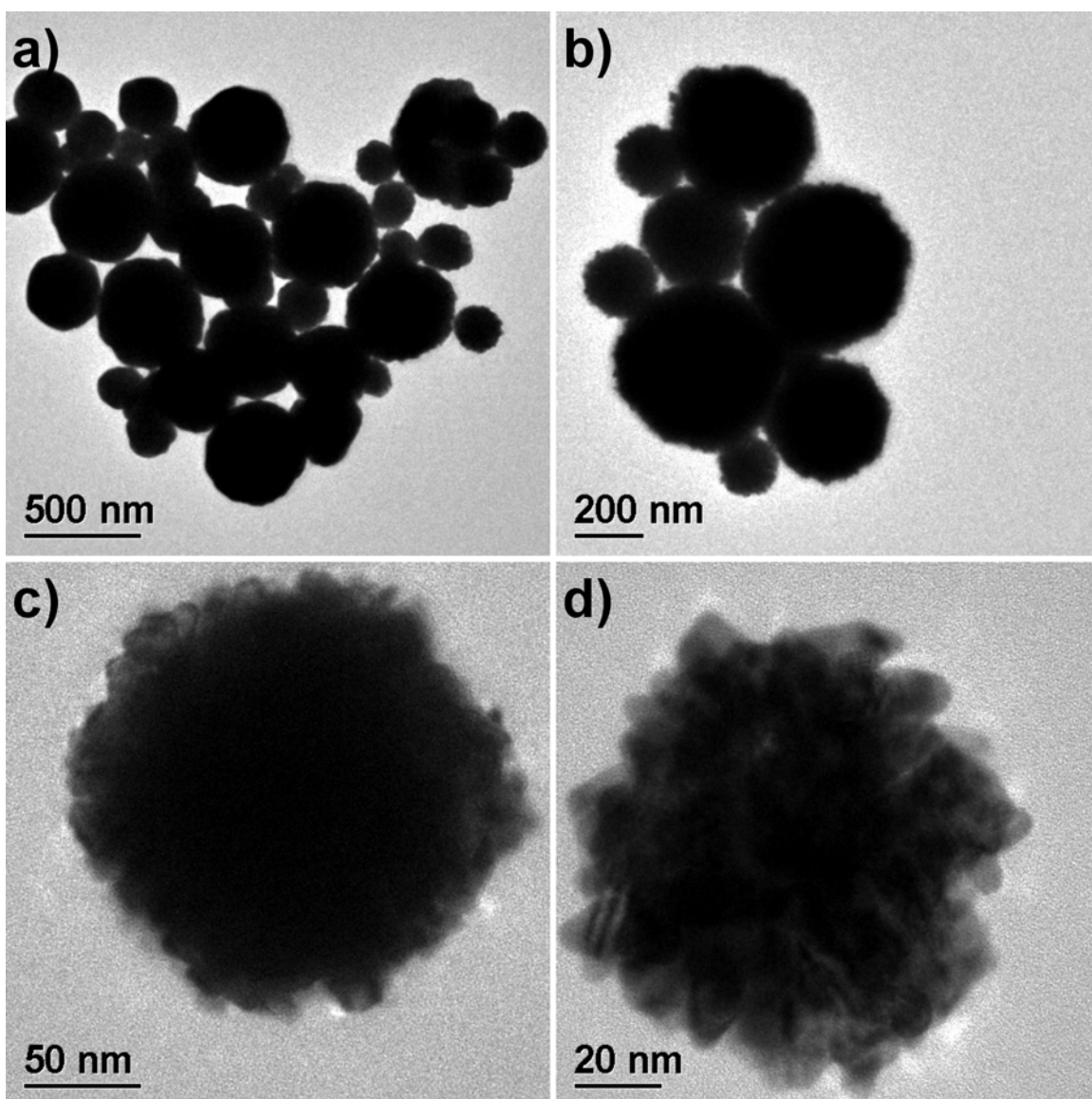


Figure 6.1: (24:1) Au:BSA at (4:1) AA:Au. (a)-(b) low-magnification TEM demonstrating the product distribution; (c)-(d) images of individual crystals.

In a solution-phase colloidal reduction, newly-formed metal atoms coalesce to form nuclei, which grow to primary-sized nanocrystals by diffusional addition of individual atoms. Two possible routes for the subsequent growth of primary-sized nanocrystals exist: (i) continued diffusion of individual atoms onto the existing

nanocrystals, and (ii) aggregation of the existing nanocrystals. (43) From TEM analysis of individual crystals (Figure 6.1c-d), it is clear these structures were formed by aggregation of primary-sized nanocrystals into large polycrystalline spheres. This type of aggregation-driven growth is commonly observed in gold nanocrystals formed by reduction in the presence of ascorbic acid. (43,147)

Since BSA was such an effective stabilizer of gold nuclei in Chapters 3 and 4, leading to purely diffusion-driven growth of primary-sized nanocrystals, we thought the use of BSA alone could be sufficient to inhibit aggregation-driven growth. However, this was not the case. The major difference between these two systems was the strength of the reducing agent. Use of a weaker reducing agent, such as ascorbic acid, entails the formation of fewer nuclei during the initial phase of reduction. For a given amount of atoms in solution, when fewer nuclei are formed, the resulting primary-sized nanocrystals will be larger. This favors aggregation-driven growth, resulting in the types of polycrystalline morphologies observed in Figure 6.1.

To overcome the effects of a weaker reducing agent, it was decided to quadruple the molar ratio of ascorbic acid to ionic gold. The results for the (24:1) Au:BSA system at a molar ratio of (16:1) AA:Au are presented in Figure 6.2. The measured distribution was 158 ± 62 nm, or a standard deviation of over 39%. Again, the product distribution was broad (Figure 6.2a-b) with crystals ranging from 75–280 nm in diameter. Compared with the previously-described (4:1) AA:Au system, the average crystal diameter in this system was half the size, although the percentage deviation from the average crystal diameter was practically unchanged. When individual crystals were analyzed by TEM (Figure 6.2c-d), it was clear these structures were also the result of aggregation-driven growth of primary-sized nanocrystals.

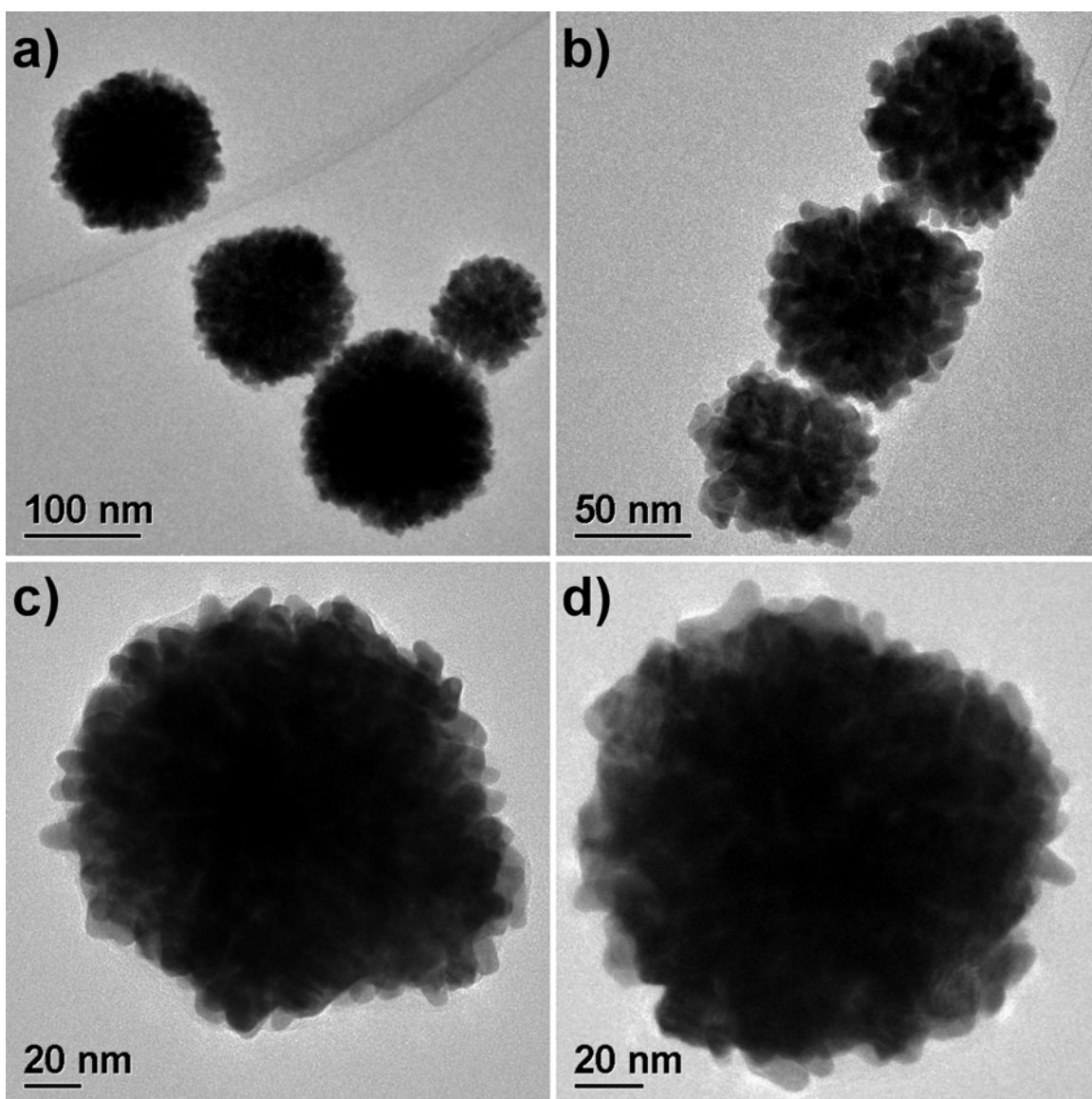


Figure 6.2: (24:1) Au:BSA at (16:1) AA:Au. (a)-(b) low-magnification TEM demonstrating the product distribution; (c)-(d) images of individual crystals.

At this point, investigation of this approach was nearly abandoned, as it appeared that a substantial yield of sub-100 nm gold crystals would not be attainable. However, in a final attempt, it was decided to again double the molar ratio of ascorbic acid to ionic gold. Representative structures from the (24:1) Au:BSA system at a molar ratio of (32:1)

AA: Au are presented in Figure 6.3. Over 95% of the product consisted of sub-100 nm gold nanocrystals, and nearly two-thirds of the crystals were less than 50 nm in diameter. Although the crystals were still the result of aggregation-driven growth, their size provided hope that by working at molar ratios of (32:1) AA: Au and greater, even smaller crystals might be obtained.

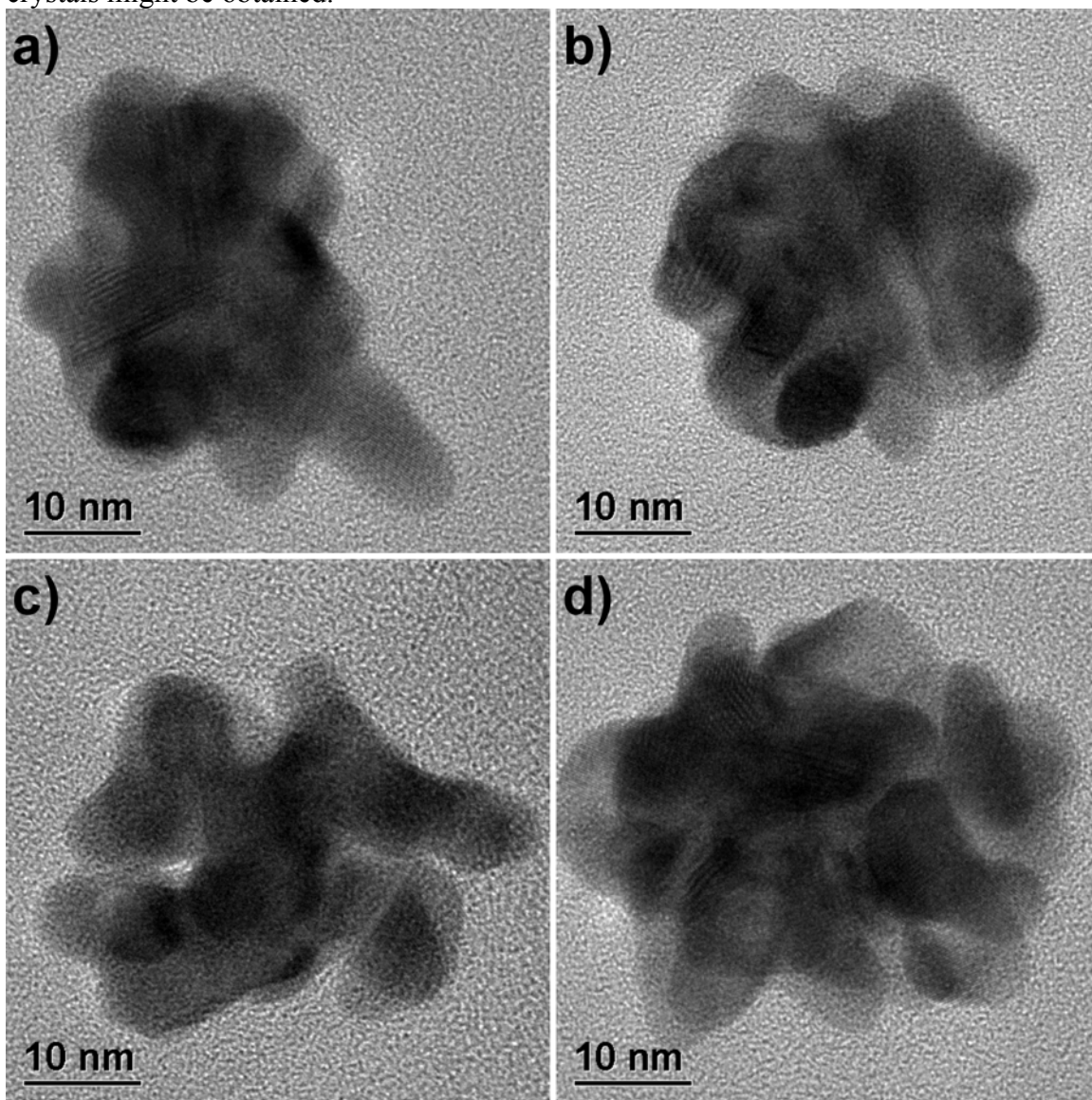


Figure 6.3: (24:1) Au:BSA at (32:1) AA: Au – polycrystalline aggregates with dimensions in the range of 40–50 nm.

(12:1) Au:BSA at various excesses of ascorbic acid

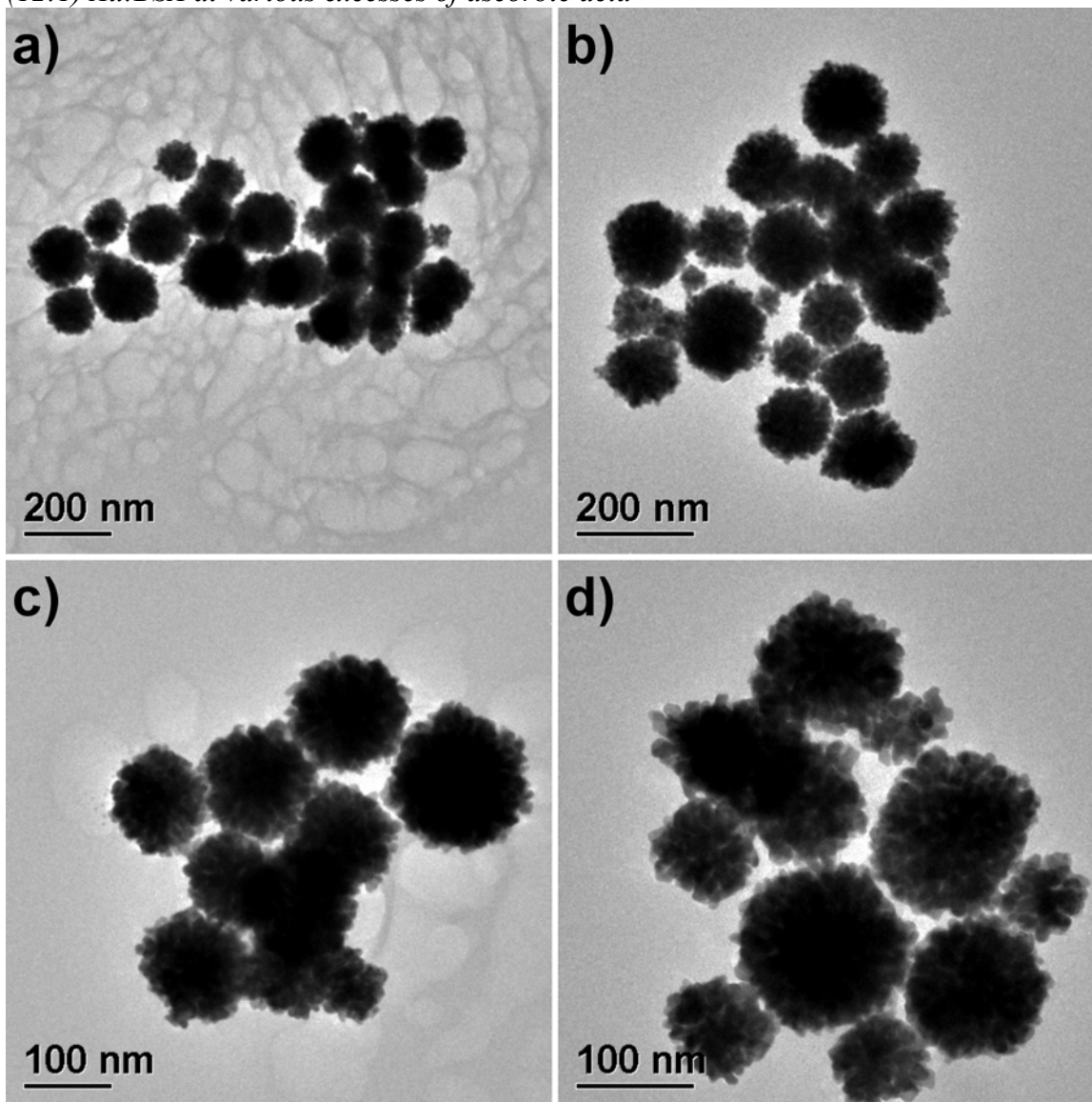


Figure 6.4: (12:1) Au:BSA at (16:1) AA:Au – TEM images.

As mentioned previously, the molar ratio of (24:1) Au:BSA was initially chosen because this had proven effective in promoting the formation of ~ 2 nm gold nanocrystals by reduction with sodium borohydride. However, recall that in Chapter 2, a molar ratio of (12:1) Au:BSA was required to obtain a near-quantitative yield of ~ 2 nm gold

nanocrystals by reduction in glycerin at 65°C. With this in mind, we repeated our preliminary investigations at a molar ratio of (12:1) Au:BSA. The results for the (12:1) Au:BSA system at a molar ratio of (16:1) AA: Au are presented in Figure 6.4.

As in the (24:1) Au:BSA system, the (12:1) Au:BSA system at a molar ratio of (16:1) AA: Au yielded polycrystalline spherical aggregates of gold nanocrystals. The measured size distribution was 122 ± 30 nm, or a standard deviation of less than 25%. The product distribution was broad, with crystals ranging from 45–185 nm in diameter. Compared with (24:1) Au:BSA at (16:1) AA: Au, the average crystal diameter in the current (12:1) Au:BSA system was 20% smaller, and the percent deviation was nearly 40% narrower.

The molar ratio of ascorbic acid to gold was again doubled. Representative structures from the (12:1) Au:BSA system at a molar ratio of (32:1) AA: Au are presented in Figure 6.5. Immediately, it was clear that the morphologies present in this system were different than any others previously observed. These nanocrystals did not form via aggregation of multiple primary-sized crystals, but resulted from the diffusional growth of individual primary-sized nanocrystals. Also, the vast majority of the observed crystals were concave, varying from nanocrystals with small, rounded peaks emerging from the crystal surface (Figure 6.5a-b), to gold multipods with clearly-defined branches emanating from the core of the nanocrystal (Figure 6.5c-d).

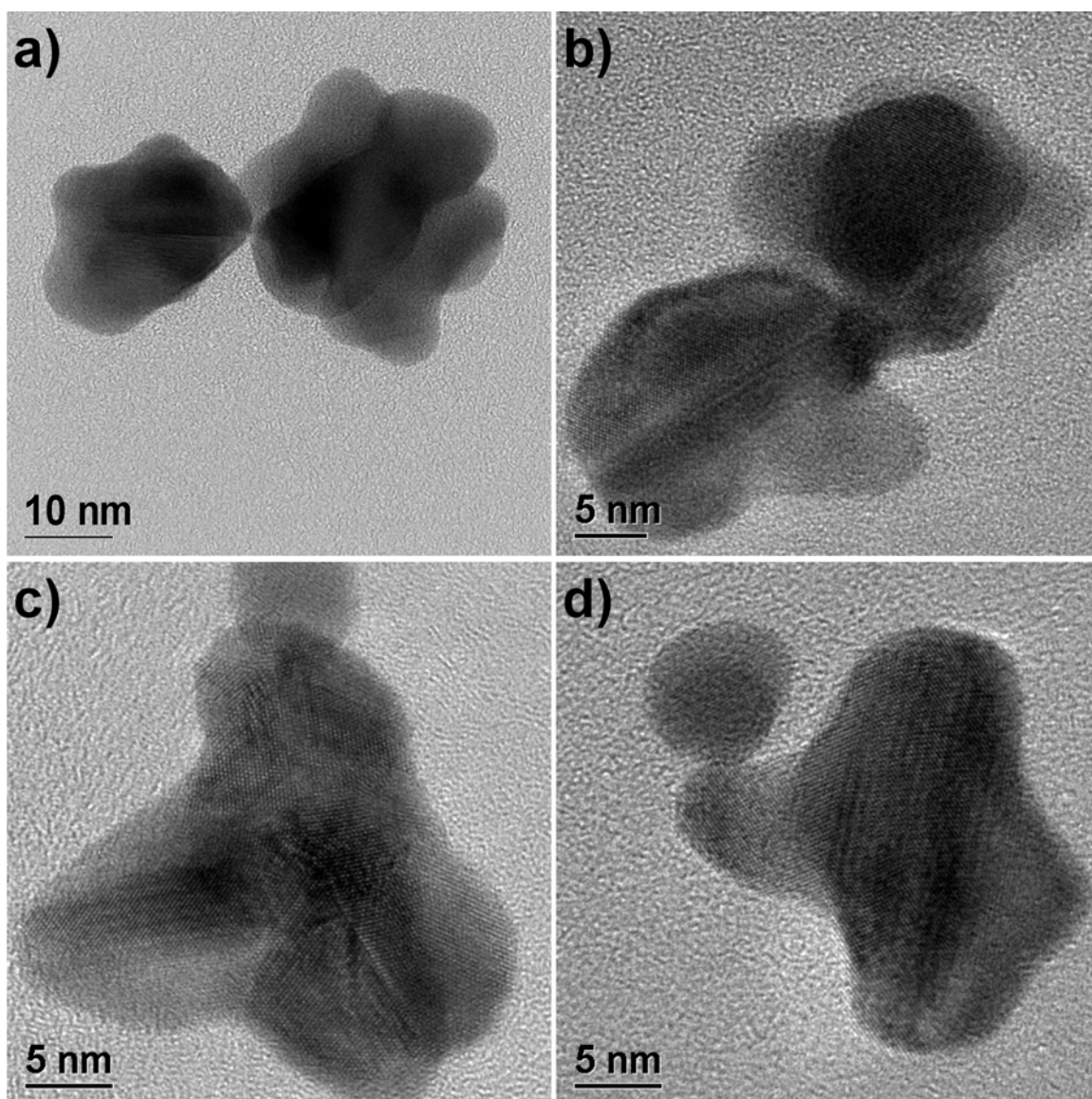


Figure 6.5: (12:1) Au:BSA at (32:1) AA:Au – TEM images.

6.3.2 Synthesis of Gold Nanocrystals in the Presence of BSA via Reduction with Ascorbic Acid

Comparing the preliminary systems investigated, one important insight emerged: larger excesses of ascorbic acid consistently favor formation of smaller nanocrystals. Therefore, we continued to increase the ratio of ascorbic acid to ionic gold, and

determined the ratio beyond which further excesses of ascorbic acid would have a negligible effect on the reaction time and the morphology of the products. For a given amount of protein, it was found that molar ratios of (40:1) AA: Au and (160:1) AA: Au were indistinguishable in terms of reaction time, final color of solution, UV-visible absorption spectra, and the distribution of nanocrystal sizes and morphologies. Therefore, all reactions in the remainder this Chapter were conducted at a molar ratio of (40:1) AA: Au, (2 mmol of ascorbic acid per 50 μ mol gold). By eliminating the amount of ascorbic acid as a variable in this system, we were able to focus solely on the role of protein concentration in determining the reaction products.

Comparison of reaction times

Reaction times were determined as follows. A fully-reacted sample was placed in a round-bottom flask under vigorous stirring, directly next to the reaction vessel. When the color and intensity of the currently-reacting solution matched the previously-reacted sample, the reaction was considered complete. All reactions were performed in triplicate, so two measures of reaction time were obtained for each system.

The reaction times for each system will be treated separately in following sections, but the overall trend in measured reaction times is presented graphically in Figure 6.6. Reaction time exhibited an exponential dependence on the concentration of BSA (as also observed in the glycerin system at 65°C described in Chapter 2). According to the regression, the reaction time in the complete absence of BSA, and with a molar ratio of (40:1) AA: Au, should be ~2 seconds. As we will find in Chapter 7, this is in agreement with the experimentally-observed reaction time.

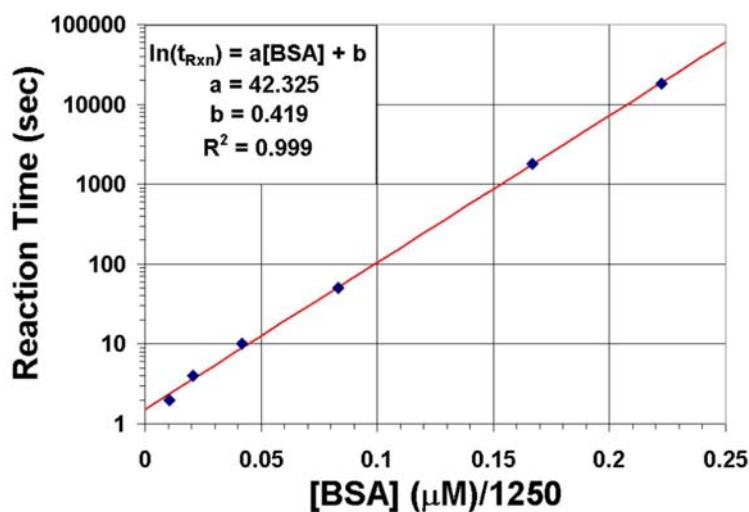


Figure 6.6: Reaction time as a function of BSA concentration for each system studied at a molar ratio of (40:1) AA: Au.

Comparison of solution appearance

In addition to reaction time, solution color was recorded at the conclusion of each reaction. Figure 6.7 demonstrates the appearance of each system investigated at a molar ratio of (40:1) AA: Au, as viewed in transmitted light. The solutions were prepared by four-fold dilution of the as-synthesized product in deionized water, and the light source for backlighting was a florescent lamp. The vial on the far left is the (7:1) Au: BSA sample from Chapter 3, produced in water by reduction with sodium borohydride in the presence of BSA. This sample demonstrates the golden-brown color characteristic of well-dispersed sub-2 nm gold nanocrystals, and is included for purposes of comparison.



Figure 6.7: Color and clarity of each system studied at a molar ratio of (40:1) AA:Au, viewed in transmitted light. The vial on the far left is (7:1) Au:BSA from Chapter 3, produced by reduction with sodium borohydride, included for comparison. From left to right, the remaining vials contain (6:1) Au:BSA, (12:1) Au:BSA, (24:1) Au:BSA, (48:1) Au:BSA, and (96:1) Au:BSA.

Clearly, the colors of the samples produced by reduction in ascorbic acid are nothing like the color expected for ~ 2 nm gold nanocrystals. The color of (6:1) Au:BSA (second from left) was red-wine, indicative of gold nanocrystals < 20 nm in diameter. The (12:1) Au:BSA solution (third from left) was violet, again suggesting the presence of gold nanocrystals in the size range of ~ 20 nm. The appearance of the (24:1) Au:BSA (fourth from left) was unique among all the solutions examined. Initially, the solution color was deep blue-violet, as seen in Figure 6.7. If allowed to sit undisturbed for two weeks, the blue color gradually migrated downwards and eventually settled at the bottom of the vial, leaving behind a violet solution very similar in color to that observed in the (12:1) Au:BSA solution. This is symptomatic of a bimodal product, with one fraction composed of ~ 20 nm nanocrystals that contributes violet color to solution, and another

fraction composed of larger crystals that contributes blue color. The (48:1) Au:BSA solution (fifth from left) had an intense blue color, and the undisturbed sample settled at the bottom of the vial within two weeks, again indicating larger nanocrystals present in this system. Finally, the (96:1) Au:BSA solution (far right) had a deep, cobalt-blue color. If left undisturbed, this sample remained uniformly dispersed for over a month. While the blue color indicates nanocrystals greater than 20 nm in diameter, their relative stability suggests they are smaller than the large crystals present in the (48:1) Au:BSA or (24:1) Au:BSA systems.

Absorption spectroscopy

UV-visible absorption spectra of gold nanocrystals <20 nm in diameter exhibit a characteristic surface plasmon resonance peak at ~520 nm that broadens and decreases in intensity as crystal size decreases. For gold nanocrystals below 2 nm in diameter, this plasmon resonance peak disappears due to the onset of quantum size effects, while for polycrystalline gold nanospheres, the plasmon resonance is progressively shifted toward the red. (10,34) As seen in Figure 6.8, each sample of gold nanocrystals produced via reduction with ascorbic acid exhibits a pronounced surface plasmon resonance, indicating the substantial presence of nanocrystals on the order of 20 nm and greater.

The absorption spectrum for (6:1) Au:BSA (Figure 6.8, Black) exhibits an absorbance maximum of relatively low intensity at ~550 nm. This spectrum is not symmetric about the absorbance maximum, and can be deconvoluted into two different curves, one centered at ~525 nm, the other at ~605 nm. The contribution at ~525 nm can be attributed to ~20 nm nanocrystals, while the contribution at ~605 nm can be attributed either to larger nanocrystals, or elongated crystals. Elongated crystals exhibit a longitudinal plasmon resonance red-shifted from ~520 nm by an amount proportional to their aspect ratio. (148,149) Since selective precipitation of a fraction of the product was

not observed in this system, we tentatively attribute the spectral contribution at ~605 nm to elongated crystals. This will be corroborated by TEM analysis.

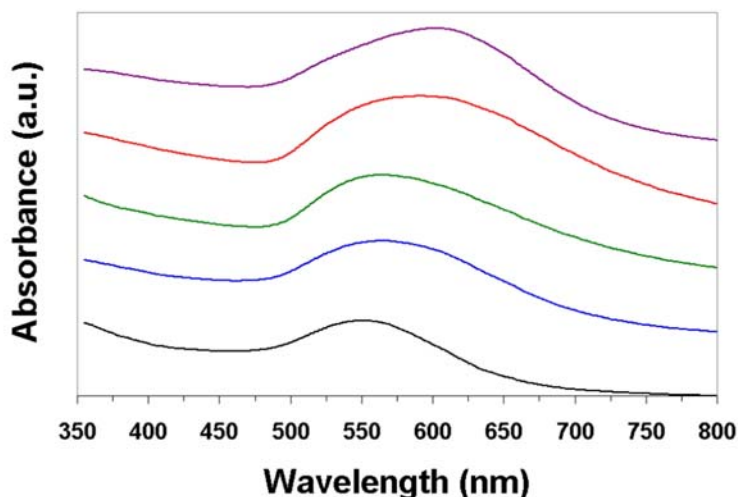


Figure 6.8: UV-visible absorption spectra of the systems studied at a molar ratio of (40:1) AA: Au. From bottom to top, the spectra are (6:1) Au:BSA (Black), (12:1) Au:BSA (Blue), (24:1) Au:BSA (Green), (48:1) Au:BSA (Red), and (96:1) Au:BSA (Violet).

By comparison, the absorbance maximum at ~565 for (12:1) Au:BSA (Figure 6.8, Blue) is much broader and more intense. However, this spectrum can be deconvoluted into the same two curves as in the case of (6:1) Au:BSA, only with a greater relative intensity for the curve centered at ~605 nm. This indicates a nanocrystal distribution very similar to the (6:1) Au:BSA system, but with a greater number of either larger nanocrystals, or elongated nanocrystals. Again, for the reasons previously cited, the curve centered at ~605 nm will tentatively be attributed to elongated crystals, to be corroborated by TEM analysis in the following sections.

The spectrum for (24:1) Au:BSA (Figure 6.8, Green) exhibits an absorbance maximum at ~560 nm that can be deconvoluted into three curves at ~530 nm, ~605 nm, and ~650 nm. This latter curve can be attributed to the larger crystals that were visually

observed to slowly precipitate from solution. The spectra for (48:1) Au:BSA (Figure 6.8, Red) and (96:1) Au:BSA (Figure 6.8, Purple) exhibit absorbance maxima at ~590 nm and ~600 nm, respectively, that can also be deconvoluted into three curves, centered at ~530 nm, ~605 nm, and ~650 nm. The (48:1) Au:BSA spectrum has the largest relative contribution from the curve centered at ~650 nm, indicating a greater percentage of large crystals, as observed visually in the form of precipitation.

Size distributions

Nanocrystal size distributions for each system were obtained from conventional TEM analysis, based on measurement of 250 crystals. Size distributions for each system studied at a molar ratio of (40:1) AA:Au, along with representative low-magnification TEM images, are presented in Figure 6.9. Analysis of the characteristic nanostructures observed in each system will be found in the following section. Presently, we limit ourselves to a brief summary of results, and some general remarks on the trends in nanocrystal size distribution and morphology.

The (96:1) Au:BSA system exhibited the narrowest percentage deviation at ~25%, and was composed primarily of ~40 nm polycrystalline aggregates, and gold multipods. With twice as much protein, the (48:1) Au:BSA system had a broader standard deviation at ~30%, and nearly two-thirds of the product was composed of 45–75 nm polycrystalline aggregates. The (24:1) Au:BSA system possessed the broadest deviation at more than ~50%. While more than half of the product was composed of gold multipods smaller than 40 nm, another 15% consisted of large polycrystalline aggregates greater than 75 nm in diameter. In comparison, the (12:1) Au:BSA system was more controlled, exhibiting a standard deviation of ~40%, and less than 5% of this sample was composed of crystals larger than 40 nm in diameter. Finally, the (6:1) Au:BSA system exhibited a deviation of ~33%, and an average crystal diameter of <20 nm.

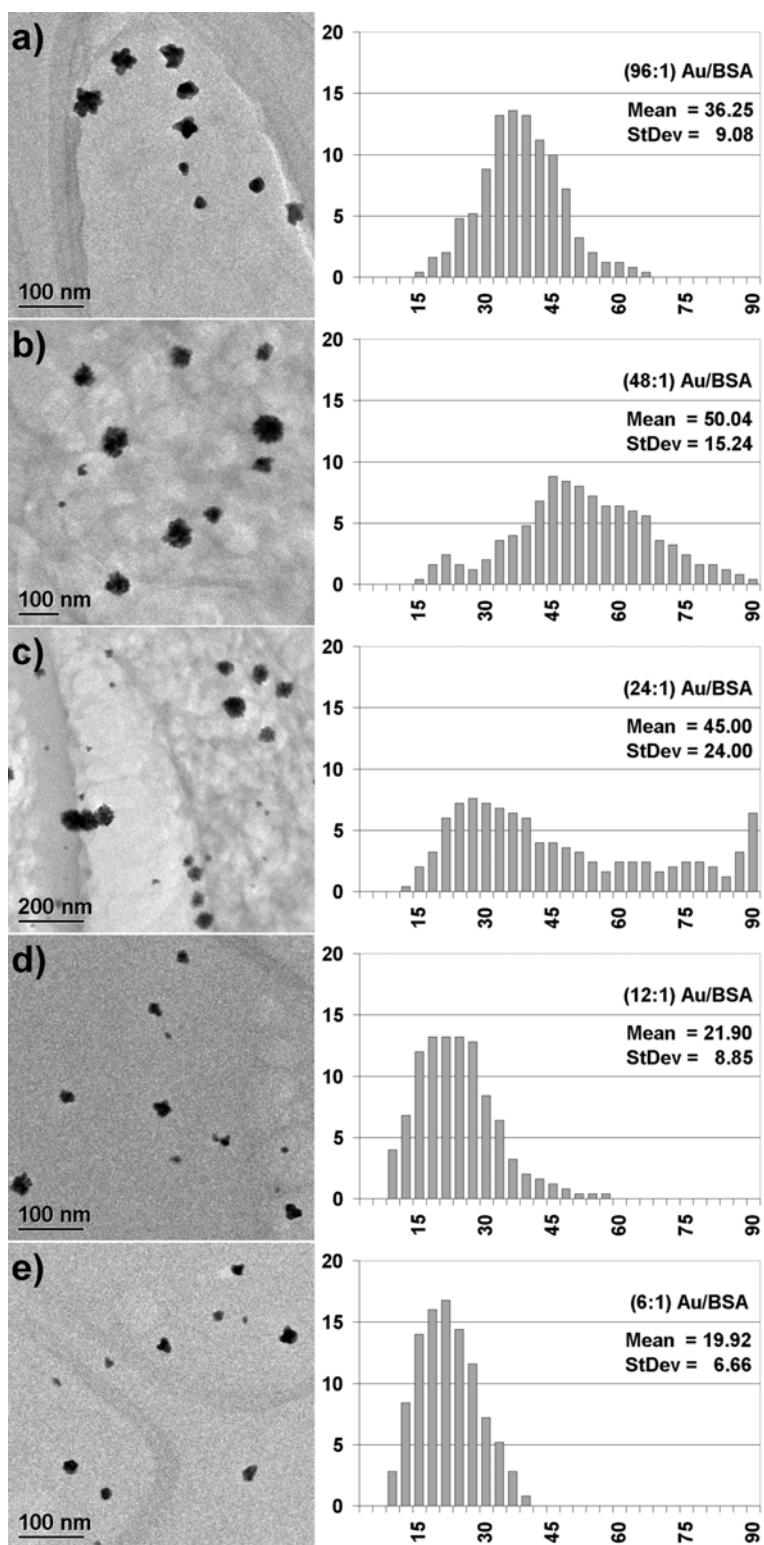


Figure 6.9: Representative TEM images and size distributions for each system studied at a molar ratio of (40:1) AA:Au. (a) (96:1) Au:BSA; (b) (48:1) Au:BSA; (c) (24:1) Au:BSA; (d) (12:1) Au:BSA; (e) (6:1) Au:BSA.

We may summarize these results as follows. With increasing concentrations of protein, gold nuclei are better stabilized, resulting in smaller primary-sized nanocrystals, which favors diffusional growth. However, increasing the protein concentration also decreases the rate of reaction, which favors the formation of fewer nuclei during the initial phase of reduction. With fewer nuclei formed, the resulting primary-sized nanocrystals will be larger, favoring aggregation-driven growth. These two competing effects determine the trends in Figure 6.9. In doubling the protein concentration from the (96:1) Au:BSA system to the (48:1) Au:BSA system, decreased nuclei formation is the dominant effect, resulting in a larger, broader distribution with a greater percentage of polycrystalline aggregates. In the (24:1) Au:BSA system, the effects of both decreased nuclei formation and increased nuclei stabilization are present, resulting in an increased percentage of both crystals smaller than 40 nm resulting from diffusional growth, and polycrystalline aggregates in excess of 75 nm in diameter. For protein concentrations greater than this, the increased stabilization of nuclei becomes the dominant effect. Thus, in the cases of (12:1) Au:BSA and (6:1) Au:BSA, the smallest average crystal sizes are obtained, and aggregation-driven growth is nearly nonexistent. We will now proceed to briefly illustrate the characteristic structures observed in each system.

6.3.3 TEM Analysis of the Gold Nanocrystals Obtained from Reduction with Ascorbic Acid in the Presence of BSA

(96:1) Au:BSA

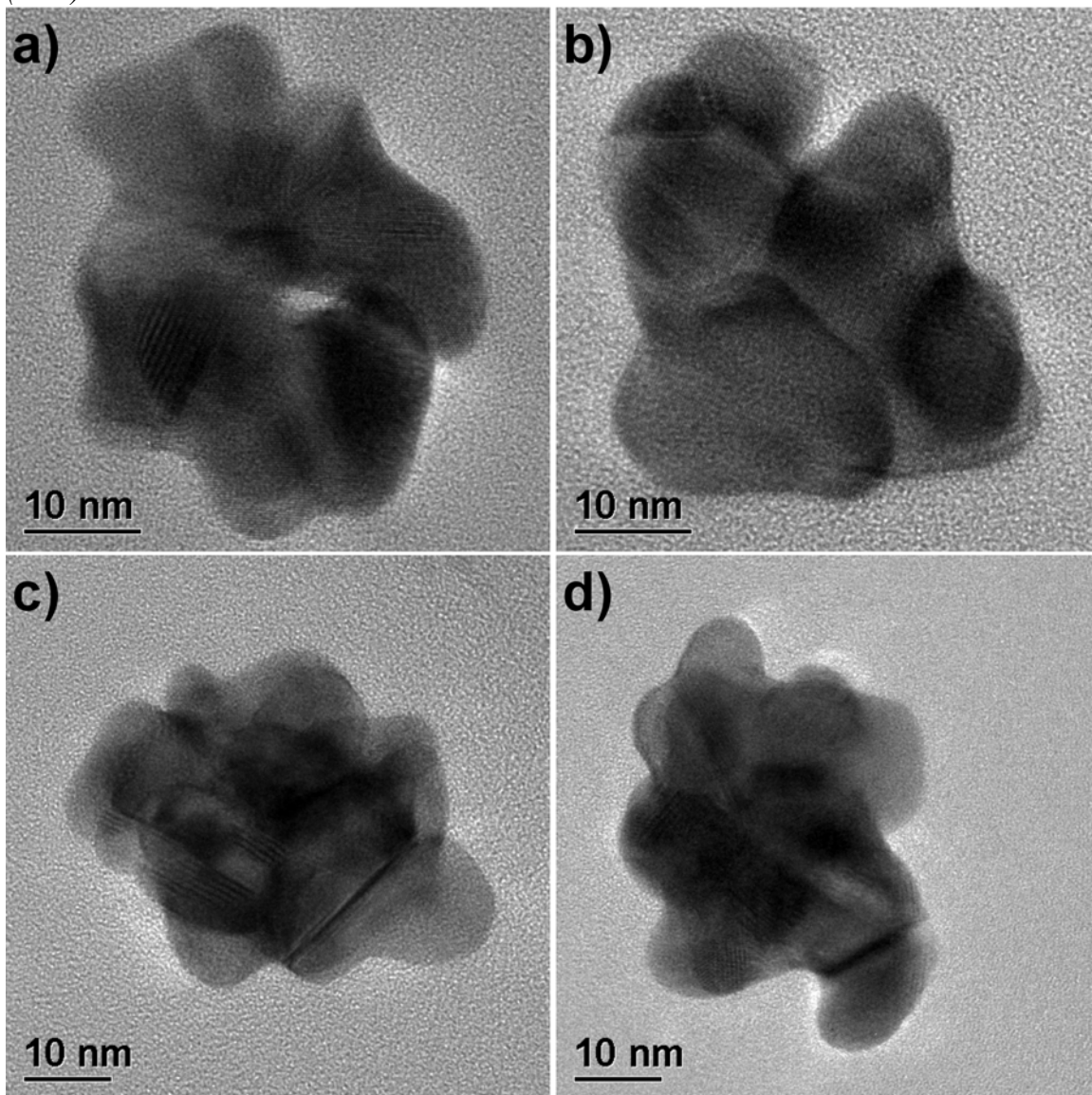


Figure 6.10: (96:1) Au:BSA – 35–50 nm polycrystalline aggregates.

The (96:1) Au:BSA system exhibited a size distribution of 36.25 ± 9.08 nm, and a reaction time of ~ 2 seconds. The product was evenly distributed between 35–50 nm

polycrystalline aggregates (Figure 6.10), and 20–35 nm gold multipods (Figure 6.11). The multipods result from diffusional growth of branched crystalline domains on pre-existing primary-sized nanocrystals. In several instances (Figure 6.11a,b,d), branches were clearly observed to emanate from a core nanocrystal whose structure was multiple-twinned with fivefold symmetry.

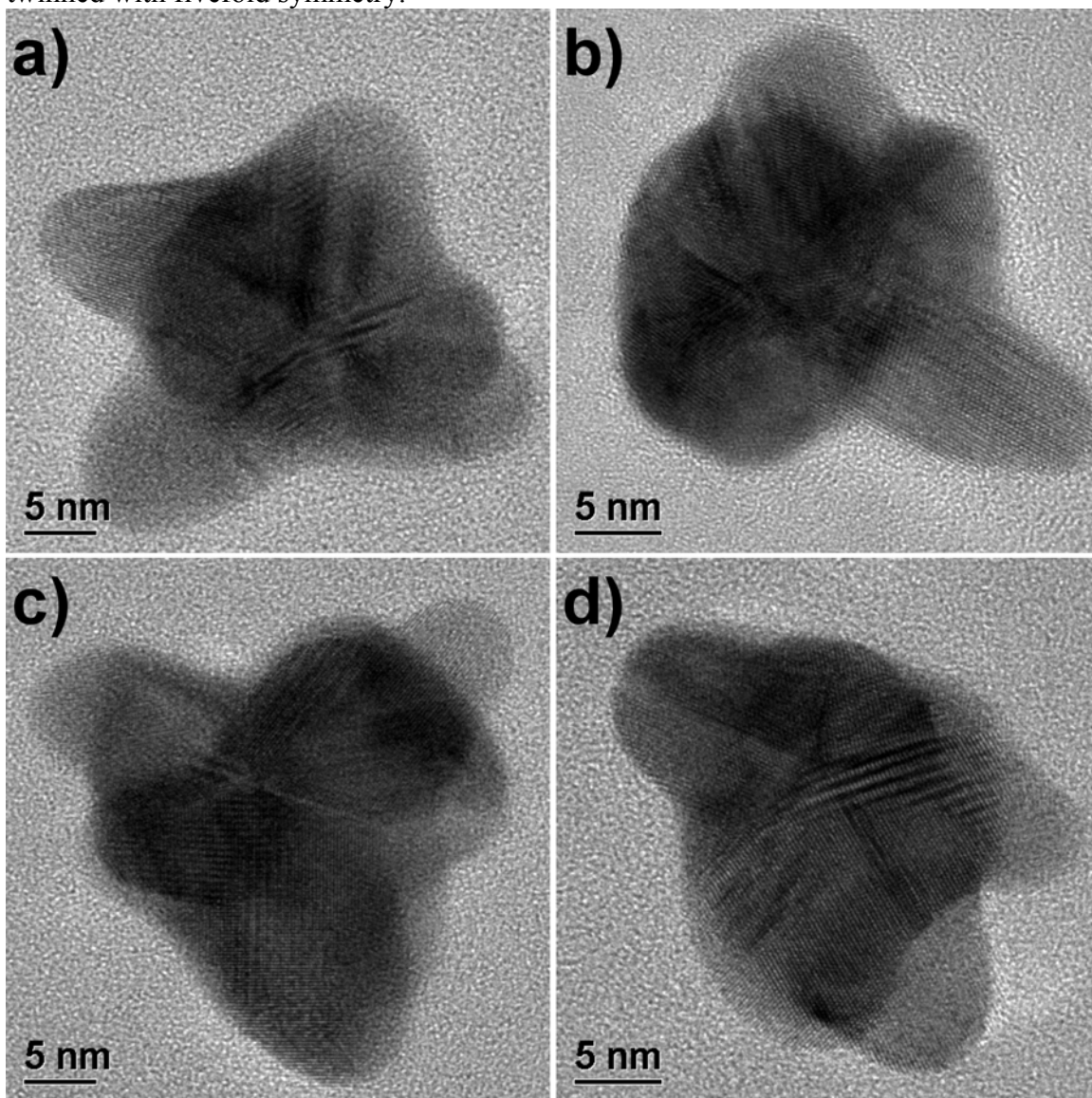


Figure 6.11: (96:1) Au:BSA – 20–35 nm gold multipods.

(48:1) Au:BSA

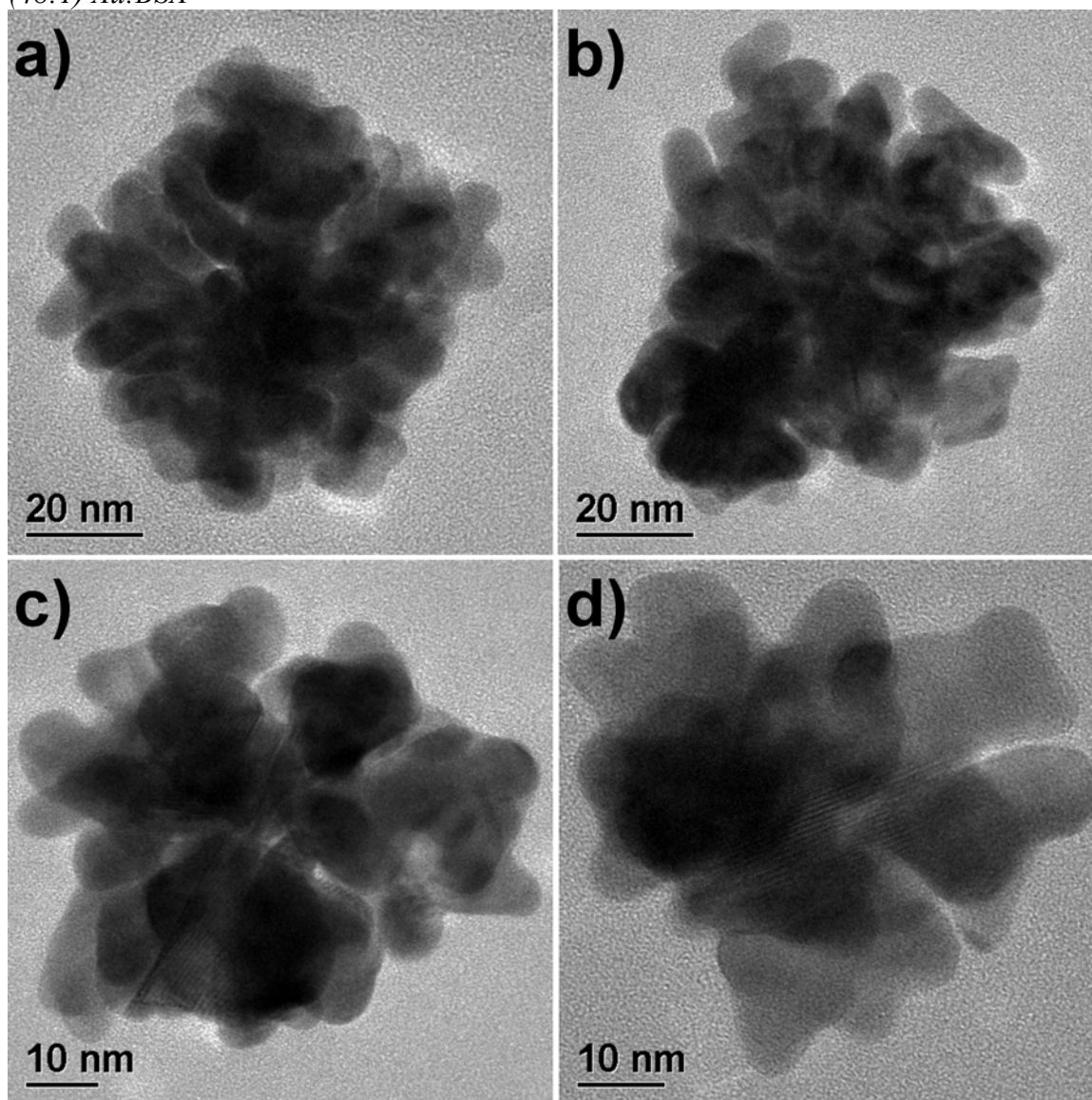


Figure 6.12: (48:1) Au:BSA – 45–75 nm polycrystalline aggregates.

The (48:1) Au:BSA system exhibited a size distribution of 50.04 ± 15.24 nm, and a reaction time of ~ 4 seconds. Nearly two-thirds of the product was composed of 45–75 nm polycrystalline aggregates (Figure 6.12). Another quarter of the product was composed of gold multipods comparable to Figure 6.11. Finally, $\sim 10\%$ of the product

consisted of 15–25 nm nanocrystals with a limited number of small pyramids protruding from the crystal (Figure 6.13). These crystals are the result of diffusional growth of primary-sized nanocrystals, with a slight degree of branching during the growth process.

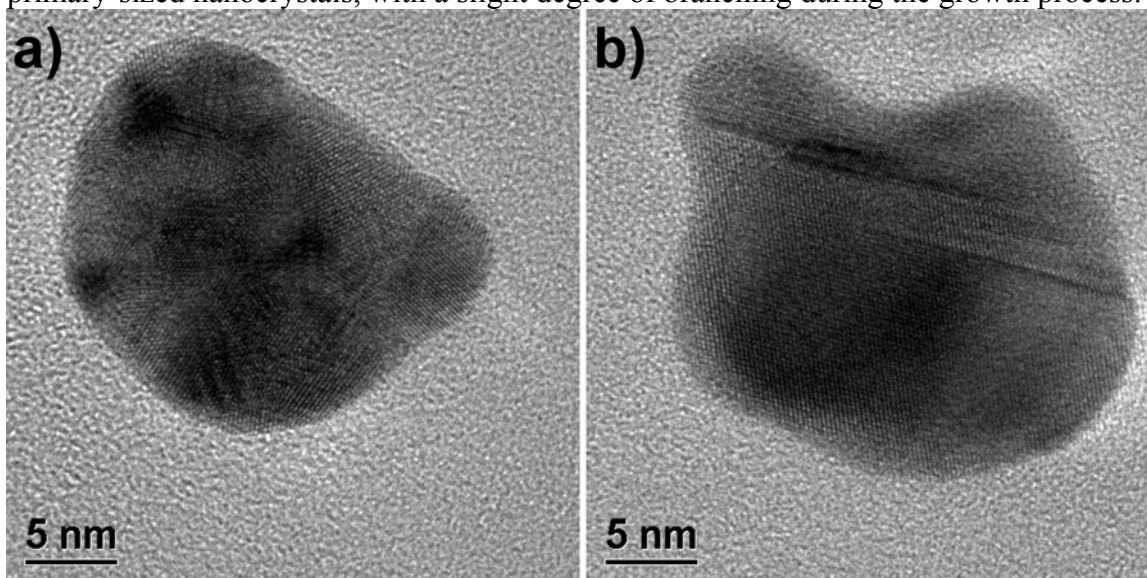


Figure 6.13: (48:1) Au:BSA – 15–25 nm crystals with small pyramids emanating from a primary-sized nanocrystal.

(24:1) Au:BSA

The (24:1) Au:BSA system exhibited a size distribution of 45.00 ± 24.00 nm, and a reaction time of ~ 10 seconds. More than half of the product was composed of gold multipods with more clearly-defined shapes than those previously described in Figure 6.10. As seen in Figure 6.14, these multipods have branches that result from the preferential diffusional growth of specific monocrystalline domains on a primary-sized nanocrystal. Nearly 30% of the product consisted of polycrystalline aggregates such as those in Figure 6.12, with sizes ranging from 60 nm to in excess of 100 nm. Finally, $\sim 20\%$ of the product consisted of nanocrystals with small, rounded pyramids, as previously demonstrated in Figure 6.13.

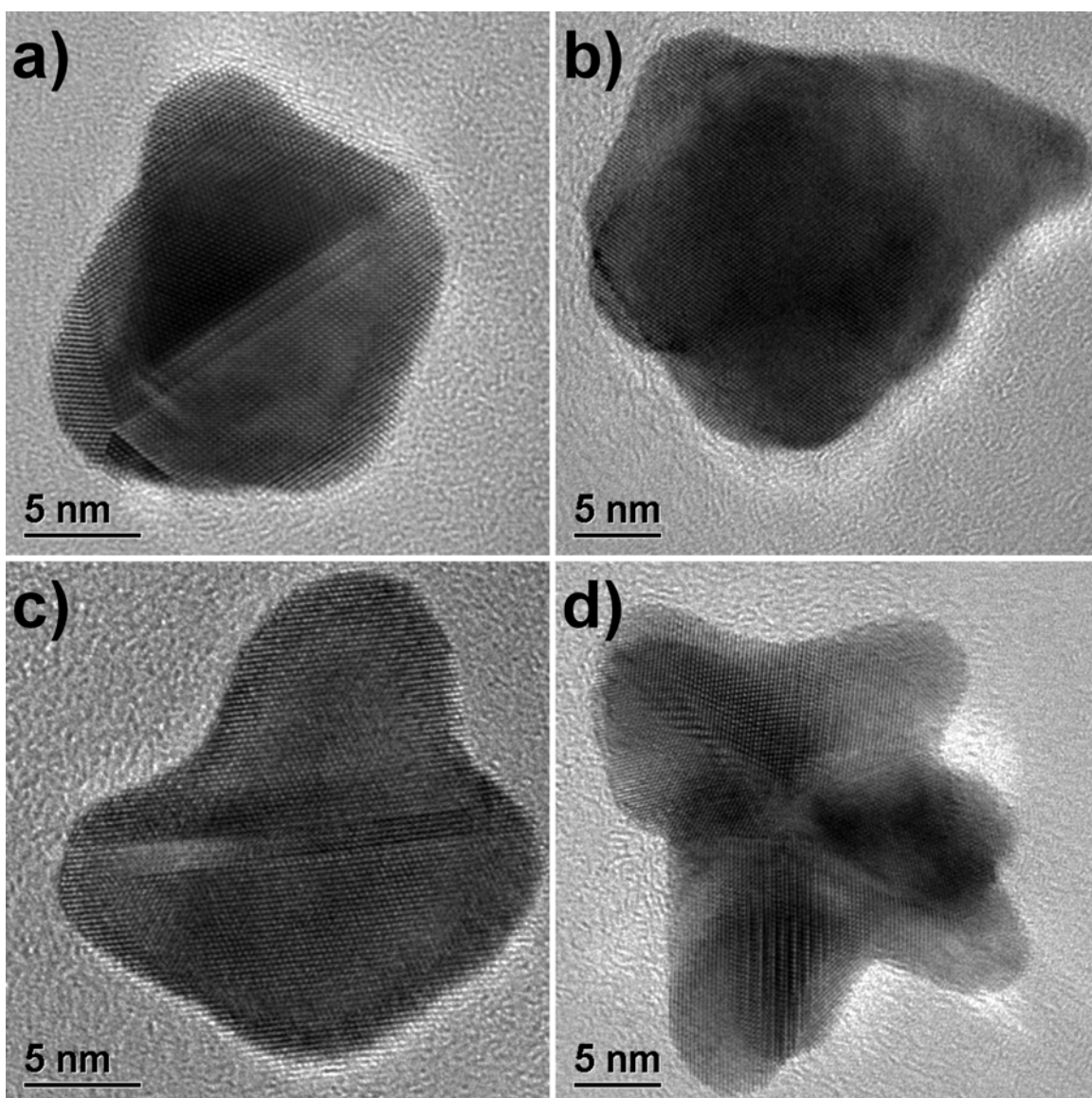


Figure 6.14: (24:1) Au:BSA –multipods with branches emanating from a common core.

(12:1) Au:BSA

The (12:1) Au:BSA system exhibited a size distribution of 21.90 ± 8.85 nm, and a reaction time of ~ 50 seconds. Over 70% of the sample was within the size range of 15–40 nm, consisting primarily of gold tripods (Figure 6.15a-b). Multipods with higher degrees of branching were also observed (Figure 6.15c-d).

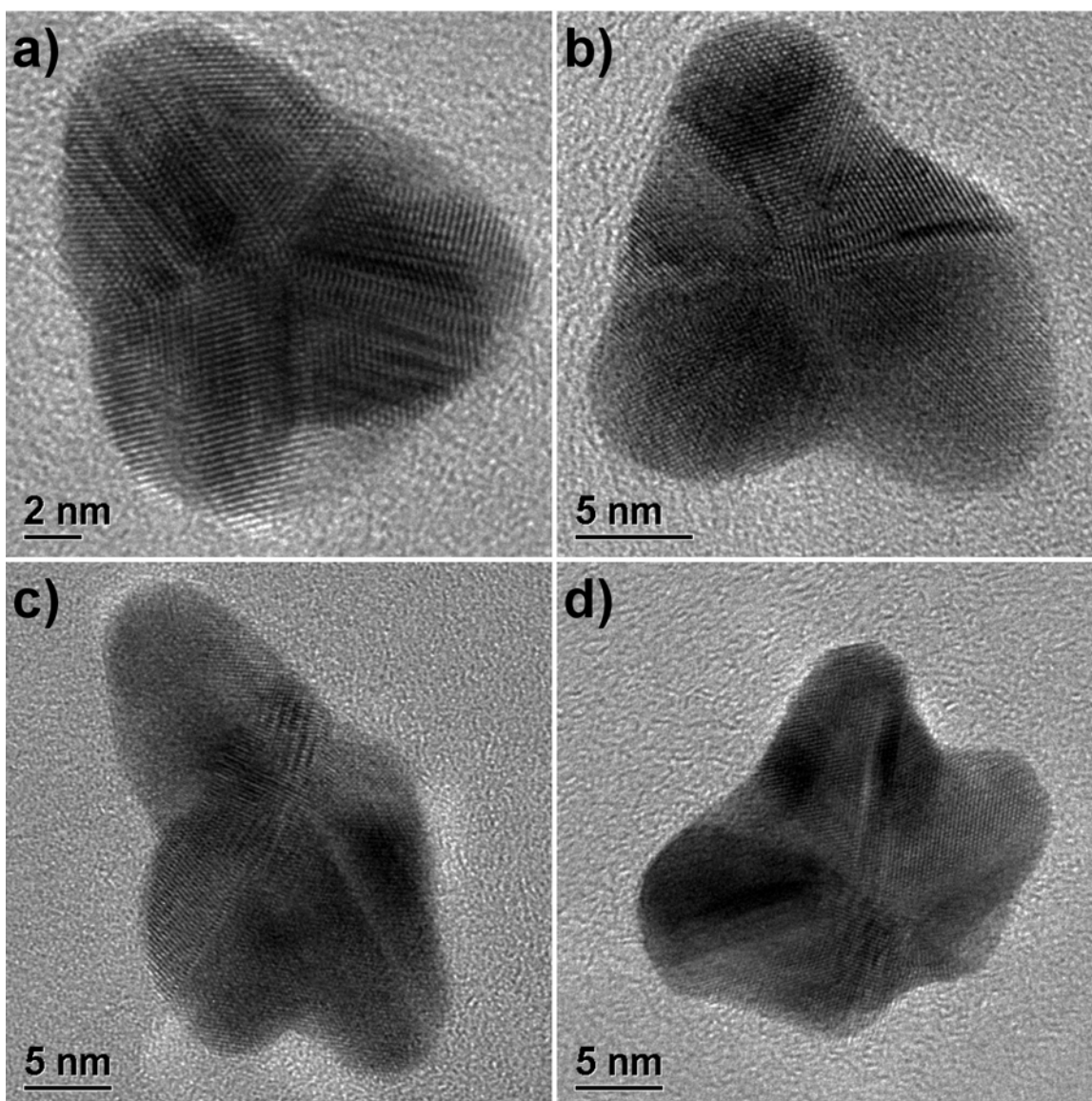


Figure 6.15: (12:1) Au:BSA – multipods. (a)-(b) tripods; (c) tetrapod; (d) pentapod.

Two distinct classes of elongated nanocrystals were identified. The first type exhibited twinning planes parallel to the direction of elongation, with lengths ranging from 20–40 nm (Figure 6.16). The second type of elongated crystals resulted from pentagonal primary-sized nanocrystals, with preferential diffusional growth of specific

monocrystalline domains (Figure 6.17). These crystals exhibited less elongation, with typical lengths ranging from 15–25 nm.

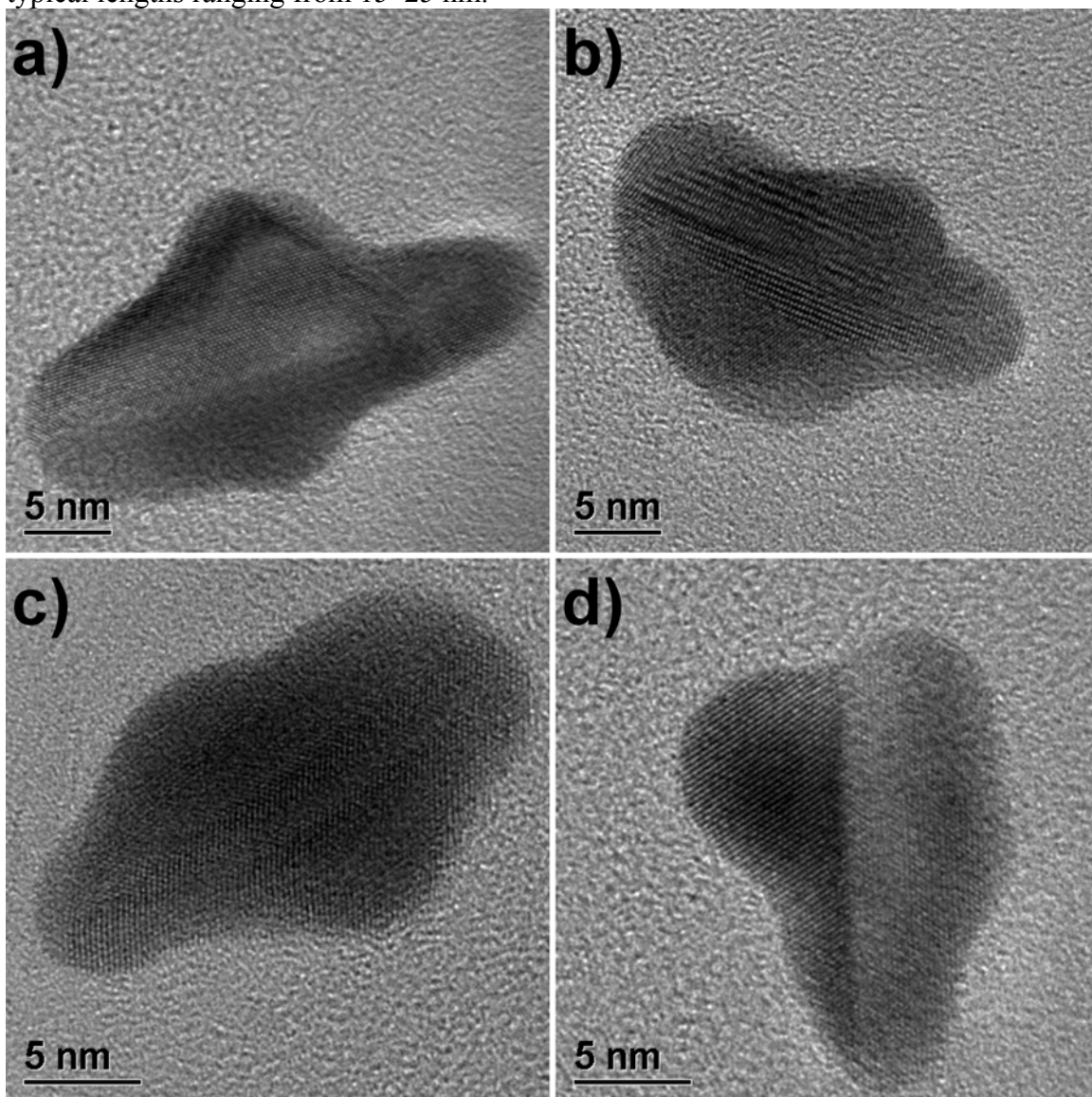


Figure 6.16: (12:1) Au:BSA – elongated crystals, with twinning planes parallel to the direction of elongation.

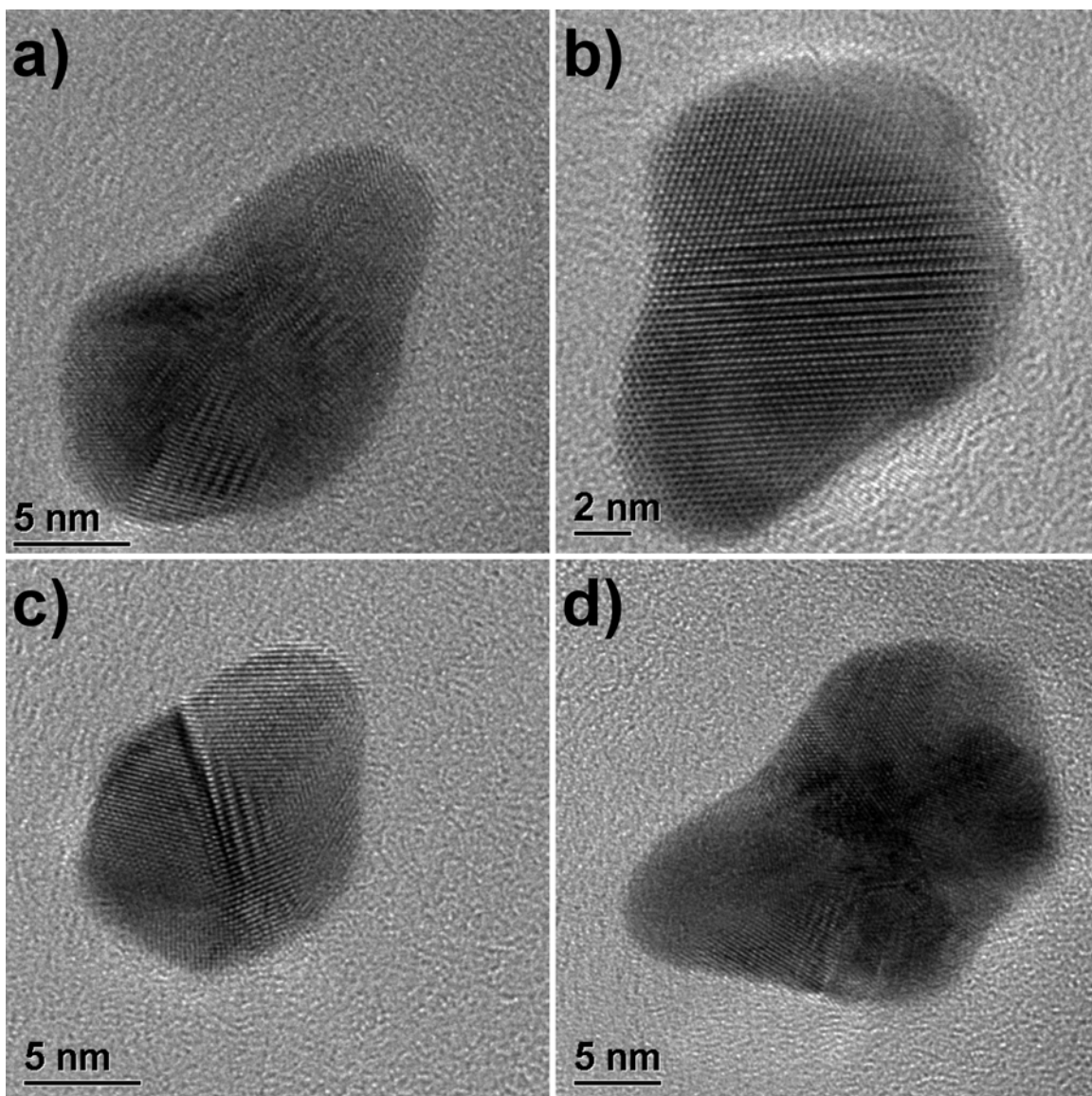


Figure 6.17: (12:1) Au:BSA – elongated crystals, resulting from pentagonal primary-sized nanocrystals with preferential diffusional growth of one or more monocrystalline domains.

In the smaller range of the distribution, ~20% of the (12:1) Au:BSA sample consisted of concave nanocrystals with nearly-rounded morphologies, and sizes of 10–25 nm, as seen in Figure 6.18. These smaller nanocrystals clearly result from the diffusional growth of individual primary-sized nanocrystals.

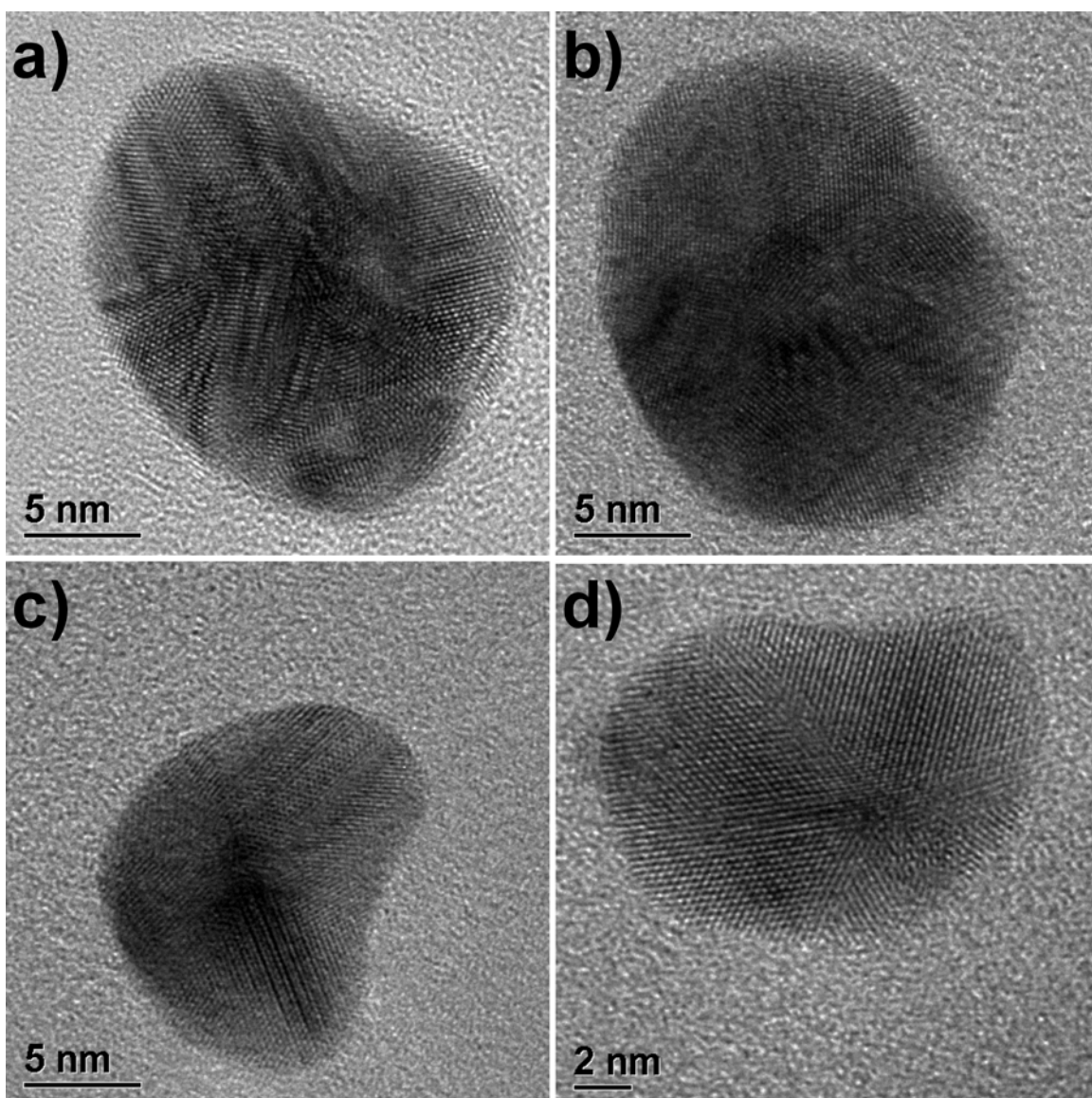


Figure 6.18: (12:1) Au:BSA – concave nanocrystals with sizes ranging from 10–25 nm.

Less than 5% of the (12:1) Au:BSA sample was composed of crystals larger than 40 nm in diameter (Figure 6.19). Interestingly, this largest fraction of crystals did not consist of polycrystalline aggregates as was observed in previous systems, but rather consisted of large concave crystals resulting from the diffusional growth of individual primary-sized nanocrystals. The overall shape of these crystals became increasingly

irregular with progressively greater degrees of internal twinning, as can be seen on comparison with Figure 6.19a and Figure 6.19c.

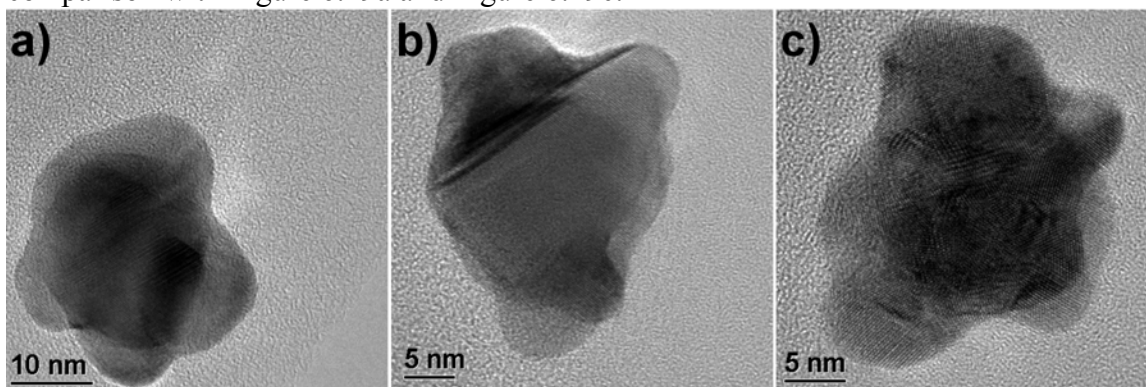


Figure 6.19: (12:1) Au:BSA – concave nanocrystals with sizes ranging from 40–55 nm.

(6:1) Au:BSA

The (6:1) Au:BSA system exhibited a size distribution of 19.92 ± 6.66 nm, and a reaction time of ~30 minutes. Nearly 80% of the sample was in the range of 10–30 nm, with the morphologies in this range evenly divided among elongated crystals, multipods, and concave nearly-rounded nanocrystals. The elongated nanocrystals were smaller than those encountered in the (12:1) Au:BSA system, with lengths ranging from 10–20 nm (Figure 6.20). Crystals with twin planes parallel to the direction of elongation (Figure 6.20a and d), and pentagonal crystals with preferential growth of specific monocrystalline domains (Figure 6.20b) were identified. Figure 6.20c presents an elongated crystal with no apparent twinning. However, it is likely that a twin plane is present along the length of the crystal, but invisible to the electron beam due to specimen tilt. (106) Figure 6.20d presents a gold nanorod with pentagonal cross-section. This is a stable morphology for elongated nanocrystals, commonly observed in nanorods of FCC-type metals. (70)

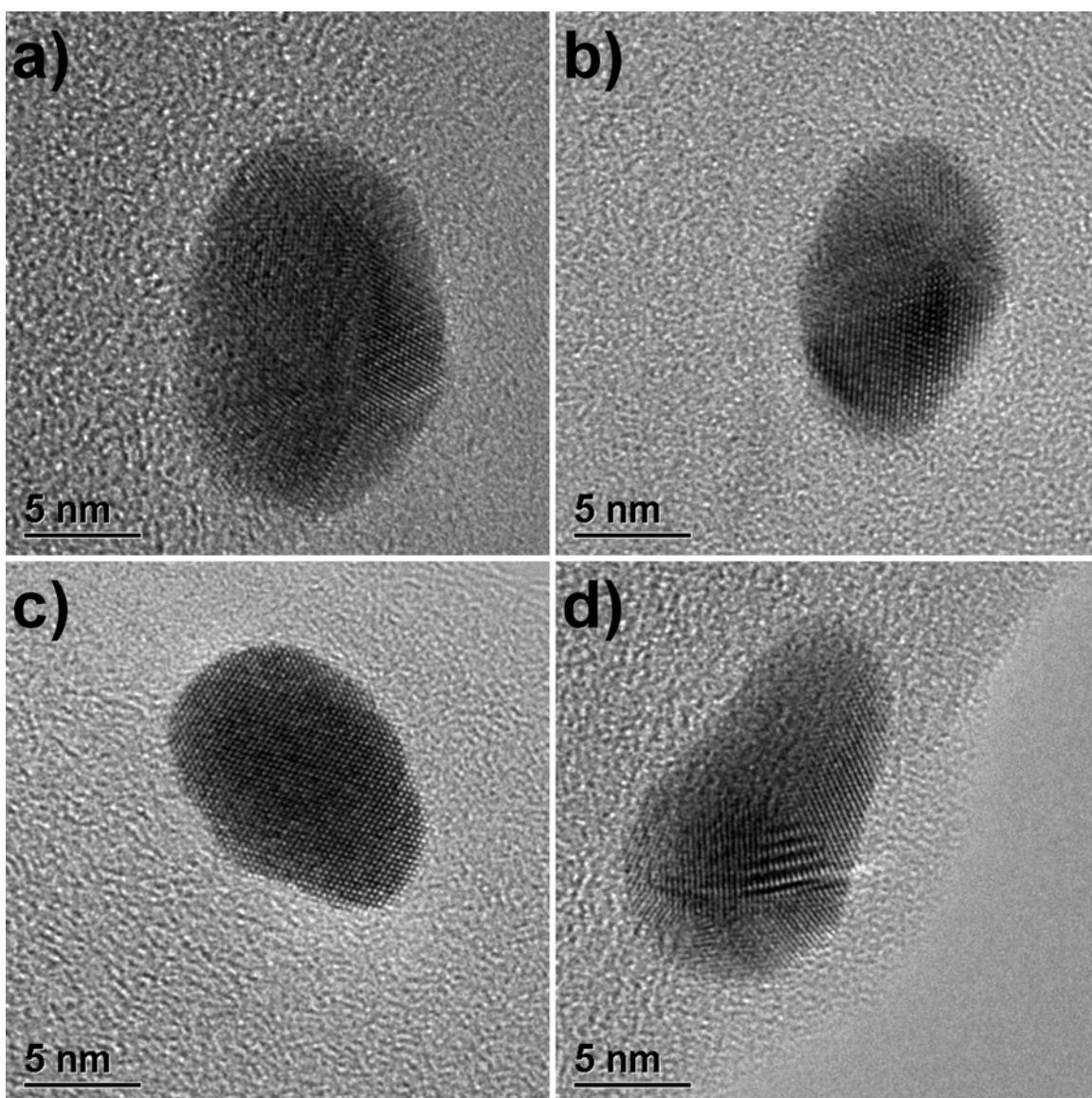


Figure 6.20: (6:1) Au:BSA – elongated crystals with lengths ranging from 10–20 nm.

The multipod nanocrystals in the (6:1) Au:BSA system ranged from 15–30 nm in length. These crystals commonly exhibited four distinct domains, some with varying degrees of branching, in a two-dimensional plane (Figure 6.21). Concave nanocrystals with nearly-rounded morphologies and with sizes ranging from 10–20 nm were also

found, as in Figure 6.22. These smaller crystals result from the diffusional growth of individual primary-sized nanocrystals.

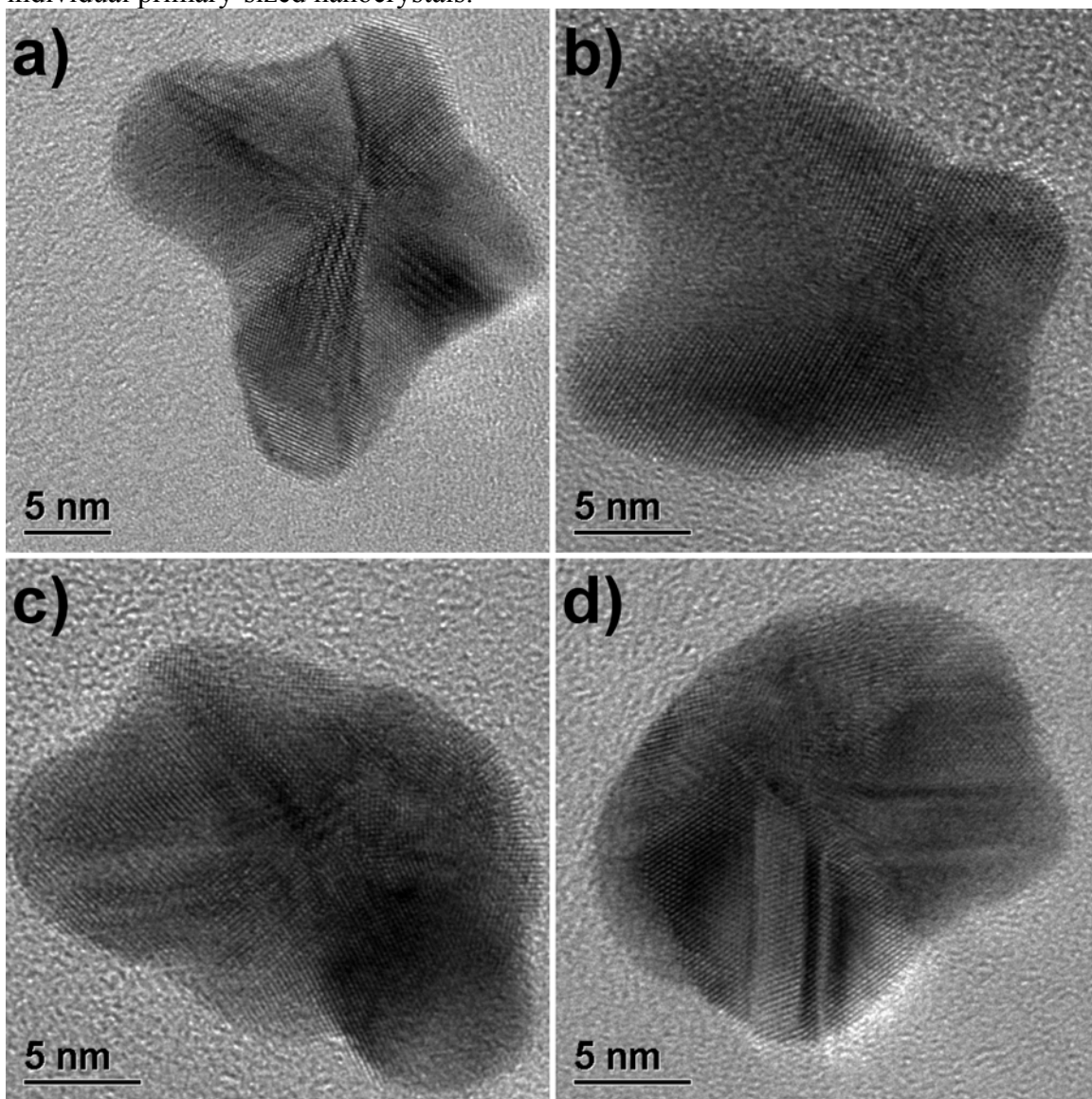


Figure 6.21: (6:1) Au:BSA – planar multipods with dimensions ranging from 15–30 nm.

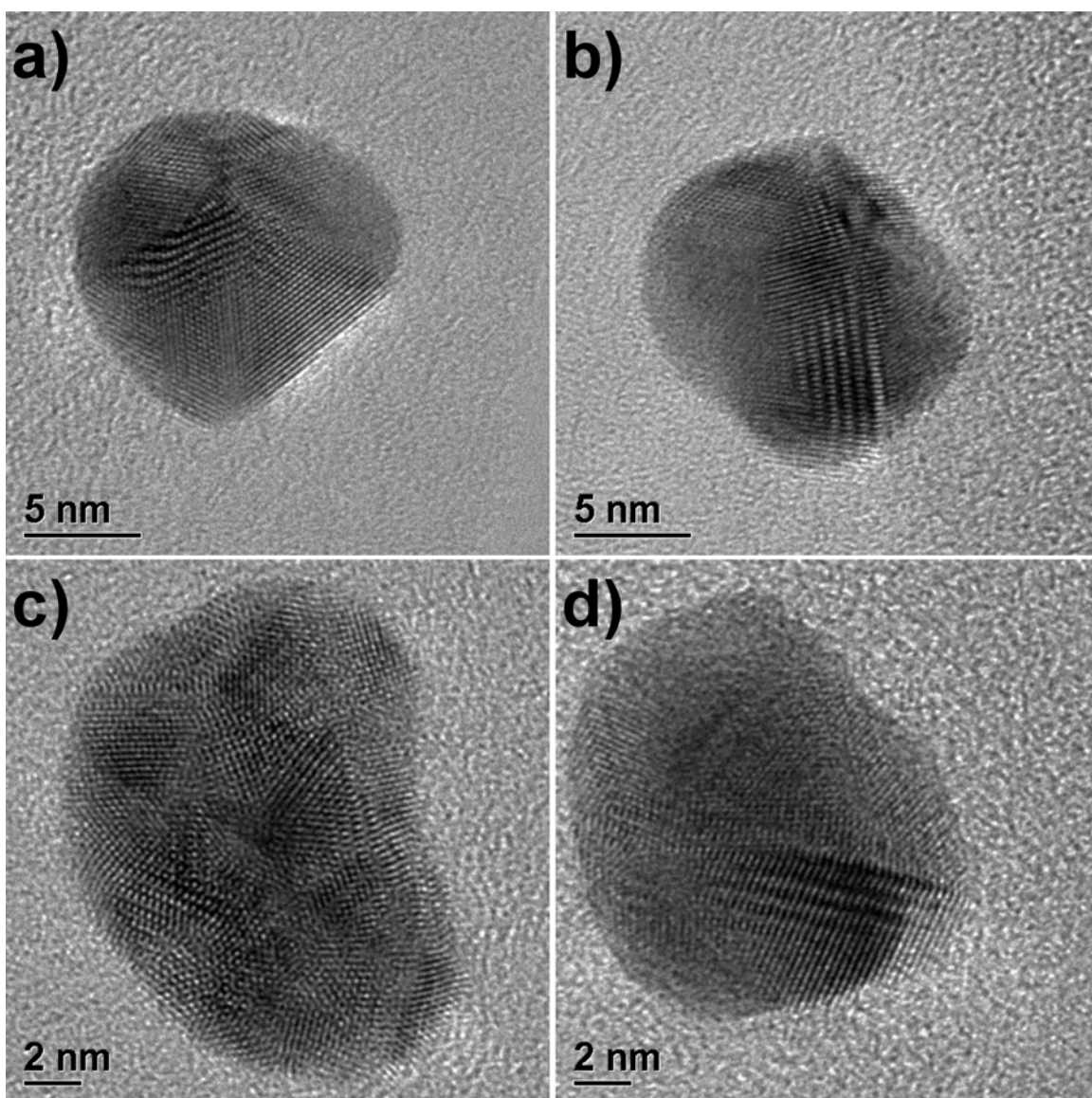


Figure 6.22: (6:1) Au:BSA – concave nanocrystals with sizes ranging from 10–20 nm.

At the larger end of the distribution, about 10% of the (6:1) Au:BSA sample was composed of crystals in the range of 30–40 nm that resulted from diffusional growth, as shown previously in Figure 6.19. Finally, at the smaller end of the distribution, about 10% of the sample consisted of rounded, convex gold nanocrystals with sizes in the range of 5–15 nm (Figure 6.23). The majority of these crystals exhibited multiple-twinned

pentagonal morphologies, including rounded decahedra (Figure 6.23a) and icosahedra (Figure 6.23b-d).

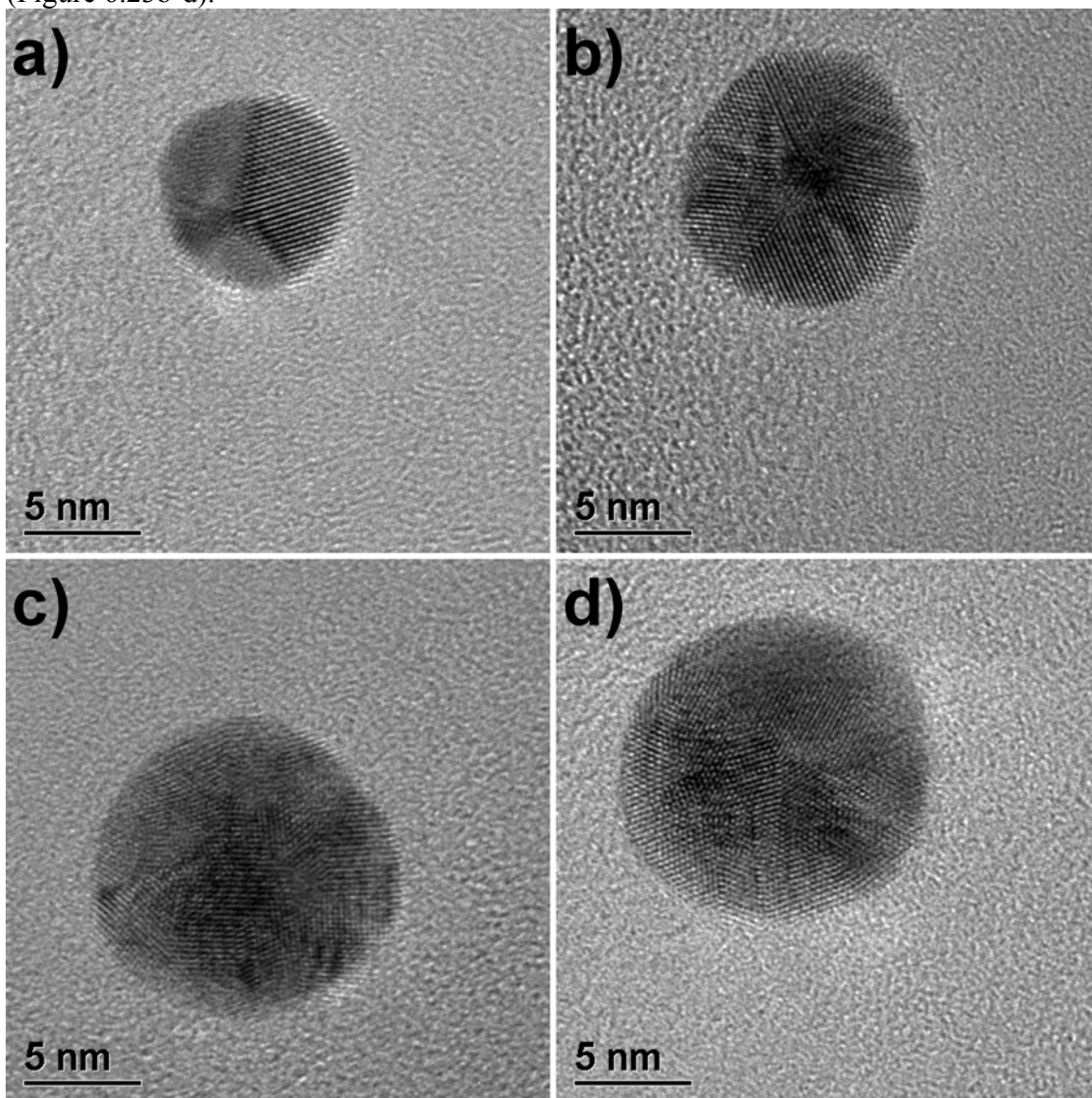


Figure 6.23: (6:1) Au:BSA – rounded convex crystals with sizes ranging from 5–15 nm.

(9:2) Au:BSA

To obtain a data point at longer reaction times for Figure 6.6, we attempted a synthesis at (3:1) Au:BSA, but no reaction was observed after 48 hours, as confirmed by

the complete reduction of gold upon subsequent addition of sodium borohydride. Thus, we attempted another reaction at (9:2) Au:BSA. In this case, the observed reaction time was ~5 hours, compared with ~30 minutes for the (6:1) Au:BSA system. Furthermore, the measured size distribution and UV-visible absorption spectrum for (9:2) Au:BSA were nearly identical to the (6:1) Au:BSA case, so no notable advantage was gained from a reaction that took 10 times longer to complete.

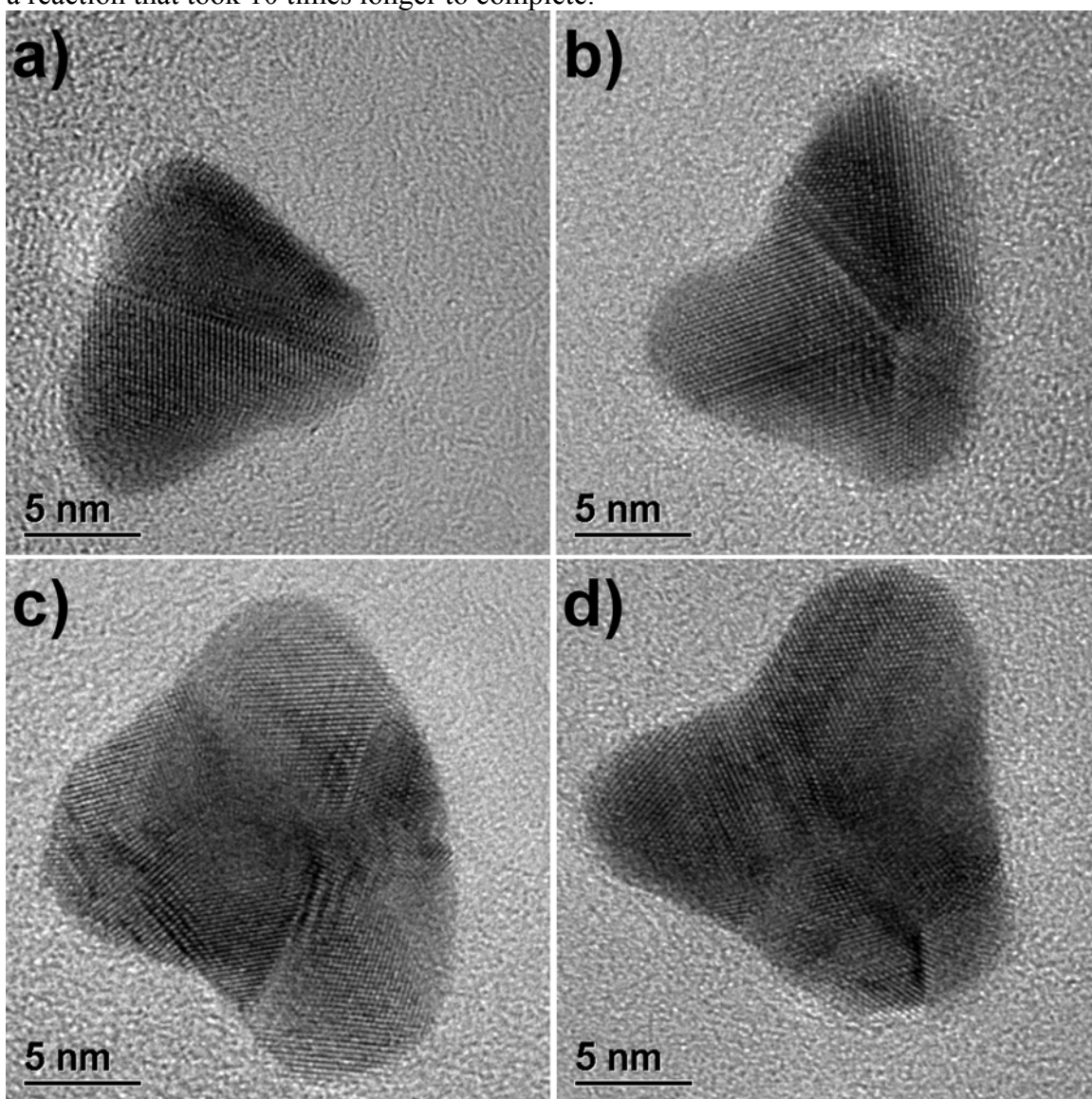


Figure 6.24: (9:2) Au:BSA – gold tripods with dimensions of 15–25 nm.

However, a slight difference in the distribution of product morphologies was noted. Fully 30% of the (9:2) Au:BSA product was composed of tripods, ranging in size from 15–25 nm (Figure 6.24). Nearly 25% of the product consisted of elongated nanocrystals, with lengths ranging from 10–20 nm (Figure 6.25). All elongated crystals observed in this system resulted from pentagonal crystals with preferential growth of specific monocrystalline domains.

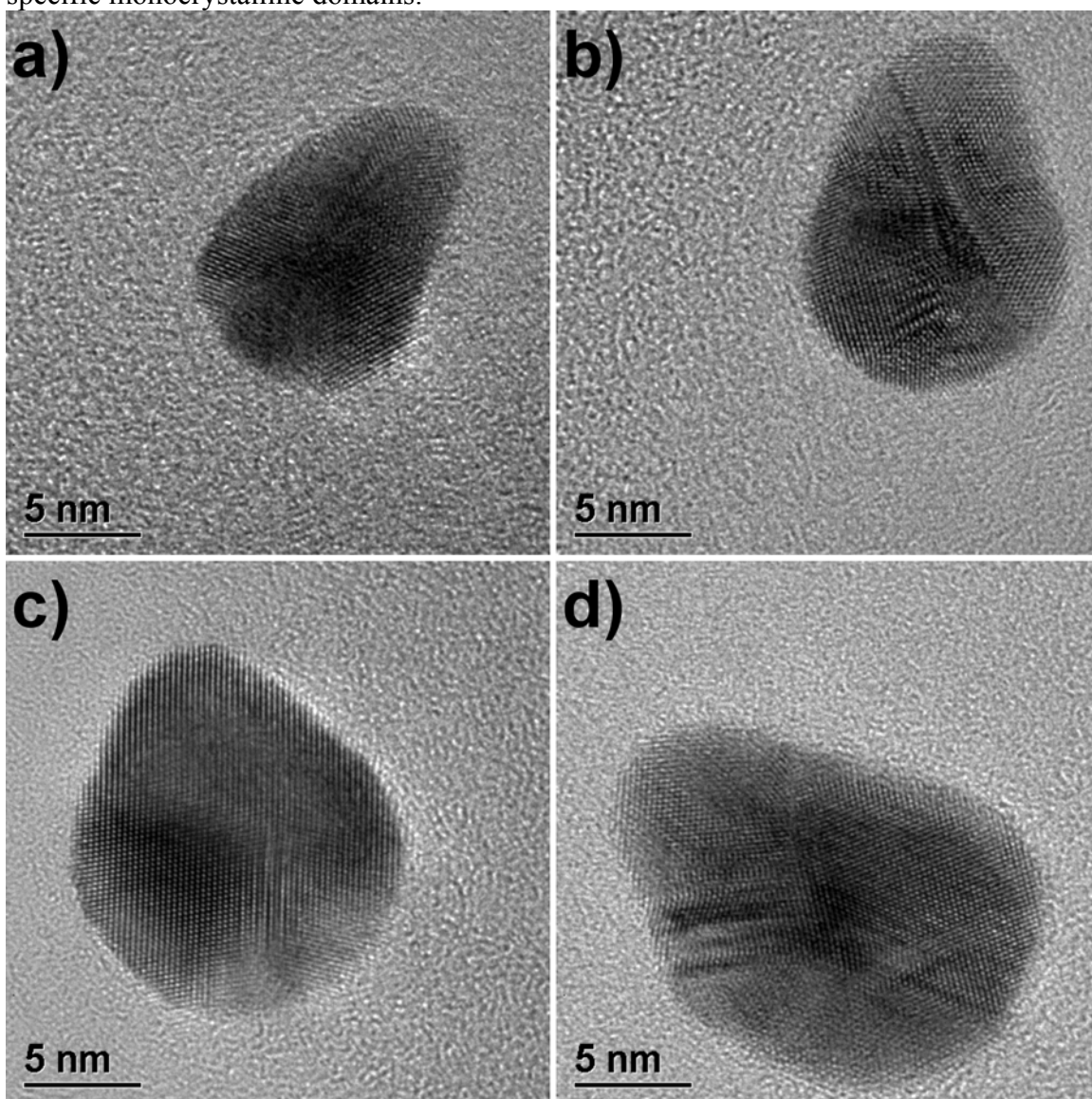


Figure 6.25: (9:2) Au:BSA – elongated crystals with lengths ranging from of 10–20 nm.

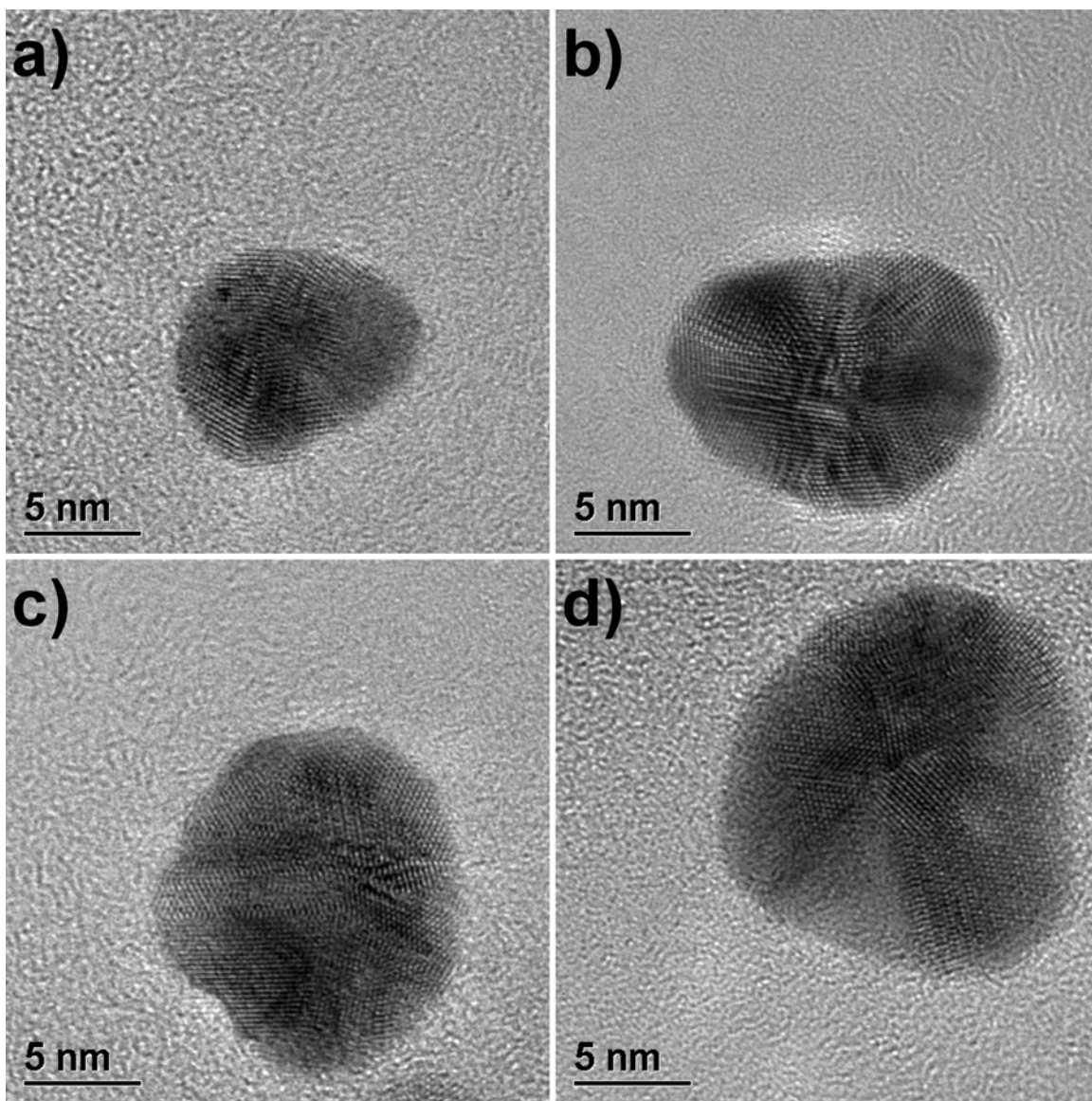


Figure 6.26: (9:2) Au:BSA – concave nanocrystals with sizes ranging from 10–15 nm.

Another 25% of the product consisted of concave nanocrystals with nearly-rounded morphologies and sizes ranging from 10–15 nm (Figure 6.26). At the larger end of the distribution, about 5% of the (9:2) Au:BSA sample was composed of crystals in the range of 20–30 nm that resulted from diffusional growth (Figure 6.27). These larger

crystals clearly exhibited twinned structures, including cyclic twinning (Figure 6.27a-b), single twinning (Figure 6.27c-d), or parallel twinning (6.27e-f).

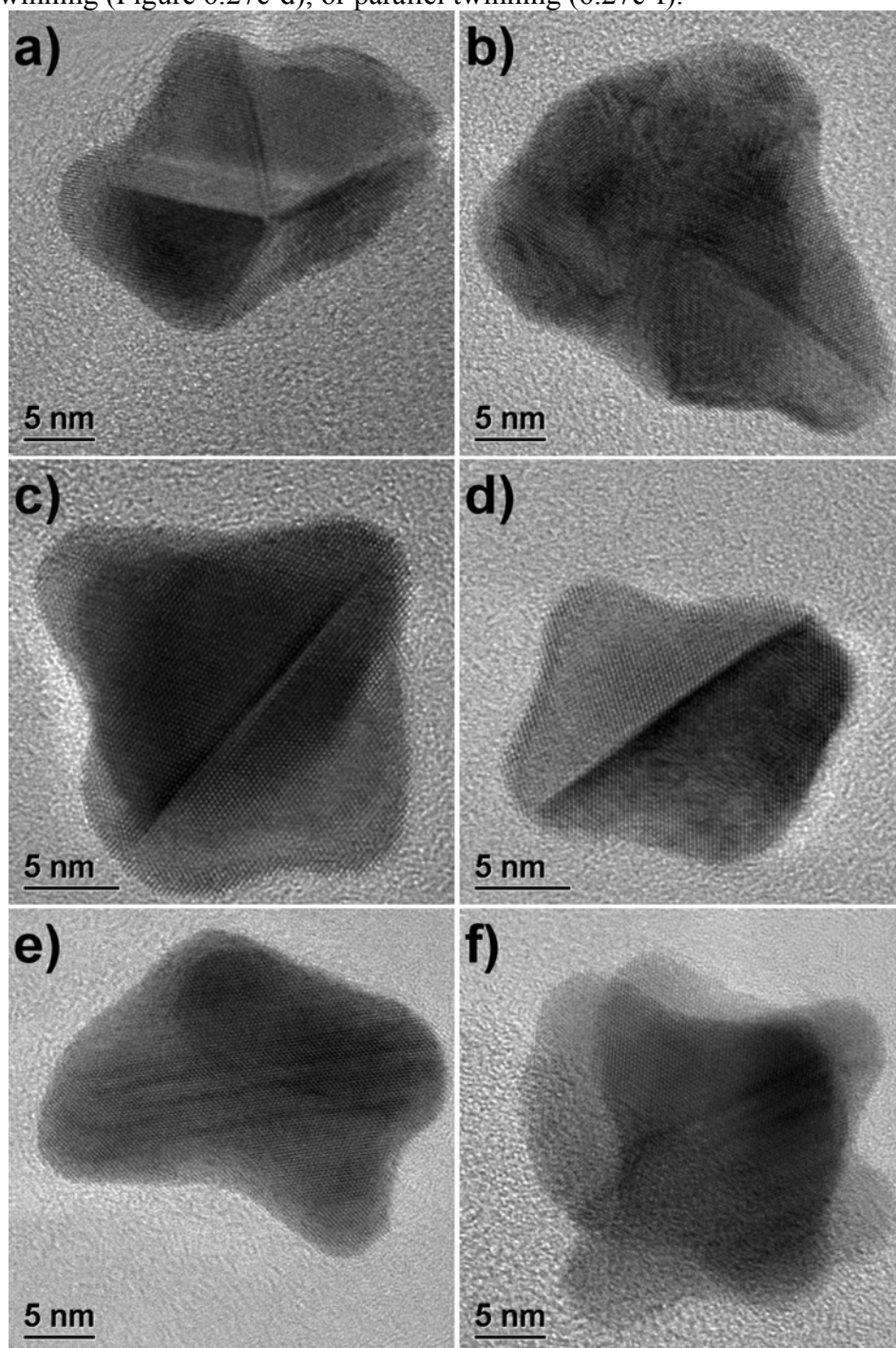


Figure 6.27: (9:2) Au:BSA – concave nanocrystals with sizes ranging from 20–30 nm.

Finally, at the smaller end of the distribution, about 15% of the (9:2) Au:BSA system was composed of rounded, convex gold nanocrystals with sizes in the range of 5–10 nm (Figure 6.28). Compared with the convex crystals from the (6:1) Au:BSA, these crystals were slightly smaller in size, but showed a broader variability in crystal structure.

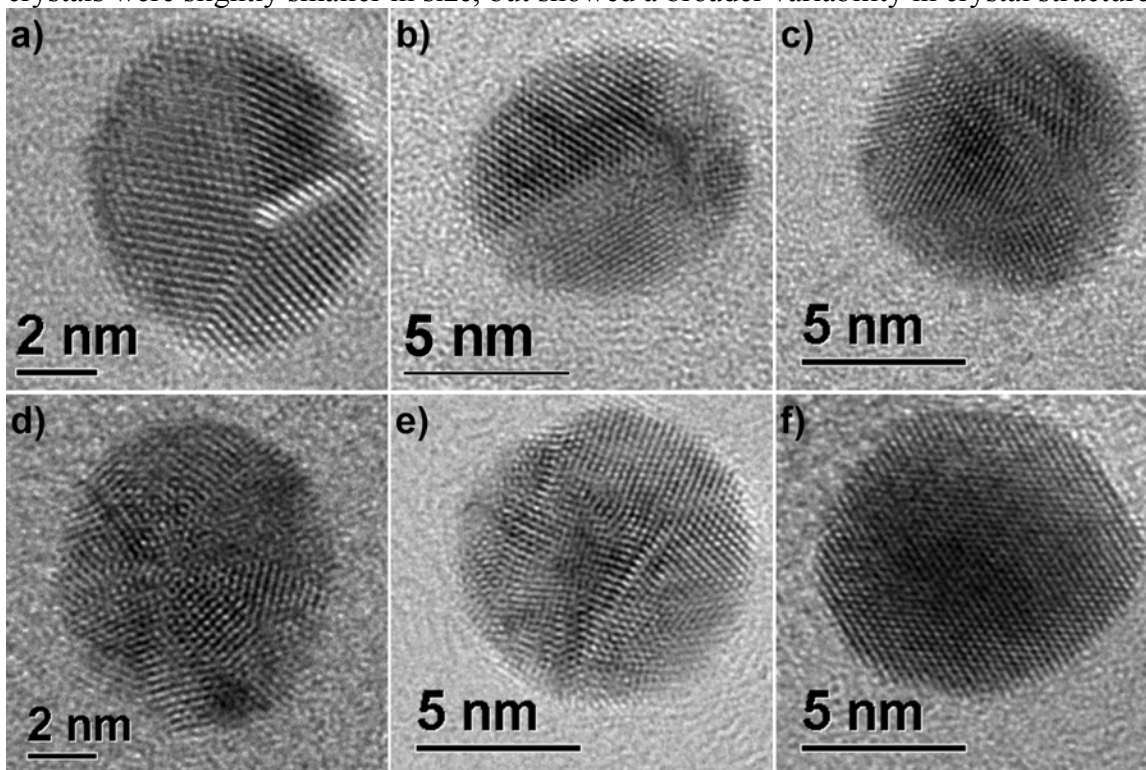


Figure 6.28: (9:2) Au:BSA – rounded convex crystals with sizes ranging from 5–10 nm.

6.4 CONCLUSIONS

In summary, I have described a modification of the aqueous-based synthesis approach described in Chapters 3 and 4, where ascorbic acid is substituted in place of sodium borohydride as reducing agent. In terms of size, gold nanocrystals produced by reduction with ascorbic acid are an order of magnitude larger than the ~2 nm nanocrystals documented in Chapters 3 and 4. With molar ratios less than (32:1) [ascorbic acid molecules]:[gold atoms], the growth of primary-sized nanocrystals is aggregation-driven.

The final product consists predominantly of gold polycrystalline aggregates, and the size of the crystals is a strong function of the ascorbic acid concentration, with greater excesses of ascorbic acid favoring smaller crystals.

For molar ratios greater than (40:1) [ascorbic acid molecules]:[gold atoms], increasing the ascorbic acid concentration has a negligible effect on the reaction. Under these conditions, reaction time exhibited an exponential dependence on the concentration of BSA. At the highest protein concentrations studied, aggregation-driven growth was avoided, and the morphologies observed all resulted from diffusional growth of primary-sized nanocrystals.

In terms of obtaining 2–5 nm nanocrystals with well-controlled morphologies, this technique in its current embodiment is a poor choice. One particularly perplexing aspect of this synthesis is the substantial presence of multiply-branched gold nanocrystals. Such crystals were not obtained in any other synthesis method described to this point. More insight must be obtained into the formation of gold nanocrystals in the presence of ascorbic acid, without additional complications from interactions with protein molecules. If the growth of branched gold nanocrystals in the presence of ascorbic acid can be more thoroughly understood, it is possible this method can be refined in the future.

Chapter 7: Aqueous Synthesis of Star Polyhedral Gold Nanocrystals via Reduction with Ascorbic Acid

7.1 INTRODUCTION

Philosophers, mathematicians, and artists have long been fascinated by regular polyhedra, and their aesthetically pleasing symmetry appeals to the academician and layman alike. The classical Greeks deduced the existence of five regular convex polyhedra (the Platonic solids), which philosophers intimately associated with the four elements and the cosmos. (150) The tetrahedron (Figure 7.1a), being the primal regular polyhedron, was associated with fire, the primal element present at the creation of the universe. The hexahedron (Figure 7.1b), with four corners on each face and its inherent stability, was associated with the stability and four corners of the earth. If a vertex is located at the center of each of the eight faces of an octahedron (Figure 7.1c), a hexahedron can be constructed within an octahedron. Each vertex of the octahedron forms a tent over each face of this interior hexahedron, much in the same way that the sky forms a tent over the surface of the earth, and so the octahedron was associated with air. The twelve faces of the dodecahedron (Figure 7.1d) were linked with the twelve signs of the zodiac, and their pentagram shape held mystical connotations. Thus, the dodecahedron was associated with the cosmos. Finally, the icosahedron (Figure 7.1e) with its twenty faces tends to roll down an inclined surface, while the other Platonic solids tend to slide. This was taken as a sign of fluidity, and the icosahedron was associated with water.

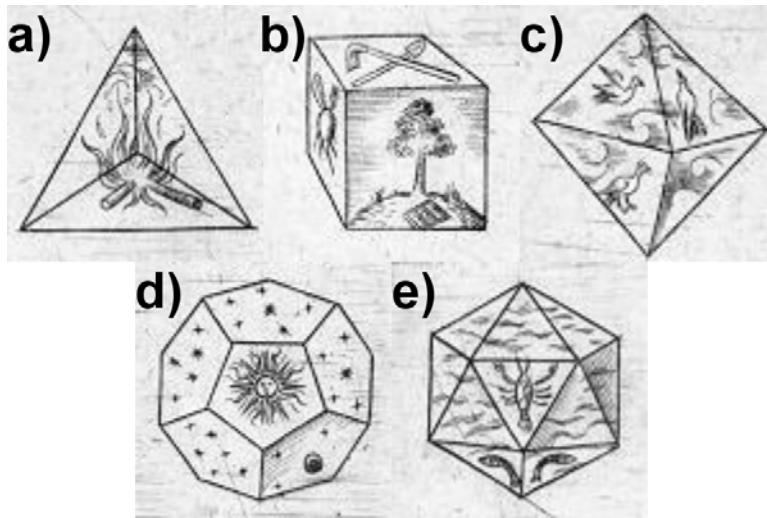


Figure 7.1: The five Platonic solids, as depicted by Johannes Kepler along with their philosophical connotations.

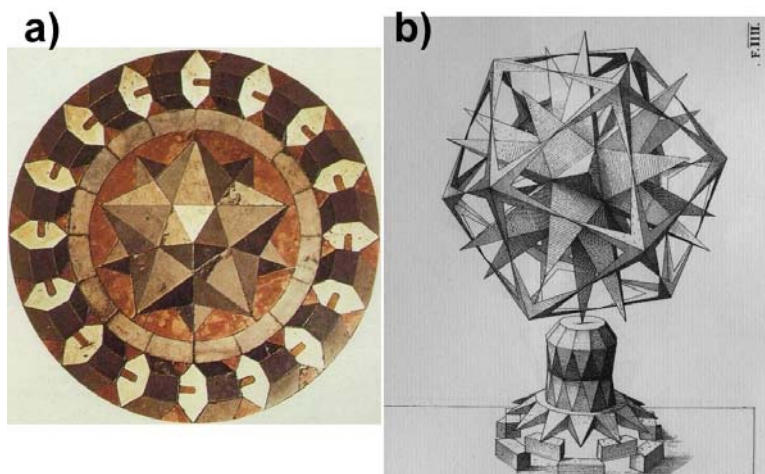


Figure 7.2: Artistic renditions of regular star polyhedra. (a) Small stellated dodecahedron as a marble inlay prepared by Paolo Uccello (Basilica San Marco, Venice). (b) Great stellated dodecahedron, in a conceptual drawing by Wentzel Jamnitzer.

The discovery of regular star polyhedra (the Kepler-Poinsot solids) dates from the Renaissance. Interestingly, regular star polyhedra were first envisioned by artists who embellished their renderings of the Platonic solids by replacing their surfaces with

pyramids. For example, a marble inlay of the small stellated dodecahedron is found in the floor of St. Mark's Basilica in Venice, and is attributed to Paolo Uccello, a fifteenth-century artisan (Figure 7.2a). The German artist Wentzel Jamnitzer produced a conceptual drawing of the great stellated dodecahedron in his *Perspectiva Corporum Regularium*, published in 1568 (Figure 7.2b).

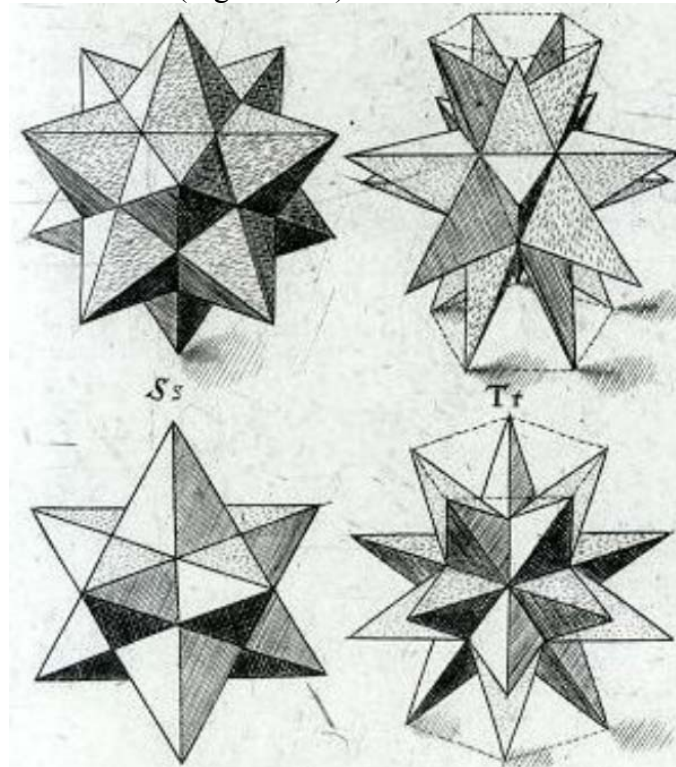


Figure 7.3: The small stellated dodecahedron (left) and great stellated dodecahedron (right), each depicted by Johannes Kepler in two different perspectives.

It was more than fifty years later when the small and great stellated dodecahedra were recognized as regular concave polyhedra from a mathematical standpoint, when Johannes Kepler described them in his landmark work *Harmonices Mundi*, published in 1619 (Figure 7.3). The dual structures of the small and great stellated dodecahedra were subsequently described by Louis Poincaré in 1810. (150)

Polyhedral crystals are also a prized pursuit in the world of nanoscience, both from an intellectual and a practical standpoint. Metallic nanostructures exhibit unique properties and are of interest in a wide range of applications including catalysis, electronics, and sensors. (32,7) The morphology of a nanocrystal strongly influences its electromagnetic, optical, and physicochemical properties, (151) and new strategies for growing nanocrystals of various shapes are continually being developed. Many promising applications will require nanostructures to be incorporated into micron-scale networks, such as electronic circuits and sensing devices, so the availability of nanostructures with specific shapes will be crucial. In this context, branched nanostructures are highly desired, and great progress has been made in the synthesis of branched semiconductor nanocrystals. (152–154)

Recently, the first branched gold nanostructures have been reported. (155,156) The synthesis methods employed were derived from the seed-mediated growth technique that has been used extensively for the production of gold nanorods. (158-160) Briefly, gold ionic salt is reduced with a weak reducing agent (typically ascorbic acid) in the presence of seed crystals, and of surfactant molecules that promote growth in a specific crystallographic direction. The morphology of the resulting crystals depends on (i) the size, shape (i.e. decahedral, icosahedral, or triangular), and type (i.e. gold or silver) of seed crystals used; (ii) the relative concentrations of seed crystals, ionic salt, and surfactant molecules; (iii) the presence of additional ions, such as sodium hydroxide or silver nitrate; and (iv) the number and duration of incubation steps.

Due to the complexity of this method, it has not been possible to discern which of the several variables involved are critical for inducing the formation of branched gold nanocrystals. In the case of semiconductor tetrapod nanocrystals, it is proposed that polytypism, or the presence of multiple crystal structures in different domains of a

crystal, facilitates the formation of branched nanostructures. (153) Polytypism exists for open, tetrahedrally bonded structures such as semiconductors, but branched gold nanocrystals possess an FCC structure, so polytypism is not involved. To date, the exact growth mechanism for branched gold nanostructures remains elusive.

We have discovered that branched gold nanocrystals can be obtained without the use of seed crystals, surfactant molecules, or successive incubation steps. Herein we report star polyhedral gold nanocrystals, synthesized by colloidal reduction with ascorbic acid in water at ambient conditions. We have identified two distinct types of star polyhedral nanocrystals, corresponding to icosahedra and cuboctahedra with preferential growth of their exposed $\{111\}$ surfaces. Specifically, the $\{111\}$ faces of the original Archimedean solids grow into tetrahedral pyramids, with the base of each pyramid being the original polyhedral face. Interestingly, icosahedrally-derived star nanocrystals possess a geometric morphology closely resembling the great stellated dodecahedron, a Kepler-Poinsot solid. Our straightforward approach has provided new insights into the fundamental process of branched gold nanocrystal formation³.

7.2 EXPERIMENTAL PROCEDURE

Synthesis. Star polyhedral gold nanocrystals were synthesized in air by colloidal reduction in a homogeneous solution at ambient conditions. Chloroauric acid trihydrate ($\text{HAuCl}_4 \cdot 3\text{H}_2\text{O}$; 99.9+%; Aldrich) was reduced in water by ascorbic acid (L-ascorbic acid; ACS reagent grade; Aldrich). An aqueous solution of ionic gold was prepared by adding 1 g $\text{HAuCl}_4 \cdot 3\text{H}_2\text{O}$ to 25 mL of deionized water. All materials were used without further treatment. In a typical experiment, 0.5 mL of 0.1M HAuCl_4 solution (50 μmol Au) was added rapidly and under vigorous stirring, to a 100 mL round bottom flask containing an aqueous solution with a 40-fold excess of ascorbic acid (2 mmol ascorbic

³ A large portion of this chapter has been published in *J. Crystal Growth* 285, 681–691 (2005).

acid), bringing the total reaction volume to 40 mL. Hereafter, this synthesis technique will be referred to as the standard reaction protocol. Upon addition of chloroauric acid, the solution rapidly changed color, becoming an opaque orange-red within approximately 2 seconds. Although no subsequent changes in color were observed, the solution was left under vigorous stirring for fifteen minutes to ensure completion of the reaction.

Characterization. Transmission electron microscopy (TEM), selected area electron diffraction (SAED), and weak beam dark field (WBDF) analysis were performed using a JEOL 2010F TEM equipped with Schottky-type field emission gun, ultra-high resolution pole piece ($C_s = 0.5$ mm), and a scanning transmission electron microscope (STEM) unit with high angle annular dark field (HAADF) detector operating at 200 kV. Scanning electron microscopy (SEM) was initially performed with an FEI Strata DB235 dual beam SEM/FIB, and subsequently with a JEOL 7401F SEM.

HAADF images are formed by electrons that have undergone high angle scattering. The two primary factors that determine HAADF image contrast for our gold nanocrystals are specimen thickness and structural defects. As electrons travel through thicker regions of the specimen and interfere with more atoms, the probability for high angle scattering increases. Therefore, thicker regions generally have brighter contrast. On the other hand, in the vicinity of crystal defects, contrast results from inelastic dispersion that occurs when the electron beam encounters atoms that deviate from their ideal lattice positions. This is known as Huang-scattering contrast. (62,63)

For WBDF, a diffraction-contrast image is formed by tilting the sample out of the Bragg condition to increase inelastic scattering. Thickness fringes are produced due to interference between scattered and transmitted beams, and the width and separation of thickness fringes is directly related to the angle of incidence between the electron beam

and the sample. Thus, WBDF illustrates how thickness changes within the crystal. (56) In the vicinity of a defect, lattice distortions cause planes to be locally tilted back to the Bragg condition, so twin boundaries are clearly delineated.

UV-visible absorption spectra in the range of 300-1000 nm were obtained with a Varian Cary 5000 UV-vis NIR spectrometer. Samples for UV-Visible absorption analysis were prepared by diluting the original reaction product with deionized water (four-fold dilution by volume). Solution-phase analysis was performed at room temperature using a matched set of quartz cuvettes (path length 10 mm), and operating the spectrometer in dual beam mode. One cuvette was filled with the diluted reaction solution, while the second cuvette contained deionized water.

7.3 RESULTS AND DISCUSSION

7.3.1 Product Overview

Recall the initial motivation for pursuing this line of investigation was to gain insight into why a substantial number of multiply-branched gold nanocrystals were found in the syntheses described in Chapter 6. Since multiply-branched morphologies had not been observed for serum albumin-functionalized gold nanocrystals formed by reduction with glycerin (Chapter 2) or sodium borohydride (Chapters 3 and 4), we hypothesized that ascorbic acid was responsible for driving this branching phenomenon.

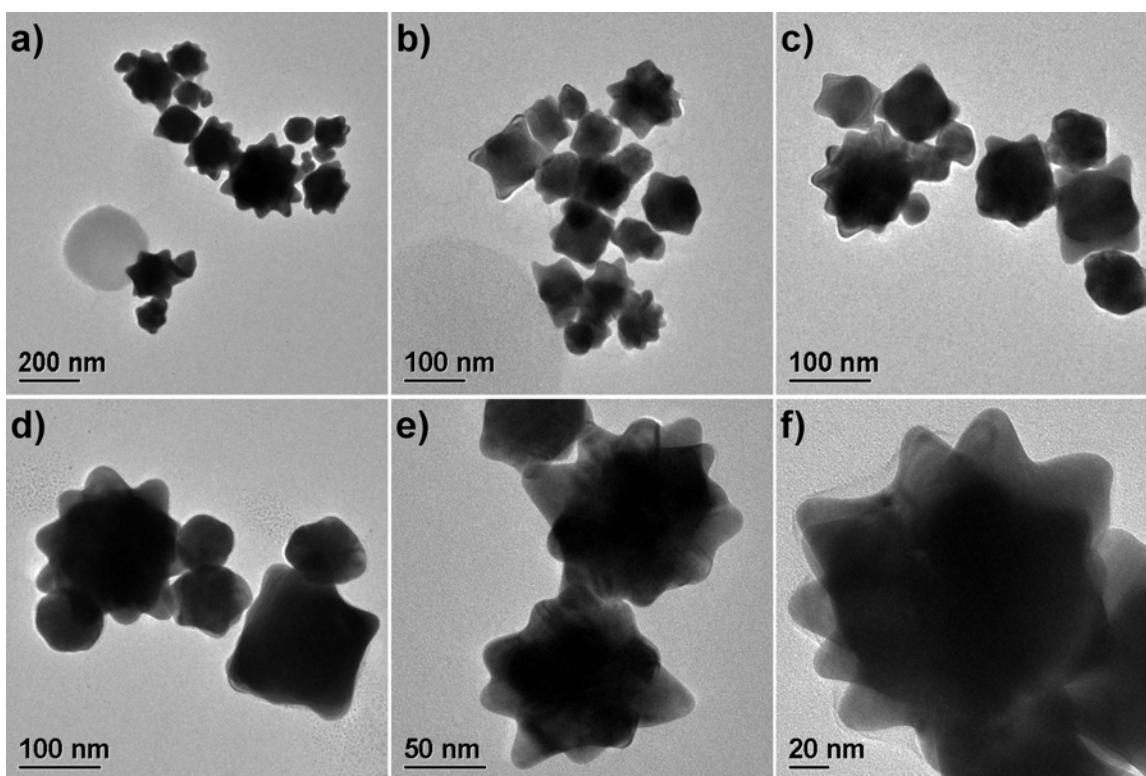


Figure 7.4: Initial TEM analysis of the as-synthesized product, formed in water at a molar ratio of (40:1) AA: Au, in the absence of any other chemical or molecular species.

We hoped to verify this hypothesis by studying the formation of gold nanocrystals in water by reduction with ascorbic acid, without additional complications from any other surface-protecting molecules. In Chapter 6, we found that for molar ratios greater than (40:1) [ascorbic acid molecules]:[gold atoms], increasing the ascorbic acid concentration had a negligible effect on the reaction, so we employed a molar ratio of (40:1) AA: Au in the present investigation. The same number of moles of ascorbic acid, gold, and water were employed as in Chapter 6, allowing for direct comparison of the two systems.

As clearly seen from Figure 7.4, one initial TEM analysis was all that was required to confirm our hypothesis. A number of multiply-branched gold nanocrystals were observed. Interestingly, several branched crystals exhibit a highly symmetric

spatial array of well-formed pyramids emanating from a central crystalline region. Figure 7.5a provides a representative low-magnification TEM image of the as-synthesized product. On average, 20% consists of rounded, multiple-twinned nanoparticles with indefinite shapes. Most of these particles are smaller than 50 nm, whereas the branched crystals range from 100–300 nm. When the branched crystals are allowed to precipitate by gravity, the smaller rounded particles remain in solution and are thus easily removed. Another 20% of the as-synthesized product consists of nanocrystals with one or more enlarged pyramids, but lacking a uniform dispersion of pyramids over the entire crystal surface. The appearance of these crystals often resembles an arrowhead. The remaining 60% of the as-synthesized product consists of star polyhedral gold nanocrystals, with 20% being multiple-twinned crystals with five-fold symmetry, and 40% being monocrystalline star polyhedra. As mentioned previously, the sizes of these crystals are in the range of 100–300 nm, but despite this broad variation, the geometric proportions of a given type of star nanocrystal are remarkably consistent from one crystal to another, regardless of size.

Figure 7.5b is an SEM image of a multiple-twinned star nanocrystal. A symmetric array of five pyramids is observed emerging in projection from the upper surface of the crystal, which confirms that the pyramids are three-dimensional features. Figure 7.5c-d are SEM images of monocrystalline star polyhedra. In Figure 7.5c, four in-plane pyramids oriented 90° from each other are observed. Additionally, two pyramids 90° from each other emerge from the upper surface of the crystal, in a plane orthogonal to that containing the other four visible pyramids. Figure 7.5d presents another monocrystalline star in an orientation which reveals a pyramid emerging from the lower surface of the crystal, also at 90° from its nearest neighbors. From these observations, and in combination with tilting sequences from TEM images, we conclude that

monocrystalline stars possess eight pyramids, two groups of four in-plane pyramids oriented 90° from each other, in two orthogonal planes.

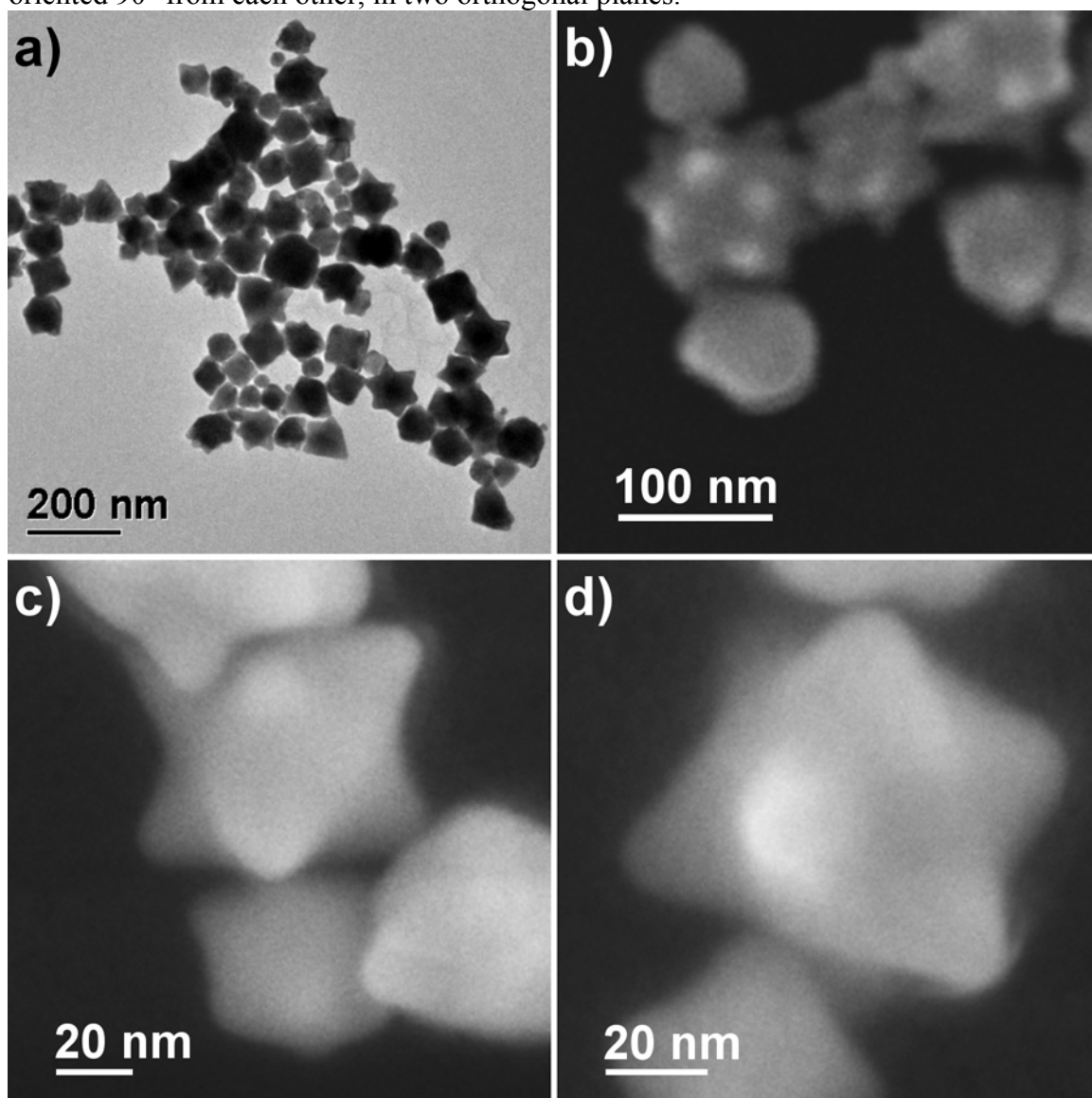


Figure 7.5: Star polyhedral gold nanocrystals. (a) Low-magnification TEM image of the as-synthesized product. (b) SEM image of a multiple-twinned star nanocrystal, revealing pyramids emerging around the perimeter of the crystal and from its upper surface. (c)-(d) SEM images of monocrystalline stars demonstrating the presence of eight pyramids, each oriented 90° from its nearest neighbors.

7.3.2 Proposed Structural Models

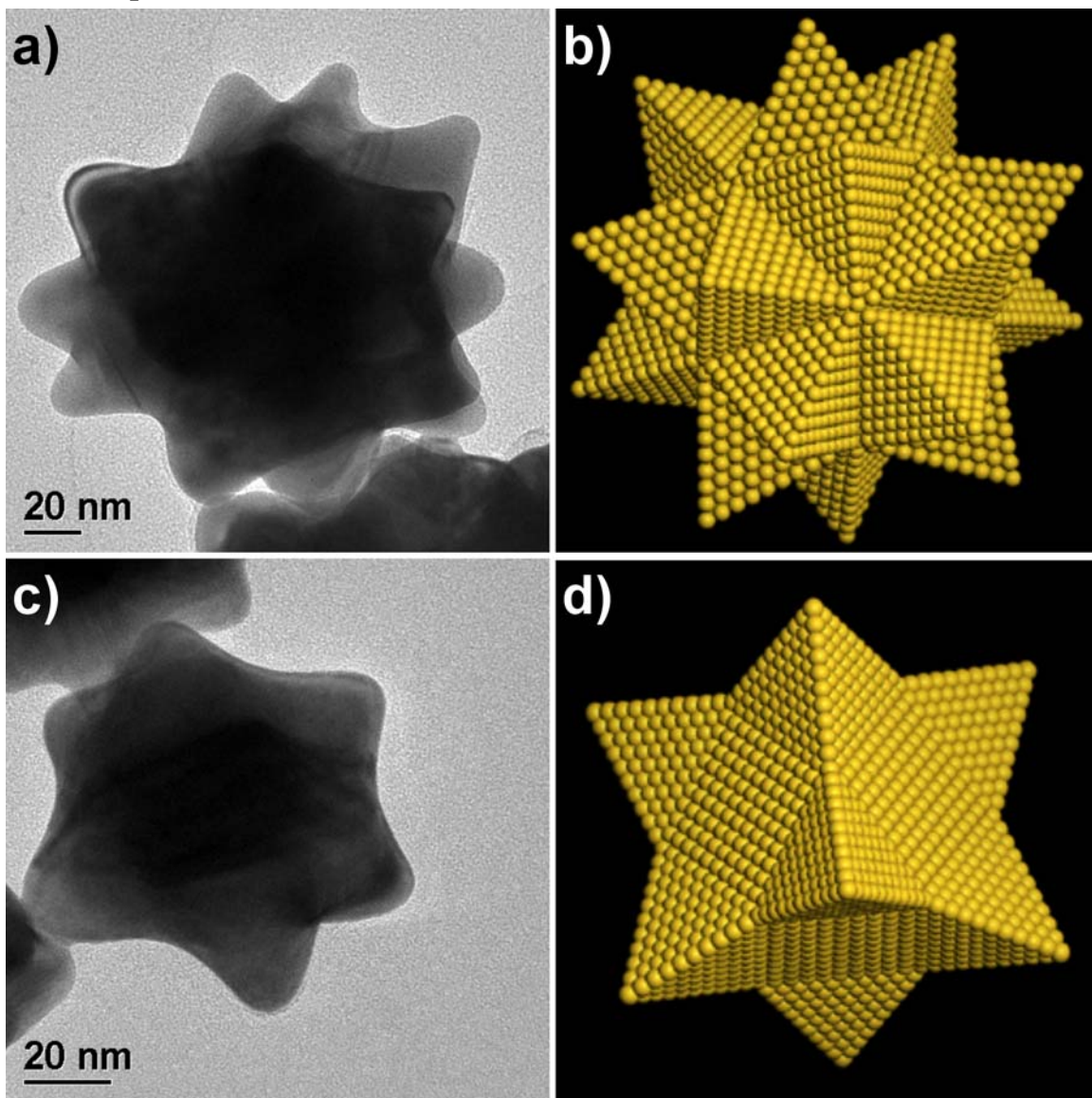


Figure 7.6: The two classes of star polyhedral gold nanocrystals. (a) TEM image of a multiple-twinned star nanocrystal, and (b) proposed model, an icosahedron with each of its twenty $\{111\}$ surfaces replaced by a tetrahedral pyramid. (c) TEM image of a monocrystalline star, and (d) proposed model, a cuboctahedron with each of its eight $\{111\}$ truncations replaced by a tetrahedral pyramid.

Employing a combination of electron microscopy techniques including scanning electron microscopy (SEM), transmission electron microscopy (TEM), weak beam dark field (WBDF) microscopy, high angle-annular dark field (HAADF) microscopy, and electron diffraction, we have identified two distinct classes of star polyhedral gold nanocrystals, as shown in Figure 7.6: multiple-twinned crystals with five-fold symmetry (Figure 7.6a), and monocrystals (Figure 7.6c). We performed tilting sequences of TEM images, and by tracking the emergence and disappearance of pyramids at various tilting angles, three-dimensional reconstructions of the crystal shape were obtained.

By combining our structural analysis with the three-dimensional reconstructions, we have proposed structural models for each class of star polyhedral gold nanocrystal. Multiple-twinned star nanocrystals with five-fold symmetry correspond to an icosahedron with each of its twenty $\{111\}$ surfaces replaced by a tetrahedral pyramid (Figure 7.6b). Monocrystalline star nanocrystals correspond to a cuboctahedron with each of its eight $\{111\}$ truncations replaced by a tetrahedral pyramid (Figure 7.6d). In the following two sections, we will provide a brief overview of the detailed structural analysis performed for each class of star polyhedral nanocrystal.

7.3.3 Structural Analysis of Multiple-Twinned Star Polyhedra

Figure 7.6a is a representative TEM image of the first specific type of star polyhedral nanocrystal we have characterized. Tilting sequences of TEM images, as in Figure 7.7a-d, were performed, and by tracking the emergence and disappearance of pyramids at various tilting angles, three-dimensional reconstructions were obtained. Twenty distinct pyramids were observed, and their spatial arrangement indicates that they emanate from an icosahedral core. Based on the observed global symmetry, we propose a structural model for this class of nanocrystal, seen in Figure 7.6b, corresponding to an icosahedron with tetrahedral pyramids extending from each of its twenty $\{111\}$ faces.

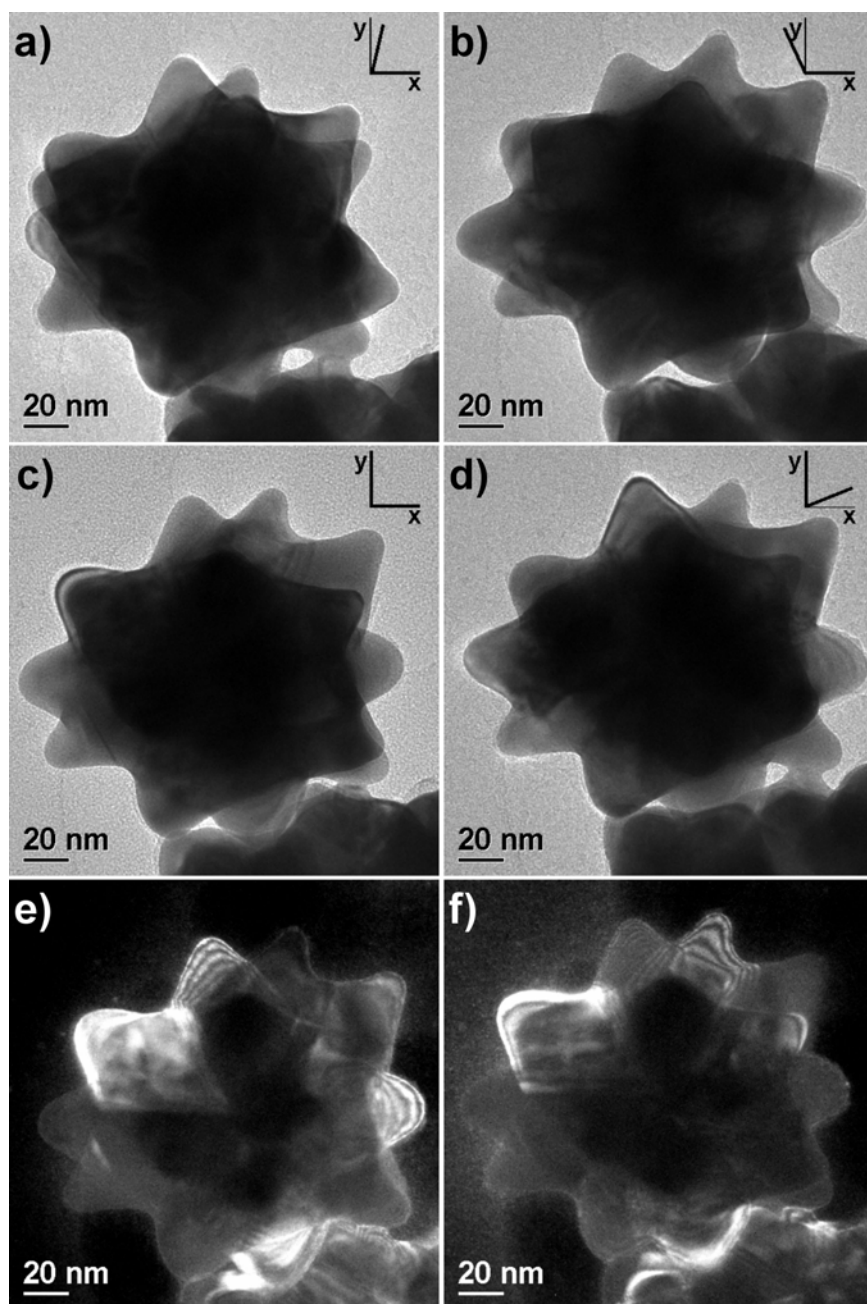


Figure 7.7: TEM tilt sequence for a multiple-twinned star nanocrystal, with $[x^\circ, y^\circ]$ tilting angles (a) $[0, -15]$; (b) $[0, 15]$; (c) $[0, 0]$; and (d) $[15, 0]$. (e)-(f) WBDF images illustrating some of the individual monocrystalline domains present within the crystal.

The structure of these icosahedrally-derived star nanocrystals resembles the great stellated dodecahedron, a Kepler-Poinsot solid. However, a great stellated dodecahedron possesses elongated pyramids, the edge length of each pyramid being related to the edge length of the icosahedral base by the golden ratio. (160) In contrast, our model was constructed by growing tetrahedral pyramids on icosahedral faces, both to satisfy FCC stacking and to match the experimentally-observed shape of the pyramids. Properly speaking, our proposed model is a sixty-faced deltahedron. (161) The peaks of the nanocrystalline pyramids have a rounded appearance. Since the corners of faceted nanocrystals grown under kinetically-driven conditions generally terminate in terraced steps, (76,77) we expect surface steps to give a rounded appearance to the peak of a tetrahedral pyramid.

Figure 7.8a-c presents a multiple-twinned nanocrystal, both in bright field (Figure 7.8a) and WBDF (Figure 7.8c-d). From the bright field image, ten pyramids are observed around the perimeter of the crystal. WBDF allows us to visualize the pentagonal array of pyramids emerging from the upper and lower surfaces of the crystal. By selecting diffraction spots corresponding to the upper or lower surfaces, we observe pyramids extending above or below the plane of the page. In Figure 7.8b there is an upward-facing pentagonal arrangement of pyramids, while in Figure 7.8c the pyramids form a downward-facing pentagon. This agrees with the geometric arrangement of pyramids in our proposed model (Figure 7.6b). WBDF also reveals the five-fold symmetry of the twin boundaries, as required for an icosahedrally-derived nanocrystal from purely geometric considerations.

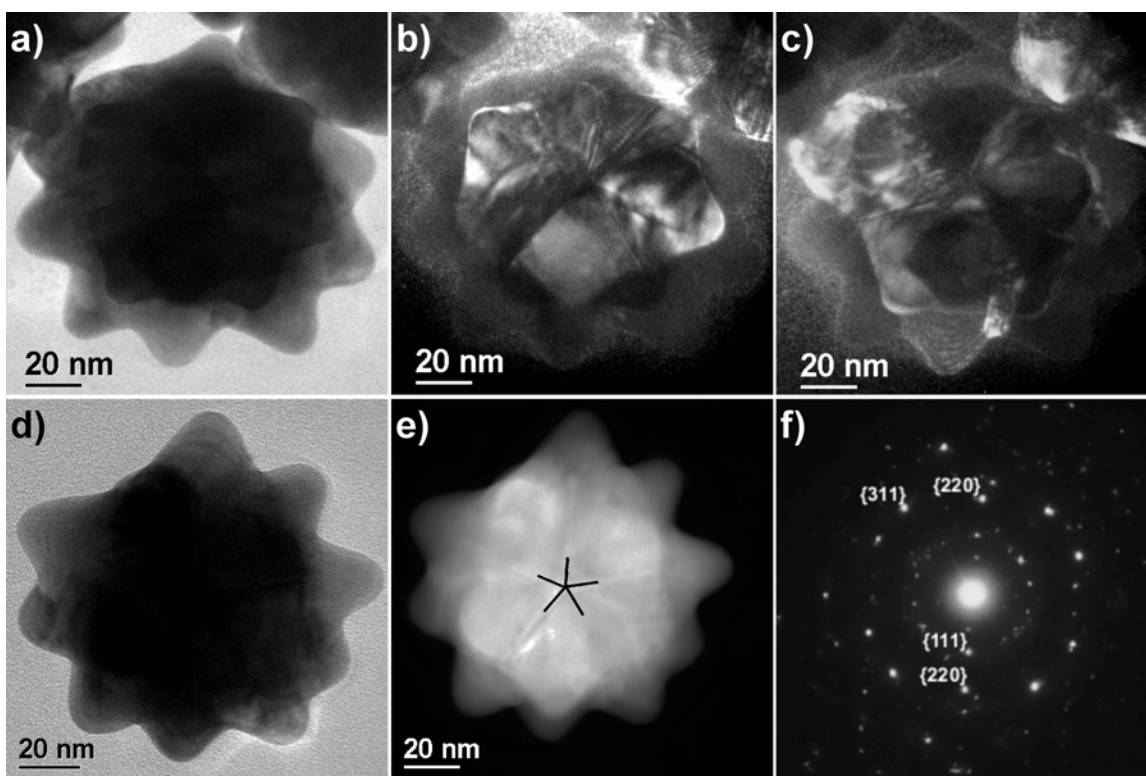


Figure 7.8: (a) TEM image of a multiple-twinned star nanocrystal. (b)-(c) Corresponding WADF images, demonstrating the five-fold symmetric twinned structure. (d) TEM image of another multiple-twinned gold nanocrystal. Corresponding (e) HAADF image and (f) SAED pattern. For clarity, black lines outline the five-fold symmetry at the center of (e).

Figure 7.8d-f present another icosahedrally-derived multiple-twinned nanocrystal. The bright field image (Figure 7.8d) reveals ten pyramids in-plane surrounding the center of the crystal (the tenth pyramid is slightly hidden due to sample tilt). In the corresponding HAADF image (Figure 7.8e), the five-fold symmetry of the twin boundaries between pyramids on the upper face of the crystal is clearly visible. The brighter contrast in the center of the crystal is due to increased thickness, which is expected since pentagonal arrays of pyramids project from the upper and lower surfaces of the crystal. In the electron diffraction pattern (Figure 7.8f), the inner ring represents

$\{111\}$, and the outer ring $\{311\}$ spots. An aperiodic sequence of diffraction spots occurs along the axis running vertically through the $\{220\}$ spots. This aperiodicity is characteristic of crystals with five-fold symmetry, and occurs when the electron beam encounters five distinct crystallographic orientations at one point, (162) such as the pentagonal array of pyramids at the center of Figure 7.8e.

The multiple-twinned structure of these nanocrystals is a direct result of their five-fold symmetry. It is not possible to fill space by joining five perfect tetrahedra to form a center with five-fold rotational symmetry, because a gap of $\sim 7.5^\circ$ remains between the final two tetrahedral units. (74) When crystals possessing five-fold symmetry are formed, such as the decahedron or icosahedron, defects must be introduced at the tetrahedral boundaries to accommodate the structure. (75) Hence, the icosahedrally-derived nanocrystals are multiple-twinned, with twenty distinct monocrystalline domains (such as those visible in Figures 7.7e-f).

7.3.4 Structural Analysis of Monocrystalline Star Polyhedra

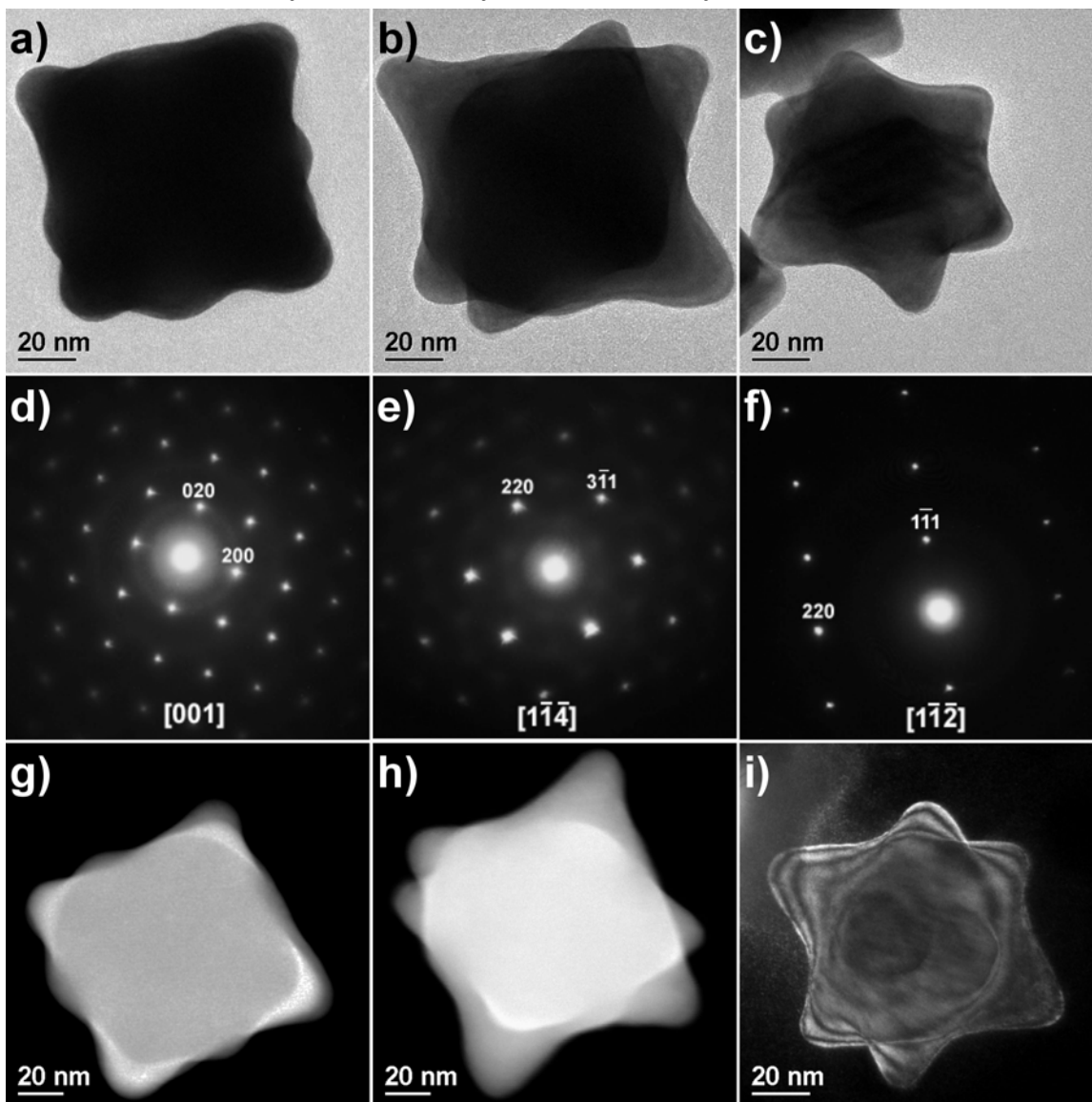


Figure 7.9: Monocrystalline star polyhedral gold nanocrystal. (a) TEM image, (d) SAED, and (g) HAADF image for the $[001]$ zone axis. (b) TEM image, (e) SAED, and (h) HAADF image for the $[1-1-4]$ zone axis. (c) TEM image and (f) SAED for the $[1-1-2]$ zone axis. (i) Representative WBDF image.

Figure 7.6c is representative of the second type of star polyhedral nanocrystal we have characterized. Based on 3D reconstructions from TEM tilting sequences, and

combined with the SEM analysis discussed previously (Figures 7.5c-d), we propose a structural model, seen in Figure 7.6d, corresponding to a cuboctahedron with tetrahedral pyramids extending from each of its eight $\{111\}$ faces. Figures 7.9a-c present three orientations for the cuboctahedrally-derived star nanocrystals, and the corresponding SAED patterns (Figures 7.9d-f) demonstrate the monocrystallinity of the structures. Figures 7.9g and 7.9h are HAADF images of the orientations in Figures 7.9a and 7.9b, respectively. The HAADF contrast in Figure 7.9h reveals the presence of two pyramids in the central region of the crystal, in addition to the six pyramids visible at the perimeter.

The orientation of the star nanocrystal in Figure 7.9a is such that the four pyramids at the upper surface of the crystal are aligned directly above the four pyramids at the lower crystal surface. In the corresponding HAADF image (Figure 7.9g), the contrast is brighter at the corners of the crystal than in the center. This contrast inversion occurs because in the center of the crystal, the electron beam travels through one continuous monocrystalline region. On the other hand, at the corners the electron beam enters one pyramid at the upper crystal surface, exits the crystal, then reenters a pyramid at the lower crystal surface with a different crystallographic orientation. This increases the local inelastic dispersion, resulting in brighter contrast at the corners even though the crystal thickness is greatest in the center.

Figure 7.9i is a WBDF image of a cuboctahedrally-derived star nanocrystal. The continuity of thickness fringes over the entire crystal structure demonstrates its monocrystallinity. In addition to illuminating the six pyramids around the perimeter of the crystal, WBDF contrast also reveals the two pyramids emerging in projection from the upper and lower surfaces of the crystal. These two pyramids are not visible in conventional TEM images at this orientation, due to the thickness of the central region of the crystal. The thickness fringe contours also illustrate rounding of the pyramid peaks,

as noted previously. Thus, in both monocrystalline and multiple-twinned stars, minimization of structural energy dictates rounded peaks for the tetrahedral pyramids.

7.3.5 Merits of the Synthesis Approach

The first reported branched gold nanocrystals were synthesized using the seed-mediated growth technique. (155–156) Due to the relative complexity of the method, it was not possible to discern which of the several variables involved were critical for the growth of branched gold nanocrystals. Our approach was to develop a greatly simplified reaction to determine the essential set of parameters required to induce branching of gold nanocrystals. Our plan was to minimize the number of variables, beginning simply by reducing gold ionic salt with ascorbic acid in water. Surprisingly, we found that adding a 40-fold molar excess of ascorbic acid was sufficient to produce branched gold nanocrystals at ambient conditions. At lower molar excesses of ascorbic acid, less branching and markedly increased aggregation was observed. For less than 8-fold molar excess of ascorbic acid, no significant branching was observed, and the product largely consisted of spherical polycrystalline aggregates of gold.

By foregoing the use of templating surfactant molecules and seed crystals, we sacrifice a degree of control over the size and shape distribution of the products. However, with our simplified approach, we know with certainty that it is exclusively ascorbic acid molecules and their oxidized derivatives that promote the preferential growth of {111} gold nanocrystal surfaces in our reaction system. Further research will be required to gain a precise understanding of the role of ascorbic acid in the branching of gold nanocrystals. Subsequently, these insights could be combined with more sophisticated synthesis techniques, such as seed-mediated growth, to develop rational design criteria for the controlled synthesis of a variety of branched gold nanocrystals.

7.3.6 Preferential Growth of {111} Surfaces

Gold nanocrystals increase the proportion of their exposed {111} surfaces by assuming star polyhedral morphologies, since each exposed {111} surface of the original Archimedean solid is replaced by a tetrahedral pyramid presenting three exposed {111} surfaces. For FCC crystals the relative surface energies of the low-index crystallographic planes are $\gamma_{111} < \gamma_{100} < \gamma_{110}$. (163) Thus, assuming a star morphology lowers the surface energy of a growing crystal, and this could be the driving force for star nanocrystal formation in our strongly kinetically-controlled system.

The sizes of our icosahedrally-derived star nanocrystals are on the order of 100–300 nm. For fivefold cyclic twinned nanocrystals, the energy introduced due to cyclic twinning is compensated by a reduction in surface energy resulting from the high proportion of exposed {111} surfaces. As the nanocrystal grows in size, the surface-to-volume ratio decreases, and the reduced surface energy of {111} surfaces can no longer compensate for the excessive strain resulting from fivefold cyclic twinning. As a result, icosahedral gold nanocrystals in the range of 100–300 nm are typically not observed.

Recently, Yang and coworkers demonstrated that by working under thermodynamically-controlled conditions and carefully regulating the growth rate for each crystallographic direction, icosahedral gold nanocrystals of 100–300 nm can be synthesized. (164) Additionally, in Chapter 2 we demonstrated that under strongly thermodynamically-controlled reaction conditions, decahedral gold nanocrystals of 100–200 nm can be synthesized. For the strongly kinetically-controlled reaction conditions currently being considered, icosahedral gold nanocrystals are stabilized by preferential growth of their exposed {111} surfaces, allowing for the formation of icosahedrally-derived star polyhedral nanocrystals on the order of 100–300 nm.

7.3.7 Characteristic Structural Defects

Although the majority of monocrystalline stars are free from structural defects, a sizable number of multiple-twinned stars contain defects and have an imperfect shape. This is to be expected, since a multiple-twinned structure inherently possesses more lattice strain, and thus a higher potential for defects. However, characteristic defects were observed for both classes of star polyhedral gold nanocrystals.

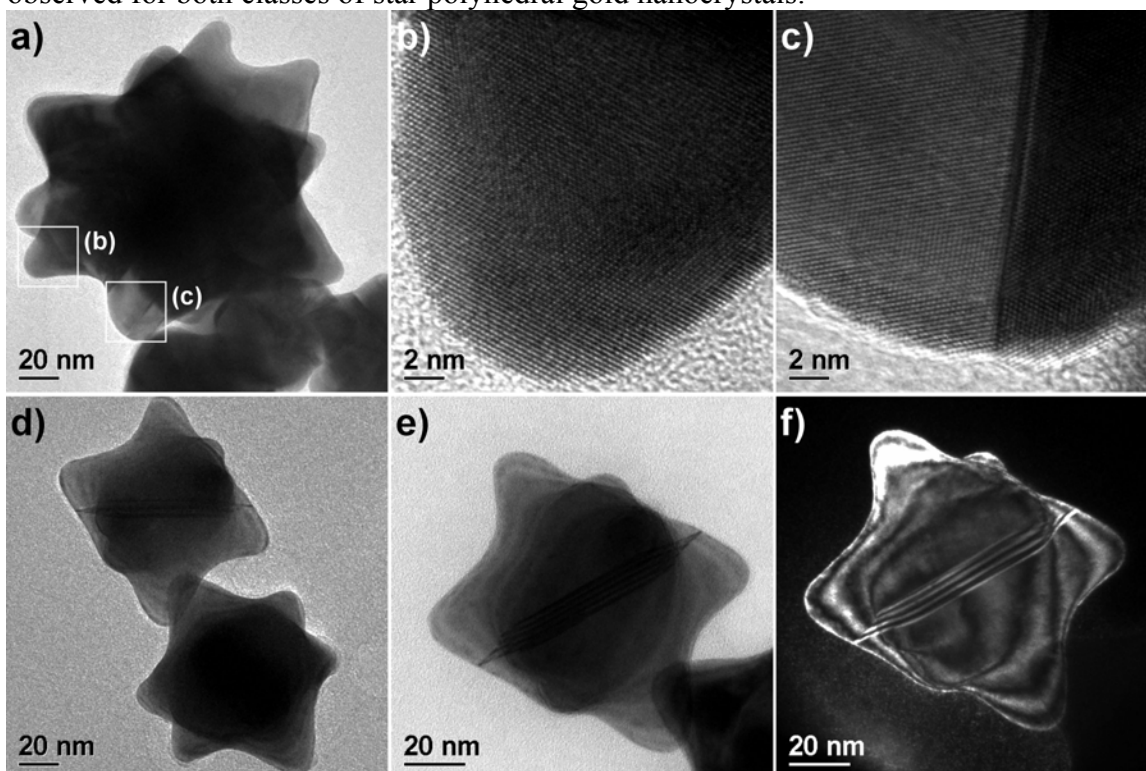


Figure 7.10: Characteristic structural defects for (a)-(c) multiple-twinned and (d)-(f) monocrystalline star polyhedral gold nanocrystals. (a) TEM image of an imperfect multiple-twinned star. (b) HREM of a well-formed pyramid, and (c) neighboring pyramid containing a twin boundary. (d) TEM image of an imperfect monocrystalline star. (e) Bright field and (f) WBDF images clearly reveal a stacking fault extending through the entire crystal.

Figure 7.10a is a TEM image of an imperfect multiple-twinned star nanocrystal. In a defect-free multiple-twinned star, each tetrahedral pyramid constitutes an individual

monocrystalline domain, as seen in Figure 7.10b. However, a common defect for multiple-twinned stars is the presence of a twin boundary within a pyramid (Figure 7.10c). Since each pyramid is a distinct crystalline domain, such defects typically remain localized within one of the twenty pyramids. Figure 7.10d is a TEM image of an imperfect monocrystalline star. A stacking fault extending through the entire crystal is evident in a bright field image at higher-magnification (Figure 7.10e). The stacking fault is vividly illuminated in the corresponding WBDF image (Figure 7.10f).

7.3.8 Absorption Spectroscopy

The UV-visible absorption spectra of star polyhedral gold nanocrystals were obtained as follows. The as-synthesized product was stored in stoppered glass vials and left undisturbed. Within four days, the larger fraction of the product (primarily branched nanocrystals) had precipitated, while the smaller fraction of the product (primarily rounded, non-branched crystals) remained in solution. The solution phase was removed, eliminating most rounded crystals from the sample, and the precipitant was re-suspended. Within two more days, a portion of this original precipitant had once again precipitated, while the remainder was still suspended. Samples for UV-visible spectral analysis were obtained from both the precipitated and suspended portions of the re-suspended branched product. From TEM analysis, the branched nanocrystal sizes ranged from 100–300 nm. We infer that the branched nanocrystals that precipitated within two days after being re-suspended were primarily from the larger end of the distribution, and crystals that were still suspended were on the smaller end of the distribution. In this way, we had a rough idea as to the effect of size on the absorption spectra of the branched gold nanocrystals.

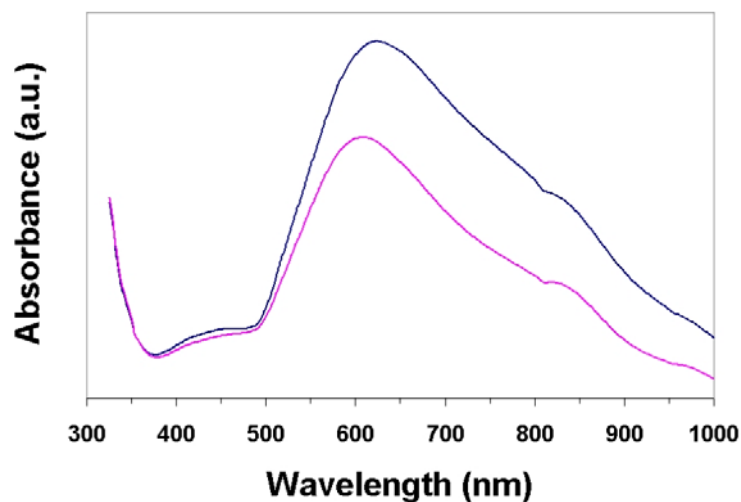


Figure 7.11: UV-visible absorption spectra of star polyhedral gold nanocrystals. Spectra were obtained from precipitated crystals (Upper, Blue), and suspended crystals (Lower, Violet) as described in the text.

Absorption spectra for the precipitated (upper spectrum) and suspended (lower spectrum) portions of the re-suspended branched nanocrystal product are presented in Figure 7.11. For the suspended fraction, a pronounced asymmetric absorbance maximum is apparent at ~ 610 nm, and a shoulder in the spectrum is observed at ~ 835 nm. The general features of the spectrum for the precipitated fraction are similar, but the absorbance maximum was red-shifted to ~ 625 nm and the intensity at this maximum was $\sim 17\%$ greater, which is indicative of a larger average crystal size.

A recent report on the optical properties of star-shaped gold nanocrystals, albeit with poorly-defined morphologies, revealed an absorption spectrum comparable to our own, with two pronounced spectral peaks observed at ~ 586 nm and ~ 773 nm. (165) For our system, the spectral peaks at ~ 610 nm and ~ 835 nm can similarly be assigned to transverse and longitudinal plasmon resonances of the pyramids protruding from the surfaces of star polyhedral nanocrystals.

7.3.9 Structural Stability of Star Polyhedral Gold Nanocrystals

Before considering potential applications for star polyhedral gold nanocrystals, it is of paramount concern to elucidate the range of conditions under which the crystals will maintain their structural stability. The structural stability of star polyhedral gold nanocrystals as a function of time was evaluated via TEM analysis, as shown in Figure 7.12. Our analysis proceeded as follows. Once the synthesis of star polyhedral nanocrystals was complete, the product solution was taken directly from the reaction vessel and transferred into stoppered glass vials for storage. That same day, samples were prepared for TEM analysis by placing a drop of solution onto a lacey carbon-coated copper TEM grid, and allowing the water content to evaporate.

The samples prepared on the day of synthesis (Figure 7.12a-d) were found to contain the distribution of star polyhedral gold nanocrystals described previously in section 7.3.1. After 60 days of storage on the amorphous carbon substrate of the TEM grid, the samples were analyzed again (Figure 7.12e-h), and no change in the product distribution was observed. Subsequent analysis of these TEM grids up to one year after preparation of the initial sample revealed no change in product distribution. This confirms the long-term stability of star polyhedral gold nanocrystals when stored as a dry product at room temperature. Additionally, the fact that a constant proportion of nanocrystals with well-defined star morphologies are observed after repeated analyses (in some cases, as many as twelve observation per TEM grid) indicates a certain degree of structural stability, inasmuch as the star polyhedral gold nanocrystals can withstand repeated irradiation by a high-energy electron beam operating at 200 kV.

A second set of TEM samples was prepared from the same original product solution 60 days after the initial day of synthesis (Figure 7.12i-l). During the intervening 60 days, the nanocrystals not only precipitated from solution, but strongly adsorbed onto

the walls and bottom of the glass vial. Therefore, the vial containing the nanocrystal solution was placed in an ultrasonic bath for one minute to re-suspend the product prior to preparing the TEM grid. Upon TEM analysis, these nanocrystals were observed to be rounded, polycrystalline, and convex; no nanocrystals with well-defined star morphologies were observed. Additionally, several nanocrystals in various stages of coalescence were identified, and in some cases coalescence was accelerated by irradiation with the electron beam during high-resolution TEM analysis.

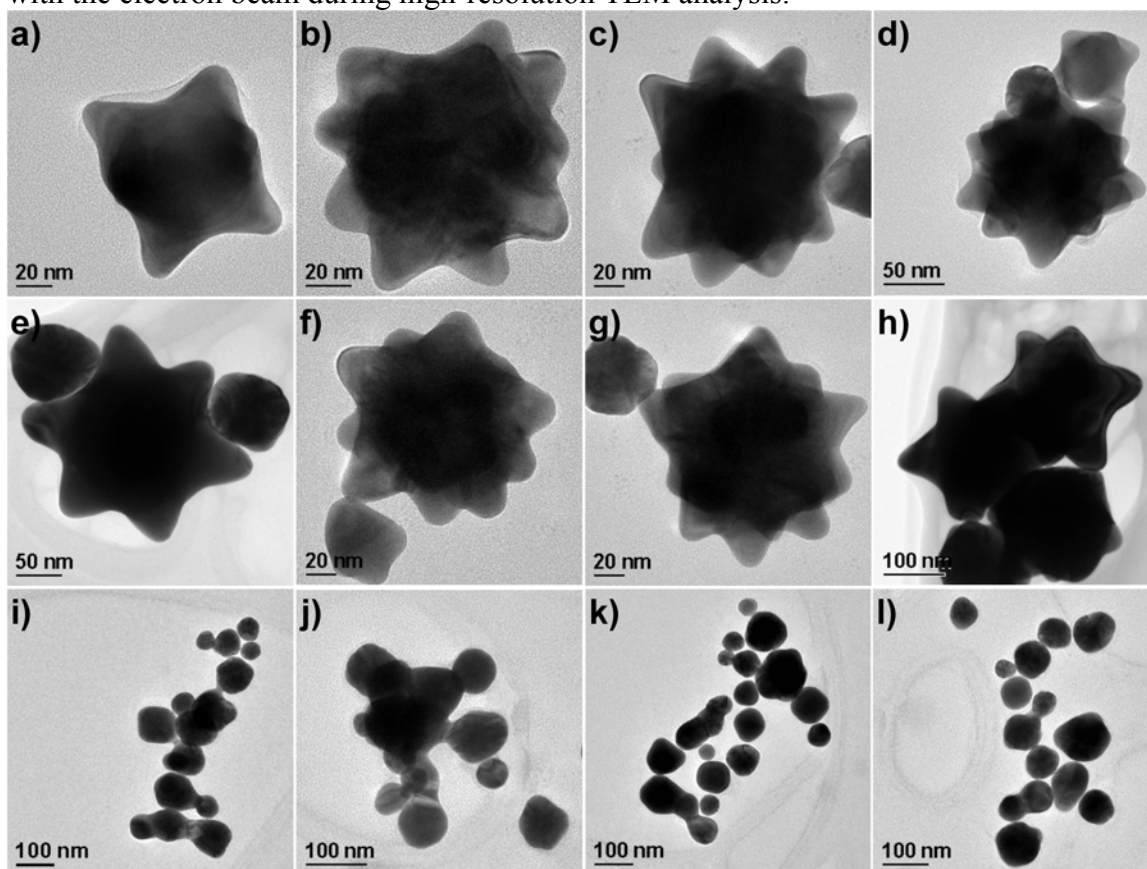


Figure 7.12: Representative TEM images illustrate structural stability of star polyhedral nanocrystals. (a)-(d) TEM grid prepared from solution on the day of synthesis. (e)-(h) The same TEM grid, 60 days later. (i)-(l) TEM grid prepared from solution 60 days after synthesis, from the same sample as images (a-h).

The appearance of these nanocrystals (Figure 7.12i-l) suggested they were rounded crystals that had undergone melting, perhaps from the thermal energy imparted to them by the ultrasonic bath. To confirm this, a second sample was prepared from another vial containing the original product solution, 60 days after the initial day of synthesis, but the nanocrystals were re-suspended via gentle manual agitation of the glass vial, rather than by an ultrasonic bath. A sample was prepared for SEM analysis, since the accelerating voltage employed (10 kV) is much less intense than for TEM (200 kV), thus reducing the extent of potential interactions between the electron beam and the sample. The results are presented in Figure 7.13. After storage in solution at room temperature for 60 days, the reaction product, which initially consisted of 60% star polyhedral gold nanocrystals, is nearly completely converted into rounded, polycrystalline, convex crystals.

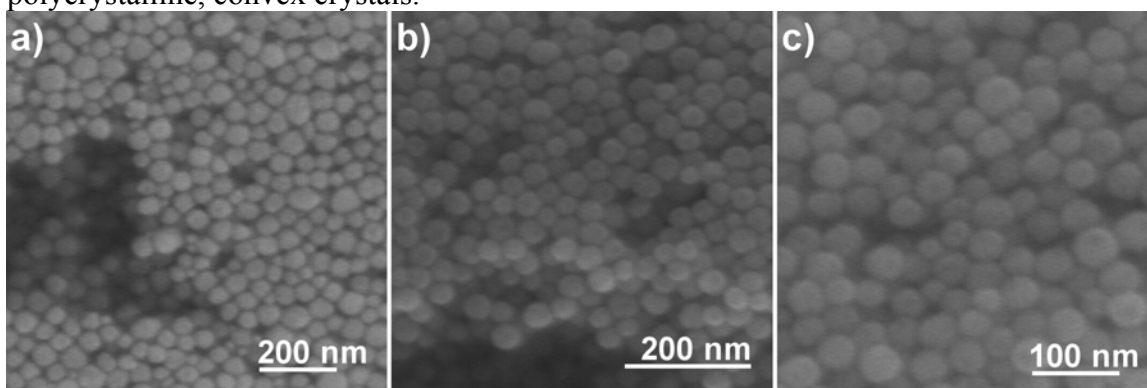


Figure 7.13: SEM images illustrating structural degradation of star polyhedral nanocrystals in solution. (a)-(c) SEM sample prepared from solution 60 days after the day of synthesis, without use of ultrasonic bath.

The distribution illustrated in Figure 7.13 led us to believe that the coalescence observed in Figure 7.12i-l was the result of exposure to the ultrasonic bath. To confirm this, a freshly-synthesized solution of star polyhedral gold nanocrystals was placed in an ultrasonic bath for 1 hour, and a TEM grid was prepared for analysis. As clearly

demonstrated in Figure 7.14, prolonged exposure to an ultrasonic bath provides the nanocrystals with sufficient thermal excitation to produce extensive coalescence.

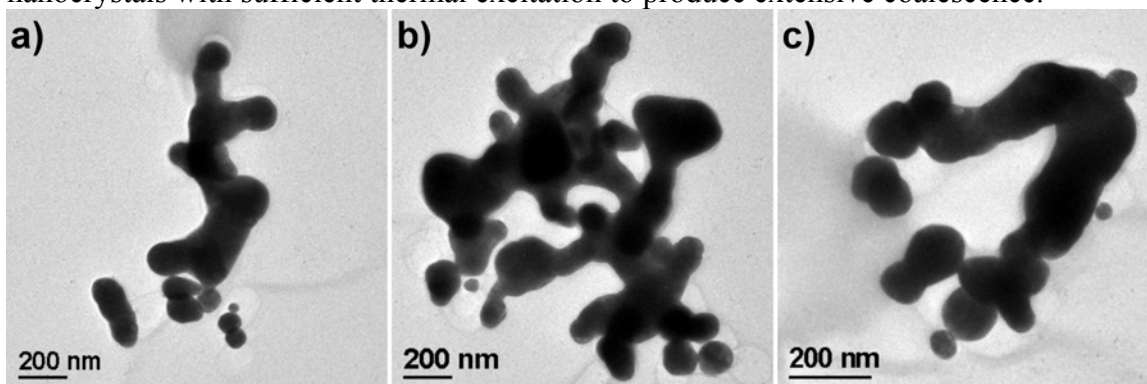


Figure 7.14: TEM images illustrating structural degradation of star polyhedral nanocrystals in an ultrasonic bath. (a–c) TEM grid prepared from solution on the day of synthesis, with use of ultrasonic bath for 1 hour.

To summarize our findings regarding structural stability, we have found that star polyhedral gold nanocrystals are metastable structures. They remain stable in solution for approximately 30 days, and within 60 days the product is nearly completely converted to rounded, polycrystalline morphologies. The energy from an ultrasonic bath is sufficient to promote extensive coalescence of the product in solution. However, when stored as a dry product on an amorphous carbon support film, star polyhedral gold nanocrystals remain stable indefinitely (in excess of one year), and are able to withstand repeated irradiation by an electron beam with 200 kV accelerating voltage. In terms of potential applications, star polyhedral gold nanocrystals would be ideally suited for long-term use in dry environments, for example as a component in nanoelectronic circuitry. For aqueous-phase applications, such as contrast enhancing agents for biological samples, long-term stability is a definite concern, as the star polyhedral morphologies are not reliably maintained in a solvated environment for longer than approximately one month.

7.3.10 On the Relative Significance of Reaction Kinetics and Solution pH

It seems highly unlikely that the branching of gold nanocrystals is the result of a unique structural or chemical property of ascorbic acid, or a highly specific interaction between ascorbic acid and gold. Rather, it is probable that branching is the result of a combination of factors, most notably the reducing strength of ascorbic acid, the rapid rate of reduction, and the pH of solution. As noted previously, upon addition of chloroauric acid, the solution rapidly changes color, becoming an opaque orange-red within two seconds after addition of the ionic gold precursor. The rapid reaction kinetics are closely related to the reducing strength of ascorbic acid, and kinetic effects have been identified as an important factor in the formation of branched gold nanocrystals. (158,159) However, in addition to kinetic effects, solution pH is also a critical parameter, as colloidal reduction in highly acidic solutions has been shown to promote the formation of anisotropic gold crystals.

The reduction potential of ascorbic acid is acutely sensitive to changes in pH, and recently Wang and coworkers have demonstrated that by varying the pH of reaction, they can selectively produce dogbone- and peanut-shaped nanostructures from gold nanorod seed crystals, using ascorbic acid as reducing agent. (166) The difference in redox potential of ascorbic acid and chloroauric acid increases as the solution pH increases, most markedly in the pH range of 8–12. (147) Accordingly, we would expect enhanced kinetics when the reaction is carried out in moderately basic conditions. However, we would simultaneously be sacrificing the highly acidic conditions present under our standard reaction protocol.

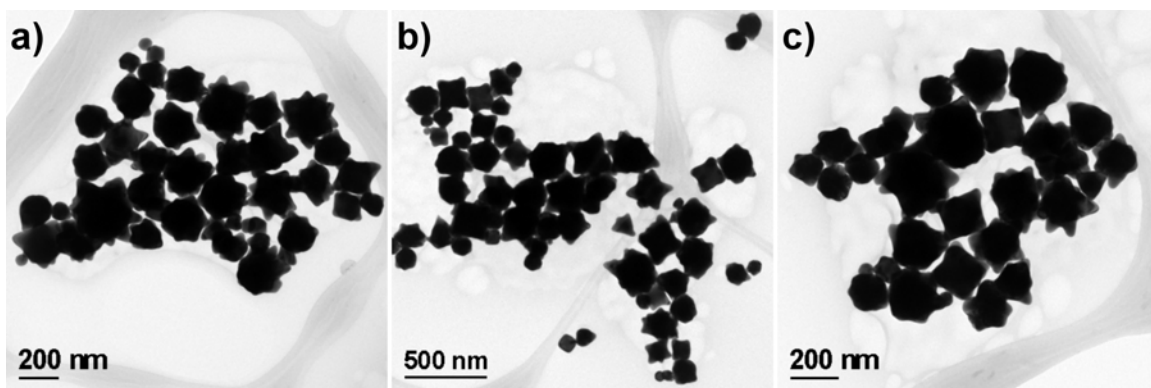


Figure 7.15: Low-magnification TEM images of the as-synthesized product, using the standard reaction protocol.

This provided an excellent opportunity to determine the relative significance of kinetic effects versus acidic solution pH in the formation of star polyhedral gold nanocrystals. Two reactions were run in parallel. In one case, illustrated in Figure 7.15, the standard reaction protocol was followed (rapid addition of 50 μmol HAuCl_4 to an aqueous 2 mmol ascorbic acid solution, with a total reaction volume of 40 mL). In the second case, illustrated in Figure 7.16, the standard reaction protocol was followed with one modification: 7.2 mmol sodium hydroxide (NaOH ; ACS reagent grade; Fisher) was added to solution with ascorbic acid, prior to the rapid addition of chloroauric acid.

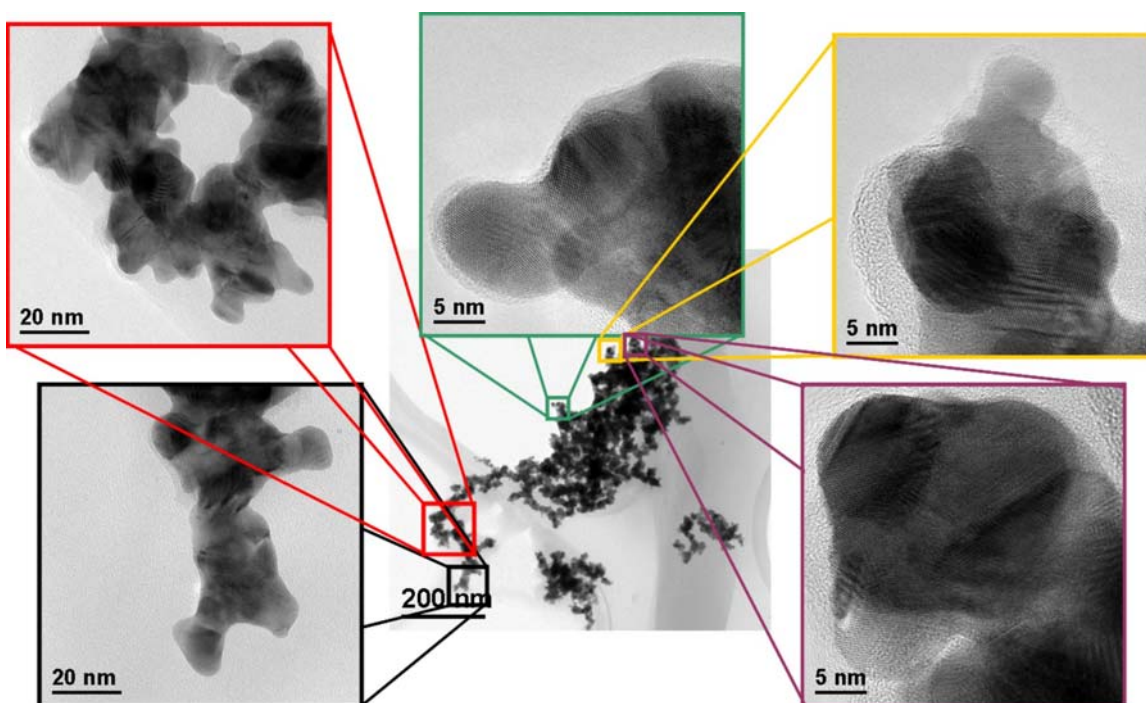


Figure 7.16: TEM images illustrating the extensive coalescence observed when sodium hydroxide is added to the reaction system.

Using the standard reaction protocol, illustrated in Figure 7.15, the reaction time as measured by visual inspection of the solution color was two seconds, and the final solution pH was ~ 2 . In the ensuing TEM analysis, the typical product distribution of nanocrystals was observed. On the other hand, with addition of NaOH (Figure 7.16), the reaction time was much less than one second, and the final solution pH was ~ 9 . Soon a large portion of this product formed greenish-black aggregates within the reaction vessel, comparable in size to dust particles, and within ten minutes the solution was completely clear with numerous aggregates in suspension. As seen in Figure 7.16, the addition of NaOH to the reaction system led not only to aggregation at the macroscopic scale, but also to extensive nanocrystal coalescence on the microscopic scale. These coalesced masses consist of nanocrystals with highly strained internal structures.

7.3.11 On the Formation and Stability of Super-Stellated Gold Nanocrystals

Having discovered that acidic solution pH is much more critical to the formation of branched morphologies than the enhanced reaction kinetics achieved by the addition of sodium hydroxide, we proceeded to consider the effects of adding greater excesses of ascorbic acid to solution. As mentioned previously, the molar ratio of (40:1) AA:Au was initially chosen for our standard reaction protocol because in Chapter 6, we found that for molar ratios greater than (40:1) [ascorbic acid molecules]:[gold atoms], increasing the ascorbic acid concentration had a negligible effect on the reaction. However, in light of our findings in section 7.3.10, we hypothesized that by adding greater excesses of ascorbic acid, it might be possible to increase the yield of star polyhedral gold nanocrystals. We thought this increased yield could result either from the increasingly acidic pH caused by increasing concentrations of ascorbic acid, or from the greater excess of ascorbic acid molecules promoting faster reaction kinetics while still maintaining an acidic reaction environment.

To test this hypothesis, the standard reaction protocol was followed with one modification: 8 mmol ascorbic acid were initially dissolved in water, providing a molar ratio of (160:1) AA:Au. In terms of reaction time, no difference was noted from the standard reaction protocol. However, in approximately one-third of the reactions carried out at (160:1) AA:Au, the final color of the solution was dark reddish-purple, rather than orange-red as typically observed for the standard reaction protocol. TEM grids of the dark reddish-purple solution were prepared for analysis, and representative images are provided in Figure 7.17.

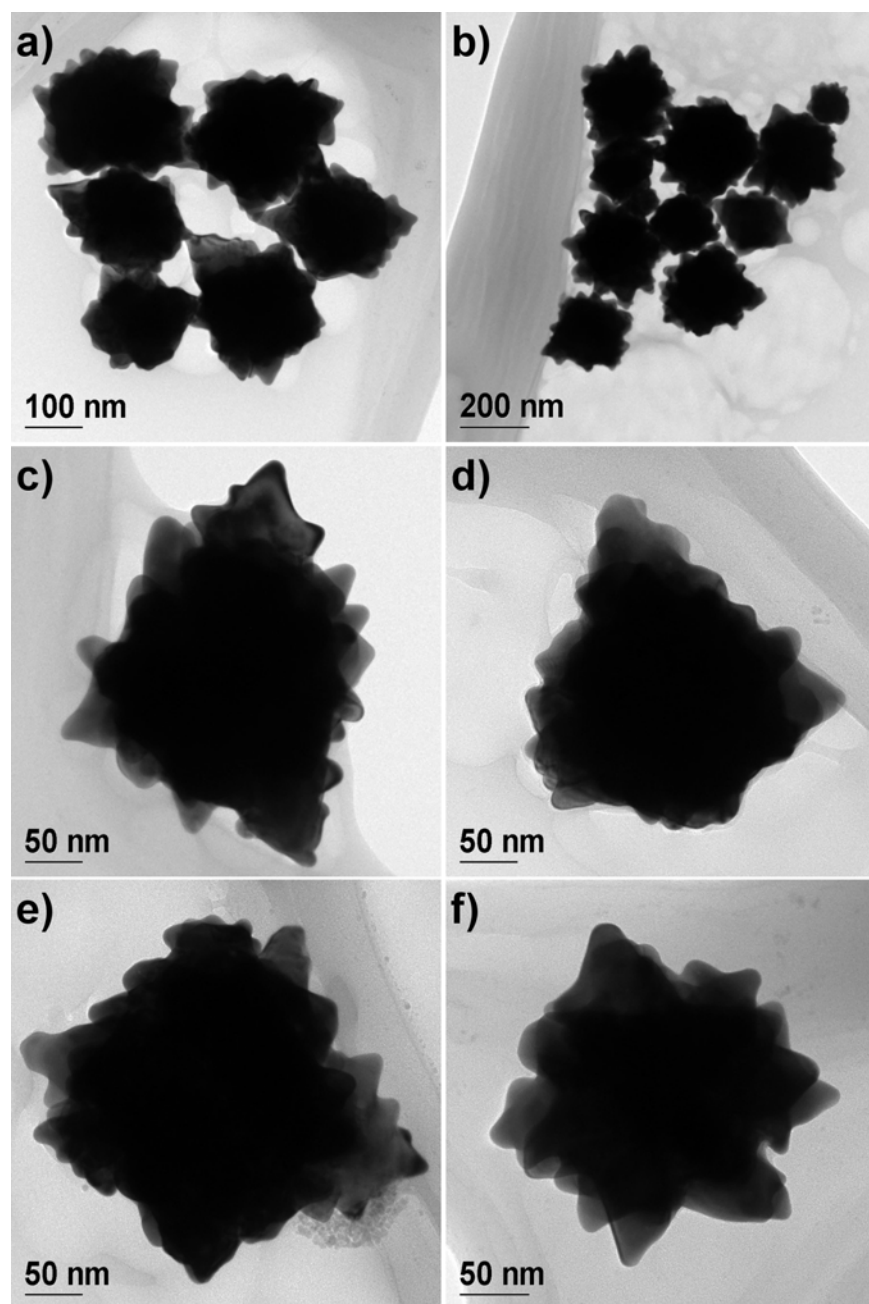


Figure 7.17: TEM images illustrating the super-stellated gold nanocrystals, formed in approximately one-third of the (160:1) AA: Au reaction systems.

Although these nanostructures are in the same size range as the star polyhedral nanocrystals observed in the standard reaction protocol, they exhibit a much higher

degree of branching, with secondary branches clearly observed growing off of primary branches emanating from the core of the nanocrystal. We refer to these nanocrystals, only observed at the (160:1) AA: Au condition, as “super-stellated” gold nanocrystals. It should be noted that the super-stellated nanocrystals were only observed in the dark reddish-purple solution, which was encountered in roughly one-third of the reactions carried out at (160:1) AA: Au. The remainder of the reactions at (160:1) AA: Au produced the typical distributions described in section 7.3.1, with no noticeable improvement in the percentage yield of star polyhedral gold nanocrystals.

As noted in section 7.3.9, although star polyhedral gold nanocrystals are metastable structures, when stored as a dry product on an amorphous carbon support film they maintain their structure indefinitely and are able to withstand repeated irradiation by an electron beam with 200 kV accelerating voltage. We undertook a comparison of the structural stability of star polyhedral nanocrystals and super-stellated nanocrystals in the electron beam. Nanocrystals were focused and centered in the optical axis of the electron beam. Then, the anode wobbler function of the TEM was employed, which modulates the current density of the electron beam. Along the optical axis, the current density periodically increases by an order of magnitude, then returns to its normal value. The frequency of modulation is approximately one cycle per second.

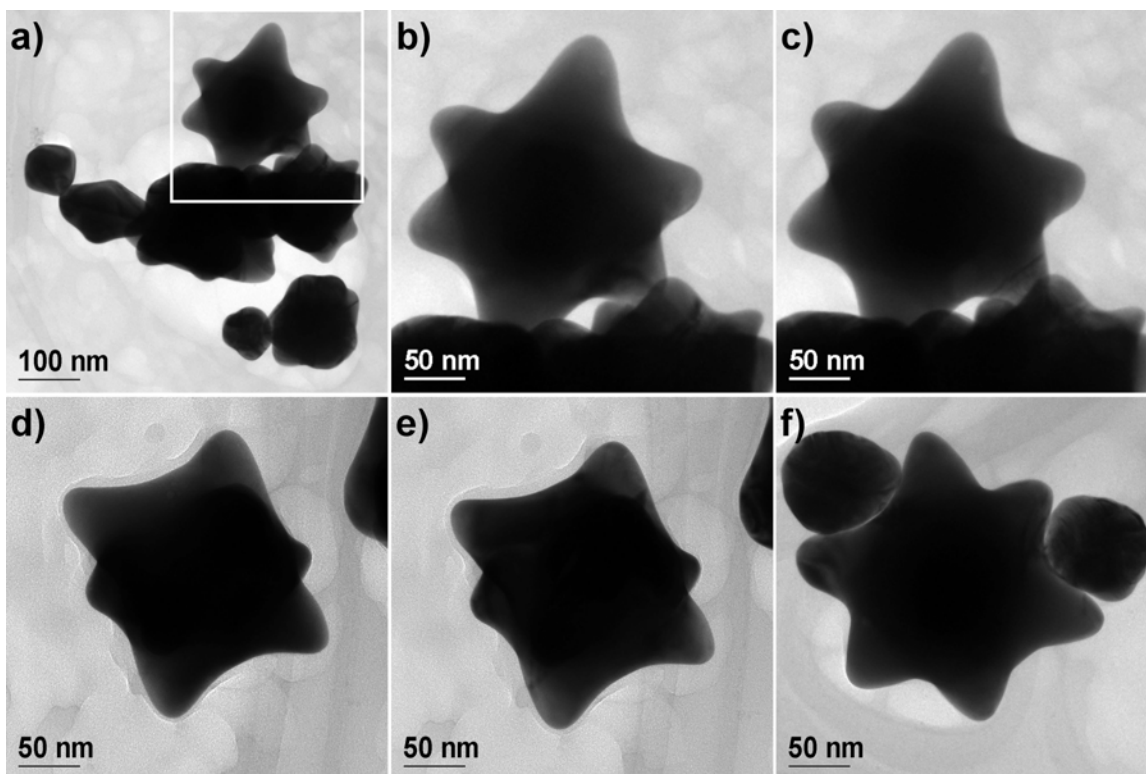


Figure 7.18: Stability of star polyhedral gold nanocrystals in the electron beam. (b) Crystal in the boxed region of (a) prior to current density modulation. (c) The same crystal as (b) after exposure to 1800 pulses of current density modulation. (d) A second crystal prior to current density modulation. (e) The same crystal as (d) after exposure to 1800 pulses of current density modulation. (f) A third crystal prior to current density modulation. Image after modulation was not obtained, due to radiation-induced destruction of the amorphous carbon support.

Figure 7.18 presents the results of this experiment for star polyhedral gold nanocrystals. The crystal in Figure 7.18a-c was chosen due to its intimate proximity to other nanocrystals. In this way, not only could we monitor the stability of the crystal itself, but we could also study its propensity to coalesce with neighboring crystals. Figure 7.18b presents the nanocrystal prior to current density modulation, and Figure 7.18c shows the same crystal after exposure to 1800 pulses of current density modulation. Clearly, no structural changes are observed, and no coalescence with neighboring

nanocrystals has occurred. Another star polyhedral nanocrystal is presented in Figure 7.18d-e, this time with no other nanocrystals in intimate contact. Again, no difference in structure is discernable in the crystal prior to current density modulation (Figure 7.18d), and after exposure to 1800 pulses of current density modulation (Figure 7.18e). A third star polyhedral nanocrystal is presented in Figure 7.18f. As in the case of Figure 7.18a, this crystal was chosen due to its intimate proximity to two small, rounded nanocrystals. Figure 7.18f shows this nanocrystal prior to current density modulation. Unfortunately, an image after 1800 pulses of current density modulation was not attainable because the amorphous carbon support was severely damaged by electron beam irradiation, and the film broke at the conclusion of the experiment, just before an image could be captured. Despite extensive radiation damage to the substrate, this nanocrystal was visually observed to be structurally unaffected, and no coalescence was observed even up to the moment the support film broke.

In comparison, the structural stability of the super-stellated gold nanocrystals resulting from the (160:1) AA:Au reaction condition is demonstrated in Figure 7.19. The images in Figure 7.19a-c and Figure 7.19g-i correspond to various super-stellated nanocrystals prior to current density modulation, while Figure 7.19d-f and 7.19j-l correspond to the respective super-stellated nanocrystals after just 1 pulse of current density modulation. The images are arranged pairwise vertically, such that Figure 7.19a is a group of super-stellated nanocrystals prior to current density modulation, while Figure 7.19d is the same group of crystals after 1 pulse of current density modulation.

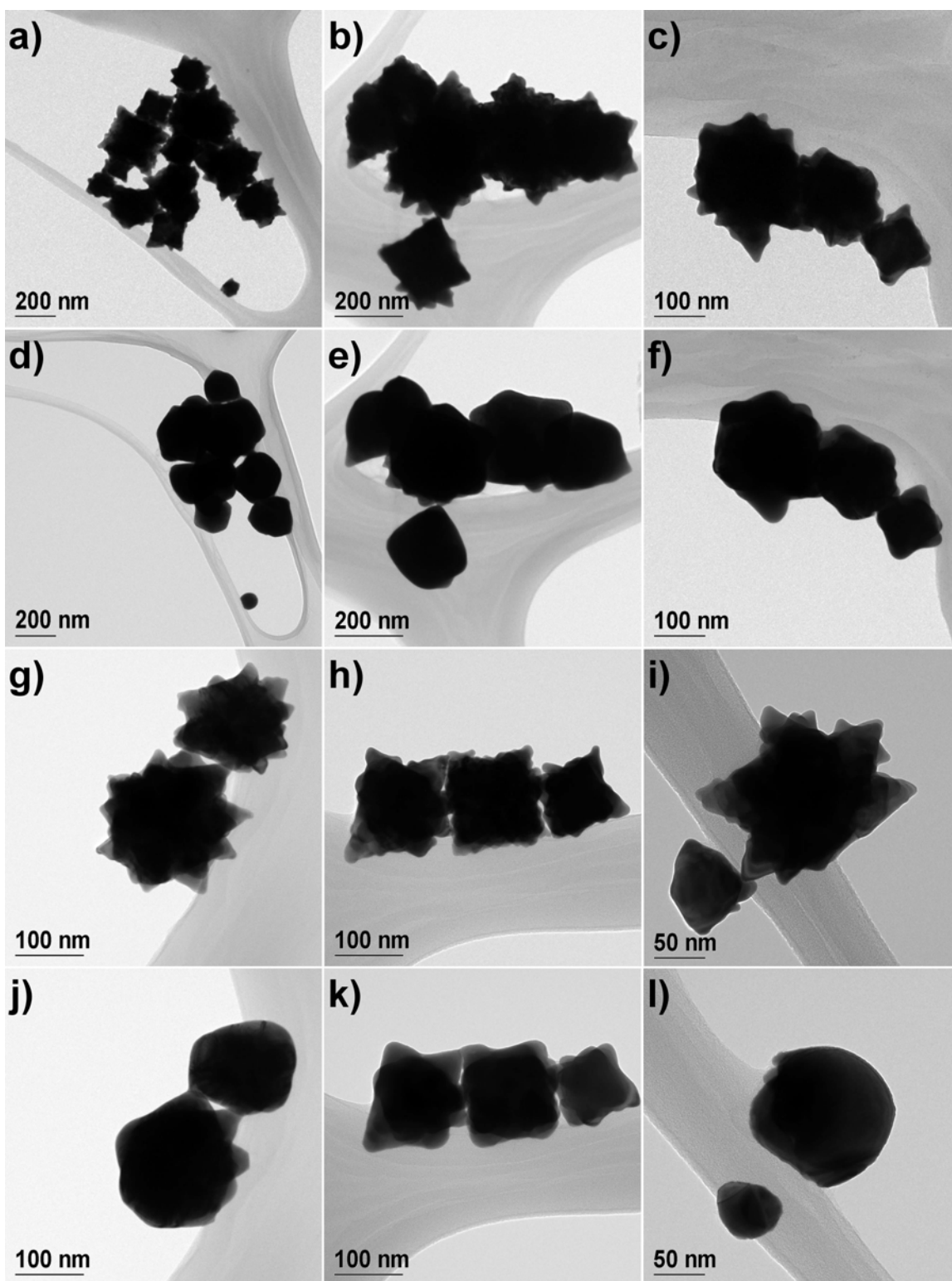


Figure 7.19: Stability of super-stellated gold nanocrystals in the electron beam. The images are arranged pairwise vertically, such that (a) is a group of super-stellated nanocrystals prior to current density modulation, while (d) is the same group of crystals after exposure to just 1 pulse of current density modulation. Likewise, images (b)&(e), (c)&(f), (g)&(j), (h)&(k), (i)&(l) constitute pairs of images prior to current density modulation, and after 1 pulse of current density modulation.

Clearly, the structural effects of just 1 pulse of current density modulation are profound, with several super-stellated structures becoming either completely rounded or irregularly faceted, with no discernable peaks. In particular, it is interesting to note that the super-stellated nanocrystals in Figure 7.19c assume morphologies closely resembling monocrystalline star polyhedra in Figure 7.19f. Similarly, the super-stellated crystals in Figure 7.19h assume monocrystalline star morphologies in Figure 7.19k. However, the two super-stellated crystals in Figure 7.19g, whose structures are reminiscent of a multiple-twinned star with fivefold symmetry, either become completely rounded, or retain only a few truncated peaks in Figure 7.19j. This suggests that the relative structural stability of the monocrystalline star polyhedral nanocrystals is greater than the multiple-twinned stars, as suggested previously in our discussion of structural defects in section 7.3.7. In summary, we can state that the super-stellated morphology is both highly irregular, and structurally unstable. Thus, further work at the molar ratio of (160:1) AA: Au was not pursued.

7.3.12 On the Initial Rate of Nucleation and Growth

At this point, we proceeded to consider the effects of temperature in the formation of star polyhedral gold nanocrystals. As described previously, we found that the star morphology is a metastable structure, and the thermal energy imparted from an ultrasonic bath was sufficient to induce nanocrystal coalescence. Thus, it was determined that working at elevated temperatures would be detrimental to the stability of star polyhedral

nanocrystals, and in our preliminary study on the effect of temperature, we used the standard reaction protocol while running the synthesis in an ice bath.

Recall that in the standard reaction protocol, the solution rapidly changed color upon addition of chloroauric acid, becoming an opaque orange-red within ~ 2 seconds. In contrast, when the reaction was run in ice bath, the solution was colorless after addition of chloroauric acid, and remained so for ~ 4 seconds. Then, the solution acquired a light blue-violet color that increased in intensity for another ~ 2 seconds. Finally, the solution color gradually changed for another ~ 4 seconds, developing the characteristic opaque orange-red color within ~ 10 seconds of the initial addition of chloroauric acid.

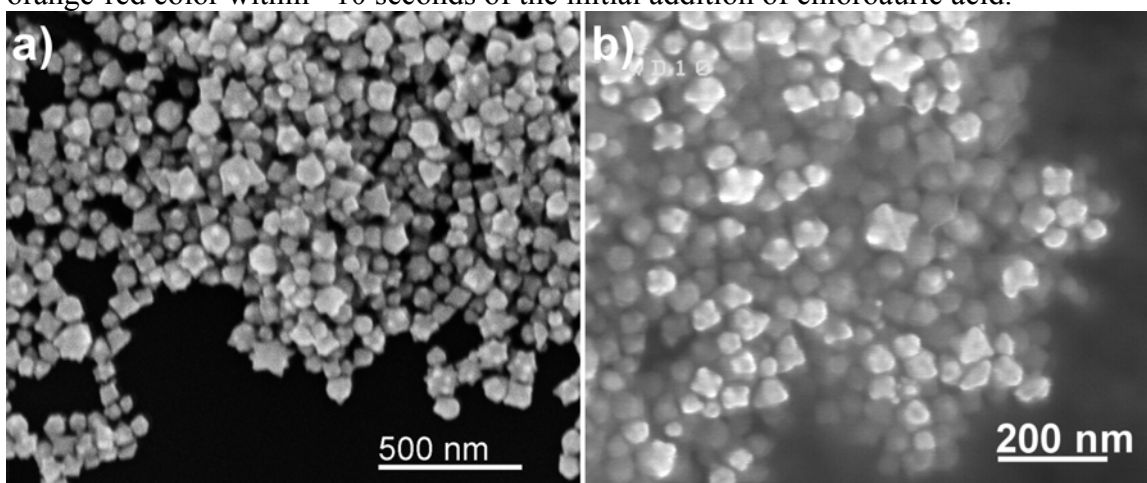


Figure 7.20: SEM images illustrating the product distribution observed when the reaction occurs (a) at room temperature, and (b) in ice bath.

Figure 7.20a provides a representative distribution for the standard reaction protocol, carried out at room temperature. Note the sizeable presence of both multiple-twinned stars with fivefold symmetry, and monocrystalline stars. Figure 7.20b is a representative distribution for the standard reaction protocol, carried out in an ice bath. From visual inspection, the presence of a large percentage of cross-shaped nanocrystals is

immediately observed. These apparently cruciform nanocrystals are monocrystalline stars in the [001] zone axis (refer to Figure 7.9a,d,g).

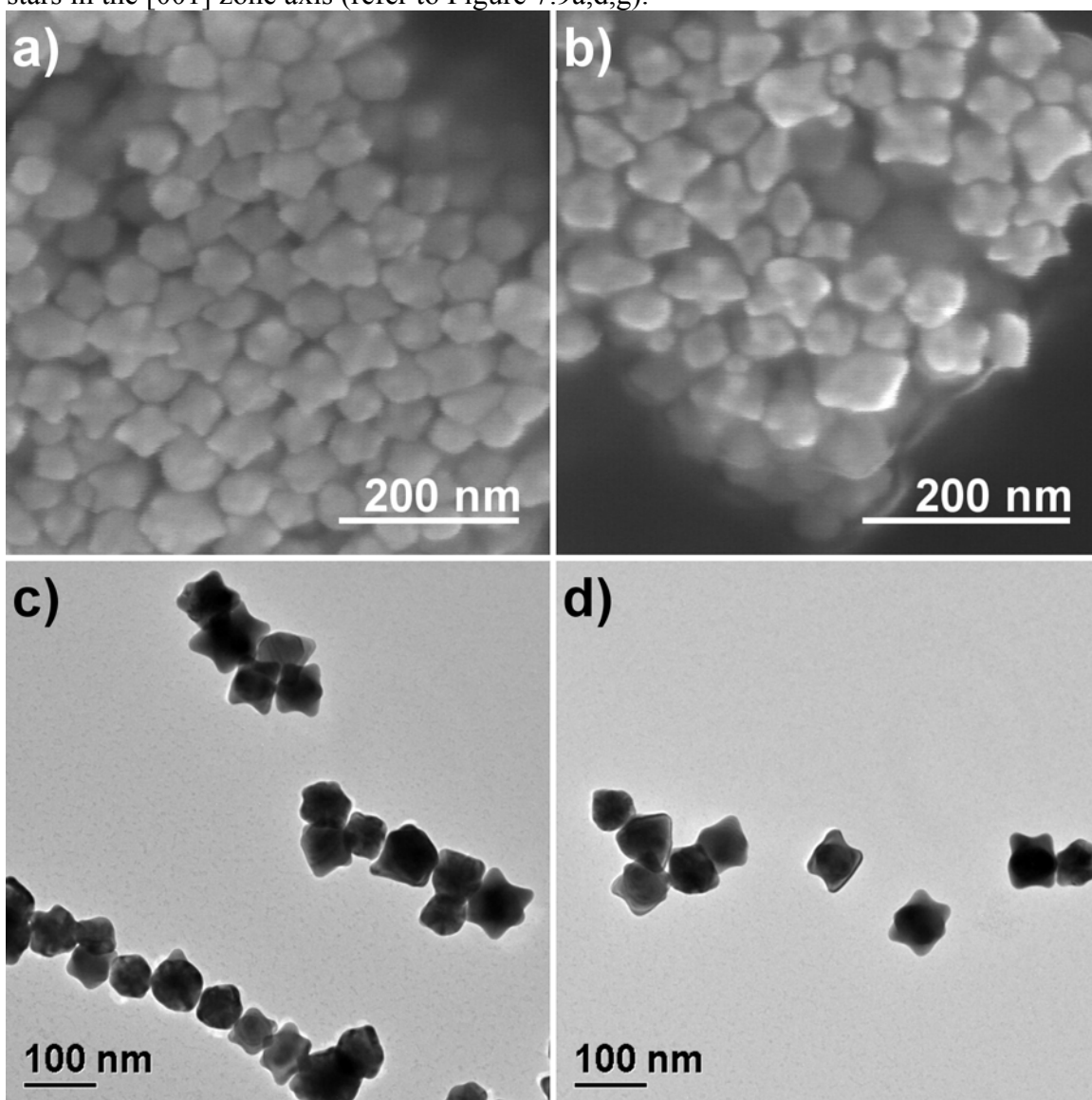


Figure 7.21: Product distribution for the standard reaction protocol carried out in ice bath. (a)-(b) SEM images and (c)-(d) TEM images. Note the large percentage of monocrystalline stars.

Reaction in ice bath favors the formation of monocrystalline stars, constituting ~70% of the as-synthesized product (compared with ~40% in the reaction at room

temperature). The remaining ~30% of the product consisted of rounded crystals, crystals with a non-uniform distribution of pyramids over their surface, or crystals with pyramids of non-uniform sizes. Interestingly, multiple-twinned stars with fivefold symmetry were largely absent from this system. From extensive SEM analysis, it appears that when a sufficiently large percentage of monocrystalline stars are present in the reaction products, they preferentially stack themselves in this cruciform orientation (Figure 7.21a-b). TEM analysis (Figure 7.21c-d) confirms the increased percentage of monocrystalline stars resulting from the standard reaction protocol carried out in ice bath.

We hypothesized that it was the slower initial rate of nucleation that favored the formation of monocrystalline stars in ice bath. To determine if this was indeed the case, independent of the reaction temperature, we conducted a second experiment in which the chloroauric acid was added dropwise to the reaction vessel. The standard reaction protocol was followed, with two modifications: the 0.5 mL 0.1M HAuCl_4 typically added to the system was diluted with 1.5 mL H_2O . Then, the 2 mL of diluted chloroauric acid solution was added dropwise to the reaction at a rate of 3 mL per minute, so the entire addition of ionic gold precursor was complete within 40 seconds.

As in the case of the reaction carried out in ice bath, the solution was colorless during the first 2 seconds of dropwise addition of chloroauric acid. The next second of addition caused the solution to acquire a light blue-violet color. Within 2 more seconds, the solution color began to change to the characteristic orange-red color. For the remaining 35 seconds of dropwise addition, the solution color increased in intensity, and the solution appearance became increasingly opaque.

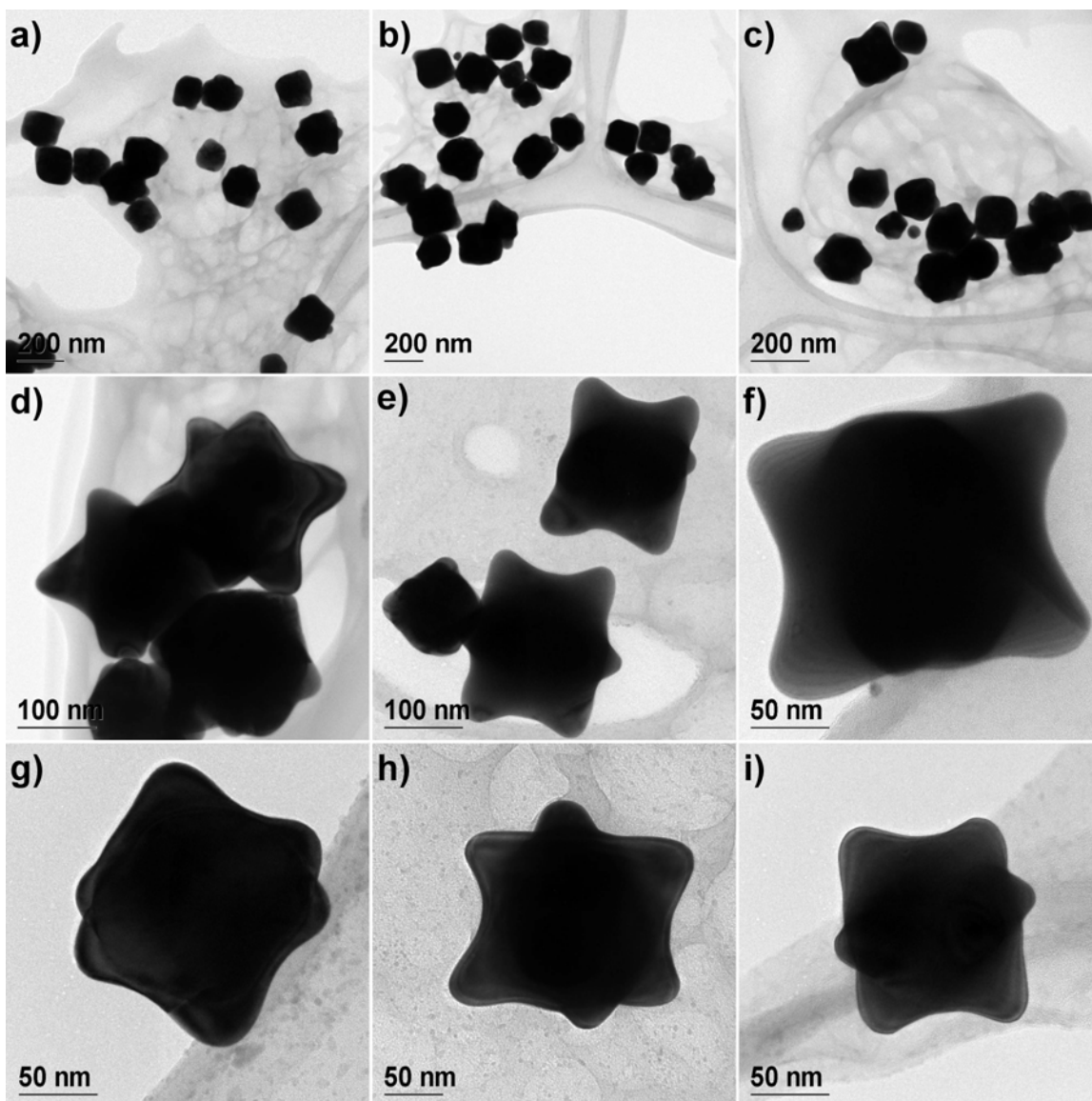


Figure 7.22: Product distribution for the standard reaction protocol carried out with a dropwise addition of chloroauric acid. (a)-(c) typical product distribution, exhibiting much smaller rounded peaks; (d)-(i) individual monocrystalline stars found within the system that exhibited more pronounced peaks.

The results for this dropwise addition are presented in Figure 7.22. As in the case of the reaction carried out in ice bath, monocrystalline stars constituted ~70% of the as-synthesized product, and multiple-twinned stars with fivefold symmetry were largely

absent from the system. However, in comparison with the reaction in ice bath, the dropwise addition of chloroauric acid over 40 seconds caused the vast majority of star nanocrystals to exhibit much smaller, more rounded, and less pronounced pyramids, as is clearly seen in Figure 7.22a-c. Some individual monocrystalline stars were found within the system that exhibited more pronounced peaks, as in Figure 7.22d-i. However, these individual crystals constituted less than 10% of the reaction product, and the vast majority of the monocrystalline stars in this system had small rounded peaks.

7.3.13 Proposed Model for Growth of Star Polyhedral Gold Nanocrystals

In light of the results of section 7.3.12, we propose a model for the growth of star polyhedral gold nanocrystals in water by reduction with ascorbic acid. Up until this point in our discussion, we have stated that our branched gold nanocrystals are obtained without the use of seed crystals. However, it is clear that branched nanocrystals on the order of 100–300 nm are not spontaneously generated in solution, but they result from the growth of primary-sized nanocrystals. Thus, a more accurate assessment would be that in our reaction system, we observe the *in situ* generation of seed crystals, which are then directly consumed in the growth of star polyhedral nanocrystals. Furthermore, we assert that it is the morphology of these *in situ* seed crystals that will determine the morphology of the final star polyhedral gold nanocrystals.

The total structural energy of a noble metal nanocrystal consists of many local minima configurations. For noble metal nanocrystals less than ~5 nm in diameter, the energy difference between these local minima is on the order of $\sim kT$ at room temperature. As a result, nanocrystals of sizes < 5 nm are characterized by a highly fluctuating structure, varying primarily between cuboctahedral, truncated octahedral, icosahedral, and decahedral. (32) As noble metal nanocrystals grow beyond this size, cyclic twinning structures become less energetically favorable, and given sufficient opportunity to sample

the various local energy minima, the crystal morphology will tend toward an FCC single crystal. For growth beyond ~ 10 nm, the fluctuating character is lost, and the nanocrystals become locked in their structural morphology.

In light of this, we can see how the initial rate of nucleation will have a critical role in determining the final distribution of star polyhedral nanocrystals. In the case of the standard reaction protocol, we propose that in the initial stage of reduction, gold atoms rapidly nucleate and form primary-sized nanocrystals of less than 5 nm in diameter. Recall that in this size range, both cuboctahedral and icosahedral nanocrystals are stable. At this point, the strongly kinetically-driven reaction conditions and high acidity of solution begin to drive the formation of branched nanostructures. The branching increases the proportion of exposed $\{111\}$ surfaces, which stabilizes the morphologies of the primary-sized nanocrystals. Thus, the final star nanocrystals observed are derived both from cuboctahedral and icosahedral seed crystals.

In the case of the reaction in ice bath, the initial rate of nucleation is slower, and the reaction is slightly less kinetically-driven. We propose that under these conditions, the primary-sized nanocrystals have more opportunity to grow before the branching phenomenon begins. If these seed crystals grow beyond ~ 10 nm in size, they will primarily assume FCC single crystal morphologies, such as cuboctahedra. The morphology of the seed crystals is stabilized by the branching process, resulting in primarily cuboctahedrally-derived monocrystalline stars.

Finally, in the case of dropwise addition of chloroauric acid, we also have a slower initial rate of formation of nuclei and a less kinetically-driven reaction. Thus, these seed crystals will also have an opportunity to grow beyond ~ 10 nm in size before branching commences, and the final morphology of the star polyhedral nanocrystals is primarily the cuboctahedrally-derived monocrystalline type. However, recall that the

entire amount of chloroauric acid was added dropwise over 40 seconds, whereas the growth of the initially-formed seed crystals may have been completed within the first five seconds of addition (from visual observations). The continued dropwise addition of gold during this secondary phase of growth seems to retard the branching phenomenon, resulting in nanocrystals with smaller rounded peaks, rather than the pronounced, well-defined branching typically observed for star polyhedral nanocrystals from the standard reaction protocol. This lends further support to our assertion that it is not only the strongly acidic pH of solution, but also the fast reaction kinetics that drive the branching phenomenon in this system.

7.4 CONCLUSIONS

In summary, we have thoroughly studied the formation, structure, and stability of star polyhedral gold nanocrystals produced in water by colloidal reduction with ascorbic acid. We have identified two distinct classes of star nanocrystals: multiple-twinned crystals with five-fold symmetry, and monocrystals, which correspond respectively to icosahedra and cuboctahedra with preferential growth of their exposed $\{111\}$ faces. In each case, the $\{111\}$ faces of the original Archimedean solid grow into tetrahedral pyramids. By assuming a star morphology, gold nanocrystals increase their proportion of exposed $\{111\}$ surfaces, and we propose that the accompanying reduction in surface energy could be the driving force behind star nanocrystal formation.

It was found that star polyhedral gold nanocrystals are metastable structures. They remain stable in solution for approximately 30 days, and within 60 days the product is nearly completely converted to rounded morphologies. The energy from an ultrasonic bath is sufficient to promote extensive coalescence in solution. However, when stored as a dry product on an amorphous carbon support film, star polyhedral gold nanocrystals

remain stable in excess of one year, and are able to withstand repeated irradiation by an electron beam with 200 kV accelerating voltage.

Star polyhedral nanocrystals can be obtained in good yield at a molar ratio of (40:1) [ascorbic acid molecules]:[gold atoms]. For much smaller excesses of ascorbic acid, no branching is observed, and the product consists of large spherical polycrystalline aggregates. At much larger excesses of ascorbic acid, the formation of super-stellated structures, or secondary branches emanating from primary branches, is observed. These super-stellated structures are irregular in shape and have poor structural stability.

We proposed that the two primary factors driving the formation of star polyhedral gold nanocrystals in this system are the strongly kinetically-driven reaction conditions, and the strongly acidic pH (~ 2) of solution. It was found that decreasing the rate of the initial phase of the reaction strongly favored the formation of monocrystalline star polyhedra. To explain this observation, we proposed a model for the growth of star polyhedral gold nanocrystals based on the concept of *in situ* generation of seed crystals, which are then directly consumed in the growth of star polyhedral nanocrystals. Slower initial rates of nuclei formation favor the formation of larger primary-sized seed crystals, which tend toward FCC cuboctahedral morphologies. The morphology of the seed crystals is stabilized by branching due to an increased proportion of exposed $\{111\}$ surfaces, resulting in primarily cuboctahedrally-derived monocrystalline stars.

Chapter 8: Aqueous Synthesis of Gold Nanocrystals via Reduction with Ascorbic Acid: Controlled Growth in the Presence of Bovine Serum Albumin

8.1 INTRODUCTION

From our study on the formation of star polyhedral gold nanocrystals in Chapter 7, we concluded that two critical conditions were required to obtain nanostructures with pronounced branched morphologies: (i) strongly kinetically-driven reaction, and (ii) strongly acidic pH of solution. I hypothesized that by negating these two conditions, we could return to the synthesis protocol outlined previously in Chapter 6, modify the reaction conditions to counteract the rapid kinetics and acidic pH, and obtain controlled dispersions of gold nanocrystals with well-defined sizes and morphologies, by reduction with ascorbic acid in the presence of bovine serum albumin (BSA). This modified synthesis protocol is the subject of the current Chapter.

To counter the fast reaction kinetics in the original synthesis, I employed a subtle approach that takes advantage of the complexation of BSA with ascorbic acid. In Chapter 6, we considered ascorbic acid molecules solely as reducing agent, and BSA protein molecules solely as surface-stabilizing agents for gold nanocrystals, without taking into account any potential interactions between ascorbic acid and BSA proteins. In fact, serum albumin is the physiological carrier of ascorbic acid through the bloodstream, (167) and the binding of ascorbic acid by serum albumin has been studied by dynamic dialysis (168,169) and ultrafiltration. (170) Ascorbic acid molecules exhibit a greatly diminished auto-oxidation rate when complexed with BSA, corresponding to 18% of the auto-oxidation rate of the unbound species. (104) In terms of our colloidal synthesis, this translates into a diminished capacity for complexed ascorbic acid

molecules to reduce ionic gold, and ultimately a slower nucleation rate for atomic gold clusters. Recall in Chapter 6, ascorbic acid was added to a pre-existing aqueous solution of ionic gold precursor and BSA protein. In the current work, we have allowed ascorbic acid to equilibrate with BSA protein in solution prior to the addition of ionic gold precursor. This will allow us to more fully exploit the effects of protein complexation on the auto-oxidation rate of ascorbic acid.

Acidic pH can easily be overcome by adding a base that lacks the capacity to reduce ionic gold, such as sodium hydroxide. The reduction potential of ascorbic acid is acutely sensitive to changes in pH. The difference in redox potential between ascorbic acid and chloroauric acid increases as solution pH increases, most markedly in the pH range of 8–12. (147) Accordingly, we would expect enhanced kinetics when the reaction is carried out in moderately basic conditions. Thus, by employing a combined approach that takes advantage of both BSA complexation and basic solution pH, we can adjust their relative contributions and ultimately achieve well-controlled synthesis conditions.

8.2 EXPERIMENTAL PROCEDURE

Synthesis. Gold nanocrystals were synthesized in air by reduction in a homogeneous solution at ambient conditions. Chloroauric acid trihydrate ($\text{HAuCl}_4 \cdot 3\text{H}_2\text{O}$; 99.9+%; Aldrich) was reduced in water and in the presence of bovine serum albumin (BSA; Fraction V – heat shock treated; Fisher) by ascorbic acid (L-ascorbic acid; ACS reagent grade; Aldrich). An aqueous solution of ionic gold was prepared by adding 1 g $\text{HAuCl}_4 \cdot 3\text{H}_2\text{O}$ to 25 mL of deionized water. All materials were used without further treatment. Three distinct sets of experiments were employed. All three types began with the preparation of an aqueous solution containing 2 mmol ascorbic acid and a variable amount of dissolved BSA protein. The solution was prepared in a 100 mL round bottom flask, and was allowed to equilibrate for 15 minutes under vigorous stirring.

In the first type of experiment, 0.5 mL of 0.10 M H₂AuCl₄ (50 μmol Au) was then added to the reaction vessel rapidly and under vigorous stirring. In the second type of experiment, 7.2 mL of 1.0M sodium hydroxide (NaOH; ACS reagent grade; Fisher) was added to the reaction vessel and allowed to equilibrate for 5 minutes under vigorous stirring prior to the addition of chloroauric acid. In the third type of experiment, chloroauric acid was added to the aqueous solution of ascorbic acid and BSA protein, followed 30 seconds later by the addition of 7.2 mL of 1.0M sodium hydroxide (7.2 mmol NaOH).

Table 8.1: Protein amounts for the various systems tested.

BSA (g)	BSA (μmol)	[Au]:[BSA]
0.2767	4.1667	12:1
0.2306	3.4722	72:5
0.1845	2.7777	18:1
0.1384	2.0833	24:1

Table 8.1 summarizes the amount of BSA protein used in each system investigated. The third column of this chart indicates the molar ratios of gold atoms to protein molecules. All ratios are calculated on the basis 50 μmol Au added to the system. For example, in the system where 2.0833 μmol BSA was added to the reaction, the ratio is calculated as [50 μmol Au]:[2.083 μmol BSA], or 24:1. For convenience, throughout this Chapter each system will be referenced by its molar ratio, for example “(24:1) Au:BSA.”

Characterization. Transmission electron microscopy (TEM) was performed using a JEOL 2010F transmission electron microscope equipped with Schottky-type field emission gun, ultra-high resolution pole piece ($C_s = 0.5$ mm), an Energy Dispersive X-

ray spectrometer (EDS), and a scanning transmission electron microscope (STEM) unit with high angle annular dark field (HAADF) detector operating at 200 kV. Samples for TEM analysis were prepared by allowing a drop of the aqueous product to evaporate on a lacey carbon-coated copper TEM grid. For the nanocrystals produced without addition of sodium hydroxide, size distributions were obtained from conventional TEM analysis, based on measurement of 100 crystals. For nanocrystals formed in the presence of sodium hydroxide, size distributions were obtained from HAADF analysis at high magnification, based on measurements of 500 crystals. The nanocrystals formed in each system were analyzed via EDS to confirm their elemental identity as gold. UV-visible absorption spectra in the range of 300-800 nm were obtained with a Varian Cary 5000 UV-vis NIR spectrometer. Samples for UV-visible absorption analysis were prepared by diluting the original reaction product with deionized water (a twenty-fold dilution by volume). Solution-phase analysis was performed at room temperature using a matched set of quartz cuvettes (path length 10 mm), and operating the spectrometer in dual beam mode. One cuvette was filled with the diluted reaction solution, while the second cuvette contained deionized water.

8.3 RESULTS AND DISCUSSION

8.3.1 Synthesis of Gold Nanocrystals via Addition of Chloroauric Acid to a Pre-Existing Aqueous Solution of Ascorbic Acid and BSA

In the initial stage of the current investigation, we decided to simply allow ascorbic acid to equilibrate with BSA protein for 15 minutes in solution prior to the addition of chloroauric acid. In this manner we studied the effects of protein complexation in our reaction system, prior to introducing a second layer of complexity with a variable solution pH. Recall in Chapter 6, the (24:1) Au:BSA system was the demarcation between aggregative and diffusional growth. Systems with greater excesses

of protein exhibited diffusional growth of nanocrystals in the size range of ~ 20 nm, while systems with smaller excesses of protein exhibited a substantial amount of aggregation-driven growth, and a larger average size ranging from ~ 35 – 50 nm. Thus, we decided to begin our study at a molar ratio of (24:1) [Au atoms]:[BSA molecules].

Comparing this system with the (24:1) Au:BSA system from Chapter 6, differences in reaction time and solution appearance were readily discernable. In the (24:1) Au:BSA system from Chapter 6, reaction time was ~ 10 seconds, and the final product was transparent with a deep blue-violet color. In contrast, when ascorbic acid and BSA were allowed to equilibrate in solution prior to the addition of chloroauric acid, the reaction time was ~ 60 seconds, and the final product consisted of an opaque gray suspension. Interestingly, if the auto-oxidation potential of ascorbic acid in the complexed form is $\sim 18\%$ of the free species, and if we assume the ascorbic molecules responsible for reduction of gold atoms in the (24:1) Au:AA system from Chapter 6 were primarily free species, we should expect a reaction time of ~ 56 seconds for the (24:1) Au:AA system where ascorbic acid molecules are complexed with BSA. This is only 6.6% less than the observed reaction time.

Characteristic TEM images of the two systems at identical magnifications are presented in Figure 8.1. The nanocrystals formed by addition of ionic gold to an equilibrated solution of ascorbic acid and BSA protein (Figure 8.1c-d) are an order of magnitude larger than those formed by addition of ascorbic acid to an aqueous solution of ionic gold and BSA (Figure 8.1a-b). The large polycrystalline spheres in the current system result from the aggregative growth of primary-sized nanocrystals. This type of aggregation-driven growth is commonly observed in gold nanocrystals formed by reduction in the presence of ascorbic acid. (43,147) Such extensive aggregation has a greater likelihood of occurring when larger primary-sized nanocrystals are involved, and

for a given number of gold atoms in solution, larger primary-sized crystals occur when fewer nuclei are initially formed. This confirms our assertion that by allowing ascorbic acid to complex with BSA and decreasing its auto-oxidation potential, we can decrease the nucleation rate for atomic gold clusters.

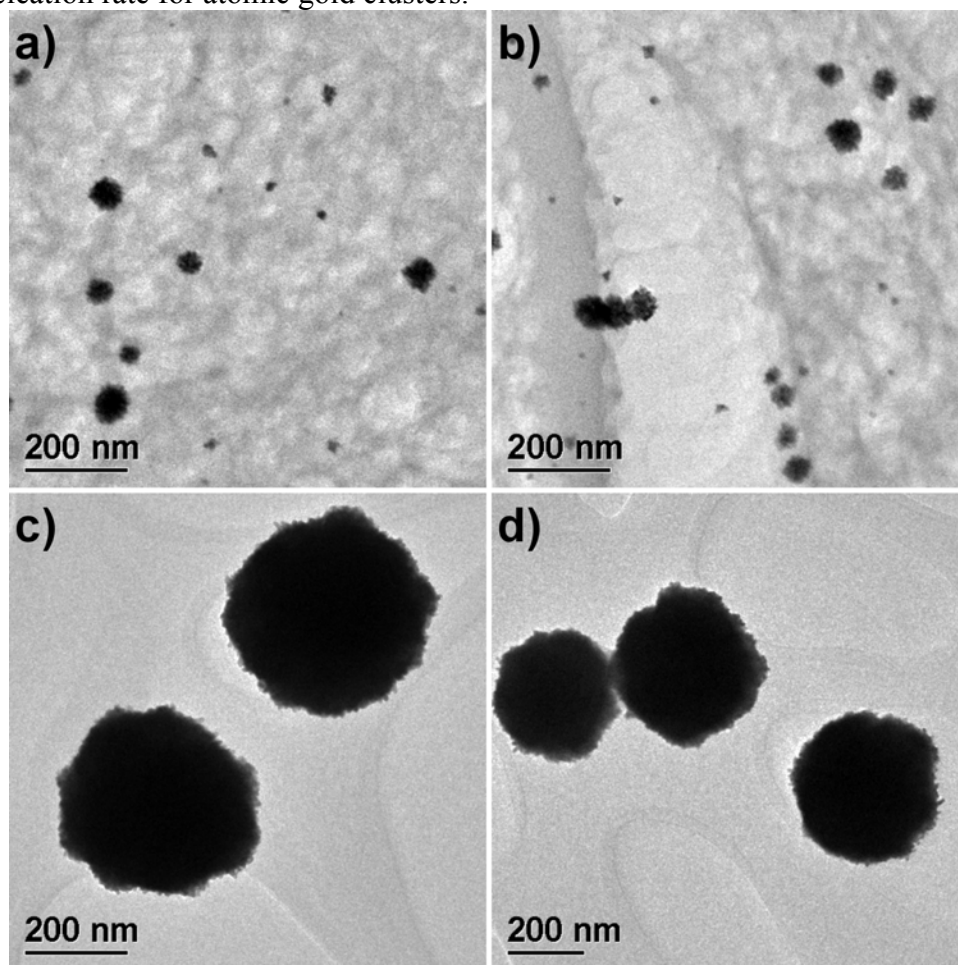


Figure 8.1: (24:1) Au:BSA systems at (40:1) AA:Au. (a)-(b) Addition of ascorbic acid to a pre-existing solution of BSA and ionic gold; (c)-(d) Addition of ionic gold to an equilibrated solution of ascorbic acid and BSA.

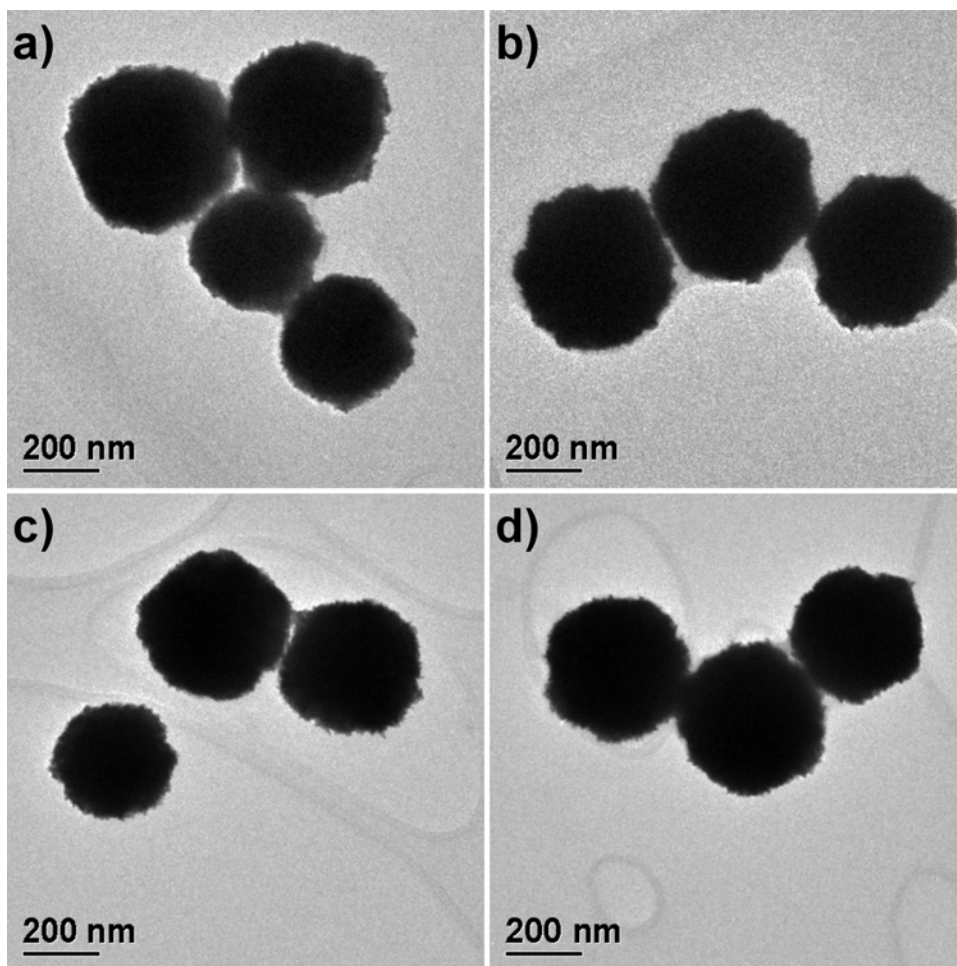


Figure 8.2: (24:1) Au:BSA systems formed by addition of ionic gold to an equilibrated solution of ascorbic acid and BSA protein. Molar ratios of ascorbic acid molecules to gold atoms (a)-(b) (40:1) AA:Au; (c)-(d) (160:1) AA:Au.

Before proceeding to study different protein concentrations, we wanted to investigate the effect of molar excess of ascorbic acid in the current system. Thus, in addition to the (40:1) AA:Au molar ratio (2 mmol ascorbic acid per 50 μ mol Au) used throughout the remainder of this Chapter, the experiments in this section were also conducted with molar ratios of (160:1) AA:Au (8 mmol ascorbic acid per 50 μ mol Au). In terms of reaction time and solution appearance, no notable difference was observed, as was the case in Chapter 6. Characteristic TEM images of the two systems at identical

magnifications are presented in Figure 8.2. The average diameter of polycrystalline spheres produced with a molar ratio of (160:1) AA: Au (Figure 8.2c-d) was ~15% less than the average diameter found at (40:1) AA: Au (Figure 8.2a-b). Since a noticeable difference was observed, we studied the remaining protein concentrations in this section at molar ratios of (40:1) AA: Au and (160:1) AA: Au.

With conventional TEM analysis, it was noted that although the majority of nanocrystals exhibited a noticeable degree of surface roughness, some crystals appeared to have smoother surfaces, such as those seen in Figure 8.3a. To determine if this was indeed the case, we turned to HAADF analysis. Recall that HAADF images are formed by electrons that have undergone high angle scattering. Thus, any feature of the crystal that increases high angle scattering will be reflected in the HAADF image contrast. (62,63) On the surface of a polycrystalline aggregate, as the electron beam passes through one primary-sized crystal and enters a neighboring primary-sized crystal with a different crystallographic orientation, the probability for high-angle scattering of electrons increases. Thus, the surface roughness resulting from the polycrystallinity of large spherical aggregates should be clearly discernable in HAADF analysis. From Figure 8.3b, HAADF imaging reveals that even spherical aggregates that appear to have smooth surfaces in conventional TEM analysis (Figure 8.3a) actually exhibit a notable degree of surface roughness.

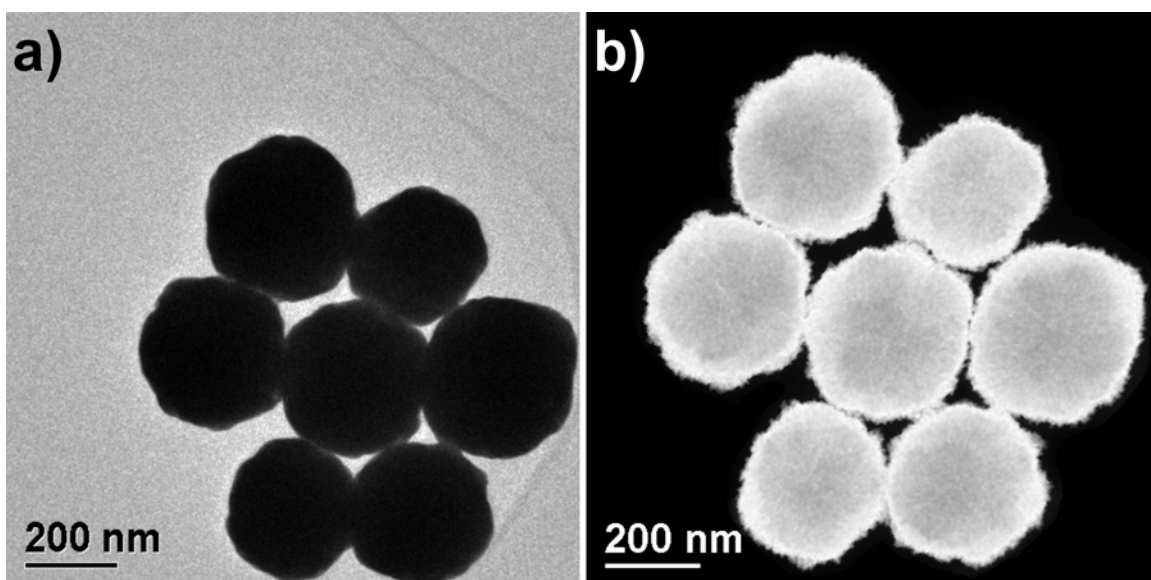


Figure 8.3: Crystals produced in the (24:1) Au:BSA system at a molar ratio of (160:1) AA:Au. (a) Conventional TEM analysis; (b) HAADF analysis, revealing surface roughness of the crystals.

Size distributions were obtained from conventional TEM analysis based on the measurement of 100 crystals. Figure 8.4 presents the size distributions for the (24:1) Au:BSA systems, where ionic gold was added to an equilibrated solution of ascorbic acid and BSA protein. The reaction time was ~60 seconds, as mentioned previously. The measured distribution of the (40:1) AA:Au system was 415 ± 45 nm, or a standard deviation of 10.8%, while for the (160:1) AA:Au system, the distribution was 355 ± 60 nm, or a deviation of 16.9%. Comparing the two reaction conditions, the (160:1) AA:Au system provides nanocrystals with an average diameter 14.5% less than the (40:1) AA:Au, but with a 6% broader percentage deviation.

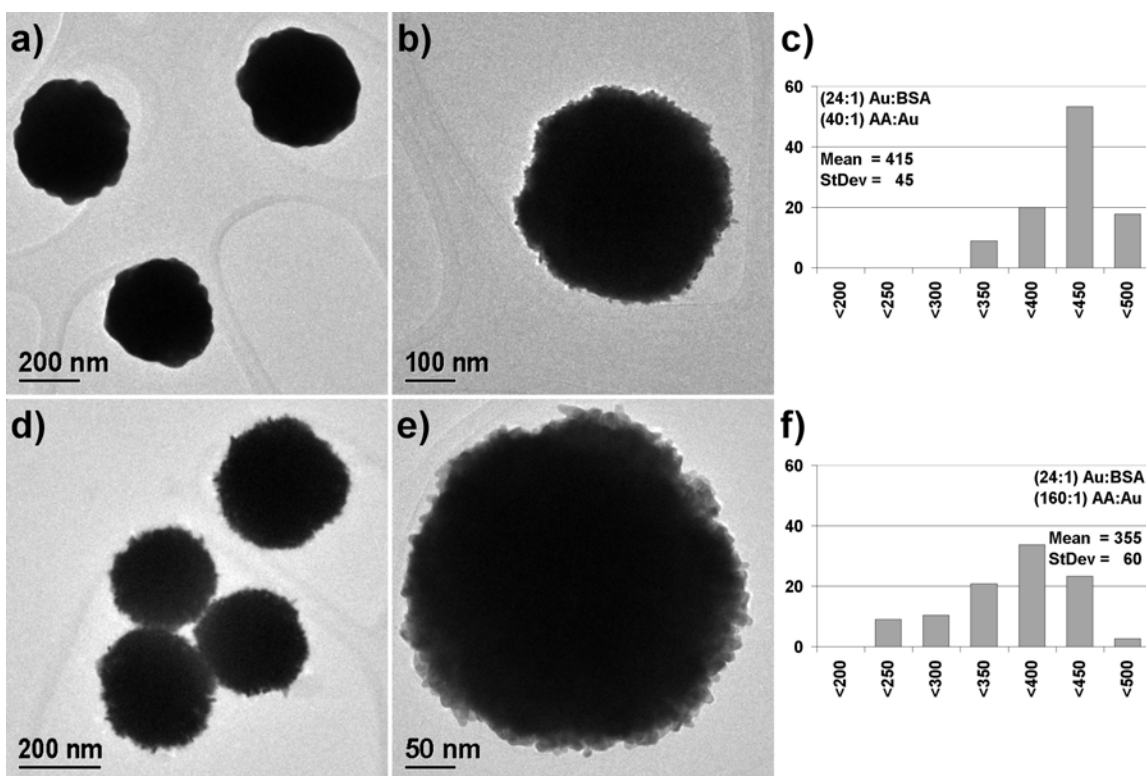


Figure 8.4: Size distributions for (24:1) Au:BSA system. (a) Low-magnification TEM, (b) TEM image of a typical nanocrystal, and (c) size distribution at (40:1) AA:Au. (d) Low-magnification TEM, (e) TEM image of a typical nanocrystal, and (f) size distribution at (160:1) AA:Au.

At this point, we wanted to explore greater excesses of protein, since in Chapter 6 we learned that more excess protein produced smaller nanocrystals resulting from diffusional growth. Accordingly, we set out to conduct experiments at a molar ratio of (12:1) Au:BSA. However, no reaction occurred at (12:1) Au:BSA in over 48 hours. The reaction time measured for (12:1) Au:BSA in Chapter 6 was ~50 seconds, and assuming an auto-oxidation rate 18% of the free species, we might expect reduction of ionic gold by BSA-complexed ascorbic acid molecules to take ~280 seconds. At first glance, the fact that no reaction was observed within two days was puzzling. However, we realized that as in Chapter 6 when we had treated ascorbic acid solely as a reducing agent and had

neglected potential interactions with BSA protein, we were now considering chloroauric acid solely as an ionic precursor, and neglecting any possible interaction with BSA protein. In fact, serum albumin binds metal ions, (83,84) as well as chlorides and chloride complexes. (85,86) With sufficient excess of protein, and combined with the diminished auto-oxidation rate of BSA-complexed ascorbic acid, many gold ions can form complexes with protein molecules before they can be reduced, severely impeding the reaction.

Since no reaction was observed at (12:1) Au:BSA, we sought the maximum relative protein concentration that would yield a reaction within 24 hours, in order to determine if any trend toward diffusional growth was discernable. We began by investigating the molar ratio of (18:1) Au:BSA. The measured reaction time was 270 seconds. From Figure 6.6, we would expect that if reduction of gold atoms was accomplished by free species, the reaction time would be ~16 seconds. Assuming an auto-oxidation potential 18% of the free species, we would predict a reaction time of 90 seconds for this system. With an actual reaction time 200% greater than predicted, complexation of ionic gold prior to reduction is already having a significant effect in the (18:1) Au:BSA system.

Figure 8.5 presents the size distributions for the (18:1) Au:BSA systems. The measured distribution of the (40:1) AA:Au system was 360 ± 35 nm, or a standard deviation of 9.7%, while for (160:1) AA:Au, the distribution was 270 ± 40 nm, a deviation of 14.8%. Comparing the two reaction conditions, (160:1) AA:Au provides nanocrystals with an average diameter 25% less than (40:1) AA:Au, but with a 5% broader percentage deviation.

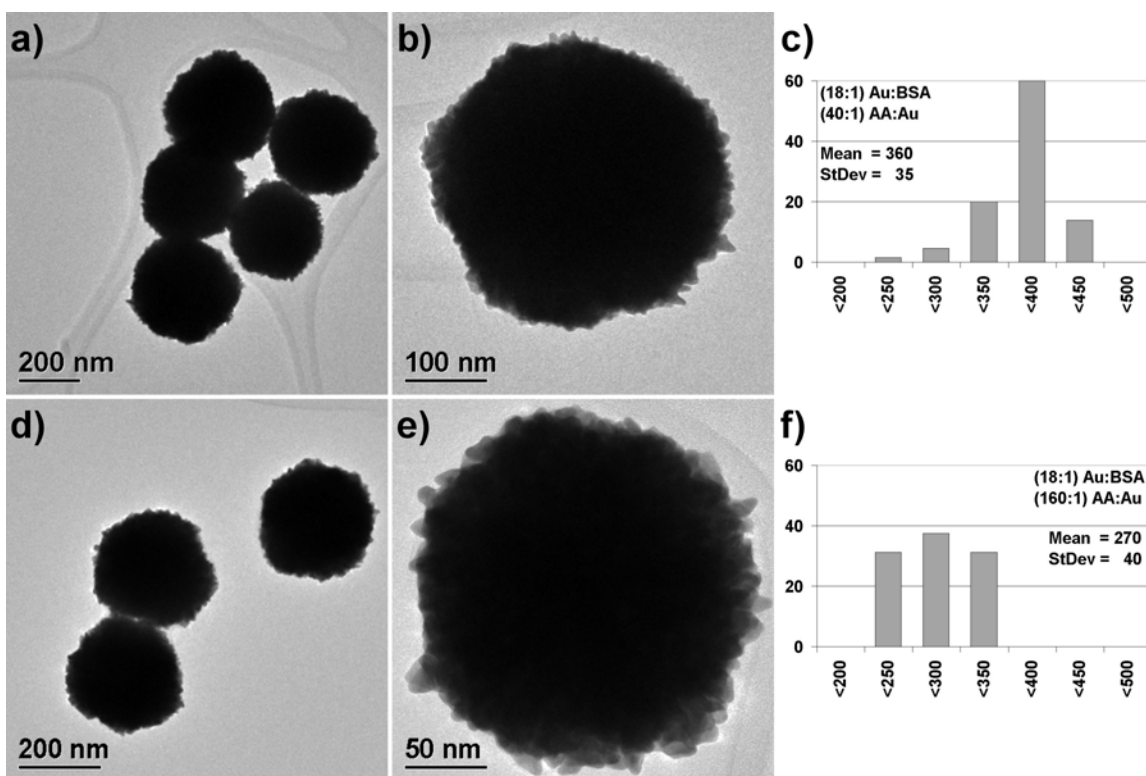


Figure 8.5: Size distributions for (18:1) Au:BSA system. (a) Low-magnification TEM, (b) TEM image of a typical nanocrystal, and (c) size distribution at (40:1) AA:Au. (d) Low-magnification TEM, (e) TEM image of a typical nanocrystal, and (f) size distribution at (160:1) AA:Au.

Finally, the measured reaction time at a molar ratio of (72:5) Au:BSA was ~24 hours. Assuming an auto-oxidation potential 18% of the free species, using Figure 6.6 we would predict a reaction time of 160 seconds for this system. Clearly, the combination of complexation of ionic gold and decreased auto-oxidation of complexed ascorbic acid has a profound effect on the (72:5) Au:BSA system. Figure 8.6 presents the size distributions for this system. The measured distribution of the (40:1) AA:Au system was 240 ± 25 nm, or a standard deviation of 10.4%, while for (160:1) AA:Au, the distribution was 170 ± 25 nm, a deviation of 14.7%. Comparing the two reaction

conditions, (160:1) AA:Au provides nanocrystals with an average diameter 30% less than (40:1) AA:Au, but with a 4% broader percentage deviation.

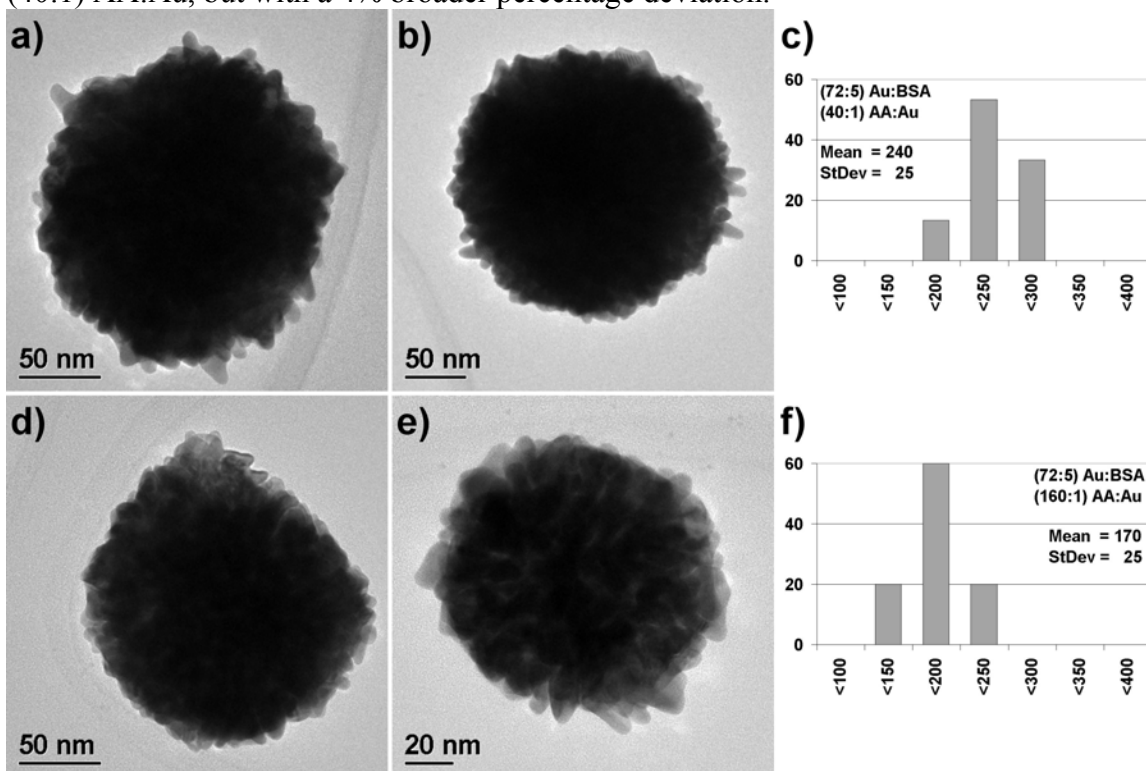


Figure 8.6: Size distributions for (72:5) Au:BSA system. (a)-(b) TEM images of typical nanocrystals, and (c) size distribution at (40:1) AA:Au. (d)-(e) TEM images of typical nanocrystals, and (f) size distribution at (160:1) AA:Au.

Comparing the (24:1) Au:BSA, (18:1) Au:BSA, and (72:5) Au:BSA systems, we make four observations. First, for all protein concentrations studied, the final product was the result of aggregation-driven growth of primary-sized nanocrystals. Second, for a given excess of ascorbic acid, the average size of the polycrystalline aggregates decreases with increasing protein concentrations. This can be attributed to BSA molecules limiting the extent of aggregative growth. Third, the reaction time increases precipitously with increasing protein concentrations. We propose this is a result of the combined effects of protein complexation with ascorbic acid and chloroauric acid, as discussed previously.

Fourth, for a given protein concentration, greater excesses of ascorbic acid result in smaller polycrystalline aggregates, but also a broader percentage standard deviation. This suggests that in the (160:1) AA: Au systems, not all ascorbic acid molecules are complexed with BSA. Free ascorbic acid molecules could increase the initial rate of reduction of ionic gold, resulting in more nuclei formed. As the free ascorbic acid molecules are consumed, the reduction rate gradually slows. In this transient phase, some primary-sized crystals continue growing by diffusion, while others begin to aggregate. This variability is reflected in a broader percentage distribution of the final product.

Returning to the (72:5) Au:BSA system, in Figure 8.6a-b and d-e, we observe several pronounced, elongated primary-sized crystals protruding from the edges of the polycrystalline spheres. These elongated structures are reminiscent of the elongated, branched, and concave gold nanocrystals previously documented in Chapter 6. It seems that the strongly acidic pH alone is sufficient to drive the formation of elongated primary-sized nanocrystals. In Figure 8.6e, we can observe variations in contrast within the body of the aggregate, corresponding to variations in the internal structural. This type of structural variation is expected for polycrystalline spheres, which possess lower internal densities and higher numbers of internal grain boundaries than crystals that result from diffusional growth. (147)

HAADF analysis was employed to examine the internal structure of the polycrystalline aggregates in the (18:1) Au:BSA system. Figure 8.7 presents an analysis of two representative polycrystalline aggregates. Variations in contrast within the body of the crystals are observed in Figure 8.7b and d. These variations appear similar to the topographical information supplied by SEM, and might be misinterpreted as resulting from surface features. However, recall that HAADF images are acquired in scanning transmission mode, and thus are formed by electrons that have passed through the entire

sample. As a result, the observed contrast results from internal density variations and internal grain boundaries that electrons experience as they travel through the polycrystalline aggregate. Additionally, note the irregular primary-sized crystals protruding from the perimeter of the polycrystalline aggregates.

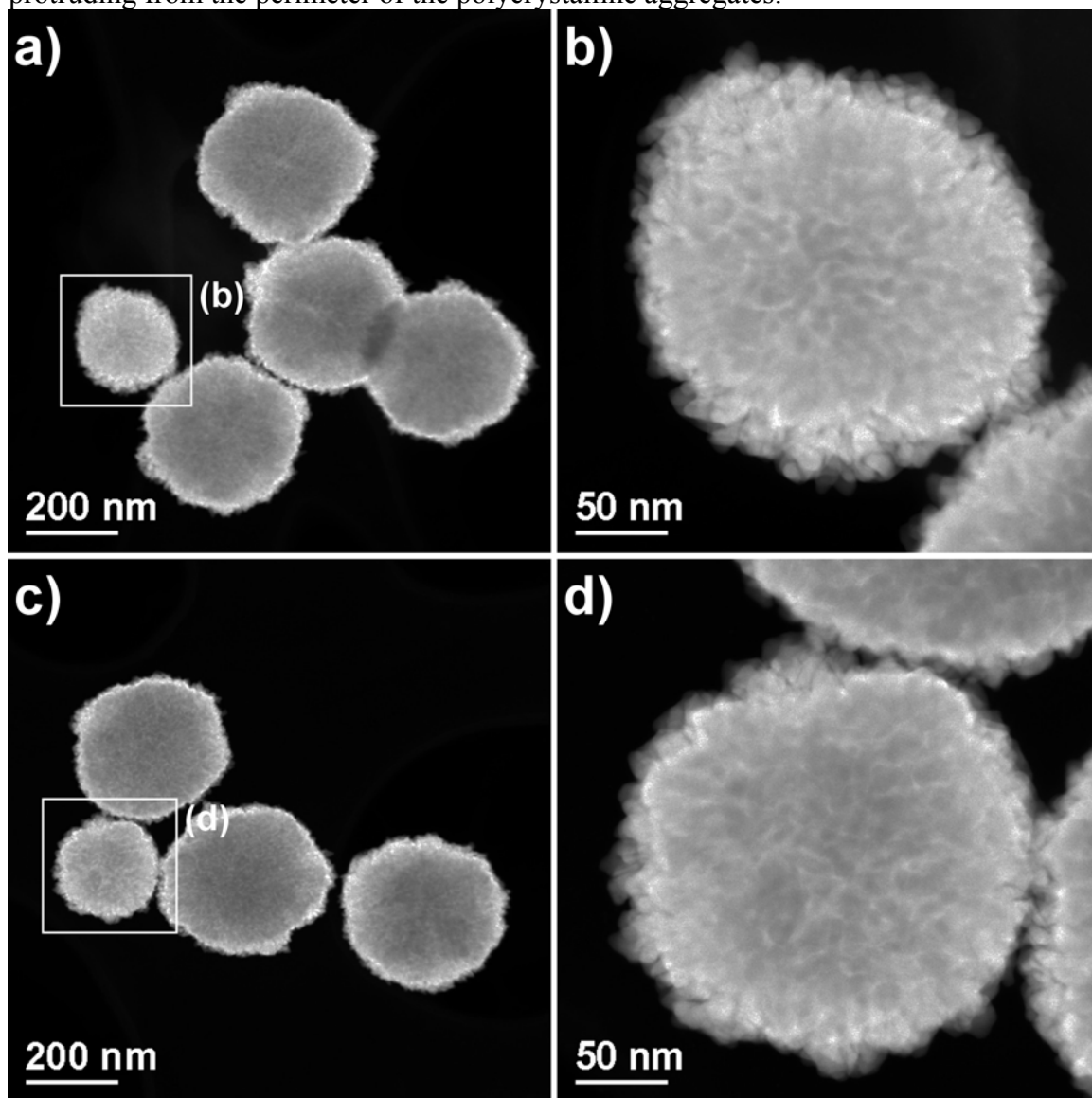


Figure 8.7: HAADF analysis of the internal structure of polycrystalline spheres in the (18:1) Au:BSA system. The boxed region in (a) is presented at higher magnification in (b), and the boxed region in (c) is presented at higher magnification in (d).

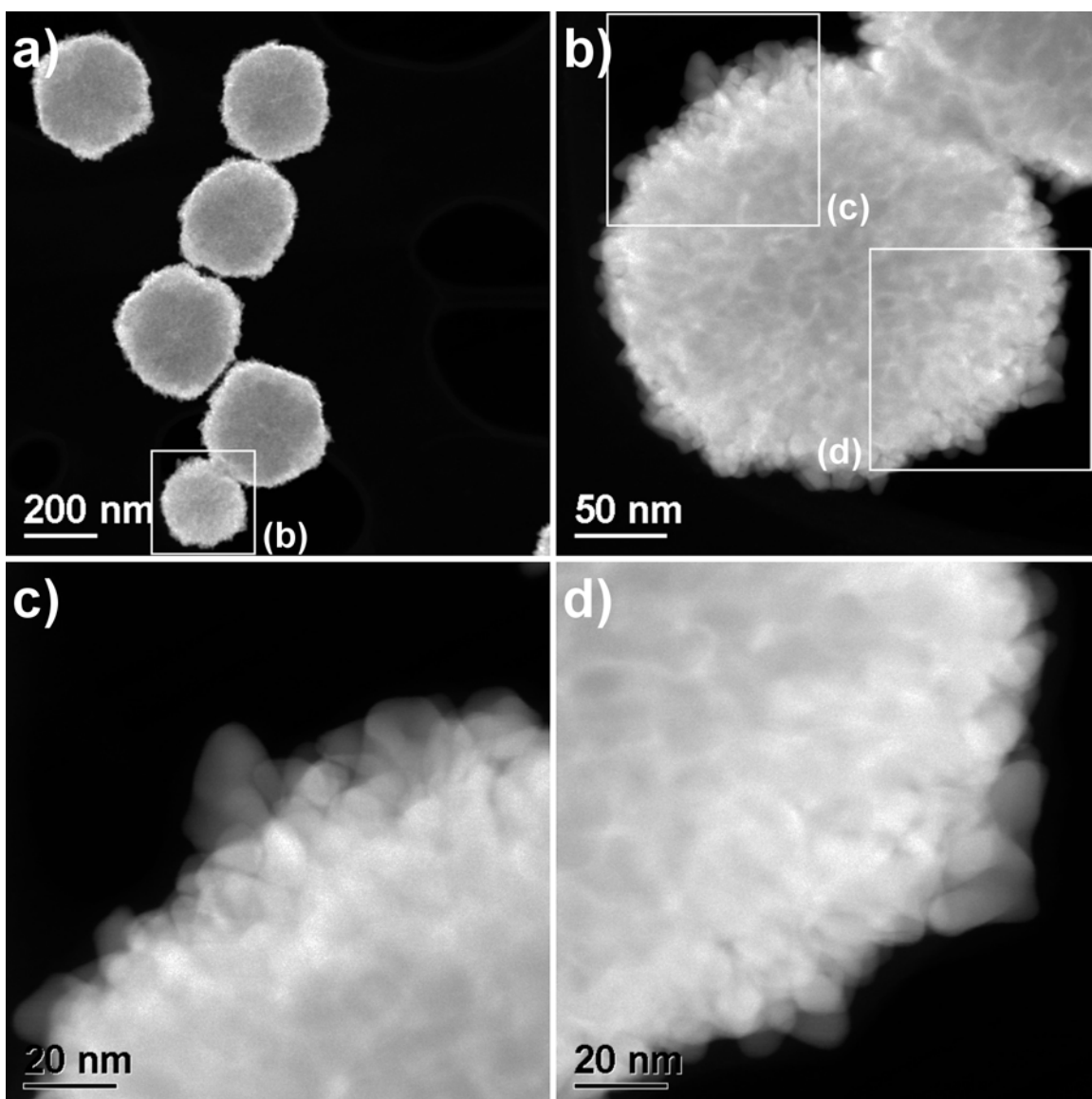


Figure 8.8: HAADF analysis of the primary-sized crystals visible along the perimeter of the polycrystalline spheres in the (18:1) Au:BSA system. The boxed region in (a) is presented at higher magnification in (b), and the boxed regions in (b) are presented at higher magnification in (c) and (d), respectively.

To further examine the structure of the primary-sized crystals constituting the overall polycrystalline structure, high-magnification HAADF analysis was employed, as demonstrated in Figure 8.8. Several elongated primary-sized crystals are visible in

Figure 8.8c-d. As noted in the TEM analysis of the (72:5) Au:BSA aggregates (Figure 8.6a-b and d-e), these elongated crystals are reminiscent of the primary-sized nanocrystals produced in Chapter 6.

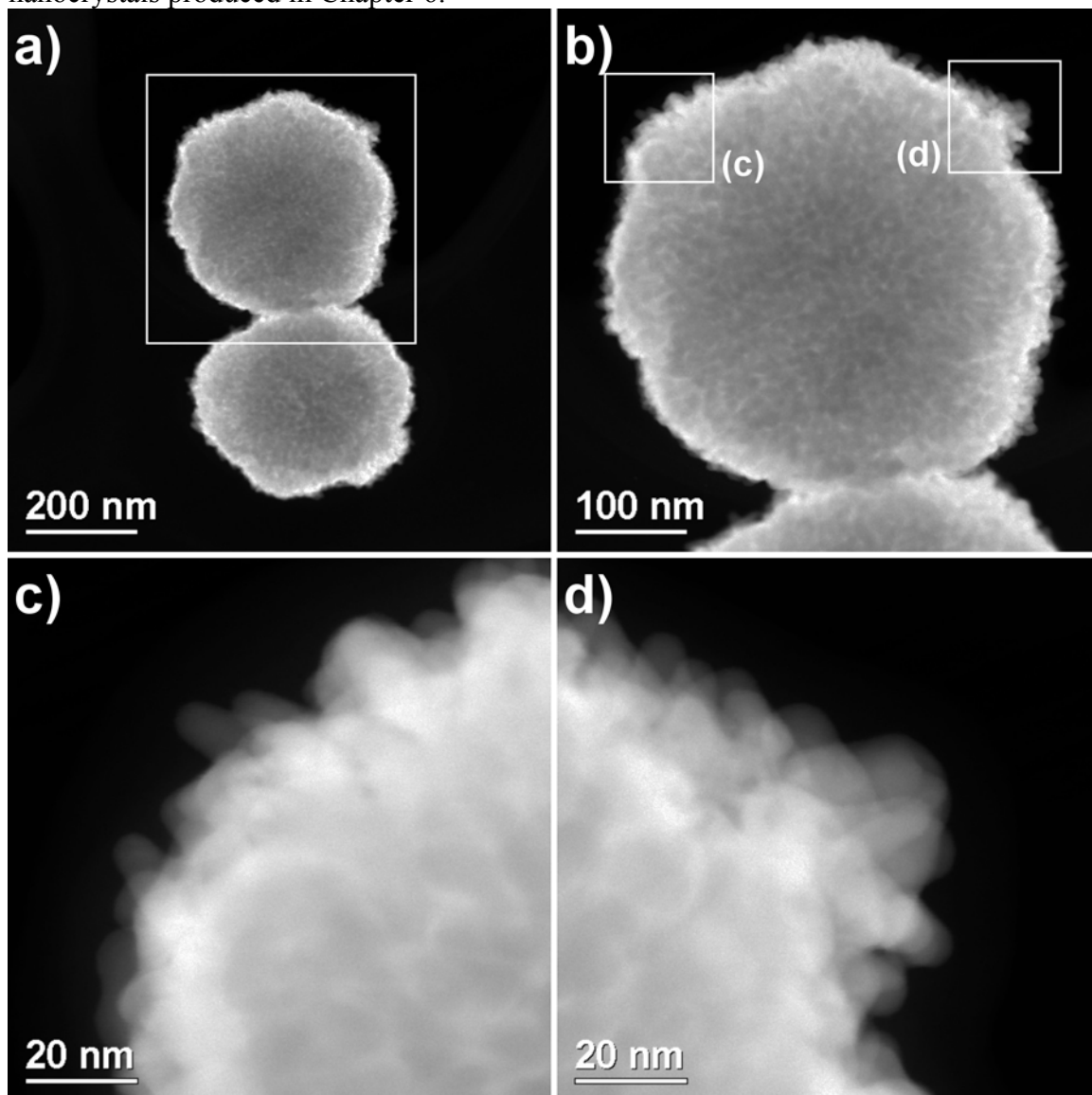


Figure 8.9: HAADF structural analysis of a polycrystalline aggregate produced in the (24:1) Au:BSA system at a molar ratio of (40:1) AA:Au. The boxed region in (a) is presented at higher magnification in (b), and the boxed regions in (b) are presented at higher magnification in (c) and (d), respectively.

To examine any potential structural variations resulting from the molar excess of ascorbic acid employed, a comparative HAADF analysis was undertaken of polycrystalline aggregates produced at (24:1) Au:BSA with molar ratios of (40:1) AA: Au and (160:1) AA: Au. Figure 8.9 presents an HAADF analysis of a typical polycrystalline aggregate in the (24:1) Au:BSA system with a molar ratio of (40:1) AA: Au. The contrast within the body of the crystal observed in Figure 8.9b results from internal density variations and internal grain boundaries. Elongated primary-sized crystals are clearly visible along the perimeter of the polycrystalline aggregate in Figure 8.9c-d.

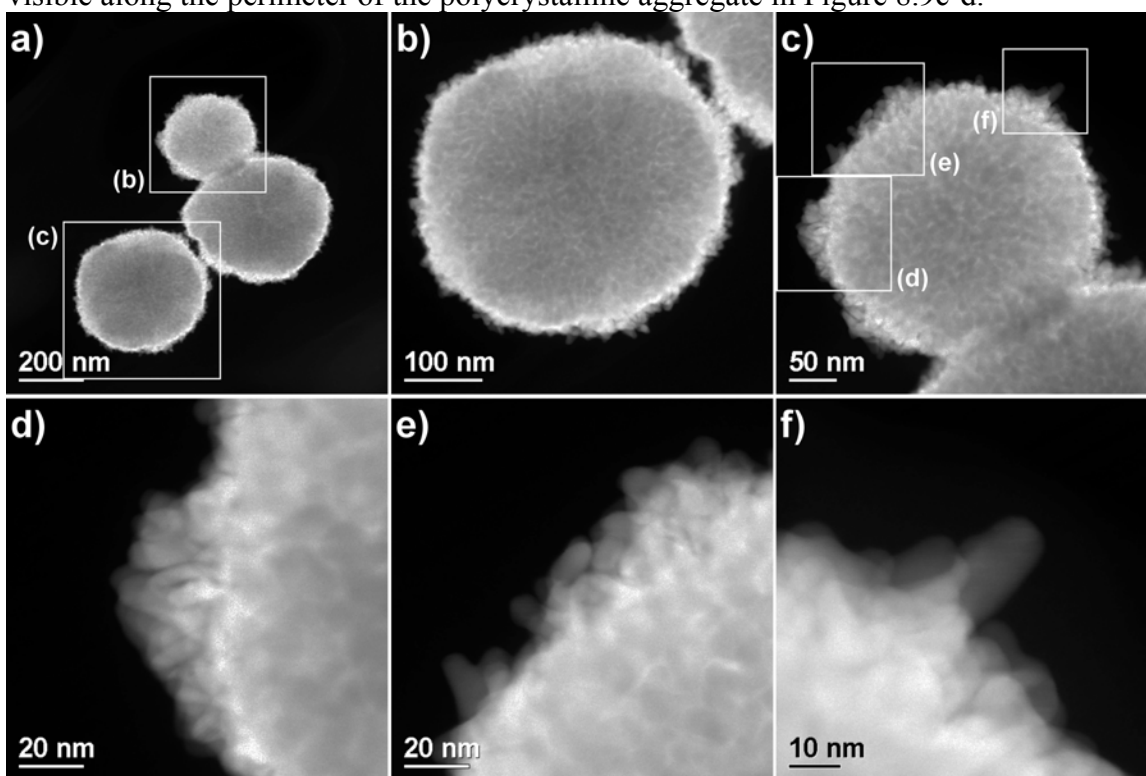


Figure 8.10: HAADF analysis of polycrystalline aggregates produced in the (24:1) Au:BSA system at a molar ratio of (160:1) AA: Au. The boxed regions in (a) are presented at higher magnification in (b) and (c), respectively, and the boxed regions in (c) are presented in (d)-(f), respectively.

Figure 8.10 presents an HAADF analysis of two typical polycrystalline aggregates in the (24:1) Au:BSA system with a molar ratio of (160:1) AA:Au. The observed contrast within the body of the crystals in Figure 8.10b-c is symptomatic of variations in the internal crystal structure. High-magnification HAADF images of the perimeter of the crystal in Figure 8.10c are presented in Figures 8.10d-f. A large number of elongated primary-sized crystals are clearly visible along the perimeter of the polycrystalline aggregate.

In summary, by allowing ascorbic acid and BSA to equilibrate in solution prior to the addition of ionic gold, but conducting the reaction at an acidic solution pH, the product consisted of large polycrystalline spheres with average diameters ranging from 170–415 nm, depending on the protein concentration. These polycrystalline spheres resulted from aggregation of primary-sized nanocrystals with pronounced elongated morphologies. Reaction times increased precipitously with increasing protein concentrations. A molar ratio of (160:1) AA:Au produced aggregates with smaller average diameters, but larger percentage deviations, which could be due to the presence of non-complexed ascorbic acid species. Since one of our stated goals in this investigation was to exploit complexation of ascorbic acid with BSA, subsequent experiments were only conducted at a molar ratio of (40:1) AA:Au.

8.3.2 Synthesis of Gold Nanocrystals via Addition of Chloroauric Acid to a Pre-Existing Aqueous Solution of Ascorbic Acid, BSA, and Sodium Hydroxide

Having studied the effects of protein complexation on our reaction system, we proceeded to introduce the second aspect of our modified synthesis protocol. In this set of experiments, after allowing ascorbic acid to equilibrate with BSA in solution for 15 minutes, 7.2 mmol sodium hydroxide was added to the reaction vessel under vigorous stirring. Recall from Chapters 3 and 4 that from the moment sodium borohydride was

introduced in the reaction solution, vigorous protein foaming was observed. In contrast, no protein foaming occurred upon the introduction of sodium hydroxide. This suggests the vigorous protein foaming observed in the sodium borohydride reduction was not a result of pH effects. As sodium borohydride is oxidized to sodium metaborate, hydrogen gas is liberated, and this evolved gas could be the source of the observed protein foaming in Chapters 3 and 4.

After allowing the sodium hydroxide to equilibrate in solution for 5 minutes, 50 μmol chloroauric acid was added rapidly and under vigorous stirring. From the instant the first drops of chloroauric acid were added, the solution turned from a transparent pale yellow to a dark black-violet color. This color change appeared to be complete precisely when the final drop of chloroauric acid entered the solution, within less than 0.5 seconds. This is in agreement with the rapid reaction time (much less than 1 second) measured in Chapter 7 when the reduction of chloroauric acid by ascorbic acid was carried out in the presence of NaOH.

Size distributions were obtained from HAADF analysis at high magnification, based on the measurement of 500 crystals. The distribution for the (24:1) Au:BSA system in the presence of sodium hydroxide is presented in Figure 8.11a. The reaction was complete within 0.5 seconds, compared with ~ 60 seconds for (24:1) Au:BSA in the absence of sodium hydroxide. The measured distribution was 6.444 ± 2.349 nm, or a standard deviation of 36.5%. Nearly 40% of the product consisted of rounded nanocrystals with diameters ranging from 2.5–5.0 nm. However, 9% of the product consisted of nanocrystals with dimensions larger than 10 nm.

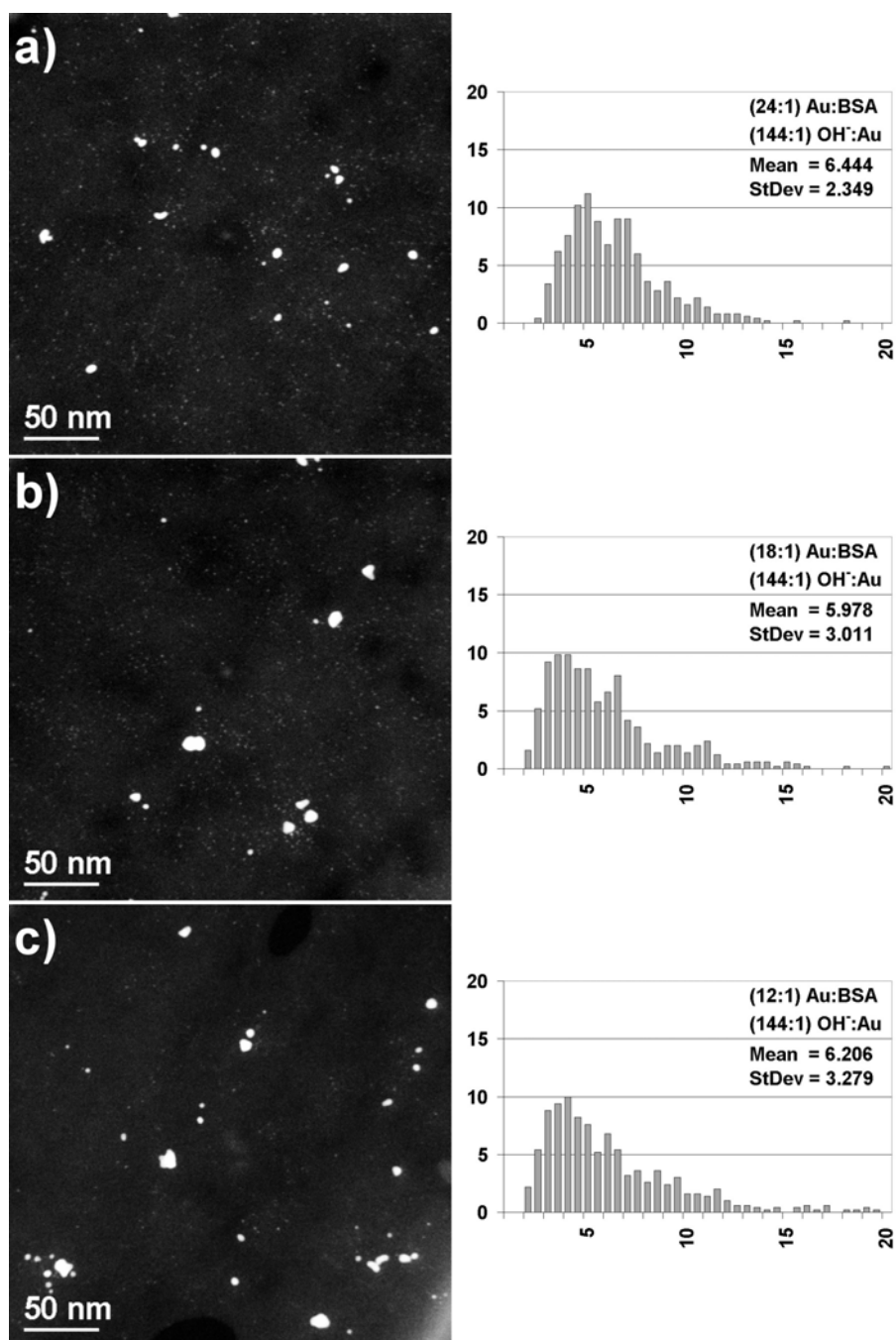


Figure 8.11: Nanocrystals formed by the addition of ionic gold to a pre-existing solution of ascorbic acid, BSA, and sodium hydroxide. Representative HAADF image and size distribution for (a) (24:1) Au:BSA; (b) (18:1) Au:BSA; (c) (12:1) Au:BSA. Size distributions depict nanocrystal diameter in nanometers versus percentage frequency.

The size distribution for the (18:1) Au:BSA system in the presence of sodium hydroxide is presented in Figure 8.11b. The reaction was complete within 0.5 seconds, compared with ~300 seconds for (18:1) Au:BSA in the absence of sodium hydroxide. The measured distribution was 5.978 ± 3.011 nm, or a standard deviation of over 50%. Nearly 53% of the product consisted of rounded crystals with diameters ranging from 2.25–5.00 nm, while 11.5% consisted of crystals with dimensions larger than 10 nm.

Finally, the size distribution for the (12:1) Au:BSA system in the presence of sodium hydroxide is presented in Figure 8.11c. This reaction was complete within 0.5 seconds, while no reaction was observed within 48 hours for (12:1) Au:BSA in the absence of sodium hydroxide. The measured distribution was 6.206 ± 3.279 nm, or a standard deviation of nearly 53%. Over 51% of the product consisted of rounded nanocrystals with diameters ranging from 2.00–5.00 nm, while 12.6% of the product consisted of nanocrystals with dimensions larger than 10 nm.

The addition of sodium hydroxide has a dramatic effect on reaction kinetics and the resulting nanocrystal morphologies. For acidic conditions, the reaction products consisted of polycrystalline aggregates with diameters ranging from 170–415 nm, while under basic conditions, the product consisted of rapidly-formed nanocrystals resulting from diffusional growth, with average diameters of ~6 nm. It was found that a minimum of 7.2 mmol sodium hydroxide was needed to eliminate aggregation-driven growth from the system. When smaller concentrations of sodium hydroxide were employed, the reaction products consisted of a mixture of small crystals formed by diffusional growth, as seen in Figure 8.11, and large polycrystalline aggregates (e.g. Figures 8.4-6). With 7.2 mmol sodium hydroxide added to the system, the pH of the reaction products was ~9. Larger concentrations of sodium hydroxide were avoided, due to the structural isomerization of BSA that occurs beyond pH~10. (89,90)

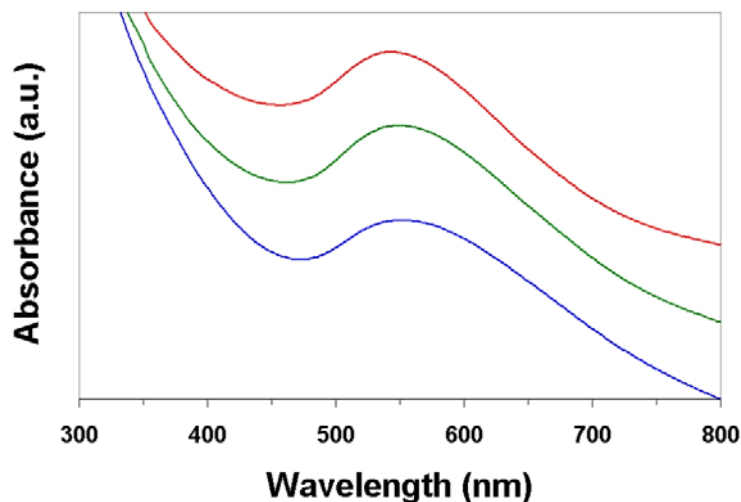


Figure 8.12: UV-visible absorption spectra resulting from addition of ionic gold to a pre-existing solution of ascorbic acid, BSA, and sodium hydroxide. From bottom to top, the spectra are (12:1) Au:BSA (Blue), (18:1) Au:BSA (Green), and (24:1) Au:BSA (Red).

UV-visible absorption spectra in the range of 300–800 nm were obtained for these three systems, depicted in Figure 8.12. Each system exhibits an asymmetric absorbance maximum that can be deconvoluted into two different curves, one centered at ~525 nm, the other at ~605 nm. As discussed in Chapter 6, the curve centered at ~525 nm can be attributed to the rounded, sub-20 nm crystals present in the system, while the curve centered at ~605 nm can be attributed to the elongated, branched, and concave nanocrystals that constitute the larger fraction of the product distribution. The location of the absorbance maximum is red-shifted from ~540 nm in the (24:1) Au:BSA spectrum, to ~550 nm for both the (18:1) Au:BSA and (12:1) Au:BSA spectra. This red-shift stems from differences in relative intensity of the deconvoluted curves, with the (24:1) Au:BSA spectrum having a smaller contribution from the ~605 nm curve than the other two systems. This is consistent with the size distributions in Figure 8.11, which indicate that (24:1) Au:BSA has a smaller percentage of nanocrystals with dimensions greater than 10

nm. Additionally, HAADF analysis revealed the largest nanocrystals in the (24:1) Au:BSA system were primarily rounded, whereas several of the largest crystals in the (18:1) Au:BSA and (12:1) Au:BSA systems were elongated, branched, or concave. Such anisotropic morphologies exhibit a red-shifted surface plasmon resonance. (148,149)

From Figure 8.11, the (18:1) Au:BSA and (12:1) Au:BSA systems possess the broadest size distributions, with standard deviations greater than 50%. These two systems also exhibit the most varied morphologies among nanocrystals with dimensions greater than 10 nm. Therefore, we determined to study these two systems via high-resolution TEM (HRTEM). We begin with the (18:1) Au:BSA system. Nanocrystals in this system larger than 10 nm primarily consisted of multiply-branched crystals (Figure 8.13), and elongated crystals (Figure 8.14).

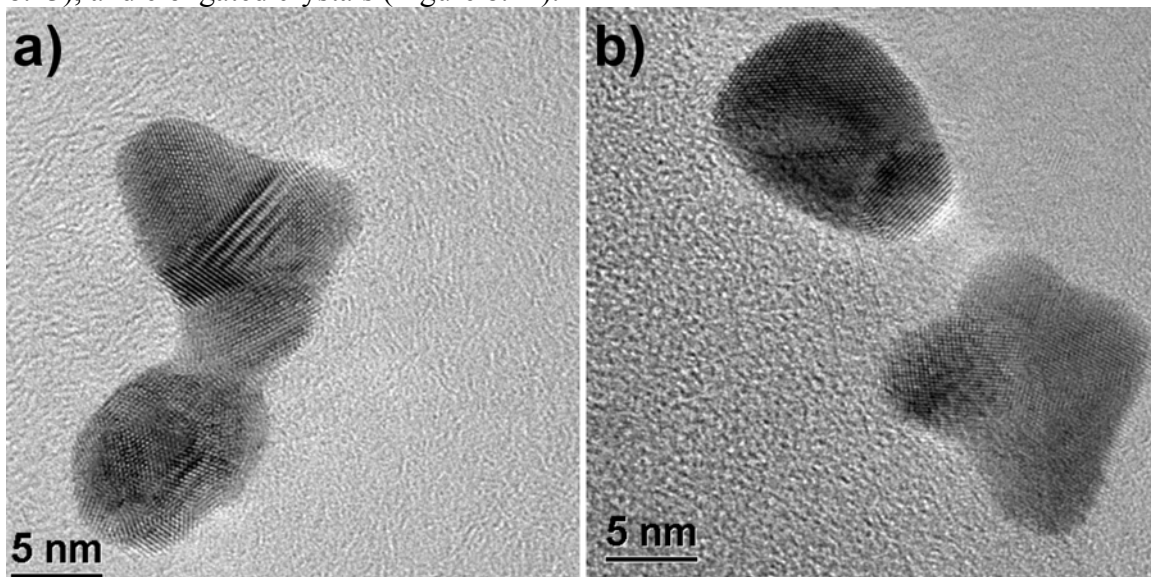


Figure 8.13: (18:1) Au:BSA HRTEM – Multiply-branched nanocrystals. (a) Gold tripod coalesced with a concave nanocrystal. (b) Gold tetrapod (lower right), in close proximity to an elongated multiple-twinned crystal with fivefold symmetry (upper left).

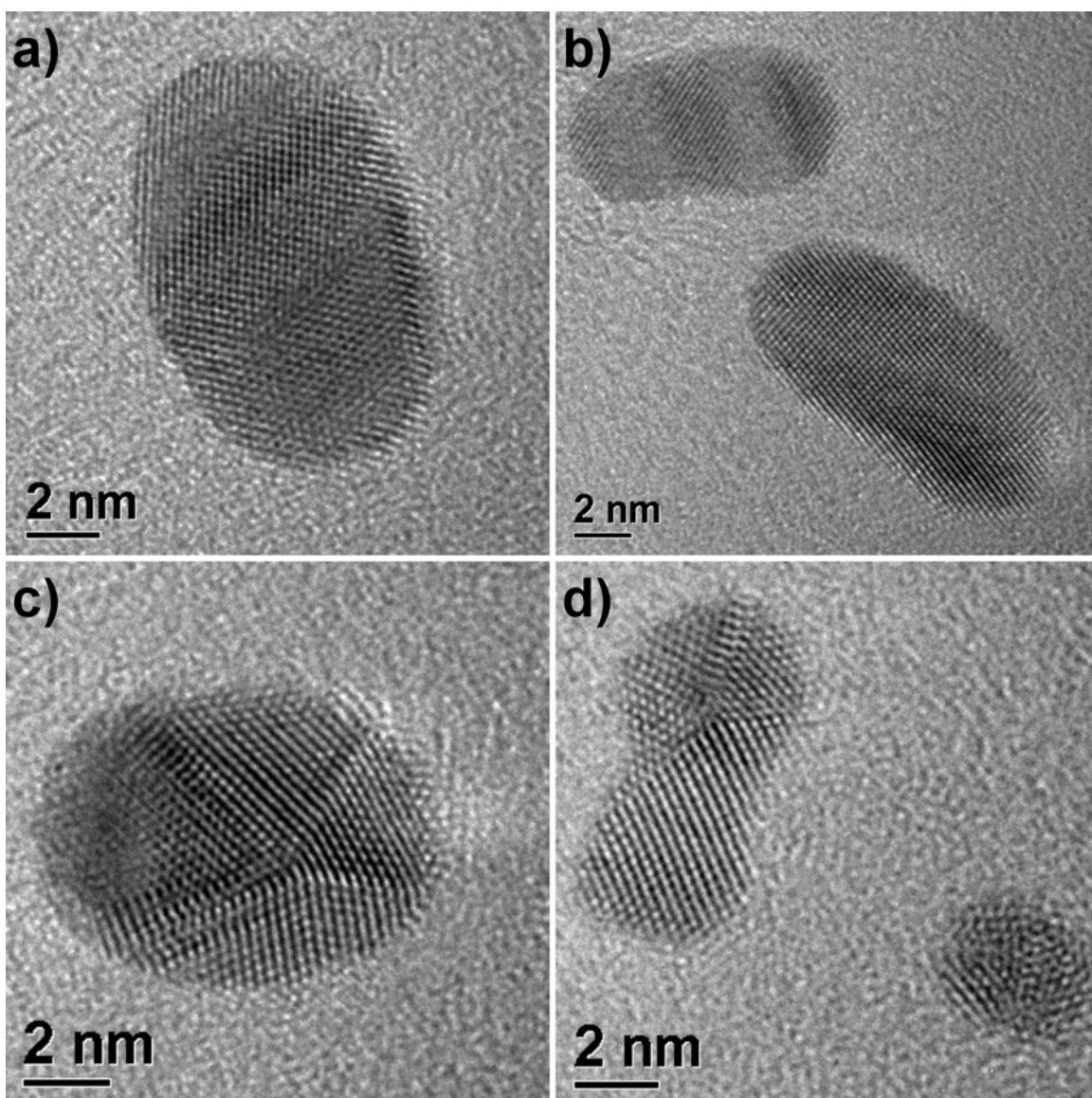


Figure 8.14: (18:1) Au:BSA HRTEM – Elongated nanocrystals. (a)-(b) Lamellar twinning orthogonal to the direction of elongation. (c)-(d) multiple-twinned crystals with fivefold symmetry, exhibiting preferential growth of specific monocrystalline domains.

Two distinct classes of elongated crystals were identified. The first type exhibited lamellar twinning planes orthogonal to the direction of elongation (Figure 8.14a-b). These crystals exhibited the largest aspect ratios, and also the most variability in length.

The second type of elongated structure arose from multiple-twinned crystals with fivefold symmetry, in which at least one monocrystalline domain exhibited preferential growth at the expense of other domains (Figure 8.14c-d). These crystals were limited to an aspect ratio of ~ 2 , most likely due to the increasing lattice strain imposed upon the growing domain by neighboring domains that do not experience preferential growth.

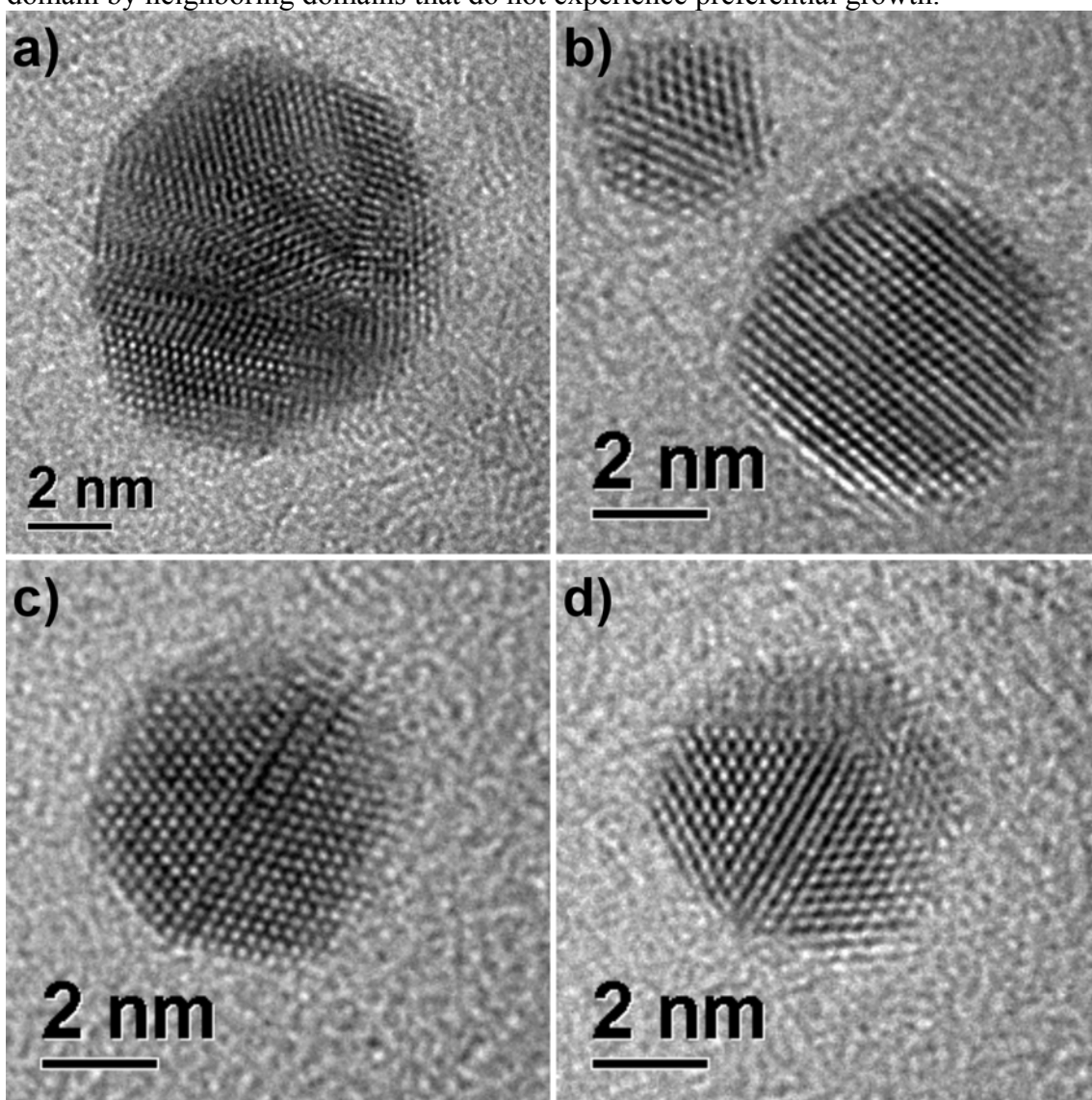


Figure 8.15: (18:1) Au:BSA HRTEM – Nanocrystals in the range of 5–10 nm. Characteristic morphologies included (a) multiple-twinned; (b) single crystal; (c) single twinned; (d) parallel twinning planes.

Nanocrystals in the intermediate size range of 5–10 nm were convex and exhibited aspect ratios of unity. The morphologies observed included multiple-twinned (Figure 8.15a), FCC single crystal (Figure 8.15b), single twinned FCC (Figure 8.15c), and crystals with parallel twinning planes (Figure 8.15d).

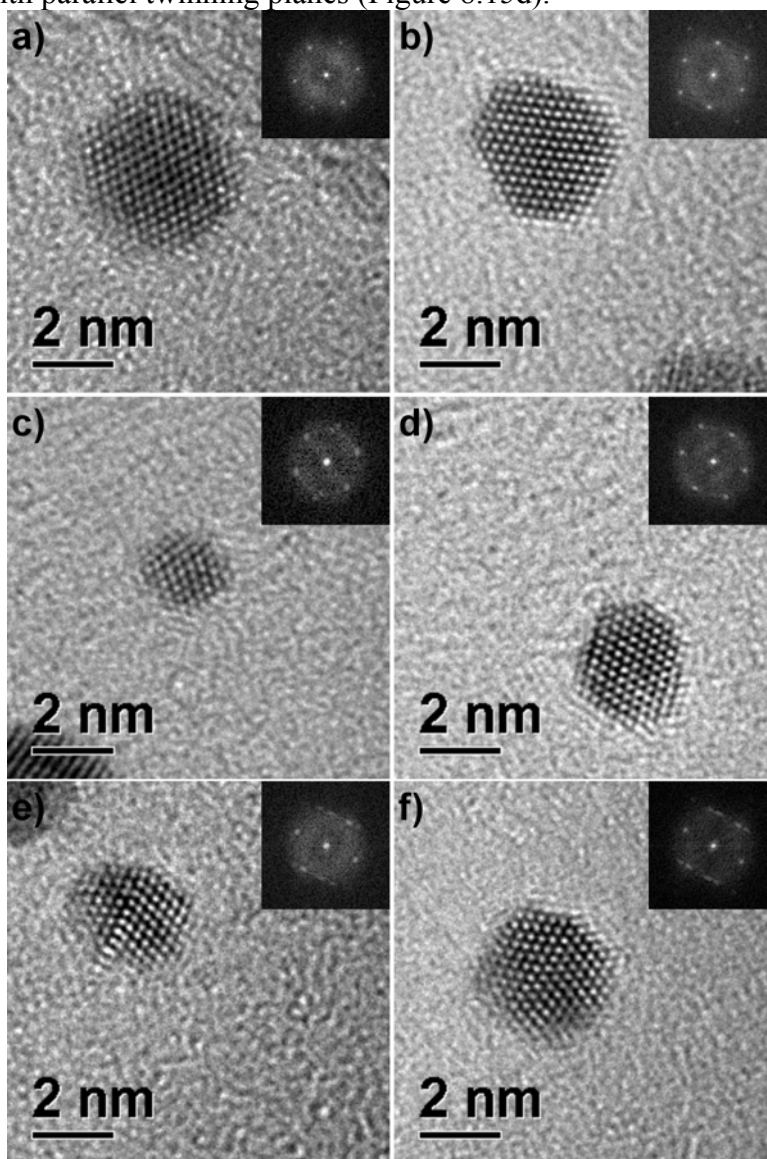


Figure 8.16: (18:1) Au:BSA HRTEM – Nanocrystals less than 5 nm in diameter. (a)-(b) FCC cuboctahedral; (c)-(d) FCC truncated octahedral; (e) single twinned truncated octahedral; (f) single twinned truncated cuboctahedral. The fast Fourier transform (FFT) of each image is included as an inset.

Finally, the morphologies for those nanocrystals less than 5 nm were quite regular and well-defined. The observed structures consisted primarily of FCC single crystals with either cuboctahedral (Figure 8.16a-b) or truncated octahedral (Figure 8.16c-d) morphologies. Single twinned truncated octahedral (Figure 8.16e) and single twinned cuboctahedral (Figure 8.16f) morphologies were also noted.

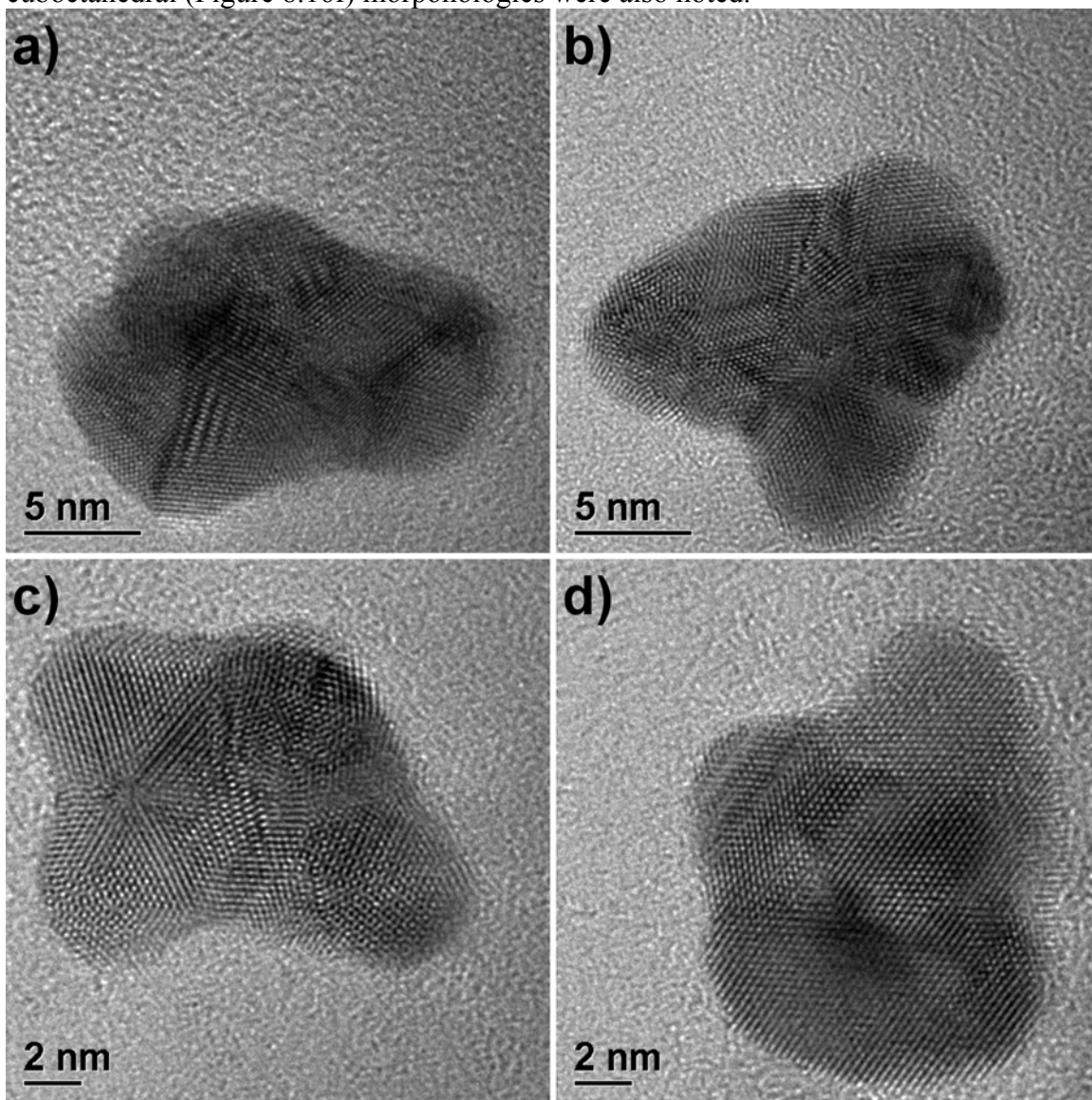


Figure 8.17: (12:1) Au:BSA HRTEM – Multiply-branched nanocrystals with irregular morphologies, and exhibiting a high density of twinning defects.

For the (12:1) Au:BSA system, nanocrystals larger than 10 nm primarily consisted of multiply-branched crystals (Figure 8.17). In comparison with the multiply-branched crystals from the (18:1) Au:BSA system (Figure 8.13), these crystals exhibit less well-defined morphologies, and a greater density of twinning defects.

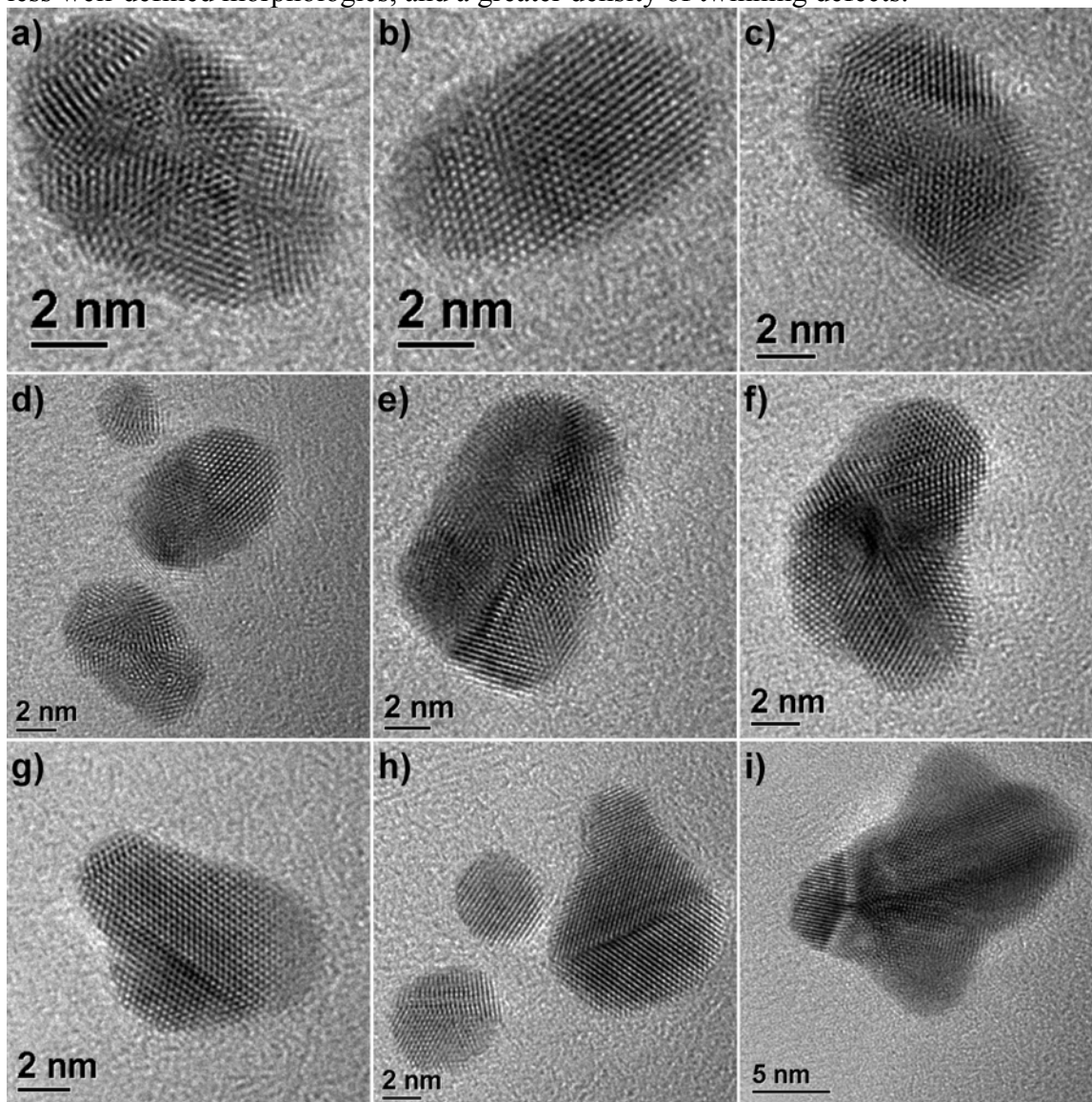


Figure 8.18: (12:1) Au:BSA HRTEM – Elongated nanocrystals. Lengths ranged from (a)-(d) less than 10 nm; (e)-(h) 10–20 nm; (i) greater than 20 nm.

Several types of elongated crystals were identified in the (12:1) Au:BSA system, ranging from 5–25 nm in length (Figure 8.18). Elongated crystals with the shortest lengths (5–10 nm) typically exhibited multiple-twinned morphologies (Figure 8.18a,c, lower crystal in Figure 8.18d), or lamellar twinning orthogonal to the direction of elongation (Figure 8.18b, upper crystal in Figure 8.18d). Crystals with lengths of 10–20 nm exhibited single twin planes running parallel (Figure 8.18g) or perpendicular (Figure 8.18h) to the direction of elongation, or combinations of the two (Figure 8.18e,f). Finally, some elongated crystals with lengths greater than 20 nm were observed (Figure 8.18i). Their morphology was reminiscent of nanowires with pentagonal cross-section, with some extra preferential growth of certain faces along the length of the crystal.

Twinned nanocrystals with aspect ratios of unity were commonly observed in the size range of 5–10 nm. The most common morphologies were single-twinned (Figure 8.19a) or crystals with parallel twinning planes (Figure 8.19b-c). Some multiple-twinned crystals with randomly-oriented twin planes were also observed (Figure 8.19d).

The morphologies for nanocrystals less than 5 nm were evenly distributed among three general categories. Several FCC single crystals were identified, such as the cuboctahedra in Figure 8.20a-b. Multiple-twinned crystals with fivefold symmetry were also present (Figure 8.20c-d). Finally, single-twinned crystals (Figure 8.20f) or crystals with parallel twinning planes (Figure 8.20e) were observed. It is interesting to note that nanocrystals smaller than ~3 nm were typically FCC single crystals, with very few twinned morphologies.

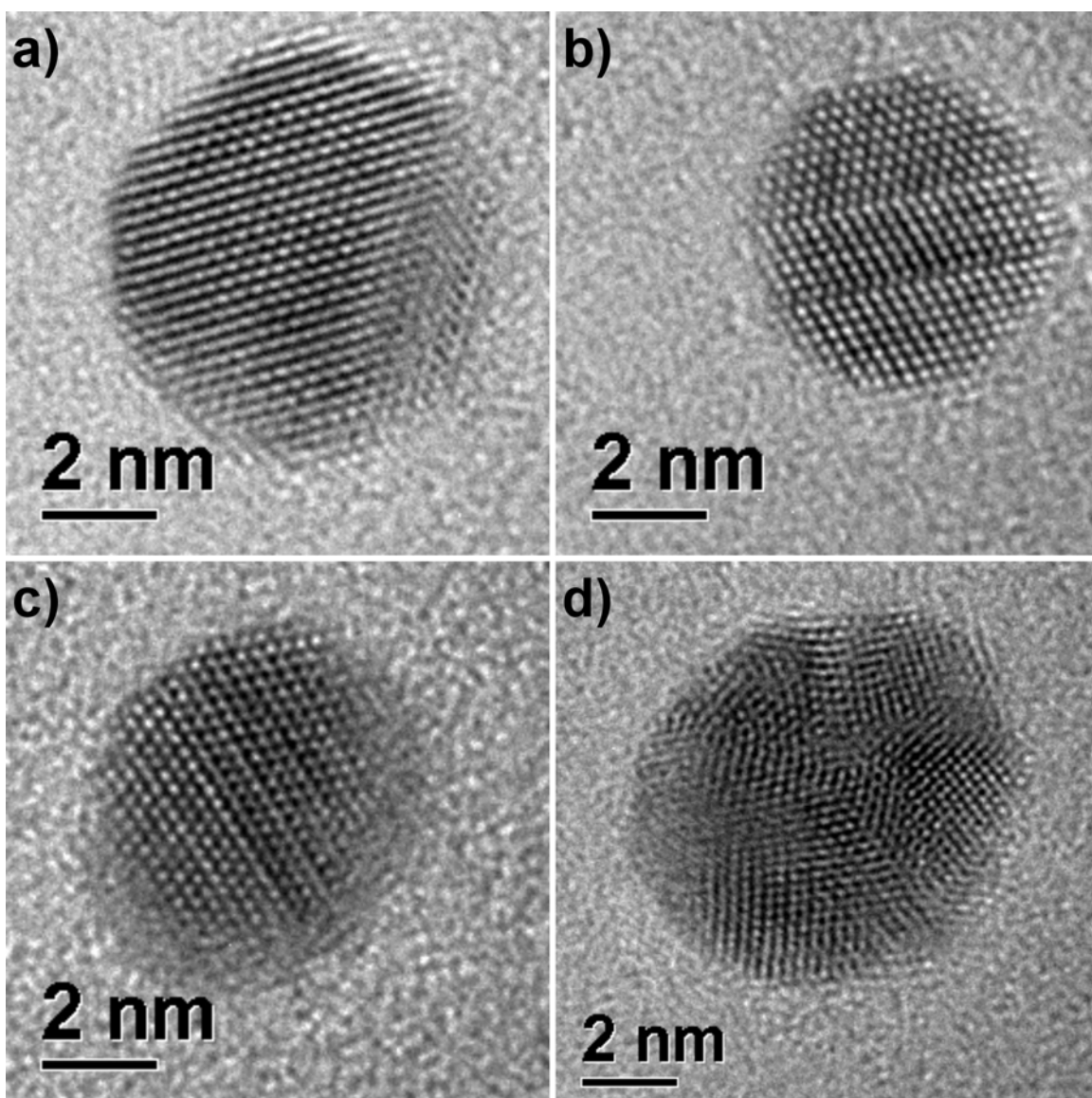


Figure 8.19: (12:1) Au:BSA HRTEM – Nanocrystals in the range of 5–10 nm. (a) Single twinned crystal; (b)-(c) Crystals with parallel twinning planes; (d) Multiple-twinned crystal with randomly-oriented twin planes.

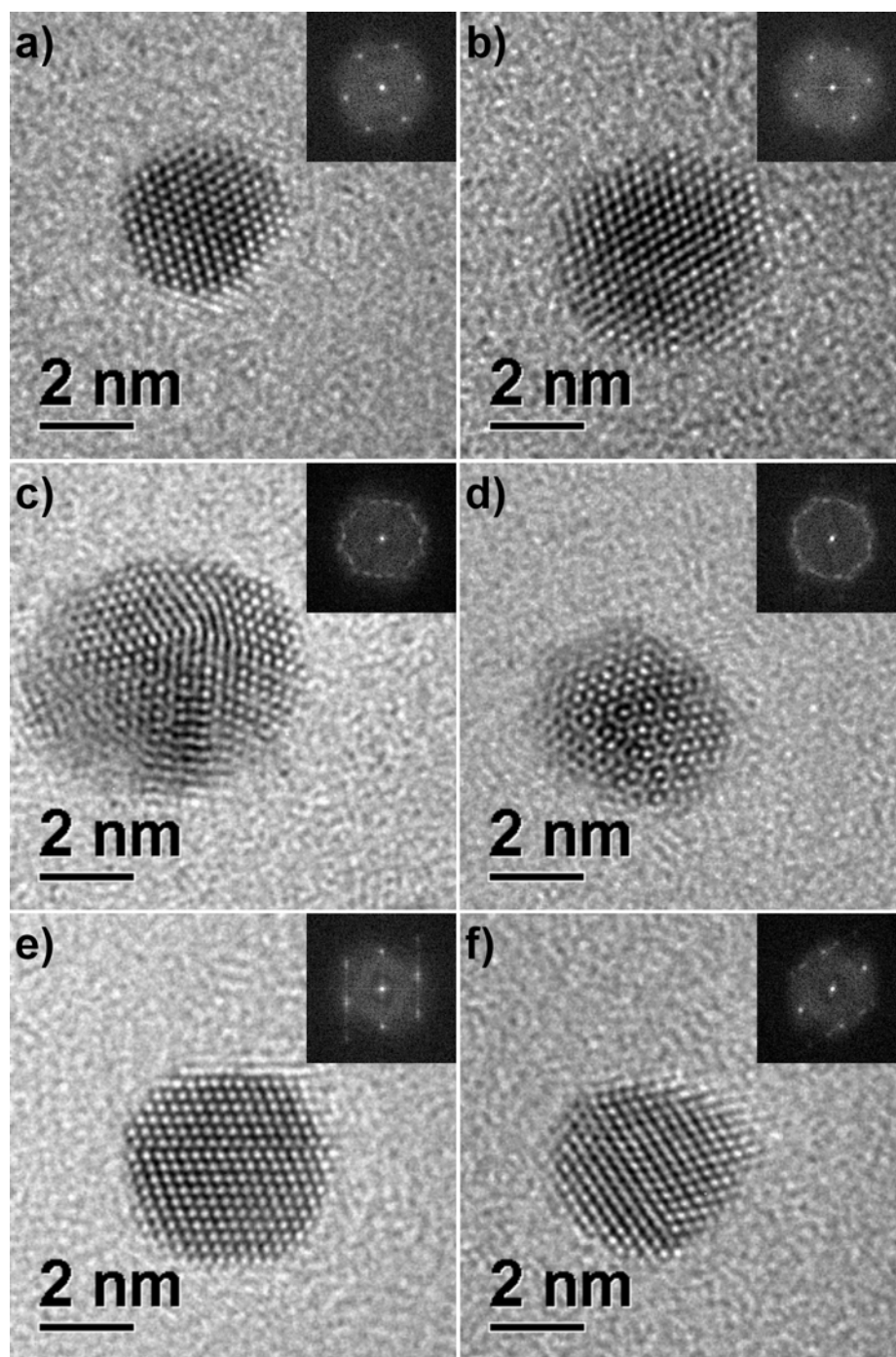


Figure 8.20: (12:1) Au:BSA HRTEM – Nanocrystals less than 5 nm in diameter. (a)-(b) FCC cuboctahedral; (c)-(d) multiple-twinned crystals with fivefold symmetry; (e) parallel twinning planes; (f) single twinned FCC crystal. The fast Fourier transform (FFT) of each image is included as an inset.

In summary, by allowing ascorbic acid, BSA, and sodium hydroxide to equilibrate in solution prior to the addition of ionic gold, nanocrystals were obtained with average diameters in the range of ~6 nm. As much as 50% of the product consisted of small, rounded crystals in the range of 2–5 nm, while the largest ~10% of the product consisted of elongated and branched nanostructures reminiscent of those described in Chapter 6. Reaction times were rapid, and the nanocrystals produced were the result of diffusional growth. In fact, the reaction at (12:1) Au:BSA was completed in less than 1 second, whereas no reaction was observed within 48 hours in the absence of sodium hydroxide. Reaction time was not observed to vary over the range of protein concentrations investigated. Clearly, the addition of sodium hydroxide to produce a basic solution pH has a significant effect on this reaction system.

8.3.3 Synthesis of Gold Nanocrystals via Addition of Chloroauric Acid to a Pre-Existing Aqueous Solution of Ascorbic Acid and BSA, with Subsequent Addition of Sodium Hydroxide

Although a substantial fraction of gold nanocrystals in the range of 2–5 nm were produced under basic pH conditions, there was too much variability in size and morphology to make this a useful synthesis method. Harkening back to our initial motivation for this investigation, our goal was to modify the reaction conditions to counteract both acidic pH and rapid reaction kinetics. In section 8.3.1 we achieved our goal of slower reaction kinetics, but at the expense of an acidic solution pH, while in section 8.3.2 we achieved our goal of a basic pH, but at the expense of rapid reaction kinetics. We needed to find a way to achieve both of our goals in one synthesis protocol.

From section 8.3.1, recall that when chloroauric acid was added to an equilibrated solution of ascorbic acid and BSA under acidic conditions, no reaction was observed at a molar ratio of (12:1) Au:BSA in over 48 hours. We suggested that with sufficiently large excesses of protein, and combined with the diminished auto-oxidation rate of BSA-

complexed ascorbic acid, the gold ions were forming complexes with protein molecules before they could be reduced. This combined complexation effect was sufficient to severely limit the reaction rate.

However, in section 8.3.2, the reaction at (12:1) Au:BSA was observed to proceed rapidly. This was likely due to two primary factors. First, the redox potential between ascorbic acid and chloroauric acid increases as solution pH increases, resulting in rapid kinetics for a basic pH. Second, BSA molecules regulate solution pH by complexing ionic species present in excess. When sodium hydroxide is added in excess, protein molecules will release some complexed ascorbic acid molecules back into solution, as they form complexes with sodium hydroxide to regulate the solution pH. As a result, the ionic gold subsequently added to solution will encounter free ascorbic acid molecules, and under basic solution conditions the reduction to atomic gold will occur rapidly, before the ionic gold species have the opportunity to form complexes with BSA.

In this final synthesis protocol, we added chloroauric acid to a pre-existing solution of ascorbic acid and BSA protein, followed 30 seconds later by the addition of sodium hydroxide. With this approach, the gold ions that first enter the solution encounter BSA-complexed ascorbic acid molecules with their greatly diminished auto-oxidation rate, and have a chance to form complexes with the large excess of protein molecules before they can be reduced. With the subsequent addition of sodium hydroxide, ascorbic acid molecules will be liberated from their protein-complexed state, and the reduction of ionic gold will commence in earnest. However, with the ionic gold stabilized by protein complexation, we hoped to induce a more gradual rate of reduction.

Molar ratios of (12:1) Au:BSA and (18:1) Au:BSA were investigated. In the absence of sodium hydroxide, no reaction was observed within 48 hours for (12:1) Au:BSA, and reaction was complete after ~5 minutes for (18:1) Au:BSA, so these

systems would provide us ample time to add the sodium hydroxide to solution before any significant reduction of ionic gold had commenced. For both the (12:1) Au:BSA and (18:1) Au:BSA systems, the solution acquired a transparent pale yellow color upon chloroauric acid. No change in color was observed in the next 30 seconds. Within 30 minutes after the addition of sodium hydroxide, the solution became colorless, acquiring a light golden hue within 1 hour. After 2 hours, the solution had a deep golden-brown color, and within 3 hours, the intensity of solution color was fully developed. These changes in color were observed in both the (12:1) Au:BSA and (18:1) Au:BSA systems.

Size distributions for both systems were obtained from HAADF analysis at high magnification, based on the measurement of 500 crystals. The size distribution of the (12:1) Au:BSA system is presented in Figure 8.21. The product is well-dispersed with a controlled size distribution, and the individual nanocrystals have well-defined morphologies. The measured distribution was 2.654 ± 0.552 nm, or a standard deviation of 20.8%. From the histogram in Figure 8.21d, we discern a bimodal distribution. In the (12:1) Au:BSA system, nearly 80% of the product was less than 3 nm in diameter, while the remaining 20% of the product was in the size range of 3.00–4.25 nm. The size distribution for the (18:1) Au:BSA system was nearly identical, but with a slightly smaller standard deviation of 14.8%, resulting from a larger fraction of nanocrystals in the size range of 3–4.5 nm. No crystals larger than 5 nm were observed in either system.

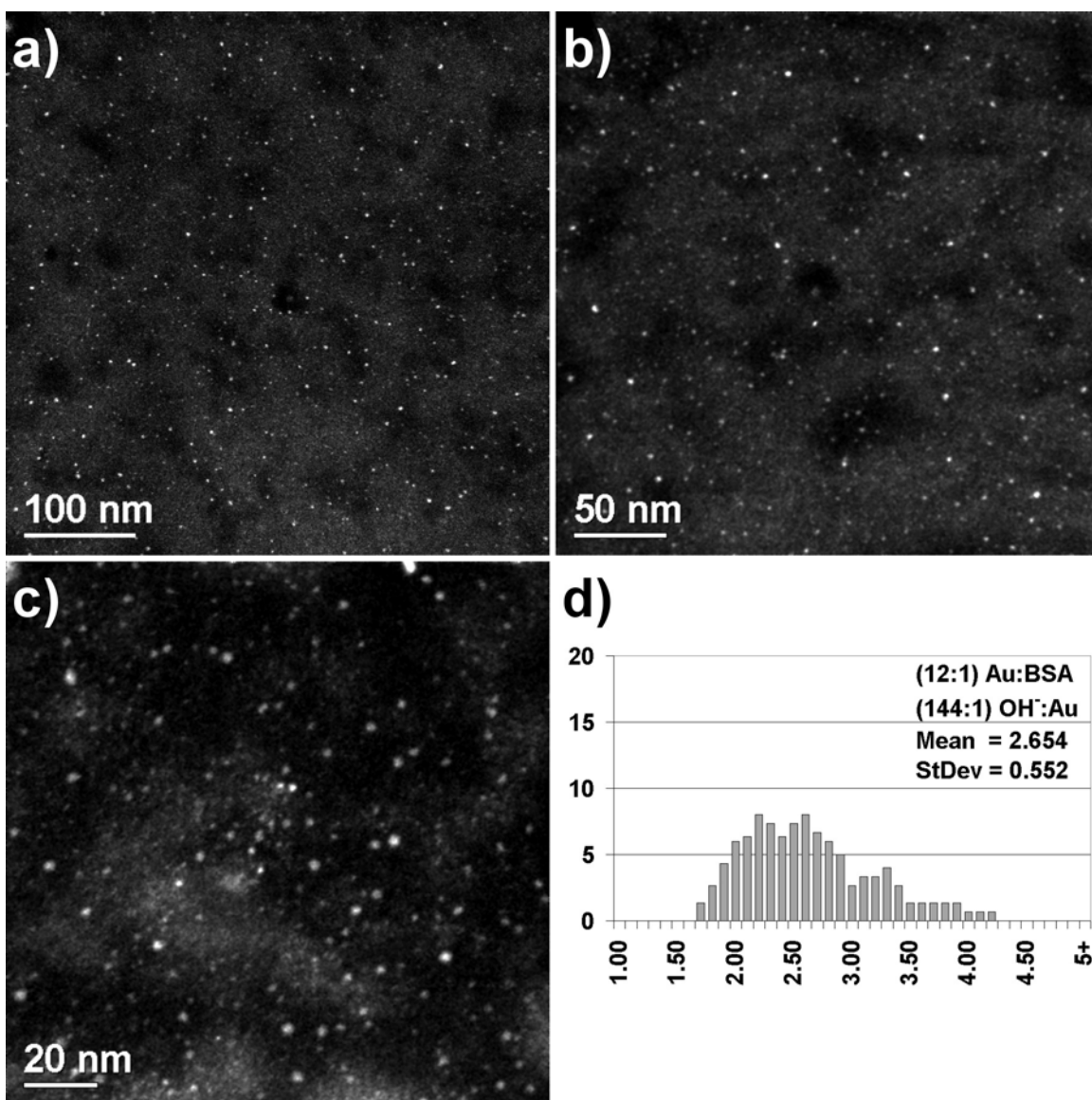


Figure 8.21: Nanocrystals formed by the addition of ionic gold to a pre-existing solution of ascorbic acid and BSA, with subsequent addition of sodium hydroxide. (a)-(c) Representative HAADF images and (d) size distribution for the (12:1) Au:BSA system. Size distribution depicts nanocrystal diameter in nanometers versus percentage frequency.

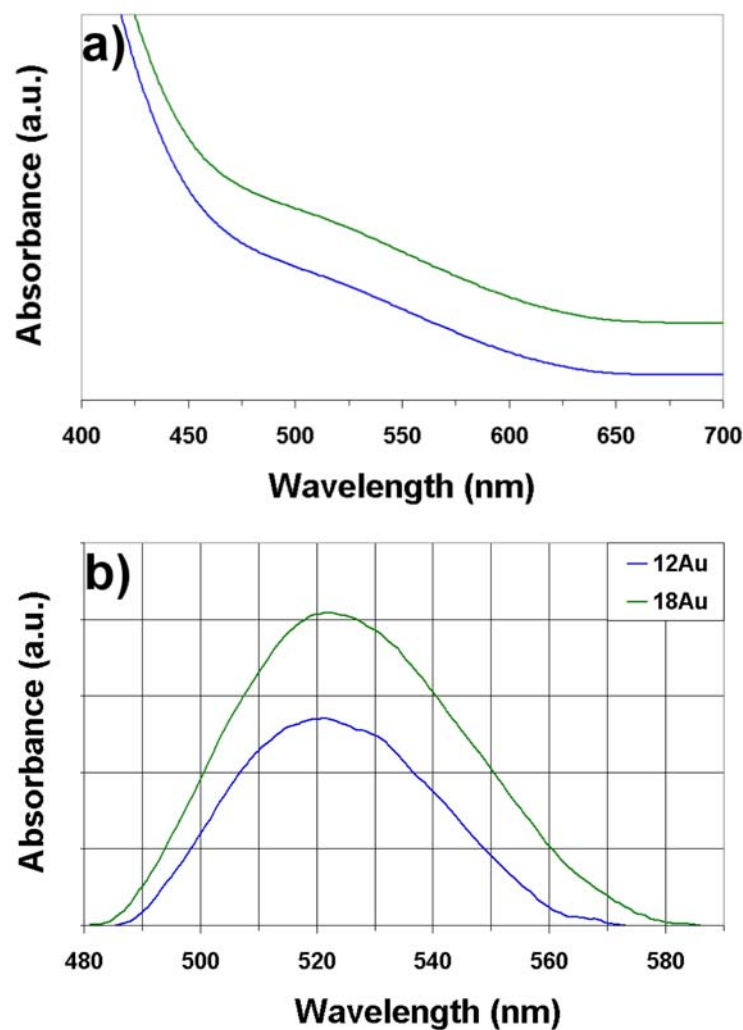


Figure 8.22: UV-visible absorption spectra resulting from addition of ionic gold to a pre-existing solution of ascorbic acid and BSA, with subsequent addition of sodium hydroxide. From bottom to top, the spectra are (12:1) Au:BSA (Blue) and (18:1) Au:BSA (Green). (b) Blow-up of the spectral region from 480–590 nm, clearly illustrating the surface plasmon resonance at ~520 nm.

UV-visible absorption spectra in the range of 400–700 nm were obtained for the (12:1) Au:BSA and (18:1) Au:BSA systems, depicted in Figure 8.22a. Each system exhibited a broad symmetric peak centered at ~520 nm. The breadth, symmetry, and small intensity of these absorbance maxima are indicative of ~2 nm gold nanocrystals.

(10,34) To better examine the spectral features of the surface plasmon resonance, a blowup of the spectral region from 480–590 nm is provided in Figure 8.22b. The maximum for (12:1) Au:BSA is centered at 520 nm, while the maximum for (18:1) Au:BSA is centered at 522 nm, and exhibits a greater intensity. This is in agreement with our HAADF analysis, where we found the (18:1) Au:BSA system had a larger average nanocrystal diameter, resulting from an increased percentage of 3.0–4.5 nm crystals.

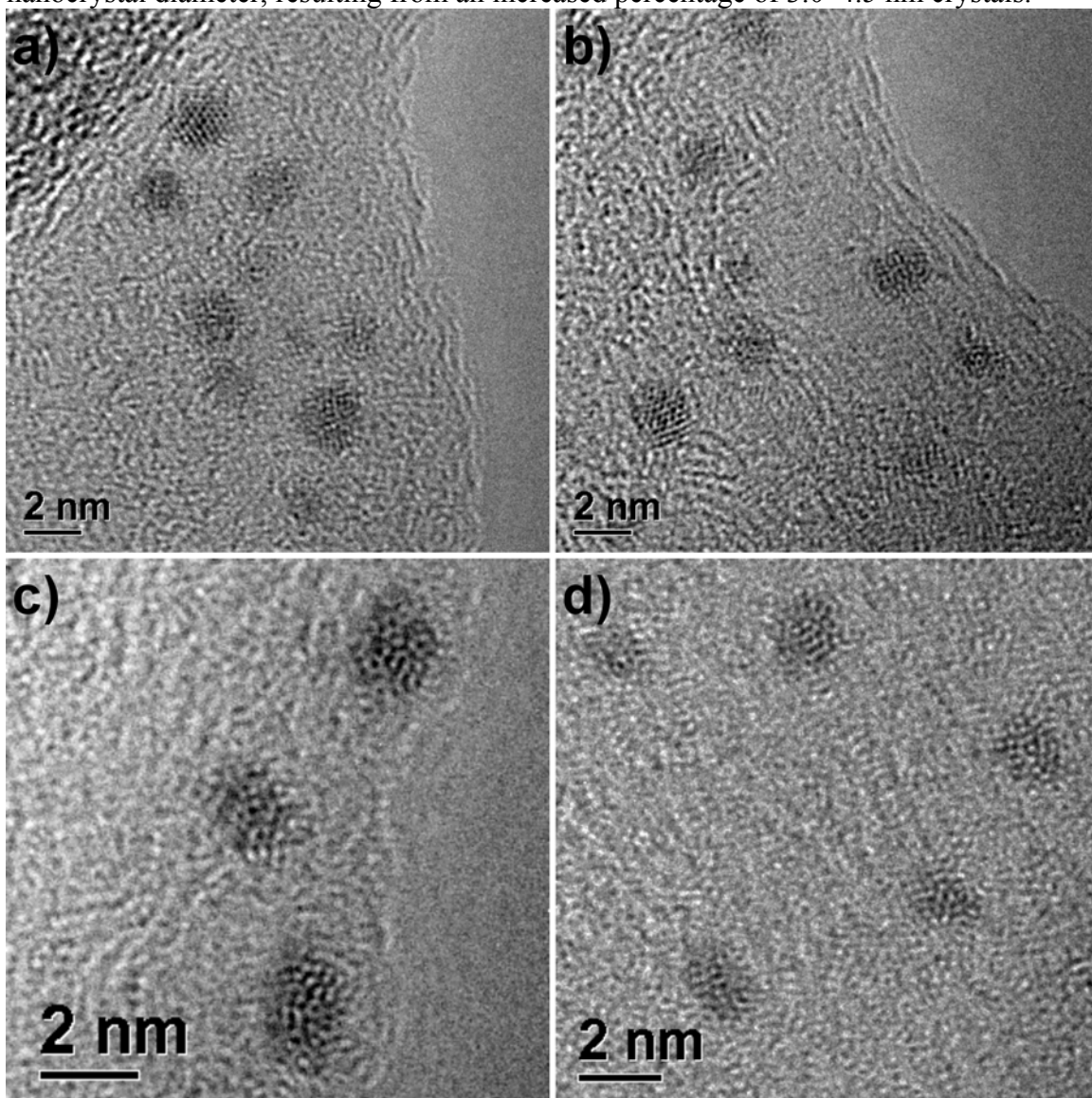


Figure 8.23: (12:1) Au:BSA – conventional TEM analysis.

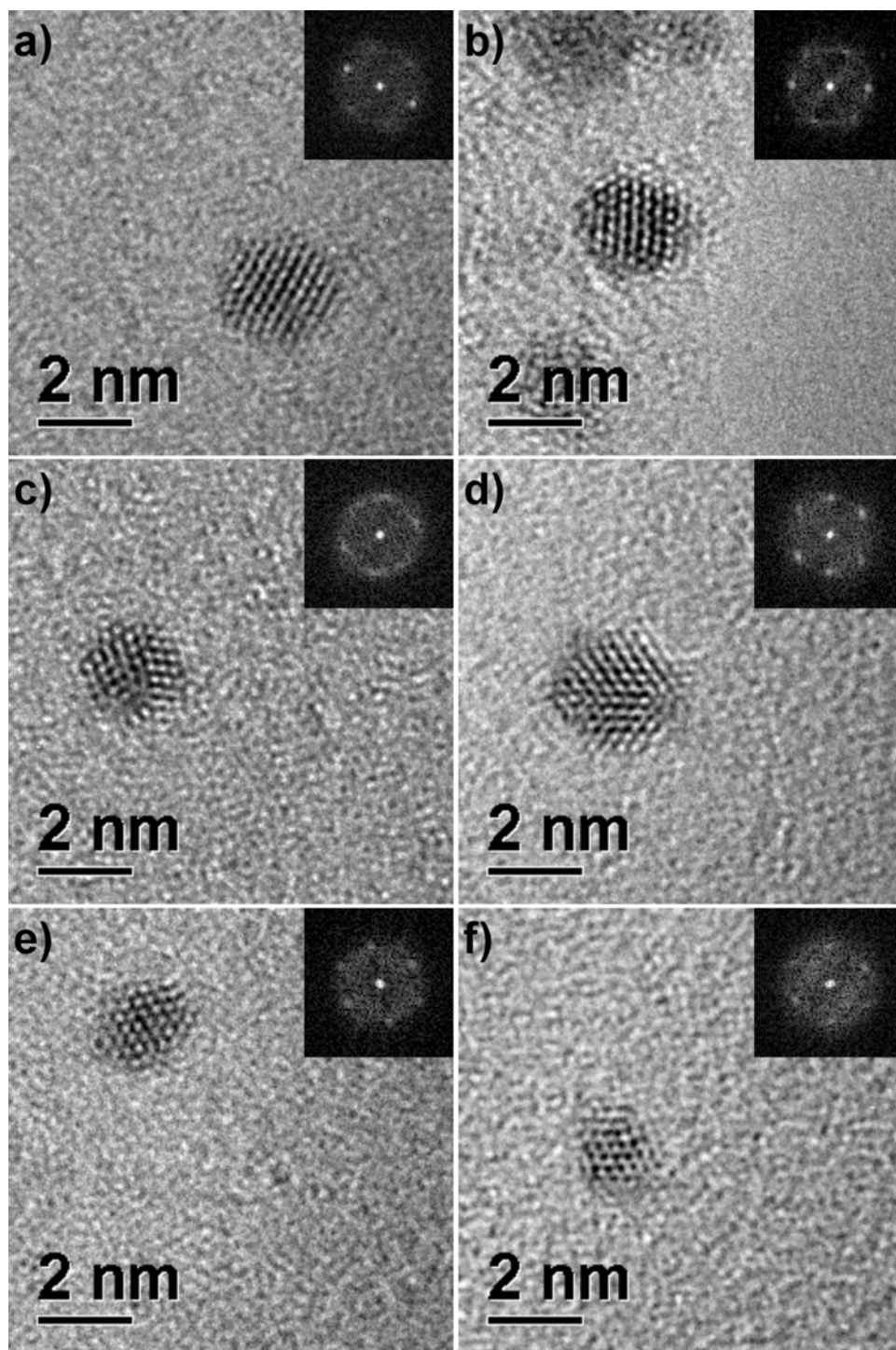


Figure 8.24: (12:1) Au:BSA – HRTEM analysis. The fast Fourier transform (FFT) of each image is included as an inset.

Due to the large excess of protein in these systems, it was difficult to obtain atomic resolution of the gold nanocrystals. However, the thickness of the protein film was less pronounced at the edges of the film, and conventional TEM images could be obtained, as presented in Figure 8.23. Although the lattice fringes of some crystals were obscured, and it was difficult to determine where the edges of some crystals terminated, TEM analysis at the edges of the protein film provided a reasonable overview of the product. The average sizes measured by conventional TEM corroborated our measurements in HAADF.

Finally, some regions of the protein film were sufficiently thin to allow for HRTEM analysis, as seen in Figure 8.24. The interplanar distances were measured from the FFT of each image in Figure 8.24, and were consistent with the expected values for FCC gold. All crystals observed in HRTEM were FCC single crystals, with $\{111\}$ and $\{200\}$ lattice planes observed. However, since only a small portion of the sample was able to be analyzed by HRTEM, we cannot exclude the possibility of other morphologies also being present in the system.

8.4 CONCLUSIONS

In summary, I have described a modification of the aqueous-based synthesis approach previously described in Chapter 6, where ascorbic acid and bovine serum albumin are allowed to equilibrate in solution prior to the addition of chloroauric acid. The auto-oxidation rate of serum albumin-complexed ascorbic acid molecules is greatly diminished when compared with the free molecular species. However, the reducing strength of ascorbic acid increases under basic pH conditions. By employing an approach that combined the effects of protein complexation and basic solution pH, we were able to select the reaction conditions best suited for the formation of ~2 nm gold nanocrystals.

Allowing ascorbic acid and BSA to equilibrate, but conducting the reduction of ionic gold at an acidic solution pH, the product consisted of large polycrystalline spheres with average diameters ranging from 170–415 nm, depending on the protein concentration and relative excess of ascorbic acid. Introducing sodium hydroxide allowed us to conduct the reactions at basic solution pH, and it was found that for a pH of ~9 or greater, aggregation-driven growth of nanocrystals was eliminated. We also found that the order of addition of chloroauric acid and sodium hydroxide had a significant effect on both reaction time and product distribution.

Addition of chloroauric acid to a pre-existing solution of ascorbic acid and BSA, followed 30 seconds later by addition of sodium hydroxide, yielded a well-dispersed product of 2.654 ± 0.552 nm gold nanocrystals, or a standard deviation of ~20%. In comparison with the BSA-functionalized gold nanocrystals produced by reduction with sodium borohydride, the crystals formed by reduction with ascorbic acid in the presence of sodium hydroxide possess a larger average diameter, a broader percentage deviation, and the reaction time was ~3 hours versus ~5 seconds. However, the current protocol has the advantage of no boronated byproducts, and after neutralizing the pH, the product should be ready for use in biological systems, without the need for extensive purification.

Chapter 9: Conclusions and Recommendations

9.1 CONCLUSIONS

9.1.1 Polyol Synthesis of Protein-Stabilized Gold Nanocrystals

We have demonstrated that bovine serum albumin, a globular protein molecule, can be successfully incorporated into a polyol method to regulate the formation and growth of gold nanocrystals with morphologies in the size range of 2–5 nm, for reaction temperatures lower than the thermal denaturation point at 75°C. Controlled size distributions and stable nanocrystal morphologies on the order of 2–5 nm were obtained at 65°C, whereas at 95°C, the nanometric size and shape distributions were broader, and the crystal structures were strained. We proposed this was a result of the thermally-induced denaturation of BSA protein above 75°C, which decreases its efficacy in protecting 2–5 nm crystals. Unfortunately, working below 75°C is a severe limitation for the polyol method, as the fastest reaction time observed at 65°C was 48 hours.

9.1.2 Aqueous Synthesis of Protein-Stabilized Silver, Gold, and Platinum Nanocrystals via Chemical Reduction with Sodium Borohydride

We have developed a new method for the synthesis of water-soluble silver, gold, and platinum nanocrystals, grown within and directly functionalized by bovine serum albumin, a globular protein molecule. This method employs aqueous chemistry at ambient conditions, and with a molar ratio of (24:1) [Ag/Au/Pt atoms]/[BSA molecules], we obtain near-quantitative yields of well-dispersed, protein-functionalized nanocrystals with ~2 nm diameters, and only ~14% standard deviation from the mean particle size. The limit of the protein in stabilizing virtually all the product as ~2 nm crystals occurs at an approximate molar ratio of (48:1) [Ag/Au/Pt atoms]/[BSA molecules]. Our analysis

suggests that for molar ratios less than (48:1), the protein molecules are controlling the nucleation and growth process of ~2 nm noble metal nanocrystals. When compared with previously-existing bioconjugation techniques, this approach has several desirable features including robust dimensional stability of the product, and a near-quantitative yield of ~2 nm protein-functionalized nanocrystals, obtained rapidly at synthesis conditions that are non-destructive for the protein.

9.1.3 Serum Albumin-Functionalized Silver Nanocrystals as Antivirals: Interaction with HIV

In the context of a broader study on the interaction of silver nanocrystals with HIV-1, we have demonstrated that BSA-functionalized silver nanocrystals can interact with an external biological system. Three types of silver nanocrystal preparations with markedly different surface chemistries were employed, which allowed us to measure the efficiency of interaction for protein-conjugated silver nanocrystals with HIV-1, as compared to conventional nanocrystal preparations. The interaction between silver nanocrystals and HIV-1 was congruent among all three nanocrystal preparations, suggesting a common mode of interaction. We proposed silver nanocrystal surfaces preferentially attach to exposed disulfide bonds of the gp120 subunit of the viral envelope glycoprotein. Since this is a specific interaction between the virus and the nanocrystal surface, these results suggest that the surfaces of BSA-functionalized silver nanocrystals are able to interact directly with an external biological system.

A size dependence of interaction with HIV-1 was noted, with only nanocrystals in the range of 1-10 nm bound to the virus. The BSA-functionalized product is completely within the proper size range to exploit this size-dependent interaction with HIV-1. Also, we noted that BSA-functionalized nanocrystals exhibited the least cytotoxicity among the three silver preparations tested. Clearly, the selection of biocompatible protecting agents,

such as plasma proteins, will be crucial for future applications involving the interaction of nanocrystals with viruses and more complex biosystems.

9.1.4 Serum Albumin-Functionalized Gold Nanocrystals: Toward In Vivo Dosage of Contrast-Enhancing Agents for the Imaging of Microorganisms

We discovered that BSA-functionalized gold nanocrystals may provide a platform for the *in vivo* dosage of contrast-enhancing agents for imaging of bacteria. Images of *P. aeruginosa* demonstrated that BSA-functionalized gold nanocrystals provide enhanced contrast to specific regions of the bacterial surface, particularly the poles. Although the microscopy technique employed in our study was destructive to the bacteria, the development of *in vivo* dosage platforms for contrast enhancing agents should open promising new alternatives for the imaging of live microbial cultures.

We proposed *P. aeruginosa* uses BSA protein as its source of nutrition, and as the bacteria consume the protein to satisfy their physiological requirements, they simultaneously accumulate contrast-enhancing gold nanocrystals on their surface. Through comparison of gold and silver, we proposed that colonization of BSA-functionalized gold solutions by *P. aeruginosa* was not due to the protein completely insulating the nanocrystal surfaces, but was a result of the inherent biocompatibility of gold. To our knowledge, this is the first report of *in vivo* dosage to microorganisms of a contrast enhancing agent directly through their nutrition source.

9.1.5 Serum Albumin-Functionalized Platinum Nanocrystals as Catalysts for the Aqueous Phase Hydrogenation of Allyl Alcohol

We demonstrated that BSA-functionalized platinum nanocrystals are active toward the catalytic hydrogenation of allyl alcohol. We documented the correlation between nanocrystal structure and catalytic performance, with elongated nanocrystals exhibiting superior activity. We attributed this difference in catalytic activity to the

relative proportions of exposed face atoms. We modeled rounded and elongated nanocrystals as cuboctahedral and cylindrical structures, respectively, and when the TOF was calculated based on the number of face atoms per crystal, the results were nearly equivalent for the cuboctahedral and elongated crystals. Comparing the activity of BSA-functionalized platinum nanocrystals with conventional preparations, the catalytic activity measured for both types of BSA-functionalized crystals was superior to the activity reported for dendrimer-encapsulated platinum nanocrystals. However, the dimensional stability of protein-functionalized platinum nanocrystals was compromised under the catalytic reaction conditions. A significant degree of coalescence was observed in the (24:1) Pt:BSA catalyst after 24 hours of reaction within the intrinsic kinetic regime, while extensive aggregation and coalescence was found after only 3 hours of reaction within the mass transfer regime. We attribute the observed protein aggregation and nanocrystal coalescence to the structural degradation of BSA molecules when exposed to the hydrogenation reaction conditions for prolonged intervals.

9.1.6 Synthesis of Star Polyhedral Gold Nanocrystals via Reduction with Ascorbic Acid

We have thoroughly studied the formation, structure, and stability of star polyhedral gold nanocrystals produced in water by colloidal reduction with ascorbic acid. We identified two distinct classes of star nanocrystals: multiple-twinned crystals with five-fold symmetry, and monocrystals, which correspond respectively to icosahedra and cuboctahedra with preferential growth of their exposed $\{111\}$ faces. By assuming a star morphology, gold nanocrystals increase their proportion of exposed $\{111\}$ surfaces, and we proposed that the accompanying reduction in surface energy is the driving force behind star nanocrystal formation.

Star polyhedral gold nanocrystals are metastable structures, although their stability is greatly improved on a dry amorphous carbon substrate. Star polyhedral nanocrystals can be consistently obtained in good yield at a molar ratio of (40:1) [ascorbic acid molecules]:[gold atoms]. For smaller excesses of ascorbic acid, only large polycrystalline spherical aggregates are observed, while for much larger excesses, the formation of “super-stellated” crystals, with secondary branches emanating from primary branches, is observed. These super-stellated structures are irregular in shape and have poor structural stability.

We proposed the two primary factors driving the formation of star polyhedral gold nanocrystals were the rapid reaction kinetics, and the strongly acidic pH of solution. Decreasing the rate of the initial phase of the reaction strongly favored the formation of monocrystalline star polyhedra. To explain this observation, we proposed a growth mechanism based on the concept of *in situ* generation of seed crystals, which are then directly consumed in the growth of star polyhedral nanocrystals. Slower initial rates of nuclei formation favor the formation of larger primary-sized seed crystals, which tend toward FCC cuboctahedral morphologies. The morphology of the seed crystals is stabilized by branching due to an increased proportion of exposed {111} surfaces, resulting in primarily cuboctahedrally-derived monocrystalline stars.

9.1.7 Synthesis of Gold Nanocrystals via Reduction with Ascorbic Acid: Controlled Growth in Basic Reaction Media and in the Presence of Bovine Serum Albumin

Employing an approach that combined the effects of protein complexation on the auto-oxidation potential of ascorbic acid, and a basic solution pH, we were able to counteract the reaction conditions required for the formation of star polyhedra gold. An ionic gold precursor was added to a pre-equilibrated aqueous solution of ascorbic acid and BSA, followed 30 seconds later by the addition of sodium hydroxide. The result was

a well-dispersed product of ~2.5 nm gold nanocrystals. In comparison with the BSA-functionalized gold nanocrystals produced by reduction with sodium borohydride, the crystals formed by reduction with ascorbic acid in the presence of sodium hydroxide possess a larger average diameter, a broader percentage deviation from the mean particle size, and the reaction time was ~3 hours versus ~5 seconds. However, the ascorbic acid-based protocol has the advantage of no boronated byproducts, and after neutralizing the pH, the product should be ready for use in biological systems without the need for extensive purification. This protocol represents a novel, environmentally benign approach to producing biocompatible nanocrystals, relying on proteins, ascorbic acid, sodium hydroxide, and water, all at ambient temperature.

9.2 RECOMMENDATIONS

9.2.1 Aqueous Synthesis of Protein-Stabilized Noble Metal Nanocrystals

Having demonstrated the feasibility of utilizing a macromolecular globular protein to regulate the formation and growth of three distinct noble metal nanocrystals, the synthesis of other types of nanocrystals in the presence of BSA via sodium borohydride reduction should be examined, including magnetic and semiconductor nanocrystals. The formation of bimetallic core-shell structures by sequential reduction should also be pursued. Furthermore, the substitution of other globular proteins with similar structures to BSA should be explored.

As for the formation of BSA-functionalized gold nanocrystals via reduction with ascorbic acid under basic solution conditions, this approach must be extended to other transition metals in order to determine if it has potential for broader application. In particular, the synthesis of ~2 nm BSA-functionalized silver nanocrystals by reduction

with ascorbic acid should be pursued in earnest, due to the clear advantages of enhanced biocompatibility for antiviral and antimicrobial applications.

9.2.2 Serum Albumin-Functionalized Silver Nanocrystals as Antivirals

The long term health effects of exposure to metallic nanocrystals are still largely unknown, despite the fact that potential applications for nanomaterials in the biological sciences are continually being discovered. Detailed toxicity studies must be undertaken in order to fully exploit the potential of nanomaterials in the biological sciences. Our preliminary study on the interaction of silver nanocrystals with HIV certainly helps provide incentive to this effect.

In the meantime, it should be worthwhile to investigate the replacement of bovine serum albumin by human serum albumin (HSA) in the synthesis protocol for protein-functionalized silver nanocrystals. HSA is a structural analog of BSA, and contains the same double-looped disulfide bridging pattern. It is highly probable that HSA will also be effective in directing the well-controlled growth of metallic nanocrystals. In anticipation of the day when the toxicology of nanomaterials is more fully understood, and in the event that silver nanocrystals are deemed appropriate for internal uses, it would be highly beneficial to have the human form of serum albumin available as a carrier molecule for targeted delivery of nanocrystal preparations within the circulatory system.

Furthermore, systematic testing should be conducted to determine the efficacy of silver nanocrystals in preventing the transmission of other retroviruses. Several retroviruses share analogous modes of infectivity, and it is possible that silver nanocrystals have the capacity to inhibit transmission of other retroviruses in a manner analogous to that discovered in the case of HIV. In particular, the broader antimicrobial efficacy of serum albumin-functionalized silver nanocrystals should be explored.

9.2.3 Serum Albumin-Functionalized Nanocrystals as Heterogeneous Catalysts

Comparing the activity of BSA-functionalized platinum nanocrystals toward the aqueous phase catalytic hydrogenation of allyl alcohol with that of conventional preparations, we found the activity of BSA-functionalized crystals was superior to the previously-reported activity of dendrimer-encapsulated platinum nanocrystals. However, the dimensional stability of BSA-functionalized platinum crystals was compromised under the reaction conditions. These observations immediately suggest that the catalytic activity of BSA-functionalized silver, gold, and platinum nanocrystals should be explored when prepared as traditional heterogeneous catalysts (deposited on a supporting substrate). The use of a solid support provides enhanced structural stability to the nanocrystals, and allows for their use in a broader range of catalytic applications.

Several applications for noble metal nanocrystals as heterogeneous catalysts exist. One of the most important industrial applications of silver is as a heterogeneous catalyst for the oxidation of ethylene to ethylene oxide, which yields ethylene glycol by the addition of water. (2) While gold is largely inert in its bulk state, gold nanocrystals are catalytically active toward several reactions including the reduction of NO_x and the oxidation of CO, which are of great importance for automobile emissions. (171) Finally, in addition to their traditional applications as hydrogenation catalysts, carbon-supported platinum nanocrystals have gained widespread attention as catalysts in fuel cells. (7)

9.2.4 Star Polyhedral Gold Nanocrystals

The formation of star polyhedral nanocrystals was strongly dependent upon reaction kinetics and pH of solution. There are numerous strategies available to obtain rapid reaction kinetics at an acidic pH without the use of ascorbic acid. Other reducing agents should be evaluated for their potential use in the formation of multiply-branched nanostructures under acidic reaction conditions. Additionally, testing should be pursued

to determine the optimal dropwise addition rate required to achieve a high selectivity for monocrystalline stars, while also providing sharply-defined pyramids.

The electronic and optical responses of star polyhedral gold nanocrystals must be thoroughly investigated. According to electromagnetic simulations by Hao *et al.*, for the case of a gold tripod with an average tip-to-tip distance of 42 nm, and using “snipped” tips to mimic the observed rounding of the crystalline peaks, electric field enhancements as great as 3900 times the applied field are predicted at the crystal tips. (172) E-field enhancement should also be anticipated for star polyhedral gold nanocrystals, which possess from eight to as many as twenty pyramids emanating from a common core crystalline region. Strong electromagnetic responses also suggest the possibility of strong non-linear optical responses, such as second harmonic generation. If enhanced electronic and optical responses are discovered, this could make star polyhedral gold nanocrystals valuable tools for applications such as chemical sensors and contrast enhancing agents.

Bibliography

1. C. Burda, X. Chen, R. Narayanan, & M.A. El-Sayed, *Chem. Rev.* 105, 105, 1025–1102 (2005).
2. R. Narayanan & M. A. El-Sayed, *J. Phys. Chem. B* 109, 12663–12676 (2005).
3. P.-A. Brugger, P. Cuendet, & M. Gratzel, *J. Am. Chem. Soc.* 103, 2923–2927 (1981).
4. J.M. Thomas, *Pure Appl. Chem.* 60, 1517–1528 (1988).
5. G. Schön & U. Simon, *Colloid Polym. Sci.* 273, 101–117 (1995).
6. G. Schön & U. Simon, *Colloid Polym. Sci.* 273, 202–218 (1995).
7. H. Bönemann & R.M. Richards, *Eur. J. Inorg. Chem.* 2001, 2455–2480 (2001).
8. F.E. Wagner, S. Haslbeck, L. Stievano, S. Calogero, Q.A. Pankhurst, & K.-P. Martinek, *Nature* 407, 691–692 (2000).
9. D.J. Barber, & I.C. Freestone, *Archaeometry* 32, 33–45 (1990).
10. S. Link & M.A. El-Sayed, *Annu. Rev. Phys. Chem.* 54, 331–66 (2003).
11. M.-C. Daniel & D. Astruc, *Chem. Rev.* 104, 293–346 (2004).
12. F. Antonii, In *Panacea Aurea-Auro Potabile*; Bibliopolio Frobeniano: Hamburg (1618).
13. H.H. Helcher, In *Aurum Potabile oder Gold Tinstur*; J. Herbord Klossen: Breslau and Leipzig (1718).
14. *Dictionnaire de Chymie*; Lacombe: Paris (1769).
15. M. Faraday, *Phil. Trans R. Soc. London* 147, 145–181 (1857).
16. M. Knoll, & E. Ruska, *Z. Physik* 78, 318–339 (1932).
17. E. Ruska, *Rev. Mod. Phys.* 59, 627–638 (1987).
18. P. Alivisatos, *Nat. Biotechnol.* 22, 47–52 (2004).

19. E. Katz & I. Willner, *Angew. Chem. Int. Ed.* 43, 6042–6108 (2004).
20. N.L. Rosi & C.A. Mirkin, *Chem. Rev.* 105, 1547–1562 (2005).
21. J.L. West & N.J. Halas, *Curr. Opin. Biotechnol.* 11, 215–217 (2000).
22. G. Bauer, J. Hassmann, H. Walter, J. Haglmüller, C. Mayer, & T. Schalkhammer, *Nanotechnology* 14, 1289–1311 (2003).
23. S.C. Tjong & H. Chen, *Mater. Sci. Eng. R* 45, 1–88 (2004).
24. T.P. Martin, *Phys. Rep.* 273, 199–241 (1996).
25. G. Schmid, In *Nanoscale Materials in Chemistry*, K.J. Klabunde, Ed.; John Wiley & Sons: New York (2001).
26. J.O. Bovin, R.L. Wallembert, & D. Smith, *Nature* 317, 47–49 (1985).
27. S. Iijima & T. Ichihashi, *Phys. Rev. Lett.* 56, 616–619 (1986).
28. A. Howie, *Nature* 320, 684 (1986).
29. P. Williams, *Appl. Phys. Lett.* 50, 1760–1762 (1987).
30. C. Cleveland & U. Landman, *J. Chem. Phys.* 94, 7376–7396 (1991).
31. U. Landman, T.G. Schaaff, M.N. Shafiqullin, P.W. Stephent, & R.L. Whetten, *Phys. Rev. Lett.* 79, 1873–1876 (1997).
32. M. Jose-Yacaman, J.A. Ascencio, H.B. Liu, & J. Gardea-Torresdey, *J. Vac. Sci. Technol. B* 19, 1091–1103 (2001).
33. L.D. Marks, *Rep. Prog. Phys.* 57, 603–649 (1994).
34. U. Kreibig & M. Vollmer, In *Optical Properties of Metal Clusters*; Springer: Berlin (1995).
35. G. Mie, *Ann. Phys.* 25, 377–445 (1908).
36. J.A. Creighton & D.G. Eadon, *J. Chem. Soc. Faraday Trans.* 87, 3881–3891 (1991).
37. T.G. Schaaff, M.N. Shafiqullin, J.T. Khoury, I. Vezmar, R.L. Whetten, W.G. Cullen, P.N. First, C. Gutierrez-Wing, J. Ascencio, & M. Jose-Yacaman, *J. Phys. Chem. B* 101, 7885–7891 (1997).

38. R. Elghanian, J.J. Storhoff, R.C. Mucic, R.L. Letsinger, & C.A. Mirkin, *Science* 277, 1078–1081 (1997).
39. J.J. Storhoff, R. Elghanian, R.C. Mucic, C. A. Mirkin, & R.L. Letsinger, *J. Am. Chem. Soc.* 120, 1959–1964 (1998).
40. S. Eustis & M.A. El-Sayed, *Chem. Soc. Rev.* 35, 209–217 (2006).
41. P.A. Frey & T.G. Frey, *J. Struct. Biol.* 127, 94–100 (1999).
42. A.G. Tkachenko, H. Xie, D. Coleman, W. Glomm, J. Ryan, M.F. Anderson, S. Franzen, & D.L. Feldheim, *J. Am. Chem. Soc.* 125, 4700–4701 (2003).
43. D.V. Goia & E. Matijevic, *New J. Chem.* 1998, 1203–1215 (1998).
44. J.S. Bradley, In *Clusters and Colloids: From Theory to Applications*, G. Schmid, Ed.; VCH: Weinheim (1994).
45. M. Sastry, *Curr. Sci.* 85, 1735–1745 (2003).
46. C.M. Niemeyer, *Angew. Chem. Int. Ed.* 40, 4128–4158 (2001).
47. A.C. Templeton, S. Chen, S.M. Gross, & R.W. Murray, *Langmuir* 15, 66–76 (1999).
48. T.G. Schaaff, G. Knight, M.N. Shafiqullin, R.F. Borkman, & R.L. Whetten, *J. Phys. Chem. B* 102, 10643–10646 (1998).
49. M.J. Meziani, H.W. Rollins, L.F. Allard, & Y.-P. Sun, *J. Phys. Chem. B* 106, 11178–11182 (2002).
50. T. Peters, Jr., In *All About Albumin: Biochemistry, Genetics, and Medical Applications*; Academic Press: San Diego (1996)
51. T. Peters, Jr., *Adv. Protein Chem.* 37, 161–245 (1985).
52. J.F. Foster, In *The Plasma Proteins*, Vol. I, F.W. Putnam, Ed.; Academic Press: New York, (1960).
53. G. Weber, *Adv. Protein Chem.* 29, 1–83 (1975).
54. S. Curry, H. Mandelkow, P. Brick, & N. Franks, *Nat. Struct. Biol.* 5, 827–835 (1998).

55. J.I. Goldstein, D.E. Newbury, P. Echlin, D.C. Joy, A.D. Roming, C.E. Fiori, & E. Lifshin, In *Scanning Electron Microscopy and X-ray Microanalysis*, Vol. 1; Plenum Press: New York (1992).
56. D.B. Williams & C.B. Carter, In *Transmission Electron Microscopy: A Textbook for Materials Science*; Plenum Press: New York (1996).
57. A.V. Crewe, J. Wall, *J. Mol. Biol.* 48, 375–393 (1970).
58. S.J. Pennycook, D.E. Jesson, *Ultramicroscopy* 37, 14–38 (1991).
59. A. Howie, L.D. Marks, & S.J. Pennycook, *Ultramicroscopy* 8, 163–74 (1982).
60. N.D. Browning, D.J. Wallis, P.D. Nellist, & S.J. Pennycook, *Micron* 28, 333–348 (1997).
61. E.M. James & N.D. Browning, *Ultramicroscopy* 78, 125–39 (1999).
62. Z.L. Wang, In *Elastic and Inelastic Scattering in Electron Diffraction and Imaging*; Plenum Press: New York (1995).
63. Z.L. Wang, *Acta Cryst. A* 51 (1995) 569–585.
64. F. Bonet, C. Guery, D. Guyomard, R. Herrera Urbina, K. Tekaia-Elhsissen, & J.-M. Tarascon, *Inter. J. Inorg. Mater.* 1, 47–51 (1999).
65. F. Bonet, V. Delmas, S. Grugeon, R. Herrera Urbina, P.-Y. Silvert & K. Tekaia-Elhsissen, *Nanostruc. Mater.* 11, 1277–1284 (1999).
66. D.L. Nelson & M.M. Cox, In *Lehninger Principles of Biochemistry*; Worth Publishers: New York (2000).
67. R. Wetzel, M. Becker, J. Behlke, H. Billwitz, S. Böhm, B. Ebert, H. Hamann, J. Krumbiegel, & G. Lassman, *Eur. J. Biochem.* 104, 469–478 (1980).
68. A.H. Clark, D.H. Saunderson, & A. Suggett, *Int. J. Pept. Protein Res.* 17, 353–364 (1981).
69. M.J. Antal, W.S. Mok, J.C. Roy, A.T. Raissi, & D.G. Anderson, *J. Anal. Appl. Pyrolysis* 8, 291–303 (1985).
70. J.L. Elechiguerra, J. Reyes-Gasga, & M. Jose Yacaman, *J. Mater. Chem.* 16, 3906–3919 (2006).
71. C. Lofton & W. Sigmund, *Adv. Funct. Mater.* 15, 1197–1208 (2005).

72. U. Dahmen, C. Hetherington, V. Radmilovic, E. Johnson, S. Xiao, & C. Luo, *Microsc. Microanal.* 8, 247–256 (2002).
73. S. Ino & S. Ogawa, *J. Phys. Soc. Jpn.* 22, 1365–1374 (1967).
74. Y. Gao, L. Song, P. Jiang, L.F. Liu, X.Q. Yan, Z.P. Zhou, D.F. Liu, J.X. Wang, H.J. Yuan, Z.X. Zhang, X.W. Zhao, X.Y. Dou, W.Y. Zhou, G. Wang, S.S. Xie, H.Y. Chen, & J.Q. Li, *J. Crystal Growth* 276, 606–612 (2005).
75. K. Heinemann, M.J. Yacaman, C.Y. Yang, & H. Poppa, *J. Crystal Growth* 47, 177–186 (1979).
76. Z.L. Wang, T.S. Ahmad, & M.A. El-Sayed, *Surf. Sci.* 380, 302–310 (1997).
77. Z.L. Wang, R.P. Gao, B. Nikoobakht, & M.A. El-Sayed, *J. Phys. Chem. B* 104, 5417–5420 (2000).
78. M. Brust, J. Fink, D. Bethell, D.J. Schiffrin, & C.J. Kiely, *J. Chem. Soc., Chem. Commun.* 1995, 1655–1656 (1995).
79. M. Brust & C.J. Kiely, *Colloids Surf. A: Physicochem. Eng. Asp.* 202, 175–186 (2002).
80. M. Brust, M. Walker, D. Bethell, D.J. Schiffrin, & R. Whyman, *J. Chem. Soc., Chem. Commun.* 1994, 801–802 (1994).
81. A.C. Templeton, M.J. Hostetler, C.T. Kraft, & R.W. Murray, *J. Am. Chem. Soc.* 120, 1906–1911 (1998).
82. M.J. Hostetler, A.C. Templeton, & R.W. Murray, *Langmuir* 15, 3782–3789 (1999).
83. J. Masuoka, J. Hegenauer, B.R. Van Dyke, & P. Saltman, *J. Biol. Chem.* 268, 21533–21537 (1993).
84. T.E. Emerson, Jr., *CRC Crit. Care Med.* 17, 690–694 (1989).
85. N. Fogh-Andersen, P.J. Bjerrum, & O. Siggaard-Andersen, *Clin. Chem.* 39, 48–52 (1993).
86. G. Scatchard & W.T. Yap, *J. Am. Chem. Soc.* 86, 3434–3438 (1964).
87. W.J. Leonard, Jr. K.K. Vijai, & J.F. Foster, *J. Biol. Chem.* 238, 1984–1988 (1963).

88. S. Era, K.B. Itoh, M. Sogami, K. Kuwata, T. Iwama, H. Yamada, & H. Watari, *Int. J. Pept. Protein Res.* 35, 1–11 (1990).
89. M. Sogami, H.A. Petersen, & J.F. Foster, *Biochemistry* 8, 49–58 (1969).
90. K. Kuwata, S. Era, & M. Sogami, *Biochim. Biophys. Acta* 1205, 317–324 (1994).
91. J. Grdadolnik, *Int. J. Vibr. Spec.* 6, 6 (2002).
92. L.O. Andersson, *Arch. Biochem. Biophys.* 133, 277–285 (1969).
93. M.C. Chen & R.C. Lord, *J. Am. Chem. Soc.* 98, 990–992 (1976).
94. K. Nakamura, S. Era, Y. Ozaki, M. Sogami, T. Hayashi, & Murakami, *FEBS Lett.* 417, 375–378 (1997).
95. S. Iijima & T. Ichihashi, *Mater. Trans. JIM* 31, 582–587 (1990).
96. H. Hofmeister, M. Dubiel, G.L. Tan, & K.-D. Schicke1, *Phys. Stat. Sol. (a)* 202, 2321–2329 (2005).
97. N. Bernstein & E. B. Tadmor, *Phys. Rev. B* 69, 094116 (2004).
98. D.C. Clark, L.J. Smith, & D.R. Wilson, *J. Colloid Interface Sci.* 121, 136–137 (1988).
99. E.B. Tadmor & N. Bernstein, *J. Mech. Phys. Solids* 52, 2507–2519 (2004).
100. R.C. Johnson, J. Li, J.T. Hupp, & G.C. Schatz, *Chem. Phys. Lett.* 356, 534–540 (2002).
101. A.A. Spector & K.M. John, *Arch. Biochem. Biophys.* 127, 65–71 (1968).
102. N.A. Attallah & G.F. Lata, *Biochim. Biophys. Acta* 168, 321–333 (1968).
103. E. Meucci, G.E. Martorana, A. Ursitti, G.A. Miggiano, A. Mordente, & A. Castelli, *Ital. J. Biochem.* 36, 75–81 (1987).
104. J.E. Fleming & K.G. Bensch, *Int. J. Peptide Protein Res.* 22, 565–567 (1983).
105. S. Damodaran & J.E. Kinsella, *J. Biol. Chem.* 255, 8503–8508 (1980).
106. H. Kohno, N. Ozaki, H. Yoshida, K. Tanaka, & S. Takeda, *Cryst. Res. Technol.* 38, 1082–1086 (2003).
107. Z.R. Dai, S. Sun, & Z.L. Wang, *Surf. Sci.* 505, 325–335 (2002).

108. Z.R. Dai, S. Sun, & Z.L. Wang, *Nano Lett.* 1, 443–447 (2001).
109. Z.L. Wang, *J. Phys. Chem. B* 104, 1153–1175 (2000).
110. S. Schultz, D.R. Smith, J.J. Mock, & D.A. Schultz *Proc. Nat. Acad. Sci.* 97, 996–1001 (2000).
111. S.Y. Liao, D.C. Read, W.J. Pugh, J.R. Furr, & A.D. Russell, *Lett. Appl. Microbiol.* 25, 279–283 (1997).
112. A. Gupta, S. Silver, *Nat. Biotechnol.* 16, 888 (1998).
113. S. Harada, Y. Koyanagi, & N. Yamamoto, *Science* 229, 563–566 (1985).
114. J. Sodroski, W.C. Goh, C. Rosen, K. Campbell, & W.A. Haseltine, *Nature* 322, 470–474 (1986).
115. H. Deng, R. Liu, W. Ellmeier, S. Choe, D. Unutmaz, M. Burkhart, P. Di Marzio, S. Marmon, R.E. Sutton, C.M. Hill, C.B. Davis, S.C. Peiper, T.J. Schall, D.R. Littman, & N.R. Landau, *Nature* 381, 661–666 (1996).
116. B. Chackerian, E.M. Long, P.A. Luciw, & J. Overbaugh, *J. Virol.* 71, 3932–3939 (1997).
117. J.P. Kaltenbach, M.H. Kaltenbach, & W.B. Lyons, *Exp. Cell Res.* 15, 112–117 (1958).
118. B. Wiley, Y. Sun, B. Mayers, & Y. Xia Y, *Chemistry* 11, 454–463 (2005).
119. M.J. Forster, B. Mulloy, & M.V. Nermut, *J. Mol. Biol.* 298, 841–857 (2000).
120. C.K. Leonard, M.W. Spellman, L. Riddle, R.J. Harris, J.N. Thomas, & T.J. Gregory, *J. Biol. Chem.* 265, 10373–10382 (1990).
121. H.R. Gelderblom, E.H.S. Hausmann, M. Ozel, G. Pauli, & M.A. Koch, *Virology* 156, 171–176 (1987).
122. A.G. Dalglish, P.C.L. Beverley, P.R. Clapham, D.H. Crawford, M.F. Greaves, & R.A. Weiss, *Nature* 312, 763–767 (1984).
123. D. Klatzmann, E. Champagne, S. Chamaret, J. Gruest, D. Guetard, T. Hercend, J.C. Gluckman, & L. Montagnier, *Nature* 312, 767–768 (1984).
124. Y. Feng, C.C. Broder, P.E. Kennedy, & E. Berger, *Science* 272, 872–877 (1996).
125. D. Elliott, *Microscopy Today*, 2007, 30–33 (2007).

126. N.S. Brodinova, A.F. Moroz, & T.Y. Luchina, *J. Hyg. Epidemiol. Microbiol. Immunol.* 27, 69–76 (1983).
127. J.R. Morones, J.L. Elechiguerra, A. Camacho, K. Holt, J.B. Kouri, J. Tapia Ramirez, & M. Jose Yacaman, *Nanotechnology* 16, 2346–2353 (2005).
128. S. Bailey & F. King, In *Fine Chemicals through Heterogeneous Catalysts*, R.A. Sheldon, Ed.; Wiley-VCH (2001).
129. J.D. Aiken III, Y. Lin, & R.G. Finke, *J. Mol. Catal. A* 114, 29–51 (1996).
130. J. Schwartz, *Acc. Chem. Res.* 18, 302–308 (1985).
131. I. Horiuti & M. Polanyi, *Trans. Faraday Soc.* 30, 1164–1172 (1934).
132. G.V. Smith, & F. Notheisz, In *Heterogeneous Catalysis in Organic Chemistry*; Academic Press (1999).
133. M. Boudart, A. Aldag, J.E. Benson, N.A. Dougharty, & C.G. Harkins, *J. Catal.* 6, 92–99 (1966).
134. M. Boudart, *Chem. Rev.* 95, 661–666 (1995).
135. J.C. Garcia-Martinez, O.M. Wilson, M.R. Knecht, J. Guerra, & R.M. Crooks, manuscript in preparation (2007).
136. O.M. Wilson, M.R. Knecht, J.C. Garcia-Martinez, & R.M. Crooks, *J. Am. Chem. Soc.* 128, 4510–4511 (2006).
137. J.D. Aiken III, & R.G. Finke, *J. Am. Chem. Soc.* 120, 9545–9554 (1998).
138. O.M. Nutt, K.N. Heck, P. Alvarez, & M.S. Wong, *Appl. Catal. B* 69, 115–125 (2006).
139. G.W. Roberts, In *Catalysis in Organic Syntheses*, P.N. Rylander, Ed.; Academic Press (1976).
140. W.R. Alcorn & T.J. Sullivan, In *Catalysis of Organic Reactions*, J.R. Kosak, Ed.; CRC Press (1984).
141. L. Lewis, *Chem. Rev.* 93, 2692–2730 (1993).
142. H. van Hardeveld, *Surf. Sci.* 15, 189–230 (1969).
143. T. Teranishi & M. Miyake, *Chem. Mat.* 10, 594–600 (1998).
144. C. Kereszszegi, T. Mallat, & A. Baiker, *New J. Chem.* 25, 1163–1167 (2001).

145. C.H. Bartholomew, *Catalysis* 11, 93–126 (1994).
146. R.W.J. Scott, A.K. Datye, & R.M. Crooks, *J. Am. Chem. Soc.* 125, 3708–3709 (2003).
147. D.V. Goia & E. Matijevic, *Colloid. Surf. A* 146, 139–152 (1999).
148. C.J. Murphy, T.K. Sau, A.M. Gole, C.J. Orendorff, J.Gao, L. Gou, S.E. Hunyadi, & T. Li, *J. Phys. Chem. B* 109, 13857–13870 (2005).
149. S. Link & M.A. El-Sayed, *J. Phys. Chem. B* 103, 8410–8426 (1999).
150. P.R. Cromwell, In *Polyhedra*; Cambridge University Press: New York (1997).
151. L.M. Liz-Marzan, *Mater. Today* 7, 26–31 (2004).
152. L. Manna, E.C. Scher, & A.P. Alivisatos, *J. Am. Chem. Soc.* 122, 12700–12706 (2000).
153. L. Manna, D.J. Milliron, A. Meisel, E.C. Scher, & A.P. Alivisatos, *Nat. Mater.* 2, 382–385 (2003).
154. Y.-W. Jun, J.-H. Lee, J.-S. Choi, & J. Cheon, *J. Phys. Chem. B* 109, 14795–14806 (2005).
155. S. Chen, Z.L. Wang, J. Ballato, S.H. Foulger, & D.L. Carroll, *J. Am. Chem. Soc.* 125, 16186–16187 (2005).
156. T.K. Sau & C.J. Murphy, *J. Am. Chem. Soc.* 126, 8648–8649 (2004).
157. N.R. Jana, L. Gearheart, & C.J. Murphy, *J. Phys. Chem. B* 105, 4065–4067 (2001).
158. C.J. Murphy & N.R. Jana, *Adv. Mater.* 14, 80–82 (2002).
159. B. Nikoobakht & M.A. El-Sayed, *Chem. Mater.* 15, 1957–1962 (2002).
160. E.W. Weisstein, “Great Stellated Dodecahedron” from MathWorld—A Wolfram Web Resource. <http://mathworld.wolfram.com/GreatStellatedDodecahedron.html>.
161. E.W. Weisstein, “Spiky” from MathWorld—A Wolfram Web Resource. <http://mathworld.wolfram.com/Spiky.html>.
162. R. Perez, J. Reyes-Gasga, & M. Jose-Yacaman, *Scripta Metall. Mater.* 25, 289–294 (1991).
163. Z.L. Wang, *J. Phys. Chem. B* 104, 1153–1175 (2000).

164. F. Kim, S. Connor, H. Song, T. Kuykendall, & P. Yang, *Angew. Chem. Int. Ed.* 43, 3673–3677 (2004).
165. C.L. Nehl, H. Liao, & J.H. Hafner, *Nano Lett.* 6, 683–688 (2006).
166. C. Wang, T. Wang, Z. Ma & Z. Su, *Nanotechnology* 16, 2555–2560 (2005).
167. S. Lewin, In *Vitamin C. Its Molecular Biology and Medical Potential*; Academic Press: London (1976).
168. T. Tukamoto, S. Ozeki, F. Hattori, & T. Ishida, *Chem. Pharm. Bull.* 22, 385–389 (1974).
169. T.P. Molloy & C.W.M. Wilson, *Internat. J. Vit. Nutr. Res.* 50, 380–386 (1980).
170. B.A. Oelrichs, C.C. Kratzing, J.D. Kelly, & D.J. Winzor, *Internat. J. Vit. Nutr. Res.* 54, 61–64 (1984).
171. M.B. Cortie & E. van der Lingen, *Mater. Forum* 26, 1–14 (2002).
172. E. Hao, R.C. Bailey, G.C. Schatz, J.T. Hupp, & S. Li, *Nano Lett.* 4, 327–330 (2004).

Vita

Justin Lockheart Burt, the son of Gary Lockheart Burt and Diana Castillo Burt, was born in Falfurrias, Texas, on December 28, 1979. After graduating from Uvalde High School (Uvalde, Texas) as class valedictorian in May of 1998, he enrolled at the University of Notre Dame. He was awarded his Bachelor of Science in Chemical Engineering, *Summa Cum Laude*, in May of 2002. In August of 2002, he began his graduate studies at the University of Texas at Austin in the Department of Chemical Engineering. In December of 2004, he was awarded his Master of Science in Engineering, and subsequently pursued his Ph.D. under the direction of Dr. Miguel Jose Yacaman. He married his beloved wife, Erika, on October 2, 2004. Erika and Justin were blessed with their firstborn child, Bernadette Genevieve, on November 15, 2006.

Permanent address: P.O. Box 186, Uvalde, TX 78802

This dissertation was typed by the author.